# Advances in Architectural Geometry 2016

Sigrid Adriaenssens, Fabio Gramazio, Matthias Kohler, Achim Menges, and Mark Pauly

Editors

**v/dlf**

Cover illustration by Frank Hyde-Antwi, based on Figure 6 in "Textile Fabrication Techniques for Timber Shells: Elastic Bending of Custom-Laminated Veneer for Segmented Shell Construction Systems" by Simon Bechert, Jan Knippers, Oliver David Krieg, Achim Menges, Tobias Schwinn, and Daniel Sonntag (ICD/ITKE University of Stuttgart, Germany).

Hosts



Main Sponsor

Workshop Sponsor



Conference Sponsors

# Advances in Architectural Geometry 2016

Sigrid Adriaenssens, Fabio Gramazio, Matthias Kohler, Achim Menges, and Mark Pauly

Editors

# Foreword

Architecture and geometry have always been intrinsically linked. However, their operational relationship has been dramatically strengthened by the recent advent of computational design and digital fabrication techniques. These distinct developments are reciprocally dependent, as the digital fabrication of complex architectural components induces the need for advanced geometric strategies, and in return the potentials of geometrical computing instils a need for efficiency in the production of complex forms. Although currently confined to the exclusive domain of specialists, such advanced geometric practices shall evolve to include a much larger and interdisciplinary professional group, including architects, engineers, computer scientists, and mathematicians. Their authorship in the creative development of specific computational tools may revolutionise the design process, all the way from initial conceptual form finding to its final fabrication and construction.

The recent passing of Zaha Hadid led to speculation that this unexpected event could herald the decline of complex form in architecture. This conjecture may be amplified by the current accumulation of global political, social, and environmental emergencies demanding fast and pragmatic architectural solutions rather than extravagant shapes; however, this critical assumption proves to be short-sighted and simplistic. As a matter of fact, geometrical complexity remains the precondition for efficient structures in architecture, and this simple paradigm can be observed in nature, beyond time-dependent stylistic and formal discourse.

Since its first edition, which was organized by Helmut Pottmann in 2008, the aim of the Advances in Architectural Geometry symposium has been to propel this research area by providing a platform for interdisciplinary debate through scientific contributions of both technical and theoretical nature. Such development of easy and elegant access to complex geometries in architecture not only demands radical progress in computational design tools and digital fabrication techniques, but primarily depends on the emergence of a novel design culture and building craft.

It is a special honour for the National Centre of Competence in Research (NCCR) Digital Fabrication to welcome the AAG community to ETH Zurich for the 2016 edition of the conference. While the workshops and the paper presentations remain the core events of the AAG symposium, the NCCR Digital Fabrication is proud of the five exceptional keynote speakers who have kindly accepted our invitation and enrich this edition with their contributions. Lord Norman Forster, who lectures together with his partner Francis Aish, represents more than half a century of persistent architectural innovation and provides a long-term perspective

on the relationship between architecture and technology. Werner Sobek, whose practice operates at the interface between architecture and engineering, contributes with his expertise in lightweight constructions and his interest in performative structures. Complementary to these highly recognised professionals, Erik Demaine and Urs B. Roth contribute distinct perspectives on geometry. While they share a deep mathematical understanding and a passion for surprising "geometric discoveries", their work methods are diametrically opposed. Erik Demaine develops his origami sculptures by engaging with computational algorithmic techniques, whereas Urs. B. Roth's heuristic search for form developed using sequences of accurate drawings and rigorous formulas that create their own peculiar aesthetic. Interesting enough, though, both consider themselves to be artists in addition to being scientists.

The peer-review process for the selection of papers was managed by the scientific co-chairs, covering the domains of architecture, structural engineering, mathematics, and computer science, with the support of the scientific committee and the AAG2106 coordinator. From a very large pool of submissions, 22 papers have been accepted and included in the present proceedings. In addition, 25 posters have also been accepted for presentation, and the workshop chair has selected 12 workshop proposals for the pre-conference sessions. We extend our thanks and acknowledgements to all authors, tutors, reviewers, and organisers for their invaluable contributions to this process.

External industry partners are vital to both the integrity and the execution of such a large conference. We are very pleased to have strong and highly supportive partners and industry sponsors for the AAG2016. We would like to especially thank our main sponsor ABB, our workshops sponsor Autodesk, and the conference sponsors Moog, Waagner Biro, ERNE, Evolute, Absolute Joint System, and Disney Research for their backing and guidance.

Finally, we would also like to thank our colleagues and co-hosts at the Institute for Technology in Architecture (ITA), the Department of Architecture, and the ETH Zurich for their ongoing support and for providing the conference venues. We hope that you enjoy your time visiting ETH and Zurich, and wish you an excellent conference.

Sigrid Adriaenssens, Achim Menges, Mark Pauly (Scientific Co-Chairs)
Dave Pigram (Workshop Chair)
Fabio Gramazio, Matthias Kohler (Conference Chairs)
Orkun Kasap, Russell Loveridge (Organisers)

# Contents

# Analysis and Design of Curved Support Structures

Chengcheng Tang, Martin Kilian, Pengbo Bo, Johannes Wallner,
and Helmut Pottmann

C. Tang
King Abdullah University of Science and Technology (KAUST), Saudi Arabia
chengcheng.tang@kaust.edu.sa

M. Kilian, H. Pottmann
Vienna University of Technology (TU Wien), Austria
kilian@geometrie.tuwien.ac.at
pottmann@geometrie.tuwien.ac.at

P. Bo
Harbin Institute of Technology at Weihai, China
bob_pengbo@163.com

J. Wallner
Graz University of Technology (TU Graz), Austria
j.wallner@tugraz.at ✉

# Abstract

Curved beams along freeform skins pose many challenges, not least on the level of basic geometry. A prototypical instance of this is presented by the glass facades of the Eiffel tower pavilions, and the interrelation between the differential-geometric properties of the glass surface on the one hand, and the layout of beams on the other hand. This paper discusses how curved beams are represented by developable surfaces, and studies geometric facts relevant to beam placement along guiding surfaces. Surprisingly, many of the curves which are interesting from the viewpoint of pure geometry (geodesics, principal curves, etc.) occur in this context too. We discuss recent advances in the modelling of developable surfaces, and show how they permit the interactive design of arrangements of curved beams, in particular the design of so-called geometric support structures.

Keywords:
developable surfaces, support structures, interactive design, Darboux frame

**Figure 1.** Freeform skins composed of developables. Left: The Disney Concert Hall consists of large, near-developable pieces. Center: The Fondation Louis Vuitton, Paris, is composed of strip sequences, each strip being made from cylindrical glass panels and approximating a continuous developable. Right: The interior of the Burj Khalifa, Dubai, exhibits a paneling by "geodesic" developable elements, using the terminology of Pottmann et al. (2008) and Wallner et al. (2010). All three designs are by F. Gehry.



**Figure 2.** Curved-crease sculptures. Left: Arum installation, 2012 Venice biennale, by Zaha Hadid architects and Robofold. Its form is defined by sheet metal folded along curved creases. Right: This virtual model of annuli folded along concentric rings by Tang et al. (2016) is motivated by actual paper objects, cf. Demaine and Demaine 2012.

# 1. Developable Surfaces in Freeform Architecture

Our objects of study are composed of *developable* surfaces, which may be informally introduced as surfaces that can be flattened without stretching or tearing. We first discuss different kinds of developables occurring in freeform architecture.

### Freeform skins composed of developables

Inextensible materials like paper and sheet metal naturally assume developable shapes, so it is not surprising that freeform skins consisting of developables have been built – see Pottmann et al. (2015, §3) for a short overview of this topic, and Figure 1 for examples. Material properties, however, are not the only reason why developables occur: Liu et al. (2006) successfully exploited the viewpoint that a sequence of planar quadrilateral panels approximates a developable. So does a sequence of cylindrical glass panels. Such sequences occur e.g. in the 2007 Strasbourg railway station, the Eiffel tower pavilions see Baldassini et al. (2013), or the 2015 Fondation Louis Vuitton (see Fig. 1, centre).

Some piecewise-smooth surfaces can be flattened without even cutting them along creases. One distinguishes two cases: (i) surfaces which locally around every point can be flattened, but a global flattening requires a certain number of cuts (Fig. 2, left); (ii) surfaces capable of flattening without a single cut (Fig. 2, right). The behaviour of such curved-crease sculptures, especially regarding degrees of freedom in modelling, is entirely different from the skins of Figure 1.

### Non-skin arrangements of developables

Developables may have other functions, in particular when they are positioned transverse to a freeform skin. Figure 5 shows the Eiffel tower pavilions, where the sides of curved beams supporting the glass facade contain developables *orthogonal* to that facade see Schiftner et al. (2012). Figure 3 shows so-called geometric support structures – using the terminology of Pottmann et al. (2015, §6.1) – which can either be smooth like the curved beams of Figure 3, left or discrete like the shading elements in Figure 3, right.

# 2. Differential Geometry of Strips

We are interested in the degrees of freedom available to a designer who wishes to lay out developables positioned either tangential to a given surface $\Phi$ or transverse to it (see Figures 1 and 3, respectively). This discussion requires studying the well known movement of the so-called *Darboux frame*, which is adapted to a curve **c**
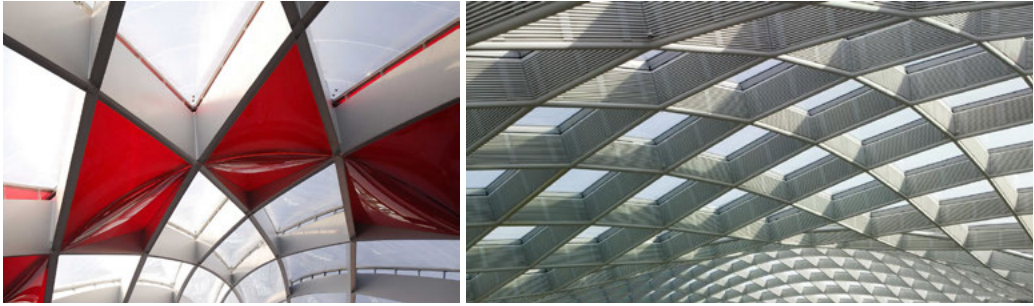
**Figure 3.** Developables which lie transverse to freeform skins. Left: Mediacité retail centre, Liege (Ron Arad Architects, structural engineering: Buro Happold). Here both families of intersecting curved beams are modeled as developables. Right: Kogod courtyard, Smithsonian Institution (Foster and partners). Quadrilateral shading elements approximate developables, and their lines of intersection approximate rulings.
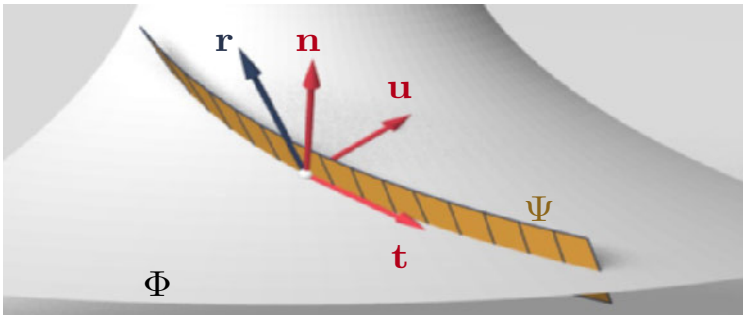


**Figure 4.** The Darboux frame associated with a curve in a surface $\Phi$ consists of the curve's unit tangent vector $\mathbf{t}$, the surface's normal vector $\mathbf{n}$ and the vector $\mathbf{u} = \mathbf{t} \times \mathbf{n}$. We also consider the developable surface $\Psi$, which follows that curve and which is orthogonal to the reference surface $\Phi$. Its rulings are indicated by the vector $\mathbf{r}$.

**12**

lying in $\Phi$. We give an introduction to this frame, for more details see textbooks like O'Neill (2006) or Strubecker (1969).

We assume that s is an arc length parameter and $\mathbf{c}(s)$ is a point of the curve under consideration. Consider the unit tangent vector $\mathbf{t}(s)$, the vector $\mathbf{n}(s)$ orthogonal to the reference surface $\Phi$, and the sideways vector $\mathbf{u}(s) = \mathbf{n}(s) \times \mathbf{t}(s)$. These vectors are used to describe a developable $\Psi$ which follows the curve $\mathbf{c}$. If $\Psi$ is orthogonal to $\Phi$, it is the envelope of the plane spanned by $\mathbf{t}$ and $\mathbf{n}$. If $\Psi$ is tangential to $\Phi$, it is enveloped by the plane $[\mathbf{t}, \mathbf{u}]$. Figure 4 illustrates this situation.

The goal of the computations which follow below is to find out the *rulings* of the developable $\Psi$. Their position is relevant to manufacturing by bending from a flat state. Figure 4 illustrates the Darboux frame $\{\mathbf{t}, \mathbf{u}, \mathbf{n}\}$ for a particular choice of curve and developable. The rulings are indicated by thin lines – it is important to note that a ruling does not have to be parallel to $\mathbf{n}$.

## The motion of the Darboux frame along a curve in a reference surface

The rotational movement of the Darboux frame is governed by a *vector of angular velocity*, called $\mathbf{d}$. Any $\mathbf{x}$ moving with the Darboux frame has a rate of change expressed in terms of the angular velocity as $\mathbf{x}' = \frac{d}{ds}\mathbf{x}(s) = \mathbf{d} \times \mathbf{x}$. Thus,

$$\mathbf{d} = \tau_g \mathbf{t} - \kappa_n \mathbf{u} + \kappa_g \mathbf{n} \Rightarrow \begin{cases} \mathbf{t}' = \mathbf{d} = \times \mathbf{t} = \qquad \kappa_g \mathbf{u} + \kappa_n \mathbf{n} \\ \mathbf{u}' = \mathbf{d} = \times \mathbf{u} = -\kappa_g \mathbf{t} \qquad + \tau_g \mathbf{n} \\ \mathbf{n}' = \mathbf{d} = \times \mathbf{n} = -\kappa_n \mathbf{t} - \tau_g \mathbf{u} \end{cases}$$

It is well known that the coefficients of $\mathbf{d}$ are the curve's normal curvature $\kappa_n$, the curve's geodesic curvature $\kappa_g$, and its geodesic torsion $\tau_g$. An insect crawling on the surface $\Phi$ can freely choose the geodesic curvature $\kappa_g$ by turning to the left or to the right, in the manner of the driver of a car can use the steering wheel. Walking straight ($\kappa_g = 0$) produces a geodesic curve on the surface.

On the other hand, the normal curvature equals $\kappa_n = \mathrm{II}(\mathbf{t}) / \mathrm{I}(\mathbf{t})$, where I, II are the first and second fundamental forms of the surface, respectively. Therefore, $\kappa_n$ is determined by the direction of the tangent vector $\mathbf{t}$ alone and can only be influenced by taking a completely different route. In negatively curved regions there are two *asymptotic* directions at each point where $\mathrm{II}(\mathbf{t}) = 0$, which are found by intersecting an infinitesimal piece of surface with its own tangent plane. In that case the above-mentioned insect can decide to follow the asymptotic line field to achieve $\kappa_n = 0$ if necessary. In positively curved regions this is not possible.

Similarly, also the geodesic torsion is already determined by the direction $\mathbf{t}$: It is known that $\tau_g = \frac{1}{2}(\kappa_2 - \kappa_1) \sin 2\varphi$, where $\kappa_1$, $\kappa_2$ are the principal curvatures and $\varphi$ is the angle between t and the vector indicating the principal direction.
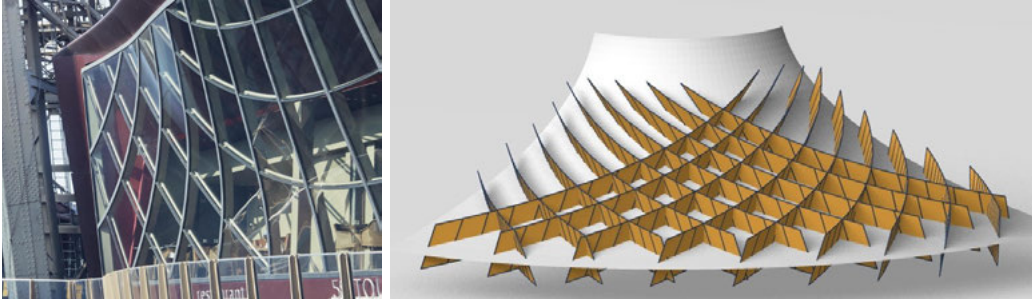
**Figure 5.** Strips with different kinds of optimality properties. Left: Eiffel tower pavilions (Moatti et Rivière architects, engineering by RFR). The top-down beams have a rectangular cross-section and are thus modeled as a union of four developable strips – two orthogonal to the glass surface $\Phi$, two tangential to them. The guiding curves are principal for $\Phi$, implying optimal rulings. Image courtesy RFR. Right: A minimal surface with two families of developable strips guided by curves with $\kappa_n = 0$, implying straight development. Rulings are not optimal, but far from bad. Further, transverse strips intersect not along rulings.
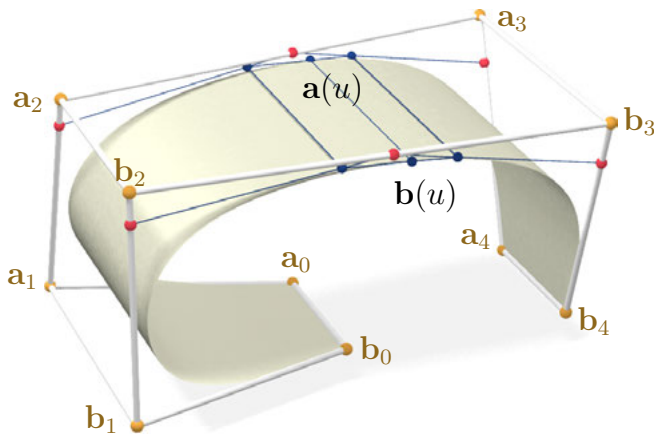


**Figure 6.** Developable strips as ruled spline surfaces which connect two B-spline curves. Here a B-spline curve $\mathbf{a}(u)$ is defined by its control points $\mathbf{a}_0, \mathbf{a}_1, \dots, \mathbf{a}_N$. This image shows the evaluation of the curve for a certain parameter value $\mathbf{a}(u)$, and similar for a spline curve $\mathbf{b}(u)$, cf. Tang et al. 2016.

We see that $\tau_g$ vanishes for the two principal directions and is highest exactly in between (i.e., if **t** bisects the principal directions).

### Developable strips along a curve; Considerations regarding flattening

A developable surface $\Psi$, which is orthogonal to the reference surface $\Phi$ and contains the guiding curve **c**, is enveloped by the planes with normal vector **u** – see Figure 4. Thus, the direction **r** of rulings is computed as $\mathbf{r} = \mathbf{u} \times \mathbf{u}'$. In more detail,

$$\mathbf{r} = \mathbf{u} \times \mathbf{u}' = \mathbf{u} \times (\mathbf{d} \times \mathbf{u}) = \mathbf{d} - (\mathbf{d} \cdot \mathbf{u})\mathbf{u} = (\tau_g \mathbf{t} - \kappa_n \mathbf{u} + \kappa_g \mathbf{n}) - ((\tau_g \mathbf{t} - \kappa_n \mathbf{u} + \kappa_g \mathbf{n}) \cdot \mathbf{u})\mathbf{u} = \kappa_g \mathbf{n} + \tau_g \mathbf{t}.$$

A similar computation applies if $\Psi$ encloses the constant angle $\alpha$ with the reference surface (we take planes with normal vector $\mathbf{n}^\alpha = \cos \alpha \, \mathbf{n} + \sin \alpha \, \mathbf{u}$ instead of u, and get rulings $\mathbf{r}^\alpha = \tau_g \mathbf{t} + (\kappa_g \sin \alpha + \kappa_n \cos \alpha)(\sin \alpha \, \mathbf{n} - \cos \alpha \, \mathbf{u}))$. For developables tangent to the guiding surface (i.e., $\alpha = 0$), we get $\mathbf{r} = \tau_g \mathbf{t} - \kappa_n \mathbf{u}$.

We would also like to say some words about *development*, i.e. flattening of a developable strip $\Psi$. It is known that geodesic curvatures of curves are invariant in this process. Thus, the guiding curve **c** is flattened to a straight line if and only if its geodesic curvature w.r.t. $\Psi$ (not w.r.t. $\Phi$) vanishes. In the notation employed above, this curvature of the development equals $-\kappa_g \cos \alpha + \kappa_n \sin \alpha$; for developables orthogonal to $\Phi$, it equals $\kappa_n$. We summarise:

### Proposition

Consider a developable $\Psi$ through a guiding curve **c** which itself lies in a reference surface $\Phi$. The rulings of $\Psi$ are called good resp. bad, if they are orthogonal resp. tangential to **c**. Then we have the following properties:

| If the curve **c** in $\Phi$ is ... | then a developable $\Psi$ through **c**, tangential to $\Phi$, has ... | and a developable $\Psi$ through **c**, orthogonal to $\Phi$, has ... |
|---|---|---|
| geodesic $\quad (\kappa_g = 0)$ | straight development | bad rulings |
| asymptotic $(\kappa_n = 0)$ | bad rulings | straight development |
| principal $\quad (\tau_g = 0)$ | good rulings | good rulings |

Actually, the conclusion about $\tau_g = 0$ applies for all angles between the reference surface $\Phi$ and the developable $\Psi$, not only in the special cases $\alpha = 0$ and $\alpha = 90°$.

**15**
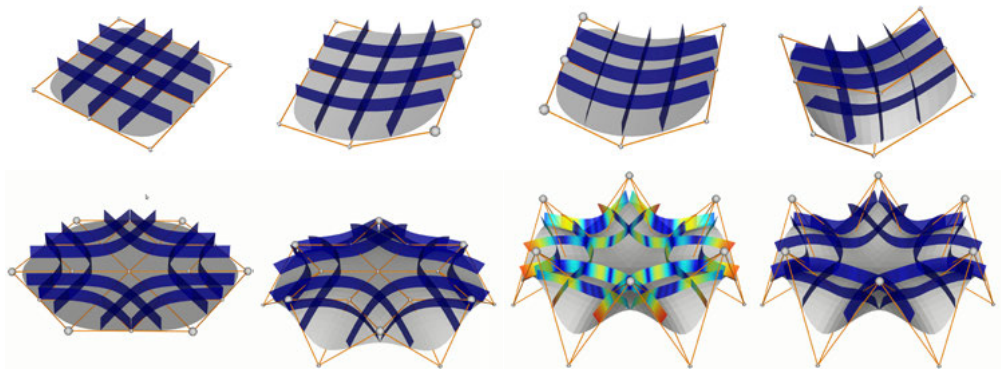
**Figure 7.** Interactive modeling of curved support structures. Top row: A configuration of strips follows guiding curves in a reference surface Φ. Starting from a very simple configuration, modelling is done by modifying the parametric representation of Φ and the guiding curve network connected to Φ. The strips follow their respective guiding curves, with their actual position in space being defined by the constraint solver. Bottom row: Such deformations destroy developability, as indicated by the colour coding (blue to green indicates sufficient developability for manufacturing purposes). After each deformation applied by the user the constraint solver re-establishes developability within seconds.



**Figure 8.** Strips which follow guiding curves. The top left image shows curves on a reference surface Φ with a constant nonzero value of $\kappa_n$ . Developables guided by these curves (middle row) have circular development. Unfortunately, the rulings of these developables are in several places rather bad (the strips are interrupted there). Our constraint solver finds a sequence of strips which, as far as they can, stay orthogonal to Φ and close to the guiding curves (bottom row). The setup of surfaces in this procedure automatically ensures good behaviour of rulings, but entails changes in the geometry. Nevertheless, the development of a sample strip is still rather circular (top, right).

# 3. Behaviour of Developables Aligned with Reference Surfaces

## Manufacturing considerations

The mathematical considerations of the previous section have practical implications regarding manufacturing and design, especially design freedom. We discuss these issues in the following paragraphs. Obviously, a developable strip is more easily manufactured if it can be flattened to a *straight* planar piece. This is because it will fit into a smaller rectangular sheet in its flattened state. We mention that examples below (Figures 8 and 9) are based on developables which will unfold not to straight planar strips, but to circular ones. The individual strip even develop to circular strips of the same radius. This property is of interest for manufacturing because it means that the unfolded state of strips has simple geometry.

The reason why *rulings* are called good or bad is that they can be seen as the infinitesimal axes of bending, when producing a developable surface from its flat state. If the rulings are tangential to the reference surface, we would have to bend longish sheets along the sheet instead of across. Obviously, bending a strip is easier if the ifinitesimal axis of bending runs across that strip.

## Examples which have been built

For a curved beam with rectangular cross-section which stays tangential/orthogonal to a reference surface Φ, optimal rulings are achieved if the beam follows the principal curves of Φ. This is exactly the case for the Eiffel Tower pavilions, see Figure 5.

Wooden panels which comprise a skin like the one shown by Figure 1 for the Burj Khalifa have straight development (simply because they were originally straight panels, before they were bent in order to fit the reference surface). They therefore follow geodesics of the reference surface. In the Burj Khalifa case the rulings on these panels are never bad, since the skin has no asymptotic directions, being of positive curvature. We would also like to point to previous work on geodesic timber constructions, see Pirazzi and Weinand (2006) and follow-up work.

## Mutual exclusivity of "good" properties

The beneficial properties of strips which are mentioned in the proposition unfortunately are mutually exclusive. For developables orthogonal to a reference surface Φ, optimal rulings are impossible if we are to have a straight development (principal curves are never asymptotic except in the special case of Φ being developable). Conversely, a straight development might imply bad rulings, if asymptotic curves happen to be geodesic (this could happen if Φ is ruled but not developable).
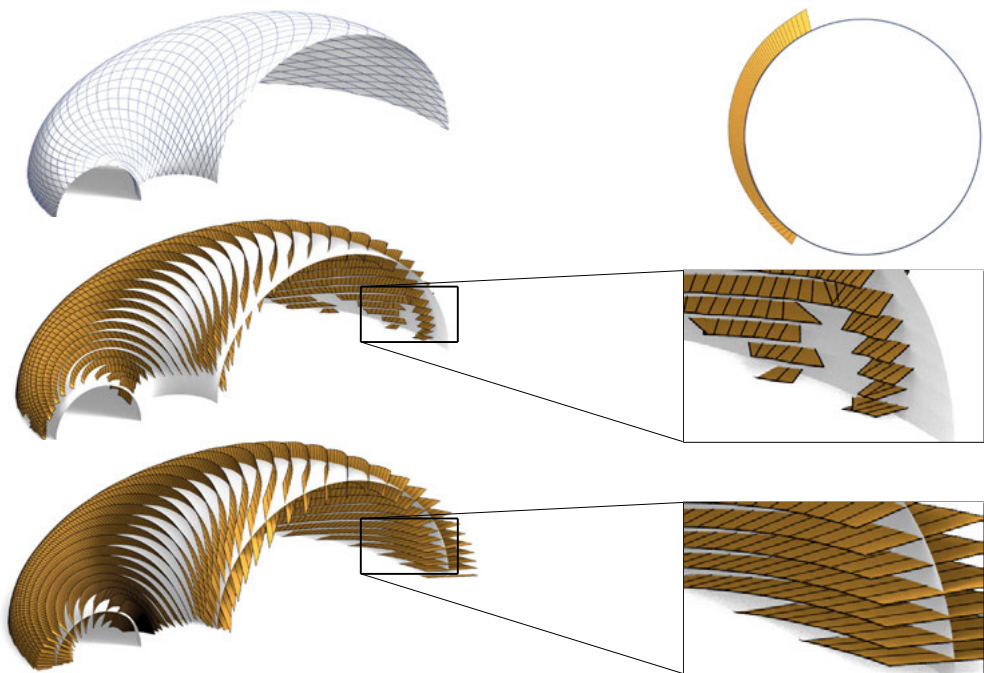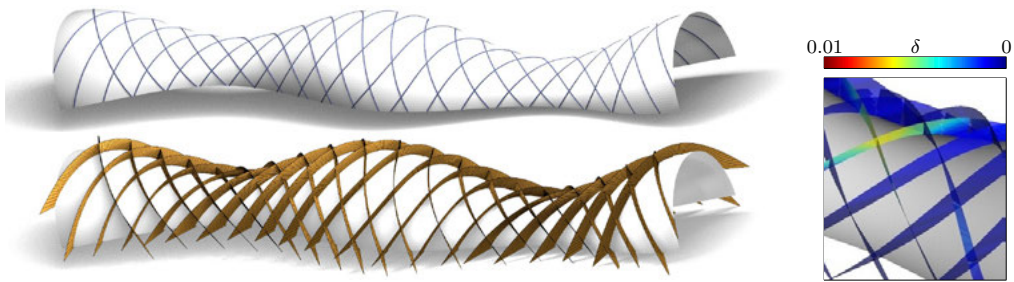
**Figure 9.** Strips which follow guiding curves. The top left image shows curves on a reference surface Φ which enjoy a constant nonzero value of $\kappa_n$ , similar to Figure 8. Constraint solving produces developable strips which, as far as they can, follow these guiding curves in addition to being orthogonal to Φ. The detail at right illustrates the degree of developability of the strips which are achieved in this way. It is measured via a quad mesh produced by regular sampling of strips. For each face of this quad mesh, we compute the value $\delta = \frac{distance\ of\ diagonals}{average\ of\ 2\ short\ edgelengths}$ . This example is sufficiently developable for manufacturing.
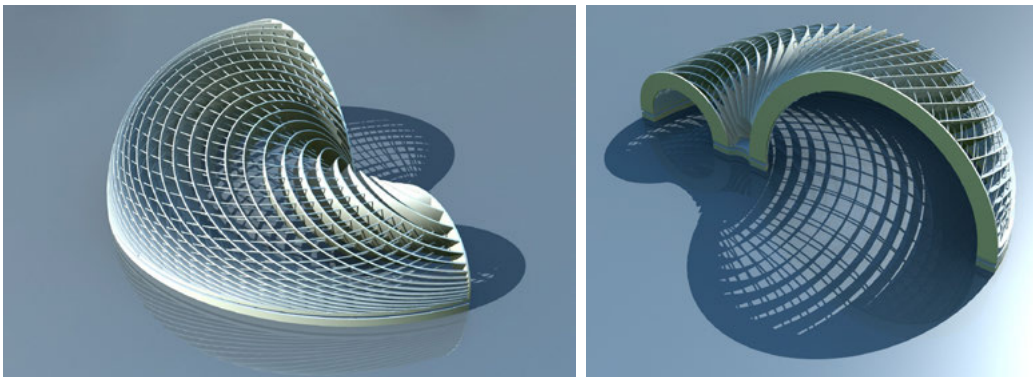


**Figure 10.** The strip sequence of Figure 8 is the basis of this system of curved beams. The individual strips, being developable with "good" rulings, can be manufactured from flat pieces by bending. As an additional geometric property, each beam unfolds into a circular strip of the same radius. The members transverse to the beams follow the system of curves shown in Figure 8 (even if there is no particular reason to do so).

Developables tangential to Φ with optimal rulings rarely have straight development (only if Φ is one of Monge's surfaces moulures, principal curves are geodesics). Straight developments might lead to bad rulings if accidentally we choose a geodesic which is asymptotic (that can happen if Φ is ruled).

The reader is advised that the previous paragraphs heavily draw on knowledge of the manifold interesting properties of curves in surfaces which are discussed in older textbooks like Blaschke (1921).

### The loss of design freedom

If one insists on optimal rulings (orthogonal to guiding curves) then the only possibility is that the guiding curves are principal, which are uniquely determined by the reference surface Φ. If Φ is already known, there is no design freedom left. This dilemma had to be solved for the Eiffel tower pavilions, see Schiftner et al. (2012).

A similar dilemma occurs if we want to construct a family of developable strips orthogonal to the reference surface which have straight development. We are stuck with using the asymptotic curves which are uniquely determined by Φ.

The fact that both the "optimal rulings" and the "straight development" requirements determine the strip layout has another consequence besides the inconvenience of loss of design freedom: This layout may be unusable. While the principal network is always right-angled, the network of asymptotic curves has no such property. Only for very special surfaces like the one of Figure 5 right does it looks nice in the sense that the angle of intersection of different asymptotic curves is close to 90 degrees (the surface shown is a minimal surface, where the asymptotic curves are exactly orthogonal).

# 4. Geometric Modelling with Developables

### Developability as a constraint on spline surfaces

Geometric modelling of developable surfaces has been a topic of interest for a long time. We refrain from giving a history of the extensive previous work in this area. The commonly used degree $m \times n$ Bézier surfaces and B-spline surfaces (see Fig. 6) make it easy to produce ruled surfaces – simply let $n = 1$, in both the polynomial and the rational cases. The conditions on the control points of these surfaces which ensure developability are not difficult, see Lang and Röschel (1992), but the nonlinear nature of these constraints has prevented truly interactive modeling until recently. Similarly, approaches to modeling of developables via discretisation and differential-geometric analysis were too slow for interactive modelling.

The constraints expressing developability enjoy mathematical properties that correspond directly to geometric design: The system has a high-dimensional solution manifold, implying design freedom. Tang et al. (2016) showed how to solve

these constraints quickly enough for interactive modelling. Following earlier work (Tang et al. 2014; Jiang et al. 2015), they modify constraints so that they are at most quadratic and still sparse; and they employ fairness energies as a regulariser for a Newton-type method in order to guide the user towards "sensible" parts of the solution manifold.

## Setup of variables

We describe our computational setup which follows Tang et al. (2016). A strip is modeled as a degree $3 \times 1$ cubic B-spline surface $\mathbf{b}(u,v)$ of $C^2$ smoothness, whose shape is determined by two rows $\mathbf{a}_0, \ldots, \mathbf{a}_N$ and $\mathbf{b}_0, \ldots \mathbf{b}_N$ of control points; each row being the control polygon of the upper and lower boundary $\mathbf{a}(u)$, $\mathbf{b}(u)$, see Figure 6. We always assume that the boundary curve a is following a guiding curve c which lies in the reference surface Φ. It does not matter if the actual strip which is to be used in applications has boundaries different from $\mathbf{a}$, $\mathbf{b}$, since developable strips may be freely extended and cropped to either side.

## Setup of developability constraints

Developability is expressed by the existence of a unit vector $\mathbf{n}_u$, for all parameter values $u$, which is orthogonal to $\mathbf{b} - \mathbf{a}$ and to the derivatives $\mathbf{a}'$, $\mathbf{b}'$. These conditions read $\mathbf{n} \cdot (\mathbf{b} - \mathbf{a}) = \mathbf{n} \cdot \mathbf{a}' = \mathbf{n} \cdot \mathbf{b}' = 0$ and are required to hold only for a finite number of values $u_1, u_2, \ldots$ and corresponding normal vectors $\mathbf{n}_1, \mathbf{n}_2, \ldots$, because the equivalent condition $\det(\mathbf{a}', \mathbf{b}', \mathbf{b} - \mathbf{a}) = 0$ is piecewise-polynomial of degree not exceeding 6, cf. the analogous discussion by Tang et al. (2016).

An arrangement of developable strips is defined by additional constraints like common intersection of strips (this corresponds to linear equations involving control points) and smooth transition of strips (more linear equations involving control points). For example, the six developable strips in Figure 7 (top row) which appear to intersect in 9 rulings are actually 24 individual strips with common boundary rulings which join smoothly.

## Constraint solving

Tang et al. (2016) show how to solve the system of constraints quickly, by linearising the constraints and solving the resulting linear system (which at the same time is under-determined and has redundant equations) via regularisation. The regulariser is a fairness energy, thus pushing the solver towards "sensible" solutions of the system. We extended their interactive modelling system for developable skins to the case of non-skin strip arrangements.

## Positioning constraints

Besides developability, further constraints can be imposed on an arrangement of strips. It is important that these constraints are linear or quadratic – otherwise the method of Tang et al. (2016) becomes slow.

An example of such a constraint is that a strip $\Psi$ encloses a certain angle $\theta$ with the reference surface $\Phi$. If the normal vectors $n_i$ and $\mathbf{n}_i^*$ of $\Psi$ resp. $\Phi$ in selected points are available, then we require $\mathbf{n}_i \cdot \mathbf{n}_i^* = \cos\theta$. This condition is neither linear nor quadratic if the dependence of $\mathbf{n}_i^*$ on the control points is nonlinear, but we can use a standard trick to make it linear: We simply consider $\mathbf{n}_i^*$ fixed during each pass of the iterative solver.

Another constraint is that a strip boundary a follows $\mathbf{a}$ guiding curve $\mathbf{c}$. We consider a sample $\mathbf{a}(u_i)$ of boundary points. The condition of closeness to $\mathbf{c}$ is highly nonlinear. Also here a well-known trick can be applied. By computing the closest point $\mathbf{c}_i^*$ on the guiding curve and the tangent vector $\mathbf{t}_i^*$ there, we require $(\mathbf{a}(u_i) - \mathbf{c}_i^*) \times \mathbf{t}_i^* = 0$. This equation expresses the requirement that the point $\mathbf{a}_i^*$, lies on the tangent of the guiding curve. It becomes linear, if $\mathbf{c}_i^*$, $\mathbf{t}_i^*$ are recomputed before each pass of the iterative solver and are kept constant.

# 5. Results and Discussion

## Applications

We discuss two main applications of the constraint solving procedure: One is the establishment of developables which follow a pre-selected curve network on a reference surface. We show two examples, namely, Figures 8 plus 10, and Figure 9. Using the formulae of Section 2, it is not difficult to compute rulings of developables which however are not everywhere nicely transverse to $\Phi$. Using this data as input for the constraint solver described in Section 4 yields a sequence of developable strips which approximates the original setup and (from construction) has nice rulings throughout.

The other main application is interactive modelling, made possible by *quickly* solving developability constraints. Figure 7 illustrates how it works.

## Limitations

The limitations which have been explained in Section 2 and Section 3 apply generally, especially the paragraph on mutual exclusivity of desirable properties. Since our procedure of computing developables always produces surfaces with "good" rulings, it is not possible to faithfully approximate developables which might have certain geometric properties, but bad rulings. The result of the computations either is not fully developable or does not entirely have the desired properties. Numerical solvers usually achieve a compromise between competing constraints. It is therefore advisable to check after computation if some properties have been lost. In fact, our implementation in its current state provides real-time feedback to the user, e.g. by colour coding the surfaces according to developability, see Figure 7. The user is able to decide on the importance of individual constraints by tuning weights which govern the constraint solving.

Examples of these limitations are shown by Figure 9, where we almost lose developability, and by Figure 8 where a circular development is not achieved exactly but only approximately. Since in the real world mathematical equalities are true only up to tolerances, such imperfections often are no obstacle.

# 6. Conclusion

We have presented an overview of the use of developables in freeform architecture – both for freeform skins and other kinds of arrangements of developable strips. After a differential-geometric discussion we showed how the computational framework of Tang et al. (2016) can be extended and subsequently applied to strip arrangements – both for modelling and for computing arrangements defined by guiding curves. It is the purpose of this paper to further the understanding of the complex geometry of developable surfaces and to show the currently available possibilities of geometric modelling.

# Acknowledgements

# References

Baldassini, N., N. Leduc, and A. Schiftner. 2013. "Construction Aware Design of Curved Glass Facades: The Eiffel Tower Pavilions." In *Glass Performance Days Finland*, pp. 406–410.

Blaschke, W. 1921. *Vorlesungen über Differentialgeometrie I.* Berlin: Springer.

Demaine, E., and M. Demaine. 2012. *Curved crease sculpture.* Exhibition catalogue. Accessed at http://erikdemaine.org/curved/GuidedByInvoices/

Jiang, C., C. Tang, M. Tomičić, J. Wallner, and H. Pottmann. 2015. "Interactive Modeling of Architectural Freeform Structures – Combining Geometry with Fabrication and Statics." In P. Block et al. (Eds.), *Advances in Architectural Geometry 2014*, pp. 95–108. Springer.

Lang, J., and O. Röschel. 1992. Developable (1, n)-Bézier surfaces. *Computer-Aided Geometric Design 9*, 291–298.

Liu, Y., H. Pottmann, J. Wallner, Y.-L. Yang, and W. Wang. 2006. "Geometric Modeling with Conical Meshes and Developable Surfaces." *ACM Trans. Graphics* 25, 3: 681–689.

O'Neill, B. 2006. *Elementary Differential Geometry* (2nd ed.). Academic Press.

Pirazzi, C., and Y. Weinand. 2006. "Geodesic Lines on Free-Form Surfaces: Optimized Grids for Timber Rib Shells." In *Proc. World Conference on Timber Engineering.* 7pp.

Pottmann, H., M. Eigensatz, A. Vaxman, and J. Wallner. 2015. "Architectural geometry." *Computers and Graphics 47*: 145–164.

Pottmann, H., A. Schiftner, P. Bo, H. Schmiedhofer, W. Wang, N. Baldassini, and J. Wallner. 2008. "Freeform surfaces from single curved panels." *ACM Trans. Graphics 27*, 3: #76, 1–10.

Schiftner, A., N. Leduc, P. Bompas, N. Baldassini, and M. Eigensatz. 2012. "Architectural Geometry from Research to Practice – the Eiffel Tower Pavilions." In L. Hesselgren et al. (Eds.), *Advances in Architectural Geometry* 2012, 213–228. Vienna, New York: Springer.

Strubecker, K. 1969. *Differentialgeometrie: Theorie der Flächenkrümmung.* Berlin: De Gruyter.

Tang, C., P. Bo, J. Wallner, and H. Pottmann. 2016. "Interactive Design of Developable Surfaces." *ACM Trans. Graphics* 35, 2: #12, 1–12.

Tang, C., X. Sun, A. Gomes, J. Wallner, and H. Pottmann. 2014. "Form-finding with polyhedral meshes made simple." *ACM Trans. Graphics* 33, 4: #70,1–9.

Wallner, J., A. Schiftner, M. Kilian, S. Fl¨ory, M. Höbinger, B. Deng, Q. Huang, and H. Pottmann. 2010. "Tiling freeform shapes with straight panels: Algorithmic methods." In C. Ceccato et al. (Eds.), *Advances in Architectural Geometry 2010*, 73–86. Vienna, New York: Springer.

# Measuring and Controlling Fairness of Triangulations

Caigui Jiang, Felix Günther, Johannes Wallner, and Helmut Pottmann

C. Jiang
King Abdullah University of Science and Technology (KAUST), Saudi Arabia
caigui.jiang@kaust.edu.sa

F. Günther
Institute of Advanced Scientific Studies (IHES), France
fguenth@ihes.fr

H. Pottmann
Vienna University of Technology (TU Wien), Austria
pottmann@geometrie.tuwien.ac.at

J. Wallner
Graz University of Technology (TU Graz), Austria
j.wallner@tugraz.at

# Abstract

The fairness of meshes that represent geometric shapes is a topic that has been studied extensively and thoroughly. However, the focus in such considerations often is not on the mesh itself, but rather on the smooth surface approximated by it, and fairness essentially expresses a mesh's suitability for purposes such as visualisation or simulation. This paper focusses on meshes in the architectural context, where vertices, edges, and faces of meshes are often highly visible, and any notion of fairness must take new aspects into account. We use concepts from discrete differential geometry (star-shaped Gauss images) to express fairness, and we also demonstrate how fairness can be incorporated into interactive geometric design of triangulated freeform skins.

**Figure 1.** Non-smoothness from geometric constraints: The Cour Visconti roof in the Louvre is a hybrid mesh consisting of both triangular and quadrilateral glass panels, for reasons of efficiency and weight optimisation. The triangle mesh originally intended by the architect is achieved by placing triangular shading elements on top of each panel. Merging of two triangular faces into a quad consumes one degree of freedom, so this mesh is not as optimally smooth as would have been possible with a triangle mesh.
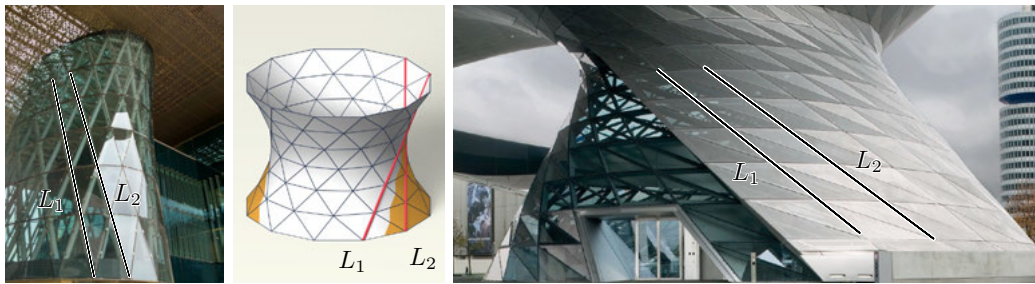


**Figure 2.** Non-smoothness from geometric constraints is exhibited by Building 16 of King Abdullah University of Science and Technology (left) and by the BMW Welt building in Munich (right). These meshes contain rows of faces whose vertices alternate between two straight lines $L_1$, $L_2$, or at least approximately so. Center: Intersection of the mesh's surface with a plane parallel to both $L_1$, $L_2$ is a zigzag polyline whose edges are parallel to either $L_1$ or $L_2$. This shows that meshes which contain straight lines in the manner described above cannot avoid a certain degree of non-smoothness.

# 1. Introduction and Motivation

**Smoothness of meshes**

Whenever a smooth shape is realised in a discrete manner, the smoothness resp. fairness of this approximation is of great importance. Depending on the application, different aspects of fairness play a role. For some applications, like the simulation of physical processes (finite element analysis) or computer graphics rendering, the vertices and edges of the mesh are only a means to an end, and "fairness" mostly refers to the suitability of the mesh for the task at hand. Typically, it involves avoiding small angles between edges, comparable edge lengths in triangles, and avoiding vertices whose number of incident edges is not 6.

**Smoothness of meshes in freeform architecture**

In freeform architecture, the purpose of meshes typically is twofold: Firstly, to make a visual statement, and secondly, to be part of the structure. The high visibility of edges and vertices makes them a much greater part of fairness resp. smoothness than in other applications. The human eye notices minimal zigzags in edge polylines which are entirely irrelevant for physical simulations or for rendering. Similarly, reflective surfaces expose even very small kink angles between faces.

Mesh smoothness is to be distinguished from smoothness of the reference shape which the mesh is thought to approximate. A wiggly mesh can mean that a smooth reference surface is approximated in a bad manner, but it can also mean that there are wiggles in the reference shape. Unfortunately, the former can sometimes not be avoided because of constraints imposed on the mesh, see examples in Figures 1 and 2.

In this paper we discuss a notion of smoothness, which we believe to be consistent with expectations of users in the field of freeform architecture. We can already draw on an existing mathematical discussion by Günther and Pottmann (2016). We further discuss the optimisation of meshes towards greater smoothness. The optimisation consists of setting up hard and soft constraints, and subsequent application of standard numerical procedures.

# 2. Measuring Smoothness

The main topic of this paper is the behaviour of meshes in the neighbourhood of vertices. This does not mean that in algorithms we neglect other contributions to visual smoothness like fairness of edge polylines (see Section 3), but these are the standard ones.
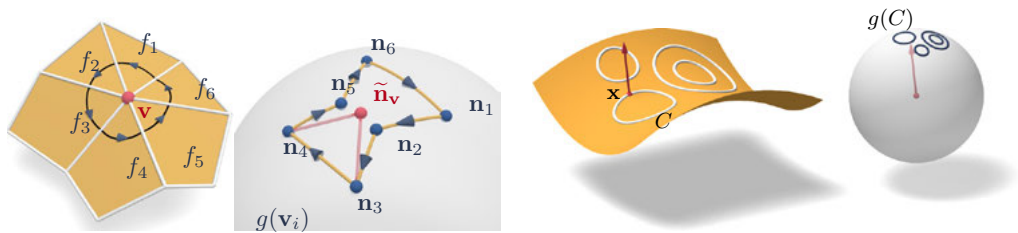
**Figure 3.** Gauss image of a vertex $v_i$. The cycle of faces $f_1, \ldots, f_6$ incident with vi defines a cycle $g(v_i)$ of unit normal vectors $\mathbf{n}_1, \ldots, \mathbf{n}_6$ on the unit sphere which form the Gauss image $g(\mathbf{v})$. The kink angle between faces $f_k, f_{k+1}$ coincides with the spherical edge length $\mathbf{n}_k, \mathbf{n}_{k+1}$. In the case shown here the Gauss image polygon $g(\mathbf{v})$ has no self-intersections, so it is the boundary of two spherical domains – one of them contains unit vectors like $\tilde{\mathbf{n}}_v$ which point to the outside of the primal mesh; it is called the interior of $g(\mathbf{v})$. We can observe the sign of curvature (negative, from the fact that the two cycles have opposite orientations). Further, any interior point $\tilde{\mathbf{n}}_v$ of the Gauss image polygon $g(\mathbf{v})$ can be viewed as an auxiliary unit normal vector associated with the vertex $v_i$. Right: The surface with point $x$ and normal vector illustrates the smooth situation.
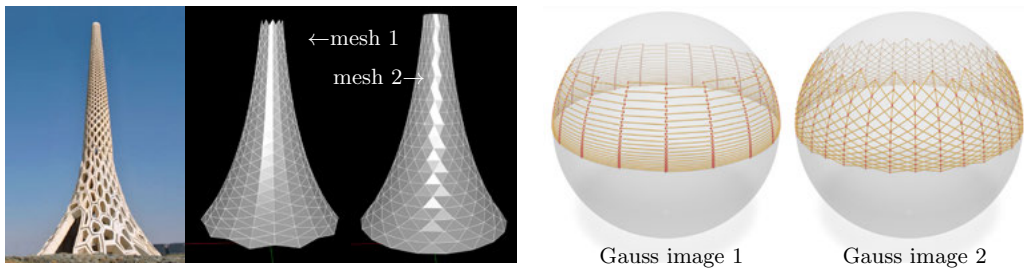


**Figure 4.** Smooth and non-smooth triangle meshes. Meshes 1 and 2 represent the same reference shape. Mesh 1 fulfills Definition 1 of "smoothness", while mesh 2 does not.

## 2.1 The Gauss Image

We endow a mesh with a *Gauss image* whose vertices are the consistently oriented unit normal vectors of the faces; we think of them as pointing to the *outside* of the mesh. The Gauss image is part of the unit sphere. Each original (primal) edge separating two faces corresponds to a Gauss image edge (dual edge) connecting two unit normal vectors. Figure 3 illustrates the Gauss image $g(\mathbf{v})$ of the 1-ring neighbourhood of a vertex $\mathbf{v}$, while Figure 4 shows Gauss images of entire meshes.

### Properties of Gauss images

There are certain obvious properties of Gauss images which correspond to visual smoothness: Long edges in the Gauss image correspond to large kink angles between adjacent faces (see Fig. 3). Also, the shape of the Gauss image cycle of a vertex (again, see Fig. 3) defines the shape of the mesh's surface in the immediate neighbourhood of a vertex. Therefore, we look for an even pattern of dual faces in the Gauss image.

If the dual Gauss image face $g(\mathbf{v}_i)$ of a vertex $\mathbf{v}_i$ is a proper polygon without self-intersections, then we might view any point in its interior as a candidate for a normal vector associated with the vertex $\mathbf{v}_i$. Further, we observe the sign of discrete Gauss curvature $K$ of the mesh: We have $K > 0$ or $K < 0$ depending on whether the Gauss image $g(\mathbf{v}_i)$, and the cycle of faces incident with the vertex $\mathbf{v}_i$, have the same orientation or opposite orientations (see Fig. 3).

This behaviour entirely corresponds to the behaviour of the normal vectors along a small circle in smooth surfaces (Fig. 3, right). If the original circle is denoted by $C$ and its Gauss image by $g(C)$, then the ratio of signed areas of $g(C)$ to $C$ is the Gauss curvature $K$. Zero Gauss curvature implies zero signed area and thus self-intersections of the Gauss image.

Coming back to the discrete case, we set aside entirely the case of developable surfaces which have $K = 0$ everywhere. Apart from the rare instances where a vertex exactly marks the boundary between $K > 0$ and $K < 0$ we have non-proper Gauss images with self-intersections only if the geometry of the primal mesh is so convoluted that it is hard to even define a normal vector. We therefore formulate the main requirement for smoothness (see Fig. 4) :

--------------------------------------------------------------

Definition 1.
A triangle mesh is smooth if all Gauss images of vertices are free of self-intersections.

--------------------------------------------------------------
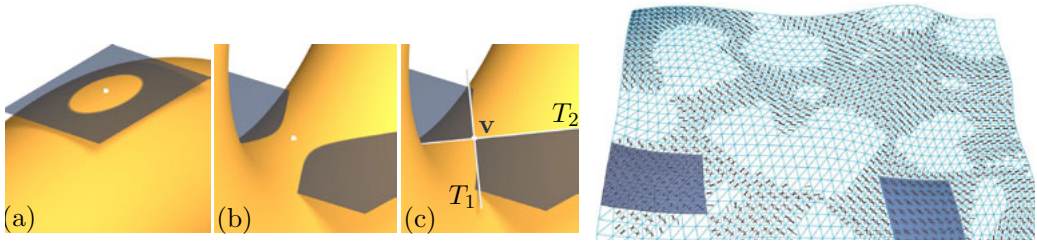
**Figure 5.** Local shape analysis of smooth surfaces: The intersection of a smooth surface with an almost-tangent plane generically approaches a conic called Dupin's indicatrix which is an ellipse in case of positive Gauss curvature (a) and a hyperbola in case of negative Gauss curvature (b). In the latter case, the intersection with a tangent plane yields two smooth curves whose tangents define the asymptotic directions $T_1$, $T_2$ in the point under consideration (c).
Right: approximate asymptotic directions of the Cour Visconti surface (Fig. 1), computed with the jet fit method of (Cazals & Pouget, 2003).
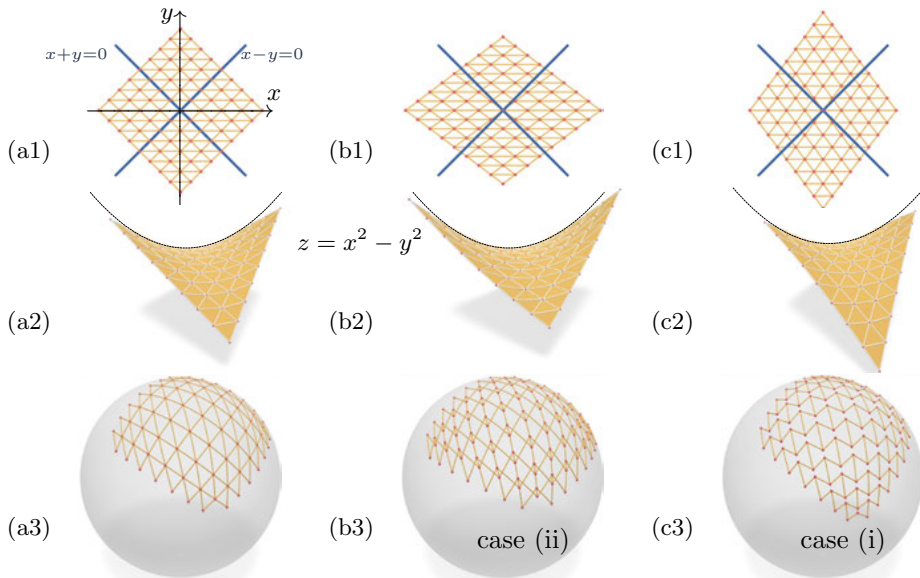


**Figure 6.** Relevance of edge orientations for smoothness. The graph of the function $z = x^2 - y^2$ carries two families of straight lines, which correspond to $x \pm y = \mathrm{const}$, and which are also the asymptotic directions. Images (a1)−(c1) show different tilings of the $xy$ plane by triangles, which in (a2)−(c2) are lifted to the graph surface and generate a mesh. Their respective Gauss images have dual faces without self-intersections in (c3) and with self-intersections in (b3). Image (a3) illustrates a boundary case where self-intersections begin to occur, and where the edges coincide with the surface's asymptotic directions.

## 2.2 Relationship Between Gauss Image and Asymptotic Lines

Closer study reveals that smoothness in the sense of Definition 1 is related to local shape properties of the surface, in particular Dupin's indicatrix and asymptotic directions, for which the reader is referred to Figure 5 or textbooks like do Carmo (1976). We state:

Observation 2.

Assume a mesh approximates a smooth saddle-shaped surface, and that the vertex $\mathbf{v}$ has face cycle $f_1, \ldots, f_6$ (indices modulo 6). Then, we typically have the following properties of the Gauss image hexagon $g(\mathbf{v})$:

(i) $g(\mathbf{v})$ has no self-intersections if the quadrants bounded by the asymptotic directions do not contain faces except for a pair $f_k$, $f_{k+3}$, which are contained in opposite quadrants.

(ii) $g(\mathbf{v})$ has self-intersections, if faces $f_k$, $f_{k+1}$ are both contained in the same quadrant between asymptotic directions, and $f_{k+3}$, $f_{k+4}$ lie in the opposite quadrant.

Figure 6 illustrates this phenomenon on a very simple surface. Situations (i) and (ii) correspond to Figure 6c and Figure 6b, respectively. Figure 7 demonstrates this observation by means of an actual freeform skin.

Observation 2 is not a mathematical statement, but it could be turned into one by specifying more clearly what is meant by "typically".[1]

### Conclusions regarding mesh design

A fundamental question is how to find a "smooth" triangulation of a given reference surface. The previous paragraphs give guidance for the combinatorially regular case with 6 edges per vertex: In the negatively curved regions of the reference surface, the positioning of edges must take the asymptotic directions into account. According to Observation 2, in each quadrant bounded by asymptotic directions we may place 1 or 2 edges, but not 3.

Thus, the layout of a "smooth" triangulation essentially experiences the same combinatorial restrictions as the layout of quadrilateral meshes with planar faces, where in the negatively curved regions of a surface, the edges cannot deviate much from the principal curves see Zadravec et al. (2010).[2]

The design of "smooth" triangulations on a reference surface is therefore an instance of a well-known dilemma: Choosing the surface determines much of the triangulation, and design freedom is limited. Further, it is generally not possible to optimise a triangle mesh towards smoothness by only slightly moving the vertices. Figure 7 is an instance of this, as will be shown below.
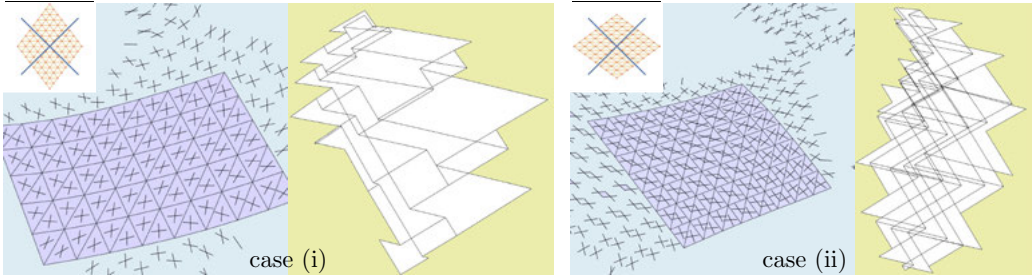
**Figure 7.** Smooth and unsmooth meshes. The blue subfigures show two patches of the Cour Visconti mesh, together with the asymptotic directions of the underlying reference surface within each face. The left and right hand patches correspond to cases (i) and (ii) of Observation 2. Consequently, their respective Gauss images (green subfigures) exhibit few self-intersections in case (i) and many self-intersections in case (ii). Thus, the left hand patch is revealed as smooth, the right hand patch as unsmooth. It must be admitted that these images are difficult to read, since this mesh has triangle pairs which together form a flat quadrilateral, so the Gauss image mesh has zero length edges.
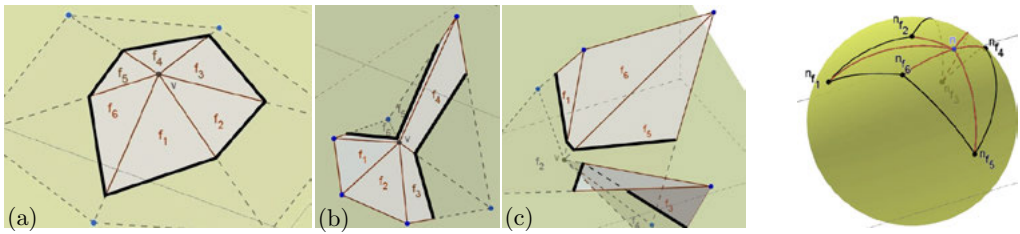


**Figure 8.** These images, taken from Günther & Pottmann (2016) illustrate Proposition 5. For a vertex v with a proper star-shaped Gauss image g(**v**), the discrete indicatrix is either a discrete ellipse (i.e. a convex polygon, subfigure a) or a discrete hyperbola (i.e. it consists of two convex arcs, subfigures b,c). The Gauss image corresponding to subfigure c is shown at right.

# 2.3 Star-Shaped Gauss Images

The constraint that Gauss image hexagons do not self-intersect is cumbersome to handle in optimisation procedures. It is fortunate that another property, which is a bit stronger, is both easier to deal with and has interesting implications on the local shape of meshes. We define:

### Definition 3.

The Gauss image $g(\mathbf{v})$ is star-shaped if it has no self-intersections and there is a point $\tilde{\mathbf{n}}_{\mathbf{v}}$ in its interior which can be connected to the entire circumference of the Gauss image by spherical arcs contained in that interior.

Figures 8 and 9 show examples. In order to properly formulate the shape properties of meshes with star-shaped Gauss images, we recall the Dupin indicatrix of Figure 5 and define:

### Definition4.

Assume that a vertex $\mathbf{v}$ in a mesh with planar faces has a Gauss image $g(\mathbf{v})$ which is star-shaped with respect to $\tilde{\mathbf{n}}_{\mathbf{v}}$ Intersecting the star of $\mathbf{v}$ with a plane close to $\mathbf{v}$ and orthogonal to $\tilde{\mathbf{n}}_{\mathbf{v}}$ yields the discrete indicatrix.

The meaning of "close to $\mathbf{v}$" is that the intersection shall not be disturbed by edges that are not incident with $\mathbf{v}$ itself. The following result, illustrated by Figure 8, has been shown by Günther and Pottmann (2016). It refers to the discrete Gauss curvature of triangle meshes (cf. Banchoff 1970).

### Proposition 5.

Consider a vertex $\mathbf{v}$ in a mesh with planar faces. Its Gauss curvature is given by $K(\mathbf{v}) = 2\pi - \sum_{f \sim v} \alpha_f$, where $\sum \alpha_f$ is the sum of all angles between successive edges incident with that vertex. Then, the following holds:
(i) If $K(\mathbf{v}) > 0$ and $g(\mathbf{v})$ is free of self-intersections, then $g(\mathbf{v})$ is star-shaped and any indicatrix is a discrete ellipse, i.e. a convex polygon.
(ii) If $K(\mathbf{v}) < 0$ and $g(\mathbf{v})$ is star-shaped with respect to some point $\tilde{\mathbf{n}}_{\mathbf{v}}$, then the corresponding indicatrix typically[3] is a discrete hyperbola, i.e. consists of two convex polygonal arcs. Also, the reverse implication is true.

We conclude that star-shaped Gauss images imply that the local shape of a mesh in the immediate vicinity of a vertex coincides with what is expected from the local shape of a smooth surface (in particular the manner of up-down oscillations
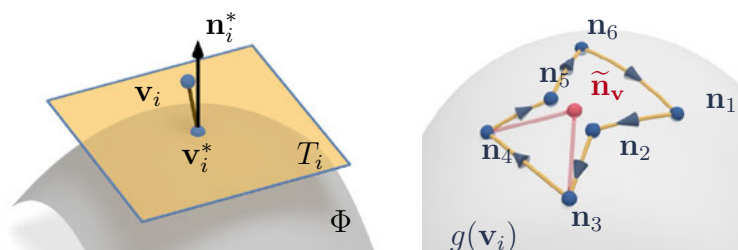
**Figure 9.** Constraints imposed on smooth meshes in our optimisation procedure. Left: For purposes of approximation, vertices $\mathbf{v}_i$ of the mesh are kept close to the reference surface $\Phi$, by adding the constraint that $\mathbf{v}_i$ lies in the tangent plane of $\Phi$ in the point $\mathbf{v}_i^*$ which was closest to $\mathbf{v}_i$ in the previous iteration of our optimisation procedure. Right: The spherical polygon $\mathbf{n}_1, \ldots, \mathbf{n}_6$ is star-shaped w.r.t. the center $\tilde{\mathbf{n}}_\mathbf{v}$ if all triangles $\mathbf{n}_k \, \mathbf{n}_{k+1} \, \tilde{\mathbf{n}}_\mathbf{v}$ have the same orientation and it winds around $\tilde{\mathbf{n}}_\mathbf{v}$ exactly once.
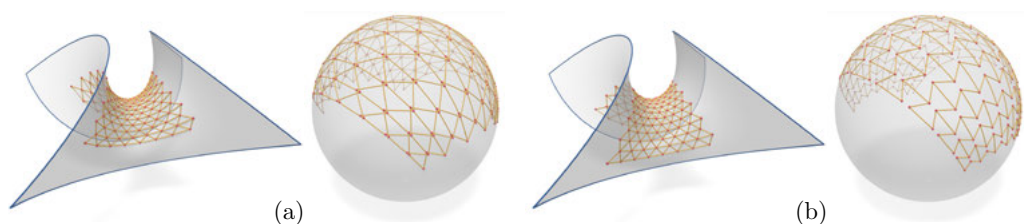


**Figure 10.** This mesh on a minimal surface together with its Gauss image (subfigure a) undergoes optimisation. All Gauss image hexagons of vertices become star-shaped (subfigure b). These images illustrate the fact that the non-smoothness of certain meshes (like the one in subfigure a) may not be visible in all renderings.
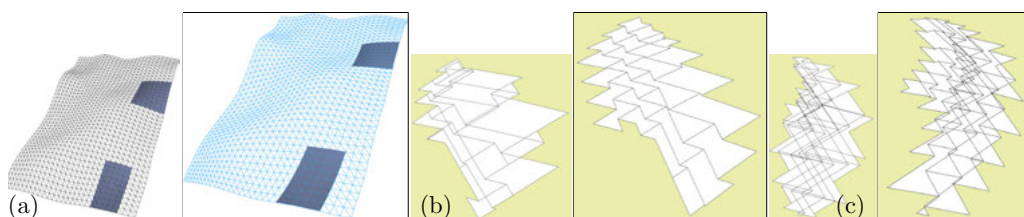


**Figure 11.** Partly successful optimisation. The three smaller images show the Cour Visconti mesh of Figure 1 (a) and the Gauss images of two selected patches (b,c) before optimisation. The larger figures show the situation after optimisation has been performed. Since the right-hand patch corresponds to case (ii) of Observation 2, optimisation can hardly be successful unless we entirely rearrange the mesh layout. Our optimisation procedure does not do that; rather, it applies small changes which may be acceptable as an augmentation of an already existing design.

w.r.t. a fictitious tangent plane, and the convexity of intersections with near-tangent planes). This means that insisting on star-shaped Gauss images makes triangle meshes even more smooth than Definition 1 already does.

# 3. Optimisation of Meshes

We have implemented a procedure to optimise a mesh such that its Gauss images become star-shaped, which makes them "smooth" as explained in detail in the previous section. The method expresses each desired property in terms of an energy function. The variables in the optimisation are positions $\mathbf{v}_i$ of vertices, normal vectors $\mathbf{n}_k$ of faces, and auxiliary normals $\tilde{\mathbf{n}}_i$ of vertices. To express the relationship between faces and normal vectors, we minimise the energy

$$E_{\text{normal}} = \sum_{\mathbf{v}_i\,\mathbf{v}_j \text{ is edge of face } f_k} (\mathbf{n}_k \cdot (\mathbf{v}_i - \mathbf{v}_j))^2 + \sum_{\text{faces } f_k} (\|\mathbf{n}_k\| - 1)^2.$$

We also ensure that these normal vectors are oriented consistently, i.e., cycling the face $f_k$ in the positive sense when looking in direction $\mathbf{n}_k$, and cycling the face $f_l$ in the positive sense when looking in direction $\mathbf{n}_k$, must assign different orientations to the common edge $f_k \cap f_l$.

Secondly, if the mesh is to approximate a reference surface $\Phi$, we should try to minimise something like $\sum \text{dist}(\mathbf{v}_i, \Phi)^2$ which is highly nonlinear. However, we replace $\Phi$ by the tangent plane $T_i$ in the point $\mathbf{v}_i^*$ of $\Phi$ which is closest to $\Phi$. Thus the highly nonlinear squared distance function is substituted by its quadratic Taylor approximation without disturbing the convergence of algorithms (cf. Pottmann et al. 2006). In each round of our iterative optimisation procedure, we recompute the closest point $\mathbf{v}_i^*$ and the normal vector $\mathbf{n}_i^*$ there. The energy expressing closeness then reads

$$E_{\text{close}} = \sum_{\text{vertices } \mathbf{v}_i} ((\mathbf{v}_i - \mathbf{v}_i^*) \cdot \mathbf{n}_i^*)^2.$$

Thirdly, the Gauss image polygon $\mathbf{n}_1, \mathbf{n}_2, \ldots$ of a vertex $\mathbf{v}_i$ is star-shaped with respect to the normal vector $\tilde{\mathbf{n}}_i$ only if all triangles $\tilde{\mathbf{n}}_i\,\mathbf{n}_k\,\mathbf{n}_{k+1}\,\mathbf{n}_i$ have the same orientation when we look at them in the direction of $\tilde{\mathbf{n}}_i$. We therefore let
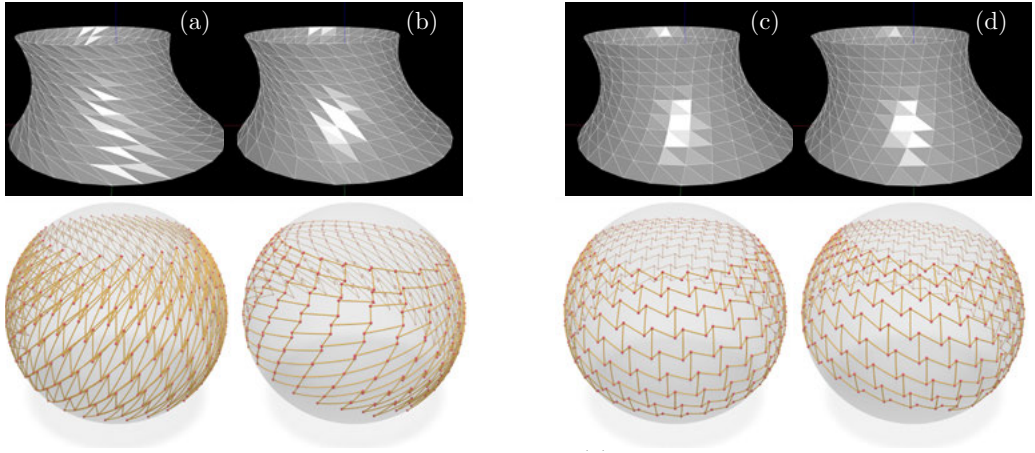
**Figure 12.** Successful optimisation. The mesh in (a) is inspired by the skin of the BMW Welt building in Munich, cf. Figure 2. It is obviously unsmooth and yields mesh (b) under optimisation. Below each mesh, the respective Gauss images are shown. Another triangulation of the same reference shape (c) is weakly smooth because Gauss images of vertices are free of self-intersections, but are not star-shaped. Optimisation yields mesh (d). The meshes are rendered as reflective surfaces, which allows visual inspection of smoothness.
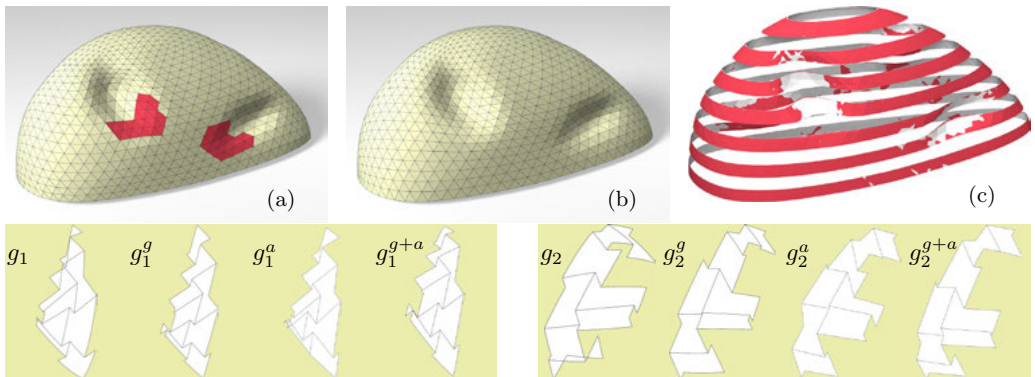


**Figure 13.** Optimization using different energies. In (a) we see the triangle mesh used for the Eindhoven Blob, together with patches No. 1 and No. 2 highlighted. The result of optimisation towards star-shaped Gauss images is shown in (b). A superimposed image of slices through original mesh and optimised mesh (c) shows approximation quality. The detailed images in the bottom row show Gauss images of patch No. $i$ ($i = 1, 2$) before optimisation (labelled $g_i$), after optimisation using $E_{\text{gauss}}$ (labelled $g_i^g$), or $E_{\text{angle}}$ (labelled $g_i^a$), or both energies (labelled $g_i^{g+a}$).

$$E_{\text{gauss}} = \sum_{\text{vertices } \mathbf{v}_i} \sum_{f_k \text{ in face cycle of } \mathbf{v}_i} (\det(\mathbf{n}_{k+1}, \mathbf{n}_k, \tilde{\mathbf{n}}_i) - \omega_{ik}^2)^2 .$$

where $\omega_{ik}$ is a slack variable. This condition is also sufficient for star-shapedness if the polygon winds around $\tilde{\mathbf{n}}_i$ exactly once (this is checked a posteriori, by computing angle sums). To prevent zigzag in edge polylines, we use the classical second order differences

$$E_{\text{polylines}} = \sum_{\text{successive vertices } \mathbf{v}_i, \mathbf{v}_j, \mathbf{v}_k} \|\mathbf{v}_i - 2\mathbf{v}_j + \mathbf{v}_k\|^2 .$$

The total energy is a weighted linear combination of the individual energies:

$$E = \omega_1 E_{\text{normal}} + \omega_2 E_{\text{close}} + \omega_3 E_{\text{gauss}} + \omega_4 E_{\text{polylines}} .$$

Figure 10 shows the result of optimisation on a simple surface.

## Implementation details

Since the limit residual of the polyline fairness energy is nonzero, it is used with a low weight, in the manner of an additional regularizer. We further use units such that the typical edge lengths in the mesh are of magnitude 1. Then we may let $\omega_1 = \omega_2 = \omega_3 = 1$ and $\omega_4 = 0.01$, but some user experimenting is necessary for good results. For the actual minimisation of the combined energy, we use a standard Gauss-Newton method (cf. Kelley, 1999, pp. 22–23).

## Discussion of results

Figures 11 and 12 show the behaviour of two different meshes which undergo optimisation. In one case optimisation is not successful, as can be seen in Figure 11c. This is not the fault of the method, but rather the fault of the design itself, which places mesh polylines relative to asymptotic directions such that case (ii) of Observation 2 applies. It depends on the nature of the mesh if optimisation manages to move vertices such that smoothness can be achieved or not. In the case of Figure 12 this works because there is not much to do: Vertices only have to move along parallel circles a bit. In the case of Figure 11 this is not possible without completely rearranging the mesh.

A more complex example is the Eindhoven *Blob* by M. Fuksas. <span style="color:magenta">Figure 13</span> illustrates how close the optimised mesh is to the original one, and illustrates the change in Gauss images.

### Comparison with other smoothing methods

There is a host of smoothing methods available in the area of geometry processing, starting with very simple methods like Laplacian smoothing a.k.a. linear diffusion (this means moving each vertex towards the average of its neighbours, see e.g. Botsch et al. (2010). However, most methods deal with removing noise from the shape, which is described by the mesh, and this is not our intention. Methods that seek to represent a reference surface by a better mesh are referred to as *remeshing*, which usually means to discard the previous mesh altogether. This is also not what we are doing. Actually, from the viewpoint of geometry processing, our smoothing procedure hardly does anything at all, which is true if one forgets the important visual role which vertices and edges play in our applications. Being aware of the different aims of other smoothing methods, we really made only few comparisons, and we only observed the behaviour of meshes as they undergo Laplacian smoothing. While for some meshes like the *Blob* of <span style="color:magenta">Figure 13</span>, this procedure produces almost acceptable results, it does not improve the meshes of <span style="color:magenta">Figure 10</span> and <span style="color:magenta">Figure 12</span> at all.

We might also ask a different question: What happens if we directly minimise the kink angles $\alpha_{kl}$ between faces $f_k$, $f_l$? With $\cos\alpha_{kl} = \mathbf{n}_k \cdot \mathbf{n}_l$ it is easy to set up an energy which directly penalises large kink angles, namely,

$$E_{\text{angle}} = \sum_{\text{edges} f_k \cap f_l} (1 - \mathbf{n}_k \cdot \mathbf{n}_l)^2.$$

The result of optimisation using this energy combined with the one producing star-shaped Gauss images is illustrated by <span style="color:magenta">Figure 13</span>. One can see that optimizing kink angles has an effect similar to making the Gauss image star-shaped, but weaker. Statistics show that between these two kinds of optimisation (or the combined optimisation of both) there is no substantial difference in kink angles. We therefore conclude that optimising $E_{\text{gauss}}$ can be augmented by adding $E_{\text{angle}}$ to the total energy, but should not be replaced by it.

# 4. Conclusion

We have presented a two-stage definition of "smoothness" of a triangle mesh in terms of the Gauss image of vertices. A weaker version requires the absence

of self-intersections, a stronger one requires that Gauss images be star-shaped. We discussed the relationship between smoothness and the placement of edges relative to the asymptotic directions. We conclude that, in negatively curved areas, we have strong combinatorial restrictions on the placement of edges if we want the mesh to be smooth. If the stronger smoothness condition is fulfilled, we can even deduce that the piecewise-flat mesh surface has local shape properties analogous to smooth surfaces (which justifies our definition of smoothness). Finally, we show the optimisation of a mesh towards smoothness and discuss in which cases this optimisation can succeed.

## Endnotes

1 We argue as follows: the observation is true for the hyperbolic paraboloid and for lifted regular triangulations (this is an easy exercise, see Fig. 6). It is true in the limit, for small faces, and limit-regular triangulations because of the hyperbolic paraboloid's capability of approximating a surface up to 2nd order (thus approximating asymptotic directions and normal vectors up to 1st order). The observation thus is true whenever the size of triangles is small enough and the triangulation is regular enough.

2 Edges of smooth planar-quad meshes must follow two families of curves which constitute a conjugate network see Liu et al. (2006) and Bobenko & Suris (2008). Theoretically, one family can be chosen arbitrarily and determines the other. However, in practice, the requirement of a minimum angle between edges ensures that edge polylines cannot cross asymptotic curves, see Zadravec et al. (2010).

3 The exceptions are cases where both $\tilde{\mathbf{n}}_v$ and $-\tilde{\mathbf{n}}_v$ are contained in the interior of $g(\mathbf{v})$.

## Acknowledgements

## References

Banchoff, T. E. 1970. "Critical points for embedded polyhedral surfaces." *Amer. Math. Monthly* 77: 475–485.

Bobenko, A., and Yu. Suris. 2008. *Discrete differential geometry: Integrable Structure*. Providence, RI: American Math. Soc.

Botsch, M., L. Kobbelt, M. Pauly, P. Alliez, and B. Levy. 2010. *Polygon Mesh Processing*. Natick, Mass.: A. K. Peters.

Cazals, F., and M. Pouget. 2003. "Estimating Differential Quantities Using Polynomial Fitting of Osculating Jets." *Proc. Symp. Geometry Processing*, pp. 177–187. Aire-la-Ville: Eurographics Association.

do Carmo, M. 1976. Differential Geometry of Curves and Surfaces. Prentice-Hall.

Günther, F., and H. Pottmann. 2016. Smooth Polyhedral Surfaces. preprint.

Kelley, C. (1999). *Iterative Methods for Optimization*. Philedelphia: SIAM.

Liu, Y., H. Pottmann, J. Wallner, Y.-L. Yang, and W. Wang. 2006. "Geometric Modeling with Conical Meshes and Developable Surfaces." *ACM Trans. Graphics 25*, 3: 681–689. Proc. SIGGRAPH.

Pottmann, H., Q. Huang, Y.-L. Yang, and S.-M. Hu. 2006. "Geometry and Convergence Analysis of Algorithms for Registration of 3D Shapes." *Int. J. Computer Vision* 67, 3: 277–296.

Zadravec, M., A. Schiftner, and J. Wallner. 2010. "Designing quad-dominant meshes with planar faces." *Computer Graphics Forum* 29 , 5: 1671–1679. Proc. Symp. Geometry Processing.

# Face-Offsetting Polygon Meshes with Variable Offset Rates

Elissa Ross, Daniel Hambleton, and Robert Aish

E. Ross, D. Hambleton
MESH Consultants Inc., Canada
elissa.ross@meshconsultants.ca ✉
daniel.hambleton@meshconsultants.ca

R. Aish
Bartlett School of Architecture, University College London (UCL), UK
robert.aish@hotmail.co.uk

# Abstract

Architectural designs are frequently represented digitally as plane-faced meshes, yet these can be challenging to translate into built structures. Offsetting operations may be used to give thickness to meshes, and are produced by offsetting the faces, edges, or vertices of the mesh in an appropriately defined normal direction. In a previous paper, we described a face-offsetting algorithm for resolving the revised combinatorics of the offset mesh produced by face-offsetting (Ross & Hambleton 2015). That is, given an input mesh with no design constraints, the algorithm computes the exact offset by determining the new geometric and combinatorial structure of the offset mesh. One of the design freedoms available in that method is the opportunity to specify different offset distances on a per-face basis. In the present paper we consider the implications of this freedom.

One question of particular interest is: Under what conditions does an offset mesh produced by variable rate face-offsetting also have a uniform distance edge-offset? To physically realise a mesh as a built structure usually requires that the mesh edges be used as the basis for structural members, with some structural depth. Therefore, given a mesh $M$ it is particularly desirable to find an offset mesh $M'$ in which the edges of $M'$ are at a uniform perpendicular distance $d$ from their corresponding edge in $M$. We present a description of meshes that admit uniform distance edge offsets as a consequence of a variable rate exact face offset, based on a graph-theoretic analysis of the underlying dual mesh. The potential advantage of this approach is that it can provide an opportunity to rationalise the physical realisation of the mesh as a constructible structure where all edge based members have the same depth.
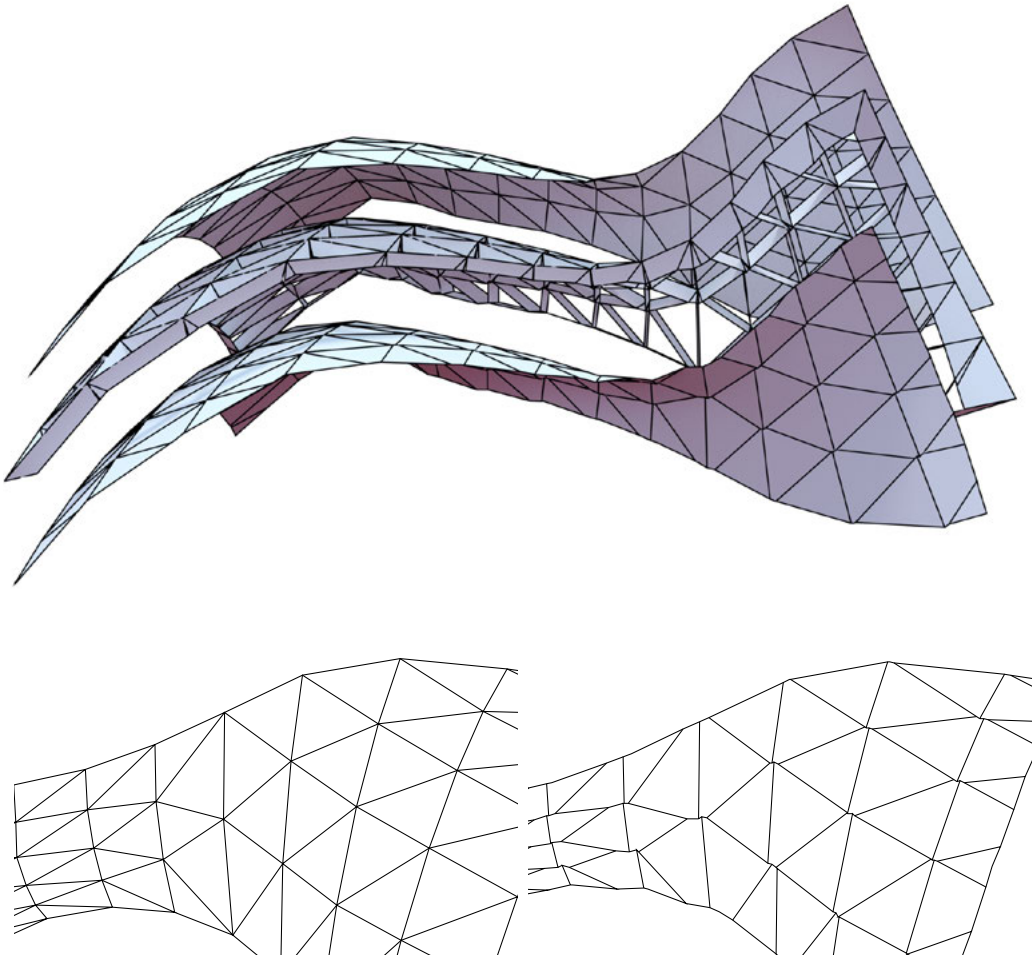
**Figure 1.** A sample mesh offset with the exact face-offsetting algorithm.
(top) The topmost mesh is the original design, and the bottom mesh is the face offset. Note that triangular mesh faces in the original have become polygonal mesh faces in the offset. The perpendicular structure can be seen in the middle layer, composed of planar quadrilateral principal members and triangular facelets.
(bottom left) Original triangular mesh.
(bottom right) Offset polygon mesh.

# 1. Introduction

Architectural geometry is a useful transitional system between the expressive intentions of the architect and the practical constraints involved in realising these intentions as a physically constructible building. Different types of geometry offer different design freedoms, but not all geometry is constructible; therefore it is also essential that geometric design tools be developed that present these freedoms and the limits to these freedoms. This is particularly important when dealing with doubly-curved surfaces which are fundamentally at odds with most standardised manufacturing processes, such as sheet metal fabrication, extrusions, and glass panel manufacturing. While it is certainly possible to employ specialised construction techniques for such surfaces, there is considerable value in developing design technology that approximate continuously curving surfaces with collections of planar elements. This *discretisation* process is of interest not just in architectural geometry, but also in computer graphics, discrete differential geometry, physical simulations, and more.

In architecture, however, it is not enough to consider only the discretisation of surface geometry. All physical objects have thickness, which is most often realised in the design phase by applying various *offsetting* techniques to the elements of the design. For surface geometry, and even planar discretisations of surface geometry, the offsetting operation is not fully understood. Of particular interest are face- and edge-offsetting techniques, which give layers or thickness to facial or edge elements, respectively. Offsetting the vertices of a mesh is also possible, although it typically introduces a 'twist' in the structural support members connecting the original mesh with the offset mesh, which may present additional fabrication challenges (Aish, Verboon, & Fagerström 2014). Some significant approaches to the face- and edge-offsetting problem have focussed on characterising the mesh geometry that produces 'well-behaved' offset outcomes (Pottmann et al. 2007; Pottmann & Wallner 2008; Wang and Liu 2010). Recently, we presented a general algorithm for face-offsetting meshes which focussed on analytically describing the offset node details for any geometry, without constraint on the input or output meshes, or any overlay of aesthetic criteria (Ross & Hambleton 2015). Each method appears to offer some advantages but may also present disadvantages.

In Section 2 we give a more detailed introduction to the face-offsetting algorithm presented in Ross and Hambleton (2015), and discuss the design considerations that arise in the context of face- and edge-offsetting. In the subsequent section, we provide several examples of one of the design freedoms of this method, specifically the ability to specify a different offset distance for each face member of the mesh. Section 4 introduces the idea of a *face-edge offset mesh*: a mesh that admits a variable rate face offset such that edge-edge distances are uniform. In that section we prove our main result, namely, the characterisation of a class of face-edge offset meshes of particular interest in an architectural
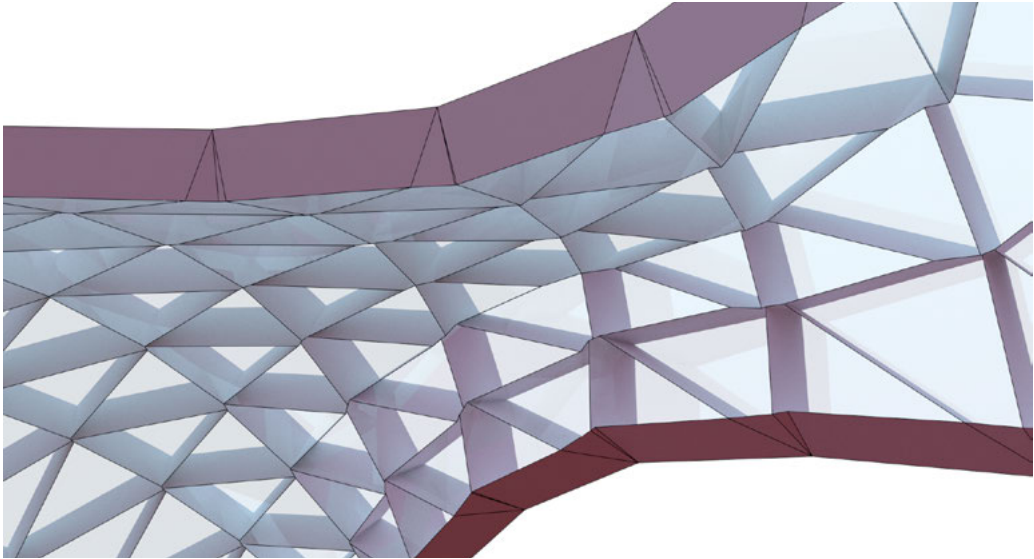
**Figure 2.** The perpendicular structure of the mesh shown in Figure 1.
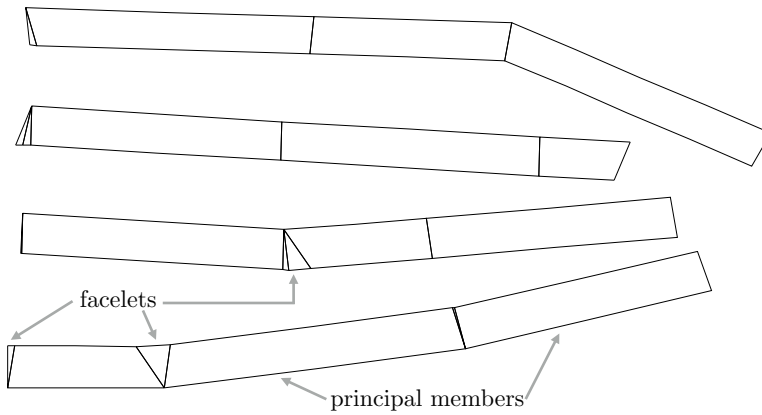


facelets

principal members

**Figure 3.** Unrolled perpendicular structure, with uniform edge offset height. Each row corresponds to a single face in an offset triangular mesh, and correspondingly has three principal members. The number of facelets depends on the offset geometry.

setting, using ideas from algebraic graph theory applied to the dual graph of the mesh. This is followed in Section 5 with a discussion about how face-edge offset meshes may be used in a design setting.

# 2. Exact Face Offsetting

A general algorithm for *exact face-offsetting* of polygon meshes was described in a previous paper by two of the authors (Ross & Hambleton 2015). Given any plane-faced polygon mesh $M$ and an offset distance $d \in \mathbb{R}$, the algorithm finds the new polygon mesh resulting from offsetting each face of $M$ in its normal direction by distance $d$ (if $d < 0$, the offset will be inward). Unlike other approaches to face offsetting (Pottmann et al. 2007; Pottmann & Wallner 2008; Wang & Liu 2010), which aim to find a *parallel mesh M'* that is combinatorially equivalent to $M$, our approach does not require that the combinatorics of the new mesh to match those of the original. In particular, the offset mesh will possess new mesh vertices and edges, although it will not possess new mesh faces (see Fig. 1). This introduces a significant relaxation of the constraints on the offsetting problem and allows us to treat all mesh combinatorics (triangular, quadrilateral, hexagon, or mixed polygon), and all underlying mesh geometry (e.g. concave, convex, hyperbolic, etc.) using a single algorithm that permits both inward and outward offsetting. Several examples of the usage of this algorithm are provided in Section 3.

## 2.1 The Perpendicular Structure

One advantage of any method of face offsetting is that it produces a planar *perpendicular structure* joining the original mesh with the offset mesh (Fig. 1 and 2). That is, given a mesh edge $e$ connecting two faces $F_i$ and $F_j$, the corresponding edge $e'$ connecting the offset faces $F_i'$ and $F_j'$ will be parallel to e.[1] Joining the mesh edge $e$ to the offset mesh edge $e'$ at their respective end points therefore creates a planar quadrilateral, which we call a *principal member* of the perpendicular structure. New edges in the offset mesh that emerge as artifacts of our general method may be connected to their originating vertex to form a triangle, which we call *facelets*[2] (Fig. 3). In this way, our offsetting method produces a perpendicular structure between the original mesh and its offset consisting only of planar quadrilateral principal members and triangular facelets. This is in contrast to other approaches to offsetting meshes which introduce a 'twist' and therefore a non-planarity in the perpendicular structure. In the work of Aish, Verboon, and Fagerström (2014), the edges of the offset mesh were used to create the primary support structure, while the edges of the original mesh were used to create a secondary 'carrier' frame for each of the glazing panels (based on the faces of the original mesh). However, connecting the primary structure to carrier frames
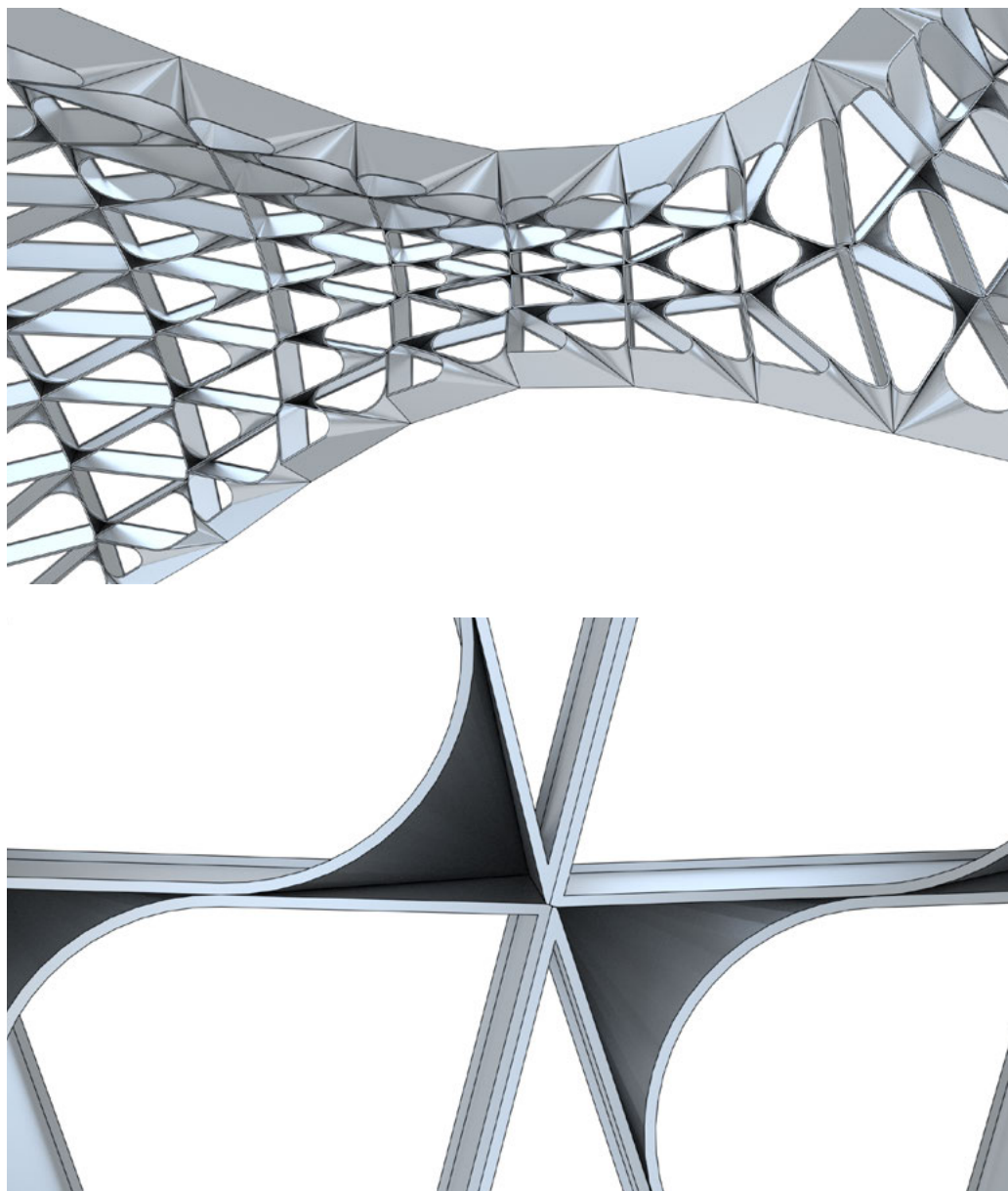
**Figure 4.** A filleting technique applied to the perpendicular structure. (bottom: detail view).

required additional elements. This significantly added to the physical and visual complexity of the resulting architecture.

A question of interest in the context of the exact face offsetting algorithm is therefore: When do the principal members of the perpendicular structure have a uniform height? That is, when is it possible that a physical realisation of the mesh as a constructible structure would have all edge-based members with the same cross-section? We answer this question in Section 4.

## 2.2 Design Considerations in the Perpendicular Structure

While at first glance, the appearance of facelets may seem undesirable from a construction point of view, there is substantial design potential within this approach. For instance, it is certainly true that facelets which create crease angles or edge lengths that fall below manufacturing tolerances need to be eliminated from the design in order for the structure to be realised. However, by using the proposed polygonal mesh as basis, such conditions may be resolved using standard modelling operations such as filleting and chamfering (see Fig. 4). Note that the planarity of the offset surface (which is guaranteed by our algorithm) becomes particularly important, since processing the planar offset faces is vastly simpler and more robust than processing more general surface geometry.

# 3. Offsetting with Variable Rates

One of the advantages of the face-offsetting method previously described (Ross & Hambleton 2015) is the ability to specify different offset distances on a per-face basis. That is, rather than specifying a single offset distance $d \in \mathbb{R}$ to be applied to all faces of a mesh $M$, we may instead specify an offset vector $\vec{d} = (d_1, \ldots, d_{|F|})$ of distances, with one distance $d_i$ for each face $F_i$. We call the vector of offset distances the *variable offset rates*.

A goal of this research is to explore how different 'design freedoms' or options might be offered to the architectural design team. In the remainder of this section we highlight the implications of the ability to specify different offset rates with several basic examples. Beyond these, one could also imagine offsetting a mesh surfaces with $\vec{d}$ determined parametrically, for example, with a trigonometric function.

## 3.1 Example: Offsetting a Single Face

In an extreme usage of variable rates, we set the offset rates of all faces to be zero, except one distinguished face which receives a positive offset rate. The

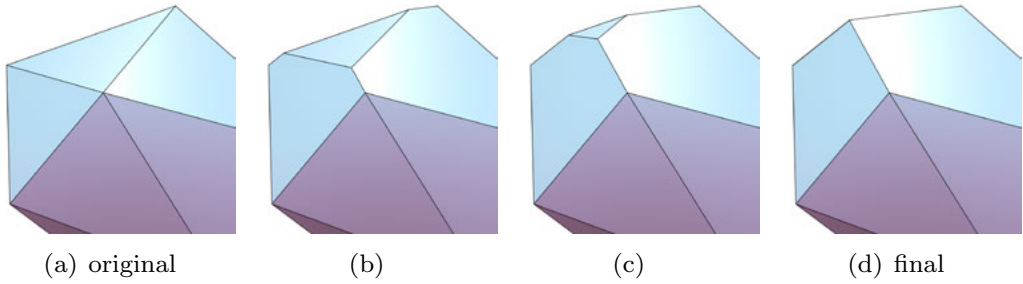(a) original       (b)       (c)       (d) final

**Figure 5.** Example of offsetting a single face only. The topmost face of the original mesh (a) will be extruded out of the mesh, leaving the final mesh (d) with one fewer face.
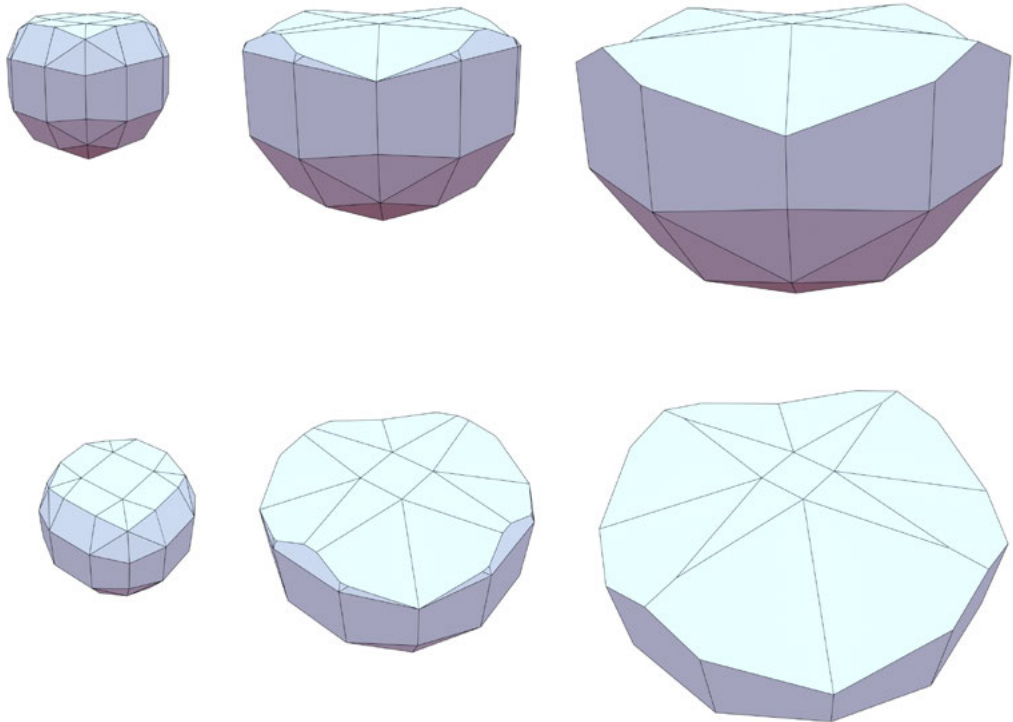


**Figure 6.** Example of offsetting with some fixed faces. Original mesh is shown at left, with the topmost faces fixed. Face-offsetting the other faces yields images at centre and right.

result of the offset procedure is to completely 'extrude' that distinguished face out of the mesh (Fig. 5).

## 3.2  Example: Fixing Multiple Faces

A second usage of variable rates might be to fix a section of a mesh, while off-setting the remainder (see Fig. 6).

## 3.3  Example:
## Rates Determined by Structural Performance

In this final example, we consider a scenario in which it might be considered important that all faces be offset uniformly. The consequence of this 'simplified' strategy is that some members will be over sized, therefore over weight, and therefore require an increase in the size of the other members. However, because all members should have the same cross-section, the whole structure may become less efficient and materially and visually heavy.

An alternative option might be to structurally optimise each member so as to reduce the face-face offset (and hence weight) of those members with less demanding role within the overall structure. Structural optimisation visually 'lightens' the architecture but may actually increases fabrication complexity. The approach of variable rate offsetting offers the architectural team both options. It does not constrain the architectural decision making, but rather defers to the team to make appropriate decision as to how to realise the mesh as a viable and efficient structure.

# 4. Edge Offsetting as a Consequence of Face Offsetting

In this section we outline a general theory for finding variable rate face offsets such that the resulting perpendicular structure has a uniform height on its principal members. More precisely, we say a mesh $M = (V, F)$ is a *face-edge-offset mesh*, or *FEO mesh* if there exists a set of rates $\vec{d} = (d_1, \ldots, d_{|F|}) \in \mathbb{R}^{|F|}$ such that face-offsetting $M$ with rates $\vec{d}$ produces a mesh $M'$ whose edges are at a uniform distance to the corresponding non-trivial edges of $M$. This ensures that the principal members of the perpendicular structure have a uniform height. Note that this definition does not require that the facelets have uniform height from their originating vertex to the new edge.
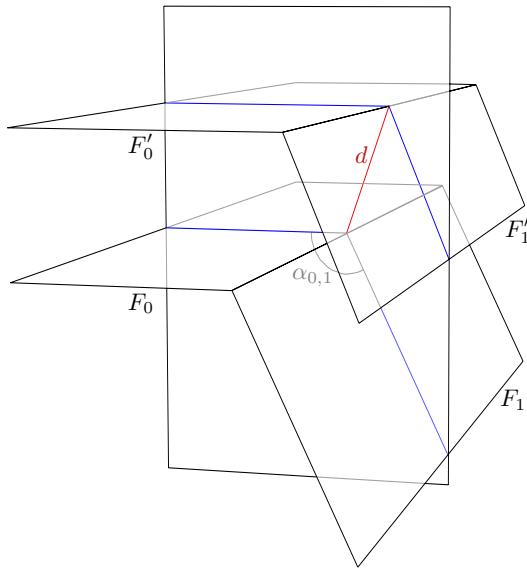
(a) Plane generated by normals of $F_0, F_1$
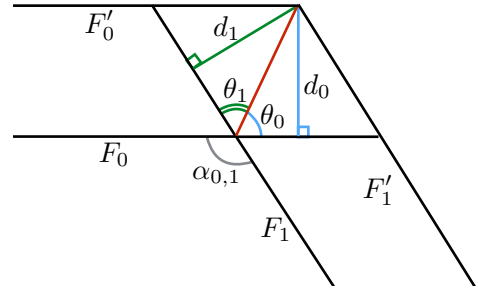
(b) $\theta_0 + \theta_1 = \alpha_{0,1}$
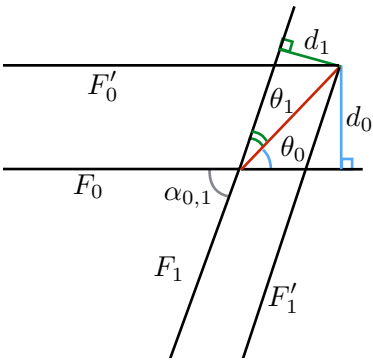
(c) $\theta_0 + \theta_1 = \alpha_{0,1}$
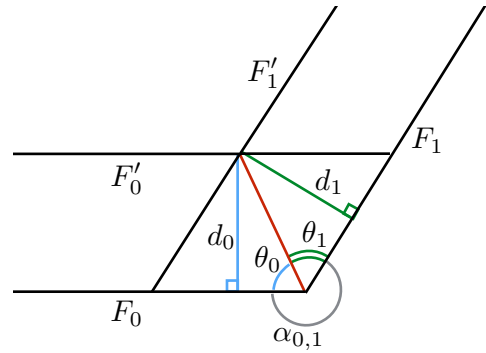
(d) $\theta_0 + \theta_1 = 2\pi - \alpha_{0,1}$

**Figure 7.** The plane $P$ generated by the normals to faces $F_0$ and $F_1$ is shown in (a). The images in (b) – (d) are assumed to be in this plane $P$. The faces are lines in $P$, and the edge offset distance corresponds to the distance from the pairs of line intersections (shown in red). If the interior angle $\alpha_{0,1}$ between the faces $F_0$ and $F_1$ is less than $\pi$, then $\theta_0 + \theta_1 = \alpha_{0,1}$, otherwise $\theta_0 + \theta_1 = 2\pi - \alpha_{0,1}$.

# 4.1 A System of Linear Equations

Let $M = (V, E)$ be a mesh. Let $e_{ij}$ be the edge connecting face $F_i$ with $F_j$. Let $\alpha_{ij}$ be the interior angle between the faces. Viewed in the plane spanned by the normals of the faces, the planes $F_i$, $F_j$ and their offsets generate a parallelogram (see Fig. 7). The diagonal that divides the angle $\alpha_{ij}$ corresponds to the edge offset distance (shown in red), and here we normalise the edge offset distance to length $d = 1$. Let $\theta_i$ be the angle opposite the perpendicular distance $d_i$, which is the offset distance of face $F_i$.

Then for each interior mesh edge $e_{ij}$ we have

(1)
$$\theta_i + \theta_j = \begin{cases} \alpha_{ij} & \text{if } 0 \leq \alpha_{ij} < \pi, \\ 2\pi - \alpha_{ij} & \text{if } \pi \leq \alpha_{ij} < 2\pi. \end{cases}$$

resulting in a system of linear equations.

If this system of equations has a solution, then we may recover the offset distances $d_i$ by the formula $d_i = \sin(\theta_i)$. Note that for $\pi < \theta_i < 2\pi$, this value will be negative, indicating an inward offsetting plane.

Let

(2)
$$\beta_{ij} = \begin{cases} \alpha_{ij} & 0 \leq \alpha_{ij} < \pi, \\ 2\pi - \alpha_{ij} & \pi \leq \alpha_{ij} < 2\pi. \end{cases}$$

Then we may record the system of linear equations:

(3)
$$e_{ij} \begin{pmatrix} & & & \vdots & & & \\ 0 \cdots 0 & 1 & 0 \cdots 0 & 1 & 0 \cdots 0 \\ & & & \vdots & & & \end{pmatrix} \overset{F_i \quad\quad F_j}{} \begin{pmatrix} \theta_1 \\ \vdots \\ \theta_{|F|} \end{pmatrix} = \begin{pmatrix} \vdots \\ \beta_{ij} \\ \vdots \end{pmatrix},$$

where $\vec{\theta} = (\theta_1 \cdots \theta_{|F|})$ is a vector of length $|F|$, and $\vec{\beta} = (\cdots \beta_{ij} \cdots)$ is a vector of length corresponding to the number of interior edges of $M$. For convenience we denote by $A$ the matrix of the linear system (3).
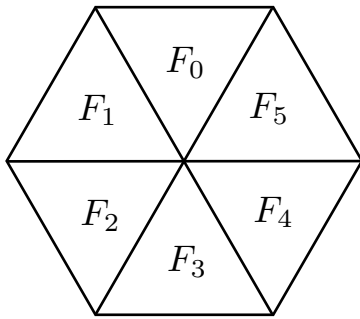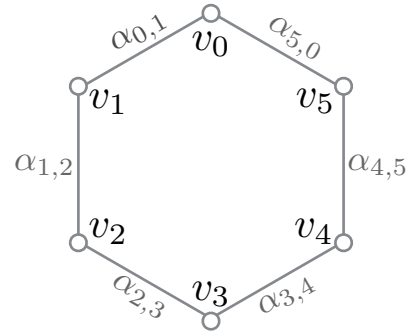
(a) $M_6$       (b) angle-labeled dual of $M_6$

**Figure 8.** A six-valent 'fully-clothed' vertex mesh $M_6$ (a) and its hexagonal dual graph (b) with vertices corresponding to the faces of $M_6$ and edges labeled by the corresponding interior angles of $M_6$.
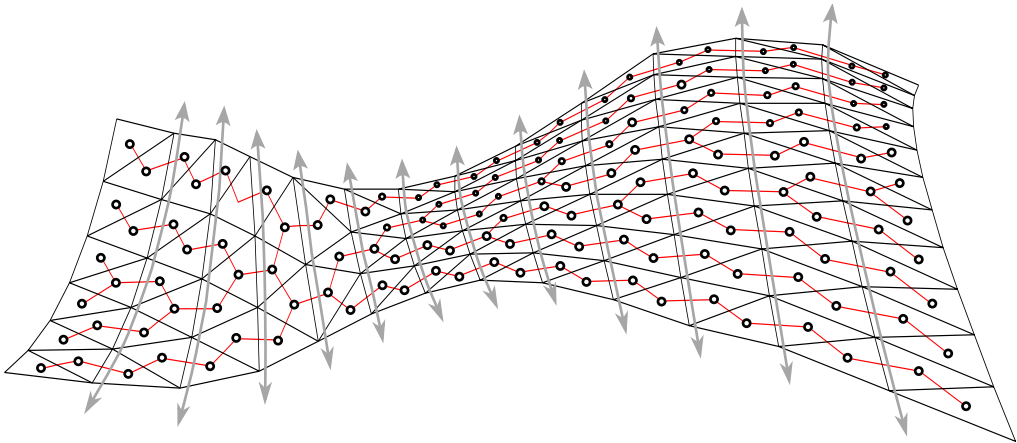


**Figure 9.** Schematic representation of the original mesh in Figure 1. The red edges form a spanning tree in the dual graph. Note that the red edges cross over every 'vertical' line of the mesh, indicated by the arrows. In this way, we can guarantee that the principal members of the perpendicular structure on these 'vertical beams' have a uniform height.

To summarise, a mesh $M$ is a FEO mesh if and only if there exists $\vec{\theta} \in \mathbb{R}^{|F|}$ satisfying $A\vec{\theta} = \vec{\beta}$. If such a solution exists, we recover the vector $\vec{d}$ of offset rates on the mesh by $d_i = \sin(\theta_i)$, for each face $F_i \in F(M)$.

## 4.2  Graph Theory Notation

Several immediate observations about FEO meshes are available from the problem set up. We first introduce some notation and vocabulary from graph theory (see e.g. Diestel 2010 or West 2001). Let $M = (V(M), F(M))$ be a polygon mesh. The d*ual graph* of $M$ is the graph $D_M = (V(D), E(D))$ formed from $M$ by introducing a vertex $v_i$ in $V(D)$ for every face of $M$. Two vertices $v_i$, $v_j$ of $D_M$ are connected by an edge if the corresponding faces $F_i$, $F_j$ are both incident to the same edge. For an open mesh $M$, the edges $E(D)$ of the dual $D$ will be in one-to-one correspondence with the interior (non-boundary) edges of $M$, and the vertices $V(D)$ will be in one-to-one correspondence with the faces of $M$. Two vertices of a graph are *adjacent* if they are connected by an edge. A *cycle* is a graph with an equal number of vertices and edges, whose vertices can be placed around a circle so that vertices appear consecutively around the circle if and only if they are adjacent.

## 4.3  Observations about FEO Meshes

We observe:

1. The matrix $A$ is the *incidence matrix* of the dual graph $D_M$ of the mesh $M$. The rows of $A$ are indexed by the interior edges of $M$, which correspond exactly to the edges $E(D)$ of the dual $D_M$. The columns of $A$ are indexed by the faces of $M$, which correspond to the vertices $V(D)$ of the dual. The incidence matrix of a graph $G = (V, E)$ is the $|E| \times |V|$ matrix $A(G)$ in which entry $A_{k,\ell}$ is 1 if vertex $v_\ell \in V$ is incident to edge $e_k \in E$, and 0 otherwise. Hence we may study the properties of $M$ via the incidence matrix of its dual.

2. Each interior edge $e$ of the mesh $M$ corresponds to an entry of $\vec{\beta}$ containing the interior angle of the faces meeting at $e$. Because each interior edge of the mesh corresponds with an edge of the dual, the interior angles of the mesh $M$ can be viewed as labels or weights on the (undirected) edges of $D_M$. In this way, the combinatorial and geometric information we require from $M$ is stored in its edge-labeled dual graph $D_M$. See Figure 8 for a simple example. A solution to (3) can be interpreted as an assignment of an angle $\theta_i$ to each vertex $v_i$ of the dual graph.

3. Unless the dual graph is a *tree* (a connected graph containing no cycles) or a connected *map-graph* (a connected graph containing exactly one cycle), the

matrix $A$ will have more rows than columns and (3) is therefore an over-constrained system of equations. In other words, no solution to the linear system should be expected to exist in general. We shall see in the Section 4.5 exactly when a solution does exist.

4. Even if a solution to (3) does exist, it need not be a positive solution. That is, it may contain a combination of positive and negative offset rates (i.e. faces moving both inside and outside the mesh), which we assume to be undesirable in an architectural context. A question of interest is to determine under what conditions we can guarantee a solution with all positive rates.

## 4.4 Small Examples

The meshes consisting of a single 'fully-clothed' vertex form an interesting class of examples. Consider a mesh $M_5$ with one central vertex, and five incident faces. Similarly, let $M_6$ be the mesh consisting of one central vertex and six incident faces (see Fig. 8a). The dual graphs corresponding to these meshes are a pentagon and hexagon respectively (see Fig. 8b). The augmented matrices for the linear system (3) are:

$$
\left[\begin{array}{ccccc|c}
1 & 1 & 0 & 0 & 0 & \beta_{0,1} \\
0 & 1 & 1 & 0 & 0 & \beta_{1,2} \\
0 & 0 & 1 & 1 & 0 & \beta_{2,3} \\
0 & 0 & 0 & 1 & 1 & \beta_{3,4} \\
1 & 0 & 0 & 0 & 1 & \beta_{4,0}
\end{array}\right]
\quad \text{and} \quad
\left[\begin{array}{cccccc|c}
1 & 1 & 0 & 0 & 0 & 0 & \beta_{0,1} \\
0 & 1 & 1 & 0 & 0 & 0 & \beta_{1,2} \\
0 & 0 & 1 & 1 & 0 & 0 & \beta_{2,3} \\
0 & 0 & 0 & 1 & 1 & 0 & \beta_{3,4} \\
0 & 0 & 0 & 0 & 1 & 1 & \beta_{4,5} \\
1 & 0 & 0 & 0 & 0 & 1 & \beta_{5,0}
\end{array}\right] .
$$

Row reduction to row-reduced echelon form already hints at some subtlety present in the problem. The incidence matrix $A_5$ of the 5-cycle row-reduces to the identity matrix $I_5$, which yields an exact solution to the system (3). In other words, for any combination of interior angles, a set of rates determining an edge offset always exists, and hence $M_5$ is always an FEO mesh.
On the other hand, row reduction of the matrix $A_6$ produces a dependent row. Therefore, for a solution to (3) to exist, we have additional conditions on $\vec{\beta}$ to ensure that it is in the column space of $A_6$. The row operations on the vector $\vec{\beta}$ yield the following condition on the adjusted interior angles:

$$
\beta_{0,1} - \beta_{1,2} + \beta_{2,3} - \beta_{3,4} + \beta_{4,5} - \beta_{5,0} = 0.
$$

In fact, this is true more generally for a vertex mesh $M_n$ with a single central vertex of valence n: if $n$ is odd, $M_n$ will always be an FEO mesh. If $n$ is even, then $M_n$ will be an FEO mesh if and only if it satisfies the alternating angle condition:

(4)

$$\sum_{k=0}^{n-1}(-1)^k \beta_k = 0,$$

where $\beta_k$ are the adjusted interior angles defined in (2) taken in cyclic order around the central vertex of $M_n$.[3]

## 4.5 Main Result

The examples of the previous section highlight the fact that the properties of the underlying dual graph of the mesh play a role in determining the solution to the system (3). Before stating our main result, we first add to our vocabulary of graph theory terminology. A graph $G = (V, E)$ is *bipartite* if its vertices can be partitioned into two sets, such that a vertex in one set is connected only to vertices of the other set. We can think of this as a colouring of the vertices of the graph into two colours, so that no two adjacent vertices have the same colour. It is not hard to see that no odd cycle (e.g. a triangle) is bipartite, but every even cycle is bipartite. In fact, the absence of odd cycles characterises bipartite graphs. Examples of meshes with bipartite duals are the planar quadrilateral meshes, and triangle meshes in which all vertices have even degree. It is straightforward to check whether a given graph is bipartite using a breadth-first search. We say a mesh is *simply-connected* if it does not have any holes.

Theorem 4.1

Let $M$ be a simply-connected mesh with a bipartite dual graph $D_M$. Then $M$ is an FEO mesh if and only if the alternating angle condition is satisfied at every interior vertex of $M$.

Before we prove this result, we require a few additional ideas from algebraic graph theory, which are adapted from the work of Grossman, Kulkarni, and Schochetman (1994). Let $G = (V, E)$ be a graph. A *circulation f* on $E$ is a real-valued function on the edge set of $G$ such that, for each vertex $v$, the sum of $f(e)$ taken over all edges incident to $v$ is zero. In particular, we may define the *circulation $f_C$ induced by a cycle $C = \{e_{j0}, e_{j1}, \ldots, e_{jr}\}$* to be

$$f(e) = \begin{cases} 0 & e \notin C, \\ 1 & \text{if } e \text{ appears in } C \text{ as } e_{j_k}, \ k \text{ odd,} \\ -1 & \text{if } e \text{ appears in } C \text{ as } e_{j_k}, \ k \text{ even.} \end{cases}$$

It is not hard to show that the set of all circulations on a graph is a vector space, and we call this the *circulant space*, denoted by $C_0$. We summarise some useful facts about this vector space in the following statement, although it should be noted that the original statements in Grossman, Kulkarni, and Schochetman (1994) are far more general (see also Remark 4.3 in this paper).

## Theorem 4.2

(Grossman, Kulkarni, & Schochetman 1994), Theorems 4.1 and 5.5). For a graph $G$, the circulant space $C_0$ is equal to the nullspace of the transpose of the incidence matrix of $G$. If $G$ is bipartite, then a basis for $C_0$ is induced by a basis of the cycle space of $G$ (which, because $G$ is bipartite, consists exclusively of even cycles).

We are now able to prove our main result.

Proof of Theorem 4.1
Let $M$ be a mesh with bipartite dual $D_M$. If $M$ is an FEO mesh, then a solution $\vec{\theta}$ exists for the linear system $A\vec{\theta} = \vec{\beta}$ (3), where $A$ is the incidence matrix of $D_M$ and $\vec{\beta}$ is the vector of adjusted interior angles of the mesh $M$. Then $\vec{\beta}$ is in the column space of $A$. The column space of $A$ is the orthogonal complement of the null space of $A^T$ (see e.g. Strang 2009). Therefore $\vec{\beta}$ is orthogonal to every basis vector of $\ker(A^T)$. By Theorem 4.2, $\ker(A^T)$ is the circulant space $C_0$ of $D_M$, which has a basis induced by the even cycle space of $D_M$. Because $D_M$ is bipartite, the even cycle space is equivalent to the cycle space of $D_M$. Because $D_M$ is the dual of a simply-connected mesh, it is planar. Therefore, a basis for the cycle space of $D_M$ is provided by the facial cycles around vertices (see e.g. Diestel 2010, 101). The circulation induced by a facial cycle is equivalent to the alternating angle condition at that interior vertex. The vector $\vec{\beta}$ of interior angles is orthogonal to a basis vector of $C_0$ if and only if the alternating angle condition is satisfied at every interior vertex. The argument reverse for the converse.

Remark 4.3
Extensions for the non-bipartite case and the case of meshes that are not simply connected are easily available using the results of Grossman, Kulkarni, and

Schochetman (1994): In the case of a mesh with dual graph that is not bipartite, a basis for the circulant space $C_0$ is generated by the even cycles and bow-ties, which consist of two odd cycles joined by a path. In the case of a mesh that is not simply connected (i.e. it has holes), the circulant space can no longer be said to be generated by the facial cycles around vertices, but there is an equivalent condition on the even cycles and bow-ties. In these broader settings Theorem 4.1 can be adapted to characterise FEO meshes using the same basic proof. In all cases, the characterisation of FEO meshes depends on an analysis of the even cycle space. Furthermore, the even cycle space of a graph $G$ can be identified using a greedy algorithm, due to the underlying matroidal structure of this space (Grossman, Kulkarni, & Schochetman 1994, 295–296).

It is known that the rank of the incidence matrix of a connected bipartite graph is $(|V| - 1)$ (Grossman, Kulkarni, & Schochetman 1994). That is, the columns of the in-cidence matrix of a bipartite graph are always dependent. This implies that, for meshes with a bipartite dual, the system of equations (3) has either no solutions or it has a one-parameter family of solutions. Provided a solution does exist, the following lemma provides us with a method for traversing the solution space of (3).

Lemma 4.4

Let $M$ be a simply-connected mesh, with bipartite dual graph $D_M$. Suppose $\vec{\theta}$ is a solution to (3), and let $\gamma \in (0, 2\pi)$. Let $\vec{\theta}'$ be the vector generated from $\vec{\theta}$ by add-ing $\gamma$ to the entries corresponding to the vertices $v \in V(D)$ of one partition and subtracting $\gamma$ to the entries corresponding to the vertices of the other partition. Then $\vec{\theta}'$ is also a solution to (3).

Proof.
The row of the matrix $A$ of (3) corresponding to the edge $e_{i,j} = (v_i, v_j)$ is:

$$\theta_i + \theta_j = \alpha_{ij}.$$

Since $v_i$ and $v_j$ are adjacent vertices in $D_M$, they must be in different partitions. Then

$$(\theta_i + \gamma) + (\theta_j - \gamma) = \alpha_{ij}.$$

From a design perspective, we wish to find the 'best' set of rates in this solution space. In most cases, this will be the set of rates that will minimise the devia-tion among the offset distances for the faces of the mesh. If two adjacent faces $F_i$, $F_j$ are offset to the same distance, then $\theta_i = \theta_j = \alpha_{ij}/2$. Therefore, to find the
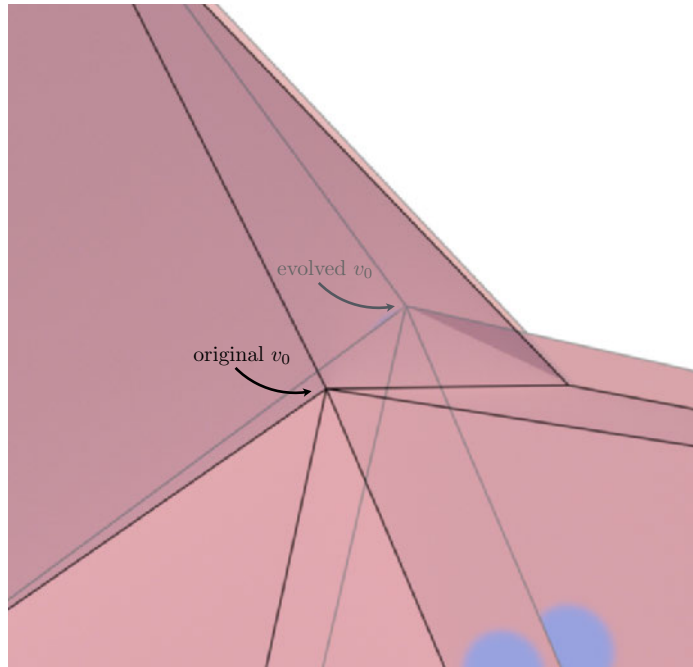
(a) Overlapped meshes. The facial cycle around the evolved vertex $v_0$ satisfies the alternating angle condition.
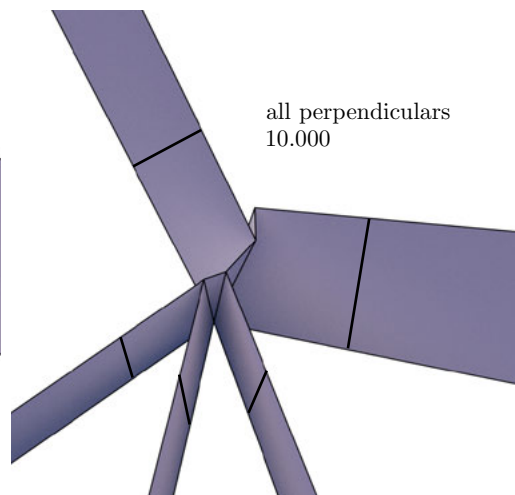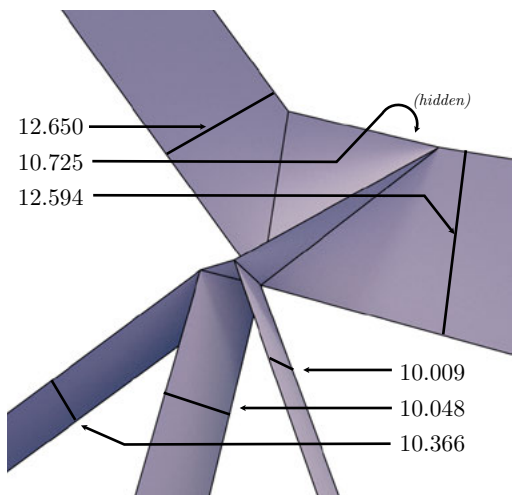


(b) Perpendicular structure, original mesh

(c) Perpendicular structure, evolved mesh

**Figure 10.** An original mesh vertex is moved to satisfy the alternate angle condition (a). The perpendicular structures of the original mesh and the evolved mesh are shown in (b) and (c).

set of face offset rates which most closely emulate this, we find γ such that the adjusted angle vector $\theta'$ minimises the sum

$$\sum_{\alpha} |\alpha_{ij}/2 - \theta'_i|.$$

# 5. Designing with Variable Rate Face Offsetting

In this section we consider several additional ways of designing using variable rate face offsetting beyond those outlined in Section 3. In particular, we consider two ways of working with FEO meshes, one which works on any mesh, and one which involves moving an original design toward an optimal solution.

## 5.1 Specifying a Spanning Tree of Uniform Edge Offsets

For any mesh with $|F(M)|$ faces, we can always ensure that $|F(M)| - 1$ edges of the mesh have a uniform edge offset. In particular, we are free to choose a spanning tree (or spanning forest) in the dual mesh that captures the edges of interest (Fig. 9). A *spanning tree* is a subgraph $T \subset D_M$ that contains no cycles and satisfies $V(T) = V(D_M)$. We then record only the edges of interest in (3), and solve to find the appropriate offset rates. In this way we could specify lines of 'beams' to offset with uniform edge distance, as indicated in Figure 9.

## 5.2 Evolving the Mesh Toward an FEO Mesh

A second way to design with FEO meshes is to evolve an original design toward an FEO mesh. This work is still in a preliminary state, but our initial explorations indicate that the alternating angle condition is quite forgiving, and that a wide range of geometries satisfying this condition are possible.

To illustrate the general idea, consider a small example mesh $M = M_6$, a single 'fully-clothed' vertex $v_0$ with six incident faces, as in Section 4.4. The dual graph is bipartite, consisting of a single hexagon cycle, and therefore by Theorem 4.1 this is an FEO mesh if and only if the alternating angle condition is satisfied on the facial cycle corresponding to the single interior vertex $v_0$ of $M$.

To find the closest FEO mesh, we fix the positions of the neighbouring vertices, and use gradient descent on the position of $v_0$ to evolve the mesh $M$ toward a new mesh $M'$ satisfying the alternating angle condition. The resulting mesh is

overlaid on the original mesh in Figure 10a. Note that this movement is 'small' in the sense that the basic geometric shape (which is hyperbolic) of the underlying mesh at that vertex is preserved.

The solution $\vec{\theta}$ to the linear system corresponding to $M'$ is a one-parameter family, and using Lemma 4.4 we add a correction vector to the solution to find a new solution $\vec{\theta}'$ of angles such that $0 \leq \theta_i' < \pi$. We recover the offset rates by taking the sine of the vector $\vec{\theta}'$, and finally offset the mesh using these rates[4]. The perpendicular structures of the original mesh and the evolved versions are shown in Figure 10b and 10c.

In a more complex example, such as an architectural shell, the neighbouring vertices would not be fixed, but rather would be moving according to their own angle optimisations. In this sense, the optimisation becomes highly nonlinear. It is possible to use the gradient descent method mentioned above on any input mesh. However, the result may not satisfy the same design criteria as the original. Therefore, a more holistic approach to the optimisation would incorporate other constraints, for example, edge length, approximate position, equal area mesh faces, planarity for non-triangular faces, etc. The development of a full-featured optimisation tool with design-based constraints is a topic for further research.

# 6. Conclusion and Further Work

Exact face offsetting with variable rates is a tool which offers a wide range of design possibilities, as illustrated through the examples in Section 3. Through the additional theory of FEO meshes, Section 5 offers several more techniques for ensuring that a mesh is not only a face offset, but is also a uniform edge offset on its principal members.

The work on FEO meshes remains in a preliminary state, and there are several questions of interest to address. Specifically, under what conditions can we guarantee that a solution to the linear system (3) corresponds to a positive set of offset rates? Based on our explorations, we conjecture that the answer may be 'always' or 'almost always', at least in the cases of primary interest in an architectural setting. A second task is to determine the best methods for optimising an original mesh toward a similar mesh that is an FEO mesh.

A common theme throughout research on offsets is the requirement of design trade-offs. Whether it is a restriction of the input geometry (Pottmann & Wallner 2008; Pottmann et al. 2007; Wang & Liu 2010), increased support structures to cover undesirable node collisions (Sevtsuk & Kalvo 2015) or the emergence of facelets as in the present work, all methods have their limitations. In turn this highlights the fact that the characterisation of the space of 'constructible' doubly- curved discrete surfaces is still an open problem. The offsetting techniques in the current paper provide the designer with the unmodified implications of their surface with respect to

material thickness, support structure, and node resolution. From this data, it is then possible to proceed with project specific processing, such as input surface optimisation, complex node design, or other techniques, thereby adding to the scope of the design freedoms available to the architectural design team.

## Endnotes

1. Provided that this offset edge $e'$ exists. One of the main ideas in our previous paper (Ross & Hambleton 2015) is the notion of global combinatorial change under offsetting. Specifically, after a sufficiently large offset step, some edges may shrink to a vertex, and faces may split into two or vanish completely. For the consideration of the perpendicular structure in the present paper, we assume no such global combinatorial change has occurred.
2. Thanks to Al Fisher for this name.
3. When $n = 4$, this is equivalent to the condition found for conical mesh vertices in Wang, Wallner, and Liu 2007. For $n > 4$, a mesh vertex is not guaranteed to be conical even when it satisfies the alternating angle condition.
4. $\vec{d} = (0:883; 0:753; 0:896; 0:905; 0:925; 0:987)$

## Acknowledgements

## References

Aish, Robert, Erik Verboon, and Gustav Fagerström. 2014. "Topo-facade: Envelope Design and Fabrication Planning Using Topological Mesh Representations." In *FABRICATE 2014 Publication: Negotiating Design & Making*, edited by Fabio Gramazio, Matthias Kohler, and Silke Langenberg. Zurich: gta Verlag.

Diestel, Reinhard. 2010. *Graph theory.* 4th ed. Berlin: Springer-Verlag. Grossman, Jerrold W., Devadatta M. Kulkarni, and Irwin E. Schochetman. 1994.

"Algebraic Graph Theory Without Orientation." *Linear Algebra and its Applications* 212: 289–307.

Pottmann, Helmut, Yang Liu, Johannes Wallner, Alexander Bobenko, and Wenping Wang. 2007. "Geometry of Multi-layer Freeform Structures for Architecture." *ACM Trans. Graph.* 26 (3). 65:1–65:11.

Pottmann, Helmut, and Johannes Wallner. 2008. "The focal geometry of circular and conical meshes." *Advances in Computational Mathematics* 29, 3: 249–268.

Ross, Elissa, and Daniel Hambleton. 2015. "Exact Face-Offsetting for Polygonal Meshes." In C*omputational Ecologies: Design in the Anthropocene Proceedings of the 35th Annual Conference of the Association for Computer Aided Design in Architecture*, edited by Lonn Combs and Chris Perry, 203–209. Cincinnati: ACADIA.

Sevtsuk, Andres, and Raul Kalvo. 2015. "Geometrical Solution Space for Grid Structures with Double-Walled Edges." In *Advances in Architectural Geometry 2014*, edited by Philippe Block, Jan Knippers, J. Niloy Mitra, and Wenping Wang, 215–231. London: Springer International Publishing.

Strang, Gilbert. 2009. *Introduction to Linear Algebra*. 4th ed. Wellesley: Wellesley-Cambridge Press.

Wang, Wenping, and Yang Liu. 2010. "A Note on Planar Hexagonal Meshes." In *Nonlinear Computational Geometry,* 221–233. New York: Springer.

Wang, Wenping, Johannes Wallner, and Yang Liu. 2007. "An Angle Criterion for Conical Mesh Vertices." *Journal for Geometry and Graphics* 11, 2: 199–208.

West, Douglas B. 2001. *Introduction to Graph Theory*. 2nd ed. Upper Saddle River: Prentice Hall.

# Marionette Mesh

## From Descriptive Geometry to Fabrication-Aware Design

Romain Mesnil, Cyril Douthe, Olivier Baverel, and Bruno Léger

R. Mesnil, C. Deute, O. Baverel
Laboratoire Navier, Champs-sur-Marne, France
romain.mesnil@enpc.fr ✉

B. Léger
Bouygues Construction, France

# Abstract

This paper introduces an intuitive method for the modelling of free-form architecture with planar facets. The method, called Marionette by the authors, takes its inspiration from descriptive geometry and allows one to design complex shapes with one projection and the control of elevation curves. The proposed framework only deals with linear equations and therefore achieves exact planarity, for quadrilateral, Kagome, and dual Kagome meshes in real-time. Remarks on how this framework relates to continuous shape parameterisation and on possible applications to engineering problems are made.

Keywords:
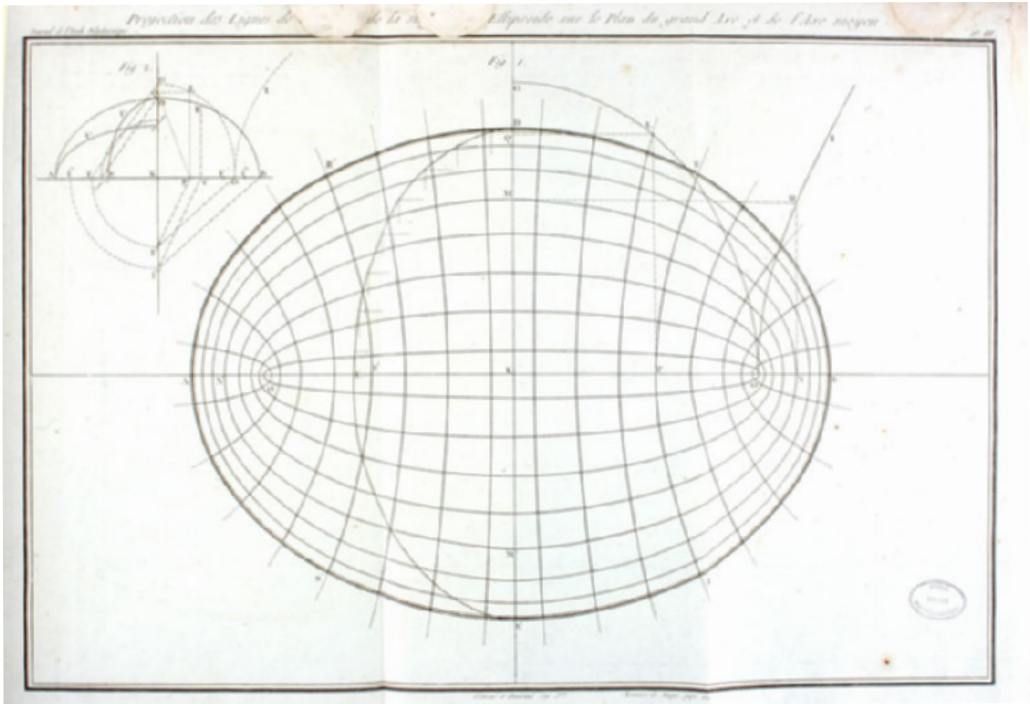structural morphology, descriptive geometry, fabrication-aware design

**Figure 1.** Lines of curvatures of an ellipsoid with descriptive geometry (Leroy 1857).

# 1. Introduction

The design of complex architectural shapes has benefited from great advances within the computer graphics community in the last decade. For instance, significant efforts were made to develop numerical methods for the covering of free-form surfaces with planar panels. These methods differ from the common knowledge of architects and engineers, making them hard use for non-specialists to use. The technique proposed in the present article aims thus at bridging this gap with a method that takes inspiration from descriptive geometry, a tool used by architects for centuries, and turns it into a real-time design tool for PQ-meshes.

## 1.1  Prior Works

### Geometrically-Constrained Approach

Planar quadrilaterals have been identified by practicians as an important optimisation target for the construction of double-curved surfaces, as they avoid using curved panels (Glymph et al. 2004). Previous research identified the need for integration of geometrical constraints within the design tools themselves and proposed methods for shape generation of PQ-meshes (Schmiedhofer 2010). Several techniques for generating exact planar quadrilateral meshes were proposed, mostly relying on affine transformations, which preserve planarity, a notion illustrated in Pottmann et al. (2007). For example, *scale-trans surfaces*, introduced in Glymph et al. (2004) use composition of two affine transformations: translation and homothetic transformations. The designer control the shape with two curves, making the process highly intuitive. Despite formal limitations, these shapes have been used in many projects.

Constrained geometric approaches use shapes that are well known and can be rationalised efficiently, for example, towards a high repetition of nodes or panels (Mesnil et al. 2015). They suffer however from a lack of flexibility and form a restricted design space. This led to the introduction of post-rationalisation strategies in order to cover arbitrary shapes with planar quadrilaterals (Liu et al. 2006).

### Optimisation-Based Shape Exploration

Most recent methods propose hence to explore design space of feasible solutions for a given mesh topology with the help of optimisation techniques (Deng et al. 2015; Yang et al. 2011). The mesh is interactively deformed by the user with the help of control handles. The overall smoothness is checked with discrete functions of the vertices. To go further, an efficient solver handling quadratic constraints was presented in Tang et al. (2014) and used in Jiang et al. (2014). Projections and subspace exploration are efficiently used for constrained-based optimisation in Bouaziz et al. (2012), Deng et al. (2013, 2015). These methods provide great design freedom, but illustrations shown in the cited references are local deformations

of meshes. Design space exploration with exact PQ-meshes was also proposed by composition of compatible affine maps assigned to each mesh face and allowed for handle-driven shape exploration (Vaxman 2012). This strategy was extended to other maps that preserve facet planarity by construction in Vaxman (2014).

The idea of this paper is to use the notion of projection, which is commonly used in architecture, especially with plane view and elevations, and to link subspace exploration techniques with representation techniques based on projections in architecture.

## Descriptive Geometry

Descriptive geometry is a technique of shape representation invented by the French mathematician Gaspard Monge (Monge 1798; Javary, 1881). It is based on planar orthogonal projections of a solid. The planes in which the projections are done are usually the horizontal and vertical planes. Figure 1 is a typical drawing of descriptive geometry: It describes an ellipsoid with a plane view, displayed with some elevations. The curve network corresponds to the horizontal projection of lines of curvature (Leroy 1857).

Because architectural objects have to deal mainly with gravity and vertical forces, it makes naturally sense to separate projections in vertical and horizontal planes. The idea to use these projections to guide structural design was used recently in the framework of the thrust network analysis, where compression-only structures are found from a planar network at equilibrium (Rippmann et al. 2012; Miki et al. 2015). The objective of this paper is to show that descriptive geometry can be turned into a general tool for the design of PQ meshes and their structural optimisation. The method, called the *Marionette method*, is presented in Section 2, where the relationship between smooth and discrete geometry for PQ-meshes is explained. Section 3 explores then some applications in architecture. Section 4 shows finally the generality of the proposed method, which can be extended to meshes other than the regular quadrilateral meshes and therefore constitute a promising versatile tool to integrate intuitively fabrication constraints into architectural design.

# 2. Marionette Meshes
## 2.1 Marionette Quad

The principles of descriptive geometry can be transposed to architectural shape modelling. The use of appropriate projections provides a simple interpretation of the problem of meshing with flat quadrilaterals. For simplification, we discuss the case of a projection in the $(XY)$ plane in this section; the generalisation to other projections is illustrated in Section 4.

Consider first <span style="color:magenta">Figure 2</span>: four points have a prescribed plane view **ABCD** in the horizontal plane $(P_1)$. Three points **A′**, **B′**, and **D′** have prescribed altitudes $z_A$, $z_B$, and $z_D$. In general, there is only one point **C′** with the imposed projection **C** so that **A′**, **B′**, **C′**, **D′** is planar.

The planarity constraint reads:

(1)
$$\det\left(\mathbf{A'B'}, \mathbf{A'C'}, \mathbf{A'D'}\right) = 0$$

Expressing coordinates in a cartesian frame of $(P_1)$, and writing $d_{BC} = det\,(\mathbf{AB}, \mathbf{AC})$, $d_{BD} = det\,(\mathbf{AB}, \mathbf{AD})$ and $d_{DC} = det\,(\mathbf{AD}, \mathbf{AC})$, if the points $A$, $B$, and $D$ are not aligned, then, one gets:

(2)
$$(z_C - z_A) = \left(\frac{d_{BC}}{d_{BD}}\right) \cdot (z_D - z_A) + \left(\frac{d_{DC}}{d_{BD}}\right) \cdot (z_B - z_A)$$

Figure 2 shows vertical lines used for construction, recalling the strings of a marionette, which gives the name *marionette quad*. Note that the system is underconstrained if the points $A$, $B$, and $D$ are aligned, which corresponds to vertical a quad. A projection in the horizontal plane thus allows only for the modelling of height fields. This limitation can be overcome by using other projections (see Section 4).

## 2.2 Regular Marionette Meshes

Consider now a quadrangular mesh without singularity as depicted in <span style="color:magenta">Figure 3</span>. The plane view in the horizontal plane is fixed, and the altitude of two intersecting curves is prescribed. Then, provided that the planar view admits no 'flat' quad (i.e. quad where three points are aligned), equation (2) can be propagated through a strip, and by there through the whole mesh. Indeed, on the highlighted strip
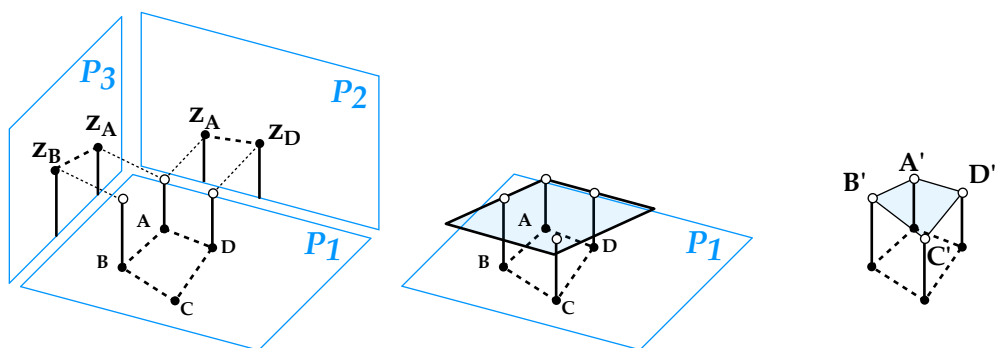
**Figure 2.** Creation of a Marionette Quad with a plane view and two elevations.
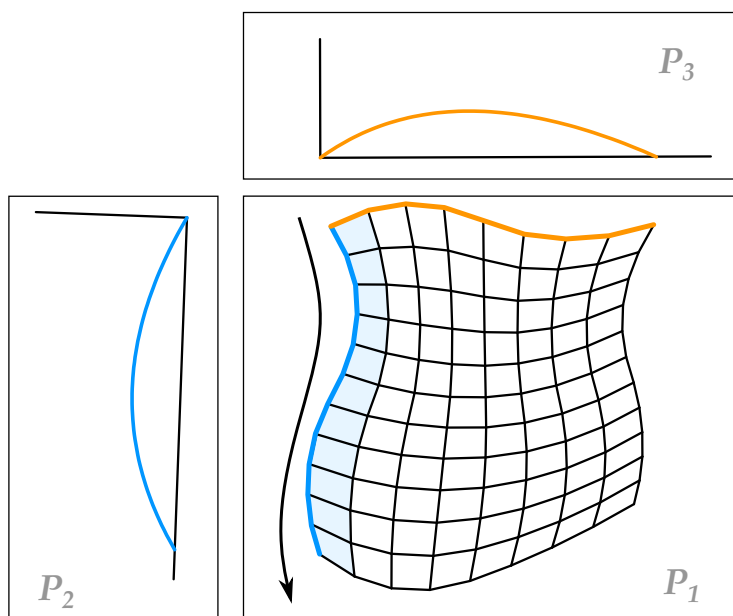


**Figure 3.** Two elevations and a planar view define a unique Marionette Mesh.

of <span style="color:magenta">Figure 3</span>, the first quad (top left) has three prescribed altitudes, and equation (2) can be used. The same applies for all the quads of the strip.

For a $N \times M$ mesh, the propagation requires $N\,M$ applications of equation (2), the memory is $3N\,M$. The marionette technique guarantees hence that the number of operations varies linearly with the number of nodes within a structure. The method performs thus in real time even for meshes with thousands of nodes, as discussed in Section 3.1.

## 2.3 Link with Smooth Geometry

The proposed method has some interesting relations with smooth geometry. The problem of covering curved shapes with planar panels is linked with the integration of *conjugate curves networks* (Liu et al. 2006; Bobenko & Suris 2008). Conjugate networks correspond to parameterisations $(u, v)$ satisfying the following equation (Bobenko & Suris 2008):

(3)
$$\det \left( \partial_{\mathbf{u}} \mathbf{f}, \partial_{\mathbf{v}} \mathbf{f}, \partial_{\mathbf{uv}}^{\mathbf{2}} \mathbf{f} \right) = 0$$

Consider now that the components in $x$ and $y$ are fixed, as in the problem solved by the Marionette technique. We are looking for the height functions $f^z$ satisfying equation 3. Adopting the notation $f_u$ to denote differentiation of $f$ with respect to $u$, equation (3) is reformulated into:

(4)
$$\det \begin{pmatrix} f_u^x & f_v^x & f_{uv}^x \\ f_u^y & f_v^y & f_{uv}^y \\ f_u^z & f_v^z & f_{uv}^z \end{pmatrix} = 0$$

Equation (4) is defined if the parameterisation in the plane $(X\,Y)$ is regular, which means if the study is restricted to height fields. An expansion of the determinant shows that the equation is a second-order linear equation in $f^z\,(u, v)$. The only term of second order is $f_{uv}^z$: the equation is thus *hyperbolic*.

Hyperbolic equations often correspond to the propagation of information in a system (think of the wave equation). It is thus no surprise that the marionette method corresponds to a propagation algorithm. Loosely speaking, it can be shown that solutions of hyperbolic equations retain discontinuities of initial conditions. The smoothness of the shape obtained by the marionette method is thus dependent on the smoothness of the input data (plane view and elevation curves).
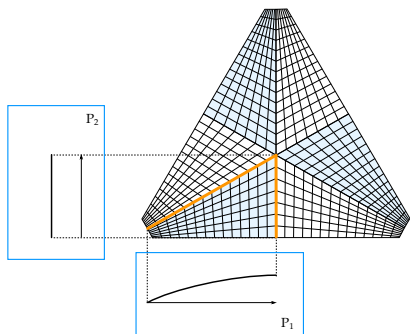
(a) Decomposition of a complex mesh into simple patches.
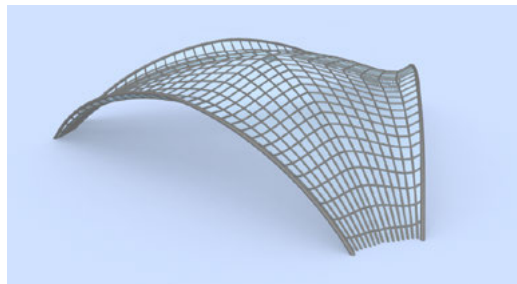


(b) The corresponding lifted mesh

**Figure 4.** A Marionette Mesh with a singularity.
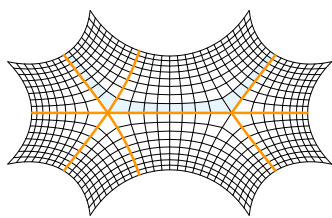


(a) Initial mesh
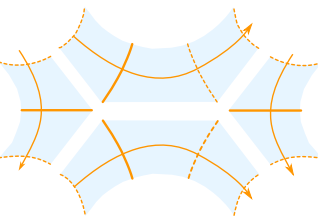
(b) Family of four strip-domains
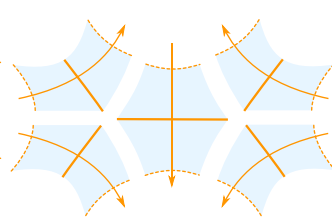
(c) Family of five strip-domains

**Figure 5.** Decomposition of a mesh into 2 families of strip-domains. Marionette Meshes can be generated by choosing one guide curve across each strip-domain.
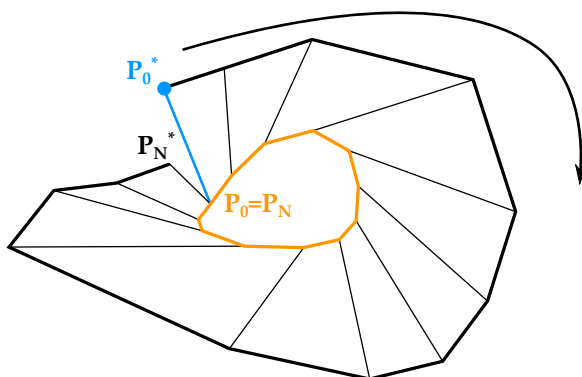


**Figure 6.** Closed Marionette Strip with incompatible closing condition induced by the prescription of the plane view of the whole strip (orange) and the altitudes of the inner curve (blue).

## 2.4 Marionette Meshes with Singularities

The modelling of complex shapes requires the introduction of vertices with a different valence, called singularities in the following. For example, the mesh displayed in Figure 4a has one singularity: the central node has a valence of six. The mesh can be subdivided into six patches with no inner singularity (in blue and white). This kind of procedure can be applied to any quad mesh. Each patch is a regular mesh, and the Marionette technique can be applied. There are, however restrictions on the curves used as guide curves due to compatibility between patches. For example, in Figure 4a, it is clear that the six curves attached to the singularity can be used as guides for the six patches, whereas choosing the 12 curves on the perimeter over-constrain the problem.

For an arbitrary quad mesh, it is possible to compute the number of guide curves that can be used to generate a Marionette Mesh. The mesh can be decomposed into simple quad domains without any singularity, for example, by using the methods described in Tarini et al. (2011) or Takayama et al. (2013). For example, Figure 4a has six domains and the mesh in Figure 5a has nine domains. These domains are four sided, and it is possible to extract independent families of strip domains, like displayed in Figure 5. Depending on the n-colourability of the mesh, the number of families varies. The example showed is two-colourable. As a result, two families of strips can be found and are shown in Figure 5b and 5c. Exactly one curve can be chosen across each strip-domain. Since strips are independent, the height of these nine curves can be chosen independently and will not over-constrain the problem.

## 2.5 Closed Marionette Meshes

### Closed Strips

Marionette Meshes create PQ-meshes by propagation of a planarity constraint along strips. One can easily figure that if the strip is closed, the problem becomes over-constrained. Indeed, consider Figure 6: The plane view of a closed strip and the altitude of the points ($P^i$) of one polyline are prescribed. If the altitude of the first point used for the propagation $P_0^*$ is chosen, the planarity constraint can be propagated along the strip. The points of the outer line are therefore imposed by the method, and the designer has no control on them. The last point $P_0^*$ is therefore generally different from the initial point $P_0^*$, leading to a geometrical incompatibility of PQ-meshes.

In the following, we develop a strategy to deal with the geometrical compatibility of closed strips. The results, however, can then be extended to general Marionette Mesh with closed strips. Suppose that the two prescribed curves are defined as the inner closed curve and one radial curve (see Figure 6). By propagation of equation (2), we easily see that the altitude of the last point $z_N^*$ depends
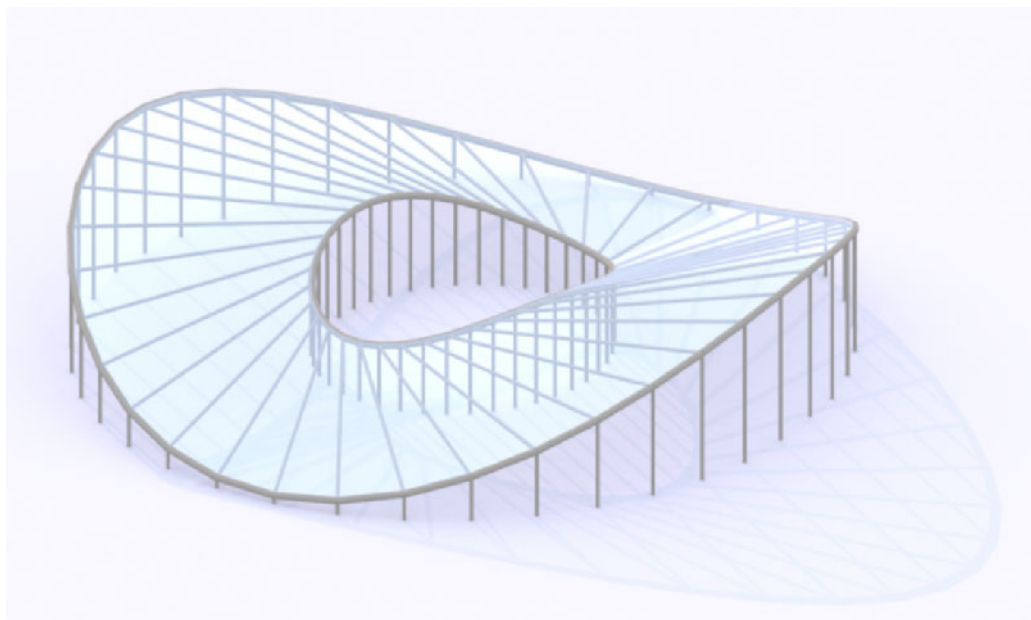
**Figure 7.** Architectural design with a closed Marionette Mesh, the altitude of the inner curve is prescribed, the designer does not have control on the outer curve.
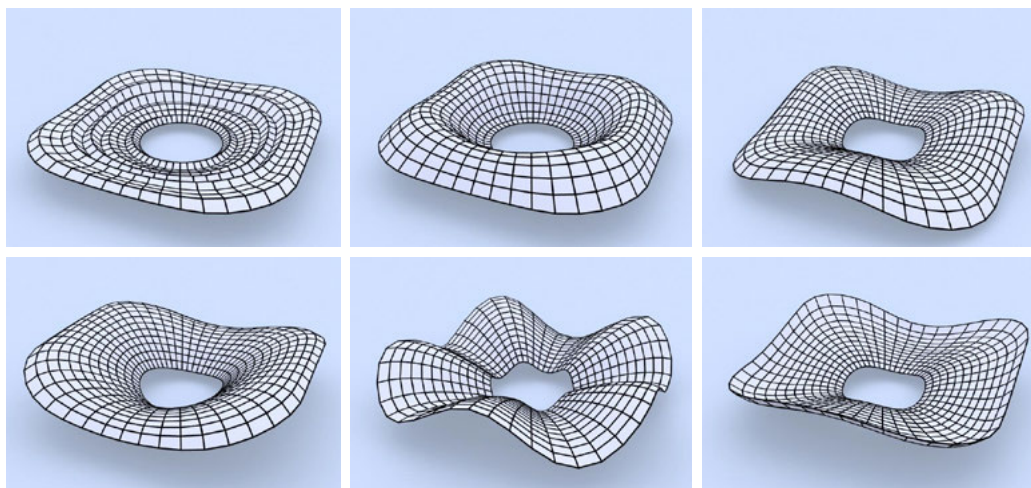


**Figure 8.** Some shapes with planar faces and a closed mesh generated with the method proposed in this paper.

linearly on the altitude of the first point $z_0^*$ and on the altitudes of the points on the inner curve $\mathbf{Z}$. It also depends on the in-plane projection of the strip. Formally, there exists a vector $\mathbf{V}$ and a scalar $a$, both functions of the plane view so that:

$$\mathbf{V} \cdot \mathbf{Z} + a \cdot z_0^* = z_N^*$$

We are interested in the case where $z_0^* = z_N^*$. There are two possibilities:

1. $a = 1$, in this case, the condition restricts to $\mathbf{V} \cdot \mathbf{Z} = 0$ and does not depend on $z_0^*$. The vector $\mathbf{z}$ is in the hyperplane of $\mathbf{V}$, which leaves $N - 1$ degrees of freedom.

2. $a \neq 1$: there is only one solution for $z_0^*$. This is the most constrained case: the designer can only control the inner curve of the strip.

### Closed Meshes

The meshes with one solution are less flexible, but they can still generate interesting shapes, like the one displayed on Figure 7, which recalls the examples of Figure 6. The designer has a total control on the altitude of the inner curve and the plane view, but cannot manipulate freely the outer curve. Note that the strings of the marionette are here materialised as columns in the rendering, illustrating the geometrical interpretation of the method.

The most interesting case occurs when the designer has potentially the control of two curves. This relies on a condition on the planar view explained above. A simple case where this condition is fulfilled is when it has a symmetry. In this case, there is a $N - 1$ parameters family of solutions for the altitude of the inner curve. The elevation of a closed guide curve can be chosen arbitrarily and projected into the hyperplane of normal $\mathbf{V}$, keeping the notations of equation (5). This operation is straightforward and allows one to control the elevation of a second curve, like for open meshes. An example of this strategy is displayed in Figure 8, where all the meshes have the same planar view.

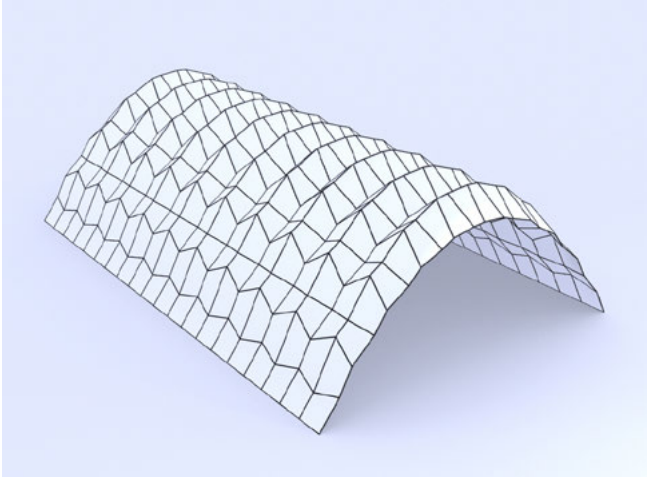**Figure 9.** A non-smooth mesh with planar facets generated with the Marionette method.
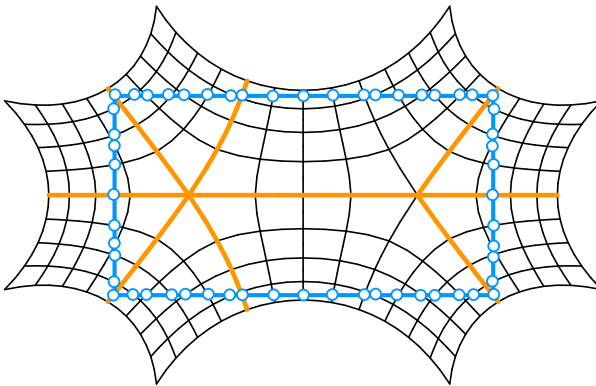


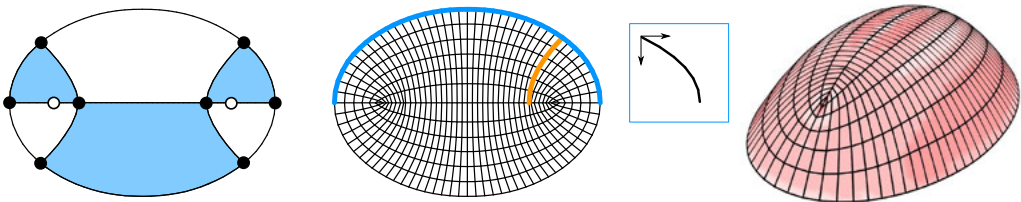**Figure 10.** A plane view (thin lines) with a prescribed boundary (thick blue lines).



**Figure 11.** A result of an optimisation procedure: the shell structure is a Marionette Mesh (top view and prescribed curves on the middle) minimising total elastic energy. On the right: red areas indicate compression.

# 3. Architectural Design with Marionette Meshes

## 3.1 Computational Set-up

The algorithms described in this paper have been implemented in the visual-scripting plug-in GrasshopperTM for the modelling software RhinoTM. This allows inter-action with other numerical tools necessary for architectural design, like finite-element analysis software. An example of interaction between fabrication-aware shape generation and structural analysis is shown in Section 3.3.

Marionette Meshes only require the solution of a linear system. The computation time is thus low; typically, it takes 3 ms to lift a mesh of 10,000 faces, with no pre-factorisation involved. Real-time computation provides great design flexibility, even for large meshes.

In our framework, the planar views are generated with NURBS patches, and the elevation curves are drawn as Bézier curves. The smoothness of the final mesh depends thus on the smoothness of the in-plane parameterisation. A $C^0$ projection yields a $C^0$ solution to the hyperbolic equation (4), so that shape functions with creases can easily be propagated through the mesh. Figure 9 shows a corrugated shape generated from a $C^0$ planar view and smooth guide curves. Such corrugations can be used in folded plate structures, and could extend the formal possibilities of methods developed in Robeller et al. (2015).

## 3.2 Shape Exploration with Marionette Meshes

The framework introduced here intrinsically accounts for the planarity of panels. Its mathematical formulation is, however, suited for many architectural constraints. Hard constraints must be fulfilled exactly, whereas soft constraints are included into the function to minimize (Nocedal & Wright, 2006). Since the planarity constraint is linear, soft constraints expressed as linear or quadratic functions can easily be included in the objective function. In this case, the optimisation problem will be similar to a classical least square problem and can be solved efficiently.

Hard constraints defined by linear equations are treated effectively within the proposed framework. Examples of linear constraints are prescribed volume or a maximal allowable altitude. The marionette method imposes $NM - (N + M - 1)$ out of $NM$ parameters, this means that another $N + M - 1$ linear constraints can be applied without over-constraining the optimisation problem.

Perhaps the most common application of hard constraint in architecture is the prescription of a boundary, as depicted in Figure 10. In this figure, the planar view is imposed and the user prescribes the altitude of some points of the mesh along a curve (white circles). In this case, the number of prescribed points is superior to

the number of degrees of freedom, and the problem might be over constrained. It might hence be preferable to turn this problem into a soft constrained problem with a quadratic function to minimize. In the same way, for really complex shapes with many singularities or highly constrained boundary, other methods will probably be more efficient, more relevant, and maybe more intuitive, like for example Jiang et al (2014).

## 3.3 Case Study: Fabrication-Aware Structural Optimisation

The formal possibilities offered by Marionette Meshes are broad enough to offer an interesting design space for engineering problems. Among them, structural optimisation is a particularly relevant. The quick generation of a parameterised design space and the coupling with advanced analysis software seems particularly promising (Preisinger & Heimrath, 2014). Indeed, non-linear criteria, like the buckling capacity, are of high importance for practical design of thin shell or grid shells (Firl & Bletzinger, 2012).

An illustration of the potential of Marionette Meshes for a structurally informed architectural design is proposed in Figure 11: The shell is a Marionette mesh spanning over an ellipse. The plane view is inspired by Figure 1. The mesh is constituted of six NURBS patches and has two singularities (white dots in the image); guide curves are found with the method proposed in this paper. The boundary curve is constrained in the horizontal plane (blue curve on Figure 11). One curve in the other direction (orange curve in Figure 11) defines the whole elevation of the dome. The shell is submitted to gravity load. All the translations at the outer boundary are restricted, and rotations at the supports are allowed (hinges). The model is computed with Finite Element software Karamba3D™. The shape generation of a 1000 faces mesh requires less than 1 ms with the Marionette technique, far less than the assembly and computation of a shell model with FEM.

The structure is optimised towards a minimum of the total elastic energy by means of genetic algorithms. The design parameters are the four altitudes of the control points controlling the shape of the guide curve. It is noticed that tension areas, depicted in blue in Figure 11, are almost non-existent on the inner and upper face of the shell. Hence, if defined properly with an accurate number of singularities, the design space offered by Marionette Meshes is wide enough to find compression-dominant shapes by the means of structural optimisation.
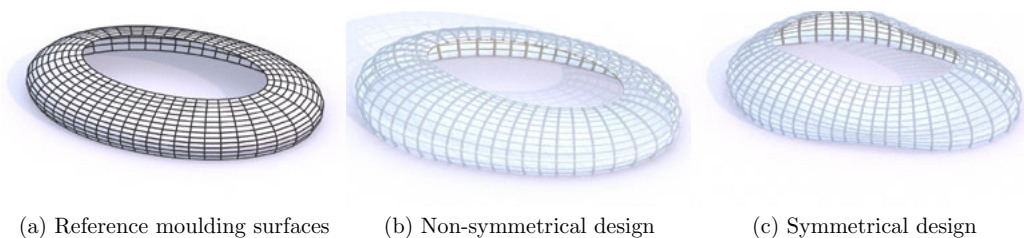
# 4. Generalisation of the Method
## 4.1 General Projections

It appeared that prescribing a horizontal view and applying the propagation technique presented here only allows for the modelling of height fields. This is a limitation of this method, although height fields surfaces are commonly used for roof covering. Other projections can be used for more shape flexibility. The planarity constraint for a quad can be extended to the case of non-parallel projections, like in Figure 12.



**Figure 12.** A Marionette quad with non-parallel guide lines.

Some projections are of practical interest for archetypal projects. Towers and facades can be modelled with cylindrical projections. Stadia can be designed using projections on torus or on moulding surfaces, the offset directions corresponding to the normals of the smooth surface. Moulding surfaces fit naturally the geometry of stadia (see Figure 13a) and have some interesting features, discussed in Mesnil et al. (2015):

- Their natural mesh contains planar curves, which are geodesics of the surface: The planarity is preserved by the marionette transformation.

- They are naturally meshed by their lines of curvatures, which gives a torsion-free beam layout on the initial surface, and on the final shape.

## 4.2 Extension to Other Patterns

The method proposed in this paper can be extended to other polyhedral patterns. As noticed by Deng et al. (2013), tri-hex meshes (also known as Kagom lattices) have the same number of degrees of freedom as quad meshes. There is therefore a straightforward way to lift Kagome lattices with the marionette technique. Figure 14a shows the guide curves for the Kagome pattern. Other isolated points are required to lift the mesh. The altitude of these points can be chosen in order to minimise the fairness energy introduced in Jiang et al. (2014), which is not difficult under linear constraints. Figure 14c shows a pattern introduced in Jiang et

(a) Reference moulding surfaces     (b) Non-symmetrical design     (c) Symmetrical design

**Figure 13.** Design of stadia obtained from a projection on a moulding surface: the prescribed curves are the inner ring and a section curve.



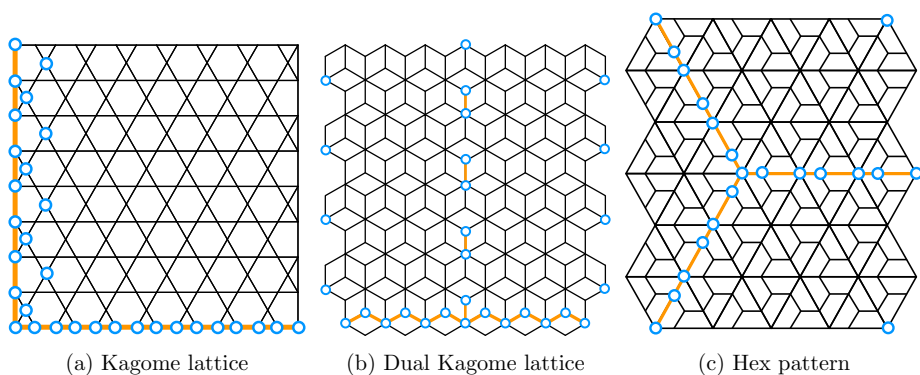(a) Kagome lattice     (b) Dual Kagome lattice     (c) Hex pattern

**Figure 14.** Marionette method applied to several patterns, white dots correspond to prescribed altitudes.
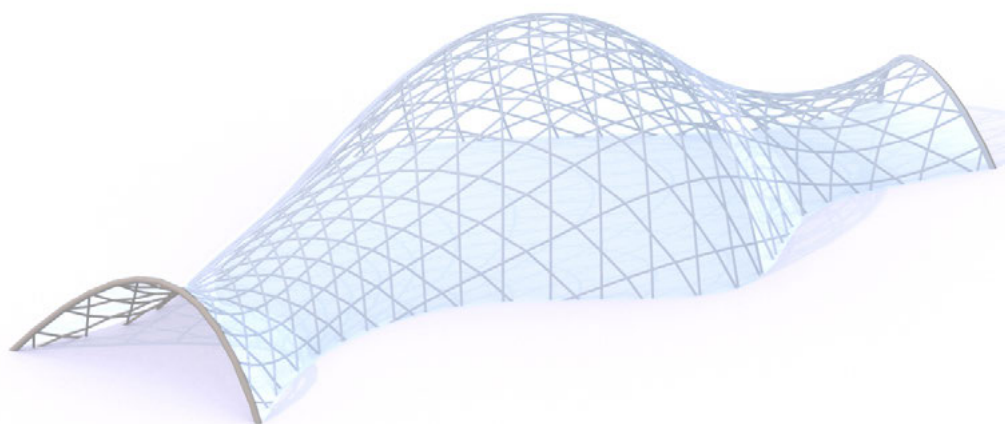


**Figure 15.** Free-form design covered by planar Kagome lattice.

al. (2014): The mesh is derived from an hexagonal pattern and three guide curves can be used to lift the mesh.

For example, Figure 15 shows a Kagome lattice covered with planar facets generated with the marionette method. The design started from a planar view generated with a NURBS patch, a Kagome was then generated following the isoparametric lines and lifted with the marionette technique. One of the guide curve is the parabolic arch of the entrance, the other is an undulating curve following the tunnel. Like for PQ-meshes, the computation is done in real time.

# 5. Conclusion

We have introduced an intuitive technique for interactive shape modelling with planar facets. It is based on descriptive geometry, which is used by architects and engineers. The concept has many applications, in particular the modelling of PQ meshes with or without singularity. Some examples show the formal potential of our method. The framework was also extended to Kagome and dual-Kagome lattices. It is likely that other polyhedral patterns can be treated with the Marionette technique. The generality of the method has also been demonstrated by changing the projection direction, a method with large potential if used on mesh with remarkable offset properties. The choice of appropriate projections, while obvious for many shapes of relatively low complexity, is a limitation to the generality of the method compared to previous methods developed in the field of computer graphics. The Marionette technique should be seen as an intuitive way to model shapes, and is complementary with other less-intuitive methods that perform well on surface-fitting or local exploration problems.

We made a comment on the smooth problem solved by the method, which gives indications on the smoothness of the shapes arising from this framework. We have seen that this smoothness depends on the smoothness of both the planar projection and the guide curves, which can be generated with any usual modelling tool based on NURBS, T-spline and Bézier curves. Moreover, it was shown that marionette meshes give an intuitive illustration on the principle of subspace exploration, a powerful tool for constrained optimisation of meshes. The underlying smooth parameterisation of marionette meshes could hence open new possibilities for efficient parameterisation of fabrication-aware design space in structural optimisation problems.

## Acknowledgements

## References

Bobenko, A. and Y. B. Suris. 2008. *Discrete Differential Geometry: Integrable Structure.* Providence RI: American Mathematical Society.

Bouaziz, S., M. Deuss, Y. Schwartzburg, T. Weise, and M. Pauly. 2012. "Shape-Up: Shaping Discrete Geometry with Projections." *Computer Graphics Forum* 31, 5: 1657–1667.

Deng, B., S. Bouaziz, M. Deuss, A. Kaspar, Y. Schwartzburg, and M. Pauly. 2015). "Interactive Design Exploration for Constrained Meshes." *Computer-Aided Design* 61: 13–23.

Deng, B., S. Bouaziz, M. Deuss, J. Zhang, Y. Schwartzburg, and M. Pauly. 201w3. "Exploring Local Modifications for Constrained Meshes." *Computer Graphics Forum* 32 (2 PART 1) :11-20.

Firl, M. and K.-U. Bletzinger. 2012). "Shape Optimization of Thin Walled Structures Governed by Geometrically Nonlinear Mechanics." *Computer Methods in Applied Mechanics and Engineering* 237–240: 107–117.

Glymph, J., D. Shelden, C. Ceccato, J. Mussel, and H. Schober. 2004). "A Parametric Strategy For Free-Form Glass Structures Using Quadrilateral Planar Facets." *Automation in Construction* 13, 2 : 187–202.

Javary, A. 1881. Traité de géométrie descriptive. Paris: Delagrave.

Jiang, C., C. Tang, M. Tomicic, H. Pottmann, and J. Wallner. 2014. "Interactive Modeling of Architectural Freeform Structures Combining Geometry with Fabrication and Statics." In *Advances in Architectural Geometry*, P. Block, W. Wang, and J. Knippers (Eds.). London: Springer.

Leroy, C. 1857. *Traité de stéréotomie, comprenant les applications de la géométrie descriptive à la théorie des ombres, la perspective linéaire la gnomonique, la coupe des pierres et la charpente, avec un atlas composé de 74 planches in folio.* Paris: Mallet-Bachelier.

Liu, Y., W. Wang, H. Pottmann, J. Wallner, and Y. Yong-Liang. 2006. "Geometric Modeling with Conical Meshes and Developable Surfaces." *ACM Transactions on Graphics* 25, 3: 681–689.

Mesnil, R., C. Douthe, O. Baverel, B. Léger, and J.-F. Caron. 2015. "Isogonal Moulding Surfaces: A Family of Shapes for High Node Congruence in Free-Form Structures." *Automation in Construction* 59: 38–47.

Miki, M., T. Igarashi, and P. Block. 2015. "Parametric Self-Supporting Surfaces via Direct Computation of Airy Stress Functions." *ACM Transaction on Graphics* 34, 4 : 1–12.

Monge, G. 1798. *Géométrie descriptive.* Paris: Baudouin.

Nocedal, J. and S. Wright. 2006. *Numerical Optimization.* New York: Springer Science & Business Media.

Pottmann, H., A. Asperl, M. Hofer, and A. Kilian. 2007. *Architectural Geometry.* Exton, PA: Bentley Institute Press.

Preisinger, C. and M. Heimrath. 2014. "Karamba – A Toolkit for Parametric Structural Design." *Structural Engineering International* 24, 2: 217–221.

Rippmann, M., L. Lachauer, and P. Block. 2012. "Interactive Vault Design." *International Journal of Space Structures* 27, 4: 219–230.

Robeller, C., A. Stitic, P. Mayencourt, and Y. Weinand. 2015. "Interlocking Folded Plate: Integrated Mechanical Attachment for Structural Wood Panels." In *Advances in Architectural Geometry 2014*, pp. 281–294. Springer.

Schmiedhofer, H. 2010. "Interactive Geometric Design of Architectural Freeform Hulls with Embedded Fabrication Information. In *Life in:formation. On responsive Information and Variations in Architecture* 348-356. New York: The Cooper Union.

Takayama, K., D. Panozzo, A. Sorkine-Hornung, and O. Sorkine-Hornung. 2013. "Sketch-Based Generation and Editing of Quad Meshes." *ACM Transactions on Graphics* 32, 4:97.

Tang, C., X. Sun, A. Gomes, J. Wallner, and H. Pottmann. 2014. "Form-Finding with Polyhedral Meshes Made Simple." *ACM Transactions on Graphics* 33, 4: 1–9.

Tarini, M., E. Puppo, D. Panozzo, N. Pietroni, and P. Cignoni. 2011. "Simple Quad Domains for Field Aligned Mesh Para-metrization." *ACM Transactions on Graphics* 30, 6; 142.

Vaxman, A. 2012. "Modeling Polyhedral Meshes with Affine Maps." In *Computer Graphics Forum*, Volume 31, pp. 1647–1656. Blackwell Publishing Ltd.

Vaxman, A. 2014. "A Projective Framework for Polyhedral Mesh Modelling." In *Computer Graphics Forum*, Volume 33, pp. 121–131. Blackwell Publishing Ltd.

Yang, Y.-l., Y.-J. Yang, H. Pottmann, and N. J. Mitra. 2011. "Shape Space Exploration of Constrained Meshes." *ACM Transactions on Graphics* 30: 124.

# Designing with Curved Creases

## Digital and Analog Constraints

Duks Koschitz

D. Koschitz
School of Architecture, Pratt Institute, USA

duks@pratt.edu ✉

# Abstract

This paper defines and describes ways of designing with curved-crease paper-folding. Curved creases are mathematically underexplored, and while many new analytic results exist, we still have no general way to geometrically predict how an arbitrary curved crease folds in 3D. We can, however, use and exploit several well-known subsets in geometry and expand on folding gadgets that include rulings or deploy analogue design methods that cannot be simulated. The paper is an investigation into four ways of designing with curved creases. The first uses developable surfaces such as cones, cylinders, and tangent surfaces, which can be manipulated in CAD software. The second focusses on 'refraction gadgets' I have derived from David Huffman's work. These sets of curves and rulings form the smallest tile of a crease pattern and can be used for digital simulation. The last two approaches focus on manual folding with the option of controlling crease patterns at the beginning or the end of a design process. The ways in which knowledge in geometry is used and to some extent abused is opportunistic in nature as the main goal consists of defining design approaches, not adequately defined mathematical models. This is important to note as many of the results may consist of ill-defined creased surfaces, for example, surface configurations made with elastic sheet materials. In this paper I introduce useful characteristics and 'design representations', the control mechanism to manipulate certain types of curved creases, for digital and analogue methods that make the design process more clear. These characteristics allow for an evaluation of the presented design approaches. This facilitates ways to teach rigorous explorations for designers and educators.

Keywords:
curved crease paperfolding, origami, developable surfaces, design

# Introduction

In order to learn how curved creases have been used, we need to investigate works in art, design, science, and engineering. Contemporary artists such as Robert Sweeney (2009), Yuko Nishimura (2009), and Matthew Shilan (2009) tend to expose personal aspects of the creative process (Klanten 2007; Nolan 1995) and don't necessarily provide productive references for defining a way of designing. Paul Jackson has published work with curved creases (Thomas & Jackson 2001), which has inspired me to try to define ways of designing rather than collecting crease pattern.

Curved creases have been explored in science and engineering with significant achievements. Regarding the foundational work, we need to acknowledge David Huffman (1976), Ron Resch and Ephriam Cohen (1970s), and Richard Riesenfeld (1974), and Dmitry Fuchs and Sergei Tabachnikov (1999). More recent work by Erik and Martin Demaine and Tomohiro Tachi (2014), Robert Geretschlaeger (2009), Jun Mitani (2009), Jeannine Mosely (2008; 2009), and Saadya Sternberg (2009) inspected specific configurations. Significant results in post-rationalising paper models exist by the team of Martin Kilian, Simon Flöry, Zhonggui Chen, Niloy Mitra, Alla Sheffer, and Helmut Pottmann (2008). Works in engineering by the teams of Simon Guest and Sergio Pellegrino (1992), Yannick Kergosien, Gotoda Hironoba, and Kunii Tosiyasu (1994) as well as Marcelo Dias and Christian Santangelo (2012) have also explored specific aspects of curved folding. Examining the work by these mathematicians and computer scientists provides insight into geometric aspects, but may not be easy to use for a designer. As the behavior of curved creases is not yet fully understood, designers face a lack of available digital tools. Investigating historical examples in art, design, and education helps to locate the time and discipline of a specific type of curved crease design, but it is not obvious how to derive design methods as we can only rely on limited documentation (Demaine & Demaine 2010), (Demaine et al. 2011).

In order to make curved creases accessible to a broader audience, including design students, I propose four design approaches that expand on specific aspects of protagonists in the field and combine them with contemporary digital tools. In order to elucidate advantages and shortcomings, I define design representations and characteristics for each approach. The relevance for architectural design is based on the convention that many building materials are manufactured as flat sheet-goods. Forming such surfaces with curved creases may have economic and energy efficiencies compared to stamping processes with molds, for example (Shelden 2002), which has been explored among others by Gregory Epps and Robofold.

# Problem Statement

How can designers learn to use curved-crease paperfolding? And which tools should be involved? Which design approaches can be included if we allow the use of surfaces that are mathematically defined in an inappropriate way? Lastly, which kind of metric can be used to qualify the proposed design approaches?

Regarding the methodology, I collected case studies in the history of curved creases and identified general design problems. I subsequently matched tools to the problems and field-tested them with students. I conducted the following workshops and seminars as a proof of concept: a 1-day workshop at the Massachusetts Institute of Technology, a 2-day workshop at Southern Polytechnic State University, Marietta, Georgia, and a seminar in the Architecture Department at Pratt Institute. The evidence is qualitative as the students had different educational backgrounds, some courses were short, and some were long. The evaluation considers and compares characteristics of each design approach. It is important to note that every design approach has intrinsic limitations and constraints, which is in part due to missing mathematical knowledge. However, if we understand the relevant constraints, as the examples demonstrate, we can still invent ways of designing with them.

# 1. Defining Design Approaches

## 1.1 Design Approaches and their Design Representation

If we want to define ways of designing with this geometry, which control mechanisms can we find? How can we define useful representations for designers? It is necessary to formalize characteristics and what I call 'design representations' for each design approach? These representations are abstractions of a curved crease design and are always related to its crease pattern. The approaches use digital and analogue methods and the rigorous definitions of representation in computer science and mathematics may not be suitable for analogue methods, for example.

The design representation of a paperfolding consists of the control mechanism that is constrained by geometric, digital, or material aspects. It is the abstraction a designer can use and manipulate in order to modify a design. These design representations relate to the crease pattern in different ways as not all geometric subsets for curved creases are well-defined. The design approaches, two fully digital and two mostly analogue, each have their own design representations (Fig. 1).

**Developable surface reflection** uses well-known configurations of cones cylinders and tangent surfaces. The 'direct digital' representation uses mirror reflections of developable surfaces in CAD software. The crease pattern is constructed at the end of the design process for fabrication.

**Refraction gadgets** is based on gadgets I have derived from David Huffman's method of drawing creases and rulings together, which can be used in simulation software. The 'indirect digital' representation relies on fixed rulings within the gadgets. The crease pattern is constructed at the beginning of the design process.

**Drawing open and closed curves** expands on the 'Bauhaus model', a design used by students of Josef Albers, and on the work of T. Roy Iwaki. A designer can draw curves and explore variations without exactly knowing what the outcome will be. The 'direct analogue' representation consists of the crease pattern that is constructed at the beginning of the design process.

**Sculpting and post-rationalising surfaces** expands on Ron Resch's crinkling by using curved creases. A designer sculpts paper or more flexible materials and defines a notational system. The 'indirect analogue' representation is based on material constraints. The crease pattern is constructed whenever a new material is introduced in the design process.
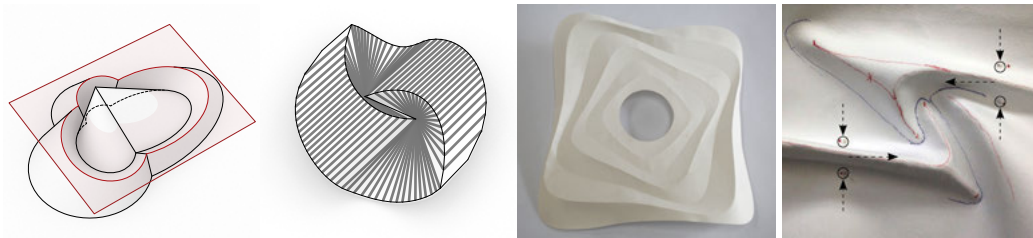
## 1.2  The Characteristics of a Design Approach

The design approaches and their explorations are presented in comparison in order for us to be able to evaluate them. The questions that arise are: Which design goals can s/he define before starting? How much knowledge is required and which digital tools are involved? The following different characteristics were used as a heuristic. In some cases, the characteristics may overlap as their boundaries can become blurry.

### Bottom-up/top-down
The first characteristic distinguishes between designing in a top-down or bottom-up way. In the case of a bottom-up approach, the designer reacts to what the curved crease gives him or her. The logics of the crease pattern and rulings drive the design process and the designer evaluates the result. The material constraints of physical paper are identified in a separate characteristic. A top-down approach demands decision making beforehand, meaning that the designer has to have made up his or her mind about what the model is supposed to look like before beginning the design process. This can in some cases represent a strong design goal, but it can also become less relevant in the process.

### A priori knowledge of geometry
The second characteristic relates to a priori knowledge of geometry, the reasoning related to previously acquired knowledge in geometry. It can play a significant role in a design approach, as a designer's decision can be influenced by the knowledge of mathematical models, for example. This knowledge is different to knowledge obtained from observation and experience, and can help in characterising a design approach.

### Exploiting material properties

The third characteristic lies in exploiting material properties. Paper resists when one folds it and the pressure in the material can guide design decisions. A designer can start to manipulate paper or felt and 'let the material fold the way it wants to fold'. The material driven process requires little mathematical knowledge, but relies heavily on tacit tactile knowledge, the knowledge that is transferred via the repeated physical manipulation or folding of paper. This can also be described as a bottom-up approach based on material logics.

### Use of digital tools

The fourth characteristic relates to the use of digital tools. The two subcategories relate to the representations defined above. The first uses direct geometric manipulation of static 3D objects in CAD software, which means that a designer looks at a static model while working on it. The second is related to the simulation of folding crease patterns that include rulings. A designer can see how a discrete version of a curved crease folds in real-time.

In the following section I discuss the design approaches in similar ways using the common headlines 'Geometry and Design Representation', 'Historical references and precedents', and 'Definition of the Design Approach'.

# 2. The Four Design Approaches
## 2.1 Developable Surface Reflection

### Geometry and design representation

We can imagine a general cylinder that is cut with a plane. We subsequently mirror and rotate the remaining part (Fig. 2). The rulings are all parallel in the crease pattern. Cones can be manipulated in a similar way, but their rulings converge in an apex. The well-known geometry includes tangent surfaces, which can be used in digital 3D models. The direct digital design representation consists of the 3D surfaces in CAD software, which are unrolled to construct the crease pattern for fabrication.

### Historical references and precedents

Students of Josef Albers made models based on general cylinders at Black Mountain College (Fig. 3 left). We can assume that the design goal consisted of creating a cylindrical shape or enclosure, which can be achieved with cylinder reflections. Haresh Lalvani provides many variations of similar configurations in the work that has been built by Milgo/Bufkin using large sheets of steel (Fig. 4) (2003). Tim Herok and Markus Schein's 'Liegengenerator' makes use of a discretised approach (2002). Their process starts by defining the constraints for input surfaces, namely, the
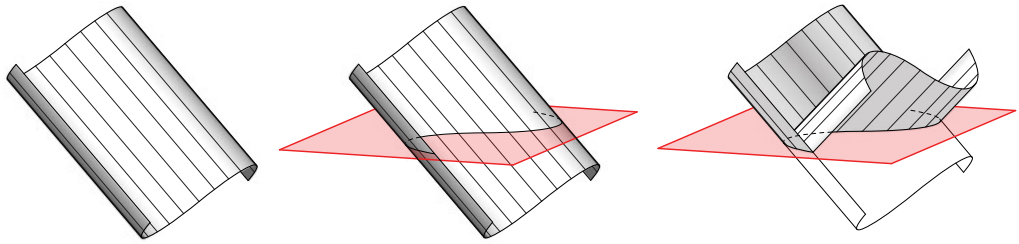
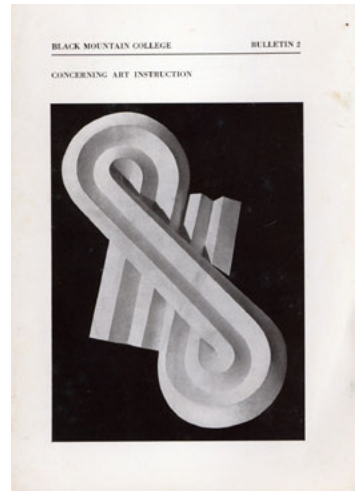**Figure 2.** Mirror reflection of general cylinder (DK).



**Figure 3.** (from left to right)
Work by students of Josef Albers, Black Mountain College (1950s – photographer unknown).
Bulletin Cover 1944 with model made in Albers' class, Black Mountain College (1944).



**Figure 4.** Metal column covers and wall panel (Haresh Lalvani).

two edges of a bench that touch the ground (Trebbi 2008). Schein sets up a digital model with user inputs for height and undulation that uses a genetic algorithm (2002). Regarding reflected cones, we can find examples by students of Josef Albers at Black Mountain College (Fig. 3 left). David Huffman based some of his designs on cone reflections such as 'Cone reflected seven times' with a gradually rotating main axis (Wertheim, 2004). The designer Poul Christiansen also uses cone reflections in one of his lamp designs (Klint 1943). Ron Resch worked with 2 cones without cutting the paper in 'Yellow Folded Cones: Kissing'.

### Definition of the design approach
Regarding cylinders, the designers begins with a 3D model of a general cylinder in any CAD software and then places a plane to cut it with. The subsequent step consists of reflecting the cut-off part and placing it on the resulting curved crease. The designer continues this process step-by-step. The approach can also be applied to cones and tangent surfaces.

I used two types of software 'ORI-REF: A Design Tool for Curved Origami based on Reflection' by the Japanese geometer Jun Mitani (2011) and Rhino3D in my seminar. ORI-REF takes cylinders, cones, and tangent surfaces as input surfaces, and the user then manipulates a local coordinate system to orient the reflection plane. The red spline in the example below with several reflections by Ashley Hickman indicates the profile of the input surface (Fig. 5). Students constructed the planes and reflections themselves in Rhino3D. Closed configurations with single and double reflections can be seen below (Fig. 6 and 7).

Corresponding examples with cones by Ashley Hickman and Kalliopi Oikonomou were made using Rhino 3D (Figures 8 to 10). The cones are cut with planes parallel to the base or the axis. The last example shows a tiling of partial cones that share an apex A.

## 2.2 Refraction Gadgets

### Geometry and design representation
Huffman's gadgets determine the position of curves and rulings in a crease pattern. If the curves are abstracted as line segments, we can create a discrete version of the gadget (Koschitz 2013), which can be used in simulation software such as 'FreefromOrigami' by Tomohiro Tachi (2013). The indirect digital design representation consists of the crease pattern that includes fixed rulings, mountain and valley folds. The crease pattern must be constructed at the beginning of the design process.

### Historical references and precedents
Huffman drew what I call 'refraction gadgets' for his designs. He interpreted rays in optics as rulings and exploited the refractive properties of the conics
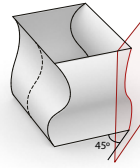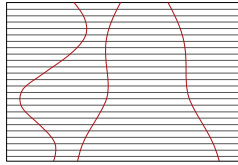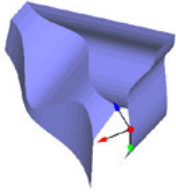
**Figure 5.** 3D model in ORI-REF, crease pattern (Ashley Hickman).



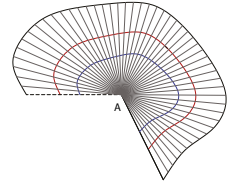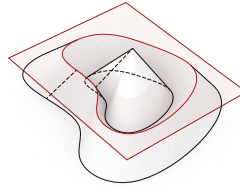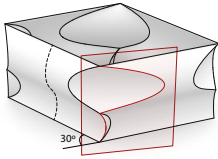**Figure 6.** 3D model in Rhno3D with reflection plane, crease pattern (Kalliopi Oikonomou).



**Figure 7.** 3D model with two reflection planes per corner, crease pattern (DK).



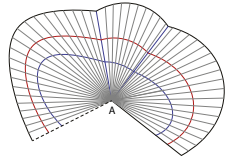**Figure 8.** 3D model of cone with two horizontal reflections, crease pattern (Ashley Hickman).
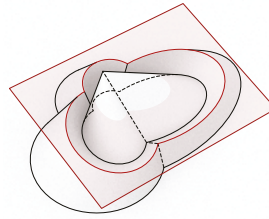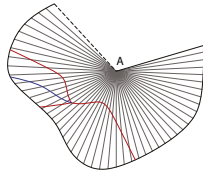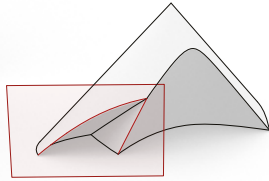


**Figure 9.** 3D model of cone with two vertical reflections, crease pattern (Kalliopi Oikonomou).



**Figure 10.** 3D models of cone reflections with two reflections, crease pattern (Kalliopi Oikonomou).

to redirect the rulings. The three available curves are ellipses, parabolas and hyperbolas and he drew all available refraction cases (Fig. 11). The diagrams on the left show how rulings get refracted, if they start in the focal point of a hyperbola, parabola, or ellipse. The cases on the right display inversions of the corresponding examples.

The foci of a hyperbola can be used to refract rays on either side of the curve (on the left). Rulings can be made to fan out on both sides of the curve (on the right). Parallel rays on the concave side of a parabola refract toward its focus (on the left). The inverse configuration pushes rulings away from the focus (on the right). Rays converging towards one focus of an ellipse get refracted to the second focus (on the left). The roles of the foci are inverted (on the right).

A rare hand-drawn sketch reveals that Huffman has the rulings in mind when designing a new model (Fig. 12 left). Huffman uses the corresponding gadget for the inner ellipse (Fig. 12 right) four times in one of his final designs (Fig. 13).

His approach can be seen as a constraint propagation system, in which 'the paper is the computer'. He sets up his designs the way a computer scientist would, namely, as a problem to be solved. Every crease pattern has the equivalent to a base case or initialisation procedure of an algorithm, in which the rulings have to follow an initial rule. He assigns the refraction scheme that will get executed on the first crease and then lets the individual rays follow the constraints given by all consecutive curves.

### Definition of the design approach

I expand on Huffman's interpretation of optics by asking a designer to use any of the gadgets and to subsequently simulate them using FreefromOrigami. A designer can alter and/or tessellate any of the gadgets. The design can be folded in software in real-time.

Many cases for which Huffman might have had a wrong mathematical conjecture can be used for simulation. The discrete representation is an approximation and thus does not necessarily follow mathematical constraints. Additionally, folding physical paper is more forgiving than its mathematically defined equivalent. The flexibility of the material allows us to create models of ill-defined mathematical foldings. This means that all of Huffman's gadgets are available for designers to explore and experiment with.

The designs produced by Kalliopi Oikonomou in my seminar consist of refraction gadgets with ellipses, parabolas, and hyperbolas. In the first example, a single ellipse is divided into two parts, one used as mountain and the other as valley (Fig. 14).

The figure below shows two examples with the same parabola gadget. A cylindrical configuration could be achieved in the bottom example (Fig. 15). The last example in this section consists of a regular tiling made with a hyperbola gadget (Fig. 16).
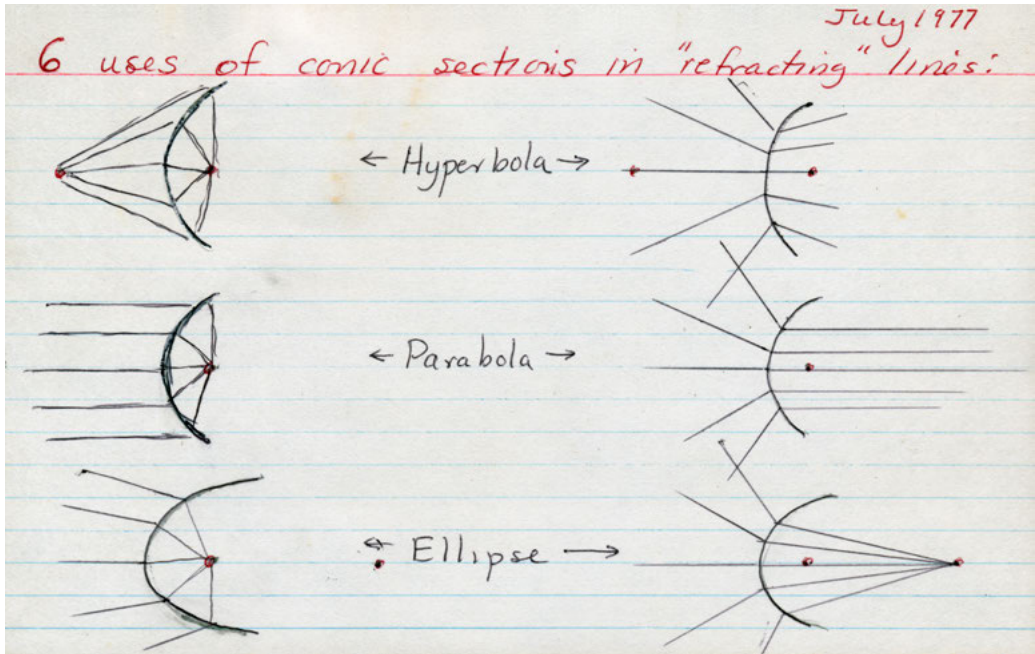
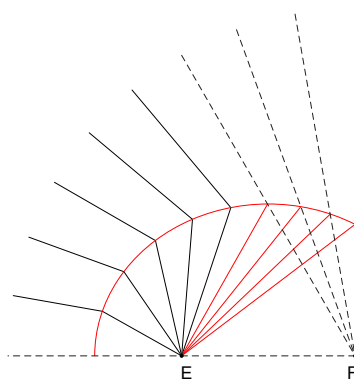**Figure 11.** Refractive properties of conic sections (1977, DAH, David A. Huffman archive).



**Figure 12.** Sketch (undated, DAH, David A. Huffman archive), Gadget (DK).

## 2.3 Drawing Closed and Open Curves

### Geometry and design representation
Designs with closed curves should consist of concentric curves and should have a hole in the centre. Recent results suggest solutions for concentric circles (Dias & Santangelo 2012). Designs based on free-hand scored curves have no constraints on curves, but they may not be foldable. No practical discrete representation exists for software, so the design approach has to be partially analogue. The models could be 3D scanned and post-rationalised using sophisticated algorithms (Kilian et a. 2008), but this might prove to be cumbersome, if it was to be part of a design process. The direct analogue representation consists of the curves drawn on the model one uses.

### Historical references and precedents
Josef Albers introduced 'The Bauhaus model' (Fig. 17 left) in his design foundation course in 1927 (Wingler 1978). Erik and Martin Demaine started to explore the model in 1998 and have made variations of it since then. Kunihiko Kasahara published his version with more creases in 2002 (2003). The model was used either as single module or in an aggregation (Fig. 17 right). It was also expanded beyond 360° with multiple joined discs (2006). In 2008 further variations of the model used quadratic curves in addition to circles (Koschitz, Demaine & Demaine 2008). Regarding curves that intersect each other, T. Roy Iwaki (2010) created a small booklet that provides a rare instance of an artist sharing his methods. He used a 'base mask', which he then modified to design specific facial features of the animals he wants to portray (Fig. 17 right). Iwaki worked from one crease to the next and allowed the paper to assume a 'natural' folded state before making a decision about the next step. He might have forced the paper on one side of the crease, but not the other, for example.

### Definition of the design approach
Regarding self-closing curves, a designer can draw any set of 'vaguely concentric' curves in CAD software. The configuration requires a hole at the centre. Regarding intersecting curves, a designer can score curves directly on a piece of paper. Every crease should be folded and evaluated prior to moving on to the next crease, if s/he wants to avoid crinkles.

Aleksandra Chechel uses concave and convex curves in 2d in CAD software in my seminar (Fig. 18). The series investigates self-closing curves with two, four, and five eccentricities. In some cases, the curves are convex only, in other cases the curvature changes direction. Once the paper has been pre-creased with a vinyl cutter, the final model is folded by hand. An important characteristic of this design approach allows designers to explore the degree to which a model can be folded. Some crease patterns fold very well and provide excellent examples to study folding motion and moving rulings.
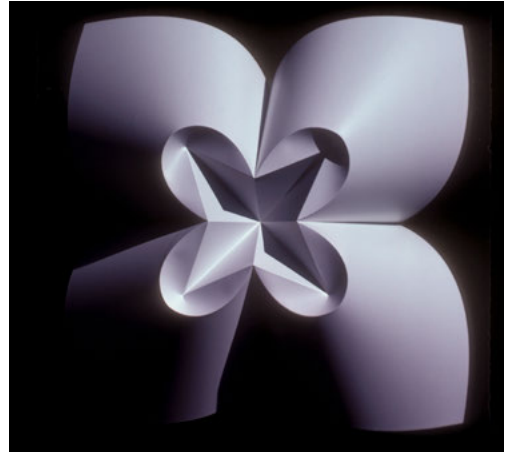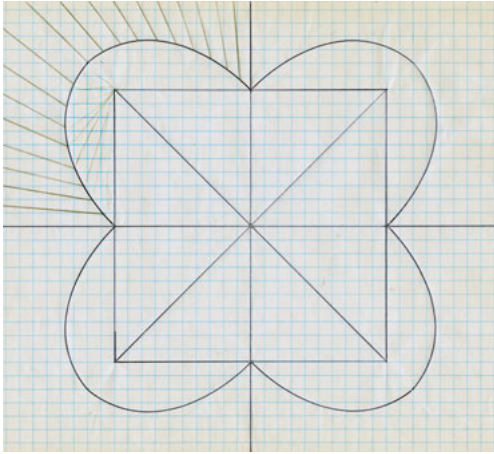
**Figure 13.** '4-lobed, cloverleaf, design' (undated, DAH), Vinyl model (1977, DAH, David A. Huffman archive).
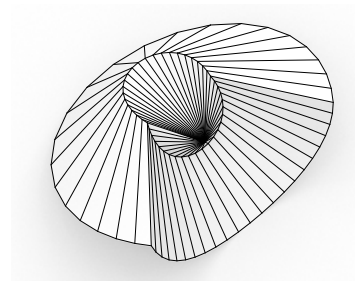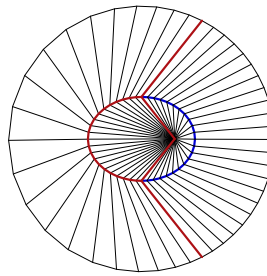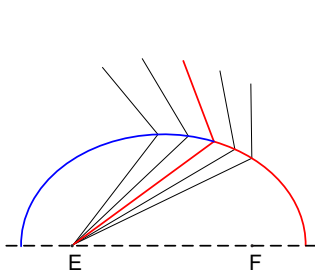


**Figure 14.** Ellipse gadget, crease pattern, simulation (Kalliopi Oikonomou).

Ashley Hickman, another student in my seminar, used the design approach with intersecting curves and simply started by making a model with several creases rather than working from one to the next (Fig. 19). She made new decisions about altering regions of paper that are wrinkled by marking options for creases in red. She subsequently folded the marked creases in the next iteration and repeats these steps until the result is satisfactory. Other students followed the initial suggestion of working step-by-step and achieved similar results.

## 2.4 Sculpting and Post-rationalising Surfaces

### Geometry and design representation

For this design approach creases and paper surfaces are created through an iterative analogue process similar to Iwaki's approach. No curve types or surface types can be defined in any practical way. Similar to the previous design approach, 3D-scanning and analytically deriving an appropriate mathematical model would slow down the process significantly. The indirect analogue design representation consists of re-constructed crease patterns on the folded model.

### Historical references and precedents

'The Ron Resch Paper and Stick Film' (Resch 1968) features a sequence in the beginning, in which he explains how he discovered paperfolding for himself. He starts with a sheet of brown paper on a table and slowly crumples it while pushing it down to the table with his fingers. Once he has achieved a desired folded shape, he flattens it, and draws simplified versions of the creases with a pen (Fig. 20). He modifies the crease pattern and tries to find regularities to eventually create tilings made of straight creases. Gregory Epps, a British designer and curved folding expert, has published similar ways of post rationalising creases (Vysivoti 2008).

### Definition of the design approach

I extend Resch's approach by using curved creases and developing a notational system to keep track of changes. The process starts with crumpling or sculpting a sheet of soft paper or felt into a desired shape (Fig. 21 and 22). A designer then marks mountains and valleys and subsequently flattens the sheet to digitize the crease pattern. The digital image needs to be traced with vector-based software. The designer can use vinyl cutters to pre-crease paper with the digitised version of the marked scan. As the model may not fold the way a flexible material might, a designer might have to go through several iterations of this process until s/he obtains a desirable result.

During my seminar, UnJae Pyon and Lauren Greer sculpt a desired shape and then mark mountain and valley creases with two different colours (Fig. 21 centre). I asked them to use a notational system that would allow them to document the
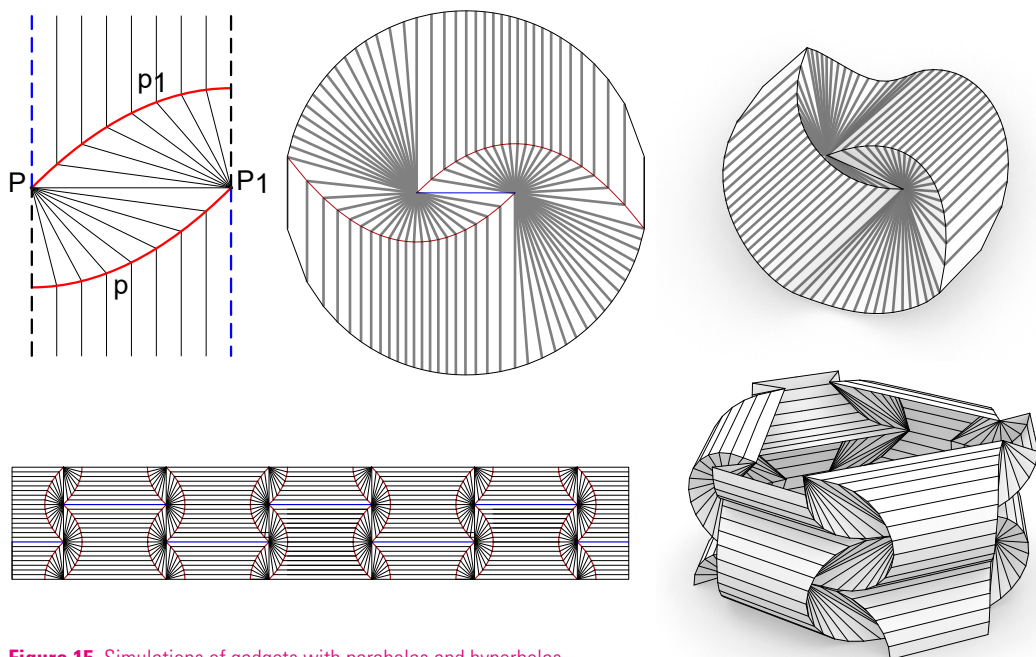
**Figure 15.** Simulations of gadgets with parabolas and hyperbolas, crease patterns (Kalliopi Oikonomou).
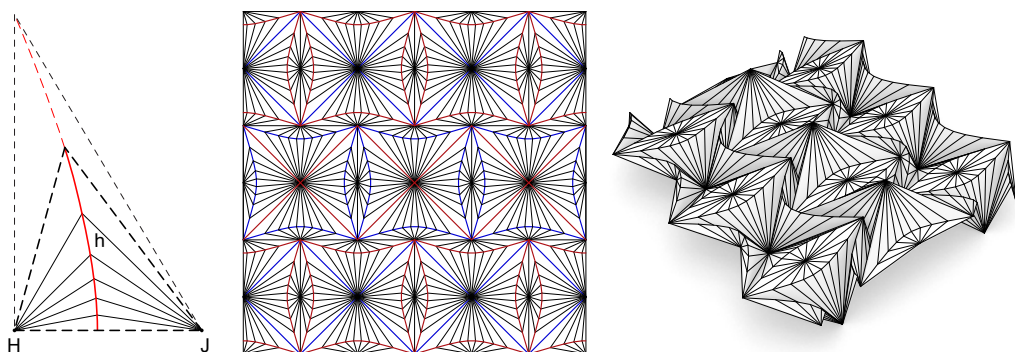


**Figure 16.** Simulations of gadgets with parabolas and hyperbolas, crease patterns (Kalliopi Oikonomou).
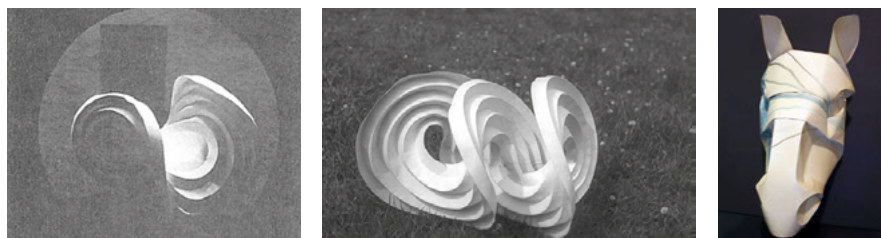


**Figure 17.** Bauhaus model, extended discs (Josef Albers Foundation), Horse head (Roy Iwaki).

necessary finger motion, if they needed to recreate the model. They photograph the drawn crease pattern in its flat state (Fig. 21 right).

The next step consists of transferring the crease pattern to CAD software (Fig. 22 left). Further steps involve making new models in paper or plastic and continuously refining the crease pattern until the paper finds an (almost) ideal configuration (Fig. 22 right).

# 3. Results and Analysis

The workshops and seminars yielded interesting observations that might be useful for instructors and designers in general. The table below shows the relationships between the design approaches and their characteristics (Fig. 23). The proposed design representations aid in identifying how a designer can work with the given constraints of the design approaches. The presented results include a brief summary of the design approach and used tools, a comment on the design process, issues relative to scalability and notes on design pedagogy.

Because developable surface reflection uses well-known configurations of cones cylinders and tangent surfaces, 3D models can easily be made with CAD software. The designer is visually confronted with the result of every cut while working on the computer, which provides constant visual feedback during this step-by-step process. The crease pattern is usually only necessary for production. Physical models can be made easily, and scaling should not be an issue. Formal explorations are limited as the designer is bound by the initial developable surface. In terms of design pedagogy, only little knowledge in geometry is required and there is no element of surprise in this approach.

In refraction gadgets the designer needs to be in full command of the crease pattern as it is designed first. The opportunity for designers lies in using simulation software to observe the folding process in real-time. The constraints produce cylinders and cones, but no tangent surfaces. The smaller mathematical solution space reduces opportunities for expressive designs as the rulings are forced to remain in their relative position, which is not how paper folds. Additionally, tangent surfaces are not represented in the gadgets. It is unclear whether this approach would scale well. The simulation may result in ill-defined surfaces, and one may have to rely on the elasticity of materials to realize these designs. The design approach is very systematic and demands a moderate level of knowledge of geometry. As a result, mastering the approach might only be suitable for a more computationally inclined designer. The exploratory potential of the design approach lies in trying out different kinds of tilings and in some cases using more or less curvature for the folded model.

For drawing open and closed curves a designer needs to draw simple curves. The direct analogue representation consists of the crease pattern that has to be
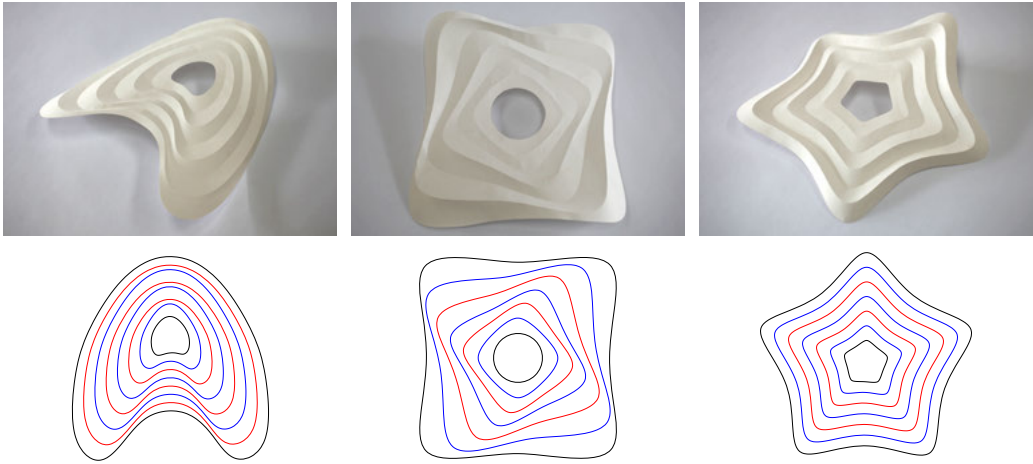
**Figure 18.** Designs with self-closing curves with varying degrees of curvature (Aleksandra Chechel).



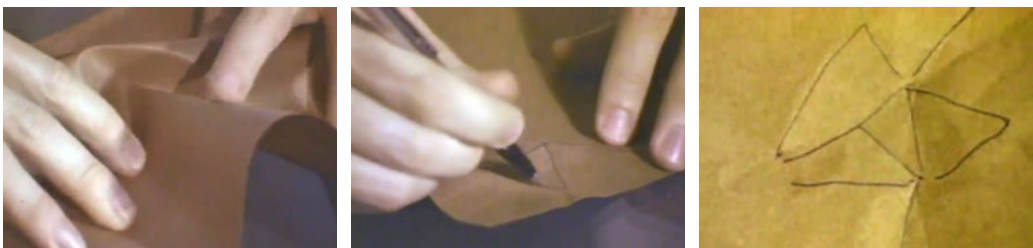**Figure 19.** Iterations of a design made with intersecting curves (Ashley Hickman).



**Figure 20.** Images from The Ron Resch Paper and Stick Film (1968, Ron Resch).

constructed at the beginning of the design process. The approach suits design-ers who are interested in tactile interaction with paper. Scaling is problematic for closed curves. The process does not require any a priori knowledge in geometry, but a designer will need to be very patient in order to master this design approach. Probably many hundreds of hours of practice are needed to gain the experience to control the shapes and their precision. It is hard to predict the folded state, and this element of surprise can raise curiosity and make the process of mak-ing a model engaging for a student. The design approach is surprisingly difficult to learn and qualifies to teach many aspects of curved creases such as folding motion and moving rulings.

With sculpting and post-rationalising surfaces one can explore designs very quickly. The indirect analogue design representation is used to cope with material constraints in a playful way. The crease pattern has to be constructed differently whenever a new material is introduced in the design process. Scaling is possible only with much iteration. The resulting shapes of this design approach tend to be irregular and display great expressive potential. Sculpting paper of more flex-ible materials and defining a notational system is easy to learn. This is the least restrictive approach that does not require any a priori knowledge of geometry.

# 4. Conclusion

The mathematical behavior of curved creases cannot be fully described yet, re-sulting in a lack of available digital tools. Designing with curved creases can oc-cur in several ways, and I propose four design approaches, two digital and two analogue, that can help designers to make curved-crease paperfoldings. Refer-ences in the history of curved creases can help in defining alternative design approaches and adhering to categories in geometry is useful in some cases.

Regarding digital design approaches, designers can easily explore cones, cylinders, and tangent surfaces. The proposed refraction gadgets can be used for simulation, but expressive explorations are difficult. It is unclear which crease patterns have well-defined surface configurations.

Analog design approaches provide the potential for formal exploration, but rely on tacit knowledge rather than a priori geometric knowledge. In these cases, it is beneficial to combine the process of making models by hand with digital tools.

The evaluation of the design approaches via characteristics and design rep-resentations may help designers who want to use this subset of geometry. Elu-cidating the limitations and constraints of the design approaches may identify future work and open problems.
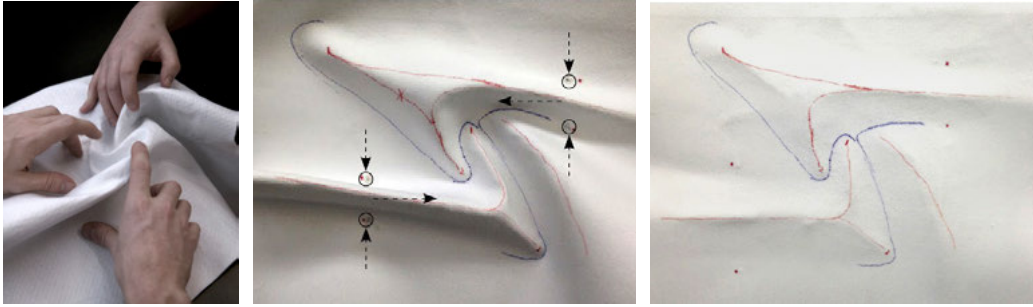
**Figure 21.** Sculpting, Notation of pinching, Crease pattern (UnJae Pyon, Lauren Greer).
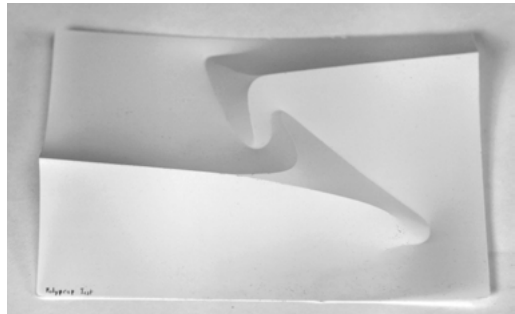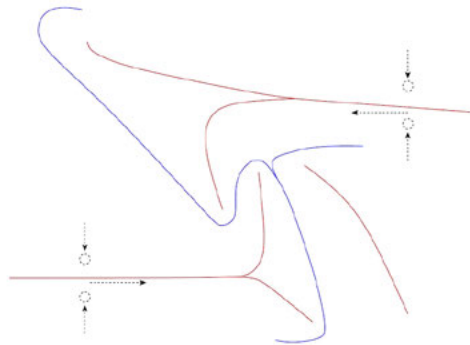


**Figure 22.** Sculpting, Notation of pinching, Crease pattern (UnJae Pyon, Lauren Greer).

| | top-down / bottom-up | knowledge of geometry | material driven | digitally driven |
|---|---|---|---|---|
| **Developable Surface Reflection** | partially top-down | medium | no | yes |
| **Refraction Gadgets** | both | high | no | no |
| **Drawing Open and Closed Curves** | bottom-up | low | yes | can be |
| **Sculpting and Post-rationalizing Surfaces** | can be top-down | low | yes | partially |

**Figure 23.** Design approaches in comparison.

# References

Demaine, E. D, M. L Demaine, David A. Huffman, Duks Koschitz, and Tomohiro Tachi. 2014. *Designing Curved-Crease Tessellations of Lenses: Qualitative Properties of Rulings*. Forthcoming.

Demaine, E. D, M. L Demaine, Duks Koschitz, and Tomihiro Tachi. 2011. "Curved Crease Folding: A Review on Art, Design and Mathematics." In *Taller, Longer, Lighter – Meeting Growing Demand with Limited Resources*. London, UK: (IABSE-IASS 2011 London Symposium Report).

Demaine, Erik, and Martin Demaine. 2010. "History of Curved Origami Sculpture." Accessed at http://erikdemaine.org/curved/history/

Dias, Marcelo A., and Christian D. Santangelo. 2012. "The Shape and Mechanics of Curved Fold Origami Structures." *EPL (Europhysics Letters)* 100, 5: 54005. doi: 10.1209/0295-5075/100/54005

Fuchs, Dmitry, and Tabachnikov, Sergei. 1999. "More on Paperfolding." *The American Mathematical Monthly* 106, 1: 27–35.

Geretschlaeger, Robert. 2009. "Folding Curves." *Origami* 4: 151–64.

Guest, S.D., and S. Pellegrino. 1992. "Inextensional Wrapping of Flat Membranes." *First International Conference on Structural Morphology*, Montpellier, R. Motro and T. Wester, Eds., 203–15.

Herok, Tim. 2002. "Foldtex_think Around the Corner: 'Liegengenerator.'" Accessed at http://foldtexdesign.blogspot.com/2009/09/liegengenerator.html

Horowitz, F. A., 2006 "Albers as a Teacher". In Frederick A. Horowitz and Brenda Danilowitz, Josef Albers: *To Open Eyes. The Bauhaus.* Black Mountain College and Yale. N. Y. and London: Phaidon

Huffman, David A. 1976. "Curvature and Creases: A Primer on Paper." *IEEE Transactions on Computers* 25, 10: 1010–19.

Iwaki, T. Roy. 2010. *The Mask Unfolds. Cavex Round Folding*. Artisans Gallery. Accessed at http://www.caroladrienne.com/roy_iwaki/the_NEW_FOLD/THE_MASK_UNFOLDS.html

Kasahara, Kunihiko. 2003. *Extreme Origami*. New York: Sterling.

Kergosien, Yannick L., Hironoba Gotoda, and Tosiyasu L. Kunii. 1994. "Bending and Creasing Virtual Paper." *IEEE Computer Graphics and Applications* 14, 1: 40–48.

Kilian, Martin, Simon Flöry, Zhonggui Chen, Niloy J. Mitra, Alla Sheffer, and Helmut Pottmann. 2008. "Curved Folding." In *ACM SIGGRAPH 2008 Papers*, 75: 1–75:9. SIGGRAPH '08. New York, NY, USA: ACM. doi: 10.1145/1399504.1360674

Klanten, Robert, Sven Ehmann, and Matthias Hubner. 2007. *Tactile: High Touch Visuals*. Dgv.

Klint, P.V. Jensen. 1943. "P.V. Jensen Klint/Le Klint Lighting." Accessed at www.ylighting.com/search/field_brand/brand-23242

Koschitz, Duks, Erik D. Demaine, and Martin Demaine. 2008. "Curved Crease Origami." In *Advances in Architectural Geometry*, 29–32. Vienna, Austria.

Koschitz, Duks. 2013. *Computational Design with Curved Creases: David Huffman's Approach to Paperfolding*. Dissertation Massachusetts Institute of Technology.

Lalvani, Hashesh. 2003. "Bend the Rules of Structure." *Metropolis Magazine* June 2003. Accessed at http://www.metropolismag.com/html/content_0603/mgo/

Mitani, Jun. 2009. "A Design Method for 3D Origami Based on Rotational Sweep." *Computer-Aided Design & Applications* 6: 69–79. doi: 10.3722/cadaps.2009.69-79

Mitani, Jun. 2011. "ORI-REF: A Design Tool for Curved Origami Based on Reflection." Accessed at http://mitani.cs.tsukuba.ac.jp/ori_ref/

Mosely, Jeannine. 2008. "Curved Origami." *ACM SIGGRAPH 2008 Art Gallery*, 60–61. SIGGRAPH '08. New York, NY, USA: ACM. doi: 10.1145/1400385.1400421

Mosely, Jeannine. 2009. "Surface Transitions in Curved Origami." *Origami 4*, edited by Robert J. Lang, 143. AWellesley, MA: A K Peters Ltd.

Nolan, J.C. 1995. *Creating Origami, An Exploration into the Process of Designing Paper Sculpture*. Haverhill, MA: Alexander Blace & Co.

Resch, Ron, and Ephriam Cohen. 1970s. *Untitled*. (David A. Huffman Archive).

Resch, Ron. 1968. "The Paper and Stick Film." Accessed at http://ww2.ronresch.com/

Resch, Ron, Robert E. Barnhill, and Richard F. Riesenfeld. 1974. "The Space Curve as a Folded Edge." *Computer-Aided Geometric Design*, 255–258. Sand Francisco: Academic Press, Inc.

Schein, Markus. 2002. "Applied Generative Procedures in Furniture Design." In *Proceedings of the 5th International Conference GA 2002*.

Schmidt, Petra, and Nicola Stattmann. 2009. *Unfolded: Paper in Design, Art, Architecture and Industry.* Basel, Boston, Berlin: Birkhäuser.

Shelden, Dennis R. 2002. *Dissertation: Digital Surface Representation and the Constructibility of Gehry's Architecture.* Massachusetts Institute of Technology.

Smith, Raven. 2009. *Paper: Tear, Fold, Rip, Crease, Cut.* London: Black Dog Publishing.

Sternberg, Saadya. 2009. "Curves and Flats." *Origami 4*, edited by Robert J. Lang, 9–20. Wellesley, MA: A K Peters Ltd. A K Peters Ltd.

Tachi, Tomohiro. 2013. "Designing Freeform Origami Tessellations by Generalizing Resch's Patterns." *Journal of Mechanical Design* 135, 11: 111006–111016. doi: 10.1115/1.4025389

Thomas, Jane, and Paul Jackson. 2001. *On Paper: New Paper Art. illustrated edition.* London: Merrell Holberton.

Trebbi, Jean-Charles. 2008. *L'art Du Pli – Design et Décoration.* Paris: Editions Alternatives.

Vysivoti, Sophia. 2008. *Supersurfaces* (4th ed.). Amsterdam: BIS Publishers.

Wertheim, Margaret. 2004. "Cones, Curves, Shells, Towers: He Made Paper Jump to Life." *New York Times*, June 22. Accessed at http://www.theiff.org/press/NYThuffman.html

Wingler, Hans M. 1978. *Bauhaus: Weimar, Dessau, Berlin, Chicago.* Cambridge: MIT Press.

# A Double-Layered Timber Plate Shell

## Computational Methods for Assembly, Prefabrication, and Structural Design

Christopher Robeller, Mina Konakovic, Mira Dedijer, Mark Pauly, and Yves Weinand

C. Robeller, M. Dedjijer, Y. Weinand
Laboratory for Timber Constructions (IBOIS), EPFL, Switzerland

christopher.robeller@epfl.ch ✉
mira.dedijer@epfl.ch ✉
yves.weinand@epfl.ch

M. Konakovic, M. Pauly
Computer Graphics and Geometry Laboratory (LGG), EPFL, Switzerland

mina.konakovic@epfl.ch ✉
mark.pauly@epfl.ch

# Abstract

This paper presents a new lightweight construction system for doubly-curved shells, built from two interconnected layers of structural wood veneer plates. The system uses integral through-tenon joints for a fast, precise, and simple assembly, allowing for the construction of a series of differently shaped shells without a costly mould or support structure. Instead, inclined joints cut with a 5-axis CNC milling machine embed the correct location and angle between plates into the shape of the parts. This constrains the relative motions between joined parts to one assembly path. To take advantage of the benefits of such connectors, the constrained assembly paths must be considered in the fundamental design of the system, allowing for the insertion of each plate. This imposes additional constraints in the segmentation process of doubly-curved shells. In order to meet the requirements and resolve the multi-constraint system, we use a global, non-linear optimisation approach. Developed as a close collaboration between architects, computer scientists and structural engineers, the paper includes an experimental analysis of the influence of parametric modifications in the shape of connectors on their load-bearing performance.

# 1. Introduction

The use of CNC-fabricated integral joints, such as through-tenons and dovetails, is a common technique in modern timber-frame constructions with linear members such as beams and posts. These connectors allow for a fast, precise, and simple on-site assembly, taking advantage of prefabrication technology, reducing and replacing increasingly expensive manual labour.

An innovative application of such joints is the construction of freeform timber plate structures, which have been the subject of recent research in the field of architectural geometry. Examples are the single-layered and double-layered Timbeer Folded Plate Structures (Robeller & Weinand 2015) (Robeller & Weinand 2016b) or the ICD/itke Landegsgartenschau Pavilion (Krieg et al. 2015) (Li and Knippers 2015). In such designs, structurally beneficial curved or folded shapes are constructed from hundreds or thousands of small and individually shaped, planar plates, made from cross-laminated wood panels such as laminated veneer lumber (LVL).

The design and fabrication of such structures is made possible by CAD programming interfaces and automatic fabrication technology. However, the assembly of the parts on site is still carried out manually. Locator features, which constrain the relative movements of parts to only one possible assembly direction (1DOF) are crucial for a fast and precise assembly of such complex designs. They allow reducing or completely replacing the need of costly support structures or moulds that prescribe the shape of the freeform structure.

In addition to the improved assembly, the previous research projects have also demonstrated that integral joints can be used to transfer forces between the plates, reducing or replacing additional connectors such as screws or nails.

This paper builds upon the previous research, demonstrating a new construction system for a double-curved shell structure built from two interconnected layers of thin LVL panels, assembled entirely with 1DOF closed-slot joints. The construction system with two thin layers takes particular advantage of the new possibility for the edgewise connection of thin plates with integral joints.
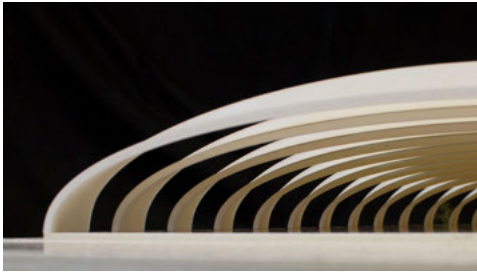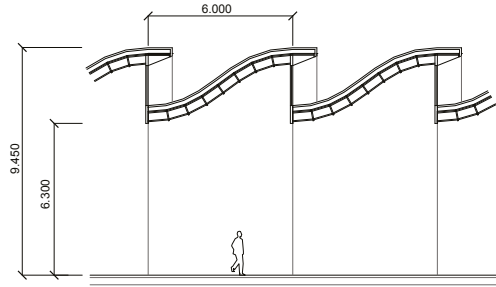
**Figure 1.** Interior view and cross-section schematic.

# 2. Project Description

The construction for a timber prefabrication facility covers an area of 5,800 m² with a series of 23 discontinuous shells, each 6 m wide and 9 m high (Fig. 1). In the transversal direction of the shells, an s-shaped cross-section curve introduces a second curvature which prevents buckling, the expected mode of failure for such a structure (Pedreschi and Theodossopoulos 2007).

The design was inspired by the famous *Gaussian Vault* masonry roof structures of the Uruguyan architect and engineer Eladio Dieste, such as the TEM factory in Montevideo, Uruguay, 1960-1962, and the Caese Produce Market in Porto Alegre, Brazil, 1969-1972 (Anderson 2004).

In addition to the structural advantages of the doubly-curved shape, it is also essential for the architectural concept. Multiple, successive shells with such a cross- section create an overlap in between, which is used as a clerestory for the natural lighting and shading of the building, much like the sawtooth roofs of 19th-century factories. However, in contrast to the Dieste's structures, where a series of shells with the same shape was built through the repetitive use of a single mould or template, our project requires the construction of 23 individually shaped shells. This is both due to the shape of the building site, which is not rectangular but obtuse trapezoidal, and the architectural program, merging from a single-story factory space on the southern wide end into a triple-storey office area at the narrow northern end of the site (Figures 2 and 3).

The span of the shells ranges from 22.5 m in the smallest, to 53.7 m in the largest shell. The cross-section profile in this main direction of loading is a compromise between the architectural program and a structurally optimised shape. With a span-to-rise ratio of 2.5-6, it deviates from the catenary line, which Dieste used for his masonry roofs (with a span-to-rise of 8-10), mostly in the first 4 m from the ground plane. Here our shells are tangential to the vertical axis, reducing horizontal forces on the supports.
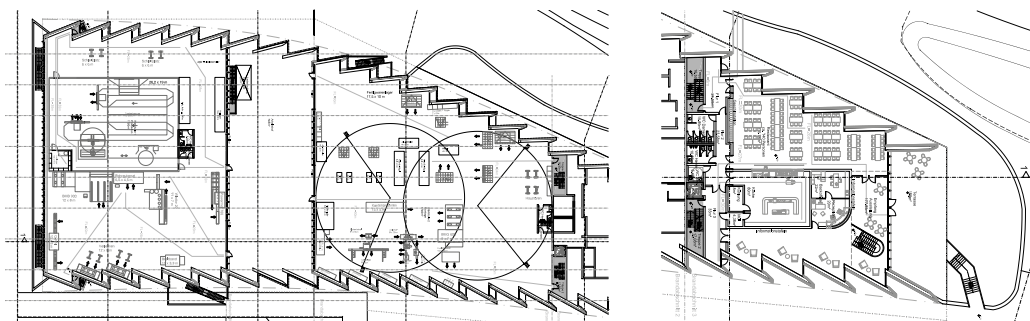
**Figure 2.** Floor plans left: production spaces, right ground floor offices.

# 3. Construction System

Our system consists of two layers of thin plates, instead of one thick layer, taking advantage of our joints' ability to connect thin plates, which already provide a high strength but are difficult to join with conventional fasteners such as screws.

A double-layered prototype was demonstrated in the ICD/itke Research Pavilion 2011 (la Magna et al. 2013), where prefabricated polyhedra made from wood veneer plates with finger joints (3DOF) were assembled to a spatial structure. In contrast to this project, our system uses 1DOF integral joints not only within segments/modules (in the previously mentioned project, prefabricated modules where joined with metal connectors), but between all of the plates, in order to take advantage of the locator and connector features everywhere in the structure.

Figure 4a shows our construction system, which approximates the curved target surface with hexahedra-shaped segments $S_i$, each consisting of four plates. Each segment is based on a centre point $P_i$ and a normal vector $n_i$. A combination of multiple parameters in the system allows for the rotation between the normal vectors of neighbouring segments, which is required by the curvature of the target surface.

Within each segment, there are two shell plates, parallel to the segment plane, ($L1$ and $L2$) which form the two layers of the shell structure. Two additional vertical shear block plates $W0$ and $W1$ are used to transfer forces between the two layers of the shell. There are no plates for the remaining two vertical faces of the hexahedron, because these plates are shared with the neighbouring segments.

Figure 4b shows how a vertical plate supports the connection of the main layers of the shell: The intersection area of the three plates is divided into alternating segments, creating slots which receive the tabs of the shell plates. This allows for a direct contact between the shell plates for the transfer of compressive forces.
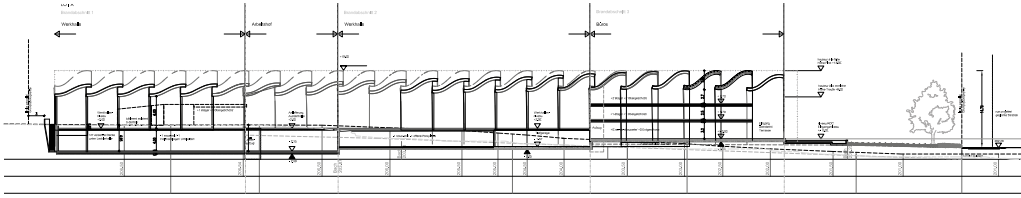
**Figure 3.** Cross-section through the building.

In between these slots and on the top and bottom face of all tabs, the vertical plate holds the shell plates.

The assembly of the segments follows their numbering. Figure 4 shows the assembly of segment $S_4$ in an $m * n$ matrix of segments. Within a segment, the shell plates are inserted first, along the segment's assembly vector $\vec{v}_i$. They connect simultaneously to the two shear block plates of the neighbouring segments $S_{i-1}$ and $S_{i-m}$. The slots in these neighbouring shear plates are oriented along $\vec{v}_i$, to receive the tenons of the shell plates $L1_i$ and $L2_i$.

## 3.1 Joints

Figure 4c shows a close-up view of the through-tenon joints that connect the shell plates. We have chosen these so-called closed-slot connectors, because they combine the benefits of dovetail joints with additional features. Like the dovetails, the shape of the through-tenon joint are kinematically classified as prismatic pins with slots, constraining the mobility of parts to one assembly motion path ($M = 1$) (Whitney 2004). This shape fully integrates a unique position of the parts within the structure and allows for a rapid and precise assembly.

While the 1DOF property is also provided by open-slot dovetail joints, through-tenon joints provide additional features for the transfer of forces. The bending strength of different types of multiple-tab-and-slot plate joints (MTSJ) has been compared by (Roche et al. 2015a), demonstrating that joints with a closed slot, also called through-tenon joints, combine the high shear strength of finger- and dove-tail joints (see Roche et al. 2015b) with a high bending strength.

Like dovetail joints, through-tenon joints connect plates in two planes. The average dihedral angle $\phi_{mean} = 6.5°$ between our shell plates is too small for the use of such joints. We solve this problem with the connection through the vertical
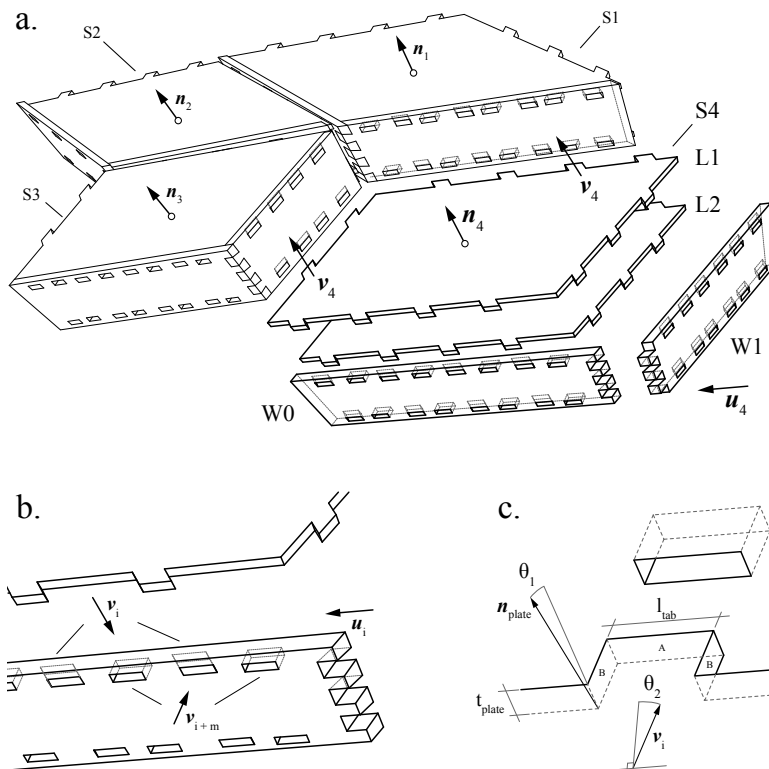
**Figure 4.** Construction system for a 2-layered shell,
a. assembly of 4-sided box segments,
b. alternating allocation of joint slots on shared vertical plates,
c. joint detail/rotations.

shear plates in between shell plates. This connection requires only a small rotation $\theta_1$ of the joint faces about the edge line (see Fig. 4c, faces marked A).

However, the assembly of our system requires a second rotation of the tabs $\theta_2$, about the normal vector of the plate, because we want to connect two non-parallel edges simultaneously, along the same direction $\vec{v}_i$.

This rotation $\theta_2$ has an influence on the shear strength of the joints, which we have analysed. Figure 5 shows our shear load test, where we have examined a joint with two tabs at a rotation $\theta_2$ from 10° to 40°, with the load applied in both directions. Graph 5b shows that the best shear strength is achieved at low rotations up to 25°, although the larger rotations of 25° to 40° also show a satisfying shear stiffness. Most specimen showed a brittle failure, while some specimen with angles larger than 30° showed a certain amount of hardening after the failure. The bottom graph shows the load/displacement behaviour in the linear elastic range of 10-40%.
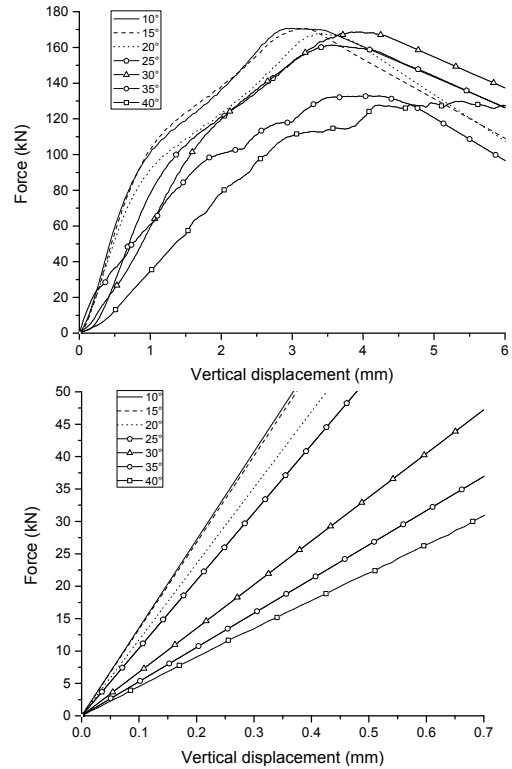
**Figure 5.** Experimental analysis of the influence of the tab rotation $\theta_2$ on the shear stiffness of the joints on 40mm cross-laminated LVL plates.
a. Load test setup
b. top: load/displacement curves for $\theta_2$ from 10° to 40°, bottom: linear elastic range (10-40%)

Figure 6 illustrates the contact surfaces between two 40 mm-thick shell plates, along an edge with a length of 1.65 m. Without integral joints, the contact area between these plates is 662 cm². In our system, neighbouring edges are slightly rotated, Figure 6 shows an example where this angle is $\kappa = 0.82°$. Without joints, this rotation reduces the contact area to 85.1%. With our integral joints (Fig. 6b), the frontal contacts (for the transfer of compression) are divided into a direct and indirect area. Through the front face of the tabs, plates are in direct contact on 222 cm² (33.5%). Additionally, an indirect contact of 383 cm² (57.5%) is established through the vertical shear plate, adding up to 605 cm² (91% of max area of two parallel edges). A distinction between the two areas is made because of the fibre-direction of the wood plates. The indirect compression is transferred normal to the shear plate, where the compressibility strength is reduced. (Fig.6, left)

Additionally, the joints provide a large contact area transversal to the edge. In Figure 6, there is an additional 220 cm² (+33%) across the plate surface, which

is relevant for shear forces, and 597 cm$^2$ (+90%) parallel to the plate, which is relevant for bending moments. The total contact area between the plates with joints is 1,422 cm$^2$ (214%).

## 3.2. Assembly-Constrained Tiling

For our assembly of multiple parts, where the mobility of each part is reduced to $M = 1$, we must find a solution where each part can be inserted without conflicts.

Additional constraints are that we want to insert each part individually, and we want to use the interlocking of elements to block the last degree of freedom of the parts with one another, avoiding long-range escape paths in the assembly, which allow for multiple segments to be detached simultaneously.

The assembly path $\vec{v}_i$ of parts is considered an *Escape Path* for the part. A part is considered *locally free*-, when the escape path of all of its connections have a common direction. In this case, the dot product of all escape paths is 1, assuming $\vec{v}_i$ as unit vectors. If this is not the case, the part is blocked and cannot be removed without prior removing other parts from the assembly. A second important situation is *global freedom*, also called long-range escape paths, where a group consisting of multiple parts can be separated from the assembly along one common direction.

Figure 7 illustrates the assembly of 4 x 2 quadrilaterals with different shapes. Figure 7a uses rectangles with prismatic pins perpendicular to their edges. In this assembly all eight pieces are locally blocked, meaning that no single element such as part *A* can be removed. In order to remove *A*, we have to either remove the four parts *E, F, G, H*, or we remove *A* together with part *E*, which shows the existence of a long-range escape path in this assembly. For our construction this pattern has two major disadvantages. The assembly of this configuration is only possible by first connecting all elements in the first row *A, B, C, D,* then connecting all elements in the second row *E, F, G, H,* and finally connecting the two groups. This means that, in the final step, the edges of four elements must be joined simultaneously, which is problematic due to the combined length of this edge, which needs to be kept parallel during the assembly. Also, tolerances of the parts themselves and caused by the connections within the two groups will make it difficult to assembly these two groups in one step.

These problems can be resolved through pins that are not perpendicular to the edges, but rotated to share one common direction per segment (Fig. 7b).

The required rotation of the pins $\theta_2$ can be obtained from the angle $\alpha$ between the edges which are connected simultaneously as $\theta_2 = 90° − (\alpha/2)$. For the array of rectangles shown in Figure 7b, all pins must be rotated at $\theta = 45°$. As discussed in Section 3.1, we want to avoid such large rotations on our joints.

We solve this problem through the use of *rhombus-shaped* elements, as shown in Figure 7c. With $\alpha = 135°$, we can reduce the rotation of the pins to 22.5°,

$\kappa = 0.82°$

a.

b.

direct    indirect

Frontal

Wood fibers

Transversal 1

Transversal 2
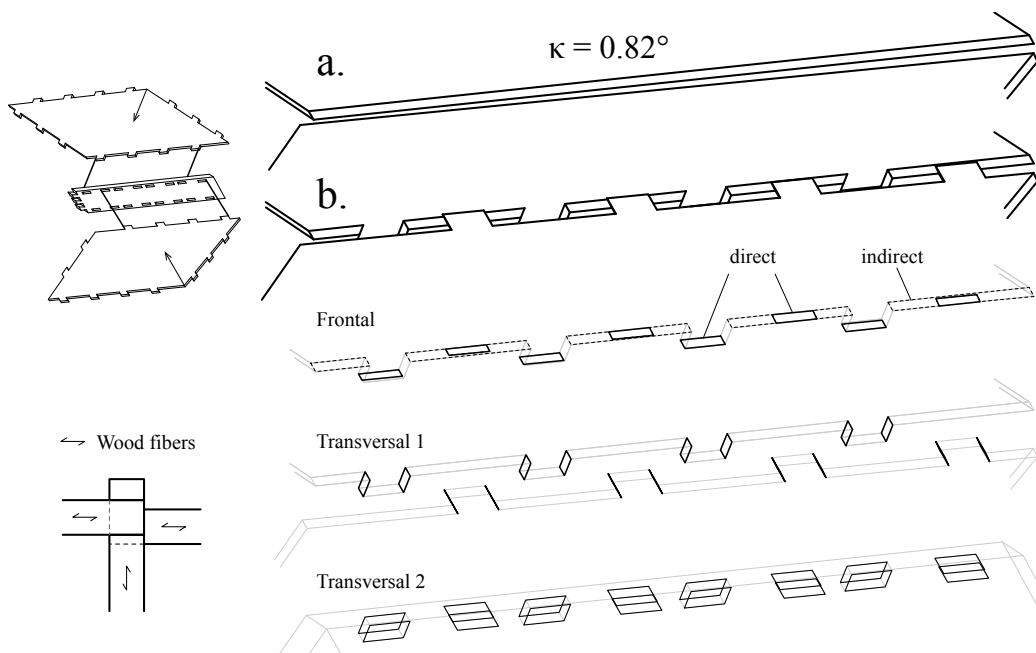
**Figure 6.** Contact area between two shell plates, without (a) and with joints (b).



a.

| A | B | C | D |
| E | F | G | H |

b.

| A | B | C | D |
| E | F | G | H |

$\theta_2$

c.

| A | B | C | D |
| E | F | G | H |

d.

| A | B | C | D |
| H | G | F | E |

$\theta_2$

**Figure 7.** Comparison of different patterns from a point of view of assembly and transfer of forces:

a. rectangular elements with pins perpendicular to the edges,

b. rectangular elements with parallel pins,

c. rhombus-shaped elements with parallel pins,

d. rhombus-shaped elements with parallel pins, alternating orientation for every second row (Herringbone Pattern).

**Figure 8.** Left: Isometric view of the first shell. The length of the blue lines illustrates the curvature of the rail curves in main direction of loading. Right: Tiling of the first shell.

half of the previous value using rectangles. However, while this configuration allows us to assemble the array piece by piece, and the shape of the elements greatly reduces the required rotation of the pins, all three configurations shown in Figure 7a,b,c share a common problem of multiple long-range escape paths.

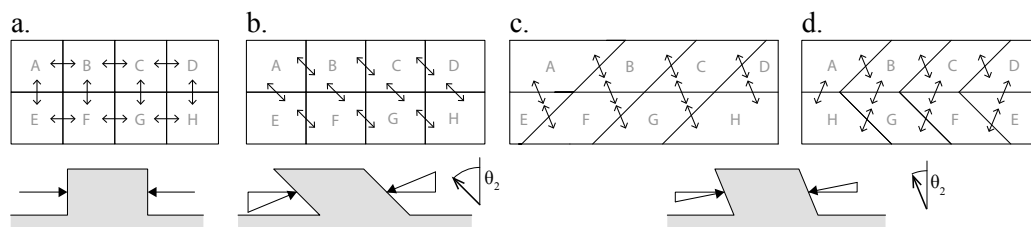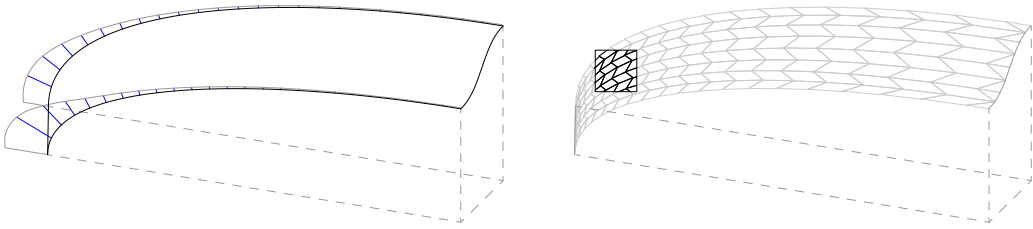This problem is greatly reduced by the *fishbone* pattern configuration in Figure 7d, where every second row of the rhombus shaped elements is mirrored. In consequence, the assembly direction is also reversed in all mirrored rows.

Except for the last row, all elements in such a configuration are connected with multiple pins with different directions, similar to the configuration a., but with the possibility of piece-by-piece assembly and without any escape paths in the vertical direction.

## 3.3  Application to Target Surface

In order to create a two-layer shell structure, we first need to segment a given design surface. To apply the previously chosen tiling pattern to our doubly curved target surface, we use a first algorithm to generate the basic pattern through the evaluation of a point grid on a NURBS surface.

We gradually increase the density of this point grid in the main direction of loading, starting with a quadratic 500 x 500 mm segment on the ground plane, with a linear increase to a maximum segment size of 500 x 2,500 mm at the top of the shell. This relates both to the increased curvature on the lower end of the shells (see the curvature graphs in Fig. 8), as well as the increased loads in this area. With this subdivision, we obtain a quad mesh for each shell, with 312 faces on the first shell, and 216 faces on the last one.

Each quad mesh of this basic pattern lies exactly on the target surface, but the quadrangular faces are not planar. Unlike in constructions with glass or metal panels, where a certain amount of non-planarity is permissible, we require very

Table 1: optimisation trade-offs

| Optimisation | A | B | C | D | E |
|---|---|---|---|---|---|
| Average kappa angle | 2.05° | 1.9° | 1.7° | 1.3° | 1.03° |
| Maximal kappa angle | 6.93° | 5.5° | 5.1° | 4.4° | 3.72° |
| Average alpha angle | 121.4° | 118.7° | 116.9° | 112.4° | 110.6° |
| Minimal alpha angle | 106.5° | 105.4° | 102.1° | 100.1° | 100.3° |
| Average surface deviation | 13.5 mm | 30.9 mm | 38.6 mm | 42.3 mm | 46.2 mm |

close to 100% planarity of the segments, due to the high rigidity of the 40 mm thick structural wood veneer panels (LVL) that we use for our construction. These plates do not allow for any significant bending or twisting.

Planar quad meshing has recently been an active area of research, see (Pottmann et al. 2015) for an overview. A common approach relies on the fact that planar quad meshes can be interpreted as discrete versions of conjugate curve networks (Liu et al. 2006). Such methods therefore optimize for the alignment of mesh edges with discrete approximations of conjugate curves. In our case study, however, the chosen tiling pattern in general does not follow conjugate directions. To overcome this problem, we do not represent our plate structure as a quadrilateral mesh, but as a collection of disconnected, but spatially coupled, planar elements. This introduces additional degrees of freedom for our global optimisation that tries to approximate the target surface as well as possible, while respecting all the fabrication and assembly constraints.

Our solution is based on the geometric optimisation framework proposed by (Bouaziz et al. 2012) and (Deuss et al. 2015). The core of this method is an iterative solver that minimizes a global non-linear energy function derived from a suitable chosen set of geometric constraints. A key feature is that constraints can be implemented via local projections that provide a modular mechanism to satisfy each constraint locally. A global step then reconciles all these local projections in a least-squares sense. Global optimisation distributes the error across the surface and thus significantly decreases locally undesirable behaviour, such as large angles κ between neighbouring edges (see Section 3.1). A comparison with a simple local optimisation approach that planarises each quad face independently is given in Figure 9.

Below we give a summary of the different constraints we use in our optimisation. These constraints are equipped with weights that allow balancing the trade-offs inherent in our over-constrained optimisation. Please refer to (Deuss et al. 2015) for a derivation of the constraints and a more detailed description of their

implementation. An open-source implementation of the solver may be found at http://shapeop.org/.

To optimise our plate assembly we use the following constraints:

- *Planarity* of the four vertices of each quadrilateral ensures fabricability. We use a high weight to respect the very high stiffness of the LVL plates.

- *Closeness* links the quads to the target surface. We set high weights for vertices on the boundary to match the site requirements. For interior vertices we use lower weights so that elements can adapt in size and shape, if necessary to satisfy fabrication and assembly objectives.

- *Angle bounds* the angles of each quad face to preserve the initial rhomboid shape and avoid rectangular faces.

- *Parallelogram* is used with a low weight for aesthetic reasons on the non-boundary elements.

- *Divergence* is a new constraint that we introduce specifically to handle our disconnected plate arrangement. This constraint couples adjacent plates by minimising the distance between neighbouring vertices. The projection operator for this constraint is simply given as the mean position of two vertices, applied on each pair of adjacent vertices as defined by the topology of the grid layout.

The global optimisation in Figure 10 and Table 1 reduces the average kappa angles $\kappa_{mean}$ by up to 50%, compared to the local optimisation. This is possible through a trade-off between multiple parameters. We allow for a controlled deviation from the base surface and for the alpha angles. Option C shows a balanced compromise, where $\kappa_{mean}$ is reduced by 17%. At the same time $\alpha_{mean}$ is well preserved with a loss of only 2.2% compared to the local optimisation (Option A), avoiding any negative effects on the mechanical strength of the joints.

We run the local-global solver that iterates between constraint projection and global linear solver for 50-200 iterations. The output of the solver is then fed into a second algorithm that creates the two-layer shell structure. We generate the four plates per face, based on local frames that we obtain from the disconnected quadrilaterals (Fig. 11). The frames show the mid-layer planes of the shear block plates W0: $e_1$, $e_3$ and W$_1$: $e_2$, $e_3$ and the insertion direction $\vec{v}_i = (e_1 + e_2)/2$. For the shell plate quads, one corner lies along $e_3$, while the other corners are found through an intersection with the shear block planes of the neighbouring segments. The final result is shown in Figure 12.
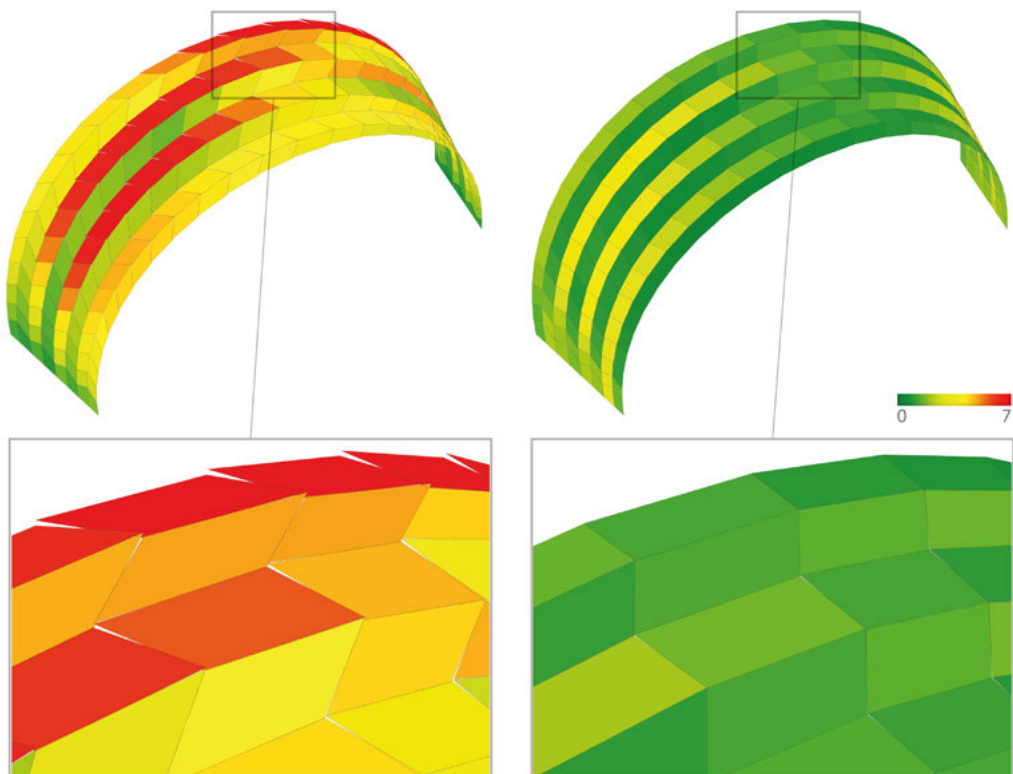
**Figure 9.** Comparison of a local and a global optimisation approach applied on the last shell. Quad faces are coloured according to a maximal angle $\kappa$ between the edges of neighbouring faces. The angle varies from 0 to 7 degrees. Left: By planarazing each face independently average $\kappa$ angle is 2.05 degrees and maximal $\kappa$ angle is 7. Right: Our global approach can reduce the average $\kappa$ angle to 1.03 degrees, and the maximal angle to 3.72.



**Figure 10.** Balancing the fabrication requirements with the optimisation. From left to right different optimisation results are given by controlling the weights of constraints. First row is the top view and the second row is the side view of the last shell. Meshes are coloured according to a maximal angle $\kappa$ between the edges of neighbouring faces. The comparison of $\kappa$ angle, $\alpha$ angle, and deviation from the target surface is given in Table 1.
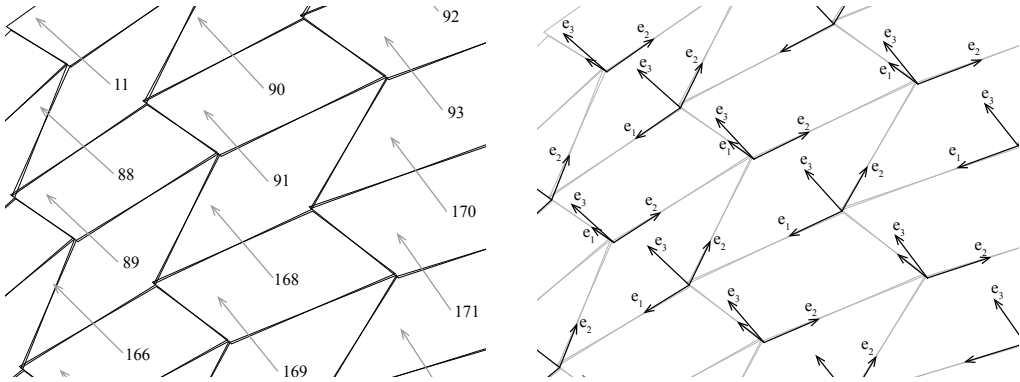
**Figure 11.** Left: disconnected planar faces, right: frames for plate generation.

# 4. Fabrication

In order to test the fabrication and assembly, a prototype of the structure was built using 15 mm birch plywood panels (scale 1:2.66). Figure 13 shows the location of the prototype within the first double-curved shell of our project. It shows the assembly of 4 x 7 hexahedron-shaped segments, consisting of 112 interlocking plates connected entirely with through-tenon and dovetail joints.

The main algorithm generates the geometry of each plate through an upper and lower polygon contour. On the shear plates, there are additional polygon contours for the joint slots. For the fabrication of the parts, the polygon contours for each plate are laid out on the World XY plane.

A second algorithm was used for the cutting of the parts with a 5-axis milling machine. It generates the G-code through a loft-like 3D offset of the plate contour polygons. On concave corners, notches are added automatically (Robeller & Weinand 2016a).

The total contour or cutting path length of the prototype (28 segments, 112 plates) is 217 meters. Parts were cut with 4 infeeds at 5 m/min (2x roughing without notches, 2x final cut with notches). Compared to a plate contour without integral joints, the contour length with the joints increases by 20% for the shell plates and 100% for the shear plates, which contain all of the slots.

On the full-scale structure, built from LVL plates with a thickness of 40 mm, the 1,248 plates of the first and largest shell add up to a total area of 1, 063 m$^2$ (without off-cuts), a volume of 43 m$^3$ and a self-weight of 32 tons.

The prototype was assembled lying on its side, inserting the tight-fitting pieces with a small mallet as shown in Figure 14. A similar prefabrication strategy is planned for the full-scale structure, dividing the 23 shells into an average of 6 pre-fabricated modules per shell, with a maximum transportation size of 20 x 2
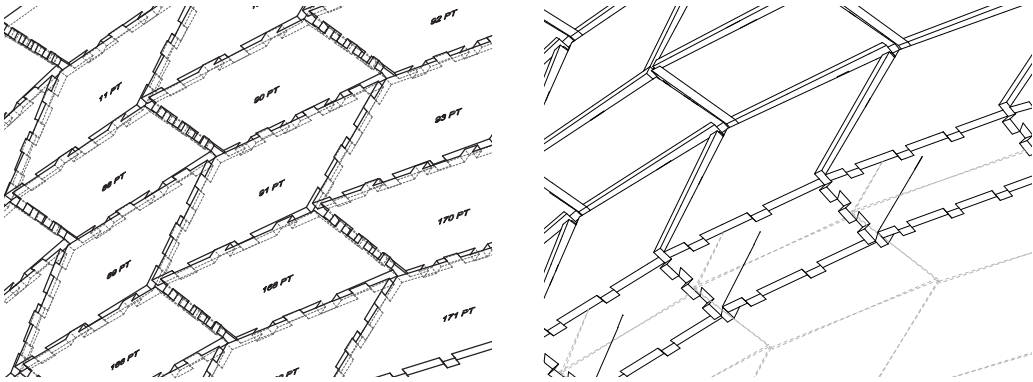
**Figure 12.** left: upper shell plates, right: cross-section view.

meters. In between these large modules, through-tenon joints cannot be used for the assembly, because no common assembly direction can be found. Instead, additional shear plates can be added and connected with metal fasteners on site. This strategy would require regular metal fastener joints on 17 % of the edge-to-edge connections on the first shell.

# 5. Conclusion

With his Gaussian vault structures, Eladio Dieste developed a highly elegant and efficient structural system, taking advantage of the local resources and technology at his time. In the same spirit, the new construction system in this paper presents a contemporary re-interpretation of a double-curved shell structure using timber, a locally sourced material that addresses the contemporary shell for sustainable building structures.

Dieste's masonry shells were based on the material and its connections, which could not resist bending forces. This was addressed through the form of the shells, but it also put a great outward thrust on the supports, requiring substantial reinforcements. Our new construction system uses integrally attached timber plates, with different material and joint properties. Our joints can resist bending forces, which is reflected in the different form of our shells, which reduces horizontal forces on the supports.

While previous projects introduced dovetail joints for the connection of timber plates, the through-tenon joints provide a high resistance to bending forces. Like the dovetail joints, the through-tenons are also prismatic joints and reduce the mobility of parts to a single motion path.
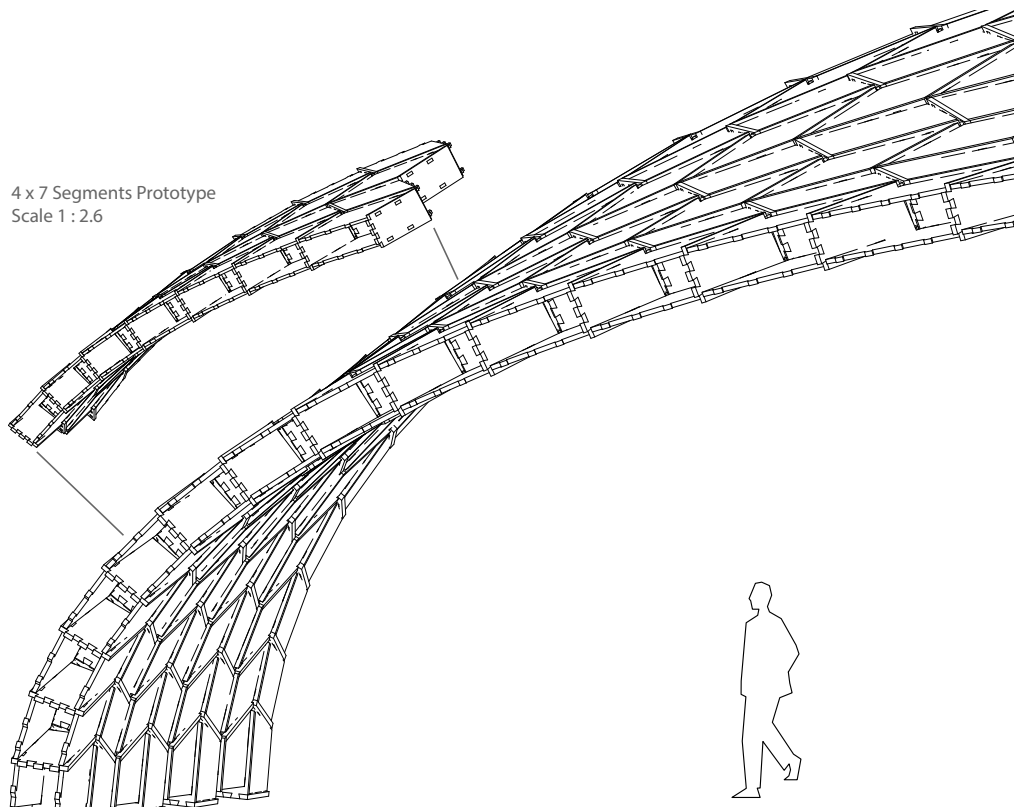
4 x 7 Segments Prototype
Scale 1 : 2.6

**Figure 13.** Isometry of arch 1 with location of Prototype A (scale 1:2.66).

The use of prismatic joints, fabricated with a 5-axis CNC-enabled cutting method, allows us to integrate the assembly instructions into the shape of the plates. Therefore, our construction system does not require a mould, which is crucial for the case study project with its 23 individually shaped shells.

The tiling with trapezoidal shaped hexahedron segments was chosen to optimize the assembly of the structure, the mechanical strength of the joints and the transfer of forces within the structure.

A rotation of the tabs allows for the piece-by-piece assembly of small plates, connecting multiple edges simultaneously. We analysed the influence of this rotation on the shear strength of the joints and optimised the shape of our plates based on the results.

The alternation of the joint rotation in every second row avoids long-range escape paths, supporting our strategy of blocking parts with one another, using their form to reduce or replace the need for additional fasteners.
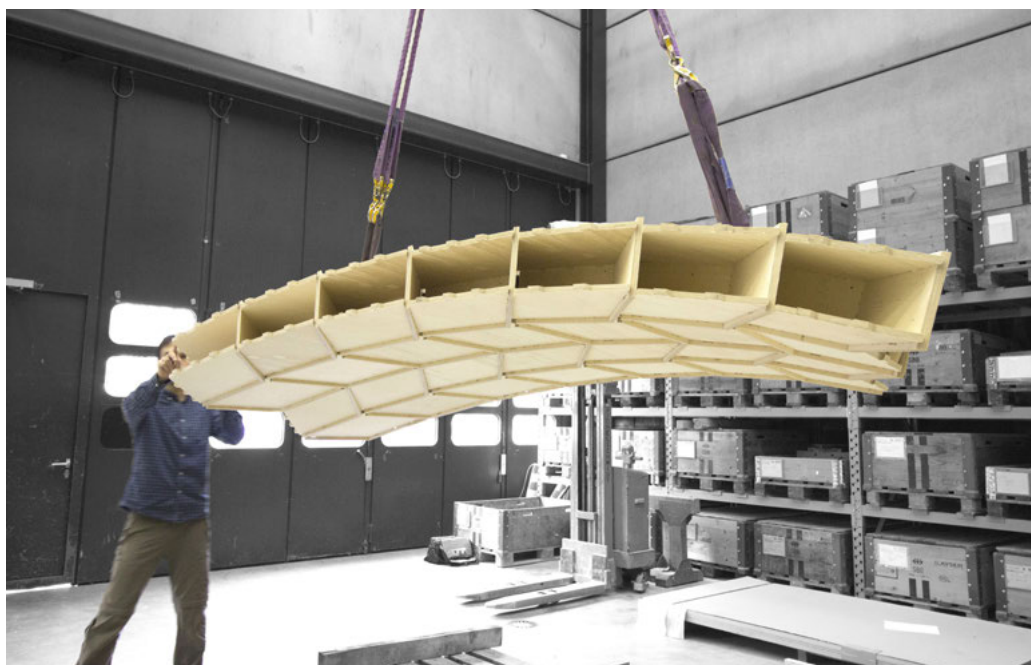
**120**

At the same time, the alternating trapezoidal shape of the segments results in an alternating rotation of all edges across the direction of span on all shells. The length of these edges is increased and continuous bending axes are avoided.

The research underlines the need for close interdisciplinary collaboration of architects, computer scientists, and engineers in the development of new types of sustainable lightweight structures, which are equally optimised for fast and precise assembly and for structural efficiency.

## Acknowledgements

## References

Anderson, S. 2004. *Eladio Dieste: Innovation in Structural Art.* New York: Princeton Architectural Press.

Bouaziz, S., Deuss, M., Schwartzburg, Y., Weise, T., and Pauly, M. 2012. "Shape-up: Shaping Discrete Geometry with Projections." *Comput. Graph. Forum 31*, 5 (Aug.):1657–1667.

Deuss, M., Deleuran, A. H., Bouaziz, S., Deng, B., Piker, D., and Pauly, M. 2015. *Modelling Behaviour: Design Modelling Symposium 2015.* Copenhagen: Springer International Publishing, Cham, ch. ShapeOp – A Robust and Extensible Geometric Modelling Paradigm, 505–515.[??]

Krieg, O. D., Schwinn, T., Menges, A., Li, J.-M., Knippers, J., Schmitt, A., and Schwieger, V. 2015. *Advances in Architectural Geometry 2014.* London: Springer International Publishing, Cham, ch. Biomimetic Lightweight Timber Plate Shells: Computational Integration of Robotic Fabrication, Architectural Geometry and Structural Design, 109–125.

La Magna et al., R. 2013. "From nature to fabrication: Biomimetic design principles for the production of complex spatial structures." *International Journal of Spatial Structures 28*, 1: 27–40. doi: 10.1260/0266-3511.28.1.27

Li, J.-M., and Knippers, J. 2015. "Segmental Timber Plate Shell for the Lan- Desgartenschau Exhibition Hall in Schwäbisch Gmünd – The Application of Finger Joints in Plate Structures." *International Journal of Space Structures 30*, 2: 123–140.

Liu, Y., Pottmann, H., Wallner, J., Yang, Y.-L., and Wang, W. 2006. "Geometric Modeling With Conical Meshes and Developable Surfaces." *ACM Trans. Graph.* 25, 3 (July): 681–689.

Pedreschi, R., and Theodossopoulos, D. 2007. "The Double-Curvature Masonry Vaults of eladio dieste." *Proceedings of the ICE – Structures and Buildings 160*, 1 (2), 3–11.

Pottmann, H., Eigensatz, M., Vaxman, A., and Wallner, J. 2015. "Architectural geometry." *Computers and Graphics 47*: 145–164.

Robeller, C., and Weinand, Y. 2015. "Interlocking Folded Plate – Integral MeChanical Attachment for Structural Wood Panels." *International Journal of Space Structures* 30, 2: 111–122.

Robeller, C., and Weinand, Y. 2016. "A 3d cutting method for integral 1d of multiple-tab-and-slot joints for timber plates, using 5-axis CNC cutting technology." In *Proceedings of the World Conference on Timber Engineering WCTE 2016.* Vienna: Curran Associates Inc.

Robeller, C., and Weinand, Y. 2016. *Robotic Fabrication in Architecture, Art and Design 2016.* Sydney: Springer International Publishing, Cham, ch. Fabrication- Aware Design of Timber Folded Plate Shells with Double Through Tenon Joints, 166–177.

Roche, S., Mattoni, G., and Weinand, Y. 2015. "Rotational stiffness at ridges of timber folded-plate structures." *International Journal of Space Structures 30,* 2: 153–168.

Roche, S., Robeller, C., Humbert, L., and Weinand, Y. 2015. "On the semi-rigidity of dovetail joint for the joinery of LVL panels." *European Journal of Wood and Wood Products 73*, 5: 667–675.

Whitney, D. 2004. *Mechanical Assemblies: Their Design, Manufacture, and Role in Product Development.* No. 1 in Mechanical Assemblies: Their Design, Manufacture, and Role in Product Development. Oxford: Oxford University Press.

# On the Hierarchical Construction of *SL* Blocks

## A Generative System that Builds Self-Interlocking Structures

Shen-Guan Shih

S. Shih
Department of Architecture, National Taiwan University of Science and Technology, Taiwan
sgshih@mail.ntust.edu.tw ✉

# Abstract

This paper explores the potential of forming hierarchical structures using just one type of element, called SL block. SL block is an octocube composed of an S-shaped and an L-shaped tetracubes attaching to each other side by side. SL blocks can be systematically assembled into variations of interlocking structures called SL strands. Multiple SL strands can be used as basic elements to build larger and stronger structures. A generative process of SL strands based on syntax-directed translation of high-level geometric specifications is defined to formalise the analysis and synthesis of forms that can be constructed with interlocking SL blocks. With the system it is not difficult to design forms that can be built by SL blocks in a top-down manner. SL blocks can be assembled to form large and firm structures without using mortise/tenon, glue, or nail. The construction can be repetitively dissembled and reassembled into various forms. The assembly process can be guided with sequential instructions so that very sophisticated structures can be encoded into compact and efficient specifications for construction.

# 1. Introduction

The research described in this paper uncovers a specific type of polycube, called *SL* block, which is an octocube consisting of an S-shaped and an L-shaped tetracubes attaching to each other side by side as shown in <span style="color:magenta">Figure 1</span>. *SL* blocks can be used to assemble extendable self-interlocking structures. Large and stable structures can be constructed with thousands of *SL* blocks without using mortar, glue, or any adhesive materials. A set of generative rules of building interlocking structures with *SL* blocks was discovered. A generative system is proposed to enable systematic methods for the design and assembly of composite structures.

     Interlocking is an interesting issue that is very useful in timber and prefabricated constructions. Advances of digital fabrication technology drive researches towards automatic generation of interlocking parts for assembly (Song et al. 2012).
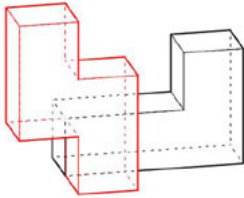


**Figure 1.** An SL block consists of an S-shaped and an L shaped tetracubes.

Interlocking levels of assembled structures can be distinguished by calculating the degrees of translational freedom for individual parts of the structure as well as the network of relations for parts engagements (Fu et al. 2015). Among these researches, polycubes were often used as the basic elements (Lo et al. 2009; Song et al. 2012; Song et al. 2015).

     The discussion is further extended to uncover the top-down design method of constructions with higher levels of hierarchy based on interlocking *SL* blocks. The generative mechanism is defined with context-free string grammars, which is fundamentally different from the shape grammar devised by Stiny (1980). Shape grammar is based on the processing of non-monotonic shapes, which are regarded as dividable constructs that allow non-deterministic recognition and processing of shape features. Shape grammar is inevitably coupled with the problem of being non-computable for which its grammar rules, with the required non-terminal shapes in the left-hand sides, are all context sensitive. For shape generative methods, Shih (1994) took a different approach by using string grammars to generate sequences of symbols that specify shape creation processes. String grammars have been successfully used for the compilation of high-level programming languages since the 1970s. Well-developed methods based on string grammars have been proven to be efficient and effective for the analysis and synthesis of syntactic structures that can be defined with context-free grammars.

# 2. Engagements, Strings and Strands of *SL* Blocks

The engagement of two *SL* blocks is defined with the transformation that transforms one *SL* block to the other block that is attaching to it. Figure 2 shows 10 types of engagements for *SL* blocks that form the basic structure of interlocking configurations. The blue (darker) one in each figure represents the host block, which receives a grey (lighter) block as the guest for the engagement. A geometric transformation can be defined to transform the blue to the gray. Each engagement is named with an upper case letter if the engaging position is at the L part of the host block, and is named with a lower case letter if the engagement takes place at the S part of the host block.



|  |  |  |  |  |
|---|---|---|---|---|
| *H* | *A* | *D* | *S* | *T* |
| *h* | *a* | *d* | *s* | *t* |
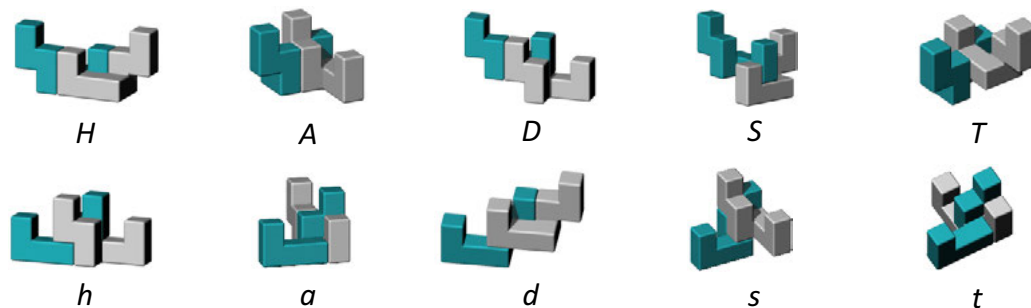
**Figure 2.** 10 types of engagements for SL blocks.

A string of engagements specifies the construction process of an *SL* string by starting with an initial block and adding on more with sequential applications of engagements in the string. For example, the string *HhH* specifies a string of four *SL* blocks lining up to form the configuration shown in the left-hand side of Figure 3. Respectively, *SL* strings of *aaa* and *ddd* are shown in the center and the right-hand side of Figure 3.



*HhH*          *aaa*          *ddd*

**Figure 3.** SL strings represented with corresponding types of engagements.

Engagements with upper and lower cases of the same letter are conjugates to each other. For every *SL* string, a conjugating string can be derived by replacing each engagement with its conjugate. Two conjugating strings of *SL* blocks can be placed against each other from the tops to form an interlocking s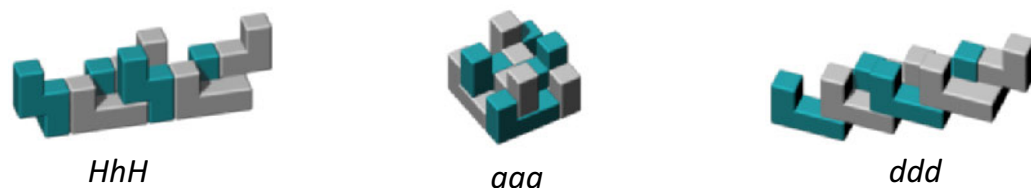tructure called an *SL* strand. Figure 4 shows three simple interlocking strands formed by placing conjugating strings against the three *SL* strings shown in Figure 3. In this paper we use # as the notation for the operation that combines two conjugates together to form a strand. Since it is trivial to derive the conjugate of an *SL* string, the second string in an *SL* strand can be omitted in the notation.



*HhH # hHh*          *aaa # AAA*          *ddd # DDD*
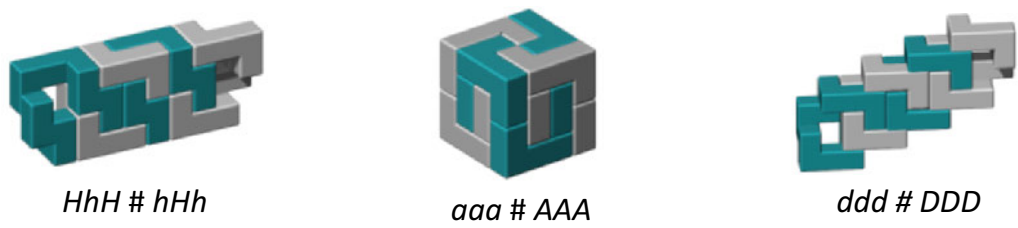
**Figure 4.** SL strands with conjugating strings of three engagements.
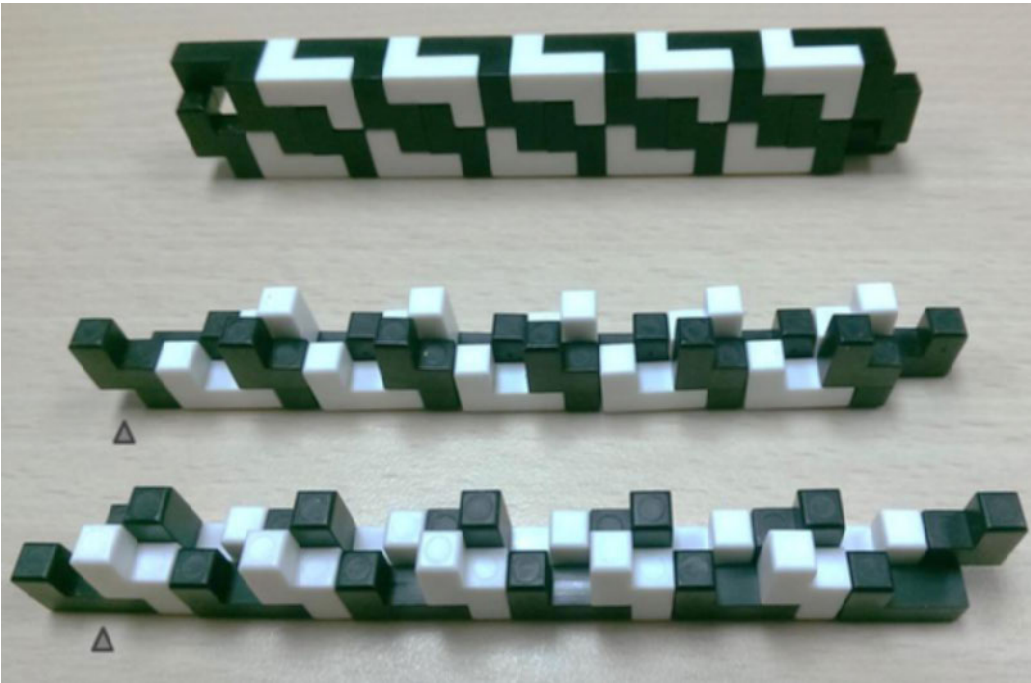


**Figure 5.** The conjugating strings of HhHhHhHhHhH (center) and hHhHhHhHhHh (bottom). The interlocking strand built with the two strings (top).

# 3. Interlocking

The interlocking mechanism of elements can be distinguished by whether it is locked by topology or by friction. With topological interlocking (Dyskin 2003), the whole structure would not be broken until some elements have already been broken. If the element is locked by friction, then the structure falls apart when the dragging force overpowers the friction. The interlocking structure of *SL* strands is not totally topological. Indeed, if any composite structure with parts that are jointed totally with topological locking, there would be no way to disassemble the structure without breaking some of the parts. Take the long strand formed by *HhHhHhHhHhH* and its conjugate (Fig. 5) as an example. Interlocking is topological when applying forces along the axial direction of the strand. The strand will
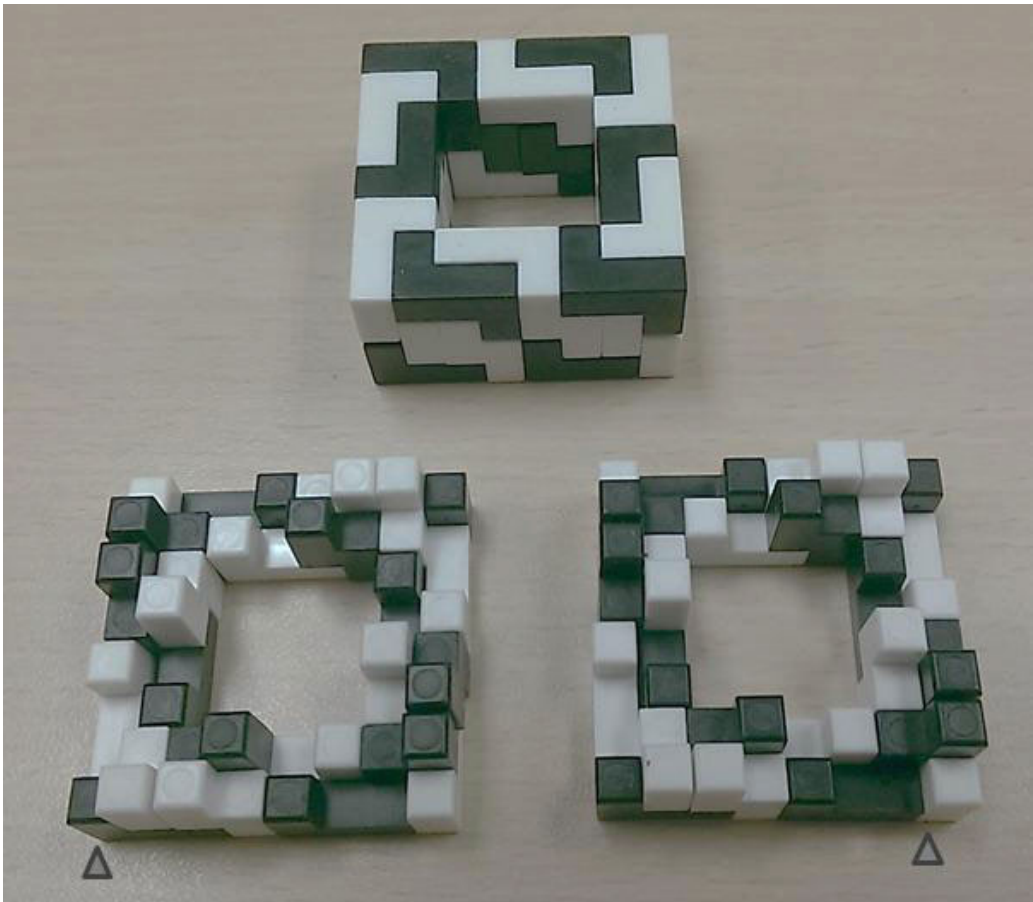


**Figure 6.** The conjugating strings of HhaHhaHhaHh(a) (bottom left) and hHAhHAhHAhH(A) (bottom right). The interlocking strand built with the two strings (top).

not be broken unless it is pulled apart along its axis hard enough to break some of the blocks. When the dragging force is applied vertically, which is along the same direction as the conjugate string is pushed into the host string, the locking is held only by friction. Even so, except for the two blocks that are located at the very ends of the strand, no single *SL* block can be pulled out of the strand without taking with it at least one other block. The weak points of the ends disappear when the strand joints its two ends to form a cyclic configuration such as the strand of *HhAHhAHhAHA(A) # hHahHahHahH(a)* (Fig. 6). The engagement enclosed by parenthesis is for the emerging engagement that takes place when the last *SL* block engages with the first.

# 4. Syntax-Directed Translation of *SL* Strings

Syntax-directed translation is a method of compiler implementation for translating the input code in one language to its corresponding code in another language. The definition of a specific syntax-directed translation requires an input grammar, which is used to derive the syntactic structure of the input, and an output grammar, which is used to generate the output. Our purpose is to derive the construction process of *SL* strands for a given shape.

With the notation we used, the plus sign represents options for what is to substitute with, and 1 represent the null string. The translation is defined as such:

| Non-terminal | Production rules for input string | Production rules for output string |
|---|---|---|
| **Init: $X_T$** | | |
| $X_T \rightarrow$ | 1. $X_S$ | $X_S$ |
| | 2. $X_L$ | $X_L$ |
| | 3. $1$ | $1$ |
| $X_L \rightarrow$ | 4. $ff\ X_S$ | $H\ X_S$ |
| | 5. $frf\ X_L$ | $A\ X_L$ |
| | 6. $dff\ X_L + fdf\ X_L + ffd\ X_L$ | $D\ X_L$ |
| | 7. $ufrf\ X_S + furf\ X_S + fruf\ X_S + frfu\ X_S$ | $T\ X_S$ |
| | 8. $dflf\ X_S + fdlf\ X_S + frdf\ X_S + flfu\ X_S$ | $S\ X_S$ |
| | 9. $1$ | $1$ |
| $X_S \rightarrow$ | 10. $ff\ X_L$ | $h\ X_L$ |
| | 11. $flf\ X_S$ | $a\ X_S$ |
| | 12. $uff\ X_S + fuf\ X_S + ffu\ X_S$ | $d\ X_S$ |
| | 13. $dflf\ X_L + fdlf\ X_L + fldf\ X_L + flfd\ X_L$ | $t\ X_L$ |
| | 14. $ufrf\ X_S + furf\ X_S + fruf\ X_S + frfu\ X_S$ | $s\ X_S$ |
| | 15. $1$ | $1$ |

The input grammar defines a language that uses letters to represent the path of the *SL* string. The definitions of letters are listed as follows:

*f*: move one step forward
*r*: turn right for 90 degrees
*l*: turn left for 90 degrees
*u*: move one step up
*d*: move one step down

With this representation, a straight line of n steps can be written as $f^n$. A square with 6 steps in width can be written as $f^5rf^6rf^6rf^6rf$. With the above syntax-directed translation, the square would be translated into the *SL* string $(HhA)^4$. With the string, it is trivial to derive the conjugate to build the corresponding strand, as the photo shows in the middle of . The deviation process of the output string is listed as follows:

## Input : Output

| Rule | Input | Output |
|---|---|---|
| $X_L$ | $X_L$ | |
| 4. | $ff\ X_S$ | $H\ X_S$ |
| 10. | $f^4\ X_L$ | $Hh\ X_L$ |
| 5. | $f^5rf\ X_L$ | $HhA\ X_L$ |
| 4. | $f^5rf^3\ X_S$ | $HhAH\ X_S$ |
| 10. | $f^5rf^5\ X_L$ | $HhAHh\ X_L$ |
| 5. | $f^5rf^6rf\ X_L$ | $HhAHhA\ X_L$ |
| 4. | $f^5rf^6rf^3\ X_S$ | $HhAHhAH\ X_S$ |
| 10. | $f^5rf^6rf^5\ X_L$ | $HhAHhAHh\ X_L$ |
| 5. | $f^5rf^6rf^6rf\ X_L$ | $HhAHhAHhA\ X_L$ |
| 4. | $f^5rf^6rf^6rf^3\ X_S$ | $HhAHhAHhAH\ X_S$ |
| 10. | $f^5rf^6rf^6rf^5\ X_L$ | $HhAHhAHhAHh\ X_L$ |
| 5. | $f^5rf^6rf^6rf^6rf\ X_L$ | $HhAHhAHhAHhA\ X_L$ |
| 9. | $f^5rf^6rf^6rf^6rf$ | $HhAHhAHhAHhA$ |

Syntax-directed translation (Aho et al. 1986) can be used to implement tools for automatic generation of *SL* strand based on figures drawn by the user. With the parser for the input grammar, the process can also check if it is possible to create an *SL* strand for the desirable form. The tool can use the input grammar to guide the form-creation process so that only forms that can be assembled with *SL* blocks would be drawn. Even when erroneous forms are given as input and the parsing fails, some syntax-directed methods such as error-correcting parsing

(Aho et al. 1972) might be able to adapt the input form so that some similar shapes that are buildable can be created. With the assistance of such tools, it would not be difficult to create more sophisticated structures using multiple *SL* strands.

# 5. Strand Hierarchy

Interlocking can be implemented at various levels, among which the lowest is built upon the engagements of *SL* blocks. Since *SL* strands are stable constructions formed by interlocking *SL* blocks, they can be used as basic elements to create super structures built upon multiple *SL* strands. The process may go on recursively for higher hierarchy still. Figure 7 shows a structure built with eight interlocking rectangular rings arranged like a cyclic chain. The ring-like strands are moveable but cannot be totally separated from each other.
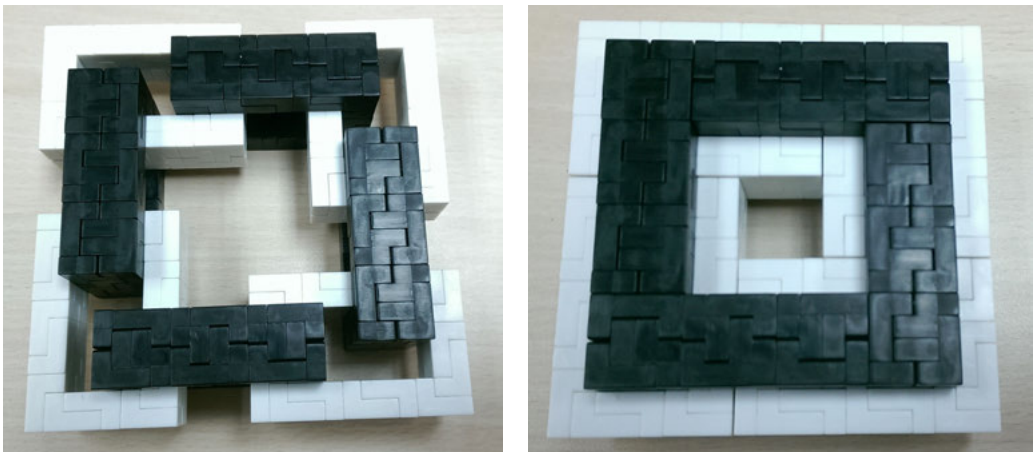


**Figure 7.** A chain structure with 8 moveable parts built with SL strands of (ahHhHahH)².
left: expanded; right: contracted.
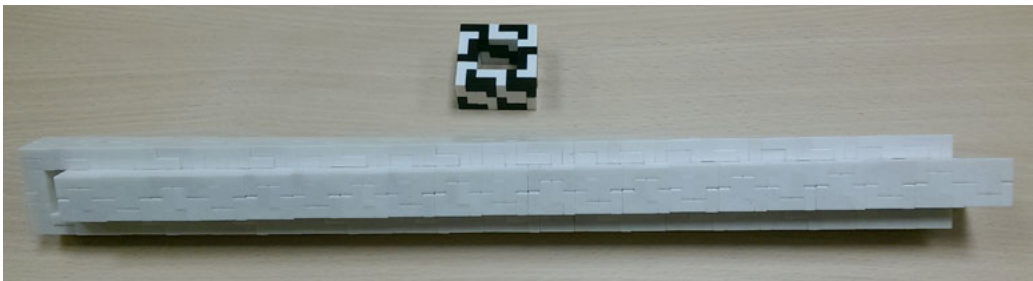


**Figure 8.** A chain structure with non-moveable parts built with 20 SL strands.

Figure 8 shows a long stick consisting of 480 *SL* blocks. The structure is formed by 20 interlocking square rings identical to the one that is shown at the top of the figure. Except for the two ends, each internal ring is locked by two neighboring rings that are oriented perpendicularly. The structure effectively prevents individual strand from breaking when forces are applied to twist the entire chain.
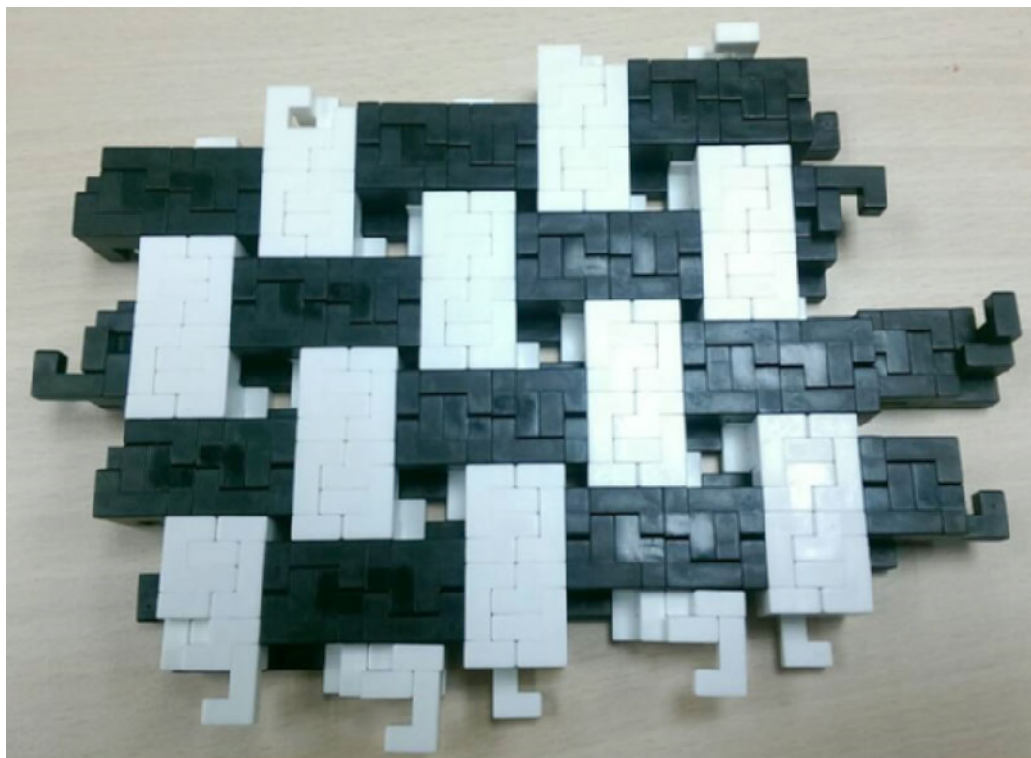


**Figure 9a.** A structure with interlaced strands.
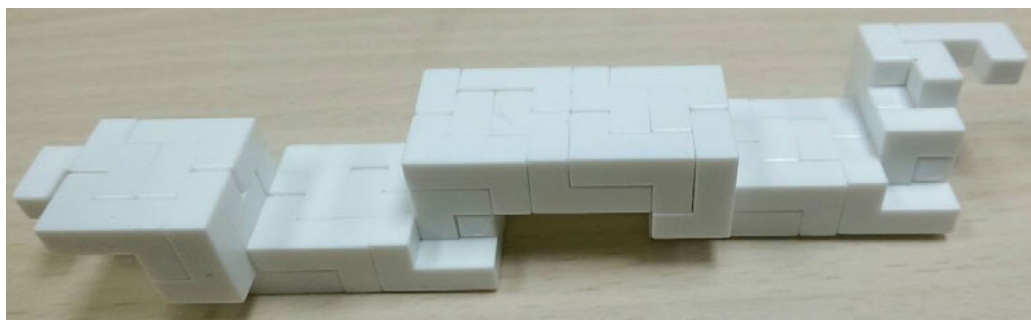


**Figure 9b.** One of the strands for the interlaced structure.

Figure 9(a) shows a structure built with 9 interlaced *SL* strands like the one shown in Figure 9(b), which can be represented as *(asHhTahH)n#(AShHtAHh)$^n$*. Interlacing could be an effective means to substentially extend the size and strength of the structure for practical applications. Each strand is strenthened by perpendicular strands that are locked with it. Except for the *SL* blocks that are located at the boundary, all internal blocks are topologically interlocked by others.

Figure 10(a) shows three structures composed of spiral strands. The one on the left consists of just one spiral strand, represented as *(St)n#(sT)$^n$*. The center one consists of two interlocked spiral strands, each of which is represented as *(add)$^{4n}$#(ADD)$^{4n}$*. The structure on the right consists of four spiral strands interlocked to form an integrity. Each of the strand is represented as (adddd)$^{4n}$#(ADDDD)$^{4n}$. (Fig. 10 b)
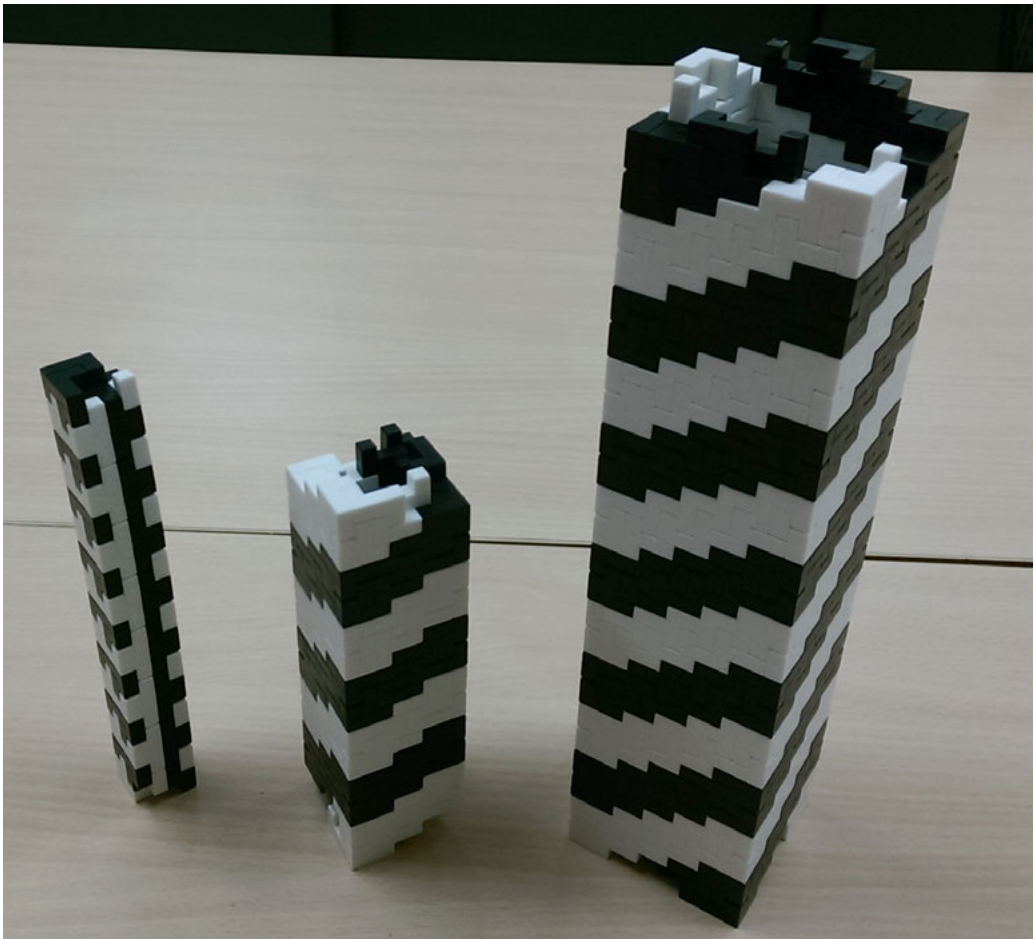


**Figure 10a.** Three structures with spiral strands.

# 6. Conclusion

*SL* block is a simple element with great potential for building larger composite structures. It is feasible to create hierarchical structures using multiple *SL* strands. Generative rules for the engagements of *SL* blocks enable efficient means for the analysis and synthesis of forms that could be built with *SL* blocks. Its usage for architecture is yet to be discovered. Various materials, details, sizes of *SL* blocks, etc., should be tested for practical applications.
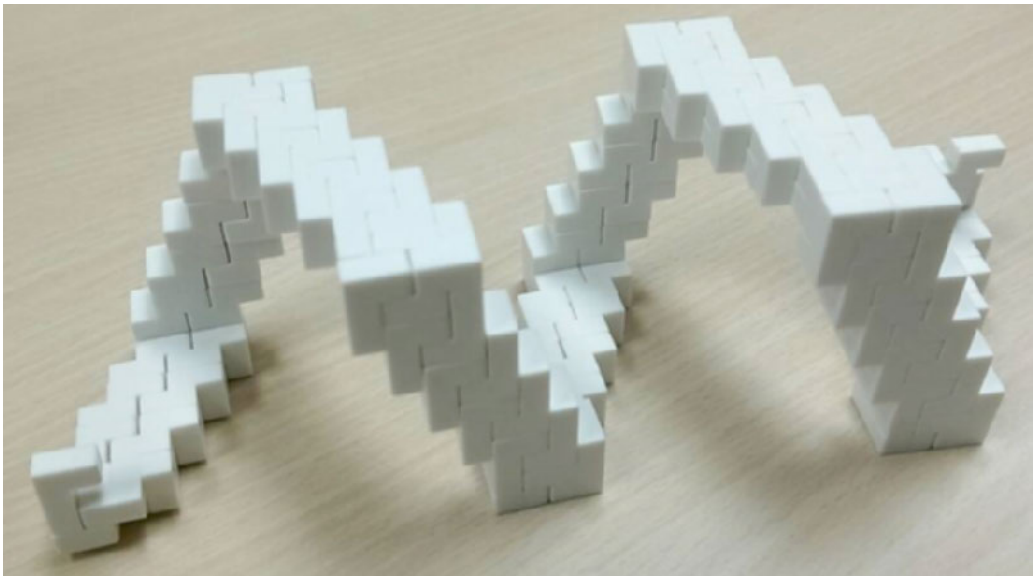


**Figure 10b.** The spiral strand of (adddd) 4n.

## Acknowledgements

## References

Aho, Alfred V., Monica S. Lam, Ravi Sethi, and Jeffrey D. Ullman. 1986. *Compilers: Principles, Techniques, and Tools*. Addison Wesley.

Aho, Alfred V., and Thomas G. Peterson. 1972. "A Minimum Distance Error-Correcting Parser for Context-Free Languages." *SIAM Journal on Computing* 1, 4: 305–312. doi: 10.1137/0201022

Dyskin, A.V., Y. Estrin, A.J. Kanel-Belov, and E. Pasternak. 2003. "Topological Interlocking of Platonic Solids: A Way to New Materials and Structures." *Phil Mag Letters* 83, 3: 197–203.

Fu, Chi-Wing, Peng Song, Xiaoqi Yan, Lee Wei Yang, Pradeep Kumar Jayaraman, and Daniel Cohen-Or. 2015. "Computational Interlocking Furniture Assembly." *ACM Transactions on Graphics* 34, 4: Article 91, doi: 10.1145/2766892

Lo, Kui-Yip, Chi-Wing Fu, and Hongwei Li. 2009. "3D Polyomino Puzzle." *ACM Trans. Graph*. 28, 5: Article 157 doi: 10.1145/1618452.1618503

Shih, Shen-Guan. 1994. "The Use of String Grammars in Computer Aided Architectural Design." Doctoral thesis, Swiss Federal Institute of Technology.

Song, Peng, Chi-Wing Fu, and Daniel Cohen-Or. 2012. "Recursive Interlocking Puzzles." *ACM Transactions on Graphics*, 31, 6: Article 128, doi: 10.1145/2366145.2366147

Song, Peng, Zhongqi Fu, Ligang Liu, and Chi-Wing Fu. 2015. "Printing 3D Objects with Interlocking Parts." *Computer Aided Geometric Design* 35–36: 137-148. doi: 10.1016/j.cagd.2015.03.020

Stiny, George. 1980. "Introduction to Shape and Shape Grammars." *Environment and Planning B* 7: 343–351.

# Tree Fork Truss

## Geometric Strategies for Exploiting Inherent Material Form

Zachary Mollica and Martin Self

Z. Mollica, M. Self
Design & Make, School of Architecture, Architectural Association (AA), UK
zacharymollica@gmail.com ✉
martself@googlemail.com ✉

All images/drawings except for Fig.13 credit of Design + Make students

# Abstract

Most recent developments in architectural geometry pursue formal complexity through non-standard building components that are digitally defined and fabricated from standardised material. An alternative approach is proposed in which non-standard materials are used a priori by exploiting their inherent geometric forms through metaheuristic optimisation placement techniques. The rationale for this approach is that the diverse characteristics of near-site material can be exploited directly without wasteful industrial processing to first standardise and then add variation back to the component geometries.

   This proposition is tested in the Wood Chip Barn project completed by Design + Make at Hooke Park, in which a series of strategies allowed the inherent natural geometries of forked wood to be exploited. The application of 3D-scanning, evolutionary optimisation of the placement of each discrete component within a structurally determined arch, and customised robotic fabrication are presented as enabling an alternative conception of material form in which inherent irregular geometries are actively exploited by non-standard technologies.

# 1. Introduction

While wood has seen a resurgence as an advanced architectural material, the complex and organic forms pursued are generally not attributable to the inherent geometric and anisotropic structural properties of wood. Instead, subtractive digital fabrication processes are often used to create complex components from standardised and homogenised wood products that have been glued together to ensure consistency (Self 2016, 1). However, before processing, trees and other organic materials already present what digitals tools are commonly employed in pursuit of: a non-standard series (Carpo 2011, p. 105). Thus, a wasteful redundancy becomes apparent in which material is processed two or more times to achieve characteristics that may already be present in the original material. Analogous to the intuitive assembly of a dry-stone wall from irregular rocks or the application of specifically curved timbers in traditional ship building, alternative conceptions of design and fabrication process have recently been proposed (Monier et al. 2013; Stanton 2010; Schindler et al. 2014) which address this redundancy.

In a standing tree the naturally occurring branching forks exhibit remarkable strength and material efficiency, able to carry significant cantilevers with minimal material. The Wood Chip Barn project revisits the traditional methods that used curved and forked timber sections in the fabrication of wooden boat hulls in the 17th and 18th centuries. In need of a range of non-linear components, shipbuilders selected appropriate materials based not only on the geometric form of pieces of wood but also an understanding of the strength of their grain. By aligning the grains of these branched members which had grown in response to

**Figure 2.** A plate from the Encyclopédie Méthodique (1782) which illustrates various naval timber components traditional boat-builders sought from curving and branched trees.
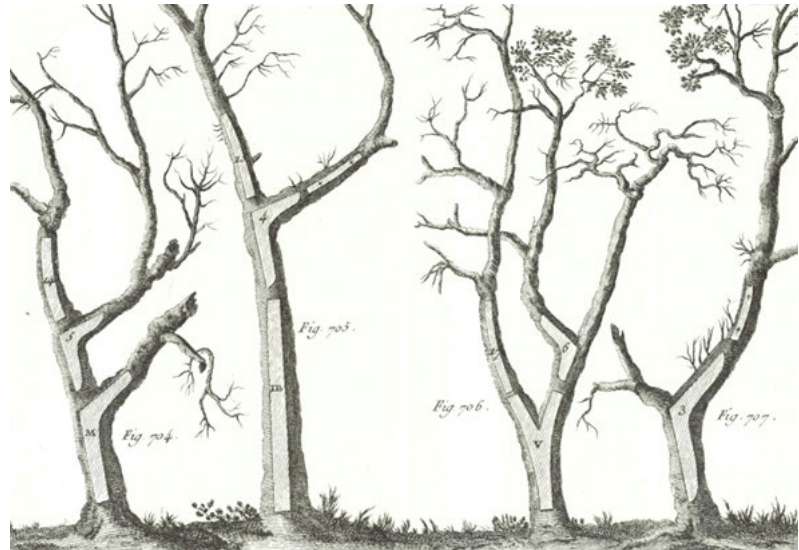
specific loads they had carried while standing into their designs, boat-builders were able to construct stronger vessels (Matthew 1831, 15).

The present work tests the premise that the integration of digital tools including 3D-scanning, parametric control modelling, and robotic fabrication enable sophisticated exploitation of the inherent qualities of natural materials such as wood. The building's primary structure is an arching truss consisting of 20 discrete beech forks that were 3D-scanned and optimally configured for structural performance before receiving robotically machined connection geometries that define their relationship to each other. The inherent geometric forms and structural potential of naturally grown tree forks (Slater & Ennos 2015) from Hooke Park's forest were deployed to create a long-span structure with minimal machine processing.

In this paper four key strategies are elaborated: the development of a precise geometric referencing system to ensure consistent placement of each component independent of its irregular surface features; the photographic and photogrammetric techniques deployed to identify and 3D-scan appropriate tree-forms to build a database of available geometries; the metaheuristic evolutionary optimisation of the placement of each discrete component within the structurally determined arch form; and the strategies employed in the robotic tool path generation for the connection fabrication to ensure overall dimensional precision independent of the local material irregularity.

**Figure 3.** Approximately scaled 2D outlines were generated for each of the 204 forks photographically surveyed.

# 2. Methods

## 2.1 Establishing a Database

Historically, shipbuilders travelled into the woods equipped with a set of templates describing the specific forms they required to construct various components. The introduction of digital tools in this project allowed the use of a wider range of geometric forms as the eventual structural form was derived from the specific character of each component found rather than finding forms which would fit within a predetermined design. Two databases of tree-fork geometries were established. First, a photographic survey of 204 standing beech trees provided approximate two-dimensional fork representations with enough detail to make informed decisions on which trees to cut down. Following the harvesting of 25 selected trees, a second more detailed 3D-scan of each fork was carried out which allowed for the development of the final truss configuration from these forks' specific geometric forms.

For the two-dimensional survey, a scaled polyline outline was generated by tracing a photograph of each fork, then correcting for parallax error according to the photograph's inclination angle and distance from the tree. An analysis of this database gave an understanding of the variations in the geometric characteristics such as the included angle between branches and minimum diameters, and, by extracting GPS location data, patterns within the forest with the aim of identifying forest compartments with the most promising forks. From this analysis a shortlist of 40 forks to be considered for felling was generated based on geographic proximity to each other, as well as a minimum angle of opening and minimum
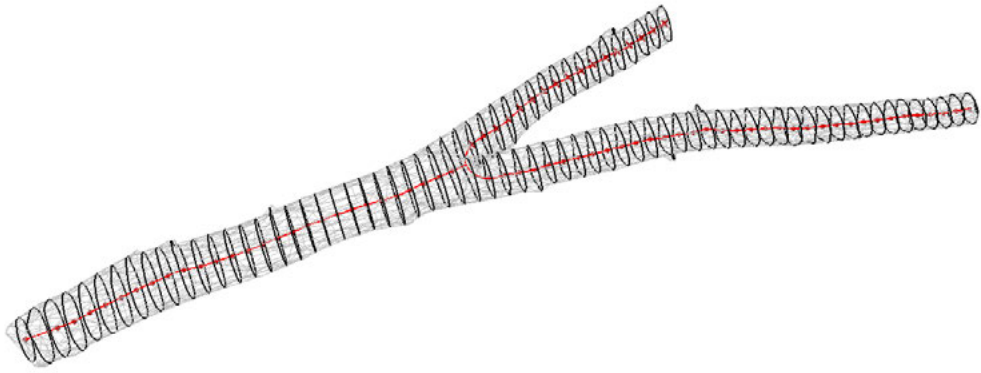
diameter which were determined in working with engineers from Arup based on early iterations of the truss form. Of these, 25 beech forks were successfully harvested. Once transported back to the yard, a detailed photogrammetric 3D-scan was made of each in order to capture their complex forms. The resulting surface mesh geometry was used as the basis of centre-curve and diameter approximations that informed the subsequent placing of the components.

Traditional timber framing methods include the projection of straight centrelines and axes onto irregular pieces of wood. Measurements are then taken outwards from this arbitrarily introduced centre geometry to ensure that variations in the tree's form have no bearing on the overall organisation. For this project, rather than straight centrelines, centre curves were defined using a polygon-based method in which transverse sections were cut through each fork at regular intervals to obtain the outer profile of their geometry and then local best-fit diameters and centroids calculated for each profiles' section which were interpolated to generate the medial curves.

Throughout the project, a fundamental consideration was how to ultimately achieve construction precision when the original material exhibited complex irregularities. The whole workflow – from standing tree to standing building – was organised around a consistent system of geometric reference (in physical and digital realms) to ensure precision in the location of the components, and thus the relative position of the fabricated surfaces, even though the actual natural form was not precisely known. This referencing system simply consisted of three points that were physically created on the tree fork components by drilling three reference holes to define a local origin point, orientation axis and plane
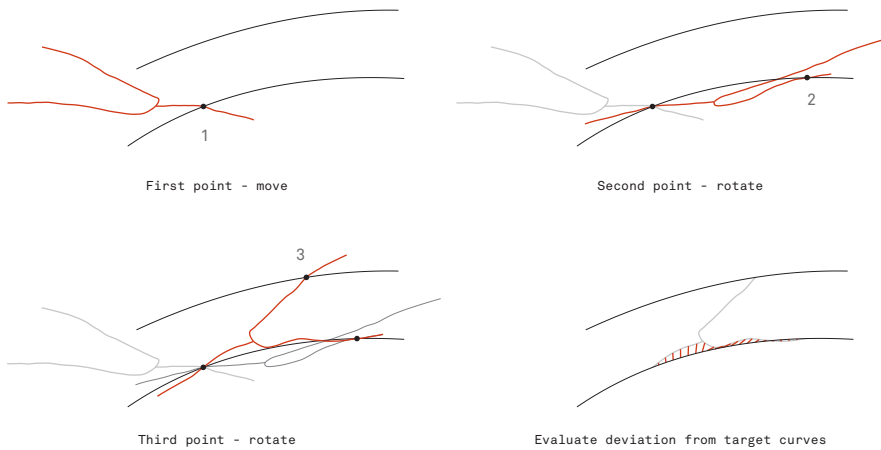
First point - move

Second point - rotate

Third point - rotate

Evaluate deviation from target curves

**Figure 5.** This image illustrates the transformations each fork underwent in being oriented to the truss target curves. Once placed, its deviation from the target curve was evaluated as a fitness parameter.

analogous to a local construction plane in 3D-modelling software. These holes were picked up in the 3D-scanning process so that they could be incorporated in the digital modelling processes and ultimately transferred back to the physical realm by being used as the supporting points when the fork component was mounted in the robot cell.

## 2.2  Metaheuristic Component Organisation

The tree forks are employed within a Vierendeel-style[1] arching truss, whose global geometry was determined to take account of the initial analysis of the available forks. The Vierendeel configuration exploits the structural capacity of the fork junction that provides the rigid moment connection that enables the construction of a non-triangulated truss. The arch structure is composed of two planar inclined arched Vierendeel trusses whose lower chords are connected by lateral elements. The structure lands at four points, the front slightly wider than the rear, with four inverted tripod legs supporting the robotically fabricated mid-section.

The Grasshopper plugin for Rhino was used to develop an organisation procedure capable of dynamically placing forks within the truss' target curves. An individual fork was located within the truss through a sequence of three transformations: (1) moved to an assigned point on the lower target curve; (2) rotated 3-dimensionally such that its stem contacts this same curve at a second point; (3) a second rotation performed using these two points to define an axis allows the branch to find its third point along the upper target curve. This placing logic was repeated for every component in each iteration of the optimisation.
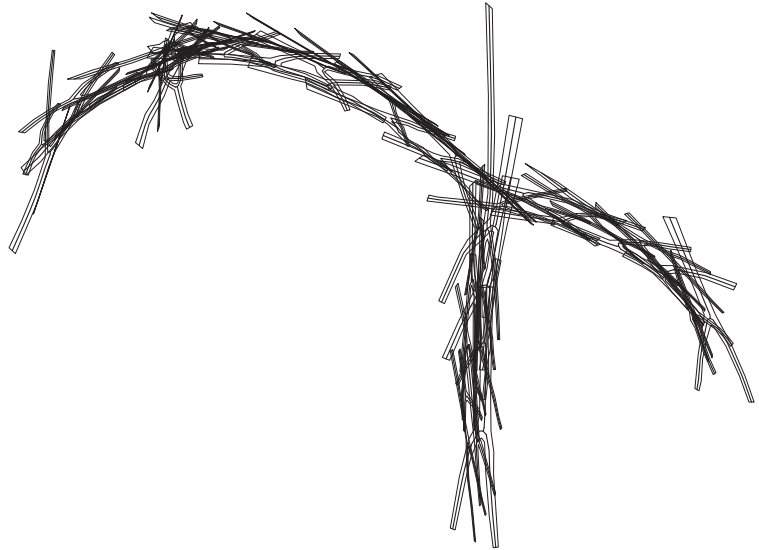
**Figure 6.** An early test of the optimisation scripting using 2D outlines of forks and their respective centrelines.

The procedure followed in organising the tree forks was to initially define the ideal ('target') inverted-catenary curves for the truss chords, and then to seek the optimum arrangement of the forks, in terms of their location within the structure and their exact local positioning, so as to best satisfy structural requirements. To minimise non-compression forces throughout the arched truss, the primary parameter evaluated in optimising the truss was the total deviation ('offset') of all 20 forks' root and stem curves from the target curves. As the placement script became more developed, a number of secondary parameters were added which addressed specific material and fabrication requirements of the truss. For example, conditions were added to ensure a minimum 300-mm gap occurred between connections as well as controls to ensure that forks which had to pass by each other did not clash.

Within the organisation process, forks were allowed to move both globally (occupying different positions within the truss) and locally (shuffling within that position) with the aim of minimising the summed offset dimension. In order to allow the truss' fitness to be optimised for the stated parameters in a controlled manner, a series of 20 integers were used as index values for selecting forks from the database of available geometries. Because the harvested forks were each longer than their required size, the individual forks were allowed to slide between the two points that define their position, to find the location where they best match the arch chord curve. The overall optimisation process was governed by 56 separate variables that would result in approximately $1 \times 10^{59}$ possible solutions. In order to address this very large search space, metaheuristic processes were implemented in an effort to find appropriate solutions through
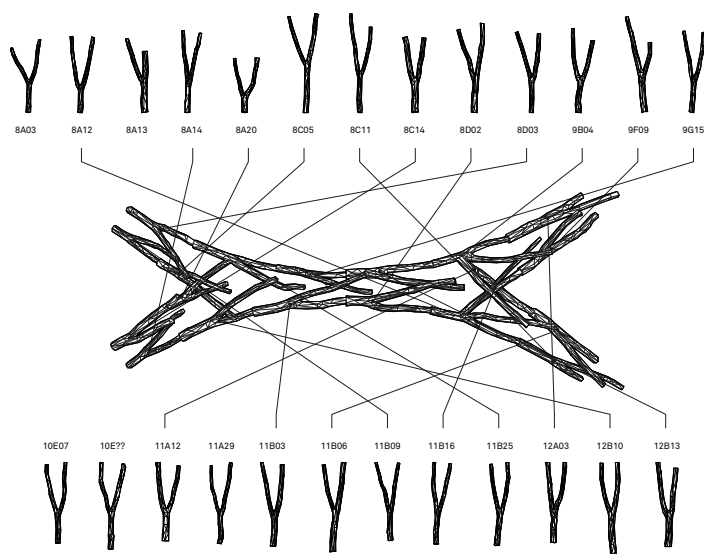
**Figure 7.** The Wood Chip Barn's arching truss.

partial searches rather than truly optimal solutions. Within the Galapagos component developed by David Rutten for Rhino-Grasshopper, both the Evolutionary and Simulated Annealing solvers were used. The role of the human operator remained significant, and a number of strategies were implemented in order to aid the solving algorithms, as discussed below.

The allocation of real physical stock within a structure presents a particular challenge to optimisation processes. Whereas adjustable variables within an optimisation typically refer to abstract quantities or proportions and building components are later derived a posteriori from a final geometry, in this case selected discrete integers refer to actual objects. As such, in order to select 20 forks to populate the truss, a list of 20 unique, non-repeating reference integers must be generated as forks cannot be in two places at once. The difficulty lies in avoiding duplication while allowing each position to select a value with equal priority. One option would be to null any iteration in which a selection is repeated but the permutations for selecting 20 objects a list means that only about 0.001 % would be admitted and thus too inefficient computationally. Another option would be to randomly assign shuffled sequences of fork objects in each iteration but this would lose any correspondence between iteration cycles, resulting in an overly stochastic search.

The strategy that proved most successful was to assign the forks to locations sequentially, accepting that the first location that was populated was likely to have better fit success than latter locations that have a smaller set of remaining available forks to choose from. This was used to our advantage by dictating that queuing sequence according to which positions within the truss were more

**Figure 8.** The final wireframe drawing output from the optimisation scripting. All of the digital fabrication information was developed from these geometries.
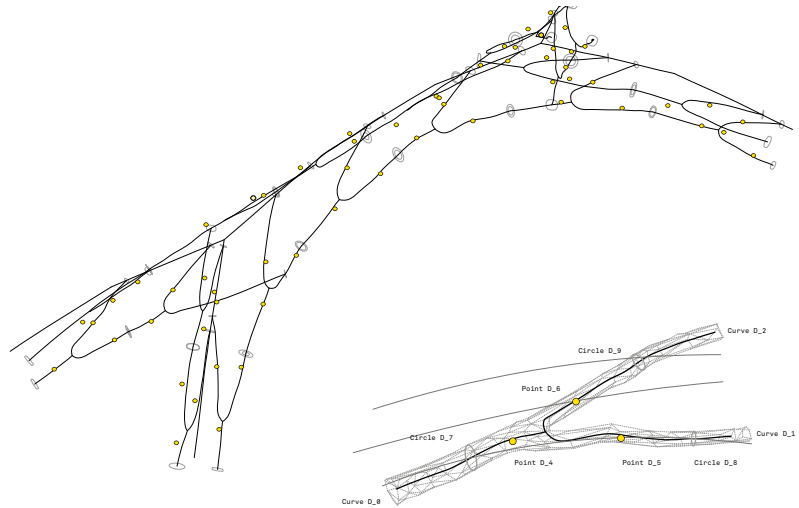
difficult to populate than others, thus requiring more specific or uncommon fork geometries (examples include those which cross each other). These positions were placed higher within the selection queue, allowing them to take priority over those positions that might be more easily filled.

A related strategy that was found to help improve the metaheuristic search was to sequence the discrete set of available forks according to their geometric similarities. This helped the optimising solver because it meant it was presented with variables in which there was a correspondence between variations between forks and their position in the integer sequence that indexed them. To generate this sequence, a script was written which, by comparing each fork's three centre curves, was able to rank the remaining 24 forks in a logical order by their geometric similarity to the first. While this 'similarity' represented a significant simplification of these complex 3-dimensional forms, it was observed that this reordering increased the ability of the solver to generate meaningful truss configurations. Although with just 25 forks the steps between them remain quite significant, it is presumed that a larger database would with surveys of enough forks begin to result in a smooth progression of geometric forms and thus enable a less stochastic search.

From the optimisation script, a series of possible truss iterations were output, and geometries provided to the engineering team for analysis and comparative quantification of the structural performance.

By automatically drawing these lines to layers based on local fork diameters, the performance of the truss could be accurately and swiftly evaluated by the engineers for a large number of iterations. In working with the engineers, one of

**Figure 9.** Development of the mortise and tenon connection.

these iterations was selected and this arrangement further refined. With a final truss geometry confirmed, the optimisation script was used to output a model with all of the geometry needed to derive the necessary digital fabrication information – 60 curves, 60 points, 60 radius circles, and 20 meshes.

## 2.3 Connection Definition and Fabrication

The strategy for the connections between the truss components was to maximise the use of compression transfer through timber-to-timber bearing and to use steel bolts and split rings to provide tension and shear capacity where needed. The connection bearing surfaces were all formed by milling using a router spindle on a six-axis robot arm. Additionally, the router was used to drill pilot holes and make locating marks for the steel hardware, and to drill further geometric reference holes for the truss assembly. Three categories of connections were fabricated. Firstly, a set of 36 axial connections between components along the truss chords were formed by milling matching planar end-faces on the pair of meeting components, which were tied together using pair of steel cross-bolts. These two planar faces, on two different pieces of irregular wood, needed to be precisely positioned and oriented 3-dimensionally so that the compression force would be transferred evenly.

Secondly, an oblique through-bolted mortise and tenon connection was used to connect the end of the branch elements to the top chords. The timber interface geometry for this connection became relatively complex as a consequence of needing to provide sufficient compression area whilst allowing for diversity in the position of the surrounding wood surface and also having a geometry that could be formed within the access constraints of the robot arm. A form similar to a truncated elliptical cone was found to best satisfy these criteria. A further subtlety was that while the compression-bearing surface was precisely milled as a smooth surface, the non-loaded surface was best milled as a series of contour

**Figure 10.** The robot arm machining one of each fork's two bearing surface.
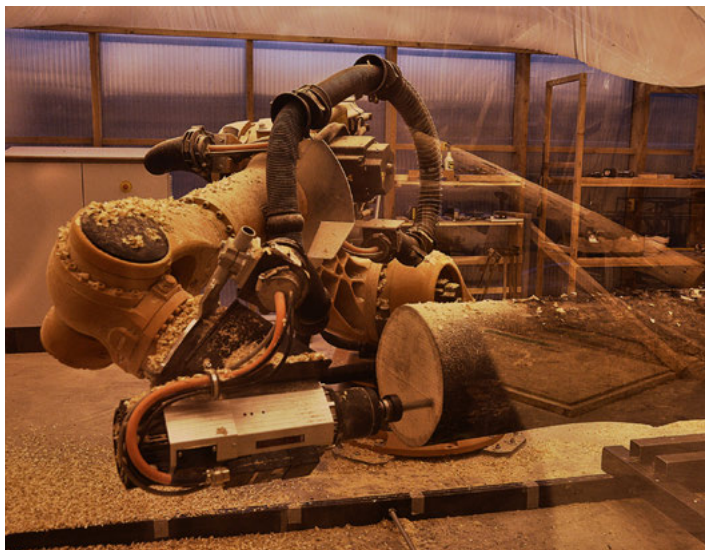
steps. Thirdly, a simpler set of planar 'seat' surfaces were defined and milled, to which smaller reinforcing timber truss members were screw connected.

To create the connection geometries, a pair of corresponding 'subtraction volumes' was defined for each of the pair of elements meeting at a given connection. These subtraction volumes – co-planar on their shared faces – consisted of geometric primitives (cuboid, cylinder, truncated cone) and represented the volume of the wood material to be removed to leave the required connection surface in its correct precise position. Intentionally, these subtraction volumes were oversized when compared to the actual pieces of wood (i.e. larger the fork's local diameter) to allow for irregularity in the wood's surface and thus ensure that all of the existing wood would be removed as required. In other words, there was always some 'milling of air' to provide tolerance for inaccuracies of the surface scan. This was one of the fundamental strategies for achieving connection precision whilst allowing for variability in the surface of the irregular natural material.

The output of the fork placement optimisation process was a 3D-model comprising sets of points, curves, and meshes that defined the component positioning, centre-curves, and surfaces, respectively. The spatial location of each fork component was defined using the three reference points from the original scan that defined its local coordinate system. A further three nodes defined the intersections of the centre-curves with the truss chord curves for each element; these nodes are shared with neighbouring elements and locate the connection geometries. At each of these connection nodes a set of vectors was defined that represented the local tangent directions of the two or three incoming elements' centre-curves.
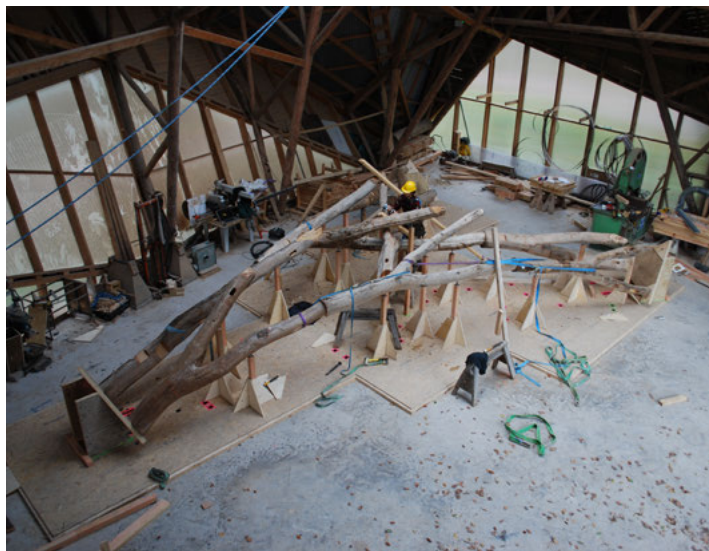
This set of minimal information for each connection – the three direction vectors and the xyz coordinate of the connection node – was the input for the generation of the connection surface geometries. Notably, the surface mesh data was not used directly in defining the connections; it was only used to check that the connection milling volumes would wholly capture the available wood. These subtraction volumes were geometric primitives defined relationally from surrounding nodal and vector information. Once defined, these volumes were populated with routing toolpaths defined using Grasshopper.

The robotic fabrication cell consisted of a fixed-position 2.7 m reach 6-axis robot arm carrying a routing spindle, and an adjustable 'trolley' that carried each fork for machining. Three vertical steel dowels, located in a horizontal plane, supported the fork at its reference holes, ensuring correct positioning of the fork within the robot workspace. The trolley itself was able to move longitudinally, acting analogously to a seventh-axis rail and enabling the robot to access the various parts of the tree for fabrication.

Machining finished, a large assembly jig made up of CNC'd sheet material and wooden studs was constructed in the Big Shed in order to precisely join together these large and complex building components. The truss was preassembled in two halves – each approximately 8 m x 6 m. This jig needed to allow the positioning of all ten forks in each half with respect to each other precisely and stably, as no connections would be made until all of the components had been loose fit together. In order to allow this, a second three-point reference system was established. The last procedure performed by the robot arm on each fork was to mill a second set of three reference holes - each drilled such that they would

**Figure 12.** A drone photo of the Wood Chip Barn's primary structure erected on site. Spanning 25 m from front to back and 10 m side to side, the arching truss rises to 8.5 m at its zenith.

be vertically oriented once the fork was properly positioned above the jig's floor. Corresponding to these points, three square pockets were cut into the 18 sheets of oriented strand board (OSB) by the CNC for each of the 20 forks, a simple vertical support then rising from each pocket to allow the reference points to be precisely set out in X, Y and Z.

Forks were lifted into place one at a time and temporarily braced. With ten forks positioned and approximately fitting, the robot-fabricated top chords were lifted in to place. With all of the major pieces held together as a loose system, the assembly team moved around the truss with hammers, straps and a Rhino model, adjusting each piece to as close to its intended position as could be achieved.

# 3. Results, Reflection, and Conclusion

With the preassembly completed, the two halves of the truss were moved to site where they were craned in to place and connected. The ease with which these large pieces came together is seen to demonstrate the success of the geometric strategies previously described in the processing of inherently non-standard materials. With its scaffolding removed, the truss was left self-supporting – its rigid, naturally formed forked components working together to allow a non-triangulated truss to stand stably. Spanning 25 m from front to back and 10 m side to side, the truss rises to 8.5 m at its zenith. Subsequently roof panels were added and the Wood Chip Barn building completed.

**Figure 13.** The structure fully loaded with its roof added. The complex form of the truss contrasts with the regular lines of the roof above. Image: Valerie Bennett.

Throughout this work digital technologies were used to convert low-value branched section of trees into complex and valuable building components while using a minimal amount of energy. In combining 3D-scanning, metaheuristic optimisation and customised robotic machining with traditional timber framing practices this has been done without significant increase in production time over a similar structure composed of standardised materials – the fabrication and construction of the building taking place in under 6 months. That the Wood Chip Barn project was realised by a student team using low-cost software and local resources is seen to prove the viability of a design-fabrication workflow in which the inherent geometric forms of materials can be exploited and deployed.

As, we believe, the first full-scale materialisation of these concepts, each of the individual processes within the workflow might be further developed and refined. For example, the survey from which components were selected for inclusion in the structure documented just 204 trees from the Hooke Park estate. A survey of this kind might be expanded to include thousands of available tree forms from a number of forests, and in doing might progress to be capable of allowing an understanding of how variables such as topography and climate affect the development of specific tree geometries for construction purposes. As

well, the optimisation process could be developed to integrate real-time structural analysis as well as a sensitive consideration of wood's unique grain patterns. In allowing the global form to be adjusted in accordance to performance and local material properties, this might allow for a greater degree of design flexibility and a return to the sensitive treatment of material in traditional buildings.

While the Wood Chip Barn project focuses on the exploitation of naturally occurring materials – in this case branched trees – the geometric strategies developed throughout might readily be applied to other materials with inherent form such as recycled industrial building components. In an era in which architects commonly seek to both add geometric sophistication to built forms as well as to reduce the embodied energy of their projects, lessons from the work outlined in this paper have significant implications. The on-site processing of near-site material by a generic industrial robot arm serves as an example of distributed manufacturing processes that fully exploit the potential of new digital tools and technologies. The non-standard aspect of the structure achieved is derived directly from a specific material's inherent forms.

## Endnotes

[1] A Vierendeel truss arrangement, more commonly found in steel structures, is one in which the truss gains stability by rigid moment resisting connections in place of triangulation.

## References

Carpo, Mario. 2011. *The Alphabet and the Algorithm*. Cambridge: MIT Press.

Matthew, Patrick. 1831. *On Naval Timber and Arboriculture.* Cambridge: Harvard University.

Monier, Vincent, Jean Claude Bignon, and Gilles Duchanois. 2013. "Use of Irregular Wood Components to Design Non-Standard Structures." *Advanced Materials Research* 671-674: 2337-2343. doi: 10.4028/www.scientific.net/AMR.671-674.2337

Rutten, David. 2010. "Evolutionary Principles applied to Problem Solving." Accessed March 25, 2016 at http://www.grasshopper3d.com/profiles/blogs/evolutionary-principles

Schindler, Christoph, Martin Tamke, Ali Tabatabai, Martin Bereuter, and Hironori Yoshida. 2014. "Processing Branches: Reactivating the Performativity of Natural Wooden Form with Contemporary Information Technology." *International Journal of Architectural Computing* 12, 2: 101–116.

Self, Martin. 2016. "Hooke Park Applications for Timber in its Natural Form." In *Advancing Wood Architecture: A Computational Approach*, edited by Achim Menges, Tobias Schwinn, and Oliver David Krieg, 138–181. London: Routledge.

Slater, Duncan, and Roland Ennos. 2014. "Interlocking Wood Grain Patterns Provide Improved Wood Strength Properties in Forks of Hazel (Corylus avellana L.)." *Arboricultural Journal* January 2015. Berlin: Springer-Verlag.

Stanton, Christian. 2010. "Digitally Mediated Use of Localised Material in Architecture." Paper presented at the 14th Congress of the Iberoamerican Society of Digital Graphics.

# Textile Fabrication Techniques for Timber Shells

## Elastic Bending of Custom-Laminated Veneer for Segmented Shell Construction Systems

Simon Bechert, Jan Knippers, Oliver David Krieg, Achim Menges, Tobias Schwinn, and Daniel Sonntag

S. Bechert, J. Knippers, D. Sonntag
Institute of Building Structures and Structural Design (ITKE), University of Stuttgart, Germany

s.bechert@itke.uni-stuttgart.de ✉
j.knippers@itke.uni-stuttgart.de
d.sonntag@itke.uni-stuttgart.de

O.D. Krieg, A. Menges
Institute for Computational Design (ICD), University of Stuttgart, Germany

oliver.krieg@icd.uni-stuttgart.de ✉
achim.menges@icd.uni-stuttgart.de

# Abstract

Recent developments in the field of segmented timber shells have shown promising structural and constructional characteristics. Advancements in computational design and digital fabrication enable architects and engineers to handle the increased geometric complexity necessary for this new construction type, integrating fabrication constraints and structural feedback in one design model. The research presented in this paper builds on new findings from biological role models for the constructional morphology, connection type, and material distribution of segmented shells. Based on the transfer of these principles, a robotic fabrication technique was developed that enables the production of elastically bent, double-layered segments made from custom-laminated beech plywood, by transferring traditional textile connection methods to timber construction. The construction system was evaluated through the design, production, and assembly of a large demonstrator.

# 1. Introduction: Segmented Timber Shells

The transfer of biological principles of constructional morphology from natural organisms into technical applications has a long tradition in engineering. However, only recent developments in digital design and fabrication have unlocked the vast possibilities and opportunities of biomimetic design strategies for architecture and construction as the generation, communication, and fabrication of complex geometry becomes a crucial aspect of the design process (Kieran & Timberlake 2004). Simultaneously, these advancements have now driven architectural design research to seek for natural examples that are characterised by both their complex, hierarchical material distributions, and their high structural performance.

Often, morphological and process-specific role models in nature lie outside or between established categories and methods in building construction. In addition, their complex shapes necessitate a digital chain from design to fabrication. Especially in the field of lightweight timber construction, biological role models have helped to redefine building systems, design methodologies, and fabrication technologies. As shown in previous research by the authors (La Magna et al. 2013; Krieg et al. 2015), segmented shells exhibit promising structural characteristics as well as architectural articulations. However, they pose challenges to the fabrication and construction and therefore require innovative and integrative design methods.

The research presented in this paper is based on a new approach to segmented shells in architecture. It builds on existing role models and integrates newly discovered biomimetic principles as well as robotic textile fabrication techniques for thin timber shells. Common connections in timber construction are usually optimised for much thicker building elements, but can hardly be applied to thin layers of veneer. Instead, much more suitable solutions were found in textile manufacturing techniques, and the construction system presented in this paper was developed based on one of the oldest techniques for fastening and attaching objects: sewing. Although sewing is used in many different industries, the degree of automation is often far less than in other production processes. The reciprocity between the sewing machine's mechanics, the thread, and the sewn material mostly require sensitive manual labour and many fast corrections in the material or tool movement. Although contemporary sensing technology and machine control allow for the necessary adaptability, only few automated solutions have been developed to date. Still, the possibilities of industrial sewing machines in architecture are promising as they can go far beyond the connection of textiles.

Timber as a construction material offers notable advantages. Not only the ecological benefits such as its negative carbon footprint (Alcorn 1996), but also its strength to weight ratio as well as its high elasticity make wood an ideal material for lightweight building construction. Further, the advancement of digital fabrication in the timber industry and its ease of machinability provides great possibilities for innovative freeform structures. As a natural fibre composite it would

seem counter-intuitive to use contemporary connection types that generally rely on subtractive fabrication that cut off and destroy the fibres and therefore weaken the material itself. In contrast, textile connections such as sewing provide the opportunity to connect timber elements while maintaining most of their fibrous material structure. Textile connection techniques have a long tradition in timber, e.g. in historical boat construction. They are often employed when geometrical flexibility is desired at the connection level, however they usually require predrilling of holes and large amounts of manual labour, making it less suitable for large scale applications. This can be avoided by employing modern robotic fabrication techniques in conjunction with an industrial sewing machine.

# 2. Biological Principles of Double-Layered Segmented Shell Structures

Previous research by the Institute for Computational Design (ICD) and the Institute of Building Structures and Structural Design (ITKE), in collaboration with the Department of Geosciences at the University of Tübingen in the field of segmented shells (La Magna et al. 2013; Krieg et al. 2015; Li & Knippers 2015) was characterised by a thorough investigation of biological role models as a basis for further structural and constructional developments. Exhibiting promising morphological features, the skeleton of echinoids was analysed to transfer functional and structural principles to the construction of segmented shells in architecture. As biological research advanced in the last years this previous work has been revisited and extended for a new type of lightweight timber construction.

Within the taxonomic phylum of Echinodermata, two species of the class Echinoidea (sea urchin) and the order Clypeasteroida (sand dollar) were identified as particularly promising for the transfer of morphological principles for the constructional morphology as well as procedural principles of growth and form-finding for an integrative design process. The biomimetic analysis of these species led to the further investigation of the following, already known, principles: (1) a double-layer skeleton, which forms in some species as so-called secondary growth and reinforces the test; (2) hierarchical material organisation and differentiation within the calcite stereom, which can be found in many biological structures (Gruber & Jeronimidis 2012); and (3) the principle of connecting segments with finger joints.

In an effort to thoroughly understand the constructional morphology, a number of previously unknown principles were also identified and integrated into this research project: (1) the differentiation of material composition for elastic or stiff material behaviour; (2) fibrous connections between segments in addition to the finger joints; (3) growth principles of plate addition and plate accretion (Raup 1968; Chakra & Stone 2011); and (4) morphological features such as internal supports and shell openings, which appear in most sand dollars and are most
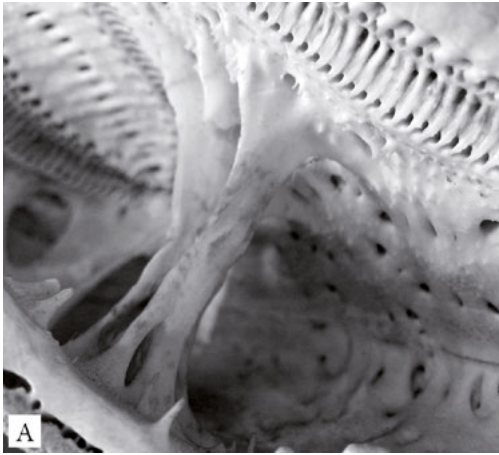
**Figure 1a.** Photograph of the interior of a Clypeaster Rosaceus with visible internal support structures connecting the top and bottom of the skeleton.



**Figure 1b.** The double-layered timber segments are most visible during the demonstrator's construction phase.

relevant in an architectural context. Although wood is a natural fibre composite with anisotropic material behaviour compared to the heterogeneous calcite with highly differentiated porosity, which makes up the skeleton of sea urchins, the analysed constructional principles can be transferred on an abstract level.

The basis of the system development was formed both by the abstraction of biological principles and the inspiration from the material. From the former a double layer construction similar to the secondary growth (Fig. 2a) in sand dollars was derived. The latter led to the choice of extremely thin and elastically bent plywood, which once bent and connected to neighbouring elements generates a stiff doubly-curved shell structure (Fig. 2b). In order to achieve sufficient interconnection between the two layers while allowing high geometric flexibility within the segment geometry, the general segment construction logic is based on three initially planar plywood strips with 3 mm to 6 mm thickness, which are bent around their longitudinal axis in order to connect on both ends with lap joints. These thin plywood strips are normally not suitable to bear significant bending moments, which is why forces are mostly transferred in form of in-plane shear forces and normal forces. This is also reflected in the joint layout. The shear forces and compression forces can be transferred between elements via finger joints. As an additional element, laces are used similar to the fibrous connection of sea urchins to withstand tensile forces.

The calcite plates of some sea urchin species are connected through fibrous elements (Fig. 3a), and it can be hypothesised that those play an important role in maintaining the shell stability during growth as well as for dynamic forces (Wester 2002). The possibility of the fibrous connections to adjust to continuously varying connection angles between the segments, and to adjust to tolerances during
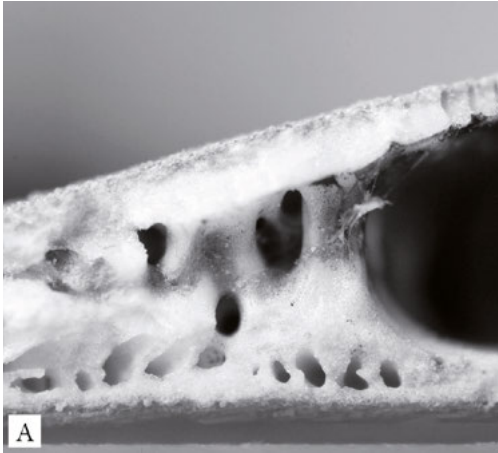
**Figure 2a.** Photograph of a cut Mellita 5-perforata with visible secondary growth inside the bottom layer. The exterior plate structure is supported by a second layer of calcite with small cavities in between.



**Figure 2b.** The principle constructional morphology of such structures is transferred into a segmented timber shell construction system with bent plywood strips.
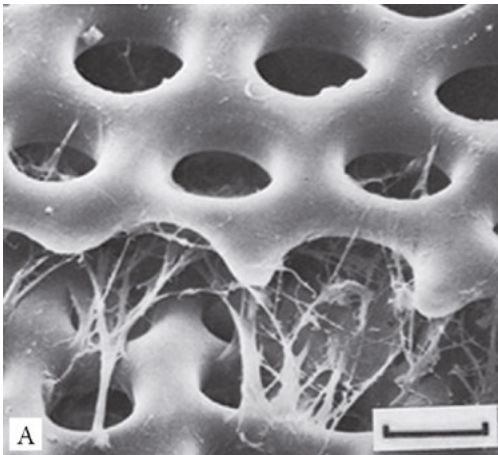


**Figure 3a**. Microscopic image of a joint between ambulacral plates, bound by collagen fibres, from a Diadema antillarum (scale bar 50 µm). From Telford (1985).
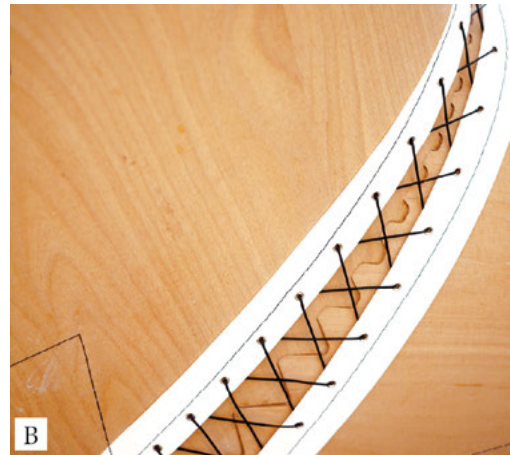


**Figure 3b.** A combination of finger joints and fibrous connection is used for the developed construction system.

assembly, can directly be compared to the biological role model, where the flexibility of the connections allows for the rearrangement and growth of the skeletal plates (Fig. 3b). In conclusion, the introduction of fibrous connections for thin plywood on multiple hierarchies turns out to be a very effective method for the robotic prefabrication of the segments as well as their on-site assembly.

**159**

# 3. Implementation of Textile Robotic Fabrication Techniques

The transfer of forces via textile connectors is implemented on two different levels of hierarchy: On the segment level, robotic sewing of laminated veneer is introduced to connect each of the three elastically bent sheets of plywood into one double-layered segment (Fig. 4). In timber construction, multiple continuous connections are generally preferable to singular ones, as the local stress concentrations of the single joints are more critical to the fibrous nature of wood. This is one of the reasons why joining thin sheets of plywood is usually achieved by gluing. However, glued connections require planar configurations or complex form work to maintain the high pressures necessary to laminate veneer sheets. Each of the geometrically differentiated segments in this research project, however, necessitate the strips to be joined while in a deformed state, making a glued connection difficult and time-consuming to achieve. In addition, the pre-bending of the strips induces high stress concentrations at the ends of the lap joints, resulting in potential delamination. To prevent this effect robotic sewing of the laminate is introduced as a manufacturing technique (Fig. 4).

With a direct connection to the digital model an industrial robot is used to position each strip of a segment and guide it through an industrial sewing machine. To attain the required shape of each segment, the height and inclination of the two opposing planes where the strips are connected are indicated by the robot in a first step of the fabrication process. After the three strips are bent into place and glued to the lap joint, the segment is mounted onto the robot using an adjustable effector. The robot then guides the segment through a stationary industrial sewing machine. To avoid breakage of the needle, the plane of the segment's part that is currently sewn has to be orthogonal to the needle's axis. Furthermore, it has to be ensured that the segment is not moving during the stitching motion of the needle. For this purpose the sewing machine controller was integrated into the robot control. It receives signals for stitching commands and sends a signal back once a stitch is completed.

Common sewing processes in industry are designed for rather soft materials such as textiles. When sewing wood, the high resistance of the plywood requires an adjustment of this process. In order to generate the required force to penetrate the veneer strips, the setup of the industrial sewing machine was modified by increasing the machine's transmission to achieve a larger torsional moment and thus a higher penetration force. In order to enable the production of a wide range of segment sizes to create more freedom in the design space, a long arm sewing machine is used. Also, to prevent needle breakage and therefore ensure a continuous fabrication process while sewing comparably strong wood, the needle has to resist high axial forces and simultaneously exhibit a certain flexibility due to
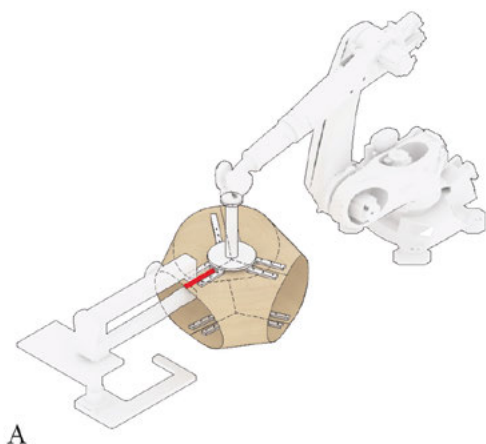
**Figure 4a.** Diagram of the robotic fabrication process. Equipped with an adaptable effector the robot holds a pre-assembled segment and guides it through the sewing machine.
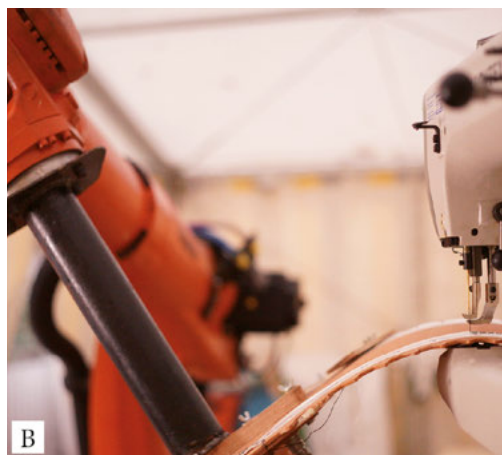
**Figure 4b.** Photograph of the process.

the deformation while puncturing the material. To achieve enough extrusion and therefore minimise the effect of abrasion or breakage of the thread, the needle tip was tested and evaluated. Thus, a titanium nitride coated needle was chosen, offering a greater hardness than standard needles and a better protection against wear and damages. In addition, a bonded polyamide thread is employed, which provides a very high breaking strength and abrasion resistance.

The robotic sewing technique offers the opportunity to directly integrate a second hierarchy of connection type. Sewing is further used to attach pre-cut, PVC-covered polyester fibre membrane strips along the finger-jointed edges of each segment (Fig. 5a). These allow to continuously transfer tensile forces between segments. They are joined using polyester-coated aramid ropes, whose density is adjusted to structural requirements. Traditional connections of membranes via laces typically require the folding of the membrane to create a keder rail, however in this case this would have been geometrically difficult to achieve. From preliminary finite element analysis estimations of the required tensile load bearing capacity of the joint are estimated. Afterwards, structural tests are performed on the connection to ensure that the membrane strips are still able to transfer those tensile forces between the elements with only a single membrane layer (Fig. 5b). The aluminium eyelets well known from membrane constructions are maintained. The laced connections between the segments allow the transfer of tensile forces and thus complement the finger joints. This connection type also has the benefit to be highly adaptable to varying geometric configurations and can ease the assembly by tensioning the laces gradually.
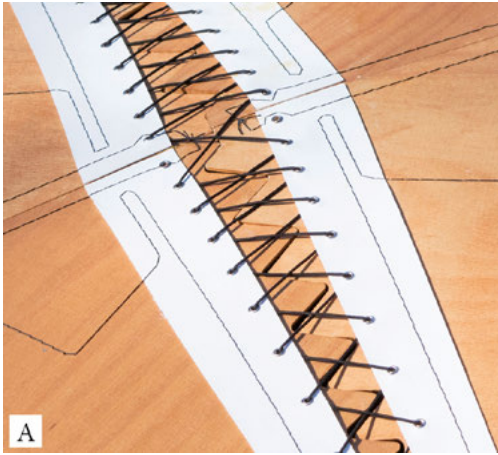
**Figure 5a.** Photograph of the membrane and lacing technique. The membrane strips are sewn onto the segments during robotic fabrication.
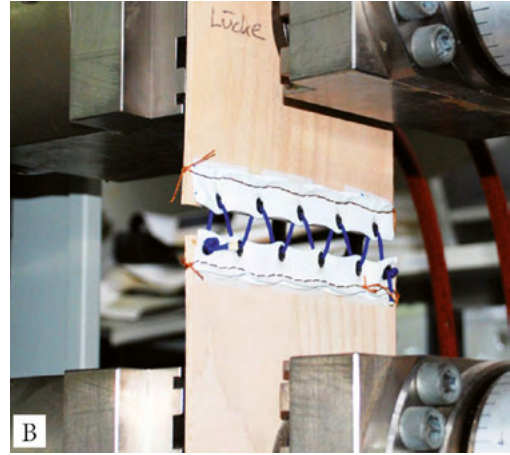


**Figure 5b.** Structural tests were performed for several lacing techniques.

# 4. Integrative Design and Hierarchy

The robotic fabrication setup in conjunction with the overall fabrication sequence is analysed for its possibilities and constraints, which are then implemented in the development process in order to determine the morphospace of possible segment shapes. For example, the element size is limited by the length of the arm of the sewing machine, and if elements become too distorted, collisions between element and robot arm are possible. This information is directly included in a computational design tool that implements the introduced principles all while staying within the solution space set by the material characteristics and fabrication constraints. It is using a form-finding process based on the biological role model of plate growth and plate addition. Compared to morphological principles, this process-based principle is abstracted for the design process in order to distribute segments over a user-defined area.

This integrative approach allows the design tool to act as an information model. It generates buildable solutions and is driven by structural and architectural requirements. It decides on the material orientation within each strip and exports fabrication information for lamination, CNC cutting, and robotic sewing. All data are automatically generated and exported into the respective file formats. This integrated digital process facilitates the production of 151 unique segments with their own differentiated material distribution, custom-fit finger-joints, and connection details (Fig. 6).

The biological role model is hierarchically organised, integrating functional aspects and constructional requirements at different levels. Similarly, the design
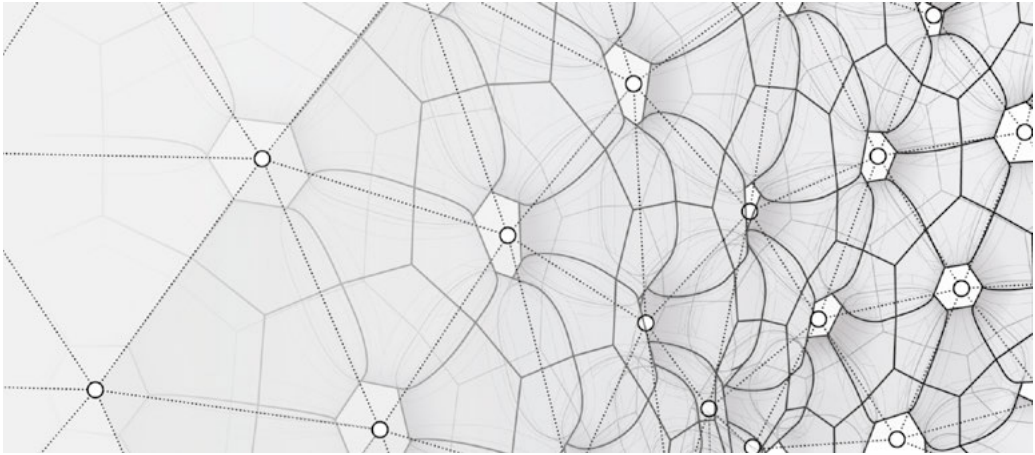
**Figure 6.** Visualisation of the geometric information in the computational design tool. A mesh forms the basis for all geometric operations that generate the final segment and membrane geometry.

tool also follows through all aspects of hierarchy from the fabrication of the finger joint to the assembly of the entire structure and integrates them in one global model. The developed construction system also allows for different morphological features similar to those from the biological role model. While the segments' arrangement is mostly characterised by openings in the shell, other types of segments form a closed arrangement. Similar to the internal supports of some species of the sea urchin, the shell can additionally form directional sub-structures that follow the material logic. In the case of the developed construction system, plywood strips bend outwards away from a segment and form a column. The structure is therefore not forced to end vertically on the ground but can cantilever horizontally above the ground while being supported by those column-like segments.

# 5. Material Differentiation and Form-Finding of Laminate Geometry

Generating doubly-curved structures from initially planar elements is of major interest in the field of architecture, as double curvature is highly beneficial to the structural behaviour, while the planarity of the elements facilitates fabrication. One possibility is to approximate doubly-curved surfaces with uniaxial elastic bending of initially planar strips (Lienhard 2011; La Magna 2016), creating the entire structure by bending it on a global level into shape. In this research project a different approach was chosen, whereby the elastic bending is used only at a segment, or local, level, thus creating complex geometries using initially planar strips. A
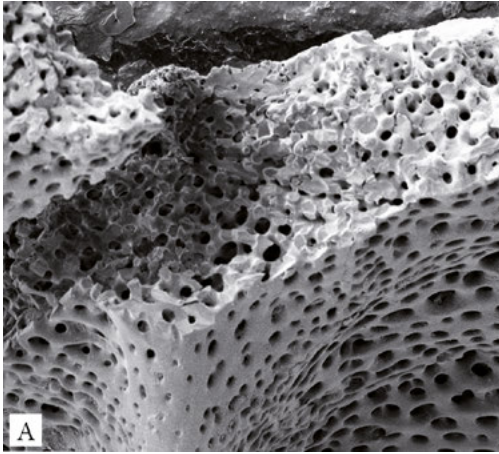
**Figure 7a.** Electron microscope image of a sand dollar's calcite structure with differentiated density (Image by Tobias Grun, 2015, from the Department of Geosciences, University of Tübingen).
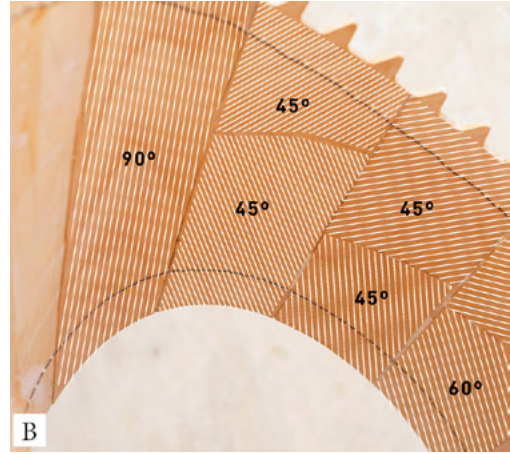


**Figure 7b.** Elastically bent plywood strip laminated with veneer layers facing in different directions.

major advantage is that the pre-bending forces are short-circuited inside the segment during fabrication and do not have to be maintained by an external device after assembly.

Biological structures often present a highly anisotropic material behaviour and characteristics that are locally adapted to comply with functional or structural requirements. In the sea urchin's case, the density of the stereom varies along the shell (Seilacher 1979) (Fig. 7a). This principle is transferred on an abstracted level, where local adaptation through a differentiated material stiffness is achieved by programming the material to comply with structural requirements. Although the role model's material has only few similarities to wood, it can be argued that the principle of material differentiation is transferred on a local level for each plywood strip. In both cases the material density is differentiated for functional requirements. In the case of wood veneer, the fibre direction is the main medium to control each strip's bending stiffness (Fig. 7b).

For the developed construction system, the shape for each segment results from the global shell layout, leading to continuously varying curvature along each strip. As the strips will be bent with an approximately constant bending moment, this results in the requirement of a gradually adapted stiffness distribution to achieve the desired 3-dimensional shape. The stiffness graduation is achieved by laminating discrete veneer strips on a base material of 3 mm beech plywood to locally reinforce and thereby stiffen the resulting laminate (Fig. 8a). For this purpose, a form-finding algorithm is developed, which allows to compute an approximate material layout as a consequence of the curvature distribution along each strip (Fig. 8b). This tool takes into consideration minimum bending radii,

**Figure 8a.** Multiple plywood strips laminated with different veneer directions to influence their elastic bending behaviour.
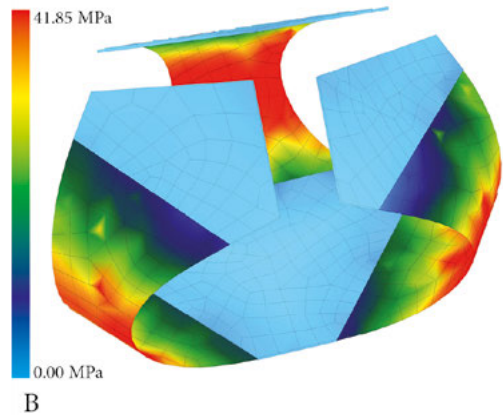


**Figure 8b.** Simulation of the bending behaviour with differentiated material make-up in finite element analysis.

veneer strip size and layer orientation to compute a material layout for the un-rolled strip, which can then be laminated and cut into shape. During an evaluation period, physical tests and digital simulations were compared in order to identify the relationship between grain direction in laminated veneer and the resulting bending stiffness. However, it is important to note that the desired shape can only be approximated. The error results from the step-like differentiated stiffness (as a consequence of the additive fabrication process) and the time-dependent material behaviour (such as relaxation of the pre-bending stress), which was not considered for simulation. This ties back to the requirement of a flexible joint connection, which allows for tolerances and further justifies the choice of the textile connection system.

# 6. Form-Finding: Integration of Procedural Biological Principles

Several studies in biology have analysed the growth process of sea urchins independent from intents of transferring the underlying principles into engineering or architecture (Johnson et al. 2002; Ellers 1993). In general, several mechanisms can be distinguished, but mainly the plate addition originating from the apical disc and accretion of calcite material around each plate's edge are responsible for the growth and distribution of the sea urchin's skeletal plates. For a living organism it is especially effective, as these principles maintain structural integrity and stability of the shell during the entire growth process. The growth process can
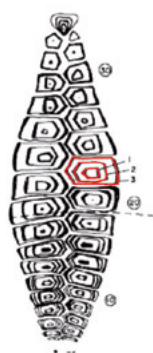
**Figure 9a.** Diagrammatic representation of plate accretion (left). A row of calcite plates is shown that grow in size while moving towards the middle. The principle of growth is abstracted in the computational design tool (right).
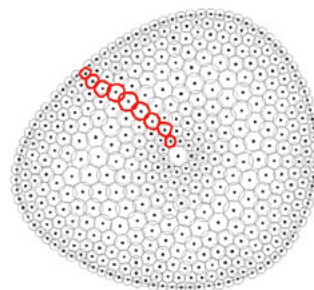
**Figure 9b.** The principle of plate addition (right) starting from the top (ambulacral plates) is also transferred to the computational design tool (right).

therefore be seen as a form-finding process that automatically respects certain geometrical and functional constraints. The principle of adding and growing segments – in the case of the research project over a pre-defined three-dimensional surface – can be transferred through a parametric circle packing approach (Zachos 2009). The geometric rules of distributing plates in a packed configuration resemble the attraction and repulsion between circles on a surface. While these circles represent segments, their radii determine the segments' sizes and keep them at distance from their neighbours. Once seeded at user-defined input areas, they grow until the surface is filled completely. In the case of the demonstrator, two opposing points were chosen at the base of the building. During the simulation the segments are seeded at those points and follow a user-defined design intent while growing and distributing over a specified area. This growth process leads to a similar segmented layout as the sea urchin's skeletal plates as segments that are further away from the starting points are usually larger. This geometric characteristic is also structurally advantageous as smaller segments lead to a higher density of interconnection and therefore to a higher structural stiffness at the base points.

A form-finding model based on procedural biological principles has several advantages for the design process. Similar to the sea urchin's growth the circle packing approach allows the control over areas where segments are seeded and hence the direction of growth. During the process segments can react to boundary conditions and follow pre-defined design intends. On a computational level, the resulting arrangement is translated into a mesh topology, which in turn forms the basis for the segment geometry. Architectural requirements are

**Figure 10.** Photograph of the demonstrator. Once assembled, the robotically sewn segments act together as a rigid, double-layered shell.

mainly implemented through the pre-defined design surface on which the segments are distributed throughout the growth process, as well as the openings between segments.

# 7. Conclusion

The presented research is a collaborative project between biology, engineering, and architecture. It is based on a bottom-up research process in biomimetics and can be summarised by two main findings: On the one hand, biological role models cannot only be transferred for the constructional morphology, but also for the design process of segmented shells in timber construction. On the other hand, textile and fibrous connections for joining thin plywood strips are a valid technique and were evaluated on a large-scale prototype building. It can be concluded that the structural and architectural solution space for segmented shells was extended through the development of the described construction system within the context of computational design and construction.

The research was evaluated through the fabrication and construction of a prototype building. With 151 segments made from 3 to 6 mm thick beech plywood, the complete structure weighs 780 kg while covering an area of 85 m² and spanning 9.3 m. With a resulting material thickness/span ratio of 1/1000 on average, the building has a structural weight of 7.85 kg/m² shell. With this new kind of fibrous connection type no metal fasteners were needed for fabrication or assembly.

As research in shells for timber construction progresses towards thinner materials, new connection types become necessary. Contemporary jointing techniques do not account for varying angles or exceptionally thin material and therefore need to be reconsidered. In addition, innovative form-finding processes allow for the exploration of lightweight and material-efficient architecture, but require a closed digital loop between design and fabrication. The developed construction system accounts for both the design process and new fabrication techniques while exhibiting the structural and architectural possibilities of lightweight segmented timber shells.

# Acknowledgements

# References

Alcorn, Andrew. 1996. *Embodied Energy Coefficients of Building Materials*. Wellington: Centre for Building Performance Research.

Chakra, Maria Abou, and Jonathon Richard Stone. 2011. "Holotestoid: A Computational Model for Testing Hypotheses about Echinoid Skeleton Form and Growth." *Journal of Theoretical Biology* 285 (1). Elsevier: 113–25. doi:10.1016/j.jtbi.2011.06.019.

Ellers, Olaf. 1993. "A Mechanical Model of Growth in Regular Sea Urchins: Predictions of Shape and a Developmental Morphospace." *Proceedings of the Royal Society London* B 254: 123–129.

Gruber, Petra and George Jeronimidis. 2012. "Has Biomimetics Arrived in Architecture?" *Bioinspiration & Biomimetics* 7: 1–2.

Johnson, Amy, Olaf Ellers, Jim Lemire, Melissa Minor, and Holly Leddy. 2002. "Sutural Loosening and Skeletal Flexibility During Growth: Determination of Drop-Like Shapes in Sea Urchins." *Proceedings of the Royal Society London* B 269: 215–220.

Kieran, Stephen and James Timberlake. 2004. *Refabricating Architecture. How Manufacturing Methodologies Are Poised to Transform Building Construction*. New York; McGraw-Hill.

Krieg, Oliver David, Tobias Schwinn, Achim Menges, Jian-Min Li, Jan Knippers, Annette Schmitt, and Volker Schwieger. 2015. "Biomimetic Lightweight Timber Plate Shells: Computational Integration of Robotic Fabrication, Architectural Geometry and Structural Design Oliver." In *Advances in Architectural Geometry 2014*, edited by Philippe Block, Jan Knippers, Niloy J. Mitra, and Wenping Wang, 1:109–25. Cham: Springer International Publishing. doi: 10.1007/978-3-7091-0309-8.

La Magna, Riccardo. 2016. *Bend9 – Bending-Active design at Pier 9*. Accessed on 05.04.2016 at http://www.itke.uni-stuttgart.de/entwicklung.php?lang=en&id=76

La Magna, Riccardo, Markus Gabler, Steffen Reichert, Tobias Schwinn, Frédéric Waimer, Achim Menges, and Jan Knippers. 2013. "From Nature to Fabrication: Biomimetic Design Principles for the Production of Complex Spatial Structures." *International Journal of Space Structures* 28 (1): 27–40. doi:10.1260/0266-3511.28.1.27.

Li, Jian-Min, and Jan Knippers. 2015. "Pattern and Form – Their Influence on Segmental Plate Shells." In *Proceedings of the IASS Symposium 2015*, 17–20 August 2015, Amsterdam, Netherlands.

Lienhard, Julian, Simon Schleicher and Jan Knippers. 2011. "Bending-active Structures–Research Pavilion ICD/ITKE." In *Proceedings of the International Symposium of the IABSE-IASS Symposium*, London, UK.

Raup, David M. 1968. "Theoretical Morphology of Echinoid Growth." *Journal of Paleontology* 42: 50–63.

Seilacher, Adolf. 1979. "Constructional Morphology of Sand Dollars." *Paleobiology* 5, 3: 191–21.

Telford, Malcolm. 1985. "Domes, Arches and Urchins: The Skeletal Architecture of Echinoids (Echinodermata)." *Zoomorphology* 105: 114 –124.

Wester, Ture. 2002. "Nature Teaching Structures." *International Journal of Space Structures* 17: 135–147.

Zachos, Louis G. 2009. "A New Computational Growth Model for Sea Urchin Skeletons." *Journal of Theoretical Biology* 259 (3): 646–57. doi:10.1016/j.jtbi.2009.04.007.

# Bending-Active Plates

## Form and Structure

Riccardo La Magna, Simon Schleicher, and Jan Knippers

Riccardo La Magna, Jan Knippers
Institute of Building Structures and Structural Design (ITKE), University of Stuttgart, Germany

ric.lamagna@gmail.com ✉
j.knippers@itke.uni-stuttgart.de

Simon Schleicher
College of Environmental Design, University of California, Berkeley, United States

simon_s@berkeley.edu

# Abstract

Aiming to support the current research on bending-active plate structures, this paper discusses the topic of form-finding and form-conversion and presents examples to illustrate the formal and structural potential of these design strategies. Following a short introduction into the topic, the authors reflect on the specific challenges related to the design of bending-active plate structures. While previous research has mainly focussed on a bottom-up approach whereby the plates first were specified as basic building blocks and the global shape of the structure resulted from their interaction, the main emphasis of this paper lies on a possible top-down approach by form-conversion. Here, the design process starts with a given shape and uses surface tiling and selective mesh subdivision to inform the geometrical and structural characteristics of the plates needed to assemble the desired shape. This new concept entails some constraints, and the paper therefore provides an overview of the basic geometries and mechanics that can be created by following this approach. Finally, to better demonstrate the innovative potential of this top-down approach to the design of bending-active plate structures, the authors present two built case studies, each of which is a proof of the concept that pushes the topic of form-conversion in a unique way. While the first one takes advantage of translating a given shape into a self-supporting weave pattern, the second case study gains significant structural stability by translating a given form into a multi-layered plate construction.

Keywords:
bending-active structures, elastic bending, plate structure,
form-finding, nonlinear analysis

# 1. Introduction

With the rise of new simulation strategies and computational tools, a new generation of architects and engineers is getting more interested in form-finding architectural systems. The key motivation of this approach is to determine a force equilibrium to generate and stabilise a structure just by its geometry. While the membrane and shell structures of pioneers like Frei Otto, Heinz Isler, and Felix Candela were often derived from model-based form-finding processes or using pure geometrical bodies (Chilton 2000, Otto 2005, Garlock & Billington 2008), today's structures often arise from advanced digital simulations and the integration of material behaviour therein (Adriaenssens et al. 2014, Menges 2012).

A good example for the new possibilities emerging from a physics-informed digital design process is the research done on bending-active structures. This type of structural system uses large-scale deformations as a form-giving and self-stabilising strategy (Knippers et al. 2011, Lienhard et al. 2013, 2014, Schleicher et al. 2015). Typically, bending-active structures can be divided into two main categories, which relate to the geometrical dimensions of their constituent elements. For instance, 1D systems can be built with slender rods and 2D systems out of thin plates (Fig. 1). While extensive knowledge and experience exists for 1D systems, with elastic gridshells as the most prominent application, plate-dominant structures have not yet received much attention and are considered difficult to design. One reason is that plates have a limited formability since they deform mainly along the axis of weakest inertia and thus cannot easily be forced into complicated geometries.

However, this obstructive limitation of the smallest building block can also be understood as special advantage. Used strategically, it offers not only more control over the global formation process, but can also be used to inform the individual parts of the assembled structure based on the features of the overall shape. This essentially means that form-finding in the context of bending-active structures could evolve from a bottom-up to a top-down approach, starting with a desired global shape first and then solving the form-force equilibrium of its parts. Following this approach renders the ability to construct a given shape by integrating local bending of its components while guaranteeing that stresses remain within the permitted working range of the material.

# 2. Typical Design Approaches and Resulting Challenges

Bending-active structures are often designed by following either a behaviour-based, geometry-based, or integrated approach (Lienhard et al. 2013). While the first category refers to traditional, intuitive use of bending during the construction process and
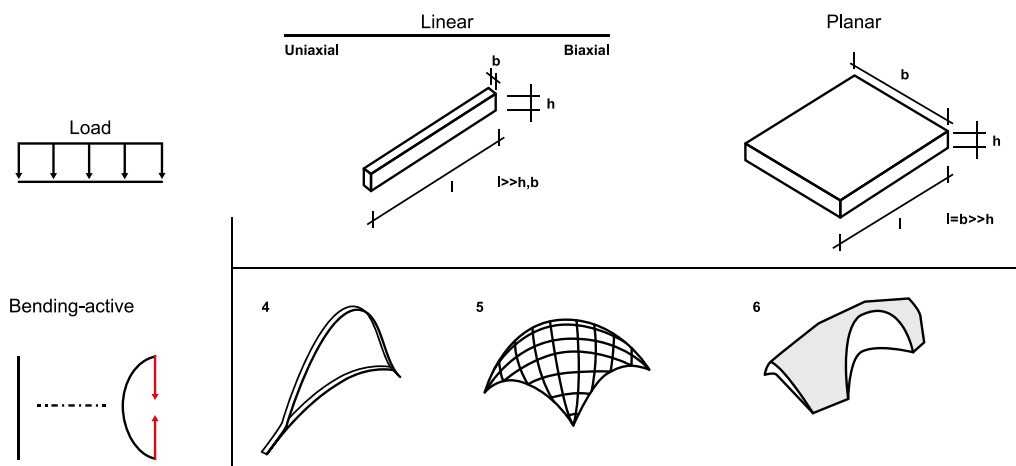
**Figure 1.** Classification of bending-active structures based on the member's geometrical dimension (from Knippers et al. 2011).



**Figure 2a.** Traditional Mudhif reed house.
**Figure 2b.** Plydome.
**Figure 2c.** ICD/ITKE Research Pavilion 2010.

relies only on hands-on experience regarding the deformation behaviour of the used building material (Fig. 2a), the latter two categories describe a more scientific take on the design of bending-active structures. Here, experimental and analytical form-finding techniques were conducted beforehand and then informed the design process.

One example for bending-active plate structures that were built by following a geometry-based design approach are Buckminster Fuller's plydomes (Fuller 1959). This construction principle is based on approximating the basic geometry of a sphere with a regular polyhedron. Its edges and angles are then used to arrange multiple plates into a spatial tiling pattern, which is fastened together by bending the plates at their corners (Fig. 2b). The resulting structure is made out of identical plates joined together by placing bolts at predefined positions. Even though this technique allowed Fuller to construct a double-curved spherical shape out of

initially planar and then single-curved plates, this methodology also had several shortcomings. First and foremost, it is limited to basic polyhedral shapes. Only because of the repetitive angles was it possible to use identical plates. Furthermore, at his time Fuller was forced to compute the needed overlap of the plates and the exact position of the pre-drilled holes mathematically. The only way to calibrate this data was by producing plydomes in series and improving the details over time.

Compared to that, following an integrative design approach for bending-active plate structures provides more flexibility and renders the opportunity for computational automatisation. A prominent example is the 2010 ICD/ITKE Research Pavilion (Fig. 2c). As characteristic for an integrative approach, this project started with intensive laboratory testing to better understand the limiting material behaviour of the used plywood. The results of these physical experiments were then integrated as constraints into parametric design tools and used to calibrate finite-element simulations. Synchronising physical and digital studies ensured that the form-finding techniques provided an accurate description of the actual material behaviour while at the same time giving more feedback on the resulting geometry of the structure. This project even went so far to re-create the actual bending process by simulating the deformation of every strip into a cross-connected and elastically pre-stressed system (Lienhard et al. 2012).

While the last project is definitely innovative, it should be pointed out that the integrated approach here was used mainly in a bottom-up way and thus narrowed the possible design space. For the future development of bending-active plate structures, however, it may be desirable to prioritise a top-down approach, which gives more weight to the target geometry and thus more freedom to the designer. However, the key challenge remains and boils down to how to assess both the global shape as well as the local features of the constituent parts for structures in which geometrical characteristics and material properties are inevitably linked together and similarly affect the result.

# 3. Form Conversion

The principal limit to the formal potential of bending-active structures lies in the restrictions on the material formability. The only deformations that can be achieved within stress limits are the ones that minimise the stretching of the material fibres. For strips and plate-like elements, these reduce to the canonical developable surfaces: cylinders and cones. Attempting to bend a sheet of material in two directions will either result in irreversible, plastic deformations or ultimately failure. Such a strict requirement severely limits the range of structural and architectural potential for plate-based bending-active systems. To expand the range of achievable shapes, it is therefore necessary to develop workarounds
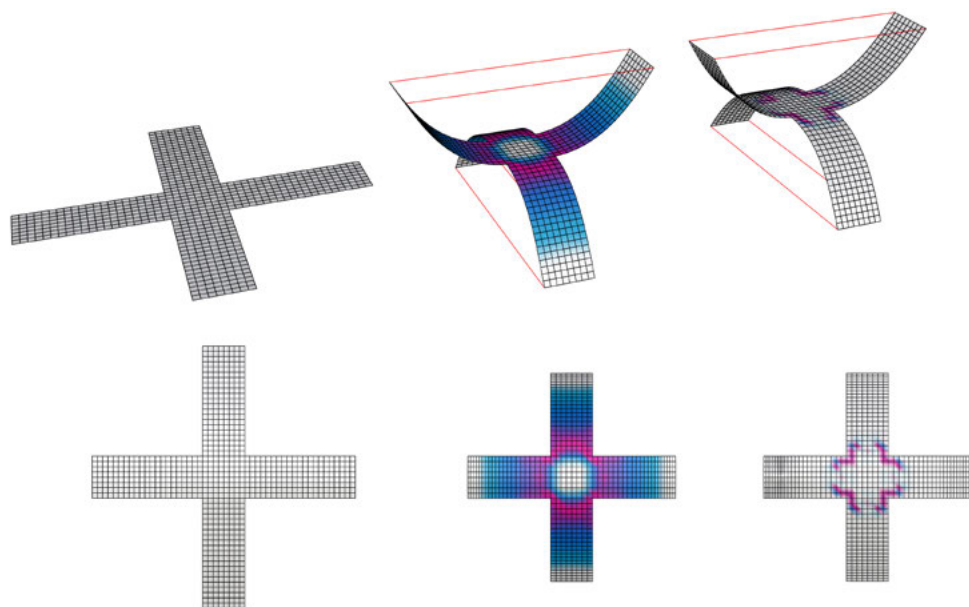
**Figure 3a.** Multidirectional strip.
**Figure 3b.** von Mises stress distribution after bending.
**Figure 3c.** Gaussian curvature.

for the induction of Gaussian curvature. To overcome such limitations, multidirectional bending can be induced by strategically removing material and freeing the strips from the stiffening constraint of the surrounding. A similar approach is presented by Xing et al. (2011) and referred to as band decomposition. The key principle is illustrated in Figure 3.

Here a continuous rectangular plate is reduced to two orthogonal strips. The strips are later bent into opposite directions in a finite element simulation using the ultra-elastic contracting cable approach based on Lienhard, La Magna and Knippers (2014). The bending stiffness of the plate, depending proportionally on its width b, results in a radical increase of stiffness in the connecting area between the strips. As a result, the connecting area almost remains planar, and therefore the perpendicular bending axis remains unaffected by the induced curvature. In this way it becomes possible to bend the strips around multiple axes, spanning different directions but still maintaining the material continuity of a single element. Figure 3b depicts the resulting von Mises stresses calculated at the top fibres. The gradient plot clearly displays an area of unstressed material at the intersection between the two strips, as expected based on the previous arguments. A local stress concentration appears at the junction of the strips due to the sharp connecting angle and inevitable geometric stiffening happening locally in that area.
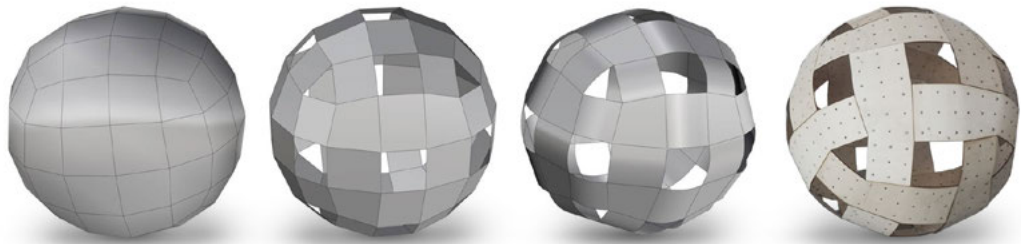
**Figure 4a.** Mesh of target surface.
**Figure 4b.** Offset and edge bridging.
**Figure 4c.** Bending of bridging elements.
**Figure 4d.** Plywood prototype of sphere test case.

This result can be compared with Figure 3c, which displays the Gaussian curvature of the bent element. From the plot it is clear that the discrete Gaussian curvature (based on Meyer et al. 2003) of the deformed mesh is everywhere zero, apart from a small localised area at the intersection of the two branches. This confirms that, within stress limits, flat sheets of inextensible material can only be deformed into developable surfaces at most.

Based on the strip approach defined so far, the general procedure for an arbitrary freeform surface is summarised in the following steps:

1. Mesh the target surface (Fig. 4a).
2. Perform an interior offset for each face of the mesh.
3. Connect the disjointed faces by creating a bridging element; two faces initially sharing an edge will be connected (Fig. 4b).
4. The bridging element is modified to take into account the bending curvature. Assuming that the start and end tangent plane of the bridging element coincide with the surfaces to be connected, the element can be defined through a simple loft (Fig. 4c).
5. Unroll the elements.

The presented method maintains general validity for any arbitrary source mesh. In the case of an Ngon mesh, its banded dual will have strips with N arms departing from the centre surface element. The geometry of the voids is defined by the valence of the mesh. For the sphere example a 4-valent source mesh produces square voids throughout the banded structure. A tri-valent hexagonal mesh would produce triangular voids and so forth.

# 4. The Geometry and Mechanics of Bending-Active Plate Structures

It is typical in engineering to distinguish between plate and shell structures, the main difference being that plates are initially flat and shells already present curvature in their stress-free configuration. Both structures can be identified as having thickness significantly smaller than length and width. In this way the geometry of a shell or plate is uniquely defined by their centre surface and local thickness (Bischoff et al. 2004). The structural behaviour of shells and plates is characterised by two main states of deformation, membrane and bending action. Membrane deformations involve strain of the centre surface, whilst bending dominated deformations roughly preserve the length of the mid-surface fibres. Under bending, only the material fibres away from the mid-surface are fully exploited, therefore the structural elements are much more flexible. Pure bending deformations are also called *inextensional deformations* as the neutral surface is completely free from longitudinal extension or compression. In mathematical terms, a transformation that preserves lengths is also referred to as an *isometry*. *Pure bending*, *inextensional*, and *isometric deformations* are all synonyms that are often used interchangeably in literature, preferring one term over another to highlight either mechanical or mathematical aspects. Strictly speaking, the only isometric transformations of the plane are into cones and cylinders, i.e. developable surfaces.

In structural applications, membrane deformation states are generally preferred as the cross-section is completely utilised and the load-bearing behaviour of the shell is significantly enhanced. On the other hand, characteristics of inextensional deformations may be exploited in certain situations, for example, deployable or tensile structures which might benefit from bending dominated transition stages. In the context of bending-active structures, inextensional deformations represent the main modality of shape shifting, as the bending elements may undergo large deformations without reaching a critical stress state for the material. Owing to the high flexibility of thin plates with respect to bending, this state of deformation may be regarded as the dominating mechanical effect for bending-active structures as having the strongest effect on the nonlinear behaviour of plates.

The relationship between large deformations and pure bending is well understood in light of energetic arguments explained in the following paragraph. An important assumption in the context of bending-active structures is that of a perfect elastic response of the material. This is the case of Hookean elasticity, which assumes a linear elastic response of the material and therefore yields a proportional relationship between strain and stress (Audoly & Pomeau 2010). This assumption is valid for small strains in general, which is commonly the case for bending-active structures. In the membrane approximation, the elastic energy of a plate reads:

$$\varepsilon_{mb} \sim Eh \iint_P (\epsilon_{\alpha\beta})^2_{cs} \, dxdy$$

where the subscript '*cs*' means that we can evaluate the density of the elastic energy along the centre surface. The approximation (4.1) can be understood as following: It is the surface integral of the squared, 2-dimensional strain along the centre surface $\epsilon_{\alpha\beta}$, multiplied by the factor $Eh$, which is proportional to the thickness $h$ and to Young's modulus $E$ of the material.

Conversely, the bending energy of a 2-dimensional plate assumes the following form:

$$\varepsilon_b \sim \frac{1}{2} \iint_P \frac{Eh^3}{12} \left( \frac{1}{R_{cs}(x,y)} \right)^2 dxdy$$

which can be read as the surface integral of the squared curvature (dependent on x and y) of the centre surface, multiplied by the factor $Eh^3$, which is commonly called *bending ſtiffness*.

Comparing the stretching energy (4.1) with the bending energy (4.2) shows that the small thickness h comes in the flexural energy (4.1) with a larger power than in the stretching energy, i.e. $h^3$ in place of h. For very thin plates, this makes the energy of isometric deformations much lower than those involving significant stretching of the centre surface. As a result, large deformations occur mainly under bending, as the low energy involved in the process is generally compatible with the strain limits of the material.

Although commonly referred to as bending-active, the term has been specifically coined to describe a wide range of systems that employ the large deformation of structural components as a shape-forming strategy. Besides bending, torsional mechanisms can also be employed to induce form, as the energy involved is of similar order of magnitude compared to bending. An essential requirement for bending-active structures is that the stress state arising from the form-finding process does not exceed the yield strength of the material. Based on the previous assumptions of perfect elastic material response and thin, slender sections, the maximum bending curvature and maximum torsional angle twist can be checked against the following relationships:
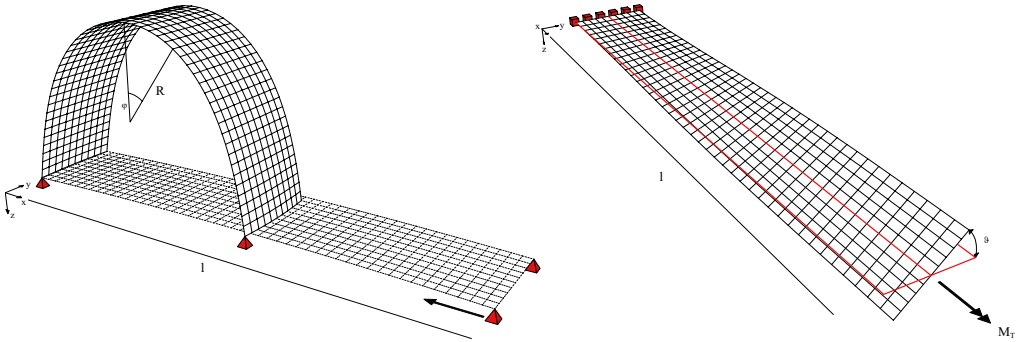
**Figure 5a.** Material strip subject to axial bending.
**Figure 5b.** Material strip subject to torsion.

$$k = \frac{d\varphi}{dx} = \frac{M_B}{EI}$$

$$\frac{d\theta}{dx} = \frac{M_T}{GJ}$$

$$\sigma_{max} = \frac{M_B}{W}$$

$$\tau_{max} = \frac{M_T}{W_T}$$

$$k_{min} = \frac{1}{R_{max}} = \frac{\sigma_{max}W}{EI} = \frac{2\sigma_{max}}{Eh}$$

$$\frac{d\theta}{dx} = \frac{\tau_{max}W_T}{GJ} = \frac{\tau_{max}}{Gh}$$

where:

| | | | |
|---|---|---|---|
| $k$ | curvature [1/m] | $\theta$ | angle of twist [rad] |
| $M_B$ | bending moment [kNm] | $M_T$ | torsional moment [kNm] |
| $E$ | Young's modulus [N/mm$^2$] | $G$ | shear modulus [N/mm$^2$] |
| $I$ | moment of inertia [m$^4$] | $J$ | torsional constant [m$^4$] |
| $W = bh^2/6$ | resistance moment [m$^3$] | $W_T = bh^3/3$ | torsional resistance [m$^3$] |
| $\sigma_{max}$ | max. allowable stress [N/mm$^2$] | $\tau_{max}$ | max. shear stress [N/mm$^2$] |
| $h$ | section height [mm] | $h$ | section height [mm] |

These equations refer to the classic Euler-Bernoulli model for bending and de Saint-Venant torsion model for beams. Both models ignore higher order effects, respectively deformations, caused by transverse shear and torsional warping. Although generally non-neglectable for large deformations, owing to the previous assumptions of slender cross-sections and elastic behaviour, it is safe to assume these values for a preliminary check of the master geometry.

The complexity of the structural systems and form-finding procedures still require an accurate numerical analysis. In general, currently available simulation tools can be subdivided into two categories. The first one, dynamic relaxation (DR), is a numerical iterative method to find the solution of a system of nonlinear equations. It has been successfully employed in engineering applications for the form-finding of membrane and cable net structures (Barnes 1999, Adriaenssens & Barnes 2001) and in modified versions also for torsion related problems in surface-like shell elements (Nabaei et al. 2013). The second method relies on finite element

**179**

simulation (FEM). Non-linear finite element routines have advanced so much lately that it is becoming more common to integrate them in the design process. All the results presented here were achieved through geometrical non-linear finite element simulations run in SOFiSTiK.

# 5. Case Studies

The following two case studies are both made out of the same material – 3 mm birch plywood. This plywood consists of three layers and has different mechanical behaviours along the main fibre orientation (stronger) and against it (softer). This is due to the fact that the fibre direction of the upper and lower layers is oriented in one direction and rotated by 90° in the centre layer. Based on this the plywood also has two values for the minimal bending radius that can be achieved as well as two values for the maximum axial twist the material can undergo. The Young's modulus of a 3 mm plywood along the grain is: $Em_{II}$ = 16471 N/mm² and against the grain is: $Em_{\perp}$ = 1029 N/mm².

## 5.1 Case Study: Berkeley Weave

The first case study investigates the design potential emerging from integrating both bending and torsion of slender strips into the design process. A modified Enneper surface acts as a base for the saddle-shaped design (Fig. 6a). This particular form was chosen because it has a challenging anticlastic geometry with locally high curvature. The subsequent conversion process into a bending-active plate structure followed several steps. The first was to approximate and discretise the surface with a quad mesh (Fig. 6b). A curvature analysis of the resulting mesh reveals that its individual quads are not planar but spatially curved (Fig. 6c).

The planarity of the quads, however, is an important precondition in the later assembly process. In a second step, the mesh was transformed into a four-layered weave pattern with strips and holes. Here, each quad was turned into a crossing of two strips in one direction intersecting with two other strips in a 90-degree angle. The resulting interwoven mesh was then optimised for planarisation. However, only the regions where strips overlapped were made planar (blue areas), while the quads between the intersections remained curved (Fig. 6d). A second curvature analysis illustrates the procedure and shows zero curvature only at the intersections of the strips while the connecting arms are both bent and twisted (Fig. 6e). In the last step, this optimised geometrical model was used to generate a fabrication model that features all the connection details and strip subdivisions (Fig. 6f).

(A) Base geometry    (B) Mesh approximation    (C) Curvature analysis

(D) Conversion to bent plates    (E) Curvature analysis    (F) Fabrication model
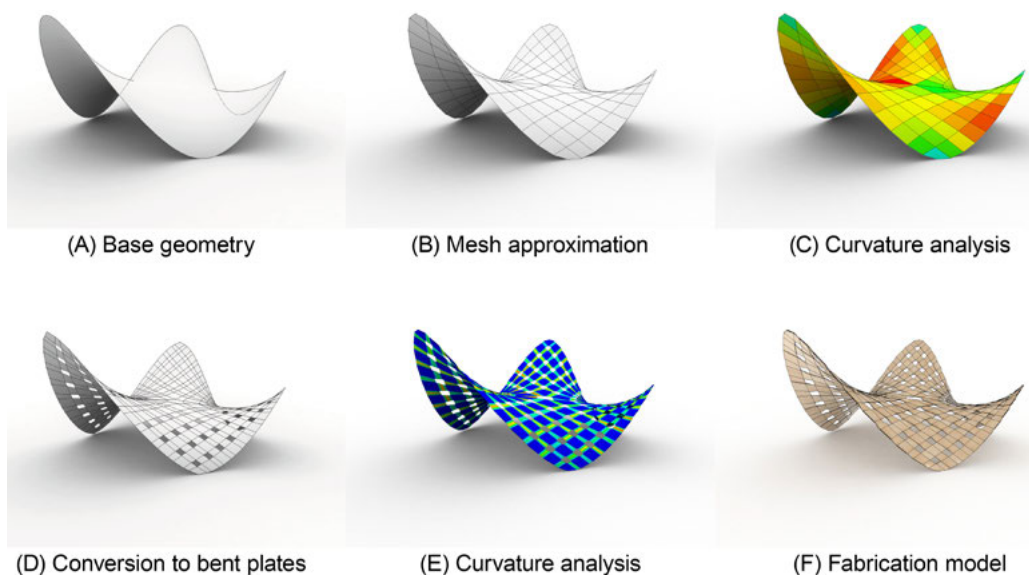
**Figure 6.** Generation process and analysis.
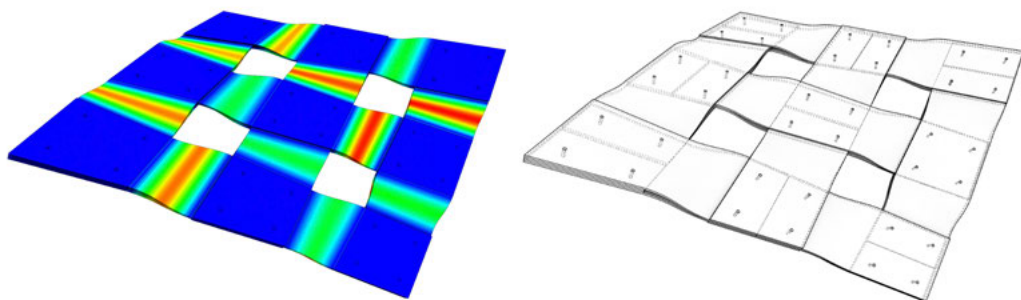


**Figure 7a.** Analysis of Gaussian curvature.
**Figure 7b.** Schematic of the weaving and technical details.

A closer look at the most extremely curved region in the structure illustrates the complexity related to this last step (Fig.7a). To allow for a proper connection, bolts were placed only in the planar regions between intersecting strips. Since the strips are composed out of smaller segments, it was also important to control their position in the four-layered weave and the sequence of layers. A pattern was created which guaranteed that strip segments only ended in layers two and three and are clamped by continuous strips in layers one and four. A positive side effect of this weaving strategy is that the gaps between segments are never visible and the strips appear to be made out of one piece. The drawback, however, is that each segment has a unique length and requires specific positions of the screw holes (Fig. 7b).

To demonstrate proof of concept for this design approach, this case study was built in the dimensions of 4 m x 3.5 m x 1.8 m (Fig. 8). The structure is assembled out of 480 geometrically different plywood strips fastened together with 400 similar bolts. The material used is 3.0 mm thick birch plywood with a Young's modulus of $Em_{II}$ = 16471 N/mm² and $Em_{\perp}$ = 1029 N/mm². Dimensions and material specifications were employed for a finite-element analysis using the software SOFiSTiK. Under consideration of self weight and stored elastic energy, the minimal bending radii are no smaller than 0.25 m and the resulting stress peaks are still below 60% of permissible yield strength of the material.

## 5.2  Case Study: Bend9

The second case study is a multi-layered arch that spans over 5.2 m and has a height of 3.5 m. This project was built to prove the technical feasibility of using bending-active plates for larger load-bearing structures. In comparison to the previous case study, this project showcases a different tiling pattern and explores the possibility to significantly increase a shape's rigidity by cross-connecting distant layers with each other.

To fully exploit the large deformations that plywood allows for, the thickness of the sheets had to be reduced to the minimum, leading once again to the radical choice of employing 3.0 mm birch plywood. Since the resulting sheets are very flexible, additional stiffness needed to be gained by giving the global shell a peculiar geometry which seamlessly transitions from an area of positive curvature (sphere-like) to one of negative curvature (saddle-like) (Fig. 9a). This pronounced double-curvature provided additional stiffness and avoided undesirable deformation modes of the structure. Despite the considerable stiffness achieved through shape, the choice of using extremely thin sheets of plywood required additional reinforcement to provide further load resistance. These needs were met by designing a double-layered structure with two cross-connected shells.

As in the previous example, the first step of the process was to convert the base geometry into a mesh pattern (Fig. 9b). In the next step a preliminary analysis of the structure was conducted, and a second layer was created by offsetting the mesh. As the distance between the two layers varies to reflect the bending moment calculated from the preliminary analysis, the offset of the surfaces changes along the span of the arch (Fig. 9c). The offset reflects the stress state in the individual layers, and the distance between them grows in the critical areas to increase the global stiffness of the system. The following tiling logic that was used for both layers guarantees that each component can be bent into the specific shape required to construct the whole surface. This is achieved by strategically placing the voids into target positions of the master geometry, as described in Section 3, and thereby ensuring that the bending process can take place without prejudice for the individual components (Fig. 9d). Although initially flat, each

**Figure 8.** View of the plywood installation Berkeley Weave.
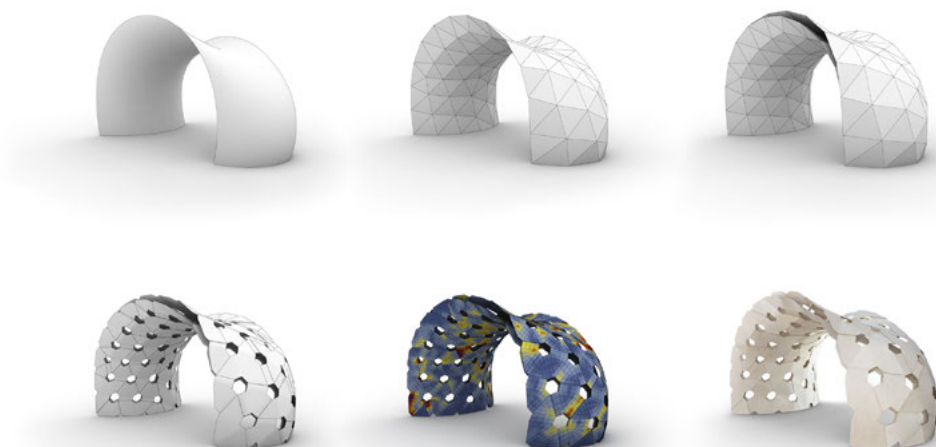


**Figure 9a.** Base geometry.
**Figure 9b.** Mesh approximation.
**Figure 9c.** Double layer offset.
**Figure 9d.** Conversion to bent plates.
**Figure 9e.** Finite-element analysis.
**Figure 9f.** Fabrication model.

element undergoes multi-directional bending and gets locked into position once the neighbours are added to the system and joined together. The supple 3.0 mm plywood elements achieve consistent stiffness once assembled together, as the pavilion, although a discrete version of the initial shape, still retains substantial shell stiffness. This was validated in a second finite-element analysis that considered both self-weight as well as undesirable loading scenarios (Fig. 9e). Finally, a fabrication model was generated and the structure fabricated (Fig. 10).

The built structure employs 196 elements unique in shape and geometry (Fig. 11a). 76 square wood profiles of 4 cm x 4 cm were used to connect the two plywood skins (Fig. 11b). Due to the varying distance between the layers, the connectors had a total of 152 exclusive compound mitres. The whole structure weighs only 160 kg, a characteristic which also highlights the efficiency of the system and its potential for lightweight construction. The smooth curvature transition and the overall complexity of the shape clearly emphasise the potential of the construction logic to be applied to any kind of double-curved freeform surface.

# 6. Conclusions

The two built case studies clearly illustrate the feasibility of a construction logic that integrates bending deformations strategically into the design and assembly process. Both structures presented are directly informed by the mechanical properties of the thin plywood sheets employed for the project. Their overall geometry is therefore the result of an accurate negotiation between the mechanical limits of the material and its deformation capabilities.

The assembly strategy devised for both prototypes drastically reduces the fabrication complexity by resorting to exclusively planar components which make up the entire double-curved surfaces. Despite the large amount of individual geometries, the whole fabrication process was optimised by tightly nesting all the components to minimise material waste, flat cut the elements, and finally assemble the piece on-site.

The very nature of the projects required a tight integration of design, simulation, and assessment of the fabrication and assembly constraints. Overall, the Bend9 pavilion and Berkeley Weave installation exemplify the capacity of bending-active surface structures to be employed as a shape-generating process. For on-going research, the buildings serve as first prototypes for the exploration of surface-like shell structures that derive their shape through elastic bending.

**Figure 10.** View of the Bend9 structure.



**Figure 11a.** Detail of the elements.
**Figure 11b.** Detail of the connecting elements.

## Acknowledgements

## References

Adriaenssens, Sigrid, Philippe Block, Diederik Veenendaal, and Chris Williams. 2014. *Shell structures for architecture: form finding and optimization*. London, New York: Routledge.

Adriaenssens, Sigrid, and Michael R. Barnes. 2001. "Tensegrity Spline Beam and Grid Shell Structures." *Engineering Structures* 23, 1: 29–36.

Audoly, Basile, and Yves Pomeau. 2010. *Elasticity and Geometry: From Hair Curls to the Non-Linear Response of Shells*. Oxford, New York: Oxford University Press.

Barnes, Michael R. 1999. "Form Finding and Analysis of Tension Structures by Dynamic Relaxation." *International Journal of Space Structures* 14, 2: 89–104.

Bischoff, Manfred, Wolfgang A. Wall, Kai-Uwe Bletzinger, and Ekkehard Ramm. 2004. *Encyclopedia of Computational Mechanics. Volume 2: Solids and Structures*. New York: John Wiley & Sons.

Chilton, John C., and Heinz Isler. 2000. *Heinz Isler*. London: Thomas Telford.

Fuller, Richard B. 1959. "Self-Strutted Geodesic Plydome." U.S. Patent 2,905,113, issued September 22, 1959.

Garlock, Maria E. Moreyra, and David P. Billington. 2008. *Félix Candela: Engineer, Builder, Structural Artist*. New Haven: Yale University Press.

Knippers, Jan, Jan Cremers, Markus Gabler, and Julian Lienhard. 2011. *Construction Manual for Polymers + Membranes: Materials, Semi-Finished Products, Form Finding, Design*. Basel, Berlin: Birkhäuser.

Lienhard, Julian, Simon Schleicher and Jan Knippers. 2012. "Bending-Active Structures – Research Pavilion ICD/ITKE." In *Proceedings of the International Symposium of the IABSE-IASS Symposium, Taller Longer Lighter*, Nethercot, D., Pellegrino, S. et al. (eds). London: Brintex Digital Publishing.

Lienhard, Julian, Holger Alpermann, Christoph Gengnagel, and Jan Knippers. 2013. "Active Bending: A Review on Structures Where Bending Is Used as a Self-Formation Process." *International Journal of Space Structures* 28, 3–4: 187–196.

Lienhard, Julian, Riccardo La Magna and Jan Knippers. 2014. "Form-Finding Bending-Active Structures with Temporary Ultra-Elastic Contraction Elements." *Mobile and Rapidly Assembled Structures IV*. doi: 10.2495/mar140091

Lienhard, Julian, and Jan Knippers. 2014. Bending-Active Structures. PhD diss., Dissertation, University of Stuttgart.

Menges, Achim. 2012. "Material Computation: Higher Integration in Morphogenetic Design." *Architectural Design* 82, 2: 14–21.

Meyer, Mark, Mathieu Desbrun, Peter Schröder, and Alan H. Barr. 2003. "Discrete Differential-Geometry Operators for Triangulated 2-Manifolds." *Visualization and Mathematics III*, 35–57. Berlin Heidelberg: Springer.

Nabaei, Sina S., Olivier Bavere, and Yves Weinand. 2013. "Mechanical Form-Finding of the Timber Fabric Structures with Dynamic Relaxation Method." *International Journal of Space Structures* 28, 3-4: 197–214.

Otto, Frei. 2005. *Frei Otto: Complete Works: Lightweight Construction, Natural Design*. Edited by Winfried Nerdinger. Basel, Berlin: Birkhäuser.

Schleicher, Simon, Andrew Rastetter, Riccardo La Magna, Andreas Schönbrunner, Nicola Haberbosch, and Jan Knippers. 2015. "Form-Finding and Design Potentials of Bending-Active Plate Structures." In *Modelling Behaviour*, pp. 53–63. Switzerland: Springer International Publishing.

Xing, Qing, Gabriel Esquivel, Ergun Akleman, and Jianer Chen. 2011. "Band Decomposition of 2-Manifold Meshes for Physical Construction of Large Structures." *Proceedings of the Siggraph Conference,* Vancouver.

# Underwood Pavilion

## A Parametric Tensegrity Structure

Gernot Riether and Andrew John Wit

G. Riether
College of Architecture and Design, New Jersey Institute of Technology, USA
griether@gmail.com ✉

A. J. Wit
Tyler School of Art, Temple University, USA
andrew.wit@temple.edu

All images/drawings by Andrew Wit and Gernot Riether

**188**

# Abstract

Recent advances in real-time structural analysis has given architects the freedom to design and manufacture forms and structures that previously would have been difficult if not impossible to achieve. Until recently these advances had not been seen as a driving force within the area of asymmetrically designed tensegrity structures. This paper presents a new design method that is integrating analysis tools into a computational design process. Through the lens of the recently completed *Underwood Pavilion* this paper demonstrates how this process of designing tensegrity structures can be streamlined. This process allows for greater access to such structures and a higher level of flexibility in designing tensegrity systems by the design community at large. Acting as a case study, the *Underwood Pavilion* describes a process where traditional methods of form finding are complimented by a new parametric approach to design tensegrity based lightweight structures and envelope systems.

Keywords:
tensegrity, parametric, membrane, pavilion, modular

# 1. Introduction

The *Underwood Pavilion* was Prof. Riether's and Prof. Wit's first successful attempt at fabricating a full-scale tensegrity prototype through a novel parametric framework. The pavilion defines a space that can comfortably be inhabited by a group of 12 people. Located close to Muncie, Indiana, it creates a permanent destination for hikers and cyclists. Accomplished through a 5-week summer workshop held at Ball State University in Muncie, Indiana, a team of 8 students and faculty collaborated in the development of the design, fabrication, and construction of the project. This paper discusses in detail the developed tensegrity design methodology and the accomplishments and difficulties encountered throughout the project's overall development. It also discusses the project's workflow and a unique design, fabrication, and assembly process created through the development utilising Rhinoceros 3d, Grasshopper, Galapagos, and Kangaroo. Through the development of an integrated digital/manual workflow, the team was able to develop a parametric design method that allowed for the design of variable tensegrity modules that, once aggregated, generated the form of the *Underwood Pavilion's* unique visual and structural envelope.

# 2. Background

Unlike conventional construction systems centred around the concept of continuous compression under gravitational loading, tensegrity structures utilise a concept of continuous tension. In contrast, tensegrity systems are similar to the assemblies within the human body, where bones act as compression struts and the muscles, tendons, and ligaments form the tension members (Ingber, 1998). What R. Buckminster Fuller (1973) previously defined as tensegrity structures is still unique: isolated compression members and a continuous path of tension members that connect all nodes.

Examples of how tensegrity structures are applied to an architectural scale are projects such as the Warnow Tower (Volkwin, 2003) in Rostock, Germany, the tallest tensegrity mast ever deployed, and the Kurilpa Bridge (Cox Rayner Architects, Arup, 2009) in South Brisbane, the world's largest hybrid tensegrity bridge. More recent research by Kenneth Snelson also exemplifies the system's unique properties and brings tensegrity into the forefront of design thinking.

Tensegrity structures are relevant to architecture since they are lighter, stronger, and more cost efficient than other structural systems such as space frames or truss systems. Additionally, the system where all struts work in pure compression while cables remain in pure tension allows for a more effective use of material and nominal dimension optimisation.

Nonetheless, the geometry of tensegrity structures is more difficult to design than other structural systems. Tensegrity structures cannot be predicted from their geometric characteristics alone. The design process must take into account that a tensegrity moment can be achieved only through a structural equilibrium within the system. Several methods of mathematically calculating tensegrity structures exist and are outlined in papers such as Tibert and Pellegrino (2003). Nonetheless, these complexities within these methods are nearly impossible to apply within a rapidly adapting design process, especially in relation to a more complex overall form, asymmetrical loading or environmental conditions.

Recent tools such as the Rhino 3D plug-in Rhino Membrane and the Grasshopper plug-in Kangaroo in conjunction with Galapagos offer for the first time graphic design interfaces for a high level of geometric complexity which also have the ability to take physical material properties into account. Both applications enable form finding and the structural solving of tensegrity systems through a methodology of finite element analysis. This provides real-time feedback of structural behavior in both individual and aggregated modules, a necessity within the geometric form-finding process of the *Underwood Pavilion*.

# 3. Parametric Tensegrity Structure

Typically, tensegrity structures are realised as a singular continuous system, where all parts are reliant on all others within the system. Although this has advantages such as material and part optimisation, the complexity inherent within solving and fabricating the overall system as a singular object was not desirable. Rather, the *Underwood Pavilion* visualised the tensegrity system as a series of self-contained modules with the ability to be individually programmed, fabricated, tensioned, and inserted/removed from the structure without causing catastrophic failure of the overall system. Through the unique programming of individual modules and the removal of modules from the overall system, the resulting pavilion was able to create formal deviations that would have been difficult to realise through a traditional continuous tensegrity system.

To facilitate the modular system, a variant of a 3-strut tensegrity module was chosen as a base constraint that helped minimise the solution space in designing the individual modules and the pavilion as a whole. The chosen base module consisted of two equilateral triangles with end faces of differing sizes parallel to one another. The upper face was named "ABC", the lower face "DEF". Tensile cables connected the node pairs "AD", "BE", and "CF", while rods connected the node pairs "AE", "BF", and "CD". Within these constraints the typology of the module could vary based on two variables that could change (defined variables) and two variables that would change as a consequence (unknown variables):

Defined variable 1:
*Scalar variation between the upper face (ABC) and the lower face (DEF).*
Defined variable 2:
*Length of the tensile members between the two faces (ABC) and (DEF).*
Unknown variable 1:
*Distance between the upper face (ABC) and the lower face (DEF).*
Unknown variable 2:
*Module rotation between upper face (ABC) and lower face (DEF), which was a consequence of the previous variables and the tension necessary to stabilise the geometry in a tensegrity state.*

To initially test the system, two physical experiments were conducted. Rubber bands were used to approximate length of cables for struts of different lengths. Based on the outcome of the first set of models, a second set of physical models were developed in which the rubber bands were replaced with strings. Within these studies, adjustments were necessary to find the final resting length of strings and their corresponding struts allowing for the models to reach a stabile tensegrity state. An aggregate of modules was built, then the variables of the module were changed, and another system was constructed. A series of aggregates showed the impact of the different module's geometry on different overall forms. Some of the aggregates twisted or curved more than others. Some aggregates started to define more enclosures than others.

These physical models created a simplistic starting point for the design method that was then developed computationally. In replacing the physical studies with a parametric model the goals were (1) to test different variations by changing one model, rather than building a separate model for each variation that the team wanted to test; (2) to achieve a more precise understanding of how varying the module may affect the overall form; (3) to test aggregations too complex to build in a physical model.

## 3.1 Parametric Form Finding

Tensegrity systems have been applied to projects at large scale before. But the examples mentioned earlier showed that only very basic overall forms had been used: In the case of the Warnow Tower or the Kurilpa Bridge, modules were assembled into a straight line. In the case of Buckminster Fuller's studies, the overall form was a sphere. The design process developed for the *Underwood Pavilion* was different. Rather than starting with an overall form, the form emerged from the aggregation of variations of modules.

To develop the design process of such a system, Rhino Membrane, Grasshopper, Galapagos, and Kangaroo were utilised. Rhino membrane, a plug-in designed for

Rhino 4.0, was used in conjunction with physical modelling as a means of initial module form finding, digital feedback, and enclosure optimisation.

Galapagos, an evolutionary solver, was utilised on singular modules to find optimal geometric fitness for the two unknown values of face rotation and distance between the upper and lower faces. The plug-in was also used as a means of obtaining real-time feedback when manipulating individual module proportions, while still maintaining a high level of mathematical accuracy (solutions within a thousandth of an inch). Through Galapagos, variation of individual modules could be created (through a series of number sliders or value inputs), compared and directly implemented into the Kangaroo solver for interpreting the overall form. Through this workflow, the designers were able to continually modify the pavilion's overall form through the manipulation of a single module's variables. To verify the parametric modules outputs and internal tensions during the aggregation process, each selected variation was fabricated and tested at small scale.

Kangaroo, a live physics engine for interactive simulation, optimisation, and form finding developed as a plug-in for Grasshopper, was used to simulate each possible outcome achieved through the aggregation of modules. By defining a series of attractor points in the location where compressive rods and tensile cable intersect, individual modules were linked, creating a single continuous system. With the connection of the cables and struts, each of the formal iterations slowly recalculated and found their form in a state of equilibrium.

Although initially the overall form is an unknown, the reconfigured and combined tools enabled the designers to define the final form through the definition of all module types in relation to their necessary points of connection as well as the desired strut and cable network forces. The overall form was also impacted by removing modules to create openings for views or an entrance, creating asymmetric deformations in the overall form, while simultaneously changing tensile forces within the aggregate.

## 3.2 Module Programming

Each individual module variation was first constructed in Rhino then parameterised: Rather than the elastic properties of the rubber bands in the physical model, the cables in the digital model were defined by a determined pre-stress value and fixed length. The modules were then connected into single rows of modules. Utilising customised computational physics simulations allowed the designers to precisely predict the curvature of linear aggregations based on specific module variations.

Following this step, single rows were doubled. This time the physics simulation visualised a shift within the arch, which was perpendicular to its curvature. The shift occurred as a consequence of the individual module's rotation. In the final simulation, the modules were arranged into aggregates of 6 x 6 modules.

The structural and formal behavior of aggregates constructed from different module variations and combinations were then compared through digital simulation.

## 3.3 Module Variation

As the overall form functions as a continuous network, simply replacing one module with another was not possible. Rather, the integration of a new module type would in turn, redefine the form and parameters of all adjacent modules. Varying a module in the physical model required the construction of an entirely new aggregate. In the digital model the team was able to instantly recalculate the formal properties of the entire aggregate and output their parameters for fabrication. In a further development one could also think about using multiple module variations within a single system.

# 4. Aggregation

Developing the pavilion from a set of varied modules allowed for easy exploration of novel strategies for aggregation through different field conditions. When connecting modules, one top face (ABC) must connect to other top face (ABC) and bottom face (DEF) to other bottom face (DEF). The smaller top triangles defined the inner surface of the pavilion, while the larger bottom triangles define the outer surface. In order to form a tensegrity structure from a pattern of individual tensegrity modules, the edges of individual triangles must always connect to midpoints of edges of neighbouring triangles.

Although during computational modelling and simulation force values were calculated to be minimal, it was found otherwise during construction. Although each module was fabricated from the exact simulated measurements, it was found that slight inconsistencies during assembly, individual module tensioning, material flexure or stretching, and finally inconsistent siting conditions created conditions where tensions could be nearly unmanageable or self-destructing. To bypass these inconsistencies, a system was developed for internal stress management.

Rather than reworking the entire tensegrity system to minimise unpredictable force accumulation, a system was developed where individual modules could be eliminated from the system creating view apertures while also reducing stress. This porosity and structural flexibility was created through the skipping of every second module in every second row. Although removing elements in a single continuous system would cause failure, even with the removal of modules within the modular based system, enough continuity still existed for the creation of a successful tensegrity system. This variable allowed the designers to create large or small apertures within the pavilion's envelope. Changing the scale between

the top face and the bottom face of each module also enabled further manipulation of the pavilions envelope.

# 5. The Role of Physical Modelling and Prototyping

Digitally confirmed results were immediately tested as physical prototypes insuring the correct translation of data. This feedback loop between physical and digital modelling allowed for previously complex complications to now be detected and solved quickly.

As modules appear very similar and can become disorienting during construction, designers learned to track the complex behaviors of individual elements and modules within the structure by creating very simple numbering, colour, and vector-based systems. Tying a simple coloured string to repeating elements in a physical model or a coloured vector in the parametric model, for example, allowed the team to easily find corresponding points of connection. Understanding methods of physically and digitally tracking behaviors of individual components within a larger system played an important role during full-scale construction, where connections become extremely complex.

Working both with individual modules and complex aggregations, the team learned to quickly visualise the effects small changes on an individual component could have on the pavilion as a whole. Varying size or tension in a single module could affect the shape, structure, and rotation of the entire form.

Full-scale prototyping was also an important feedback mechanism. If an individual or group had a proposed design idea, it was immediately necessary to test its workability, availability as well as cost effectiveness. If any of these could not be found or achieved, it was necessary for the designers immediately revise their idea to make it feasible.

Initial testing also aided the team in the rapid prototyping of joints, connectors, and details. As prototyping happened simultaneously with the design process, the team was able to test large numbers of variations within the mock-up of a single module. For example, a single module contained a total of one piece of fabric, six joints, nine cables and 27 connectors. Therefore, in the testing of one module, designers could test a variety of connections and parts for aesthetics, compatibility, and structural integrity. Because of this integrated process, many potential on-site construction issues were confronted early on in the design process.

With only a single week for fabrication and construction, it was imperative that a robust production system be designed and implemented. While prototyping, the team developed a step-by-step fabrication process utilising individual strengths, machines and space to maximise efficiency.

# 6. Module Construction

The final tensegrity state of a module can be reached only when all members are in tension or compression. The entire system remained loose and in a flat pack orientation until one final turnbuckle per module was connected and tightened. In the untensioned state, the modules can be easily stacked and transported as a loose low-volume bundle of bars and cables (roughly 3″ x 3′ x 6′). At the site of construction, only a single cable per module was joined creating the final module's form. Each of the 40 individual modules described a volume that varied between 3′ x 3′ x 3′ and 4′ x 4′ x 4′, respectively, and weighed less than 5 pounds. This ease of assembly and scale of module allowed for the module to be maneuvered around the site in a compressed form, then simply tensioned and moved into its corresponding location by a single individual.

Since cables were in pure tension and struts in pure compression, the axial deformation of struts and cables was visually negligible under full loading conditions. This enabled the use of lightweight materials such as 1″ diameter aluminium tubes and 1/8″ braided galvanised steel cables were used for the pavilion's final structure.

The cables were pre-cut to length for each of the 9 nodes per module. Precise grooves and holes within the aluminium tubes were created though the implementation of a flexible jig and facilitated the fixing of the cable positions, through the use of simple crimped cable stoppers and pins.

Through the inserting of a turnbuckle in the centre of the final connecting cable, stress was easily regulated within individual modules until each unit had snapped into its predicted final geometry; individual modules tension could be adjusted in place to achieve the final form.

During the process of connecting modules, after every few connections it was necessary to lift the pavilion in progress off the ground to allow the structure to find its equilibrium. This process also aided in keeping internal stresses down was achievable all the way to the end with only three to four individuals.

The *Underwood Pavilion* was fabricated from 40 interconnected tensegrity modules. After all of the modules had been connected, the overall structure was anchored. Standard 30″ earth anchors were used to secure the pavilion from wind and snow loads.

# 7. From Tensile Enclosure to "Tensegrity Fabric"

With all of the modules assembled on the site, each individual module was fitted in an elastic fabric. The ends of the three struts were used to span the fabric. As
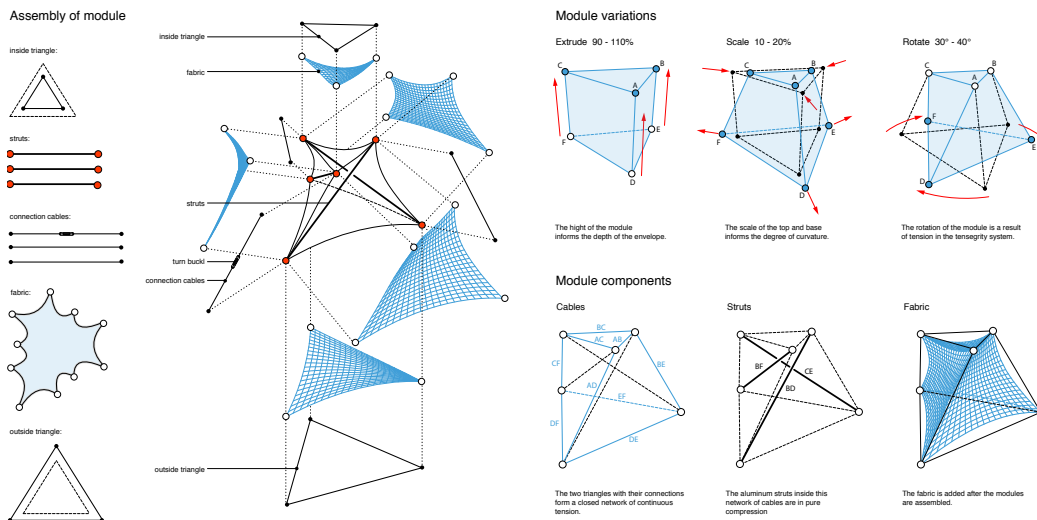
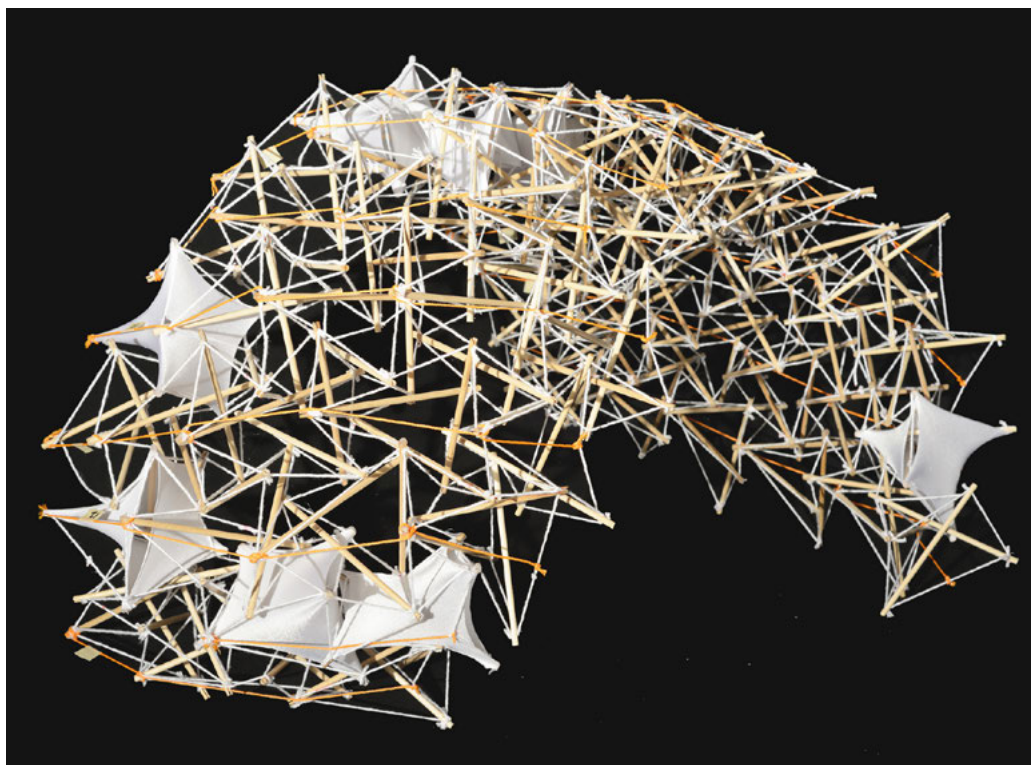**Figure 3.** Assembly and variations of module.



**Figure 4.** Physical study model of pavilion.

a result, the fabric enclosed the struts within a minimal volume defined by the elastic qualities of the fabric.
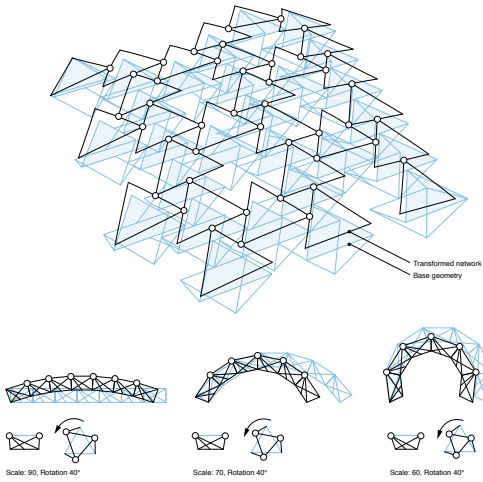
Elastane, a stretchable environmentally friendly fabric originally used for sportswear was adapted to create the pavilion's skin. Created by filaments that are more durable than non-synthetic materials such as rubber, Elastane can also be derived from 84 % recycled polyester.

Finding the precise pattern for cutting the fabric required taking a stretch factor of 40 % into account. This was derived from experiments utilising a 1/1-scale module prototype. Having studied the elastic behavior of the material, the team digitally modelled the fabric in Rhino Membrane. The 3D model was then unrolled with the holes necessary to connect the fabric to the struts. The final fabric pattern was calculated to a width of 62", the same width of the fabric roll offered by the supplier. This minimised material waste.

The modules were "dressed" after the entire structure of the pavilion was assembled. This affected how the fabric was unrolled and the pattern was developed. After the dressing of the pavilion, each module divided an enclosed volume that as a pattern created a self-shading system. The self-shading structural envelope created a cool environment in the hot summer months of Indiana, and as a windbreak in the cooler fall months.
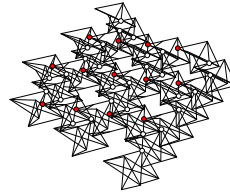
With the successful completion of the *Underwood Pavilion*, the authors envision the next steps for further development moving towards (1) the creation of more complex formal solutions through the utilisation of new module and aggregation variables; (2) the elimination of tensile cables through the introduction of a structural tensile membrane. Although the formal goals are more obvious, the elimination of the tensile cables could have several benefits. In the current configuration, the membrane serves only as a shading device. The use of reinforced tensile membranes could allow for the simplification of the overall structure while simultaneously introducing a more robust, material necessary for larger scale structures. Additionally, the introduction of reinforced fabrics would eliminate the current condition where aluminium and stainless steel interact eliminating long-term problems of fatigue and corrosion. In part, these principals were tested recently in the Noda Pavilion by Prof. Kazuhiro Kojima and his students from the Tokyo University of Science. This pavilion was constructed from a single sheet of fabric. Also, developing the *Underwood Pavilion* further in this direction would create a novel outcome. Rather than building a pavilion from a single sheet of fabric, each module would be developed as an independent tensegrity system. Advantages of that are that such a system would be easier to assemble, expand, modify and change in scale. Using fabric and struts to form a tensegrity module would be a new type of tensegrity structure.
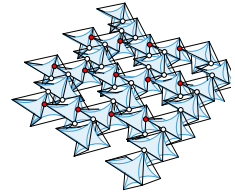
Simulation of aggregate deformation

Transformed network
Base geometry

Scale: 90, Rotation 40°    Scale: 70, Rotation 40°    Scale: 60, Rotation 40°

Aggregate

Struts and cable network

Cable network and fabric

The base pattern for the structure consists of a tensegrity module that is aggregated into a two dimentional field.
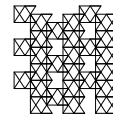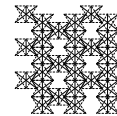
The struts of each module are covered by an elastic fabric that is streched between the ends of the struts.
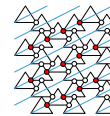
Base pattern    Cable network    Struts    Cable network and fabric
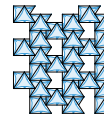
**Figure 5.** Schematic of the simulation algorithm for one iteration step Figure 5. Aggregation of different module variations.



Assembly diagram:

Sequence of assembly:
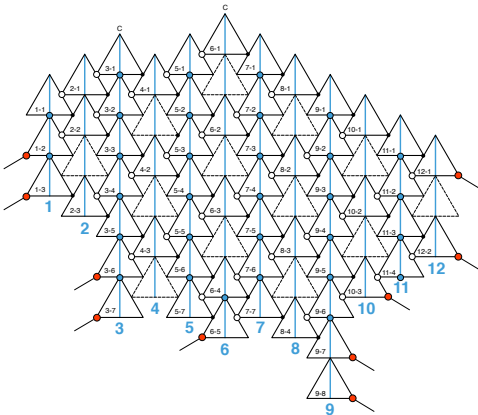
Dressing of module:

Each module is dressed in an elastic fabric after the pavilion is assembled.

Move fabric over cable B-C and attach to A.

Move fabric inside E-F and attach to E and F.

Attach fabric to D.

Move loose ends inside D-E and D-F and attach A, B and C.

**Figure 6.** Assembly diagrams.

# 8. Findings

Rather than rationalising a given geometry such as a line or sphere into a tensegrity system, the intention of this project was to use simulation tools for a form-finding process. The form in such a process emerges from changing the module's proportion or the configuration of the pattern causing a twisting and bending in the aggregate which was used to define the pavilion's spatial enclosure.
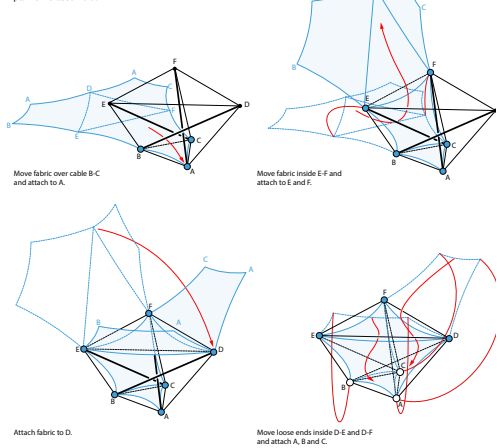
Enclosing the module with an elastic fabric created a unique perception of the structural system. Appearing as volumes that visually do not touch each other created a perception of weightlessness, architecturally articulating a tensegrity system in a new way. Enclosing the modules with a fabric also suggests using the fabric structurally. This would create a novel method of constructing modular based tensegrity structures.

The use of a parametric tensegrity structure had in the case of the *Underwood Pavilion* proven effective as a temporary structure because of its self-erecting behavior along with its ease and range of adapting its geometry. The creation of simplistic and precise details within the pavilion allowed for a fast and accurate assembly process, while also maintaining the possibility of collapsing a mobile pavilion into lightweight bundles of cables and rods for easy transportation. The findings will allow for further prototypes to explore the possibility of more irregular tensegrity systems that respond to new sets of parameters in the future.

# Acknowledgements

# References

Donald, Ingber E. 1998. "The Architecture of Life: A University Set of Building Rules Seems to Guide the Design of Organic Structures – From Simple Carbon Compounds to Complex Cells and Tissues." *Scientific American* 278:1: 48–57.

Fagerstrom, Gustav. 2009. "Dynamic Relaxation of Tensegrity Structures." In *Between Man and Machine: Proceedings of the 14th International Conference of Computer-Aided Architectural Design Research in Asia CAADRIA*, 553–562.

Fuller, Buckminster R., and Robert Marks. 1973. *The Dymaxion World of Buckminster Fuller*. New York: Anchor Books.

Kojima, Kazuhiro. 2012. "Minimalistic Lightweight Construction: Temporary Pavilion in Noda." Accessed May 31, 2016, at http://www.detail-online.com/article/minimalistic-lightweight-construction-temporary-pavilion-in-noda-16465/

Liapi, Katherine A. 2004. "A Computer Based System for the Design and Fabrication of Tensegrity Structures." In *Proceedings of 23rd Annual Conference of the Association for Computer Aided Design in Architecture*, 100–109.

Tibert, Gunnar A., Sergio Pellegrino. 2003. "Review of Form-Finding Methods for Tensegrity Structures." *International Journal of Space Structures* 18, 4: 209–223.

Tomohiro, Tachi. 2012. "Interactive Freeform Design of Tensegrity." In *Proceedings of the Advances in Architectural Geometry Conference*, 259–268.

# Safra Neuron Screen

## Design and Fabrication

Josef Musil, Darron Haylock, Matthew Hayhurst, Samuel Wilkinson, Xavier De Kestelier, and Eilon Vaadia

J. Musil, D. Haylock, M. Hayhurst, S. Wilkinson, X. De Kestelier
Foster + Partners, UK

jmusil@fosterandpartners.com ✉
dhaylock@fosterandpartners.com
mhayhurs@fosterandpartners.com.
swilkinson@fosterandpartners.com
xdekeste@fosterandpartners.com

E. Vaadia
The Edmond and Lily Safra Centre for Brain Sciences, Jerusalem, Israel

eilon.vaadia@elsc.huji.ac.il

# Abstract

This paper provides an overview and an analysis of research in progress on automated facade pattern generation for The Edmond and Lily Safra Centre for Brain Sciences. This pattern is derived from accurate microscopic scans of brain tissue and is architecturally reconstructed with the implementation of structural and fabrication constraints. A single automated work-flow and pattern reconstruction is presented here.

Keywords:
cortical column reconstruction, parametric design, digital fabrication

# 1.  Background

A strong desire to accurately and iconically represent a building's function is often found in architecture. Such a desire faces the hardship of doing so, once considering architectural, structural, and manufacturing constraints. In this paper we introduce an automated work-flow that integrates these two criteria together to design, generate, and manufacture a neural facade pattern. The result of this work-flow is an architectural reconstruction of a section through brain tissue, specifically the visual neocortex area. This section, also known as cortical column, is scaled up to a full height of four floors and serves as the building's facade element.

Finding the right balance between the correct representation of original neuroscientific data and its architectural representation is facilitated by cooperation with the client itself, the Centre for Brain Sciences. Two main types of neurons are used to build the network, pyramidal cells with triangular shape and stellar cells with rounded shape. Pyramidal cells connect different layers within the cortical column by its apical dendrite (Fig. 5).

Currently built projects use different ways of rationalisation to allow for the fabrication of complicated patterns. Repetition of panels, such as Francis Soler's Ministere de la Culture et de la Communication in Paris, or incorporation of frames, such as Jakob + Macfarlane's Euronews headquarters in Lyon, are the most common solutions. Here we look at free-form, non-repetitive, frame-less panels.

## 1.1  The Safra Centre

The Edmond and Lily Safra Centre for Brain Sciences at The Hebrew University of Jerusalem is a pioneering research facility for the scientific exploration of the brain. Physically, the building (Fig. 1) acts as a gateway between the university campus and city - its dynamic social spaces and laboratory facilities are designed to attract exceptional scientists, as well as to foster an interest in the centre's research activities within the wider community.

The building is arranged as two parallel wings around a central courtyard. The upper levels house 28 highly flexible laboratories linked by social hubs, which are conceived to encourage interaction and the exchange of ideas between students and staff. The centre's progressive environmental strategy makes use of passive techniques to naturally reduce energy use.

Local materials, such as Jerusalem stone, are utilised where possible, and the building is orientated East-West to reduce solar gain. The upper three levels are shaded by a perforated aluminium screen, with a pattern derived from the neurological brain structure. Further passive cooling of the building is provided by translucent ETFE canopies to the West and East, which form distinctive markers for the main entrances.

**208**

## 1.2  Design Objectives/Brief

The design objective is to generate a facade screen and shading element that iconically represents the Safra building's function. For this purpose a reference image which is identifiable and meaningful within the research community (Fig. 2 left) of Santiago Ramon y Cajal's drawing of a cortical column (y Cajal 1899, y Cajal 1928) from the beginning of 20th century is selected. This image was hand drawn by the scientist while observing brain tissue under a microscope and is an important image within the field of neuroscience. Using this image directly for a facade element raises many issues like difficulty of scaling up to building height, avoiding repetition when applied multiple times and difficulty to incorporate any manufacturing or architectural constraints.

To facilitate all of these aspects, a fully generated pattern representing a cortical column is proposed and designed (Fig. 2 right). This pattern shows the first five out of six layers of visual neocortex. Each layer is presented by a carefully selected type of neuron and placed so as to create a whole network of neurons.

# 2. Design Methodology
## 2.1  Neuron Library

The original neuroscientific scans of neurons are downloaded from www.neuromorpho.org (Ascoli 2006, Ascoli et al. 2007, neu). This webpage provides an open library of neurons. These are 3D computer reconstructions of microscopic scans of neurons sorted by brain area or author. The reconstructed format we use is a *\*.swc file*, which stores information as a text file and describes neurons like a 3D network of points (nodes) and their linear connections (edges) with given radii for each connection.

Additionally, each line has a tag about what kind of structure it is – apical dendrite (branches going to higher layers mainly receiving signals, basal dendrite (branches going to lower layers mainly receiving signals) or axon (branches sending out signals). Each node has an x,y,z coordinate, its own index and an index of a connected node.

All models used are from the primary visual cortex area of the neocortex of a rat, provided and reconstructed by Markram (Markram 2006). In total we use 70 unique files, each representing one neuron. These are grouped into types by layers.

## 2.2  Parametric Neuron Model

All neurons are first fully reconstructed in Grasshopper andRhinoceros (Fig. 3), the primary software used throughout the whole project. Raw data from downloaded files are parsed as a sequence of numbers that define locations of points in 3D

space. Indices of connected nodes are reconstructed in the same way and are used to build an initial network of lines that represent centre-lines of dendrites. This is done in Python programming language and stored in a custom object class, which also stores a radius read in original raw data file for each of these lines.

To correctly reduce the number of branches in the final pattern, a sub-section of the neuron is created. The depth of this section is a variable that trims off any branches that are outside this range.

Five key steps (Fig. 4) is used to simplify the centrelines and build surfaces. The pseudo-code (implemented in Python) for neuron generation is described by Algorithm 1.

---

**Algorithm 1** Neuron generation
_____

  **while** next branch in neuron available **do**
      rebuild center polylines by connecting nodes as points from the raw data
      **if** distance of this point not close to existing point **then**
         skip
      **end if**
      store points as a list in a neuron class
      sample these polylines
      interpolate these points to smooth the centreline
      sort these curves by their length and distance from the origin of the neuron
      count number of branches
      **if** length or distance $>$ target value **then**
         skip curve
      **end if**
  **end while**

---

## 2.3 Constraining Parametric Model

Incorporating some of the structural and manufacturing constraints is necessary and most efficient on the level of centre-lines. To allow all spigot locations to be on a given grid or within predefined zones, which is discussed later, all these centre-lines have to go through specified points, representing a possible spigot location. Another advantage of introducing these fixed points is that more branches intersect at those locations, thus minimising the number of free branches which structurally act as cantilevers and thus have limited performance. A Python function rebuilds the centre-lines and forces them to go through these fixed points. Only a small maximum movement is allowed to keep the original visual characteristics of branches. Each fixed point finds a point closest on a centre-line, and if within given tolerance, the centre-line is split into two halves, shortened and the newly created gap is replaced by a new curve that goes through the fixed

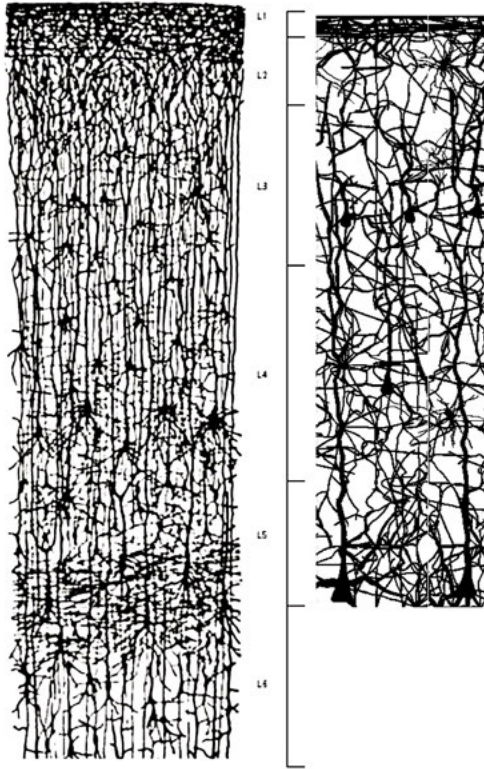**Figure 3.** All 70 reconstructed neurons used to generate the pattern.

**Figure 2.** Vertical alignment of the facade screen (right) with Ramon y Cajal's drawing (left) of cortical column showing generated target layers.
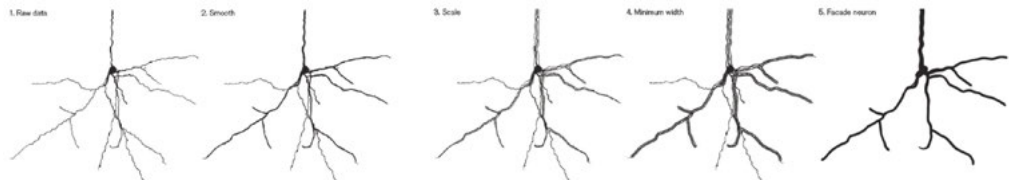


**Figure 4.** Five key steps in the process of simplifying and smoothing the raw data.

point and is tangent to the two parts of the original centre-line. The new three curves are joined and rebuilt into a new single centre-line.

Three main groups of fixed points are introduced because of required manufacturing and structural constraints. Each panel is attached by spigots on its vertical edges, top and bottom horizontal edges and a single point in the centre of the panel.

Once the selection and modification of centre-lines is finished, these are offset to create surfaces. The amount of offset is primarily driven by the original radius from the raw data. Because each branch has to have a minimum thickness to work well structurally and another minimum thickness to hide a connection detail on the back side of each panel, the original raw radius is first scaled up by a fixed number. Scaling all radii by the same number keeps the characteristic tapering of dendrites. Fixed number scaling also keeps the characteristic average thickness of branches that varies between neurons in different layers – neurons in lower layers tend to be thicker and larger compared to neurons in higher layers. To minimize noise in the raw data, this tapering is further forced by a function that checks for a gradient along the centre-line. Each centre-line is sampled to a dense list of points; each point is then offset along a normal vector to both sides to a distance driven by the radius of the closest raw line. A list of points on either side is generated and an interpolated curve created from those points.

These two offset curves define edges of a loft B-spline surface of degree 3, which creates the actual fill of branches. Additional surfaces at the end of each centre-line creates a smooth ending filet. This end surface is generated from a curve that is tangent to the two offset curves and goes through a point on a prolonged original centre-line to create a tip of the branch.

## 2.4 Generating Somas – The Cell Bodies

As somas are not described by enough points in the raw data file and at the same time have a shape crucially characterising each neuron type, they are drawn manually for each of the 70 neuron files. There are two main shapes of somas: a circular one for interneurons and a triangular one for pyramidal cells. Further somas are significantly larger in lower layers then in higher layers, e.g. somas of large pyramidal cells in layer 5 have larger somas than small pyramidal cells in layers 3 and 4. These manually drawn templates of somas are then positioned to the centre-point of neurons within the pattern and a small noise is applied to remove any repetition when the same neuron is used more than once. This noise is generated by scaling the soma by a small random number different in x and y directions and in a plane that is rotated by a small random angle to introduce skewing.
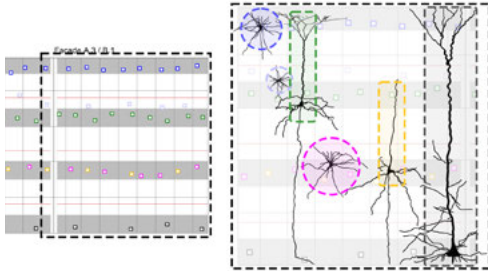
**Figure 5.** Centre-points of neurons, e.g. soma's locations, placed within the solid areas of facade. Colours represents different neuron types with a typical sample shown to the right. Neurons with circular marker represent interneurons (stellar cells) in different layers, rectangles represent pyramidal cells.
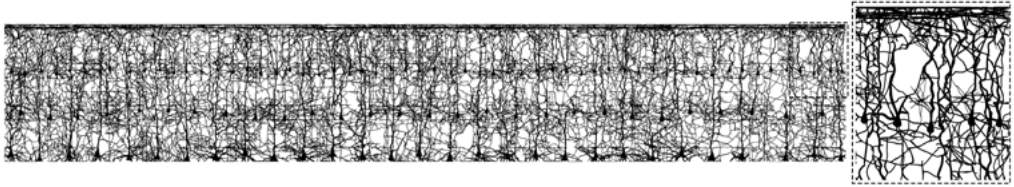


**Figure 6**. Visualisation of the pattern itself showing three facades connected together into a single pattern. Few panels shown with larger scale to the right.
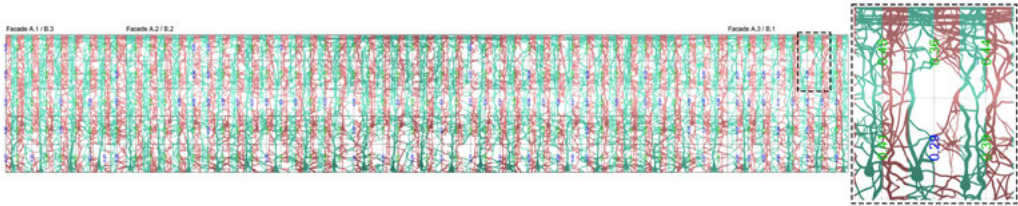


**Figure 7.** Added solidity of two halves of panels attached to an adjacent vertical mullion determines the number of spigots along that mullion. Few panels shown with larger scale to the right.



**Figure 8.** All 290 panels shown in different colours. Few panels shown with larger scale to the right.
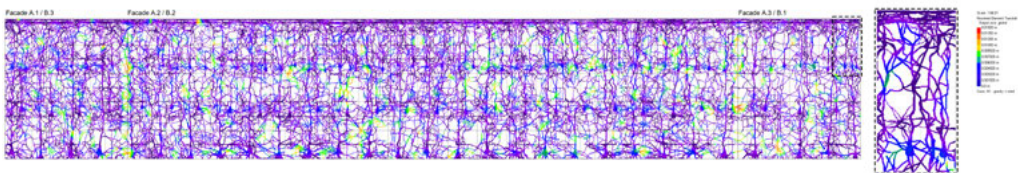


**Figure 9.** Structural analysis of all 290 panels analysing combined dead load and wind load. Few panels shown with larger scale to the right.

## 2.5 Layer Mapping and Neuron Size

Another key characteristic of pyramidal cells is what layers within the cortical column they connect by their apical dendrites. Pyramidal cells in layer 3 are connected to layer 1, pyramidal cells in layer 4 are connected to layer 3 and large pyramidal cells in layer 5 are connected to layer 1. Although the raw data puts neurons to the correct layer and gives it the right size to connect to the correct layer, as the generated screen pattern has the cortical column layers aligned with building's floor levels, a small modification needs to be done to match the distance of correct connecting layers. This is simply done by scaling the neurons along its centre-point by a ratio that is calculated as a ratio between the height of a bounding box of all apical dendrites within a neuron and the target height given by a distance between connecting floor levels.

## 2.6 Horizontal Branches in Cortical Layer 1

The very top layer 1 is filled by separate horizontal branches, which are directly generated by a Python script and connects random points within allowed vertical zones for spigot locations along the vertical mullions. These points define centre-lines that are offset by a fixed number to create two edges of resulting surfaces.

## 2.7 Network

Neurons in the neocortex are of multiple different types. The type defines its shape, size, and connectivity to other neurons and other layers. The cortical column is made of 6 layers. Our pattern rebuilds five of them, leaving out layer 6. As each neuron has two key parts – the soma (central nucleus) and dendrites and axon (branches) – and the facade's objective is to keep all parts of the pattern within a standing or sitting person's field of view more open (less dense), we deliberately place somas into areas in front of solid parts of facade. Because these are mainly floor and ceiling constructions and we cover three floors, we have in total four separate height levels for placing somas (and thus neurons). These height levels drive positions of neurons in levels 2, 3, 4, and 5. Layer 1 is made by thin horizontal branches and thus is put jointly above layer 2 on the very top floor of the building.

For structural reasons somas are placed close to potential structural supports, because somas are a large solid piece and so the heaviest part from a structural point of view. This is considered when generating the initial grid of points based on a structural grid of possible support locations. These are defined by the window mullions behind the pattern. A centre-point of each neuron is then generated as a random offset from this structural point within a predefined range along x
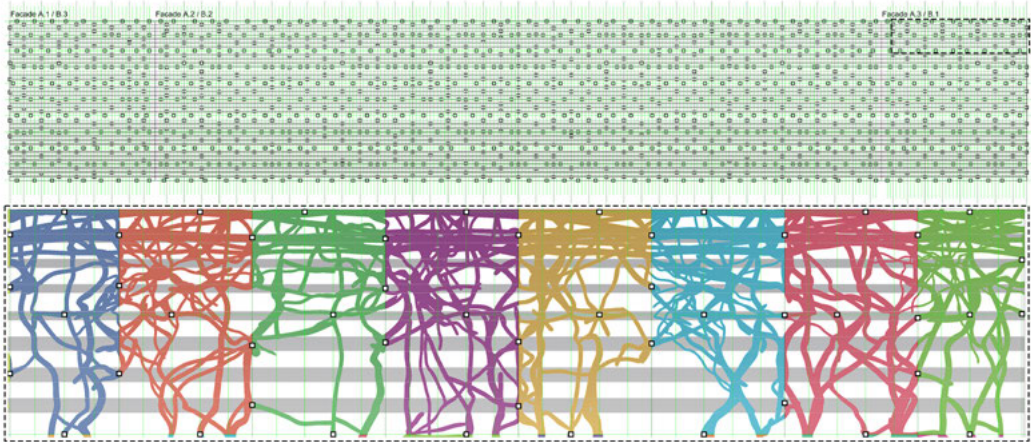
**Figure 10.** Location of all spigots overlaid with corresponding vertical grid and horizontal target zones required for spigot placement.

and y axes (y axis is z axis in the building's coordinate system). At the same time these centre-points are constrained to the facade's solid areas only for transparency reasons (Fig. 5). Only small stellar cells in layer 2 with thin branches and small somas are placed off the solid zone.

The y coordinate of each centre-point then defines the layer within the cortical column and thus the type of neuron used in that location. For layer 2 (the very top floor / roof level of the building) a random selection among 20 neurons is made. 50% of those neurons are small Basket cells and the other 50% are small Martinotti cells. Both are sub-types of inter-neurons, which are neurons characterised by rounded shape of soma and missing the apical dendrite, the thicker vertical branch coming out of soma.

Layer 3 (second floor level from the top) is made of neurons selected from 20 different small pyramidal cells. Pyramidal cells in this layer are characterised by smaller somas of triangular shape and thicker vertical branch (apical dendrite) connecting this neuron to layer 1.

Layer 4 (third floor level from the top) is made of combination of inter-neurons and pyramidal cells. Both neurons in this layer have larger somas compared to previous layers. We use 50% of each type, so there is always one pyramidal cells followed by one inter-neuron. Inter-neurons are further selected from a group of Martinotti and Basket cells. Pyramidal cells in layer 3 are connected to layer 2 by apical dendrites, so the cell is forced to be the correct height.

Layer 5 (the very bottom floor level in the building) is made of large pyramidal cells only. Because the density of neurons in layer 5 is smaller, we place cells only to every other structural point, leaving more space in between. We have 10

different pyramidal cells to choose from and they are forced to be the correct height to connect to layer 1.

Layer 1 is generated separately as a number of thin horizontal branches spanning over the whole width of the building. They are placed above layer 2 cells and also create a solid visual ending of the pattern at the top edge.

After initial generation of centre-points (Fig. 5) of cells and assigning a type of corresponding neuron, random rotation of each neuron is applied. This rotation is along the z axis of the neuron and provides further diversity in the pattern when the same neuron is used more than once – on average each neuron is used three times to reach the total number of 230 neurons. This rotation is within plus-minus 10 degrees additionally to 180 degrees used for mirroring. Somas are generated separately as discussed in previous sections.

The final network (Fig. 6), which is generated in original dimensions and is 900 nm in height, is scaled up to 14093 mm to match the facade's height. This gives a scale of 15659:1.

## 2.8 Workshop

To facilitate the search for the right balance between architectural representation and accuracy, we collaborated with the client directly, which is the Centre for Neuroscience. We held two separate workshops with the leading neuroscientist to discuss and develop the logic behind the pattern.

During these workshops (Fig. 11), it proved to be very useful to have a parametric model of the work in progress pattern and do live changes to the pattern. We developed a pseudo-code for further development that resulted in the algorithm described here. Having a descriptive rather than prescriptive understanding of the logic of the pattern helped to find flexible areas in both fields and intersect them.
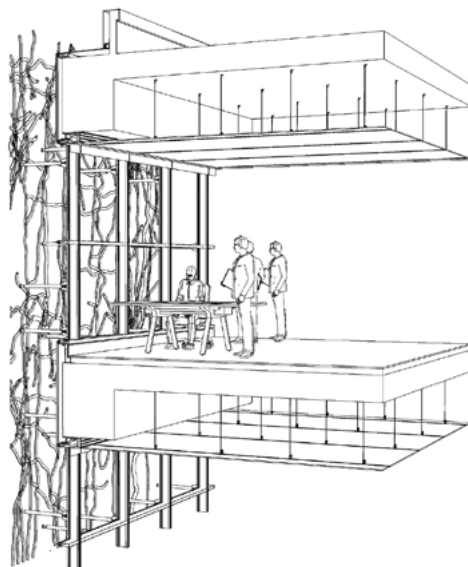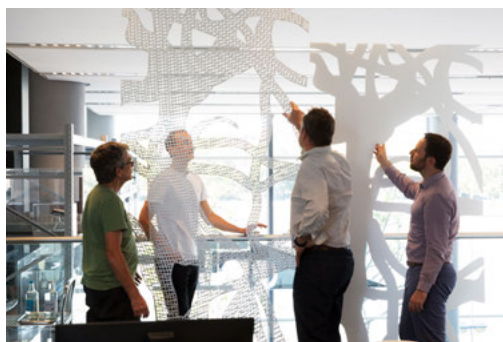
## 2.9 Fabrication

All panels will be water jet cut from 1500 mm x 3000 mm sheets of 12 mm thick aluminium.

The overall pattern goes around the whole building but is split into two identical halves. This makes it easier to manufacture by reducing the number of unique panels to half, but cannot be seen anywhere on the building, because one half is rotated 180 degrees relative to the other.

In total there are 600 glass panels. Every two of these are covered by one aluminium panel of double size, which gives 290 unique aluminium panels (Fig. 8).

Each aluminium panel is attached by a number of steel spigots. These spigots are attached to the glass mullions and transoms behind. Spigots on vertical mullions transfer dead load as well as wind load. Spigots attached to the horizontal transom take only wind load.
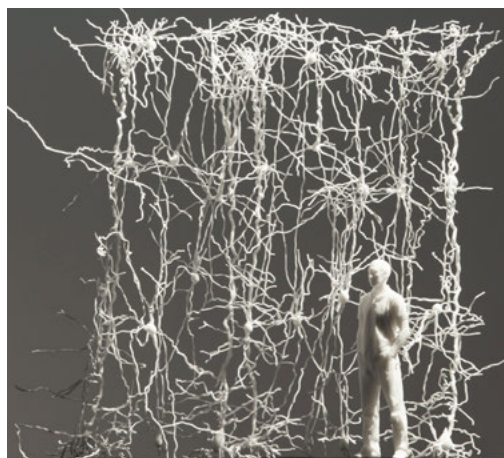
(from left to right and top to bottom)

**Figure 11.** Design and process review workshop with client, neuroscientist, and fabricator.

**Figure 12.** Section of facade and interior.

**Figure 13.** Scaled foamboard mock-up of the full screen.

**Figure 14.** Scaled 3D printed model of a portion of the screen reconstructed in 3D before flattening.

A key constraint is to achieve a total optimal number of spigots carrying the whole pattern. This divided by the number of panels gives an average number of 4.8 spigots per panel. As all spigots on the outer border carry two adjacent panels, while only one spigot in the centre of a panel carries only itself, the average number is 8.8 spigots per panel. The pseudo-code for placement of spigots on vertical edges is described by Algorithm 2.

---

**Algorithm 2** Placement of spigots on vertical edges

---

**Require:** solidity for each vertical edge as a sum of two halves of adjacent
    panels (Figure 7)
**Ensure:** solidity of all edges $< 0.5$
    **while** next panel edge available **do**
        **if** solidity of this edge $< 0.33$ **then**
            assign spigot at 1/3 of the edge length
            assign spigot at 2/3 of the edge length
        **else**
            assign spigot at 1/5 of the edge length
            assign spigot at 1/2 of the edge length
            assign spigot at 4/5 of the edge length
        **end if**
        find closest point from these points on any center-line $\rightarrow$ output actual
        spigot location
    **end while**

---

For additional strength against wind load, one spigot is positioned on the top, one on the bottom edge, and one on a horizontal line going through the centre point of each panel. The initial rule of placing the spigot to the widest branch is replaced by a spigot closest to the midpoint of the edge, which gives best structural performance. All of those spigots are localised in one of the four possible locations on a transom. This allows the transoms to have only four different types and is therefore cheaper to manufacture.

Because centre-lines are already forced to go through the zones allowed for spigot placement, the closest point on them is also within those zones (Fig. 10).

To simplify installation of the panels and to ensure that each panel is supported by at least three points not on line, each panel must be made of a single piece. This is achieved by having the pattern dense enough, which is controlled by the parameter number of branches. This parameter is different for each of the neuron types, so slightly different densities within the pattern are achieved. Additionally, if there are still any small pieces left, an algorithm removes them completely.

It was calculated that a maximum length of any cantilever must be less than 500 mm. This is controlled by a Python function that splits all centre-lines against all other centre-lines, and if any of the end pieces is more than 500 mm, it shortens it to 500 mm minus a small additional random number to avoid a regular look.

A structural analysis of all 290 panels was done (Fig. 9) in General Structural Analysis (GSA). An automated link from Grasshopper creates a GSA file that is then analysed and gives information about overall displacement. Having this as a Grasshopper component allows us to easily define locations of different supports. Spigots on vertical edges work as pins fixed in x, y, and z directions. Spigots on horizontal transoms are fixed only in x and y direction, thus not taking any dead load. Further settings for the analysis are 12 mm thick aluminium and 1430 Pa wind load on each face, which is the highest wind in Jerusalem.

The analysis itself is mesh based. For this each panel that is drawn as a B-spline surface so far has to be meshed and the mesh needs to be as regular as possible. This is again done automatically in Grasshopper as well as finding the support location as a closest point on the mesh from a spigot location.

To achieve the target maximum deflection of 15 mm, multiple full cycles of geometry generation, panelisation, and analysis had to be done. The interim results and careful observation redefined the rules for spigot placement and overall density as discussed before. This made around 95 % of the panels perform well.

To effectively fix the last few percent of panels as well as to incorporate and visually integrate openings for the escape windows, which are 12 windows that need to be completely clear, manual modifications of the generated surfaces were necessary. All surfaces are baked into Rhino, modified, and then loaded back into Grasshopper, panelisation and analysis is automated again.

# 3. Physical Prototypes

Multiple methods were used for evaluation of the aesthetic and structural properties of the pattern.

## 3.1 Foam-Board Zund Cuts

A scaled full-facade model was done from a foam board and cut on a Zund machine (Fig. 13), which allowed us to quickly and cheaply create 1:1 pattern prototype. The whole facade was split into 10 boards of size 1200 mm x 2400 mm. This was used to evaluate the overall density, complexity and correctness of the pattern (Fig. 13).

### 3D Prints

Because the very initial raw data are 3-dimensional, few experiments were done to visualize the pattern in 3D (Fig.14). This is the same pattern as the facade pattern before applying any manufacturing or structural rules. A sample of such structure was 3D printed on an SLS machine (Fig. 14).

### Mock-up

A full scale mock-up of multiple glass and aluminium panels was done on site in Jerusalem (Fig. 15). This shows the final detailing and surface treatment.

# 4. Discussion

The ability to have a smooth work-flow including a structural analysis and automatic processing of raw scientific data allows content accuracy to be implemented and aligned with manufacturing and architectural constraints.

The overall size of the final pattern is 86,313 mm (width) x 14,093 mm (height). As the height of the pattern would be 900 nm, that gives a scale of 15,659:1. Minimal solidity of the panels is 10%, average 36% and maximum solidity 61%. 41% of all vertical edges have two spigots, 59% have three spigots. The total number of spigots is 1,403 per half, 2,806 in total. The number of neurons used to generate the full pattern is 207, based on 70 unique raw files.

The pattern is designed so it performs well for 1,430 Pa wind load and 15 mm maximum deflection, fabricated from 12 mm aluminium panels. The minimum width for unsupported branches is 38 mm, otherwise 49 mm. The initial pattern before implementing the manufacturing constraints has 8320 branches with 39,749 intersections and would need 7,216 spigots. This was reduced after geometry modifications by 63% to 2,685 spigots. And this was reduced further by 48% after careful spigot location selection to 1,403 spigots.

The overall process could be further optimised by having a two-way closed loop with GSA. In this case the initial strategy was good enough to handle around 95% of panels.

As the project developed in complexity, more consultants got involved, and deadlines approached, the usefulness of the digital workflow became obvious and allowed for rapid changes to the design; this meant it was necessary to keep the model up to date right through to fabrication.

# 5. Conclusion

The digital and practical work-flows presented here proved to be relatively productive for multiple design and construction criteria to be integrated into a single work-flow. It allowed a pattern derived from accurate microscopic scans of brain tissue to be generated and architecturally reconstructed with integration of structural and manufacturing constraints.

## Acknowledgements

## References

Neuromorpho.org online library.

http://neuromorpho.org/.

Ascoli, G. A. (2006). "Mobilizing the base of neuroscience data: the case of neuronal morphologies." *Nature Reviews Neuroscience 7* (4), 318–324.

Ascoli, G. A., D. E. Donohue, and M. Halavi (2007). "Neuromorpho. org: a central resource for neuronal morphologies." *The Journal of Neuroscience 27* (35), 9247–9251.

Markram, H. (2006, Feb). "The blue brain project." *Nat Rev Neurosci 7* (2), 153–160.

y Cajal, S. R. (1899). *Comparative study of the sensory areas of the human cortex*.

y Cajal, S. R. (1928). *Degeneration & regeneration of the nervous system, Volume 1.* Oxford University Press, Humphrey Milford.

# Scissor Mechanisms for Transformable Structures with Curved Shape

## The "Jet d'Eau" Movable Footbridge in Geneva

Etienne Bouleau and Gabriele Guscetti

E. Bouleau, G. Guscetti
INGENI SA, Switzerland

etienne.bouleau@ingeni.ch ✉
gabriele.guscetti@ingeni.ch

# Abstract

In this paper we focus on transformable structures and more specifically on structures that can change from a flat shape to a curved shape in a continuous process. We present a method for building a mechanism from any kind of curve that can be flattened by modifying only one degree of freedom. Such mechanisms are based on scissor-pair mechanisms; recently, their technology has been improved to be able to match all sorts of curved shapes. We applied this method in a contemporary ongoing project at the "Jet d'Eau" in Geneva, a structural footbridge spanning 12 meters over a thin lake channel. This footbridge consists of 30 couples of stainless-steel scissors that can be either flat or raised and in the raised position looks like a wave with a sinusoidal geometry. This footbridge resolves a public mobility issue and combines wheelchair and gentle mobility with boat passing in the lake channel: When the footbridge is horizontal, the deck is flat and pedestrians can pass even if in a wheelchair while the boat traffic is closed; when the footbridge is raised, the deck becomes stairs so that pedestrians can pass on it and boats can navigate underneath.

# 1. Introduction

There are many different types of movable bridges around the world, most of which use basic movements such as translation or rotation. Generally these bridges allow only one traffic mode: The pedestrian traffic is stopped when fluvial traffic is active and vice versa. Indeed, most movable bridge structures are made with discontinued mechanisms, so that the deck is interrupted by a gap when the bridge is raised.

In June 2013, an association for the mobility of handicapped people launched a project to provide a large public access to the "Jet d'Eau" in Geneva. The aim was to build a timber deck 4 m wide to enlarge the existing jetty from the early 20th century made of stone which provides access to the harbour.

In its place, we developed a movable footbridge to allow the passing of wheelchairs and pedestrian traffic in the resting position, while boat-passing and non-wheelchair pedestrian traffic remain possible in its raised position. Construction on site commenced in October 2015 and should be finished by the end of June 2016. Figure 1 shows two renderings of the footbridge in the resting and raised positions.

# 2. Issue

In order to avoid an interrupted structure with a gap in the deck, we needed to develop a mechanical system with continuous transformation of its shape, such as stretch movements or homothetic transformations. Our research focussed on a fundamental issue: *How to build a curved structure that can transform itself into a flat structure?* The aim was to build a structure with only one degree of freedom that can be transformed without stress or damage to its continuity, as shown in Figure 2. We focussed our study on structures of constant height.

# 3. Sources of Inspiration

Mechanical systems with one degree of freedom are rare. The most popular is the scissor mechanism found in engines such as cranes, man-lift platforms, accordion barriers, trivets, and toys.

One of the objects inspiring our structure was the Hoberman Sphere, a small toy invented in the 1990s by Chuck Hoberman (Hoberman 1991, US Pat. 4942700) based on a pair of scissors that maintain a constant angle while moving and allows the creation of expanding circles. Chuck Hoberman carried out several projects using this mechanical concept, some of which reached architectural dimensions such as the Iris Dome (Hoberman 1991, US Pat. 5024031).

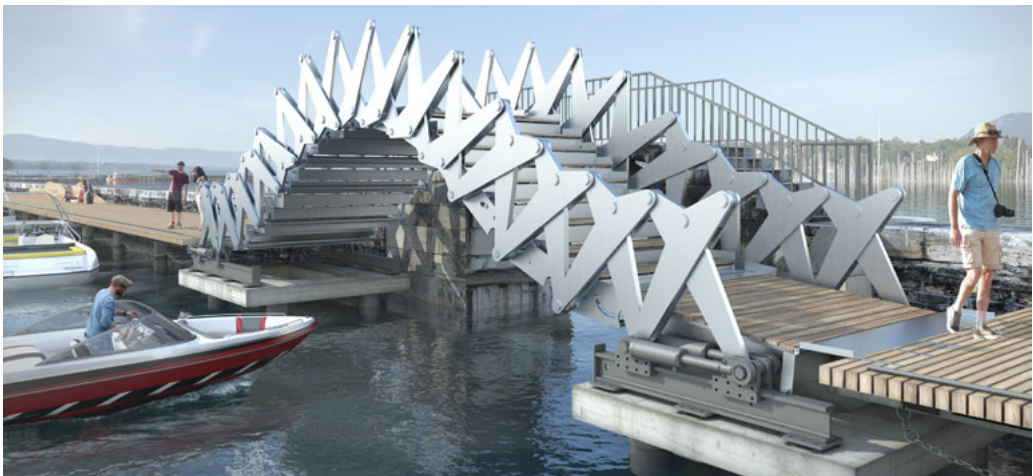**Figure 1.** Top: In the resting position the footbridge is flat and allows wheelchairs and pedestrian traffic to pass. Bottom: In the raised position the footbridge is curved and allows boat-passing underneath the bridge as well as non-wheelchair pedestrians to pass over the bridge by walking on stairs. Courtesy of Christian Tellols.
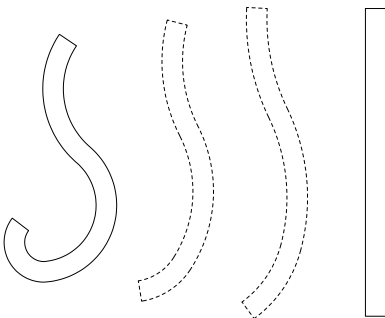


**Figure 2.** The expected transformation must be continuous, dictated by only one parameter.

The scissor mechanism was developed in 1965 by Perez Pinero (Pinero 1965, US Pat. 3185164) as a movable theatre structure and rediscovered in 1974 by Theodore Zeigler (Zeigler 1974, US Pat. 3968808) for a collapsible structure. It has since been intensely studied and improved, in particular by Escrig and Valcarcel (1993, 71-84), and then by Kassabian, You and Pellegrino (1999, 45-56). It has also been widely used in applications for deployable/retractable roof structures. Called pantographic scissors by Hanaor and Levy (2001, 211-229), this mechanism led to many derived concepts as a pair of scissors where the pivot is in the centre, a pair of scissors where the arms do not have the same length, a pair of scissors where the arms are angulated as in Hoberman Sphere, and a pair of scissors where the pivot can slide along one arm in a slot. Not to forget all the combinations of the various scissors concepts. Indeed, despite the huge range of existing scissors concepts, seldom did they actually lead to a concrete project.

In a recent article, X. Chen and L. Liu (Zhang et al. 2016) present a topological method for building a scissor structure that matches a target shape as precisely as possible starting from a given source shape. Unlike this global generative approach, we propose a simplified approach that allows us to choose a solution by exploring different possibilities.

Another source of inspiration is the Rolling Bridge, located in London and designed by Thomas Heatherwick in 2004. This footbridge consists of a structure moved by seven pairs of hydraulic cylinders that can transform themselves into a circle by rolling.

This interesting project opens up new possibilities by using engine technology and robotics in architecture and structural engineering.

# 4. Curve with Scissor Mechanism

First of all, we looked at traditional scissor mechanism whereby the scissor pair comprises two arms linked together at a central pivot. Here, the scissor always forms a rectangle, with the length of each side changing when the arms revolve around the pivot. Since we only studied structures with a constant height, each scissor must have the same height h.

When the central pivot is shifted vertically, the scissor changes its shape from a rectangle to a trapezium, as shown in Figure 4.

The trapezium is an interesting element that allows us to build curved shapes thanks to its two inclined sides.

It is possible to build many different trapezium chains to run along any curve. For a standard path $p$ and a common height $h$ for each trapezium, the chain results upon choosing a starting angle $\gamma$ for the first element; each following angle is then determined by symmetry, see Figure 5.
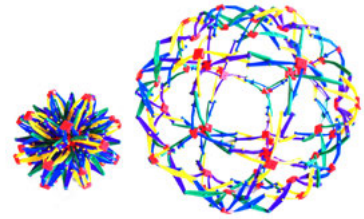
**Figure 3.** Sources of inspiration using a scissor mechanical system. Left: a scissor crane. Middle: a widespread trivet. Right: the Hoberman sphere.
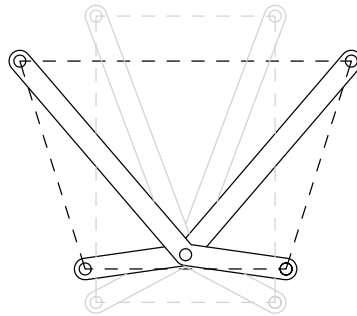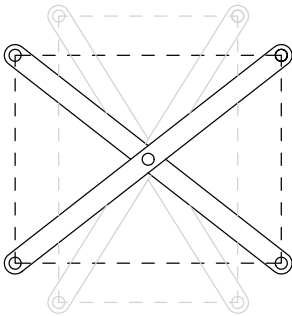


**Figure 4.** Left: the traditional scissor maintains a rectangular geometry while moving. Right: a scissor with the central pin shifted down, causing the geometry to change from a rectangle to a trapezium.



**Figure 5.** Elaboration of a trapezium chain. A given curve is discretised into a polyline with a constant path, the angle $\gamma$ determining the trapezium chain. Many chains are possible. It is also possible to have a different path $p$ for each trapezium.

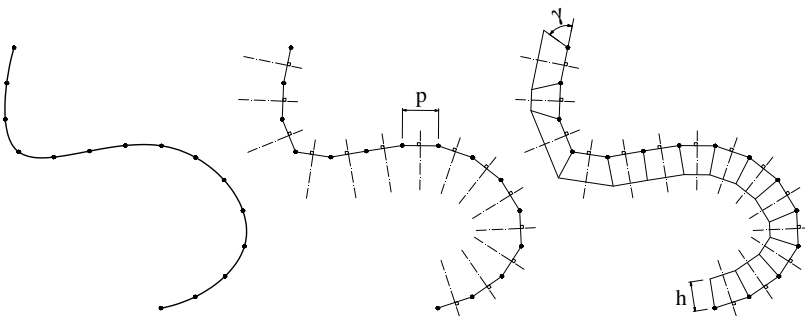In order to build the scissor inside the trapezium chain, we have to solve an equation with several parameters. Indeed, all scissors are linked by one side so they have to fit the same conditions: same height h, path p, and angle a between both inclined sides.

# 5. Solution of the Trapezium Equation

Even if each trapezium has a different shape, they have the same height $h$ and a base $b$, which corresponds to the polyline path; only the angle $\alpha$ is different. The goal is to find the position of the central pivot $C$ such that, when arm $L$ and arm $l$ rotate of $\theta$, their horizontal projections match to form a rectangle (see Fig. 6).

The result of transforming the trapezium into a rectangle led us to build all existing scissors possibilities for a given trapezium, even though these possibilities might not be compatible with one another for building a chain. The next step consisted of choosing the valid solution among all these possibilities.

The whole family of possibilities is drawn on the left side of Figure 7 for a theoretical case. For each angle $a$, the curve represents the rectangle height $h'$, depending on the pivot position ratio $\rho$; each curve represents a family of scissors that have the same angle $\alpha$ and can transform itself into a rectangle.

From these curves we have to choose which ones match the expected height and intersect the horizontal line $h' = 1.7\,m$. Some angles might not intersect this line. Typically, on this graph, it is not possible to find the same height $h'$ for an angle $a = 6°$ and an angle $a = 40°$. This means that, if the curvature of the shape leads to a trapezium with both angle values in the same trapezium string, there is no way to find a solution.

To solve that problem, it is possible to bring down a curve that does not intersect the expected height $h'$ by decreasing the trapezium base b and with it path $p$.

At the top right of Figure 7, several curves are shown for a path decreasing from *1.34 m* to *0.50 m*. When $p$ reaches that last figure, the curve intersects the horizontal line $h' = 0.17\,m$, making it possible to embed the scissor with $\alpha = 40°$ into the trapezium chain.

Varying the path of the trapezium makes it is possible to target a wide range of angle $\alpha$ and allows it to work on a wide range of curves.

# 6. Helix with a Constant Path

As an example from the previous section, we apply the method described to a helix (see Fig 8).
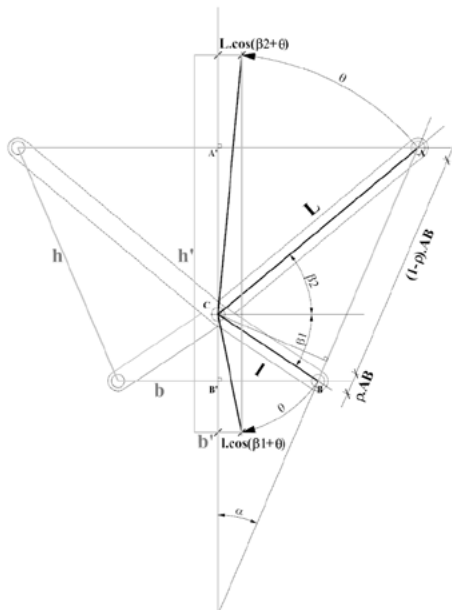
Boundary conditions:

$l + L > h'$

$|CA'| \geq |CB'|$

$\beta_2 + \theta < \pi/2$

$\beta_1 + \theta < \pi/2$

Rectangle condition:

$L.\cos(\beta_2 + \theta) = l.\cos(\beta_1 + \theta)$

Rotation solution:

$$\theta = atg\left( \frac{l.\cos\beta_1 - L.\cos\beta_2}{l.\sin\beta_1 - L.\sin\beta_2} \right)$$

**Figure 6.** Diagram of the trapezium. By turning $\theta$, the arms $L$ and $l$ form a rectangular geometry.



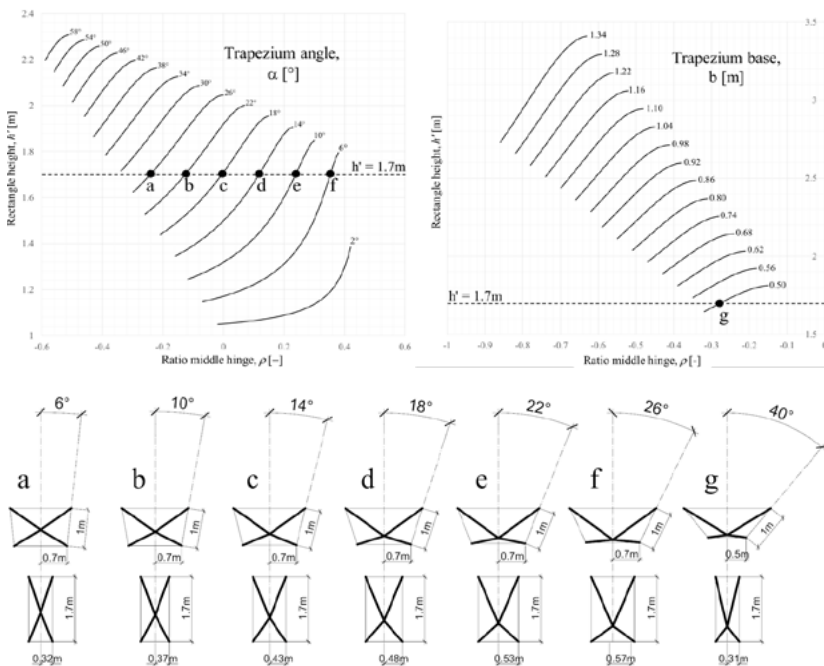**Figure 7.** Top left: Graphic of the whole string of trapezium possibilities for different trapezium angles. In this theoretical case, the graphic is based on a trapezium base b = 0.7 m and a side length h = 1 m. Top right: Graphic of the whole string of trapezium possibilities with a = 40° for different trapezium bases. Bottom: Images of the scissors in the trapezium position and in the rectangle position.
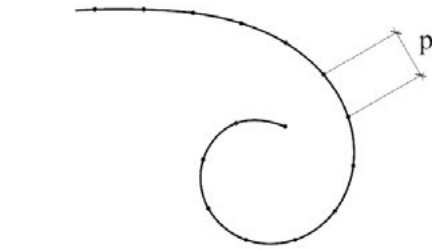
The helix curve is segmented into a polyline with a constant path $p = 25\ cm$.
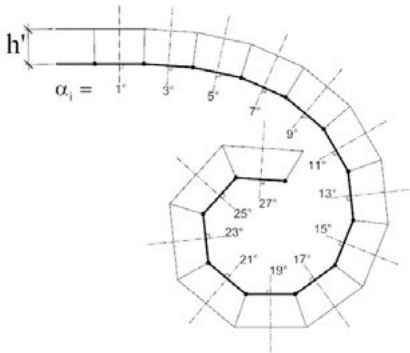


A trapezium string is built with a single height $h' = 18\ cm$ and each angle of trapezium is determined.

The height $h'$ is chosen according to the graphic at the top of Figure 7, to produce a solution for every angle $\alpha_i$.
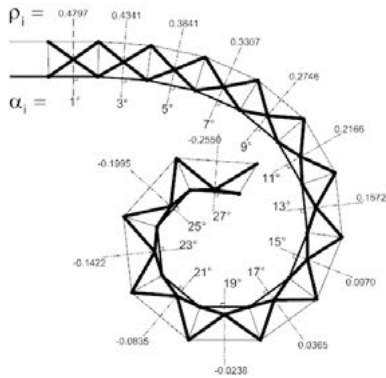


For each trapezium we place the central pivot according to the ratio $\rho$, which is calculated based on the trapezium angle $\alpha$.

The scissor geometry is unique once the parameters $h$ and $p_i$ have been chosen.
Angles $\alpha_i$ are not chosen, but rather depend on the curve geometry.
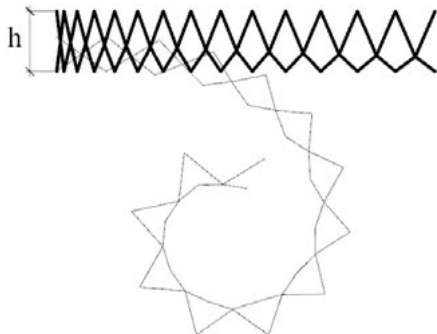


When one scissor rotates, the whole scissor chain flattens. The rectangle height $h = 31$ cm.

In this example the first scissors are narrower to the left; this could be modified by increasing the path in this area.

**Figure 8.** Construction sequence of the scissor string construction for a helix example.
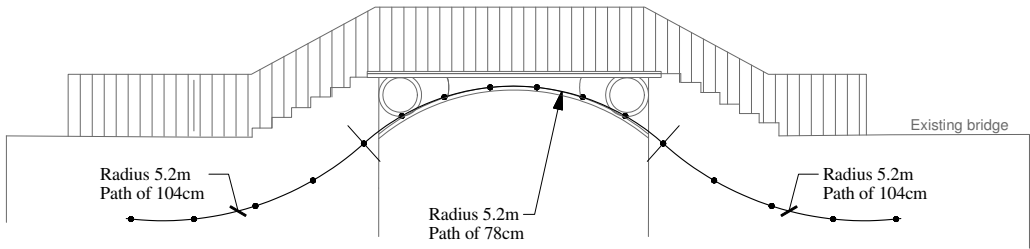
**Figure 9.** The curve for the scissor string is copied from the shape of the existing bridge, which remains unchanged. The height for clear boat passage is a strong requirement, leading to the shape of the curve, which consists of three circular arcs with identical radius r = 5.2 m.
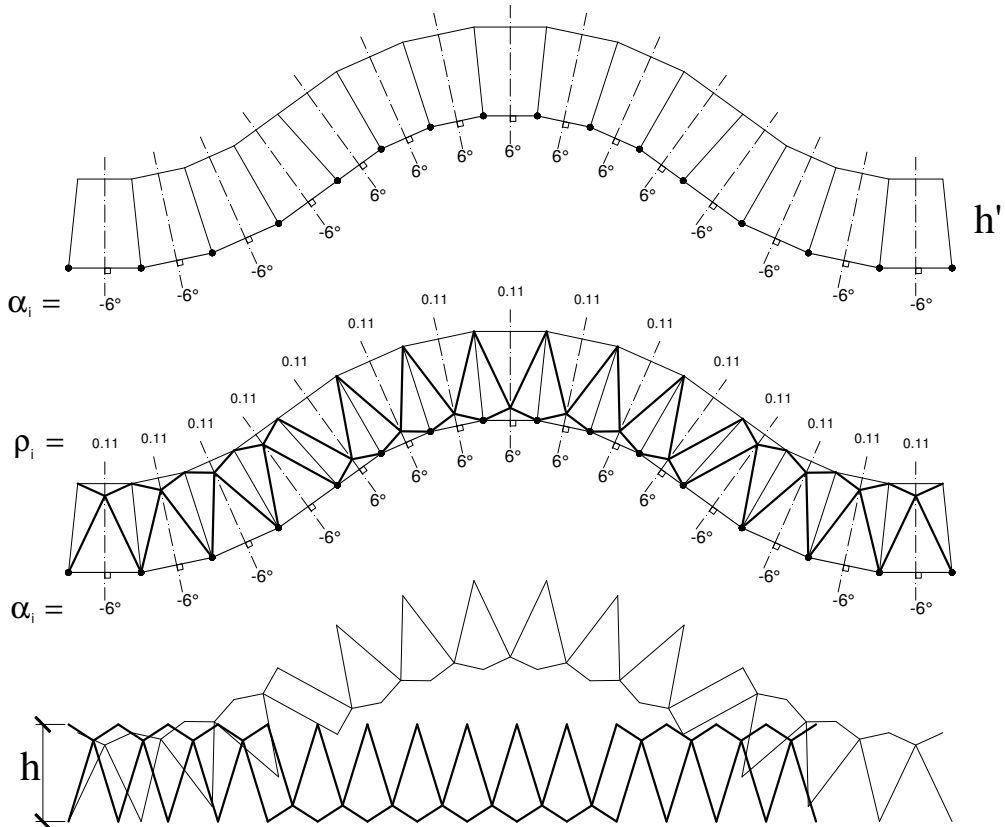


**Figure 10.** The initial curve permits building 15 trapeziums with same height h = 1.20 m and same angle $\alpha = \pm 6°$. The path is p = 74 cm in the middle and p = 104 cm at both edges.

# 7. The Curve of the Geneva "Jet d'Eau" Footbridge

At the beginning of the project, we had no preconceived idea of what material should be used to construct the footbridge. In order to keep the range of possibilities open, we decided to make all the scissors with the same geometry, in particular to allow for moulding process or jig fabrication.

The fact that every trapezium is identical means having every pair of scissors identical. The scissors in the middle are turned down and the scissors on the edges are turned up. One very interesting feature of this footbridge is that for the footbridge to be raised the mechanism has to be extended and for the footbridge to come back to its flat position it has to be shortened.

Once the scissor string was known, we built a structure from the mechanism. Each scissor became a structural beam. This structure must respect standard requirements for footbridges, in particular be stiff enough to carry the usual loads.

# 8. Static Condition

Supports for a moving bridge can be a decisive issue for the structural design. Here the mechanism has only one degree of freedom, so it does not need many supports to stand erect. However, in order to provide enough stiffness and control the deflections, we decided to vertically fix two points at each edge. Of these four support points, one has to be fixed and the three others have to slide horizontally (see Fig. 11).

The hydraulic cylinder acts as a structural section that can change its length by changing the inside pressure. Because of the four support points and the two hydraulic cylinders, the mechanism becomes statically indeterminate.

The sliding points are made of bronze wear plates between a rail and the scissor support plates. They add a further difficulty to the calculation because even if the wear plates have a low friction coefficient, the hydraulic cylinder has to fight the friction resistance in order to raise the footbridge.

The finite element model must simulate the friction since it has an important impact on the structural behaviour. When the horizontal reaction is lower than the friction resistance, the sliding support points become fixed and the footbridge changes its support behaviour. The finite element model demonstrates that maximum stress in the hydraulic cylinder occurs during the detachment phase at the start of the movement.
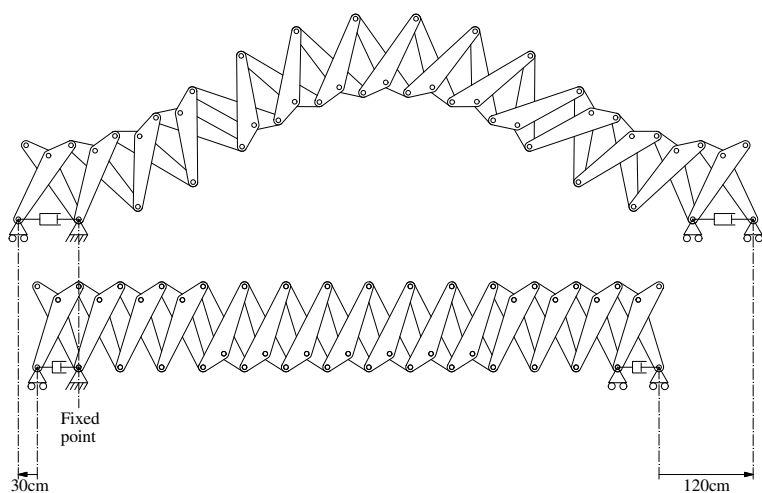
**Figure 11.** Diagram of the support system. Because of the fixed point position, the sliding points induce 30 cm of translation on the left and 1.20 m on the right.
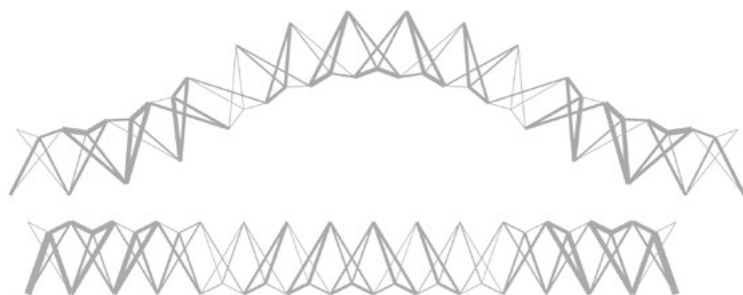


**Figure 12.** Optimisation of the structural members for the two positions accomplished with a strain-energy minimisation routine. The thickness of the line represents where steel must be placed to improve the stiffness of the whole structure.
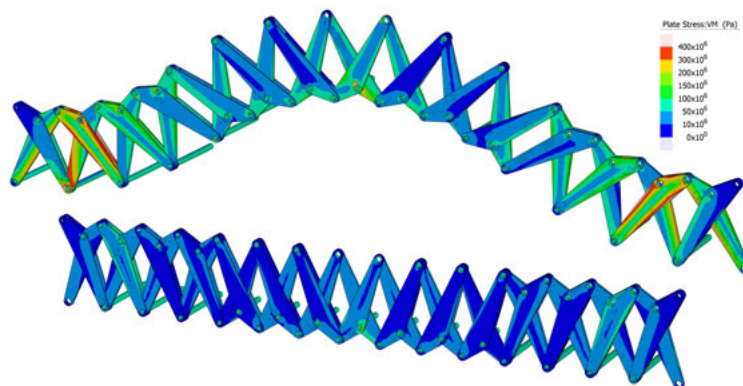


**Figure 13.** View of the final element model made with strand7, coloured with the VonMises stresses for the ultimate load state.

# 9. Structural Behaviour

While the shape is transforming, the span increases and each scissor rotates, so the distribution of stress changes significantly during the rise. The raised position causes higher stress in the scissors than the horizontal position, though for the joining components it is different. The structural design must cover all middle positions of the movement; we proceed to a non-linear analysis with Strand7 by increasing the length of each cylinder and then analyse the results at each increment.

Figure 12 shows the material repartition needed to obtain the best structural behaviour. The situation is almost the same for both positions though slightly different at the edges. Obviously, all scissors do not work the same, so even with the same shape we need to find a way to adapt the resistance differently to each of them.

At this point of the project, the materials used in the structure become the main concern. For durability reasons we choose a stainless steel suited to outside exposure, the lake atmosphere and the Jet d'Eau clouds. We agreed on duplex stainless steel 1.4462, which has the advantage of having a good corrosion resistance, high toughness to limit wear and high proof strength ($R_{p0,2}$ = 500 MPa) (see Fig. 13).

The scissors plates are linked on each side with transoms Ø88 mm and 12 mm thick, which create a steel frame for transversal stability. The transoms belong to the primary structure and also support the deck and the stair frames.

A model analysis shows that the structure has a low frequency in both positions, especially for the first lateral mode. The footbridge should thus be sensitive to pedestrian traffic excitation, but in reality no such effect can be felt when people walk on it in the flat position. In the raised position, the horizontal vibration is perceived only at the very top of the stairs. Further measurements showed that employing most assemblage in bronze strongly increases the damping ratio and limits the discomfort due to the dynamic excitation (see Fig. 14).

The overall weight of the footbridge is about 16 tons, which breaks down as follows:

- Scissor plates : 10,130 kg
- Pin connectors : 800 kg
- Transoms : 1,220 kg
- Actuators : 750 kg
- Stair and deck : 3,400 kg

The force in the hydraulic cylinders reaches 11 tons when raising the footbridge; maximum reaction in the support is about 21 tons in serviceability state.

|  | Raised position | Flat position |
|---|---|---|
| First lateral mode | 1.8 Hz - 1.7 Hz | 2.3 Hz - 1.8 Hz |
| First vertical mode | 3.6 Hz - 4.4 Hz | 5.7 Hz - 7.5 Hz |

**Figure 14.** Table of the natural frequency of the structure. The first value is calculated from the FE model, and the second value is measured in situ.
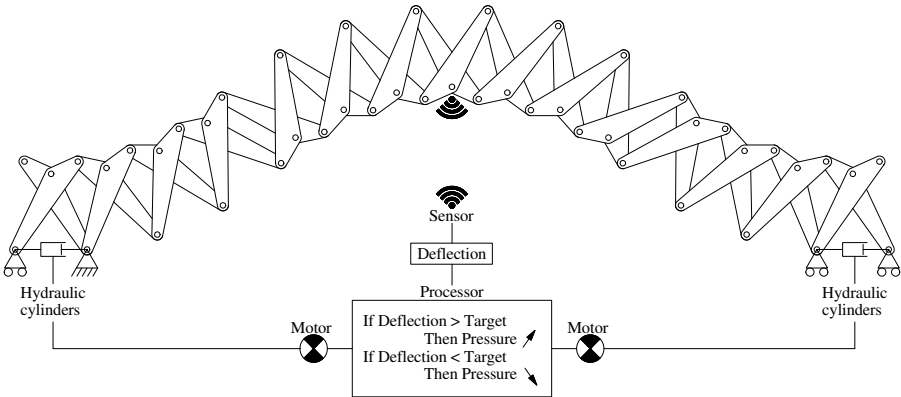


**Figure 15.** Scheme of the hyperactive concept. The sensor, the processor, and the motors are part of the structure and must be permanently active.



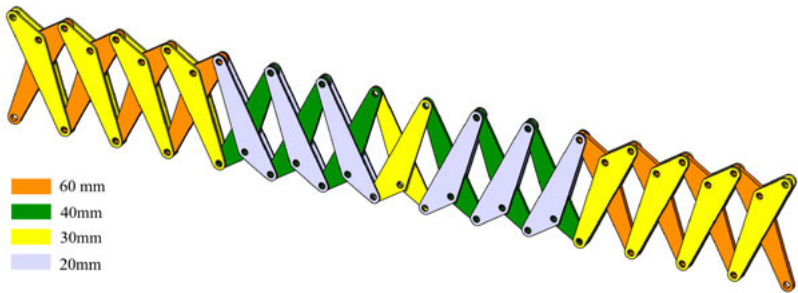Figure 16. Left: The 2 x 30 mm thick plates. Right: The 60 mm thick plates, which comprise the edge scissors.



**Figure 17.** The scissors' colour depends on the thickness value. At the edges, the plates are 60 mm thick and 2 x 30 mm thick. In the middle, plates are 40 mm thick and 2 x 20 mm thick.

# 10. Hyperactive Structure

Having hydraulic cylinders in the structural system means that the structure is permanently active, like a muscle in a living being. This opens a huge field of innovation for structural design called hyperactive structures.

One of its first applications is the clear distinction between ultimate state and serviceability state. The resistance of the structural element can be designed according to the ultimate limit state; the serviceability limit state could be managed separately.

Indeed, in order to respect the serviceability or to reduce the deflection, we have to manage the stress inside the hydraulic cylinders because it acts directly on the shape. In practice, when deflection is too high, we can increase the pressure in the cylinders to balance the deflection and vice versa (see Fig. 15).

Sensors are necessary to analyse the structure state and to determine the deflection value. A post-process state is also necessary to inform the hydraulic cylinder, which is commonly used in robotics and in mechanical engineering. These technologies can also be used for bridges.

One of the main advantages of this scheme is to provide a lightweight structure with high performance and reactive behaviour. In his paper "Pumping vs. Iron", Gennaro Senatore et al. (2011) presented some interesting results about this topic.

As explained above, the weak point of such structures is the dynamic behaviour. With dynamic excitation, the hydraulic cylinders don't have time to be reactive to stop the vibration. In such a case, a complete dynamic study must be done by taking into account the damping, which is very high and helpful for these mechanisms.

# 11. Double Shear Plate

To produce the pair of scissors, we had to find a method providing high accuracy. Even a tiny deviation or distortion in a pivot positioning could stop the assembly or prevent the mechanism from working correctly. Welds and laser cuttings are prohibited in that degree of accuracy as they would distort the steel plates too much. Therefore, we chose water-cutting technology, which can cut plates up to 100 mm thick with a low temperature and thus not cause damage to the form. Then, the plates were machined to drill the holes for the pivot pins (see Fig. 16).

To manage the difference of stress distribution inside the structural scissors, we decided to change the plate thickness: More stress implies more thickness. In the middle, we put a thin plate to reduce the weight, because this area has a major influence on the vertical deflection.

In the end we chose four different plate thicknesses (20, 30, 40, and 60 mm) for building the structure. Each plate is joined in double shear with the next
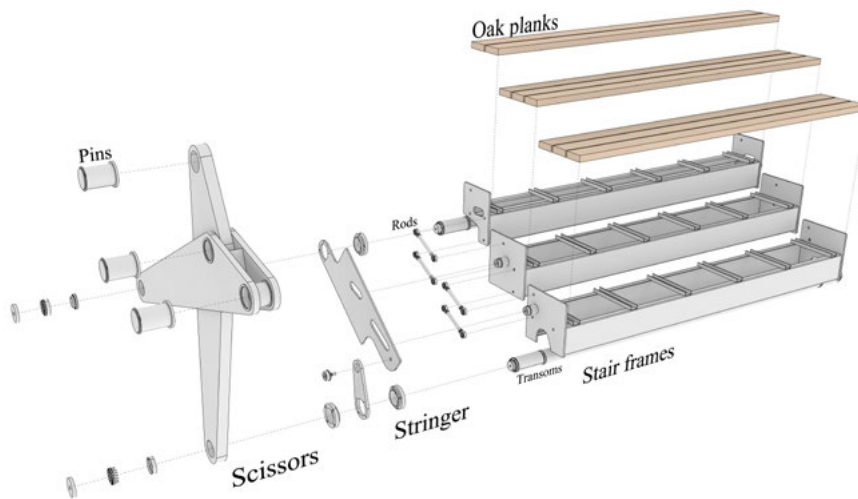
**Figure 18.** Exploded view of the fabrication model. Stringers control the vertical position of each stair frame with a slot. Each stair frame is linked with two rods to next frame. The frames slide into the slots of the stringer. There is no gap between the treads.

neighbour plates; for instance, the 60 mm plate is joined to 2 x 30 mm plates in order to transfer correctly the stress and to avoid eccentricity in the pin rods (see Fig. 17).

In the middle, the thickness of the plates is reduced to 40 mm and 2 x 20 mm, respectively, in order to give more lightness in this area and have greater influence on the deflection. The middle scissor is different from the others: It is a scissor with single shear plates of 30 mm, which allows it to have a fully symmetric structure.

# 12. Stair and Deck

The particularity of the footbridge is the transforming deck. As mentioned above, we wanted to allow pedestrians to cross the footbridge even when it is raised. To this end, we put a mechanical deck in place which follows the bridge transformation by evolving into a stair. This mechanism comprises two basic parts: The first is the stair stringer, which is linked to the scissor with a rod to rule the slope of the stair; the second is the stair frame, which slides in the stair stringer to reach the correct position. The treads are made of oak planks, and the rises are included in the stair frame.

The stair is thus like a sheet lying on the footbridge; it follows the bridge transformation without resistance. The stability of the stair frame is provided by the rods that link the frames together (see Fig. 18).

# 13. Conclusions

The "Jet d'Eau" footbridge of Geneva was specially designed to provide different traffic modes, such as wheelchair and gentle mobility, pedestrian traffic, and boat-passing. The traffic mode can't be active at the same time, but the project serves to reconcile the needs of all users according to their attendance rates.

The method we developed to build the scissors mechanism can be used for any kind of curved shape. In our project we used the sinus shape, though we can imagine different shapes for other applications. The method is flexible, since it is possible to modify a single parameter, like path or height, in order to discover different solutions. The scissors mechanism does not have high stiffness, but the deflection can be managed by a hyperactive behaviour and the vibration are balanced by the high damping ratio.

This project is an application of technologies stemming from the mechanical field to a civil-engineering task. The use of hydraulic cylinders is rare in civil engineering, but we have shown that it is effective for changing the geometry of the structure and also for enhancing the structural behaviour. It is relevant for the future development of buildings and civil works that can evolve in their forms and also adapts to suit multiple needs (see Fig. 19).

## References

Escrig, F., and J.P. Valcarcel. 1993. "Geometry of Expandable Space Structure." *International Journal of Space Structures* 8, 1–2: 71-84

Hanaor, A., and R. Levy. 2001. "Evaluation of Deployable Structures for Space Enclosures." *International Journal of Space Structures* 16, 4: 211–229.

Hoberman, Chuck. 1990. "Reversibly Expandable Doubly-Curved Truss Structures." US Pat. 4942700.

Hoberman, Chuck. 1991. "Radial Expansion/Retraction Truss Structures." US Pat. 5024031.

Kassabian, P.E., You, Z., and S. Pellegrino. 1999. "Retractable roof structures." *Proc. Instn Civ. Engrs Structs & Bldgs Feb.*: 45–56.

Pinero, Emilio Perez. 1965. "Three Dimensional Reticular Structure". US Pat. 3185164.

Rosenberg, Daniel. 2009. *Designing for Uncertainty: Novel Shapes and Behaviors Using Scissor-Pair Transformable Structures.* Thesis. MIT. Dept. of Architecture. Accessed at http://web.mit.edu/d_rosen/www/Designing_for_Uncertainty.pdf

Sennatore, Gennaro, Philippe Duffour,, Sean Hanna,, and Fred Labbe. 2011. "Pumping vs. Iron, Adaptive Structures for Whole Life Energy Savings." *7th International Conference on Intelligent Environments, IE 2011*. Nottingham, UK.

Zeigler, Theodore Richard. 1974. "Collapsible Self-Supporting Structure." US Pat. 3968808.

Zhang, Ran., Shiwei Wang, Xuejin Chen, Chao Chen, Luo Jiang, Jie Zhou, and Ligang Liu. 2016. "Designing Planar Deployable Objects via Scissor Structures." *IEEE Transactions on Visualization and Computer Graphics* 22, 2: 1051–1062.
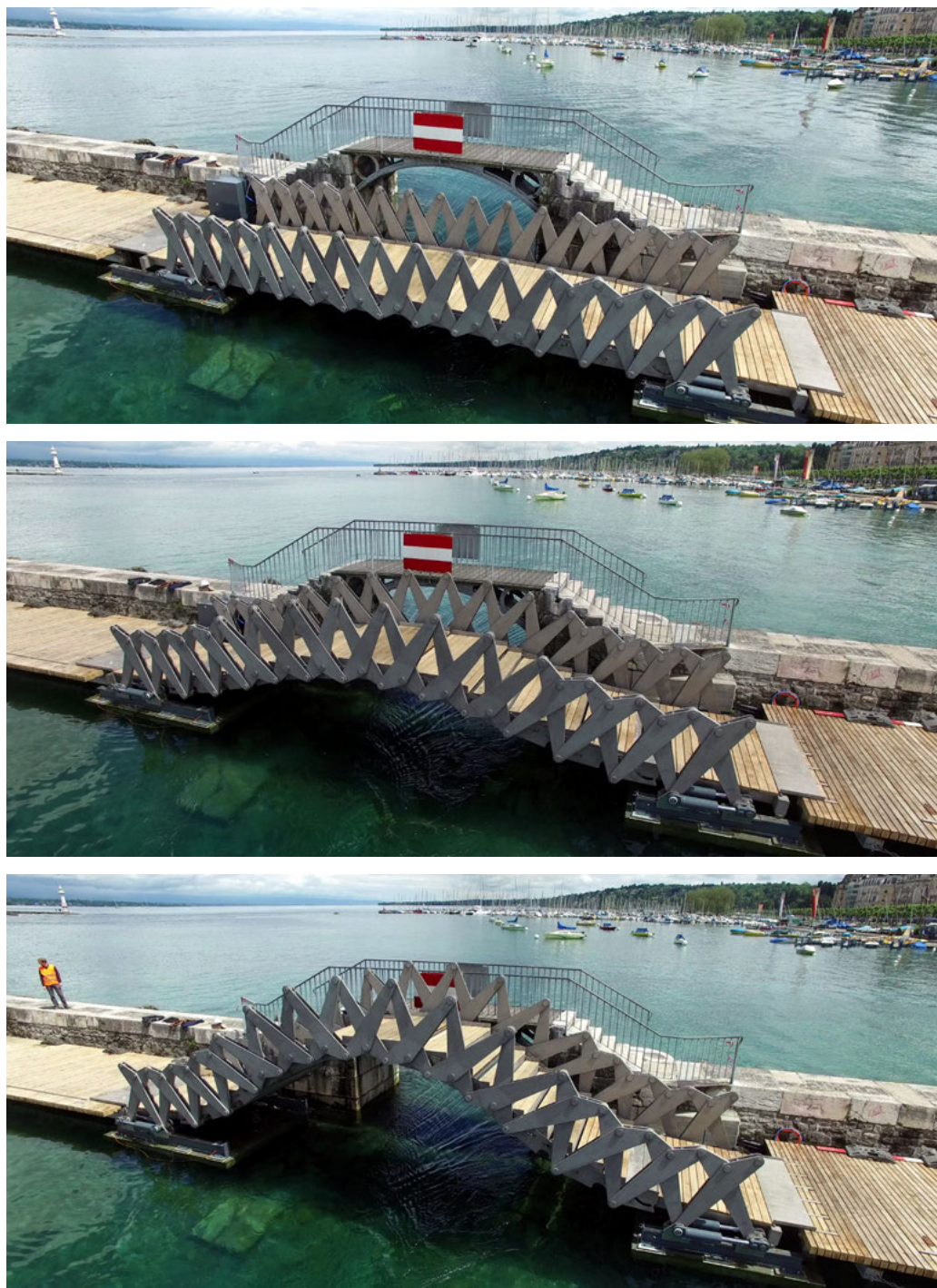
**Figure 19.** The footbridge in situ during the rise. The movement from flat to raised takes around 90 s.

# Mastering the "Sequential Roof"

## Computational Methods for Integrating Design, Structural Analysis, and Robotic Fabrication

Aleksandra Anna Apolinarska, Ralph Bärtschi, Reto Furrer, Fabio Gramazio, and Matthias Kohler

A. A. Apolinarska, F. Gramazio, M. Kohler
Gramazio Kohler Research, ETH Zurich, Switzerland

apolinarska@arch.ethz.ch ✉
gramazio@arch.ethz.ch
kohler@arch.ethz.ch

R. Baertschi
ROB Technologies AG, Switzerland

baertschi@rob-technologies.com

R. Furrer
Dr. Lüchinger+Meyer Bauingenieure AG, Switzerland

rfu@luechingermeyer.ch

# Abstract

This paper gives insight into a cross-disciplinary computational workflow developed and implemented in the recently completed "Sequential Roof" project at ETH Zurich. The project is a 2308 m² freeform, load-bearing timber structure consisting of nearly 50,000 members, robotically assembled layer-by-layer into trusses. The design and analysis of the highly differentiated structure required bespoke computational methods combined into an iterative process to solve the complex interrelations between geometry, structural behaviour, and fabrication constraints. Here, we describe this process, starting with (1) the geometric definition of the roof and (2) its structural model representation and evaluation with respect to the used connection method. Further we elaborate on (3) a randomised vertex population algorithm for the nail connection, and (4) the greedy algorithm to determine the necessary modifications. Ultimately, we explain how this computational workflow was implemented in the construction design phase of the project and discuss transferability of the approach and the architectural outcome.

# 1. Introduction
## 1.1 Project Description and Context

The "Sequential Roof" was developed by the group Gramazio Kohler Research at ETH Zurich for the new "Arch_Tec_Lab" building of the Institute of Technology in Architecture (ITA) at the ETH Hoenggerberg Campus. The building itself was planned and realised as a multidisciplinary research project (ITA 2016). The concept behind the roof's design was to investigate possibilities and constraints of computational design and robotic assembly on a full architectural scale (Willmann et al. 2015). Following previous, smallerscale experiments of the group, the design concept focussed on using ordinary, low-engineered softwood elements with a simple, linear geometry and notch-free joints, to create complex, versatile, and highly articulated structures (Gramazio, Kohler & Willmann 2014).

   The roof structure, covering an area of 2,308 m$^2$, consists of 168 individual trusses, spanning maximum 14.70 m between steel box beams of the primary structure (Fig. 1) (Adam 2014). Each timber truss is composed of average of 370 geometrically unique timber slats, stacked in a layerwise alternating way and joined together by nails connecting each two overlapping slat ends. Using a robotic setup, the elements are fabricated and assembled sequentially in a fully automated process, where each slat is cut to size and then directly placed and joined with the rest of the truss structure (Fig. 19) (Apolinarska et al. 2015). Using simple elements that require minimal and fast processing (simple cuts) and focussing on full automation in assembly are key features that distinguish the project from other recently realised nonstandard timber structures, which make intense use of multiaxis CNC woodworking techniques to produce complex, curved elements with intricate connections and which are then assembled manually.

## 1.2 Computational Workflow

Such fabricationdriven design addressing a novel construction method radically challenges the conventional, phase-based process where the level of detail increases with each planning stage. Here, it was mandatory that design, analysis, and execution planning are tightly integrated and developed concurrently because of the obscure and complex dependencies between geometry, structural behaviour, and fabrication details. In consequence, it was not possible to generate a valid (structurally sound, feasible to fabricate, and architecturally correct) solution explicitly from a given set of input parameters.

   With a "heavy" digital model, large data sets, long calculation times, and tight schedule to produce a final model ready to fabricate, our strategy was to start with a simple and mostly underdimensioned model, and to iterate through the loop of analyses and local modifications until all problems were resolved. The key challenge was therefore to establish an integrated workflow to facilitate this
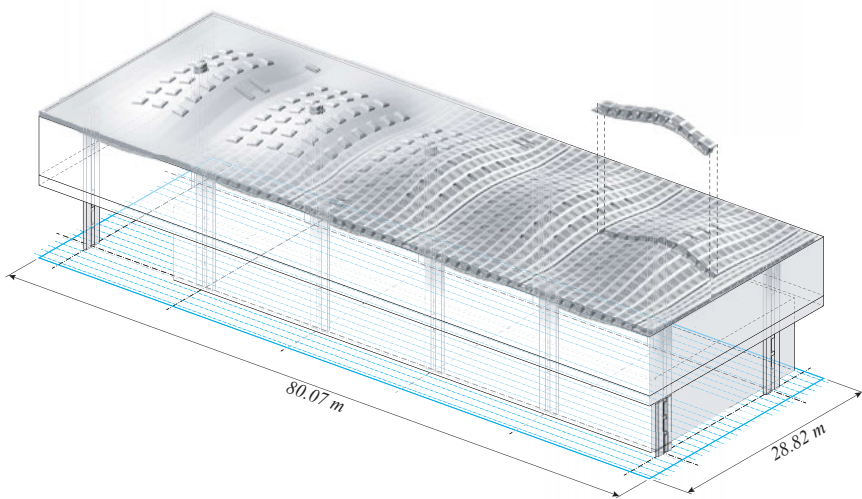
**Figure 1.** Isometric overview of the roof. It is composed of 168 timber trusses supported by a primary steel structure.
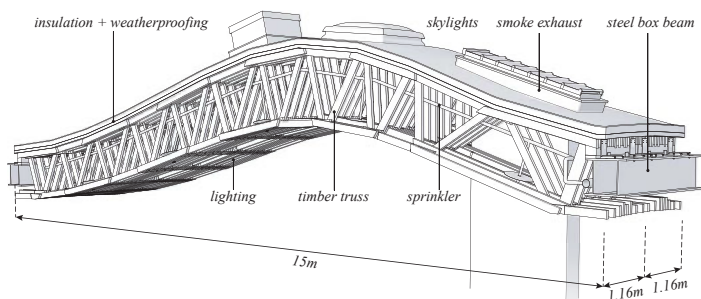


**Figure 2.** A pair of timber trusses with subsystems (sprinkler system, smoke exhaust, electrical, lighting, skylights). Insulation and weatherproofing layers are applied directly onto the structure, without additional boarding. Each truss rests on steel box beams, with one fixed bearing and the other movable in the longitudinal direction.
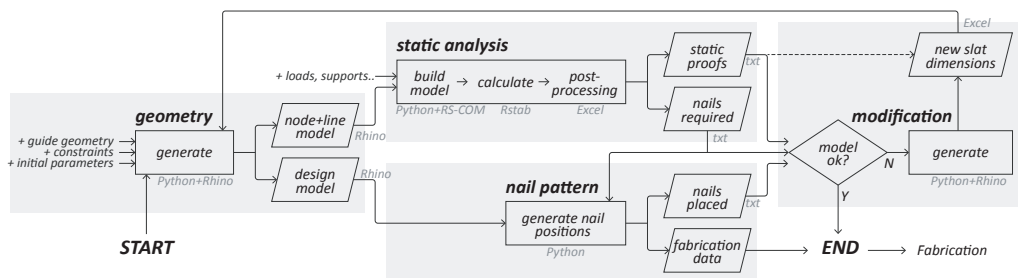


**Figure 3.** Schematic of the established computational workflow.

process. In short, each iteration consisted of four steps: First, generate the model given the current parameters (see Section 2). Then, perform structural calculations and evaluation (see Section 3). Next, generate nail pattern for each connection, observing structural and fabrication constraints (see Section 4). Finally, assess the results of both simulations and perform modifications (see Section 5). Apart from several bespoke algorithmic methods, the workflow involved data management and data exchange, error-proofing and evaluation methods.

# 2. Geometric Design
## 2.1 Geometry Setout

The overall undulating form of the roof is defined layerwise by pairs of cubic Bézier curves. The curves are discretised by *setout points P* (Fig. 4), which are then used as direct and fix reference for the truss geometry. Their position is derived from a possibly uniform triangulation of the truss and locally compromised by interfaces with building components such as skylights, exhaust shafts, sprinkler pipes, or primary structure (Fig. 2). With setout points referring to the outer boundary of the roof shape, the position of a slat's axis line *L* depends on its width *w* (Fig. 5). The given *setout points* and widths create a geometric stencil for elements in a layer. Due to the free-form overall shape of the roof, in each layer the *stencil* is different, and there is a slight shift between slats in neighbouring layers.

## 2.2 Layering

While the *stencil* is needed to determine geometry of the elements (axes, node points, end cuts of each slat) in each layer, the layering pattern defines which elements actually occur in the truss – it defines the composition of chord and diagonal slats through all 23 layer of a truss. For example, structural logic imposes continuity of the top and bottom chord, which could here be achieved by concatenating the individual elements into a symmetrically layered belts (Fig. 6) (Apolinarska et al. 2015). The resulting pattern consists of a repeated sequence of three layers of chord slats followed by a layer of diagonal slats. Local exceptions to this pattern occur when some slats need to be removed, for example, below the skylights (to let more light in) or to let smoke exhaust shafts through the roof structure (Fig. 2). In general, the geometric setup is relatively flexible, and its principles could easily be adapted to use in other projects.
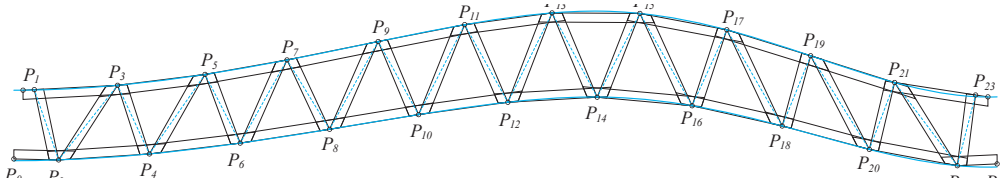
**Figure 4.** Setout geometry for a layer: a pair of Bézier curves, setout points P and stencil geometry.
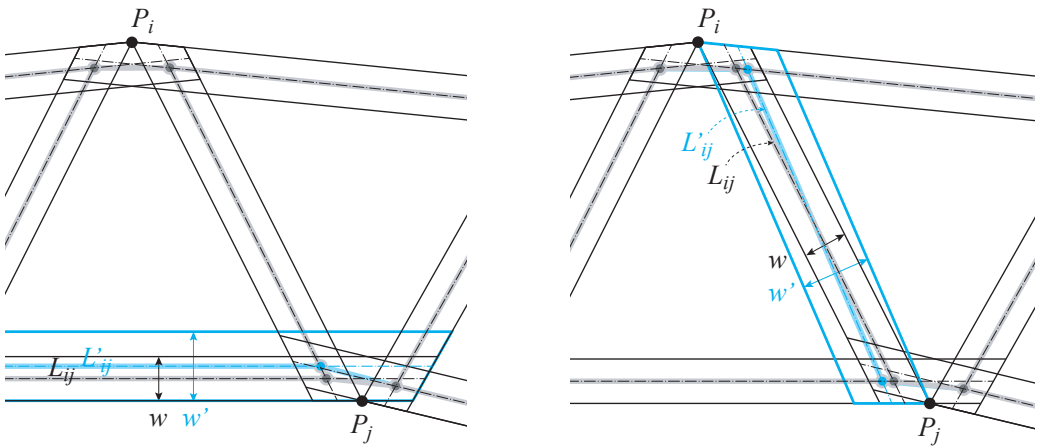


**Figure 5.** Detail of the geometric stencil. With setout points P fixed, the position of the slat's axis L depends on its width w.
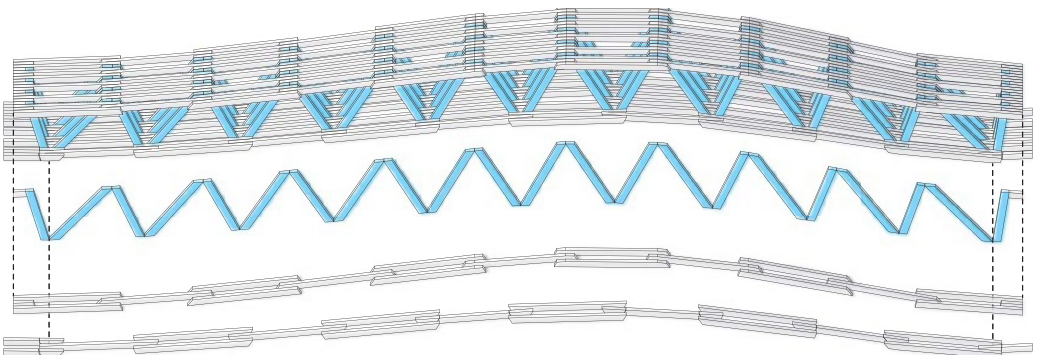


**Figure 6.** Layering pattern. (Apolinarska et al. 2015).

# 3. Structural Analysis

## 3.1 Structural System

Through the layered buildup, the structural system of the timber trusses differs slightly from that of a typical truss, where the axes of diagonal and chord members usually intersect at nodal points. This is not the case here (Fig. 7), and the resulting eccentricity causes considerable shear forces and bending moments. Additionally, the load flow in cross direction (which is also wood's weak direction) is diverted, because the axes of connecting member do not intersect as they lie in different layers. Thus, the connections are modelled as *connector*-beams. Further, *connector*-beams have to be geometrically decomposed into segments so that the *connector* is normal to the shear plane (Fig. 8) to get the right section forces. Together, all these phenomena were challenging to represent and interpret with a beam statics program.

## 3.2 Analysis

The structural analysis process consisted of three steps: model setup, calculation, and post-processing. The model setup included acquiring the geometry (node points and members) into a structural analysis software and defining loads, load cases, supports, cross-sections, etc. From the calculation results, the internal forces were post-processed to produce twofold output information. The first output information was derived from beam proofs based on buckling, bending, normal and shear forces, and indicated which slat had to be wider to satisfy these. The second output information was the required number of nails per *connector* as a result of the internal forces in the *connector* beams.

## 3.3 Connection

The specific structural and fabrication logic of the structure required a connection method that would be both geometrically flexible and fully automatable. Further, because the static system of the coupled trusses is statically highly indeterminate, ductile connections were necessary to transfer loads – a brittle failure of connections could lead to a progressive collapse of a truss. Therefore, a connection technique using 90 mm long grooved nails, with a shaft diameter of $d = 3.4$ mm, proved to be both the simplest and the most applicable solution for this project. Automated nailing is a fast, cost-effective, and well-established CNC technology in timber construction. Compared to bolts, screws, or bulldog connections, resistance of one nail is quite smal; however, due to their relatively small diameter nails can be placed closer together and fit better in the connection's overlap area. In result, the sum of the nails can create enough resistance, more than the alternatives. The downside of this connection technique is the exceptional complexity that arises from combining multiple layers with different geometries.
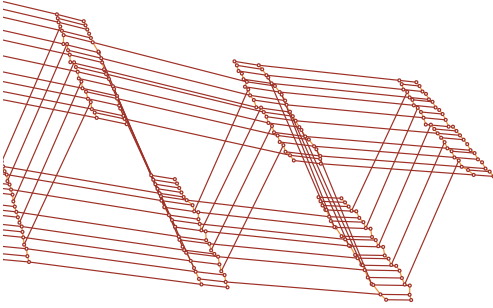
**Figure 7.** Point-and-line model generated for Rstab input.
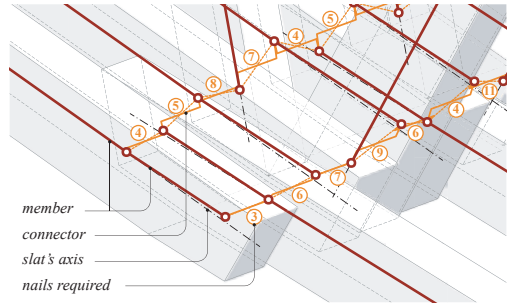


**Figure 8.** Detail of point-and-line model. The number of nails required is given individually for each connectorbeam. Through the eccentric connection, chord slats are represented by three (in general not colinear) members.
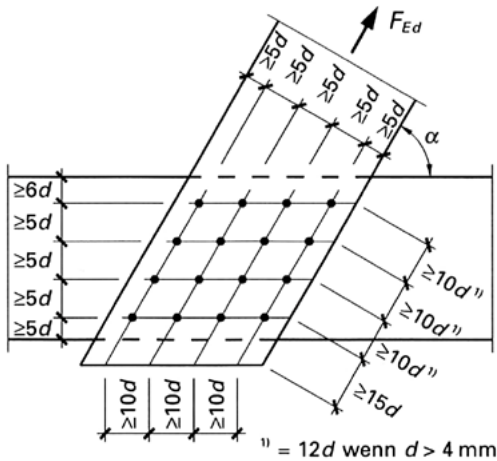


**Figure 9.** (left) Minimal distances for nailed connections according to the Swiss timber code (SIA 265:2003 Timber Structures 2003). For this project, both slats are considered loaded, so the edge offset are 6d (cross to fibre) and 15d (along fibre). Distances between nails are 5d and 10d respectively.
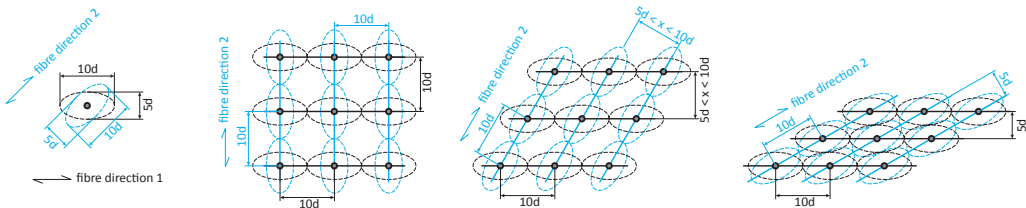


**Figure 10.** Interpretation of the spacing rules as elliptic lockout areas and comparison with a rhombic grid layout.

The Swiss timber code (SIA 265:2003 Timber Structures 2003) specifies rules for nailed connections, including minimum distances to slats' edges and between nails, depending on the fibre direction and the nail's shaft diameter $d$, as represented by a rhombic grid in Fig. 9. This distribution, however, is inefficient if multiple slats are overlapping with different angles between them. Instead, the distances were interpreted as a pair of elliptic lock-out areas around each nail, with long axes of the ellipses aligned with fibre directions of the two corresponding slats (Fig. 10). The edge offsets, resulting in a polygonal *feasibility region*, were calculated individually for each pair of connecting slats.

Still, the nails in each connection had to observe nails from the layer above and below. With a total of 129,840 *connector*-beams, each with individual geometric conditions, distribution of all the required nails in a reasonable, efficient, and compliant way could only be solved with computational methods. The next section describes the algorithm developed for this purpose.

## 3.4 Testing

The various assumptions mentioned above needed to be refined and confirmed by physical tests. First, small specimens consisting of three slats were tested to determine shear and bending stiffness parameters for connectorbeam elements in the calculation model. Also, connections with asymmetrically distributed nails were tested to determine the impact of symmetry on the performance of the connection – strongly asymmetric distribution of nails increases the risk of splitting of wood fibres due to onesided lateral tension forces. Finally, 15 full-scale trusses were load tested to get further assurance in regard to statics, and production processes. With the use of statistics the failure mode and the corresponding load could be predicted quite precisely.

# 4. Nail Placing Algorithm
## 4.1 Problem Description

Given the geometry of connecting slats, the challenge for the nail-placing algorithm is to find a solution to how to distribute the required number of nails in the connections in a way that is compliant with the spacing rules described in the previous section. Moreover, the nails should be distributed evenly (symmetrically). Also, a fabrication requirement is that each slat has at least one *fix-nail* at each end – a nail that lies exactly on the slat's axis line. As the trusses are assembled by a robot, the first nail has to be placed when the gripper holding the slat is still closed in order to fix the slat in place precisely. The fact that the gripper is still holding the slat in that moment constraints the *fixnail's* position (Fig. 20).
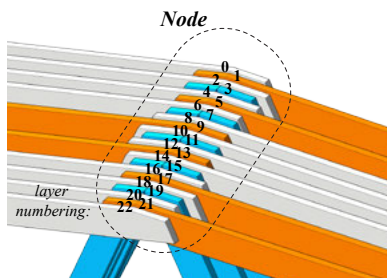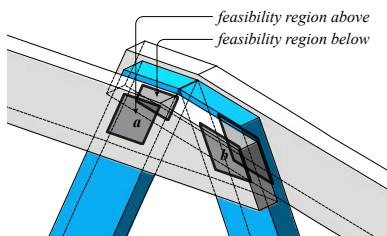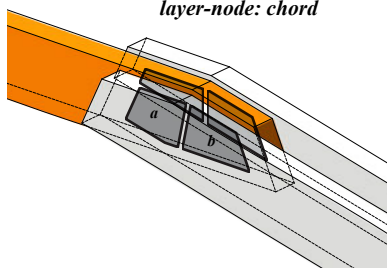
**Figure 11.** Node and layer-node.

```
Def VertexPacker(AlreadyPlacedNails, GeometricalSituation, RequiredNails):
     Generate the initial feasibility areas
    Loop as long as there is some nonempty feasibility area:
        Choose either upper or lower connector
         Pick m random vertices on the border of the feasibility area
        Discard vertices harming symmetry
        Pick best vertex
        Place a nail
        Recalculate both feasibility areas affected by this nail


counter = 0
solutions = []

While counter < 15:
    counter += 1

    If counter==3 and not solutions:
        DeleteRedundantNailsOnDifferentLayers(AlreadyPlacedNails)

    packing = VertexPacker(AlreadyPlacedNails, GeometricalSituation, RequiredNails)

    If enough_nails:
        result = [#redundant_nails_upper + #redundant_nail_lower, symmetry, packing]
          solutions.append(result)
```

**Figure 12.** Nail placing algorithms pseudocode.

## 4.2 Splitting the Problem into Sub-problems

Each *node*, understood as the sequence of connections of 23 layers of slats, refers to 22 pairs ("a" and "b") of *connectors*. The nail-placing problem is independent for each *node*. The problem of placing nails in the entire *node* can be split into a set of *layer-node* nail problems (Fig. 11). By *layer-node* we denote an abstraction that describes all nails going through a certain slat in the *node*, i.e. those placed in this slat (lower *connector*) and those from the slat above (upper *connector*).

There are two types of connections: between a chord slat and a diagonal, and between two chord slats. The nails inside diagonal slats (in diagonal *layer-nodes*) are placed first (layers 3-4, 7-8, 11-12, 15-16, and 19-20). The remaining nails are placed by solving for the chord slat in the middle of the belt (chord *layer-nodes* in layers 1-2, 5-6, 9-10, 13-14, 17-18, and 21-22) – this task is partially constrained by the already placed nails from the diagonal *layer-nodes*.

## 4.3 Random Vertex Population

Our first studies to solve the nail spacing problem were based on physical systems, for example, floating circles (Hockney & Eastwood 1981). However, it soon became apparent that the problem is too stacked to get a good floating behaviour. Also, the nail spacing task is not an optimisation problem, but one aiming at finding a feasible solution.

Therefore, an alternative approach was pursued: Nails are added to the solution one by one, placed on the border of the *feasibility region*. At the beginning, the *feasibility region* is constructed by edge offsets of the overlapping slats. When a nail is placed, and a corresponding nonconstant offset of its lockout zone is subtracted (Fig. 13). This means that the resulting new *feasibility region* may as well be disjoint. Experience shows that Boolean clipping in 3D CADsoftware lacks robustness (Schirra 2000). In order to get a robust polygon clipping behaviour, we decided to use a 2D polygon clipping library based on Vatti's algorithm (Vatti 1992; Murta 1997). For this, the lock-out zone ellipses are represented by a polygon with 72 vertices. The resolution of the ellipses, and of the resulting shape of the *feasibility region*, is an important parameter in the subsequent algorithm (Fig. 12).

The nail-placing procedure starts by finding a feasible fixnail configuration for all layers. After that, the remaining nails are distributed. For each layernode there are two feasibility regions, so first we choose whether the new nail should be placed in the upper or lower one. If both *feasibility regions* are non-empty, let $\Delta := n_R - n_P$ (where $n_R$ = number of nails required, $n_P$ = number of nails placed). If both connectors do not yet have enough nails (i.e. $\Delta_u > 0 \wedge \Delta_l > 0$), then the lower of the ratios $A/\Delta$ (where $A$ = area of the feasibility region) wins; otherwise, the higher of ($\Delta_u >$ , $\Delta_l$) wins. Next, we randomly choose from vertices on the border of the selected *feasibility region*, restarting the algorithm a few times
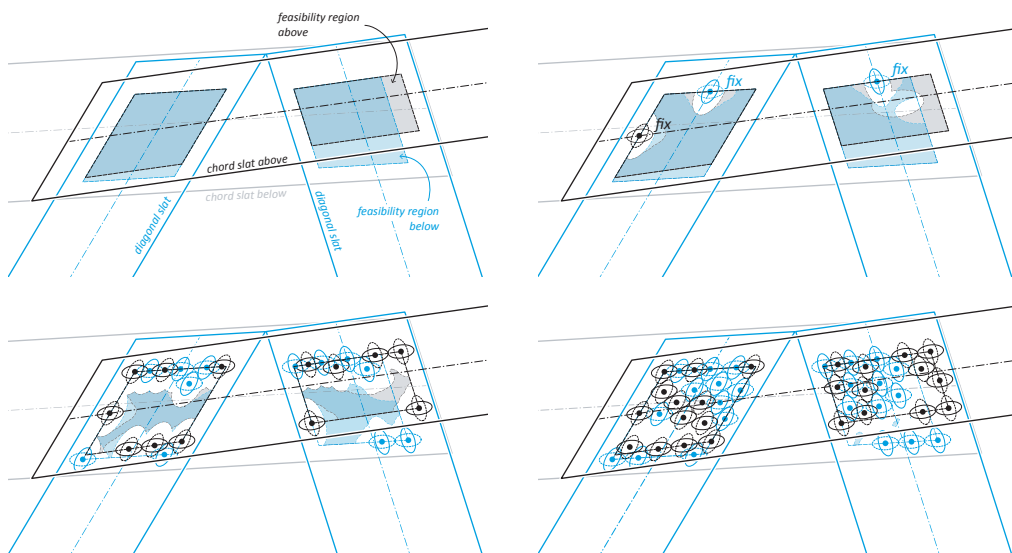
**Figure 13.** A step-by-step example of solving a diagonal layernode. Top left: Initial situation. Shaded areas denote the initial feasibility regions created by edge offsets. Top right: Fixnails placed at axis lines. New remaining feasibility regions after subtracting the offsets of lock-out areas, including those from nails from other layers not shown here. Bottom left: Situation after 10th iteration. Lockout areas of the same colour cannot intersect. In the lockout areas of different colours, only the ellipses in the layer they share cannot intersect, which is here the layer of the diagonal slats (ellipses aligned with axes of diagonals). Bottom right: Situation near completion. On the right there is still a non-empty feasibility region where two more nails could be placed.
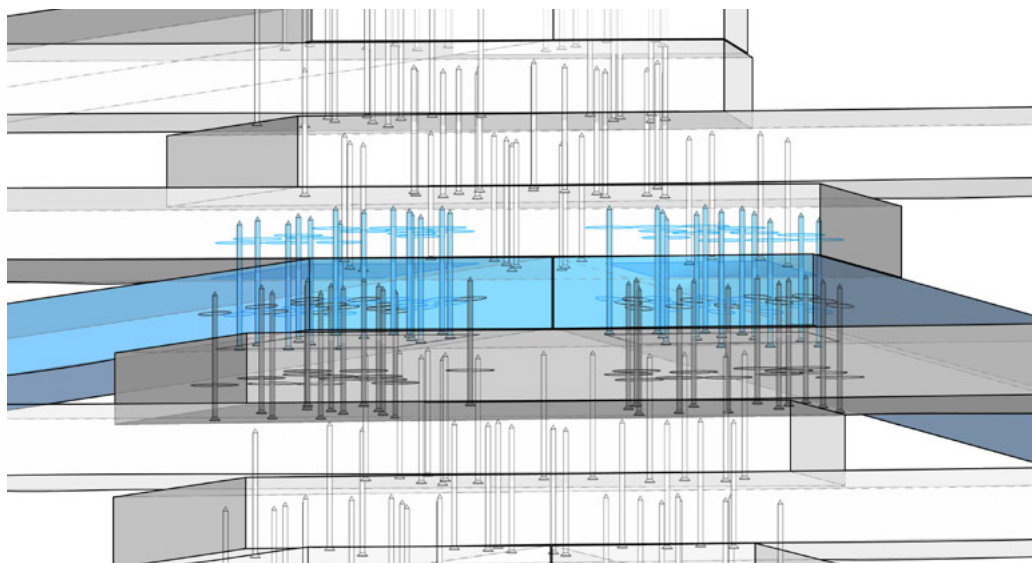


**Figure 14.** Final distribution of nails in a diagonal layer-node from the example in Figure 13 (isometric view from top).

with different seeds. Using randomness helps to avoid bias and thus proved to improve the overall behaviour of the algorithm. Next, we evaluate the randomly selected candidates in terms of symmetry and discard solutions below the acceptable threshold. The symmetry of a nail pattern with respect to a slat is defined as the average of signed distances of the nails to the axis line. From the remaining candidate points, we pick the best solution to place a nail. Alternatively, one could restrict the choice of the random vertex to the convex hull of the *feasibility region*. This would automatically solve the dependence on the resolution.

The nail-placing algorithm iterates as long as the *feasibility regions* are non-empty. It may not be able to place all the required nails, or it may fail to place a fix-nail, or it may be able to place more nails than needed. This can cause problems: Redundant nails placed when solving for diagonal slats can impair the completion of the vertex population algorithms in the chord slats. To avoid this, if no solution was found after two trials, redundant diagonal nails which intersect the considered *feasibility region* are deleted. A surplus of more than 50% of required nails is also economically undesirable. The superfluous nails above the +50% threshold are therefore deleted. The selection is done carefully to maximise the symmetry in distribution around slat's axis.

# 5. Modification Strategies
## 5.1 Challenge

Both structural analysis and nail-placing procedure can yield negative results, meaning that the model needs some modification. Since the problems proved to be highly differentiated, no generalised solutions could be found. Also, as the overall form of the structure and the setout points were overconstrained, possible spectrum of modifications was confined to dimensioning (incrementing the slat's width) and geometric details (extending the slat's end cut) (Fig. 15). The choice of slat sizes was limited to three: 115 x 50 mm, 140 x 50 mm and 180 x 50 mm, which is a compromise between the necessary differentiation and economy of the fabrication process.

The problems of the first type – the failed beam proofs (as described in Section 3) – are explicit and non-negotiable. They are treated in the first place by changing the indicated slats' sizes as required by structural analysis. The second type of problems concerns the connection: Either some of the required nails or a fixnail could not be placed. In general, the solution is to change (usually increase) the feasibility area of the connection. These problems are far less trivial to solve. One of the reasons is that the problem does not explicitly indicate which element to modify – each connection is shared by two elements and in most cases changing only one of them is sufficient. Also, increasing the size of a slat to solve a problem at one end changes the situation in all of its connections at
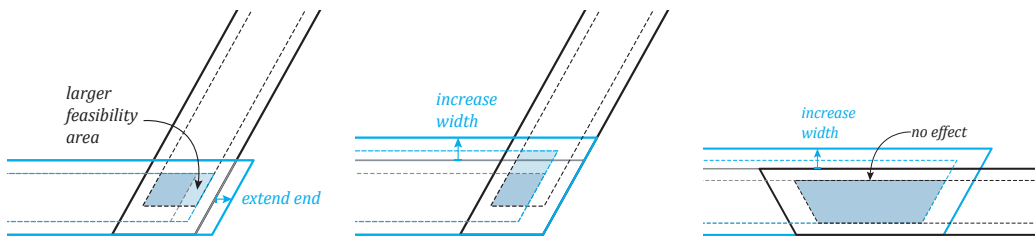
**Figure 15.** Two possibilities of modifying the overlap zone geometry: by extension and by increasing the size of a timber element. Extensions are preferred for the sake of material economy, but cannot be applied to diagonal members (as it would increase the eccentricity) and were not allowed in lower chord (for visual reasons) and certain further exceptions. Increasing size in chord-chord connections may be ineffective. (Apolinarska et al. 2015).

the other end too. Moreover, the effect of the modification cannot be evaluated exactly; this would require repeating the structural and fabrication analysis for each considered choice – technically possible, but inefficient. The actual number of nails that fit into the initial *feasibility region* cannot be directly deduced from its area (because it depends on the situation in other layers) – an estimate must suffice instead. In some cases, the modification does not increase the overlap area at all (Fig. 15). Again, modifying the size of a slat changes its axis and moves the structural *node* points.

## 5.2 Method

The solving procedure can be applied to each truss individually, which considerably reduces the complexity and speeds up the process. For each truss, first we try to solve all fixnail problems. Fortunately, they are rare, and their cause is easy to identify and eliminate. Next, we try to solve the "missing nail" problems, starting with the most economical method: extending the slat's end. For each *connector* there is only one possible slat to extend, and the problematic *connectors* are treated in the order according to the number of missing nails.

For each modification, the new *feasibility region* is calculated to check if its area really increased. For any applied modification, areas of all affected (shared by the slat) *feasibility regions* must be recalculated to estimate the number of nails that they could additionally accommodate and to add this amount to each connector's number of nails already placed ($n_P + n_A$).

The remaining "missing nail" problems are solved by enlarging the slat's width. Here, to establish a solving order, we chose a "greedy algorithm" mechanism in which the "worst" elements are treated first. The "worst" slat is determined with a heuristic approach by combining various parameters to sort all slats according to four criteria in the following sequence: difficulty ($S_1$), then the sum of all nails required ($n_R$) in all connectors ($c$) attached to a slat ($S_2 = -\sum_{i=1}^{c} n_{iR}$),

followed by slat's current size ($S_3 = w$), and finally nails overload ($S_4$), which is a ratio of the sum of missing nails ($n_M$) to the required nails ($n_R$): $S_4 = \sum_{i=1}^{c} n_{iM} / \sum_{i=1}^{c} n_{iR}$. Difficulty ($S_1$) is a sum of three values: sum of all nails missing in all its *connectors* ($\sum_{i=1}^{c} n_{iM}$), nails missing ($n_{kM}$) in slat's worst *connector* (*connector* with the highest number of nails required, and nails missing ($n_{qM}$) in slat's worst *node* (node with highest number of nails required in its *connectors*): $S_1 = \sum_{i=1}^{c} n_{iM} + n_{kM} + n_{qM}$. If the worst slat cannot be modified (because it has already maximal size) or the modification is not effective, try other slats connected to its worse end. After each modification, we sort the list of elements again and remove all "resolved" ones. The process iterates until the list is empty.

## 5.3 Results

Although each truss was processed individually (see example in Fig. 16) and problems were considered on a local level, the algorithm yielded consistent solutions throughout all trusses, producing similar patterns in similar trusses (Fig. 18), thus proving to be sufficiently robust to minor differences in input parameters, such as rounding errors. In terms of efficiency, the number of problems reduced by over 95% between iterations (Fig. 17). Most of the trusses were cleared after already three to four iterations, though, some required as much as seven iterations. With one full iteration costing almost 24 hours of work and calculation time, solving the model with as few iterations as possible was favourable. At the same time it is difficult to conjecture whether a method converging more slowly would yield a solution that is more efficient in terms of material consumption, because with the given slat sizes the size increment is often larger than needed, especially for minor problems. In the final model, the wood volume increased by +13% to 385 m³ compared with 339 m³ of the initial model. Nevertheless, if the roof had to be realised with one size only and dimensioned to the worst case, the increase would have been an estimated +59% (539 m³). It is worth pointing out that, as it is often the case in timber structures, also here the connections were the driving factor in dimensioning of the slats. In total, 815,984 nails were placed, with an overhead of +45.73% making use of the surplus area to increase the stiffness of the connections and improve the transferring loads.

## 6. Implementation

The entire roof model consisted of 49,858 slat elements (represented by extrusions, axis lines, outlines) generated based on 3,808 pairs of input curves. The structural representation involved 135,840 node points, 91,286 members, and 129,840 *connector*-beams. Handling such a "heavy" and differentiated model
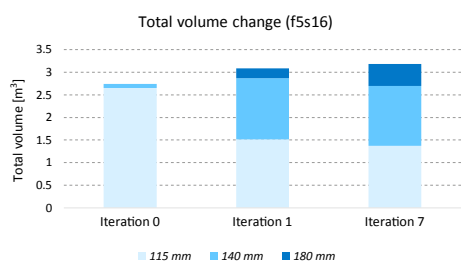
**Figure 16.** Solving steps for an exemplary truss: an initial model, after first and after last iteration (Apolinarska et al. 2015). Corresponding resulting wood volume with respect to the three slat sizes: 115–50 mm (light blue), 140–50 mm (blue), 180–50 mm (dark blue).
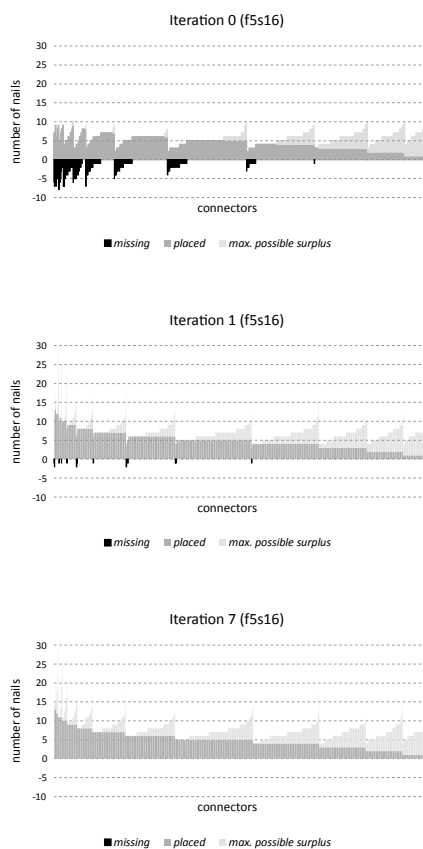
**Figure 17.** Solving steps for an exemplary truss. Number of nails missing (black), placed (grey) and maximal possible surplus (light grey) at different iterations.
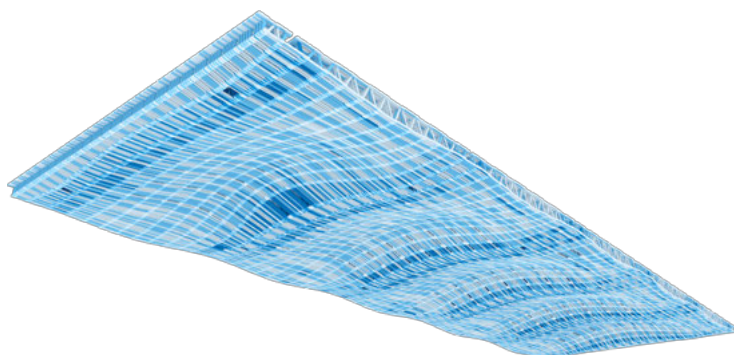


**Figure 18.** Final, resolved model of the entire roof structure, colour-coded according to the slat's width (see legend Fig. 16) (Apolinarska et al. 2015).

required a high degree of automation in modelling and an efficient and intuitive data management strategy for query, survey, and control.

The architectural geometric model was generated using custom-made libraries based on RhinoCommon SDK of the 3D Modelling software McNeel Rhinoceros©. For the structural analysis in the software Dlubal Rstab©, the model was assembled with bespoke scripts using API modules that directly access the application (RS-COM) to overcome the hurdle of manually setting the extremely high amount of individual properties for each element. The post-processing of the calculation results was carried out in Excel with help of VBA macros.

The computational workflow relied heavily on intense exchange of large amounts of data, and the output format of the processed data at different steps of the workflow could be tailored accordingly, be it a 3D model or a data-set in text or spreadsheet format. Conventional representation methods such as 2D plans, elevations, and sections were mostly unfit to portray the relevant information.

Needless to say, error-proofing demanded special consideration, and cross-checking procedures had to be established. For example, the development of the highly complex nail pattern algorithm required an independent control script to examine the reported nail pattern results with the geometric solution, by redrawing the fibre-aligned ellipses and checking if they are collision-free. Additionally, at all stages the geometry and calculations were inspected at random, including visual control, and checked for consistency.

As mentioned earlier, the final, completely resolved model provided not only all calculations and detailing, but also output data for fabrication (Fig. 3). This feature is a radical difference to the conventional execution planning process and a major step forward to a complete, gapless digital chain. These output data were then converted into machine code of the large scale 6-axis gantry robot with which the roof trusses were built (Kramer 2016) (Fig. 19).

# 7. Conclusions

The project exemplifies the specific *modus operandi* needed for fabrication-driven design, which requires a concurrent collaboration between disciplines that are usually involved at different project stages (design, detailing, structural analysis, fabrication, and execution planning). It also highlights the importance of team-work as soon as challenges and risks faced by planners and stakeholders go beyond the standard code of practice.

Overall, although many of the developed methods are very case specific, the core ideas of the project, i.e. the computational workflow, should be easily transferable to future projects. Still, the established computational framework holds a lot of potential for further development, for example by tighter integration of programming interfaces to simplify data exchange.

**Figure 19.** Automated fabrication and assembly using a 6-axis gantry robot (ERNE AG Holzbau) (Willmann et al. 2015).
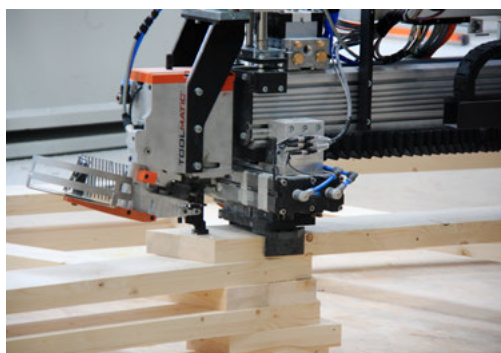


**Figure 20.** Fixing a slat with a fix-nail. After all slats in the layer have been placed and fixed, all remaining nails are shot.



**Figure 21.** Interior view of the completed roof.



**Figure 22.** Detail soffit view of the completed roof. The varying width of the diagonal slats manifests itself in the connections. The shadow gaps between the timber trusses allow for building tolerances and shrinking and swelling of wood.

257

## Acknowledgements

## References

Adam, Hubertus. 2014. "Holzkonstruktionen, Digital Fabriziert." *Zuschnitt – proHolz Austria*. Accessed at http://www.proholz.at/zuschnitt/53/holzkonstruktionen-digital-fabriziert/

Apolinarska, Aleksandra Anna, Michael Knauss, Fabio Gramazio, and Kohler Matthias. 2016. "Arch_Tec_Lab Roof." In *Advancing Wood Architecture*. London: Routledge. (in press)

Gramazio, Fabio, Matthias Kohler, and Jan Willmann. 2014. *The Robotic Touch – How Robots Change Architecture*. Zurich: Park Books.

Hockney, R. W., and J. W. Eastwood. 1981. *Computer Simulation Using Particles*. New York: McGraw-Hill.

ITA. 2016. "Arch_Tec_Lab." Accessed March 30 at http://ita.arch.ethz.ch/index.php/de/arch-tec-lab

Kramer, Martin. 2016. "Individual Serialism Through the Use of Robotics in the Production of Large-Scale Building Components." In *Robotic Fabrication in Architecture, Art and Design*, 460–67. Cham: Springer International Publishing.

Murta, Alan. 1997. "GPC – General Polygon Clipper Library." Accessed at http://www.cs.man.ac.uk/~toby/alan/software/

Schirra, Stefan. 2000. "Robustness and Precision Issues in Geometric Computation." In *Handbook of Computational Geometry*, edited by J.-R. Sack and J. Urrutia, 597–632. Amsterdam: Elsevier.

*SIA 265 : 2003 Timber Structures. 2003*. Switzerland. Accessed at http://www.webnorm.ch/normenwerk/ingenieur/sia 265/e/D/Product

Vatti, Bala R. 1992. "A Generic Solution to Polygon Clipping." *Commun. ACM 35 (7)*. New York, NY, USA: ACM: 56–63.

Willmann, Jan, Michael Knauss, Tobias Bonwetsch, Aleksandra Anna Apolinarska, Fabio Gramazio, and Matthias Kohler. 2015. "Robotic Timber Construction – Expanding Additive Fabrication to New Dimensions." *Elsevier: Automation in Construction*, 16–23. doi:10.1016/j.autcon.2015.09.011

# Adaptive Meshing for Bi-directional Information Flows

## A Multi-Scale Approach to Integrating Feedback between Design, Simulation, and Fabrication

Paul Nicholas, Mateusz Zwierzycki, David Stasiuk, Esben Nørgaard, Scott Leinweber, and Mette Thomsen

P. Nicholas, M. Zwierzycki, D. Stasiuk, E. Nørgaard, S. Leinweber, M. Thomsen
Centre for Information Technology and Architecture (CITA), Denmark

paul.nicholas@kadk.dk ✉
mzwi@kadk.dk
dsas@kadk.dk
enor@kadk.dk
slei@kadk.dk
mette.thomsen@kadk.dk

# Abstract

This paper describes a mesh-based modelling approach that supports the multi-scale design of a panelised, thin-skinned metal structure. The term multi-scale refers to the decomposition of a design modelling problem into distinct but interdependent models associated with particular scales, and the transfer of information between these models. They are applied in this architectural context as a means to manage complex information flows between scales. We describe information flows between the scales of structure, panel element, and material via two mesh-based approaches. The first approach demonstrates the use of adaptive meshing to efficiently sequentially increase resolution to support structural analysis, panelisation, local geometric formation, connectivity, and the calculation of forming strains and material thinning. A second approach shows how dynamically coupling adaptive meshing with a tree structure supports efficient refinement and coarsening of information. The modelling approaches are substantiated through the production of structures and prototypes.

Keywords:
meshing, discrete models, tree, optimisation, multi-scale modelling

# 1. Introduction

Thin panelised metallic skins play an important role in contemporary architecture, often as a non-structural cladding system. Strategically increasing the structural capacity – particularly the rigidity – of this cladding layer could offer significant savings for secondary and primary structural systems. Achievable through the specification of geometric and material properties, skin-stiffening techniques marked the early development of metallic aircraft (Hirschel et al. 2012), and are currently applied within the automotive industry, where selective local differentiation of sheet thickness and yield strength combine with locally specific rigidising geometries that increase structural depth.

To improve the rigidity of thin-skinned metal structures requires a modelling approach that guards against instabilities due to buckling at three distinct scales: buckling of the structure, buckling within panel elements which have to carry compressive load, and also buckling and tearing that can occur during the sheet forming process itself (Nicholas et al. 2016). In this paper we discuss a multi-scale approach in which a mesh connects distinct models associated with each of these scales. A particular challenge is related to the fabrication technique used to form the steel sheet. A robotic incremental sheet forming (ISF) process is used to form all connections and rigidising geometries in a given panel. The ISF process has material implications related to thinning and change in yield strength, which means that a panel cannot be accurately modelled as geometrically or materially homogeneous. This leads to a requirement for multiple mesh resolutions, which go beyond that of a typical architectural model, and for effective flows of information about both geometric and material properties.

The paper is organised as follows: Section 1 describes the ISF process as well as the geometric and material transformations that it implicates. Section 2 describes the multi-scale modelling approach. Section 3 presents two adaptive mesh-based approaches, the first supporting unidirectional information flow and the second bi-directional information flow through a coupled meshing/tree traversal.

# 2. Background: ISF Process

The modelling process addresses the design of a thin-sheet steel structure fabricated via a specific fabrication method – robotic ISF. ISF is an innovative fabrication method for imparting 3D form on a 2D metal sheet, directly informed by a 3D CAD model. In the ISF process, a simple tool moves over the surface of a sheet to cause localised plastic deformation (Jeswiet et al. 2005) (Fig. 1). The primary advantage of ISF is to remove the need for complex moulds and dies, which only become economically feasible with large quantities (Wallner & Pottmann 2011). For
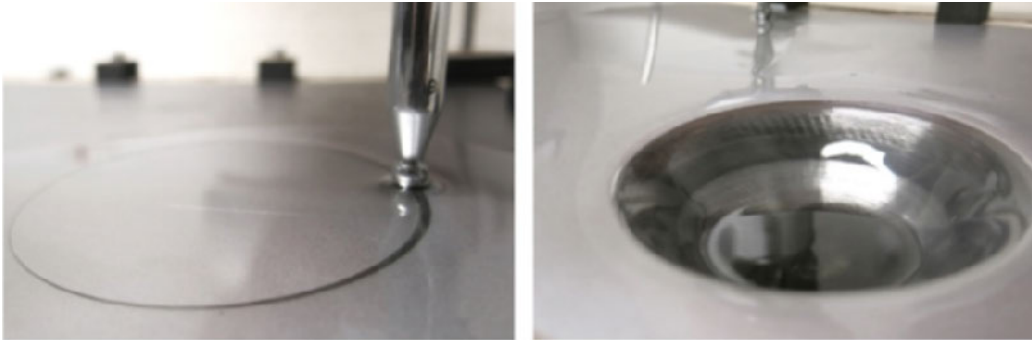
**Figure 1.** ISF process.
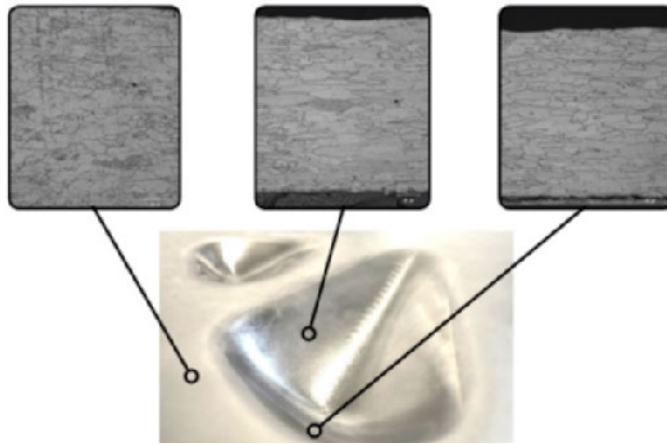


**Figure 2.** Grain elongation and thinning at selected wall angles.
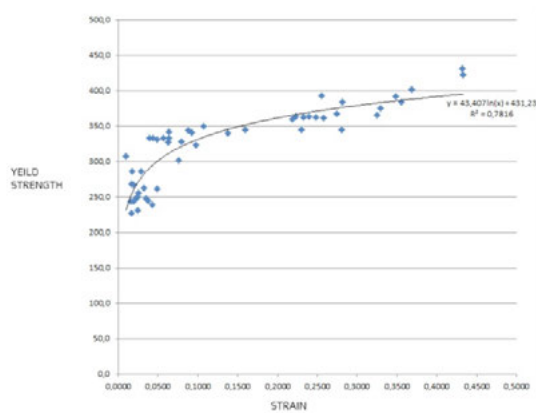


**Figure 3.** Increase in yield strength as a result of cold working during the ISF fabrication process.

this reason, in contexts such as automotive, ISF is explored for its potential to dramatically reduce the costs of prototyping.

Transferred into architecture, ISF moves from a prototyping technology to a production technology. Within the context of mass customisation, it provides an alternate technology through which to incorporate, exploit and vary material capacities within the elements that make up a building system.

## 2.1 Transformative Implications of ISF

The ISF process has effects that are both geometric and materially transformative. Geometric features can be introduced by locally stretching the planar sheet out of plane. These increase structural depth and therefore increase rigidisation and can also provide architectural opportunities for connection and surface expression.

As the steel is formed, there is an increase in surface area and a corresponding local thinning of the material. It is important to calculate this change in thickness so that the material is not stretched too far and tears or buckles as the thickness approaches zero. Forming also activates a process of work hardening – a deliberate application of deformation that helps resist further deformation – with the effect of raising the yield strength of the steel. Depending on the geometric transformation, the effects of the material transformation are locally introduced into the material to different degrees, depending on the depth and angle attained through the ISF process. At an extreme, yield strength for steel can almost double, while material thickness can reduce to zero (Fig. 2, Fig. 3). Because the transformative implications of ISF fabrication are significant, it is very important to incorporate them into the design phase.

## 2.2 Design Application

The context of this research is the application of ISF to the forming of panels within unframed, panelised, stressed-skin structures. Stressed skins are lightweight, thin sheet structures in which the skin is structurally active, and bears tensile, compressive and shear loads as well as providing rigidity.

A full scale demonstrator was installed at the Designmuseum Danmark in May 2015 (Fig. 4), and prototype panels that also test the meshing methods described in this paper were produced afterwards. The panels are produced by robotic ISF based on production information drawn directly from the meshing methods described in Section 3. The basis of the customised toolpathing algorithm is the established method of a spiral descent (Jeswiet et al. 2005), which can be run on different levels of mesh resolution to achieve different aesthetic effects (Fig. 5), but extended to vary stepping and tooling speed in relation to wall angle, measured from the normal of the mesh face.

**Figure 4.** Demonstrator in the Designmuseum Danmark.



**Figure 5.** Toolpath generated from different levels of mesh resolution.

# 3. Method: Multi-Scale Modelling Approach

The design context described above necessitates a multi-scale approach. Multi-scale models aim to describe a problem by separating it into discrete models, typically of different type (E 2011). They leverage that, for some applications, a model does not require the full complexity of the object. Each model addresses a particular feature of the design problem (Nicholas et al. 2012). These models parameterise one another, either sequentially or simultaneously. A key concern is therefore those techniques that enable the information generated within each of these models to flow to others.

The modelling framework for StressedSkins defines three scales – macro, meso, and micro – that coincide with the considerations regarding rigidity outlined above. In addition, the macro-scale encompasses the resolution of global design goals, overall geometric configurations, a full-scale understanding of structural performance and discretisation, and is informed by the available scale of production. The meso-scale considers the project at an assembly and sub-assembly level, and is concerned with material behaviours tied to geometric transformation, detailing and component-level tectonic expression. The micro-scale is concerned with relevant material characteristics at the most discretised level. To act as a communicative substrate and efficiently bridge between different levels of resolution to capture the required dynamics, small-scale geometry and scale-sensitive calculations, the adaptation of a non-structured grid is pursued. This mesh supports all relevant outputs for form-finding, analysis, fabrication and representation.

## 3.1 Communication Across Scales Through Half-Edge Mesh Structure

The first approach focusses on incrementally refining a mesh subdivision so that one mesh can support understandings of coarser topological relationships between individual panels, granular understandings of local material behaviours, and refined geometries for defining digital fabrication drivers and toolpaths. The basis of the approach is a half-edge (or directed-edge) mesh data structure. Half-edge meshes enable the deployment of N-gon faces (rather than more standard triangulated or quadrilateral faces). This opens up the possibility for designing with more complex topologies.

The sequential increase in resolution is shown in Figure 6. Initial increases in resolution are achieved through node insertions related to specific geometries, and later refinements by Loop subdivision (Loop 1987). The refinement of the mesh maintains anchored nodes, seams, and creases as they are established at different levels of resolution. At a first resolution, two layers of pentagonal tiling are distributed across a base surface. The nodes of this base mesh are positioned
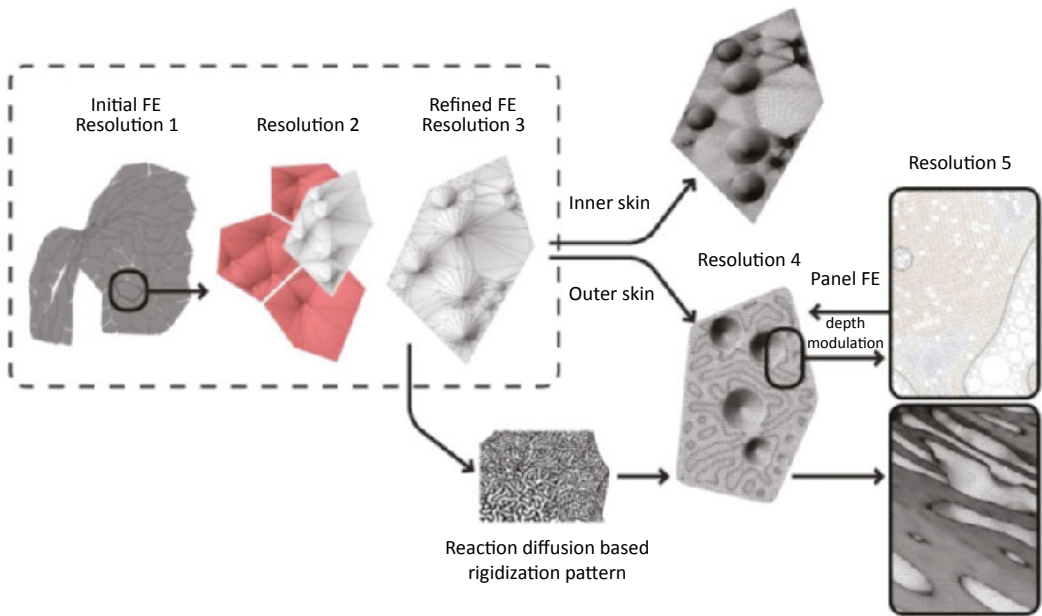
**Figure 6.** Information flow. Mesh resolution is adaptively increased to support scale specific computational processes.
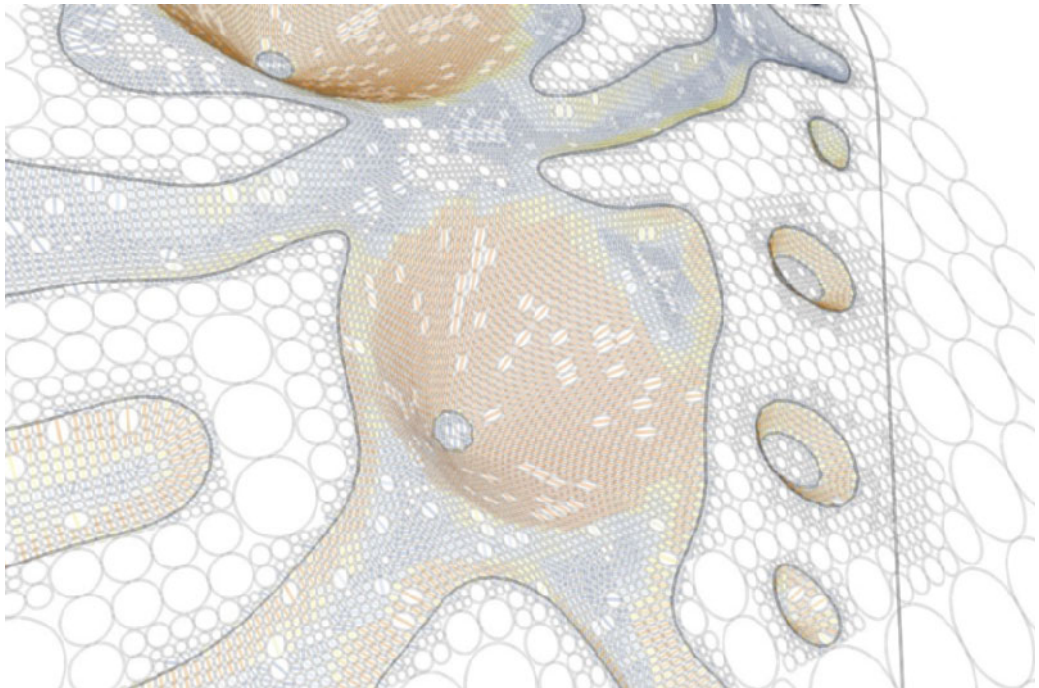


**Figure 7.** Calculation of strains and material thinning.

so that edges are oriented to minimize any global hinge effects using constraint based form-finding. At a second resolution, nodes describing low-resolution details related to connection are added to the mesh. These conical geometries are integrated with the panels and connective faces – with inherited data structures – into a coarse triangulated mesh. An iterative process of finite element analysis performed upon this mesh refines the number and distribution of connection elements, which are located in as great a number as possible near high-shear forces, and aligned perpendicular to them.

A third resolution introduces new nodes that more accurately describe all connection geometries, and the mesh is then subjected to finite element analysis. The results of this analysis – utilisation and bending energy – directly drive the tectonic patterning of the skins, which introduces a fourth resolution. For this, utilisation forces within each panel are used to drive the depth of either oriented dimples or a non-orientated pattern within the structure.

The complex geometries that result are informed by the calculation of thinning and increased yield strength, on the basis of strain measurement via circle projection (Fig. 7) and numeric models generated from Vickers hardness testing. Empirical testing provided a means to accurately inform the model at this scale, as available theoretical models such as the sine law do not yet provide accurate models (Ambrogio et al. 2005). A final skin fabrication model at a fifth scale of resolution is synthesised, and each panel systematically arrayed for extracting toolpaths.

## 3.2  Communication Across Scales Through Coupled Meshing / Tree Traversal

The second communication approach is focussed on refining two phases of the modelling process: mesh subdivision and data transmission between different scales.

As experienced with the first modelling workflow, the geometries produced by subdivision can become computationally expensive, whereas their high resolution is necessary only locally within each panel, specifically where the out-of-plane deflection occurs. To reduce the mesh density without coarsening the geometry, an adaptive Loop Subdivision algorithm (Pakdel & Samavati 2004) was implemented and further developed to incorporate additional constraints. The subdivision method was extended to support creases (chains of edges which break the curvature continuity) and anchor points (points that stay in place during the process), which are utilised to efficiently and precisely model the deformation. Using this adaptive subdivision strategy, the resolution of a typical mesh used in the first demonstrator can be reduced by up to 30%, yet still maintain the shape (Fig. 8). Structural analysis occurs at different mesh resolutions/scales: The structural efficiency of the global shape is optimised at the macro level, where
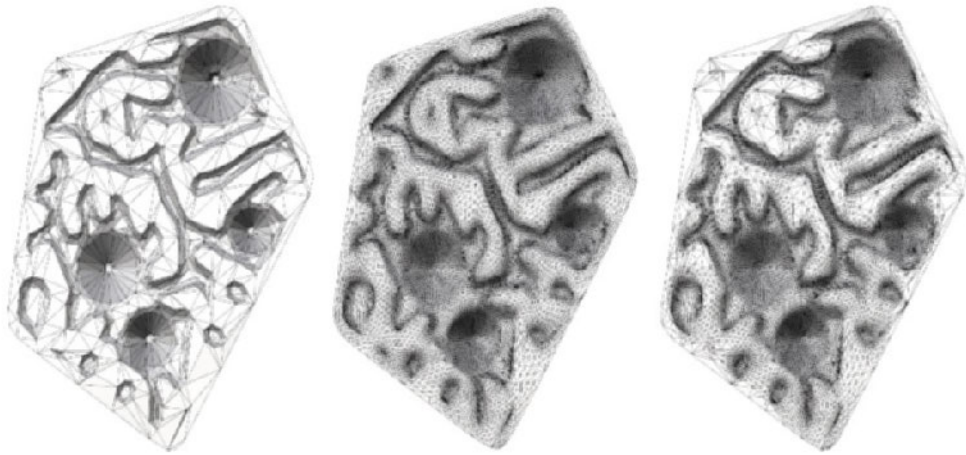
**Figure 8.** Face count comparison. From left: original mesh, Loop subdivision, adaptive Loop subdivision.
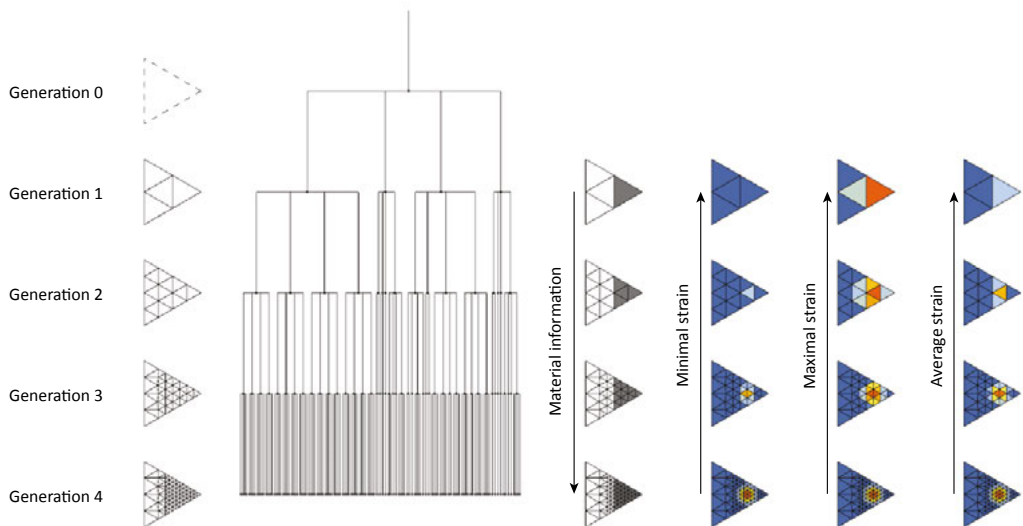


**Figure 9.** Bi-directional data propagation between low and high resolution.
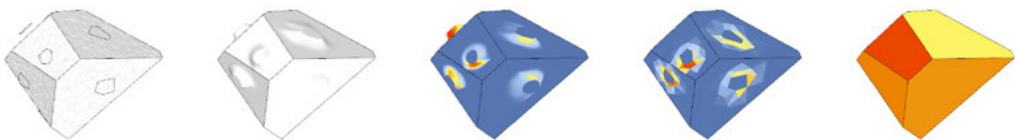


**Figure 10.** Upstream data propagation result. From left: original mesh, subdivided mesh, strain calculation, results propagated up the subdivision tree, colourizing the panels with respect to the maximal strain value.

the low resolution mesh is sufficient. On the other hand, the plastic deformation is computed at the micro-level, being analysed for a single panel at a time. The meso-level information accounts for connections between layers and analysis of relationships between panels. It is highly desirable to tie the analysis information with the discrete model produced by the subdivision algorithm, since the efforts to transition of data back and forth between different models/scales should be minimised. The ultimate goal is to consider multiple various scale representations as a single model.

The HNode Class is developed to support continuity of information between different resolutions. The modelling framework is based on Grasshopper, where the principal collection type is called Data Tree. Contrary to its name, this object is not a proper tree-like collection (rather a dictionary), as it doesn't have a query method for parent and child nodes. A custom-tailored class provides a better foundation to accomplish geometry-data coupling through a recursive tree object. The HNode Class (Hierarchy Node) is a type of a tree data structure that can be traversed efficiently. As with tree structures, all of the data are stored in the root-level node. In our case, the root represents the complete demonstrator structure composed of multiple panels, which are stored separately as the second level of the tree. The third level represents the initial low-resolution mesh, where each node keeps information for each mesh face. To keep track of different resolutions, the subdivision algorithm introduces new layers to the tree: For each subdivided face, multiple children are added (2-4 for adaptive loop subdivision), and to keep the tree easy to read and manipulate, the nodes of the faces which are not subdivided are given a singular child. Additionally, to storing information about its children, an HNode collection can store and/or convey some more information just like a binary tree (Fig. 9). Contrary to that kind of structure, the values are decoupled from the topology of the tree (in our case the topology is derived from the subdivision process) and come from structural analysis at various levels. As the analysis can be done for any of the levels of the tree at any time, various upstream and downstream methods of propagation have been implemented.

One example of upstream data propagation is the minimal wall thickness information gained from strains calculation. This process happens at the lowest level of the tree, and to visually inspect the results it is easiest to recursively query each top-level parent to get the lowest value of each of its children. At this highest level, this results in an easy to verify visualisation (Fig. 10).

Two ways of keeping the data up to date within the tree have been tested: active and passive. The active way means that the value of dependent parents and children is updated automatically each time any value in the tree is changed; the passive method requires the user to manually trigger the upstream or downstream propagation from a selected level of the tree. During the tests, it came clear that the passive method is more adequate for computational efficiency and clarity.

**Full resolution mesh**

Average strain   Minimal strain   Maximal strain
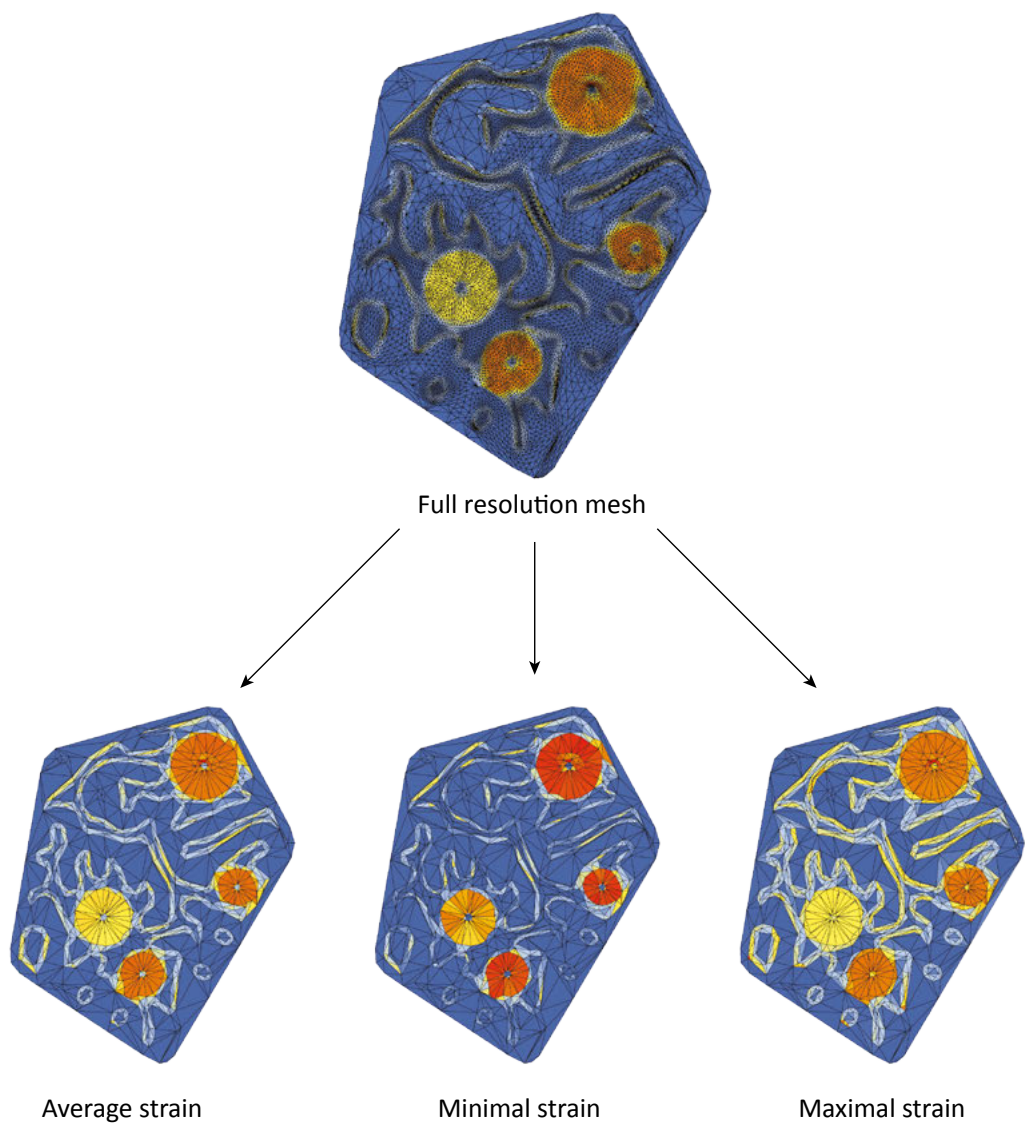
<span style="color:magenta">**Figure 11.**</span> Various methods of data propagation.

The HNode library is written in .NET, and the implementation wraps it up as a data type compatible with Grasshopper. The generic nature of this collection type bears a premise of its being useful in other applications, where keeping track of dependencies and relationships might not be as easy to achieve with the native to Grasshopper Data Tree collection because of the previously stated dictionary-like characteristics.

# 4. Reflections and Conclusions

This paper examines adaptive mesh-based modelling as a means to support the computational design of panelised thin-sheet structures built using the ISF process. Two approaches are described: The first is characterised as unidirectional and the second as bi-directional. The context of the research exemplifies the need for a back and forth between fabrication, design, and analysis. With multiple scales of material organisation – multiple parts, highly heterogeneous in terms of their shape, their surface geometry, and their material properties, modelling necessitates a discretisation for reasons of control, accuracy and workability. However, a successful discretisation relies on retaining as many possibilities for information flow as possible, and on an efficient and effective organisation of that information flow.

The tree-based approach we have described avoids the separate storage and lookup of information, as this can be produced directly from the hierarchy. The approach is generalisable. For example, although applied here to a technique of manipulative fabrication, the methods we described would also support material specification and optimisation for additive fabrication, specifically within the emerging territory of functionally or mechanically graded materials. Because digital fabrication offers increasing possibilities for bespoke material design that corresponds to desired performances, complex information flows between design, specification, and analysis at multiple scales become required.

One could ask why it is necessary to have multiple scales of resolution and not simply compute every aspect at the highest level of resolution. Beyond pragmatic reasons, which include limitations of computation time and legibility, there is a greater issue of efficiency. The generation of unnecessary data can render a design workflow unusable, or simply displaces effort into subsequent filtering.

The first approach sequentially varies a single mesh topology to manage the complexity of bridging scales and functions while maintaining the continuity of information flows down scale. However, a realisation of this approach is that, for each scale, there is some data that the designer wants to pass up or down. This is because a model does not necessarily have the possibility to recognise or even correct a problem within the model itself. Instead, geometry needs to be passed to another level of resolution for its implications to be tested accurately. Equally, something can be learnt on a lower level that forces adjustment on the upper level, which cannot be tested for at the resolution of prior levels. This cannot be well addressed by a unidirectional model.

In the second approach described, the bi-directional workflow ties multiple scales together in a more consistent and manageable way compared with the previous method. The ability to reference the data through common interface to other levels makes an element on one level aware of information at any other level of the tree. This enables adaptation of any particular element based on

higher or lower-level information. Future research will connect this bi-directional workflow with an automated feedback loop, and develop visualisation techniques that allow analysis and comparison at different resolution levels.

## References

Ambrogio, Giuseppina, Luigino Filice, Francesco Gagliardi, and Fabrizio Micari. 2005. "Sheet Thinning Prediction in Single Point Incremental Forming." *Advanced Materials Research* 6-8: 479–86. doi: 10.4028/www.scientific.net/AMR.6-8.479

E, Weinan. 2011. *Principles of Multi-Scale Modeling.* Cambridge University Press.

Hirschel, Ernst Heinrich, Horst Prem, and Gero Madelung. 2012. *Aeronautical Research in Germany.* Berlin Heidelberg: Springer. doi: 10.1007/978-3-642-18484-0

Jeswiet, J., N. Alan, F. Bramley, J. Micari, J. Duflou, and J. Allwood. 2005. "Asymmetric Single Point Incremental Forming of Sheet Metal." *CIRP Annals – Manufacturing Technology* 54, 2: 623–49. Accessed at http://opus.bath.ac.uk/2137/

Loop, Charles Teorell. 1987. "Smooth Subdivision Surfaces Based on Triangles." *Department of Mathematics, The University of Utah, Masters Thesis.* Accessed at http://research.microsoft.com/apps/pubs/default.aspx?id=68540

Nicholas, Paul, David Stasiuk, Esben Nørgaard, Christopher Hutchinson, and Mette Ramsgaard Thomsen. 2016. "An Integrated Modelling and Toolpathing Approach for a Frameless Stressed Skin Structure, Fabricated Using Robotic Incremental Sheet Forming." *Robotic Fabrication in Architecture, Art and Design 2016*, 62-77, doi: 10.1007/978-3-319-26378-6

Nicholas. Paul, and Martin Tamke. 2012. "Composite Territories: Engaging a Bespoke Material Practice in Digitally Designed Materials." *eCAADe – Digital Physicality*, Prague 2: 691–699.

Pakdel, Hamid-Reza, and Faramarz Samavati. 2004. "Computational Science and Its Applications." In *ICCSA 2004: International Conference, Assisi, Italy, May 14–17, 2004, Proceedings, Part III.* Ed. by Antonio Laganá, Marina L Gavrilova, Vipin Kumar, Youngsong Mun, C J Kenneth Tan, and Osvaldo Gervasi, 237–46. Berlin, Heidelberg: Springer. doi: 10.1007/978-3-540-24767-8_25

Wallner, Johannes, and Helmut Pottmann. 2011. "Geometric Computing for Freeform Architecture." *Journal of Mathematics in Industry* 1, 1: 4. doi: 10.1186/2190-5983-1-4

# Dimensionality Reduction for Parametric Design Exploration

John Harding

J. Harding
University of The West of England (UWE), UK

johnharding@fastmail.fm ✉

# Abstract

In architectural design, parametric models often include numeric parameters that can be adjusted during design exploration. The resulting design space can be easily displayed to the user if the number of parameters is low, for example, using a simple 2- or 3-dimensional plot. However, visualising the design space of models defined by multiple parameters is not straightforward. In this paper it is shown how dimensionality reduction can assist in this task whilst retaining associations between input designs at a high-dimensional parameter space. A self-organising map (SOM), a type of unsupervised artificial neural network, is used in combination with Rhino Grasshopper in order to demonstrate the potential benefits for design exploration.

# 1. Introduction

Dimensionality reduction (DR) is the study of reducing the number of variables that define any system. This is typically divided into two methods, feature selection and feature extraction. For the former, the task involves selecting a subset of variables, typically those that have the greatest influence on the output. Feature extraction, on the other hand, transforms the data into a new set of lower dimensional variables.

Techniques for feature extraction of high-dimensional data sets are well known in data-mining for both reducing storage space of complex data and visualising high-dimensional data sets. Examples in speech (Kumar & Andreou 1998) and image recognition (Yu & Yang 2001; Hinton & Ruslan 2006) are now standard references in pattern recognition, and research into using DR methods for solving engineering design problems (Bekasiewicz et al. 2014) is continuing at pace.

Dimensionality reduction has strong links to research in neuroscience and cognition, for example, in mapping sensory experience to associated three-dimensional locations in the brain, the so-called *somatotopic map* (Grodd et al. 2001). In AI research, some artificial neural networks attempt to artificially recreate this process by mapping complex inputs into a lower dimensional spaces, one example being the SOM introduced by Kohonen (1982). This paper therefore investigates whether SOMs can be used effectively in combination with architectural parametric models defined by high-dimensional parameters.

# 2. Background

Visualising high-dimensional data for human cognition is hard. Examples without resorting to reducing dimensions include the use of colour on plots or by combining multiple plots representing different combinations of variables. Due to this mixed mode of representation, such diagrams can often be difficult to understand and get an overall picture of the data set.

With feature extraction, reducing the high-dimensional data can be converted to a lower dimensional space. Feature extraction methods can be classified into two sets, linear and non-linear. Popular linear methods include K-means cluster analysis and principal component analysis (PCA). PCA, for example, transforms the data set to a lower dimensional orthogonal coordinate system that maximises variance (Jolliffe 2002).

Whilst linear methods are often comparatively fast, they struggle to maintain associations between data that is distributed non-linearly in the high-dimensional space. A classic example is in handing the so-called *Swiss-roll* data set, for which PCA in particular is known to struggle (Tenenbaum et al. 2001). Some examples of non-linear dimensionality reduction (NLDR) methods that retain
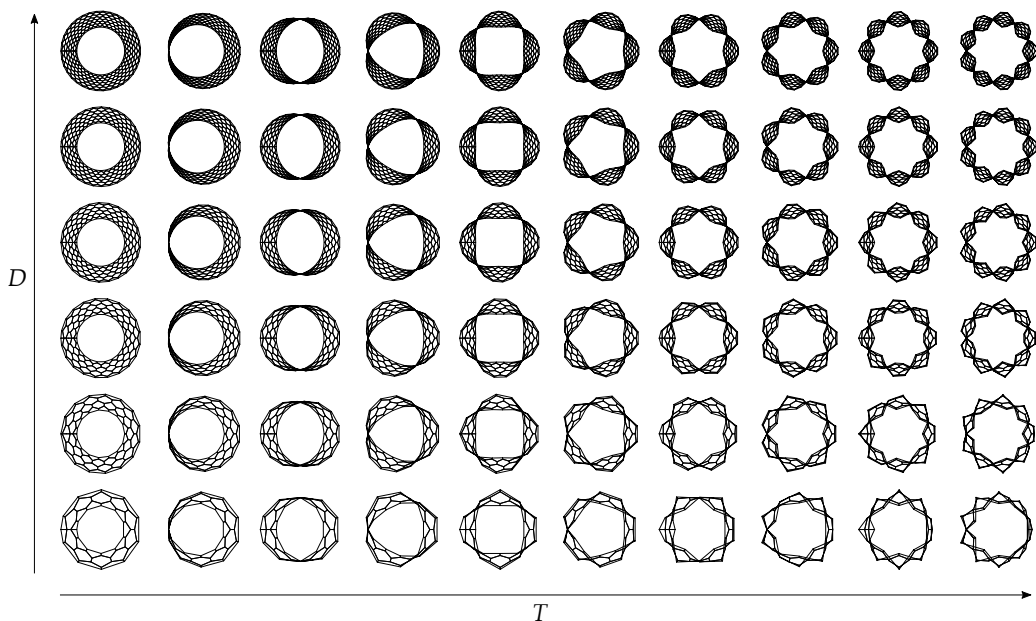
**Figure 1.** Visualising the design space of a simple parametric model with two parameters.

non-linear relationships include Sammon mapping (1969), Isomaps (Tenenbaum et al. 2001), elastic maps (Gorban & Zinovyev 2009), and SOMs (Kohonen 1982).

## 2.1 Precedents in Architectural Design

In architectural design, DR has been implemented predominantly in spatial analysis. Coyne (1990) first used the idea of connectionism to display differences between abstract residential plans. Petrovic and Svetel (1993) generated 3-dimensional layouts based on higher dimensional semantic associations. More recent work by Derix and Thum (2000) investigated a spatial machine that could build autonomous representations of space using SOMs. Methods for the classification of architectural plans have been investigated using both PCA (Hanna 2006; Hanna 2010) and SOMs (Jupp & Gero 2006; Harding & Derix 2010). More recently, Derix and Jagannath (2014) have used SOMs to capture and classify spatial descriptions.

Although these applications have shown the high potential of using DR methods in design, they are yet to have a wider impact in architectural computing. This has in part motivated this research in returning to existing parametric modelling tools, offering new ways to enhance their use. The work presented here focusses on visualising parameter and not objective space (for example, performance criteria).

**277**
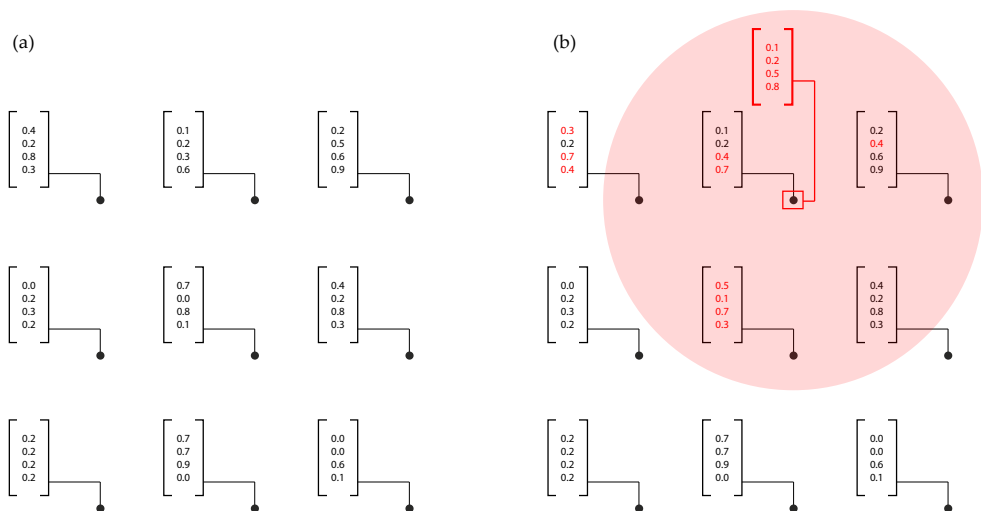
**Figure 2.** Each neuron in the map has an associated feature vector at the same dimension as the inputs (a). Learning takes place after the 'winning' node is identified (b).

## 2.2 Potential for Parametric Models

A subset of parametric modelling tools based on dataflow programming associates input parameters and explicit functions to form a directed acyclic graph (DAG). The structure of the DAG typically describes a mapping of numbers into geometry, setting out a possible design space to be explored when parameters are adjusted (Aish & Woodbury 2005). Well-known examples of such DAG-based tools used in architecture include Rhino Grasshopper (McNeel and Associates) and Autodesk Dynamo (Autodesk).

Visualising the design space of parametric models can help users to understand both the bounds of the model and how each parameter guides variation. For low-dimensional models, a simple plot is often sufficient to understand the parameter space inherent in the model. Such an example is shown in Figure 1. The design space of shapes defined by a set of parametric equations similar to Möbius bands is visualised. A parameter (T) governs a number of twists in the surface which is then discretised into a hexagonal pattern with increasing density (D). In this particular case, it is possible to include semantic information to each parameter/axis, for example *twist* and *density*.

When models begin to increase in terms of independent variables (parameters), it becomes increasingly hard to understand the extent of the model. One is sometimes left adjusting different combinations of parameters and observing their effect on the output geometry. This is where DR techniques such as SOMs can potentially help visualise the bounds of a parametric model definition.

# 3. Self-Organising Maps

SOMs are a type of unsupervised artificial neural network that can be used in reducing the dimensionality of data whilst attempting to retain non-linear associations. Samples in the high-dimensional input *feature space* are presented to a map in a lower dimensional *map space*, with the map learning over time from the inputs presented to it.

Typically, the map has either a hexagonal or rectangular topology arranged on a 2D plane, although this depends on the application. Each location in the map has an associated *feature vector* (sometimes known as a synaptic vector) at the same dimension as the input samples. In the example shown in <span style="color:magenta">Figure 2</span>, a 2-dimensional 3 x 3 map contains feature vectors in 4 dimensions. Before learning takes place, these feature vectors are typically randomised, meaning resulting maps for the same set of inputs, although similar, are never identical.

## 3.1 Learning

At each iteration, the inputs are presented to the map with the node with the closest feature vector to each input declared the winner. Determining this distance can be done using various methods, including finding the Hamming distance (binary comparison) or simply taking the dot product for small input dimensions. The most common method, however, and that used here is to take the smallest Euclidean distance (in feature space) to determine a *winning node*.

Once identified, a winning node adapts its feature vector slightly towards the input at a given rate (winner learning rate), with neighbouring nodes also learning depending on a radial function, typically a Gaussian radial basis function. These learning rates decay (exponentially) over time, with the map converging as learning approaches zero. As the map changes, so the inputs move between winning nodes, making the SOM more than simply a form of high-dimensional diffusion.

The SOM algorithm has various parameters that govern the nature of learning in the map. These include:

- Map dimension, size, and topology.
- Winning node learning rate.
- Winning node learning decay rate.
- Neighbourhood learning function (e.g. Gaussian radial basis function).
- Neighbourhood learning decay rate.
- Neighbourhood decay rate (affected neighbours shrinks over time).

Setting these parameters depends on the nature of the inputs and requires either manual adjustment based on visual inspection of the final map outcome or by using various adaptive methods (Berglund & Sitte 2006). For the applications
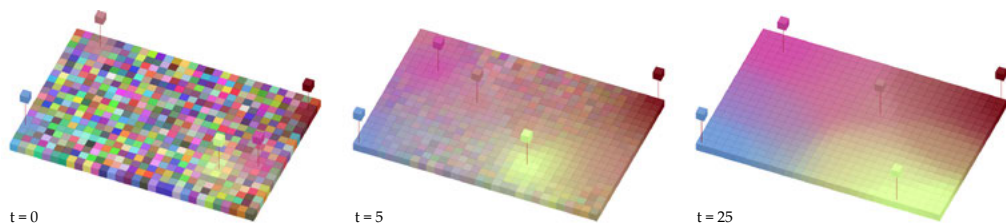
**Figure 3.** A 2D self-organising map being trained with five RGB inputs.
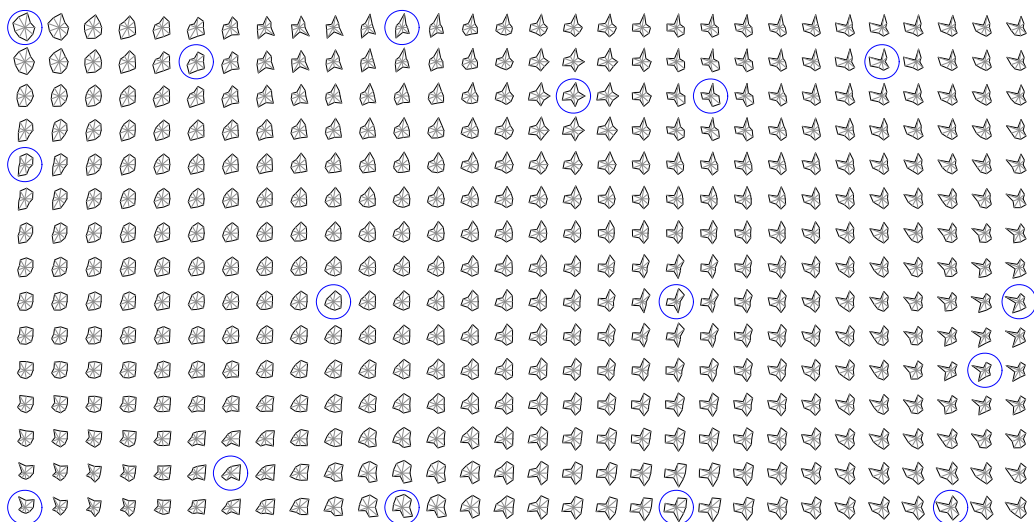


**Figure 4.** 9-dimesional 'glyphs' reduced to a two-dimensional map. The final 16 input locations are highlighted.

discussed here, manual adjustment of the parameters were adequate to produce suitable maps for visualising parametric model design spaces. A more thorough background to the SOM algorithm can be found in Kohonen (2001).

## 3.2 Reduction to 2D

The chosen map dimension can in theory be any equal or below the input space dimension. In this paper, 2-dimensional plots for the map were chosen in order to best visualise the design space for human cognition. Figure 3 shows an example of a 2-dimensional SOM on a rectangular grid being trained with five inputs. Each input is defined by a 3-dimensional vector corresponding to RGB values.

After 25 iterations learning has completed and the locations of the inputs on the map are distributed with similar colours being closer to each other and

those most different being furthest away. This associativity between inputs is maintained, despite a reduction from 3 dimensions to 2. As well as the input distribution, the map itself contains a smooth gradient between inputs, revealing colours that were not explicitly defined by the inputs.

Although non-linear DR can maintain associativity in the form of map regions, it is important to note that the original orthogonal structure of the data is lost. For example, one cannot associate axes to the sides of the 2-dimensional map, or in other words the mapping cannot be defined by a linear combination of the three original variables. Another important aspect is that the whole visible spectrum as we know it is not shown; the map can only learn from the inputs presented to it.

Figure 4 shows a higher dimensional geometric example with sixteen random 9-dimensional input 'glyphs' being used to train a 2-dimensional map. Glyphs are similar to radar or spider plots in that each radial axis defines the value of a given parameter. The resulting map produces a similar result to multi-dimensional scaling (MDS) methods (Buja et al. 2008). In the example shown, in theory the nine parameters could in theory control any aspect of a parametric model with the resulting geometry located at each map node.

# 4. Application in Parametric Design

The use of DR methods in architectural design to date is relatively niche, so combining such techniques with popular parametric design software was the motivation behind developing a tool for use in the architectural computing community. Written in C#, a freely available Grasshopper component was developed by the author for producing 2-dimensional SOMs with a rectangular topology (Harding 2016). The component consists of the control parameters as discussed in Section 3.2. Figure 5 shows the use of the component to generate the glyph plot shown in Figure 4.

## 4.1 Parameter Encoding

In general, parametric design models map numbers to resulting geometry. The amount of indirectness in this mapping can vary, for example, a parameter that controls the height of a box can be seen as direct and linear – i.e. increasing the parameter also gradually increases the height of the output gradually. At the other end of the scale, parameters that are seeds for pseudorandom functions result in a completely indirect mapping between parameter and final geometry – a concept similar to that of continuous functions or smooth fitness landscapes in evolution.

Parametric models that use dataflow programming such as Rhino Grasshopper do not typically allow cycles and therefore have a so-called *explicit embryogeny* (Bentley and Kumar, 1999). The topology of the graph in a parametric model is fixed when
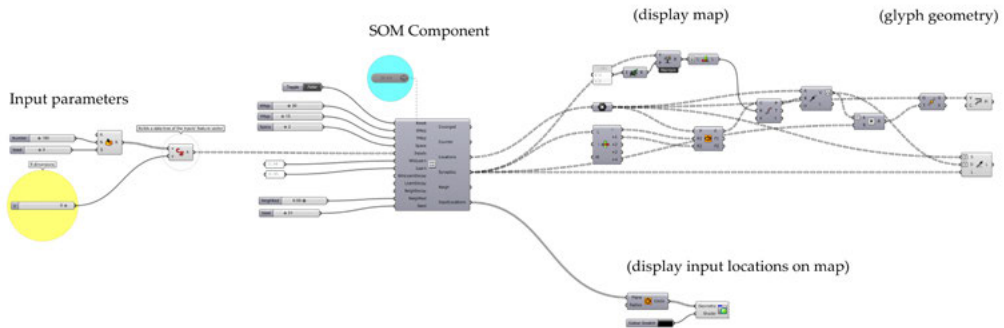
**Figure 5.** Grasshopper definition with self-organising map component in use.

parameters are adjusted, and this usually helps in maintaining a direct mapping between number and form. This is in contrast to chaotic (Lorenz 1963) or complex systems such as class IV cellular automata (Wolfram 1986) that have a highly indirect mapping between parameter and resulting form.

So-called *developmental encodings* are generally more indirect than parametric models, for example, superformulas (Gielis 2003) and compositional pattern-producing networks (CPPNs) (Stanley 2007; Clune & Lipson 2011) that vary graph topology. In architectural design, Vierlinger (2015) has recently showed how such developmental encodings can help evolve neural networks that produce drawings in anticipation of the user.

The nature of the mapping is therefore an important consideration when visualising a design space and will inevitably vary depending on the parametric definition. For example, if the parametric model is many-to-one, i.e. two values of a given parameter map to the same design (a periodic function, for example). In such cases, a method such as shape analysis (Costa & Marcondes 2000) is likely to be more appropriate for classifying geometry and forming a feature vector.

## 4.2 Sampling of Models

As with the examples given in Section 3.3, for high-dimensional parametric models, a selection of samples (saved parameter states) selected at random from the design space can be used to produce a lower-dimensional map. Figure 6 shows a tower massing form defined by three parameters with a direct mapping that alter the twist, height, and tapering of a box. By using several inputs with normalised parameter values, the resulting 2-dimensional map can offer an overall visualisation of the design space inherent in the parametric model.

The spaces between the inputs are interpolated by the map itself. Again, note that we have lost the structure of the original 3 dimensions during the process,
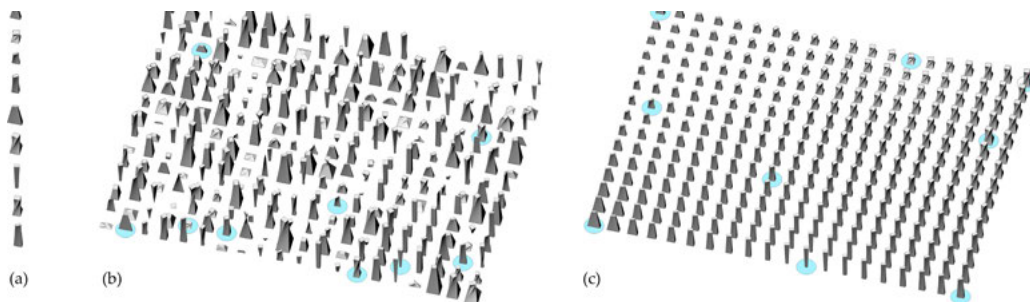
**Figure 6.** Reducing three dimensions (twist, height, and taper) to a plane. Random selection of inputs (a), initial state of the map (b) and following learning (c).

i.e. no particular direction now indicates twist, density, or height, rather there exists *regions* in the map that have higher values of these parameters than others.

In this example, as the choice of inputs is random, there exists no prevalent structure or clustering in the high-dimensional space that requires maintaining. However, if particular designs (or parts of design space) are more desirable then these can be selected as the inputs to the map. As the specific sampling may vary, one must anticipate that linear methods may not be sufficient. Sampling such as the Swiss-roll data set (Tenenbaum et al. 2001) requires a non-linear method to maintain high-dimensional clustering. This is discussed further in the next section.

## 4.3  Selective Sampling

If certain parameter combinations are preferred by the designer, then there exists a bias towards certain clusters in the data. These could be selected automatically using an objective function and/or selected artificially. Figure 7 shows the design of a structural node as part of the UWE 2016 Research Pavilion. Each node is defined by five parameters, two controlling colour and three defining the mesh geometry. As opposed to random sampling, seven designs were selected from the parametric model by the design team by adjusting parameters in the traditional way and saving parameter states.

The selected designs were then used as inputs in the SOM. The resulting map (Fig. 8) interpolates designs between the inputs as well as locating similar designs closer to each other on the map and dissimilar designs further apart. Again, although it is not possible to define linear axes on the map (as we could in 5-dimensional feature space), associations between designs are evident by viewing the map as a gestalt. The associative map gives an overview of the latent possibilities within the parametric definition. Without resorting to laborious slider

tweaking resulting in user fatigue (Piasecki & Hanna 2011), the map suggests possible design combinations that might have been otherwise missed.

## 4.4 Artificial Selection

Evolutionary algorithms with artificial selection often employ a visual interface for engaging with the user. Dawkins' biomorphs (1986), for example, involve selecting designs which are then crossbred and mutated at each generation. Such *interactive* evolutionary algorithms are known to be useful for exploring design problems with no clearly defined goal. At each iteration, SOMs could potentially be used to display the design space to the user as part of a human-computer interactive process. In addition, associating a fitness landscape at this lower dimensional parameter space could also potentially help better visualise the effect of parameters on different performance measures for different designs.

# 5. Conclusions

In this paper DR has been used in combination with a parametric modelling environment in order to visualise high-dimensional parameter spaces. As well as creating associations between inputs, the SOM can suggests possible design avenues beyond that easily achieved by adjusting numeric parameters manually. Future research in linking parametric design with DR includes the following:

- The use of a hexagonal map topology which is known to improve the performance of the map (Länsiluoto 2004).
- Incorporating fitness plots in order to make comparisons between parameter and objective space for architectural designs.
- Incorporate a form of sensitivity analysis to understand effect of parameters on the final geometry (i.e. the directness of mapping from parameters to design).
- Incorporating analysis measures as inputs to the map.
- Development of the SOM tool to generate 1- and 3-dimensonal maps.
- Testing of complex parametric models where the 'curse of dimensionality' can make adequate sampling difficult.

Although popular in other fields such as engineering, machine learning techniques are still relatively niche in architectural design. It is therefore hoped that by combining dimensionality reduction methods with mainstream parametric modelling software, this can benefit the wider architectural community through future experiment and application.

Parameters:

B: blue colour index
G: green colour index
R: pipe radii
S: central node size (convex hull)
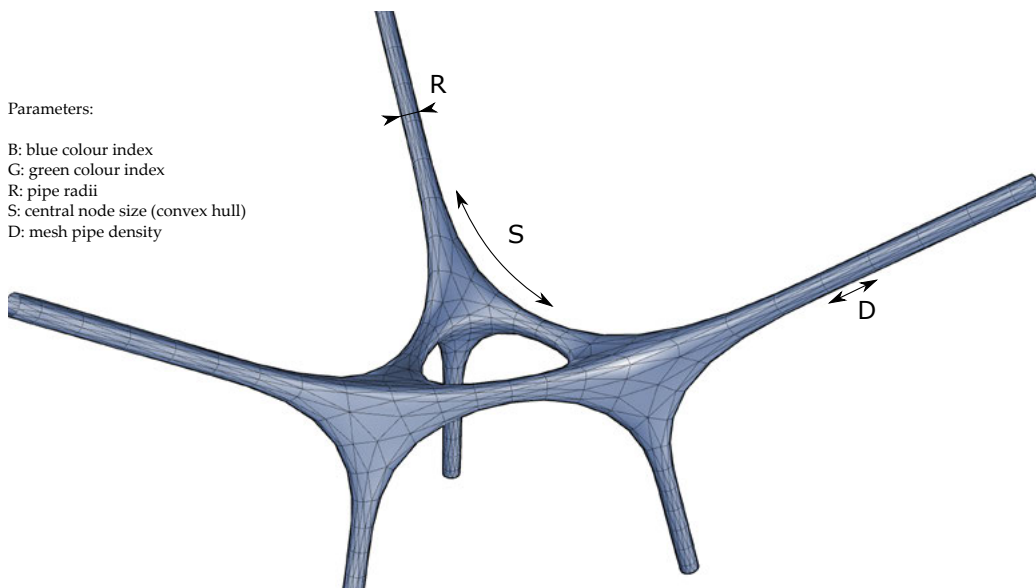D: mesh pipe density

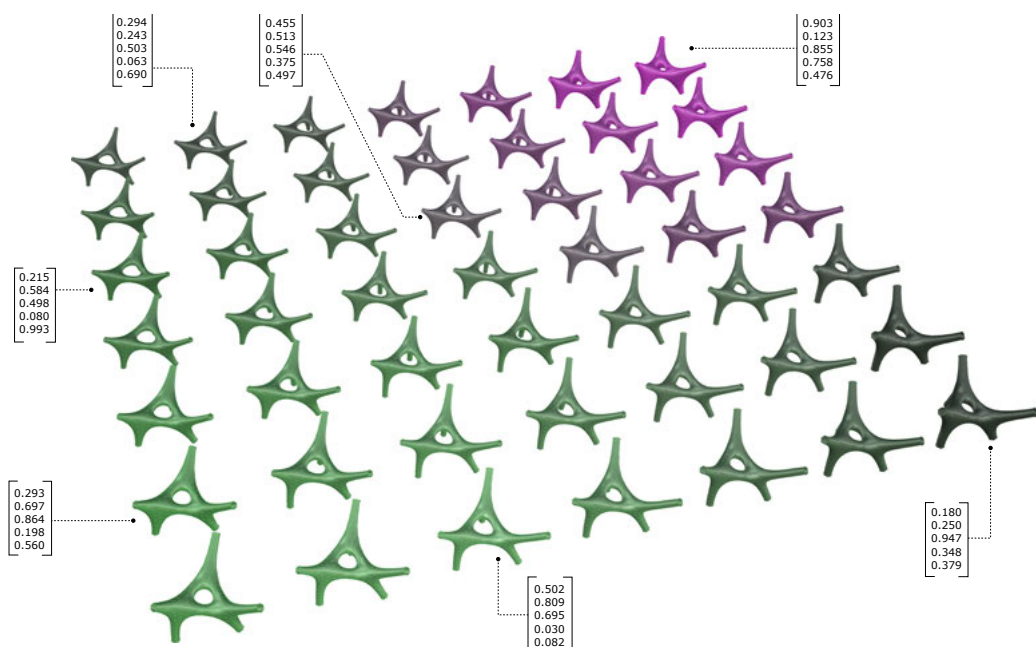**Figure 7.** Structural node joining six elements controlled by five parameters.



**Figure 8.** A 7 x 7 2-dimensional SOM trained with seven inputs chosen by the design team. The input locations at the map when learning has completed are shown.

## Acknowledgements

## References

Aish, Robert, and Robert Woodbury. 2005. "Multi-level interaction in parametric design." In *Smart Graphics*, 151–162. Berlin Heidelberg: Springer.

Bekasiewicz, Adrian, Koziel Slawomir, and Zieniutycz Wlodzimierz. 2014. "Design Space Reduction for Expedited Multi-Objective Design Optimization of Antennas in Highly Dimensional Spaces." In *Solving Computationally Expensive Engineering Problems: Methods and Applications* 97: 113–120.

Bentley, Peter J., and Sanjeev Kumar. 1999. "Three Ways to Grow Designs: A Comparison of Embryogenies for an Evolutionary Design Problem." In *GECCO*, 99: 35–43.

Berglund, Erik, and Joaquin Sitte. 2006. "The Parameterless Self-Organizing Map Algorithm." *Neural Networks, IEEE Transactions* 17, 2: 305–316.

Buja, Andreas, Deborah F. Swayne, Michael L. Littman, Nathaniel Dean, Heike Hofmann, and Lisha Chen. 2008. "Data Visualization with Multidimensional Scaling." *Journal of Computational and Graphical Statistics*, 17, 2: 444–472.

Clune, Jeff, and Hod Lipson. 2011. "Evolving Three-Dimensional Objects with a Generative Encoding Inspired by Developmental Biology." In *Proceedings of the European Conference on Artificial Life*: 144–148.

Costa, Luciano da Fontoura Da, and Roberto Marcondes Cesar Jr. 2000. "*Shape Analysis and Classification: Theory and Practice.*" Boca Raton, Florida: CRC Press, Inc.

Coyne, Richard D., and A. G. Postmus. 1990. "Spatial Applications of Neural Networks In Computer-Aided Design." *Artificial intelligence in Engineering* 5, 1: 9–22.

Dawkins, Richard. 1986. "*The Blind Watchmaker: Why the Evidence of Evolution Reveals a Universe Without Design.*" New York: WW Norton and Company.

Deb, Kalyanmoy, Amrit Pratap, Sameer Agarwal, and T. A. M. T. Meyarivan. 2002. "A Fast and Elitist Multiobjective Genetic Algorithm: NSGA-II." *Evolutionary Computation, IEEE Transactions* 6, 2: 182–197.

Derix, C., and P. Jagannath. 2014. "Near futures: Associative archetypes Architectural Design." *Wiley Online Library* 84: 130–135.

Derix, C., and R. Thum. 2000. "Self-Organizing Space." *Proceedings of the Generative Arts Conference 3*, Milan :1-10.

Gielis, Johan. 2003. "A Generic Geometric Transformation That Unifies a Wide Range of Natural and Abstract Shapes." *American Journal of Botany* 90, 3: 333–338.

Grodd, Wolfgang, Ernst Hülsmann, Martin Lotze, Dirk Wildgruber, and Michael Erb. 2001. "Sensorimotor Mapping of the Human Cerebellum: fMRI Evidence of Somatotopic Organization." *Human Brain Mapping* 13, 2: 55–73.

Harding, John, and Derix, Christian. 2011. "Associative Spatial Networks in Architectural Design: Artificial Cognition of Space Using Neural Networks with Spectral Graph Theory." In *Design Computing and Cognition '10*, edited by John S. Gero, 305–323. New York: Springer.

Harding, John. 2016. "A Self-Organising Map Component." Accessed March 3, 2016. http:// http://www.grasshopper3d.com/profiles/blogs/self-organising-map

Hinton, Geoffrey E., and Ruslan Salakhutdinov. 2006. "Reducing the Dimensionality of Data with Neural Networks." Science 313, 5786: 504–507.

Jolliffe, Ian. 2002. *"Principal Component Analysis."* New York: Springer.

Jupp, Julie, and John S. Gero. 2006. "Visual Style: Qualitative and Context-Dependent Categorization." *AIE EDAM: Artificial Intelligence for Engineering Design, Analysis, and Manufacturing* 20, 3: 247–266.

Gorban, Alexander N., and Andrei Y. Zinovyev. 2009. "Principal Graphs and Manifolds." In *Handbook of Research on Machine Learning Applications and Trends: Algorithms, Methods and Techniques*, edited by Emilio Soria Olivas, José David Martín Guerrero, Marcelino Martinez-Sober, Jose Rafael Magdalena-Benedito and Antonio José Serrano López, 28–59. Hershey, Pennsylvania: IGI Global.

Kohonen, Teuvo. 1982. "Self-Organized Formation of Topologically Correct Feature Maps." *Biological Cybernetics:* 43, 1: 59–69.

Kohonen, Teuvo. 2000. "*Self-Organizing Maps.*" Berlin: Springer-Verlag.

Kumar, Nagendra, and Andreas G. Andreou. 1998. "Heteroscedastic Discriminant Analysis and Reduced Rank Hmms for Improved Speech Recognition." S*peech Communication* 26, 4: 283–297.

Länsiluoto, Aapo. 2004. "*Economic and Competitive Environment Analysis in the Formulation of Strategy: A Decision-Oriented Study Utilizing Self-Organizing Maps*". Turku: Publications of the Turku School of Economics and Business Administration.

Lorenz, Edward N. 1963. "Deterministic Nonperiodic Flow." *Journal of the Atmospheric Sciences* 20, 2: 130–141.

Piasecki, M., and S. Hanna. 2011. "A Redefinition of the Paradox of Choice." *Design Computing and Cognition 2010 :* 347–366.

Sammon, John W. 1969. "A Nonlinear Mapping for Data Structure Analysis." *IEEE Transactions on Computers* 5: 401–409.

Stanley, Kenneth O. 2007. "Compositional Pattern Producing Networks: A Novel Abstraction of Development." *Genetic Programming and Evolvable Machines* 8, 2: 131–162.

Tenenbaum, Joshua B., Vin De Silva, and John C. Langford. 2000. "A Global Geometric Framework for Nonlinear Dimensionality Reduction." S*cience* 290, 5500: 2319-2323.

Vierlinger, Robert. 2015. "Towards AI Drawing Agents." In *Modelling Behaviour: Design Modelling Symposium 201*5, edited by Mette Ramsgaard Thomsen, Martin Tamke, Christoph Gengnagel, Billie Faircloth, and Fabian Scheurer, 357–369. Switzerland: Springer International Publishing.

Yu, Hua, and Jie Yang. 2001. "A Direct LDA Algorithm for High-Dimensional Data – With Application to Face Recognition." *Pattern recognition* 34, 10: 2067–2070.

Wolfram, Stephen. 1986. *Theory and Applications of Cellular Automata, Vol. 1.* Singapore: World Scientific.

# Force Adaptive Hot-Wire Cutting

## Integrated Design, Simulation, and Fabrication of Double-Curved Surface Geometries

Romana Rust, Fabio Gramazio, and Matthias Kohler

R. Rust, F. Gramazio, M. Kohler
Gramazio Kohler Research, ETH Zurich, Switzerland

rust@arch.ethz.ch ✉
gramazio@arch.ethz.ch
kohler@arch.ethz.ch

# Abstract

This paper discusses a robotic cutting technique – Spatial Wire Cutting (SWC) – performed by the coordinated movement of two six-axis robotic arms which control the curvature of a hot-wire adopting itself against the resistance of the processed material. By escaping from the linearity of the cutting medium, combined with an integrated approach towards computational design, simulation and automated fabrication, this technique fosters the efficient manufacturing of double-curved surface objects by single cutting procedures and significantly expands the set of possible hot-wire cutting geometries. This paper presents a custom fabrication-informed computational design and simulation framework. It also outlines comparative analytical studies between digitally created SWC objects and their physically fabricated counterparts. Finally, it concludes with the architectural potentials of the discussed technique.

Keywords:
computational design, digital fabrication, hot-wire cutting,
feedback-based automated manufacturing, multi-robot control,
dynamic simulation

# 1. Introduction and Background

Recent technological advances have fostered the relationship between digital design and fabrication of architectural freeform shapes, opening a cross-fertilizing field from which various research directions are evolving. However, fabricating bespoke double-curved surfaces with commonly used fabrication techniques such as CNC-milling or 3D printing still comes at a high cost due to inefficient material use and time consumption (Schipper et al. 2014). The consequences are the simplification and post-rationalization of a specific design proposition. Digitally controlled cutting techniques, however, which have become very common in the larger fields of architecture, design and construction (Pigram & McGee 2011; Rippmann & Block 2011; McGee, Feringa & Søndergaard 2012), offer a fast, low-cost and material-efficient fabrication of non-standard volumetric elements for diverse applications (such as bespoke formwork components, prototype construction, etc.). These elements are created through the repeated movement of a cutting medium (e.g. hot-wire, steel cutting wire, hot-blade; Broek et al. 2002) through a synthetic material (e.g. expanded polystyrene) that melts the material just in advance of contact (thermal cutting). However, depending on the cutting medium, the range of geometries is limited. The project 'BladeRunner' (GXN 2016) is one of the most recent approaches, in which a hot-blade is dynamically bent to cut "surfaces swept out by continuously varying families of planar Euler elastica" (Søndergaard, et al. 2016), that reduces the geometrical restrictions.

The research presented in this paper focuses on Spatial Wire Cutting (SWC), a novel cutting technique performed by two six-axis lightweight robotic arms connected through a single hot-wire, which is attached to their end-effectors (see Fig. 1). Contrary to the above-mentioned approaches, it operates in transition states between thermal cutting and thermo-mechanical cutting to utilize the forces opposite to the moving direction to manipulate the hot-wire, which takes up the form of a curve. This curve is controlled by the robot's coordinated movement and is constantly altered throughout the procedure. Hence, this technique allows to significantly expand the set of possible hot-wire cutting geometries to certain double-curved surfaces, in particular sweep surfaces, which can be defined by the motion of a changing profile curve along two trajectory curves.

To efficiently control this multi-robotic cutting process, an advanced robotic control system is developed that monitors occurring forces during the manufacturing process and adapts the velocity of the cooperating arms accordingly. The dynamic change of these forces throughout the whole cutting procedure determine the absolute geometry of the surface being cut. To design those artefacts, it is crucial to predict the physical behaviour, as an evolving interplay between velocity, heat input, and reaction forces. As such, the project proposes an integral approach towards adaptive fabrication, design and simulation.
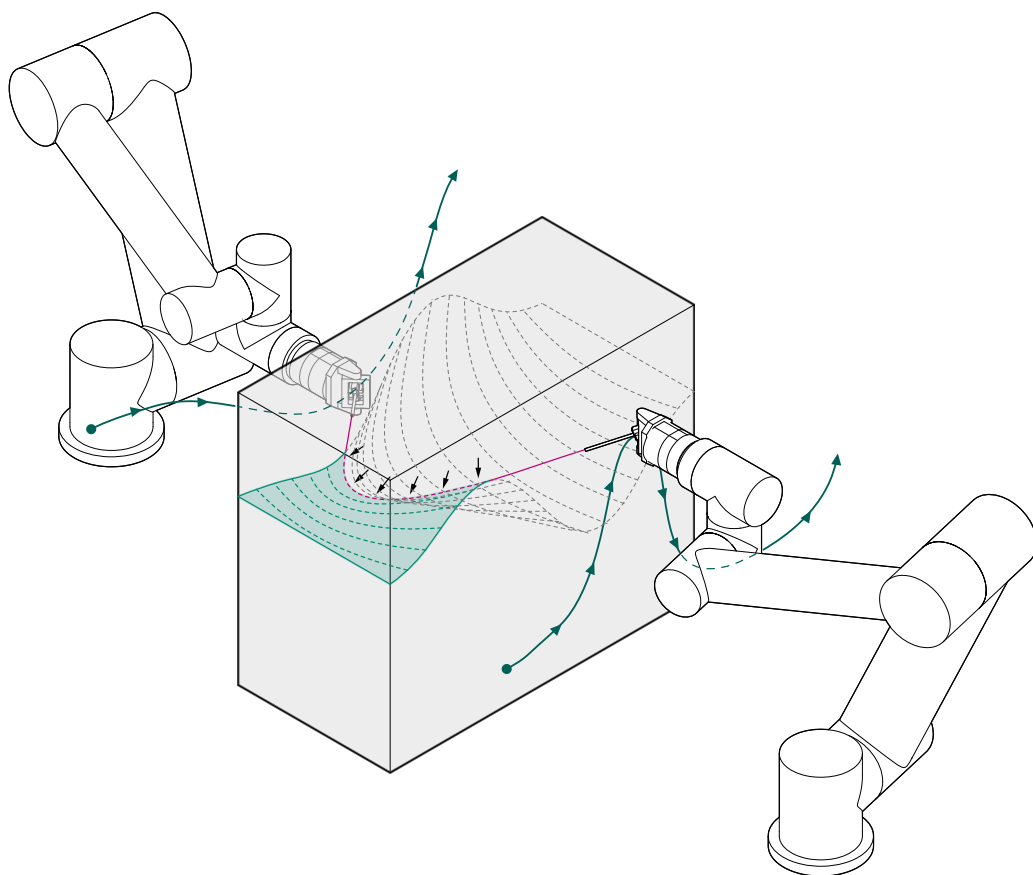
In the next section (Section 2) the process variables and relationships that guide the procedure as well as their integration into the simulation framework, and further its embedding into the computational design setup, is presented. Section 3 outlines comparative studies of four surface objects, which have been simulated, fabricated, and 3D scanned. The analysis focusses on simulated and measured process data and a quantitative geometrical comparison. Section 4 discusses the results and addresses strategies to improve the combined simulation framework and fabrication system. The conclusions and outlook are summarized in Section 5.

$$F_{left} = T_{left}\ sin(\alpha)$$

$$F = F_{left} + F_{right}$$
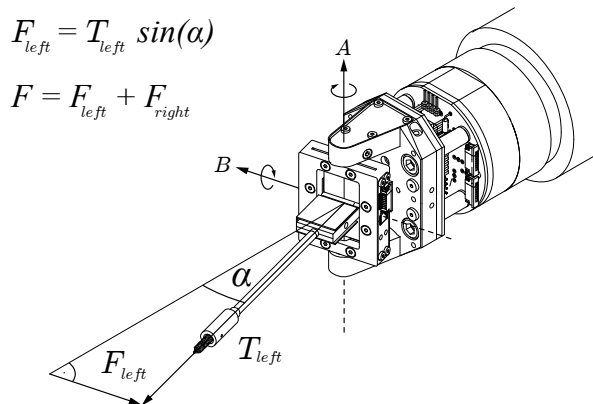


**Figure 2.** Cardan joint end-effector with axes (A, B), measuring angle α about axis A.

# 2. Fabrication-Informed Design and Simulation Framework

The shape of the wire and therefore the resulting surface is determined by forces acting on it throughout the cutting procedure. The magnitude of these forces as well as the force direction do not only vary along the cut, but also along the engaged wire in the foam. Their calculation is dependent on multiple factors such as the current speed, the heat input, the actual wire shape and the material properties of both the polystyrene and the hot-wire. In order to efficiently control the procedure and predict the resulting geometry, a digital model of the physical process has to be developed.

## 2.1 Process Variables

To identify the relationships between the most influential variables, such as heat input $Q_l$ [W/m], speed $v$ [m/s], and resulting cutting force, a first series of cutting tests was performed. According to Ahn, Lee, and Yang (2003), $Q_l$ and $v$ can be considered together as the effective heat input $Q_{eff}$ [J/m$^2$] ($= Q_l/v$). In these tests the tension force $T$ was recorded in steady state conditions[1], in which it levels off (Brooks 2009, 91). Additionally, the deflection[2] of the wire about the mounting points was logged (using a custom Cardan joint tool head with magnetic encoder sensors and a force sensor in the centre of the axes, see Figure 2). Thus, it was possible not only to map the tension force according to a given $Q_{eff}$ in an exponential model (Bain 2011, 176–78), but also the resultant of all forces acting perpendicular onto the wire (see Fig. 4). The coefficients ($a$, $b$, $c$, resp. $\bar{a}$, $\bar{b}$) were found by model fitting and are material dependent (properties of polystyrene and hot-wire[3]).
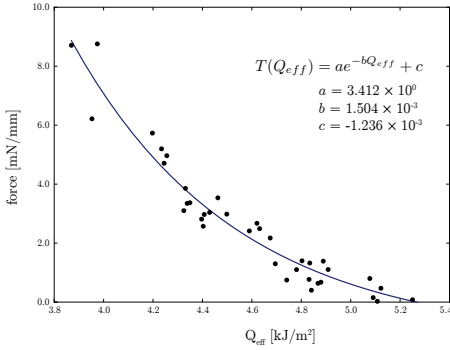
**Figure 3.** Model of relationship between $Q_{eff}$ and tension force $T$ in the steady state per unit of engaged wire length (Rust et al. 2016).
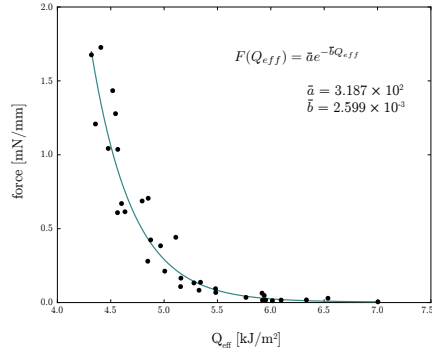


**Figure 4.** Model of relationship between $Q_{eff}$ and material force $F$ in the steady state per unit of engaged wire length.

(1)

$$T\big(Q_{eff}\big) = a\,e^{-b\,Q_{eff}} + c$$

(2)

$$F\big(Q_{eff}\big) = \bar{a}\,e^{-\bar{b}Q_{eff}}$$

## 2.2  Force Distribution

As the wire is exposed to variable forces, it deforms dependent on the magnitude, the direction, and the location of those forces, which ultimately influences the shape. For the fabrication process it is necessary to keep the wire always under a certain tension (based on empirical testing 2.0 N at each mounting point was defined as optimal value) to achieve a corresponding surface quality and, ultimately, to efficiently control the procedure.

   To calculate the force distribution for a wire with a given shape of length $s$ at a given moment $t$ in time, it is discretized into $n-1$ segments and $n$ nodes, with constant edge length $l$ [mm] ($l = l_i$) between the nodes. Furthermore, for each node $i$ the unit tangent vector $\hat{\mathbf{t}}_i$ is calculated. Assuming that the unit force direction $\hat{\mathbf{f}}_i$, the node speed $v_i$ and heat input $Q_i$ are known, the force vector $\mathbf{f}_i$ acting on one individual node $i$ can be estimated as follows

(3)

$$\mathbf{f}_i = F(v_i, Q_i)\,l_i\,\big\|\hat{\mathbf{t}}_i \times \hat{\mathbf{f}}_i\big\|\,\hat{\mathbf{f}}_i,$$

$$F_{res} = \left\| \sum_{i=0}^{n-1} \mathbf{f}_i \right\| = k \left\| \hat{\mathbf{t}}_0 + \hat{\mathbf{t}}_{n-1} \right\|$$

$$\mathbf{f}_i = F(v_i, Q_l) l_i \left\| \hat{\mathbf{t}}_i \times \hat{\mathbf{f}}_i \right\| \hat{\mathbf{f}}_i$$

$s$ ... wire length
$n$ ... number of nodes
$l_i$ ... length between nodes
$\hat{\mathbf{f}}_i$ ... force directions
$\hat{\mathbf{t}}_i$ ... tangents
$v_i$ ... speeds

**Figure 5.** Force distribution on the nodes of the discretized wire.



**Figure 6.** Schematic of the simulation algorithm.

where $F(v_i, Q_i)$ is the force [N/mm] acting perpendicular to the engaged wire length according to equation (2) and $\| \hat{\mathbf{t}}_i \times \hat{\mathbf{f}}_i \|$ a ratio between 0 and 1 depending on the angle between $\mathbf{f}_i$ and the edge tangent $\hat{\mathbf{t}}_i$. Since the target tension force in the endpoints of the wire with tangents $\hat{\mathbf{t}}_0$ and $\hat{\mathbf{t}}_{n-1}$ is constrained to $k(=2\,\mathrm{N})$, it is possible to calculate the resultant force $F_{res}$, which is the magnitude of the sum of all force vectors from equation (3):

(4)

$$F_{res} = \left\| \sum_{i=0}^{n-1} \mathbf{f}_i \right\| = k \| \hat{\mathbf{t}}_0 + \hat{\mathbf{t}}_{n-1} \|.$$

## 2.3 Shape Calculation

Since operating forces and shape are mutually dependent, it is assumed that the form of the wire at every moment $t$ along the cutting trajectory is in an equilibrium state. Therefore, the force density method (Schek 1974) is applied to calculate its form. The two endpoints of the wire are set to fixed nodes with known positions $\mathbf{X}_f$, and according to applied forces $\bar{\mathbf{F}}\,[\,n \times 3\,]$, a vector $\mathbf{q}$ of force densities is sought, so that the length between each individual node matches the edge length $l$. The approach to find the target force densities $\mathbf{q}$ is performed iteratively (Veenendaal & Block, 2012): Starting with an estimated vector $\mathbf{q}_0$ the equation in (7) is solved for the unknown positions $\mathbf{x}_{u0}$:

(5)

$$\mathbf{D}_u = \mathbf{C}_u{}^T \mathbf{Q}_0\, \mathbf{C}_u$$

(6)

$$\mathbf{D}_f = \mathbf{C}_u{}^T \mathbf{Q}_0\, \mathbf{C}_f$$

(7)

$$\mathbf{D}_u \mathbf{X}_{u0} = \bar{\mathbf{F}}_u - \mathbf{D}_f \mathbf{X}_f$$

(8)

$$\mathbf{q}_{k+1} = \mathbf{Q}_k\, \mathbf{L}^{-1}\, \mathbf{p}_k$$

$n_u, n_f$ …number for free (n − 2) and fixed (2) nodes
$m$ …number of edges (= $n - 1$)
$\mathbf{C}_u[m \times n_u]$ …connectivity matrix of n − 2 free nodes
$\mathbf{C}_f[m \times n_f]$ …connectivity matrix of 2 fixed nodes
$\mathbf{X}_u[n_u \times 3], \mathbf{X}_f[n_f \times 3]$ …coordinate matrices of free and fixed nodes
$\mathbf{Q}_k[m \times m]$ …diagonal matrix of $\mathbf{q}_k$
$\mathbf{L}^{-1}[m \times m]$ …inverted diagonal matrix of the target edge lengths

According to $\mathbf{X}_0 (= [\mathbf{X}_{uo}, \mathbf{X}_f])$, the edge length vector $\mathbf{p}_k$ is calculated and the next force density vector $\mathbf{q}_{k+1}$ is estimated by (8), which is again inserted into equations (5) and (6) as diagonal matrix $\mathbf{Q}_{k+1}$, and the linear system in (7) is solved to calculate the new coordinates $\mathbf{X}_{k+1}$. This process is continued until a certain tolerance is reached and the sum of all edge lengths matches the wire length $s$.
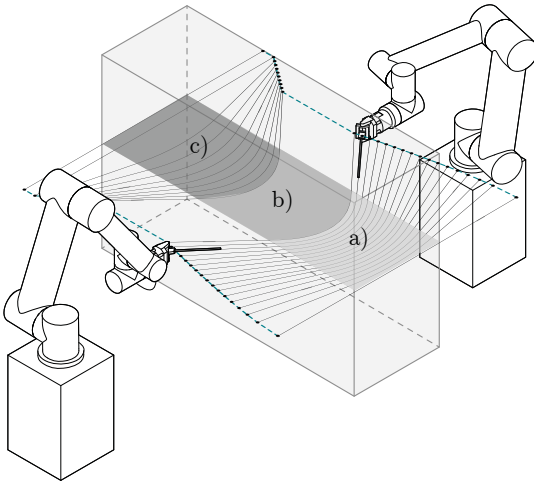
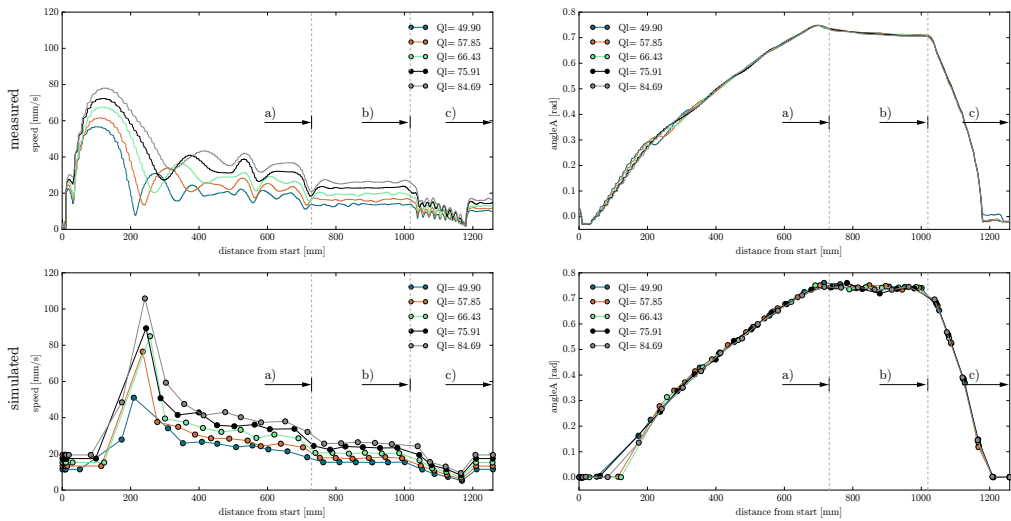**Figure 7.** a) Entry, b) steady and c) exit phase.



**Figure 8.** Measured and simulated process data (speed and angle) from five cutting tests with same path curves but different heat input.

## 2.4 Simulation Model

The simulation model builds upon the simplified physical models as described in Sections 2.1 and 2.2. It is employed to predict the physical process to improve the control of the fabrication and to predict the resulting geometry.

The wire moving through the foam is a dynamic system. The boundary conditions are the path curves, respectively the synchronized positions on those curves, the size and position of the foam block as a volume, and a defined heat input. As mentioned in Section 2.1, the forces $\mathbf{F}$ (= matrix of all $\mathbf{f}_i$) in equation (4) are the steady-state forces that act at a certain moment. However, the shape is also dependent on the dynamic forces, and therefore the transient behaviour of the wire. The total forces $\bar{\mathbf{F}}$, used to compute the shape result from all forces that have occurred since the entry of the wire into the foam at $t_0$ to the current timestamp $t_j$. Therefore, a numerical integration is performed to integrate the forces over time.

The integration model for the simulation is a combination of the explicit Euler method with the trapezoidal rule and the predictor – corrector method (Heun's method). The steady-state forces $\mathbf{F}$ are a function of the shape and the speeds $\mathbf{v}$, $\mathbf{F} = \mathbf{F}(\mathbf{v}, \mathbf{X})$ acting at time $t_j$. The step size is denoted by $h_j$ and initial forces $\bar{\mathbf{F}}_0 = \mathbf{F}(t_0, \mathbf{X}_0)$. In the predictor step, starting from the current forces $\bar{\mathbf{F}}_j$, the next forces $\mathbf{F}_{j+1}$ are estimated with the Euler method:

(9)

$$\tilde{\mathbf{F}}_{j+1} = \bar{\mathbf{F}}_j + h_j \mathbf{F}(\mathbf{v}_j, \mathbf{X}_j),$$

from which the shape $\widetilde{\mathbf{X}}_{j+1}$ is calculated as described in Section 2.3. In the corrector step the initial guess is improved by using the trapezoidal rule:

(10)

$$\bar{\mathbf{F}}_{j+1} = \bar{\mathbf{F}}_j + \frac{1}{2} h_j \left( \mathbf{F}(\mathbf{v}_j, \mathbf{X}_j) + \mathbf{F}(\tilde{\mathbf{v}}_{j+1}, \widetilde{\mathbf{X}}_{j+1}) \right),$$

from which the shape $\widetilde{\mathbf{X}}_{j+1}$ is calculated. In each iteration step, the speed $\tilde{v}_{ij+1}$ for one node $i$ is estimated by $r\tilde{d}_{ij+1}$ ($r$ factor, distances $\tilde{d}_{ij+1} = \| \mathbf{X}_{ij} - \mathbf{X}_{ij+1} \|$, $\mathbf{X}_{ij}$ position of node $i$ at iteration step $j$). The secant method is applied to find the factor $r$ and the root to the nonlinear equation (11), so that forces $\mathbf{F}(\tilde{\mathbf{v}}_{j+1}, \widetilde{\mathbf{X}}_{j+1})$ acting in the moment $t_{j+1}$ comply equation (4).

(11)

$$g(r) = \left\| \sum_{i=0}^{n-1} F(r\tilde{d}_{ij+1}, Q_i) \, l_i \, \| \hat{\mathbf{t}}_{ij+1} \times \hat{\mathbf{f}}_{ij+1} \| \, \hat{\mathbf{f}}_{ij+1} \right\| - k \| \hat{\mathbf{t}}_{0j+1} + \hat{\mathbf{t}}_{n-1j+1} \| = 0.$$
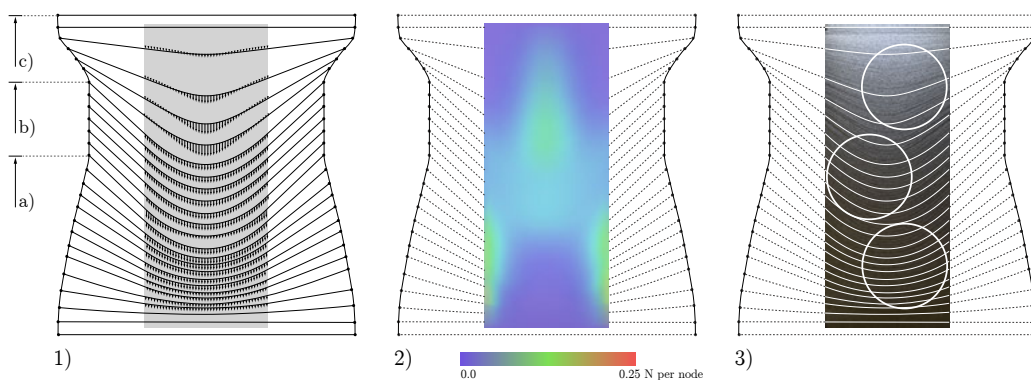
**Figure 9.** 1) Force vectors and curves from simulation, 2) force magnitudes coloured to visualize the differences and 3) overlay of surface picture with simulated curves.
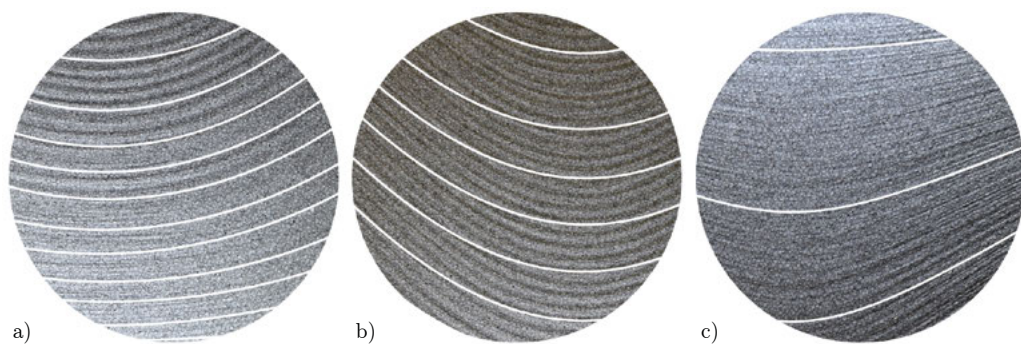


**Figure 10.** Details from the overlay between simulated curves and surface picture, from a) entry, b) steady and c) exit phases.

The step size $h_j$ is calculated as the reciprocal value to the solution $r(h_j=d_{ij}/v_{ij})$, as the time between two iteration steps. After each iteration step, $\overline{\mathbf{F}}_{j+1}$ is down-scaled, so that equation (4) is met and then multiplied by $h_j$; otherwise, the relation to the new force vectors $h_{j+1}y(\mathbf{v}_{j+1},\mathbf{F}_{j+1})$ in the next iteration step wouldn't correspond.

## 2.5 Physical Validation

A series of cutting tests were performed a) to validate the force distribution model as stated in (3) and b) to verify if the force density method and the calculated wire shapes are coherent with the physical shape. Multiple cuts were performed with different foam block sizes (300, 400, and 500 mm in width and 1200 mm in length), different heat inputs (50–85 [W/m]) and different path curves. The robots' path curves were designed in such a way that all positions lay in the same horizontal plane but have different distances to each other, generating three phases that are of interest to the analysis, due to expected distinctive differences in the force distribution:

a) **Entry phase:** the wire starts straight but the wire's endpoints are continuously moving towards each other
b) **Steady phase:** the wire is in shape and the endpoints of the wire are moving parallel to each other
c) **Exit phase:** the endpoints of the wire move off each other

Results from the simulation are node positions of the discretized wire, from which NURBS curves are created, force vectors (magnitude and direction), estimated speeds and, according to the curves, also estimated angles of the wire's deflection about the mounting points. As such, it was possible to compare the measured speeds and measured angles with the simulated speeds and angles (see Figure 8). To uncover the wire's shape from the cut surface, it was illuminated from a sloped angle, the distortion of the picture taken was reversed, and the simulated curves were overlaid for comparison (see Figure 9).

The force magnitude colouring is an efficient analysis tool for the resulting surface and clearly exemplifies what happens inside the foam block. In the entry state, the outer nodes of the wire have to move faster than in the centre, producing higher forces in exit zones of the foam, while in the centre they reach zero force. Whereas in the steady zone, the force distribution is almost equal along the engaged wire and in the exit zone the reversed picture to the entry zone is visible, where the force in the exit zones are low, since the speed is lower than in the centre. Low forces can also be recognized on the physical surface, e.g. in the detail picture of (Figure 10, c): Low or zero force means thermal cutting, more material melted, producing more rills.
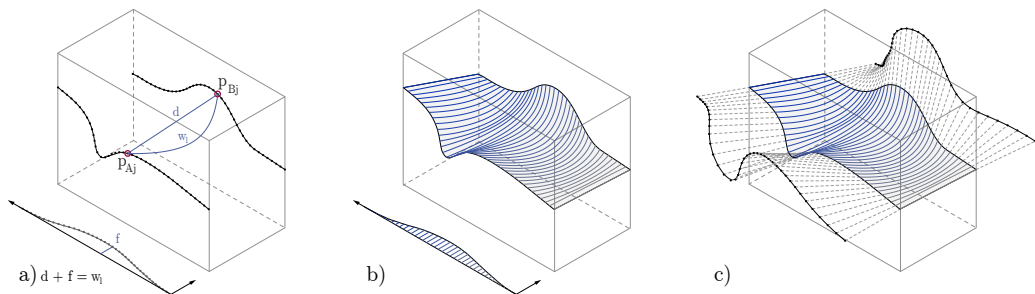
**Figure 11.** a) Edge curves, distribution of positions and wire length extension function, b) simulated curves and lofted surface thereof, c) extension of tangents to calculate path curves.
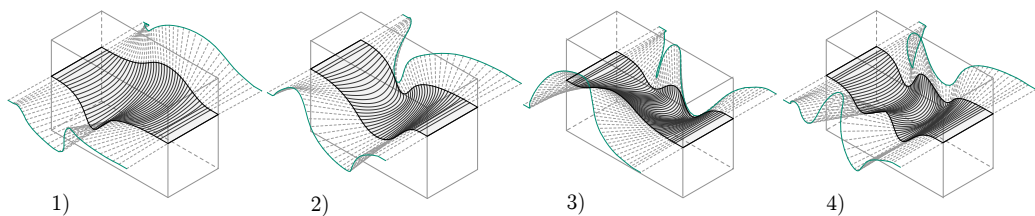


**Figure 12.** Surface design of different edge curve settings and robotic path curves.



0.0            1.0 N
per node
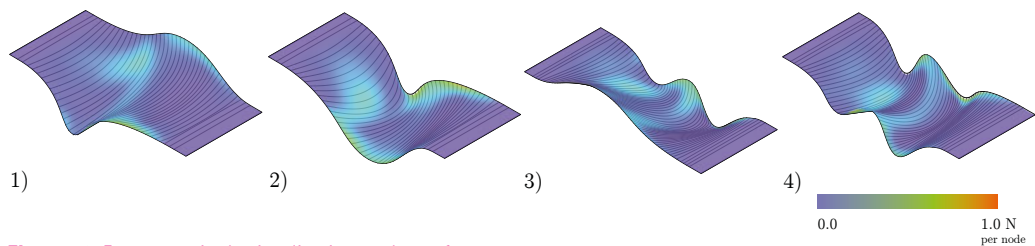
**Figure 13.** Force magnitude visualisation on the surfaces.
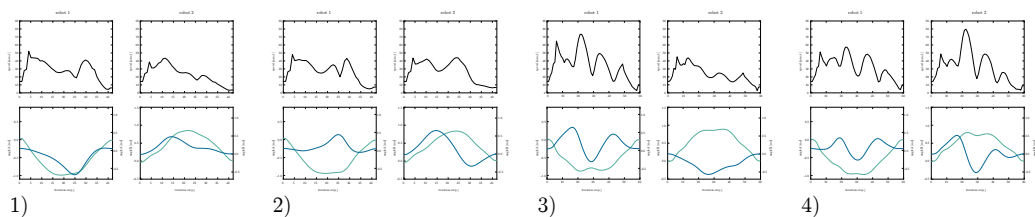


**Figure 14.** Estimated speed trajectories (black) and angles (blue, turquoise) for both robots.

The results from the comparison of simulated process variables and measured process data of 20 cutting tests (as in Fig. 8) was very successful. Although the shape of the wire in the foam could just be visually compared, the simulated angle α, as the deviation of the wire about the mounting point had a normalized root-mean-square deviation (NRMSD) of just 0.06. The estimated speed trajectory also produced very good results and a similar NRMSD of 0.08 in the cutting tests. Thus, these tests proved physical coherency for the force distribution equation (3).

## 2.6 Computational Design

The procedure creates a specific set of double-curved surfaces. In order to design within this constrained design space, it is necessary to integrate design and simulation. The inputs for the simulation framework, as described in Section 2.4, are the path curves, respectively the positions on the curves and a defined heat input. But there is a counter-intuitive relationship between designing these curves and the resulting surface. Therefore, the initial simulation setup was altered to facilitate designing these surfaces: Instead of designing path curves, the edge curves of the surface on the foam block are designed, which are discretized into a number of points. Further, a function is created, that defines the additional length of wire to the distance between the points $\mathbf{P}_{aj}$ and $\mathbf{P}_{bj}$ (see Fig. 11, a).

As such, the simulation calculates the forces for nodes that are constantly in the foam, and the fixed nodes are the defined positions on the edge curves. However, since the length from one iteration step to the other changes, the nodes and their forces have to be redistributed. After all node positions have been calculated and NURBS curves have been created, a surface is lofted through the curves (see Fig. 11, b). To generate the path curves, a minimum distance to the foam block is defined and the simulated curves are extended at both ends in such a way that all curves have the same length (see Fig. 11, c).

This simulation framework was empirically tested and validated in a 2-week design and building workshop with students, which focussed on the development of novel façade typologies using bespoke cut polystyrene blocks as moulds. It was applied to design and generate a parametric model for the aggregation of robotically cut prototypes (Rust et al. 2016).

## 3. Comparative Studies

The potential of the cutting technique can clearly be expressed in cutting freeform shapes. Therefore, four different sample surfaces were designed, simulated, fabricated, and 3D scanned to provide an additional quantitative geometrical comparison between simulated surface and physical artefact.
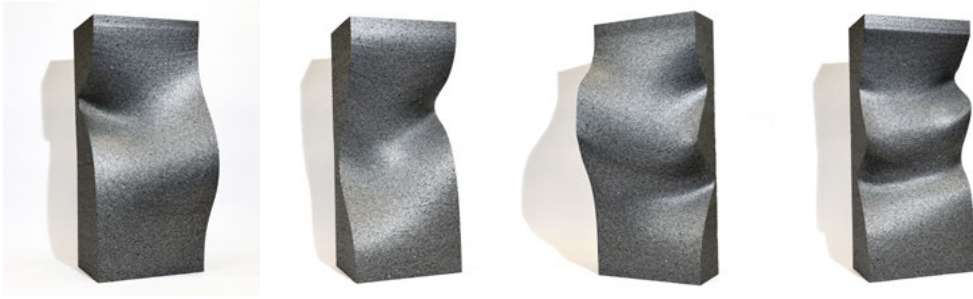
**Figure 15.** Fabricated objects 1) – 4), 400 x 900 mm (width x length).



1)          2)          3)          4)

900    400

0.0          42.0 mm
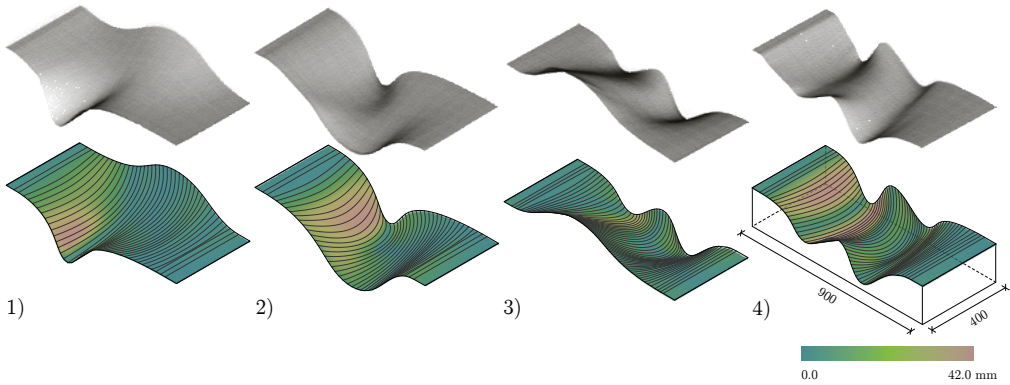
**Figure 16.** Simulated surfaces and point cloud data from the scanning process. The colours on the surface indicate the closest distance to the reconstructed mesh from the point cloud.



**Figure 17.** Surface detail.

For the design of these surfaces, the edge curves and the wire length extension function, as input for the simulation, were designed in such a way to provide variability between moving directions and varying distances (see Figure 12). The estimated speed trajectories for the robots (see Fig. 14), calculated in the simulation, served as input for the fabrication procedure, which uses a combined feedback-feedforward control to tare the speed according to the force measurement about this estimated speed trajectory. After the fabrication the surfaces (see Fig. 15) were scanned and per surface an average over 1 million scan points were registered. From these point clouds a surface was reconstructed (Poisson surface reconstruction) and the closest distance to the simulated surface was calculated (see Fig. 16).

# 4. Results and Reflection

The comparison between simulated and measured process data, such as angles and speed trajectories, was similarly successful (speed: 0.14, angle $\alpha$: 0.09, angle $\beta$: 0.06 NRMSD) as in Section 2.5. These results are clearly visible in the surface quality (see Fig. 17), proving a very good estimation of process variables and an efficient adaptive control. The maximum deviation in the geometrical comparison was 42 mm, which is still very high in terms of building tolerances. Areas of high deviation could be identified where the path curves show high curvature and at later moments in the procedure where deviations accumulate.

The simulation model is a simplification and an abstraction to the physical process. Factors that have not been integrated may have affected an accurate result. Amongst others, for example, the material force model (see Fig. 4) estimates the force under steady-state conditions, but actually the temperature of the wire is changing and constantly in transition states. These factors were assumed to have negligible influence, but small inaccuracies sum up along the process. Although the developed computational simulation framework cannot predict the resulting physical surface with absolute precision, the results are visually identical, and therefore it can be employed for digital design explorations that are coherent with their fabrication.

# 5. Conclusion and Outlook

A fabrication-informed design and simulation framework was presented and physically evaluated. It was demonstrated that the project's combined design and fabrication methodology allows for the efficient fabrication of unique and differentiated double-curved surface geometries, which brings forward a new geometric capability to existing hot-wire cutting techniques. The particular set

of geometries imposes a constrained design space, which allows to reveal the specific tectonics of the process.

A coherency between digital and physical model was established. A further topic of research is to investigate methods to make these two models complementary, which is already partly achieved by correcting the estimated speed trajectory according to the force measurements. Thus, strategies to overcome the physical tolerances could either be the improvement of the simulation by integrating more physical behaviour or the improvement of the adaptive fabrication control to not only regulate the speed, but also to dynamically adjust the path curves to fulfil the desired geometric target. This opens up the question to which extent a process needs to be modelled in advance to be able to efficiently control it, which means either adapting the digital model to the physical process control, vice versa, or even both. Material and process-informed design methods are inherently soft design methods. They do not necessarily describe exact geometry but the constraints and rules that create geometry. A subject of further research, which relates to the question above, will be the investigation of such a soft control in respect to architectural design.

## Endnotes

1 Steady-state conditions are reached at constant speed when the temperature and the cutting force level off.

2 In these tests the deflection, respectively the angle $\alpha$, was kept below 10 degrees to mainly induce perpendicular forces on the wire.

3 The described experiments were performed with the foam swissporLAMBDA Vento (density: 15 kg/m³) and the material for the hot-wire was Kanthal A with a diameter of 0.15 mm.

4 Since the measured data was oscillating in the beginning of the entry phase, the investigated phase was shifted thereafter. RMSD represents the sample standard deviation of the differences between the simulated values and measured values. NRMSD is the normalized RMSD according to the range of the measured data (= maximum – minimum value).

## Acknowledgements

## References

Ahn, D.G., S.H. Lee, and D.Y. Yang. 2003. "A Study on the Influence of the Sloped Cutting Angle on Kerfwidth and Part Quality in the Hotwire Cutting of EPS Foam for the VLM-s Rapid Prototyping Process." *International Journal of Machine Tools and Manufacture* 43, 14: 1447–464. doi: 10.1016/s0890-6955(03)00170-6

Bain, J. 2011. "Thermomechanical Hot Tool Cutting and Surface Quality in Robotic Foam Sculpting." PhD diss., University of Canterbury. Christchurch, New Zealand.

Broek, J. J., I. Horváth, B. De Smit, A. F. Lennings, Z. Rusák, and J. S.M. Vergeest. 2002. "Free-form Thick Layer Object Manufacturing Technology for Large-Sized Physical Models." *Automation in Construction* 11, 3: 335–47. doi: 10.1016/s0926-5805(00)00108-4

Brooks, H. 2009. "Plastic Foam Cutting Mechanics for Rapid Prototyping and Manufacturing Purposes." PhD diss., University of Canterbury. Christchurch, New Zealand.

GXN. 2016. 3xn – BladeRunner. Accessed May 27 http://gxn.3xn.com/#/projects/by-name/213-bladerunner

McGee, W., J. Feringa, and A. Søndergaard. 2012. "Processes for an Architecture of Volume." Edited by S. Brell-Çokcan and J. Braumann. In *Rob/Arch 2012: Robotic Fabrication in Architecture, Art and Design*, 62–71. Austria, Vienna: Springer.

Pigram, D., and W. McGee. 2011. "Formation Embedded Design: A Methodology for the Integration of Fabrication Constraints into Architectural Design." In *Integration through Computation: Proceedings of the 31st Annual Conference of the Association for Computer Aided Design in Architecture (ACADIA)*, 122–31. ACADIA. Calgary/Banff, Canada: The University of Calgary.

Rippmann, M., and P. Block. 2011. "Digital Stereotomy: Voussoir Geometry for Freeform Masonry-Like Vaults Informed by Structural and Fabrication Constraints." In *Proceedings of the IABSE-IASS Symposium 2011*, London, UK.

Rust, R., D. Jenny, F. Gramazio, and M. Kohler. 2016. "Spatial Wire Cutting – Cooperative Robotic Cutting of Non-ruled Surface Geometries for Bespoke Building Components." Edited by S.-F. Chien, S. Choo, M. A. Schnabel, W. Nakapan, M. J. Kim, and S. Roudavski. In *Living Systems and Micro-Utopias: Towards Continuous Designing, Proceedings of the 21st International Conference on Computer-Aided Architectural Design Research in Asia (CAADRIA 2016)*, 529–38. Australia, Melbourne, 30 March–2 April.

Schek, H.-J. 1974. "The Force Density Method for Form Finding and Computation of General Networks." *Computer Methods in Applied Mechanics and Engineering* 3, 1: 115–34. doi: 10.1016/0045-7825(74)90045-0

Schipper, H.R., S. Grünewald, P. Eigenraam, P. Raghunath, and M.A.D. Kok. 2014. "Optimization of the Flexible Mould Process for the Production of Double-Curved Concrete Elements." Edited by H. Justnes. *Program and Book of Abstracts for the 1st Concrete Innovation Conference (CIC), Oslo*, June 11–13, 1988.

Søndergaard, A., J. Feringa, T. Nørbjerg, K. Steenstrup, D. Brander, J. Graversen, S. Markvorsen, A. Bærentzen, K. Petkov, J. Hattel, K. Clausen, K. Jensen, L. Knudsen, and J. Kortbek. 2016. "Robotic Hot-Blade Cutting – An Industrial Approach to Cost-Effective Production of Double Curved Concrete Structures." Edited by D. Reinhardt, R. Saunders and J. Burry. In *Robotic Fabrication in Architecture, Art and Design 2016*, 151–63. Sydney: Springer International Publishing.

Veenendaal, D., and P. Block. 2012. "An Overview and Comparison of Structural Form Finding Methods for General Networks." *International Journal of Solids and Structures* 49, 26: 3741–753. doi: 10.1016/j.ijsolstr.2012.08.008

# Designing for Hot-Blade Cutting

## Geometric Approaches for High-Speed Manufacturing of Doubly-Curved Architectural Surfaces

David Brander, Andreas Bærentzen, Kenn Clausen, Ann-Sofie Fisker, Jens Gravesen, Morten N. Lund, Toke B. Nørbjerg, Kasper Steenstrup, and Asbjørn Søndergaard

D. Brander, A. Bærentzen, A. Fisker, J. Gravesen, T. B. Nørbjerg, K. Steenstrup
Technical University of Denmark, Denmark

dbra@dtu.dk
janba@dtu.dk
ansofi@dtu.dk
jgra@dtu.dk
tono@dtu.dk
khor@dtu.dk


K. Clausen
3XN Architects, Denmark

kec@3xn.dk


A. Søndergaard
Odico Formwork Robotics, Denmark

asbjorn.sondergaard@aarch.dk ✉

# Abstract

In this paper we present a novel method for the generation of doubly-curved, architectural design surfaces using swept Euler elastica and cubic splines. The method enables a direct design to production workflow with robotic hot-blade cutting, a novel robotic fabrication method under development by authors of the paper, which facilitates high-speed production of doubly-curved foam moulds. Complementary to design rationalisation, in which arbitrary surfaces are translated to hot-blade-cuttable geometries, the presented method enables architects and designers to design directly with the non-trivial constraints of blade-cutting in a bottom-up fashion, enabling an exploration of the unique architectural potential of this fabrication approach. The method is implemented as prototype design tools in MatLAB, C++, GhPython, and Python and demonstrated through cutting of expanded polystyrene foam design examples.

Keywords:
robotic fabrication, hot blade, digital design, EPS-moulds, cost-efficiency, concrete structures
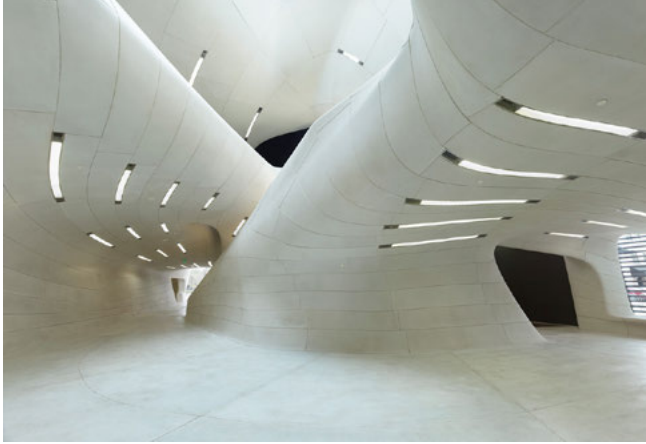
**Figure 1**. Louisiana State Museum and Sports Hall of Fame, courtesy Trahan Architects (top). Kagamigahara Crematorium, Courtesy Toyo Ito Architects (bottom).
Copyright, Figure 1a: Trahan Architects. Copyright, Figure 1b: Toyo Ito Architects.

# 1. Introduction

In contemporary architectural practice, a rising number of projects employ advanced building geometries, which departs from the orthogonality of mainstream construction, incorporating digital design tools and manufacturing for the realisation of expressive or dynamic design features (Pottman 2007). A group of projects within this category, such as Kagamigahara Crematorium (Toyo Ito Architects, 2006) and Waalbridge Extension (Zwart & Jansma, 2015), rely on the doubly-curved geometries, which may be constructed either via production of manual formwork, which relies on digitally produced guides to bend plate material in place over large radii. Alternatively, large-scale CNC-milling of either foam molds for concrete casting or direct milling of construction materials are employed enabling the realisation of shorter radii designs with more detail and surface controls. Such projects include, for example, Spencer Dock Bridge (Amanda Levete Architects, 2010), Louisiana State Museum and Sports Hall of Fame (Trahan Architects 2013), Museum Foundation Louis Vuitton by Gehry & Associates (Paris, 2014); the Nordpark cable railway by Zaha Hadid Architects (Nordpark 2007), the Metz Pompidou by Shigeru Ban (Metz 2010).

However, none of these general construction processes provides a cost-effective option for general construction, and projects of this type therefore require extraordinary budget frameworks for realisation: Manual onsite formwork processing in this category is a highly laborious and demanding process, with resulting difficulties in cost-engineering to follow. Large-scale CNC-milling on the other hand, provides cost transparency due to the digital nature of the process – although the mechanical principle of CNC-milling, which subtracts material through incremental removal, is inherently slow when applied to architectural scale production, and results in exuberant machining times and high costs.

Recent developments in architectural robotics and digital manufacturing have seen the emergence of a number of approaches to diversify the machining options available, with the purpose of realizing structures of more advanced geometries. This includes actuation of a flexible membrane as a casting surface (Jepsen et al. 2011; Hesse 2012); dynamic slip-casting for column elements (Lloret et al. 2014), as a variant of the additive manufacturing of concrete structures (Khosnevic 1998, Lim et al 2012); fabric formwork applied as an alternative technique for the casting of advanced designs (Veenendaal et. al 2011); spatial wire cutting (Rust et al. 2015) as well as large-scale robotic hot-wire cutting of EPS molds by authors of this paper. None of these approaches however, are capable of delivering combined (1) unconstrained degrees of freedom which enables general purpose realisation equivalent to that of CNC-milling; (2) machining efficiencies which significantly supersedes that of CNC-milling; (3) process predictability which ensures the delivery of a pre-controlled geometry.
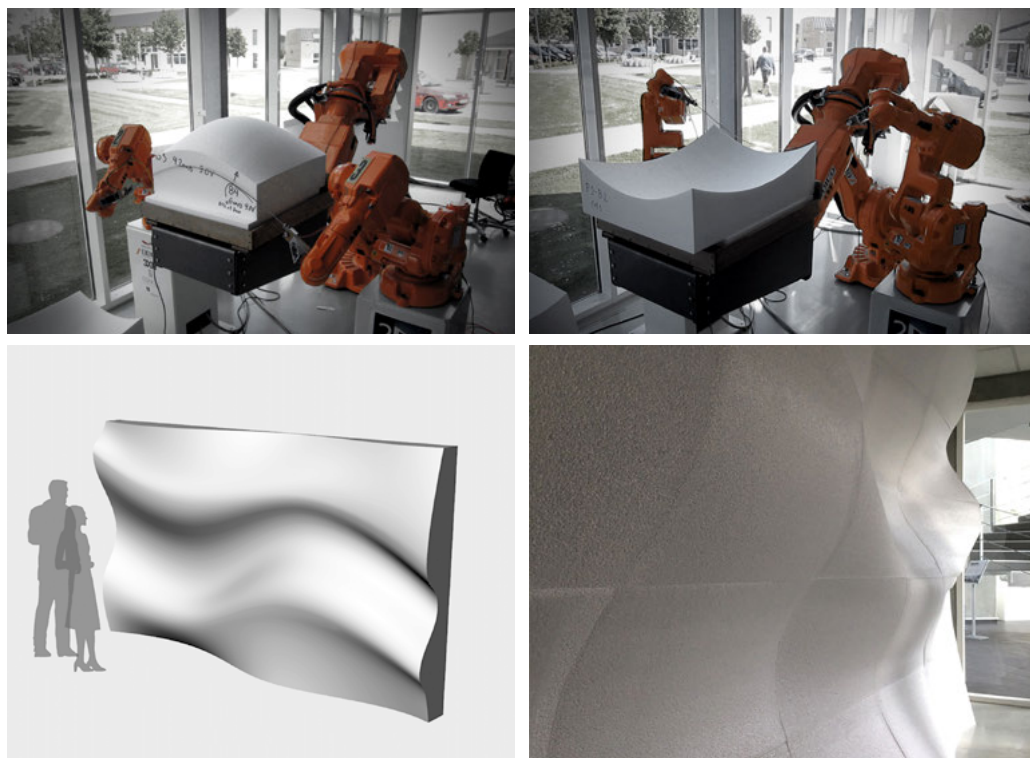
**Figure 2.** Bladecutting experiments in progress.
Top: 18-axis tri-robot hot-blade pilot-cell.
Below: concrete panel design and cut foam result.

# 2. Robotic Hot-Blade Cutting

In an effort to develop a new manufacturing process which would satisfy these criteria, the authors of this paper initiated in 2012 the Bladerunner project, which targets the cost-effective production of double-curved foam moulds. The technique developed in this effort – dubbed robotic hot-blade cutting – employs a multi-robotic process, in which an 18-axis cell consisting of 3 industrial manipulators translates a flexible, heated blade through expanded polystyrene blocks in a thermal cutting process, while controlling the distance and rotation of end-effectors to achieve variable cross-section curves along the trajectory of cutting sequences. Pilot production experiments currently under development seek to explore and demonstrate the applicability of this method for production of pre-fabricated concrete elements under a general CAM paradigm, in which arbitrary design input – understood here as geometry which is conceived without particular regard to the specific constraints of the process – is rationalised for hot-blade production using a set of algorithms developed within the project. These early developments point to the perspective of a highly time-efficient production method, up to 126 times faster than comparable CNC. However, complementary to a top-down process of rationalisation, a second trajectory is also possible, in which the geometric constraints of the hot-blade cutting is incorporated already in the design process, thus operating under a generative design paradigm. The work in the following chapters outlines tools and processes that can facilitate such an approach.

# 3. Designing with Elastica

An Euler elastica is the shape assumed by an elastic rod with planar constraints of position and tangents placed only on its endpoints. A planar curve is geometrically determined by an angle function $\theta(t)$, the angle between the tangent and some fixed direction. The angle function for the elastica are given by solutions of the normalised pendulum equation $\ddot{\theta} = -\sin\theta$, a nonlinear equation the solutions of which can fortunately be given explicitly in terms of elliptic functions.

Mathematically, the correct model for an elastica was given by James Bernoulli in 1691 (see Truesdel 1983). He approximated the solution for the case that the ends of the rod are perpendicular to each other, recognizing that non-standard functions were needed for an analytic expression. The problem was subsequently suggested to Leonhard Euler in 1743, who gave all possible shapes for the elastica in his famous treatise on the calculus of variations (Euler 1744).

People have in fact been designing with elastica for centuries, albeit in a physical rather than mathematical format. Prior to the introduction of computers for draughting in the shipping, aviation, and automobile industries, which began in the
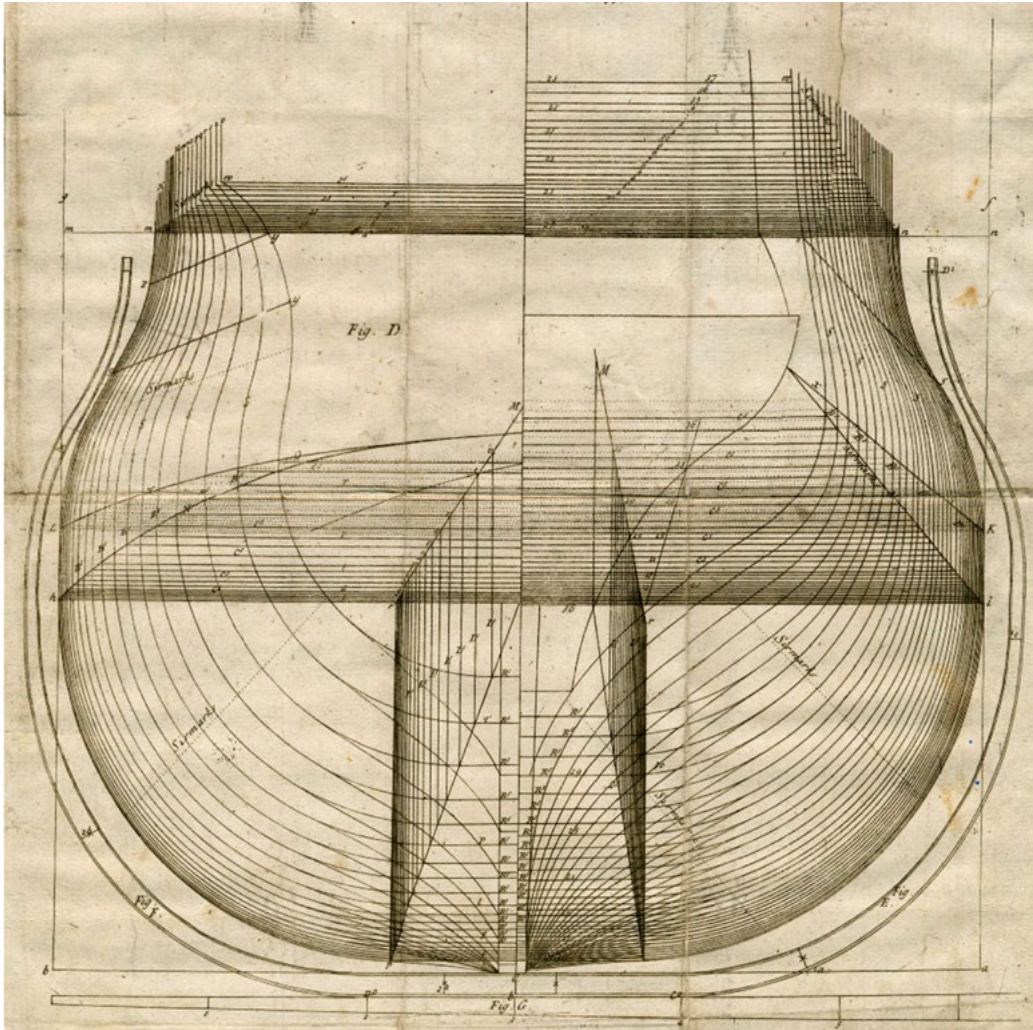
**Figure 3.** Use of physical splines for ship-hull manufacturing.
Copyright: William Sutherland, The Shipbuilders Assistant: or, Some Essays Towards Completing the Art of Marine Architecture (London, 1711).

1950s, the curves needed in the designs were created by tracing the shapes of thin wooden rods, known as splines, manipulated by the placement of so-called 'ducks' at various points to create a naturally smooth curve. This practice started in the ship-building industry, where the placement of the ducks simulates the placement of ribs in the hull of the ship; hence the curve drawn by following the spline is an accurate reflection of the natural shape adopted by the planks forming the ship's hull. The drawing took place at the loft of the shipyard, hence the word 'lofting', now used in the CAD industry. Going further back in time, splines were used for the storage and transmission of designs in ancient Rome, in the form of physical templates for the ribs of ships (see Farin 2002).

When computers became cheaper and more powerful, a desire for electronic storage and editing appeared. The word 'spline' now began to be used for piecewise polynomial or rational curves used in design. Paul de Casteljau at Citroën and Pierre Bézier at Renault used what are now known as Bézier curves to describe the designs. In the USA, Carl de Boor at GM used B-splines (basis splines) for the designs. In the aircraft industry, at Boeing, similar developments took place.

## 3.1 Design vs. Rationalisation for Hot-Blade Cutting

For a CAD surface to be produced using hot-blade cutting, it needs to be segmented into suitable pieces and each surface segment then swept by planar curves that are subsequently approximated by elastic curve segments. We described this rationalisation process in recent and forthcoming work.

An alternative to the rationalisation of a CAD design is to provide design tools that allow designers to create fabrication-ready surfaces. There are a number of reasons for doing this: Firstly, the rationalisation of an arbitrary design is non-trivial and in general can result in some regions of the surface needing to be produced by another method such as milling. Secondly, a design tool can give the designer control over the cast-lines between the segments, which will in many cases be visible from close range.

A third reason is the additional complexity arising when we consider a surface created by more than one cut to the same EPS block. For example, consider the surface shown on the left in Figure 4. By cutting the same EPS block twice, the second time with a 90 degree rotation, the surface on the left in Figure 5 is produced. Now the surface on right in Figure 4 approximates the first surface very well at the end-points of the cutting blade, but deviates slightly in the middle. Such an approximation is likely to arise in surface rationalisation, because we will usually need the patches to fit together with tangent continuity, which requires a little more freedom away from the patch edges. Doing the same two cuts with the new surface results in the surface on the right in Figure 5, and here we can see that the intersection curves are no longer the same as the design.
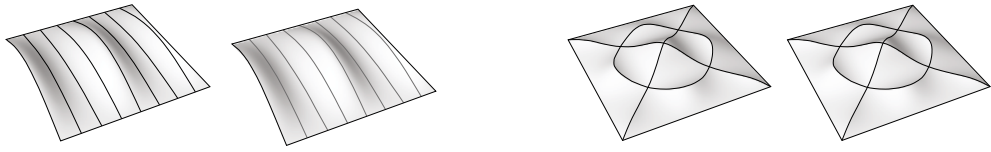
**Figure 4 & 5.** (right) Matlab generated surface. (left) rotated double cut of the same design.



001
Design domain and Hot-Blade-Cutting domain

002
Elastica Curves (Generating Cutting-Domain)
Data:
Start and End points
Start and End tangents
length

004
End Effector Movements.
Blade flexibility

003
Robot-Setup
From Design to Production
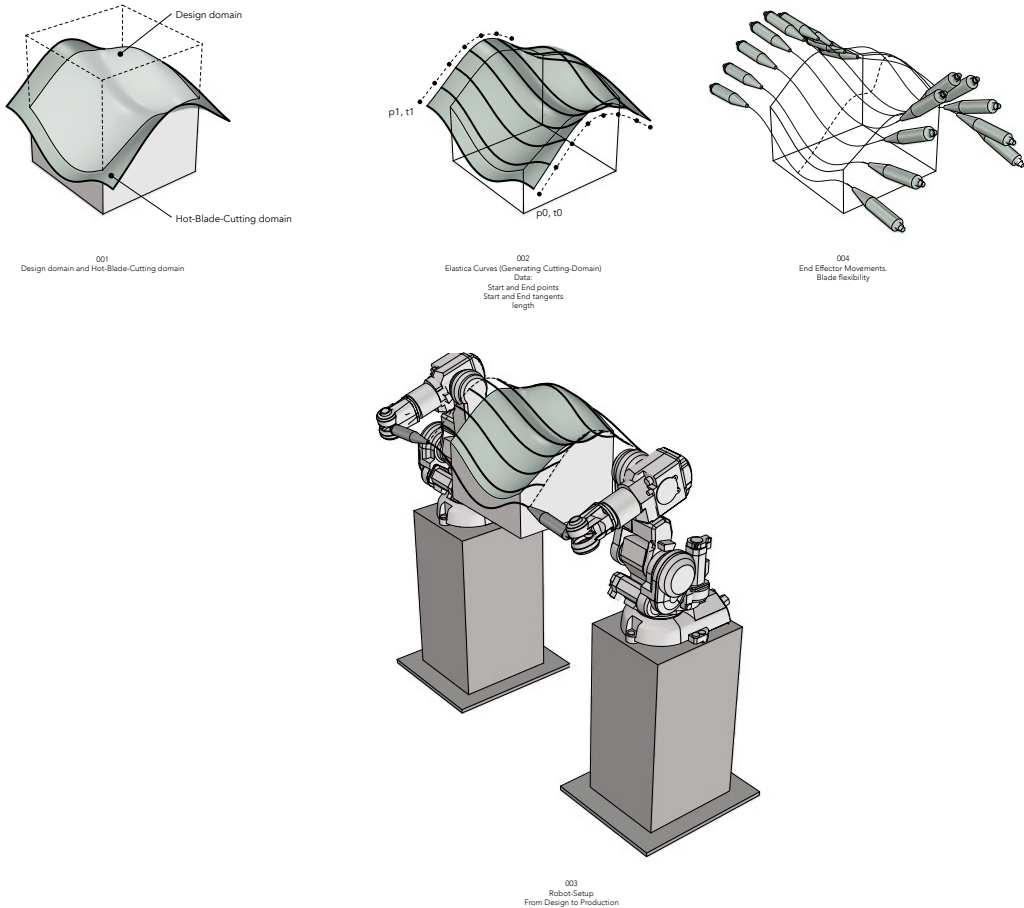
**Figure 6.** Configuration of input data.

Of course there are solutions for this kind of issue in the rationalisation approach, but this scenario illustrates the kind of advantages one has with a fabrication-ready design tool.

## 3.2 Single Block Designs

For the simple case of just one block, we design with curves of the desired length, i.e. the length of the cutting tool. During cutting the cutting tool is kept in a horizontal plane perpendicular to the cutting direction. The data needed for the robot movement are thus simply the positions of the ends of the blade and the angles of its ends relative to horizontal. The positions are given as $y, z\text{-}coordinates$ (the $x\text{-}coordinate$ describes how far the curve is in the cutting direction), see <span style="color:magenta">Figure 6</span>. In the design space (e.g. Rhino) we know the position of the design curves relative to the EPS block, so we can obtain the robot data directly from the design curves by computing the positions of the endpoints relative to the EPS block, and their angles relative to horizontal.

The plugin for the discrete elastica ensures that we get a representation of the final design in Rhino, before going to production. In the following, we describe the numerical algorithm used to find this solution given end points, tangents at the end point, and the length of the curve (see Bruckstein et al. 2001). This method does not find the elastica in terms of the elliptic functions; instead we return to the defining property of elastic curves, namely that they minimize $\int \kappa^2 ds$. In a discrete setting where we represent the curve using line segments of equal length, the analogous energy for the piecewise linear curve is:

$$F_a(\alpha) = \sum_{i=0}^{n-1} \alpha_i^2$$

where $\alpha^i$ is the turning angle at segment $i$ as illustrated in <span style="color:magenta">Figure 7</span>.

Thus, to find the discrete curve, we minimize $F_a$ subject to two constraints that both serve to enforce the boundary conditions. To ensure that the tangent at the last point has the correct direction, we require that

$$0 = F_t(\alpha) = \sum_{i=0}^{n-1} \alpha_i - (\alpha_n - \alpha_{-1})$$

where $\alpha_{-1}$ and $\alpha_n$ are the angles that correspond to the direction of the first and last line segment, respectively. Clearly, we also require that the curve ends at the right point. This is taken care of by the second energy

**Figure 7.** Turning angles.



**Figure 8.** Turning angles for a discrete elastic.
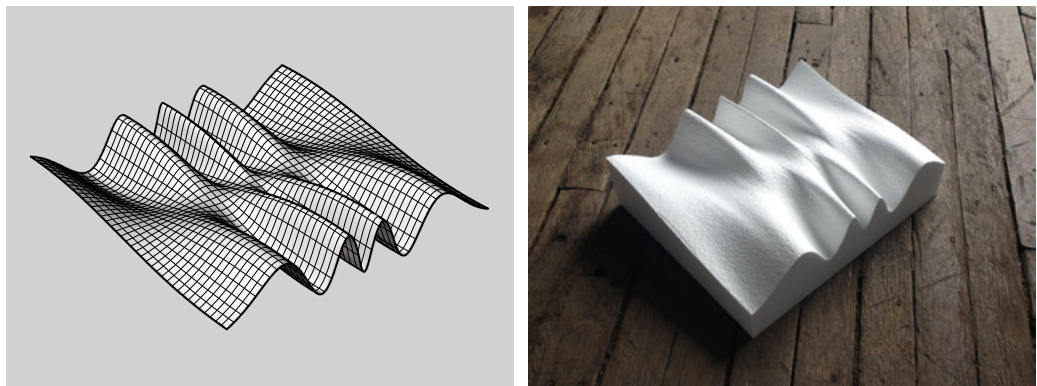


**Figure 9.** Examples of a generated and a cut surface.



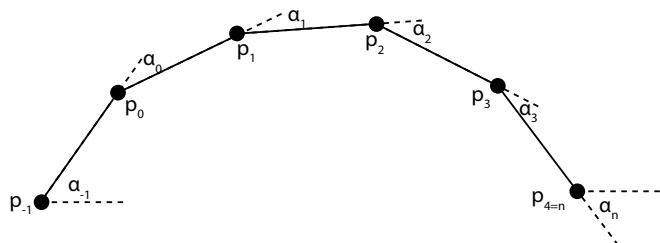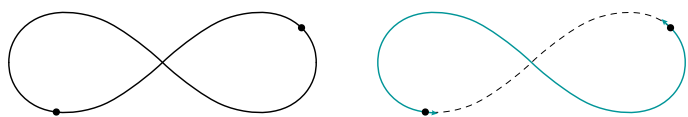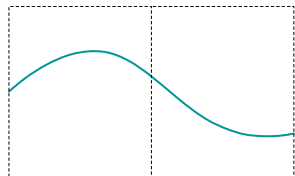**Figure 10.** In blue an exact elastic curve and in black a discrete approximation calculated from the boundary conditions shown in yellow.
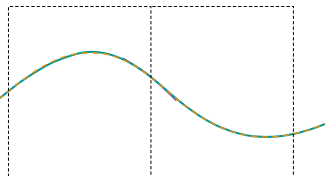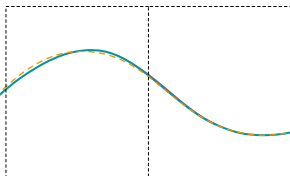
**Figure 11.** Transitions between elastica.

$$F_{p(\alpha)} = \left\| \sum_{j=-1}^{n-1} \left[ \cos\left(\sum_{k=-1}^{j} \alpha\_k\right), \sin\left(\sum_{k=-1}^{j} \alpha_k\right) \right]^{\mathrm{T}} - (p_n - p_{-1}) \right\|$$

We can construe the discrete elastic curve problem as an inverse kinematics problem. In this light, $F_p$ simply ensures that the end of the curve (end effector) coincides with $p_n$ – the end point of the elastic curve.

In practice, we find the elastic curves using a two-step procedure. In an outer loop, we reduce $F_a$ and in the inner loop, we solve for $F_p=0$ and $F_t=0$. $F_a$ and $F_p$ are minimised using gradient descent, whereas $F_t$ can be solved exactly in each step. The outer loop runs for a fixed number of iterations whereas the inner loop terminates when a desired tolerance has been reached. Figure 11 shows a test. The green figure-eight is an analytic elastic curve. The black curve on top is the discrete approximation computed from the boundary conditions shown in red.

## 3.3 Examples

The images below show a surface defined as the graph of a bivariate function

$$z = f(x,y) = k \cos\left(2\left(\frac{\pi}{2} - y\right)^4\right) \sin(x) \exp(-0.1x^2) \quad [x,y] \in \left[-\frac{\pi}{2}, \frac{\pi}{2}\right] \times (-0.75, 0.75)$$

z = f(x,y) =k(2(/2-y)4)(x)(-0.1 x2)   (x,y) (-/2, /2)(-0.75,0.75)

As the initial design created using a Python script in Rhino, as a rationalized surface and as a styrofoam block cut with the hot blade.

## 3.4 Design Using Multiple Blocks

For the more complex case with several blocks, a more advanced procedure is used to ensure a smooth transition from one block to the next. Consider a curve design that passed over two blocks (see Fig. 10, left). We need to produce this in two cuts – one per block – and we want the two block segments to match at the boundary after cutting.

If we run our plugin independently on the two parts of the curve, we would automatically obtain the smooth transition, but we would be unable to get the necessary data for the robots, since the curves (which are inside the blocks) are shorter than the cutting tool, and we have no quick way to extend these while preserving the elastic properties. If we simply extend the original curve and then use our plugin on parts with the desired length, we do not ensure smooth transition (see Fig. 10, right).
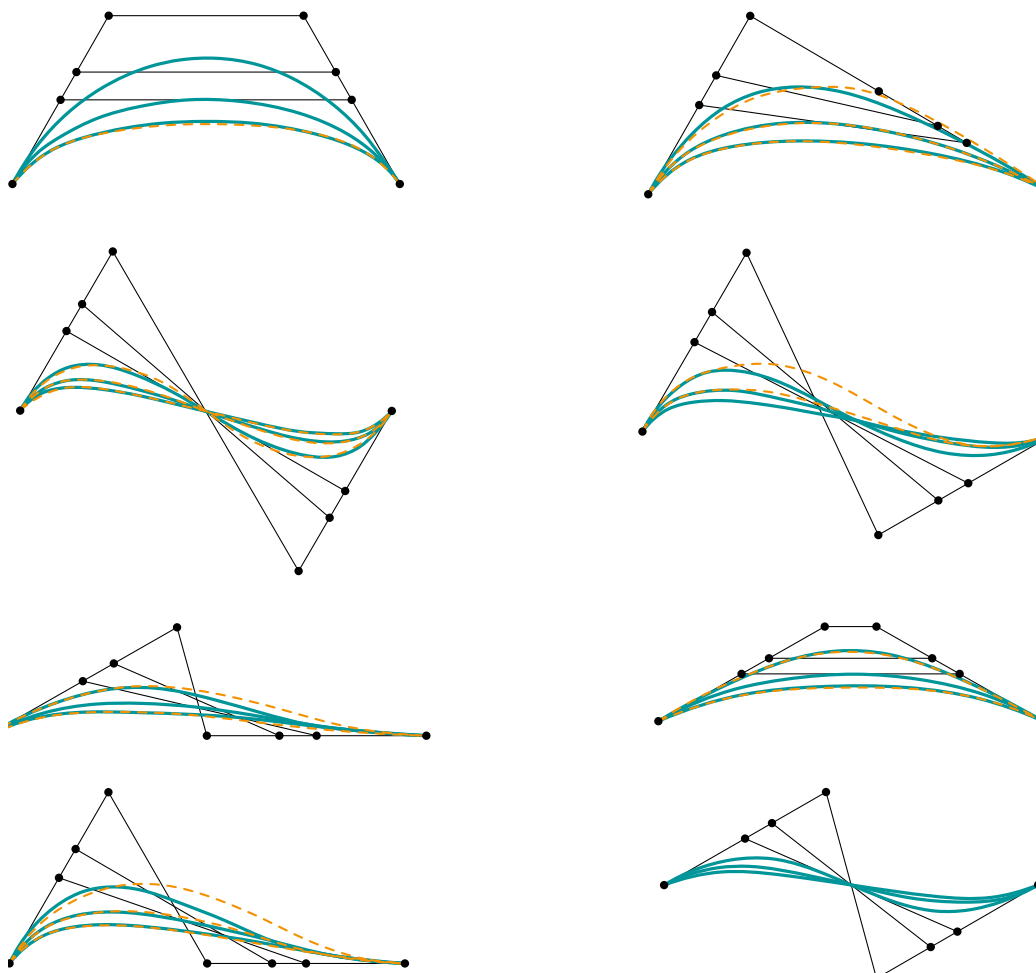
**Figure 12.** In blue Bézier curves, in black their control polygons, and in dashed red elastic curves with the same endpoints, end tangents, and lengths.
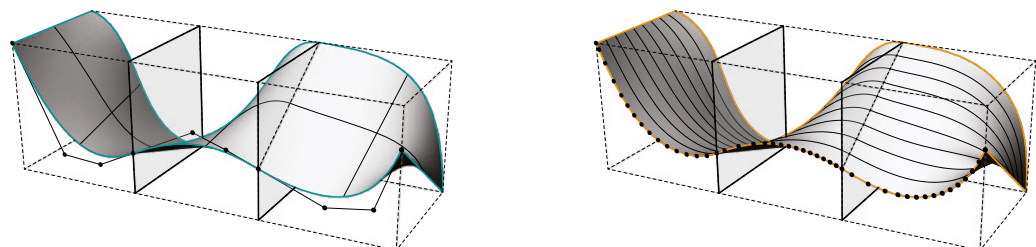


**Figure 13.** A Rhino design tool. Top: three blocks with two tangent continuous curves. Lower left: lofted Bézier curve surface. Lower right: rationalized elastica curve surface.

The solution is, instead of finding a discrete representation of the elastic curve that models the shape of the cutting tool, we find an analytic mathematical description of the elastic curve in terms of elliptic functions. This requires a more cumbersome optimisation in order to find the parameters that describe the rationalised curve. However, when these parameters are found, the entire (infinitely long) elastic curve that contains the required segment is known. It is then simple to extend the segment to an elastic segment of the length of the blade (see Fig. 11) and from this extract the position data for the robots.

# 4. An Alternative Approach:
## Bézier Curves as a Proxy for Elastic

Historically, the use of cubic splines as a design tool was often motivated by saying that they are a good substitute for real physical splines. This is justified by the fact that, if the speed of a curve is constant, then the square of the curvature is the same as the square of the second derivative, and if the latter is minimised we obtain exactly a cubic spline (see Yamaguchi 1988). Now a cubic curve does not have constant speed unless it is a straight line; but if the control polygon of a cubic Bézier curve is reasonably well behaved, then the curve is close to an elastica. See Figure 12, where 24 Bézier curves are plotted together with elastic curves having the same endpoints, end tangents, and length.

If the angles in the control polygon are not too acute, then there is very little difference between the Bézier curve and the elastic curve of the same length and end conditions.

Based on this observation, we implemented a design tool in Rhino™ where the surfaces and their rationalisation are very close. The idea is that we imagine space filled with EPS-blocks and define our surfaces such that the parameter curves have exactly one planar cubic piece in each block. As a simple example consider Figure 13, where we have three blocks and have defined three Bézier curves at both the front and the back of the blocks in such a way that they have common endpoints and tangents, i.e. they form two tangent continuous curves (see Fig.14). The surface is defined by a lofting process. We can of course have several layers of blocks, and we could also have included more curves in the middle of the blocks. The inputs are planar curves with exactly one cubic piece in each block, and the surface is defined by lofting.

One can achieve a curvature continuous construction by replacing the sequence of Bézier curves by a single planar cubic spline (with simple interior knots). Between the knots we have a cubic polynomial, so we if we require that the image of the knots is on the block boundaries then we obtain a single cubic polynomial piece in each block (Fig. 15).
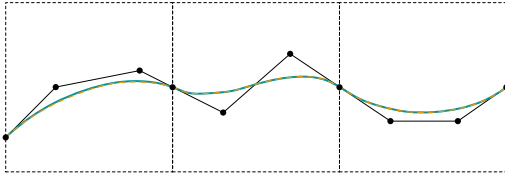
**Figure 14.** The tangent continuous construction. In each block we have a cubic Bézier curve and we require that adjacent curves have control polygons the first and last legs of which form a single line segment. In dashed red we have plotted the true elastica having the same length and boundary conditions as the Bézier curves.
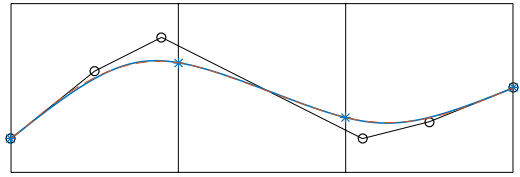
**Figure 15.** The curvature continuous construction. A single cubic spline curve where the images of the knots are on the block boundaries. In dashed red we have plotted the true elastic curves that have the same length and endpoints as the polynomial pieces. The tangents corresponding to the extreme points of the cubic curve are also prescribed.
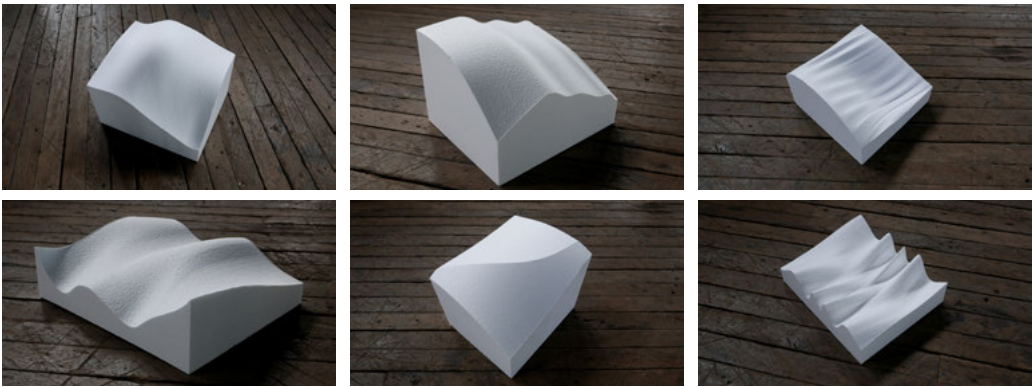


**Figure 16.** pre-test cuts from the workshop. From the left: while single, continuously swept surfaces are readily achievable through rationalization, the ripple and curvature effect on the right most samples requires careful alignment with the blade directions, and hence is difficult to obtain aside from directly controlling it in an elastica-swept surface.
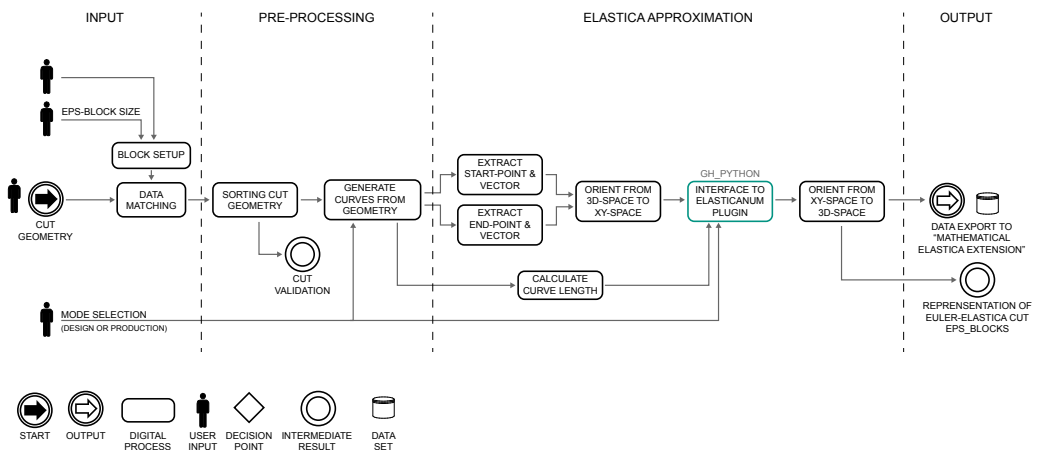


**Figure 17.** Data workflow chart.

If we replace the spline with an elastica having the same length in each block as the spline, passing through the images of the knots, and having the same tangent angles in the beginning and end as the spline curve, we obtain almost the same result. This corresponds exactly to the classical design using a physical spline and ducks. We just have to place the ducks at the images of the knots.

# 5. GH Workflow

For the development of design experiments as well as participatory workshop design sessions, a toolset is developed in McNeel Grasshopper, implementing the above approaches. The toolset is linking the full cycle of research, innovation, implementation and production, creating a framework for geometric operations consistent with the robotic setup. The overall logic of the workflow connects conventional digital modeling approaches with the robotic hot-blade process. This requires the identification and rationalisation of geometry types before rebuilding the geometry to the accuracy of the robot, EPS-segmentation and tolerances.

The Grasshopper-definition is developed with the purpose of designing with rationalisation through Euler elastica. It is a Real-Time process that allows for fast interpolations from design to production and ensures a smooth curve continuity transition from one block to the next. The tool is very flexible and allows for large variation of form typologies when designing with single or multiple cuts in the design explorations.

The setup is part of a larger digitised workflow; *'Interpolation of Geometry'*, *'Euler Elastica Approximation'*, *'Mathematical Elastica Extension'*, which is is a linear process that allows for feedback loops when data or geometry are outside of preset conditions and/or needs changes. The Grasshopper tool *'Design with Elastica'* inputs arbitrary surfaces and/or curves, converts them into planar elastica curves that describe the cut-direction and the movement of the robot-setup. The setup is structured in four overall processes; *'Global Parameters'*, *'Input'*, *'Process (Machine)'*, *'Output (Export)'*.

## 5.1 Global Parameters

The backbone of the setup is the global parameters that are changeable within the workflow environment. Its settings, syntax, and data are adapted in both the approximation plugin and the extension script while the workflow recalibrates when global settings are re-configured or need additional inputs. The global parameters allow you to toggle between *'Design'* or *'Production'* which are value bases and changes the resolution of the Elastica approximation.

One block is locally defined by its XYZ-values (dimensions), cut-plane (orientation) and its local location in the XYZ-world-coordinate system and global

001
EPS-Block (XYZ-dimensions)
Cut-Planes and Orientation

002
Multiple EPS-Block setup (Design Framework)

003
Data-Tree-Structure
Export data-system

004
Cut-Planes (Directions)
Orientation of Blocks
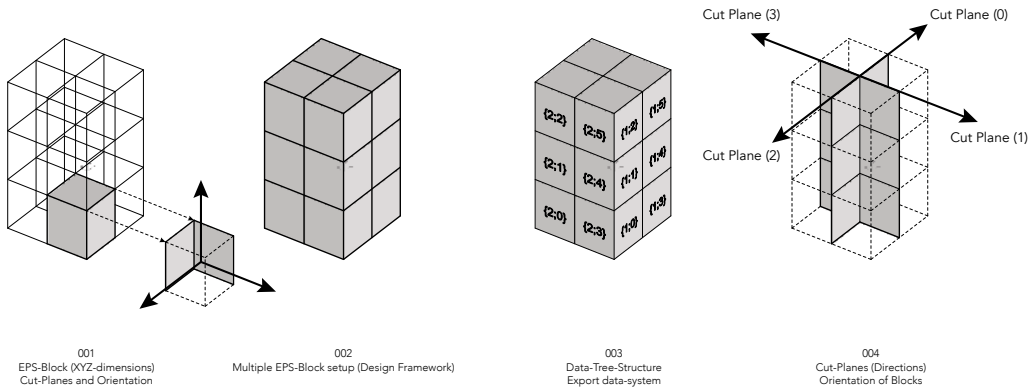
**Figure 18.** Work object configuration.



005
Design Framework

006
Geometry for cutting blocks (Design input)

007
Multiple Design "Inputs"
Data-Tree-Structure matches Design Framework

008
Brep represntation of 3Dimensional design
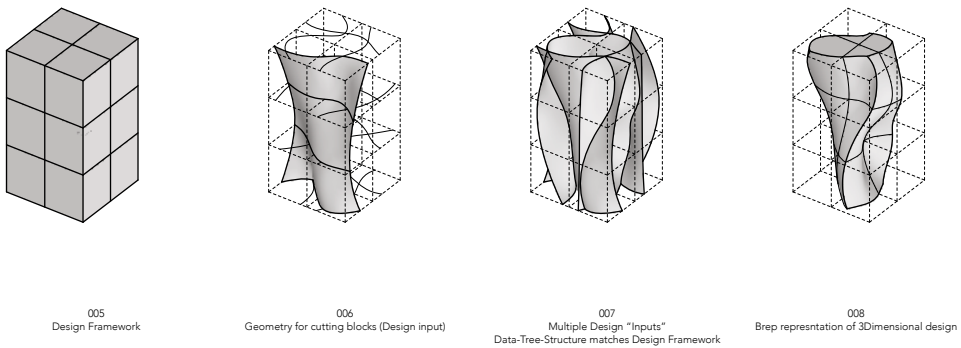
**Figure 19.** Generation of elastica design surfaces.



009
Sorting Cut-Geometries
Location and rotation of EPS-blocks in 3D space and block X and Y domain in the plane
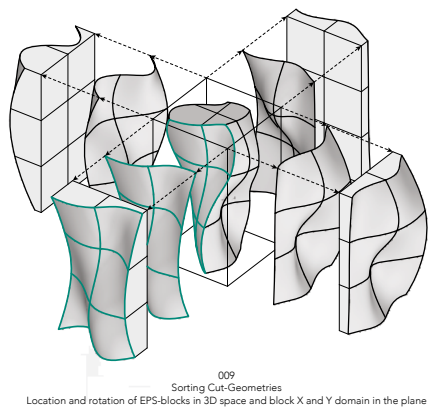
**Figure 20.** Configuration of demonstrator design.

location in a multiple-block-system. The block and blade length are interconnected to each other, if too short, the robot will move into the EPS-block, while too large the physical implications will increase and affect the precision.

## 5.2 Input

A multiple block configuration is developed as a framework for the generation of continuous surfaces over several blocks. The *'block setup'* is framed in a data-tree structure that matches and sorts the input designs for each block and subsequently for each face of the block (6 sides). The procedure generates a data-list for each block containing cut-plane, cut-direction, number of cuts, rotation, and location. By defining a clear data-flow from the input step you gain full control from design intent till export code and production.

## 5.3 Preprocessing of Geometry

The pre-processing step first matches each block (nested in a data-tree-structure representing the design framework and block number within the design framework) with cutting geometries related to the blocks design framework. The cutting geometry is then sorted according to cut priority, the primary cut being closest to the blocks base, and the remaining cuts are checked for collision with the primary cut and removed if no collision occurs. The final operation generates a number of planar curves for each cut by sampling the cut geometries in the X direction of the blocks. The sampling is extended beyond the block domain to allow the robots to have lead-in and lead-out of each block. The number of sampling points is triggered by the current mode selected (design or production).

## 5.4 Elastica Approximation

To approximate the Nurbs curves we made a Rhino plugin. The *ElasticaNum Plugin* operates on curve start-, end-points, tangent vectors at start- and end-points, and the desired length of the elastica curve. The *ElasticaNum Plugin* is interfaced through the Rhino command-line and python code using a custom data structure. The final operation in the *Elastica approximation* is reorienting the curves back into 3D space.

## 5.5 Output

The *'Design with Elastica'* tool generates two outputs that work parallel within the workflow and connect the designer with the final rationalisation output while still designing in the beginning of the process. Output one is data-driven

010
Surface representing the desired cut geometry

011
Curves for Elastica-Approximation
Select resolution (Design or Production)

012
Rotation of Element to ensure adaptability with
Elastic-Approximation and Data-Flow

From XYZ to XY orientation

013a
Planar curves for Elastica-Approximation

013b
Extract Start- and End-Point and tangent Vectors:
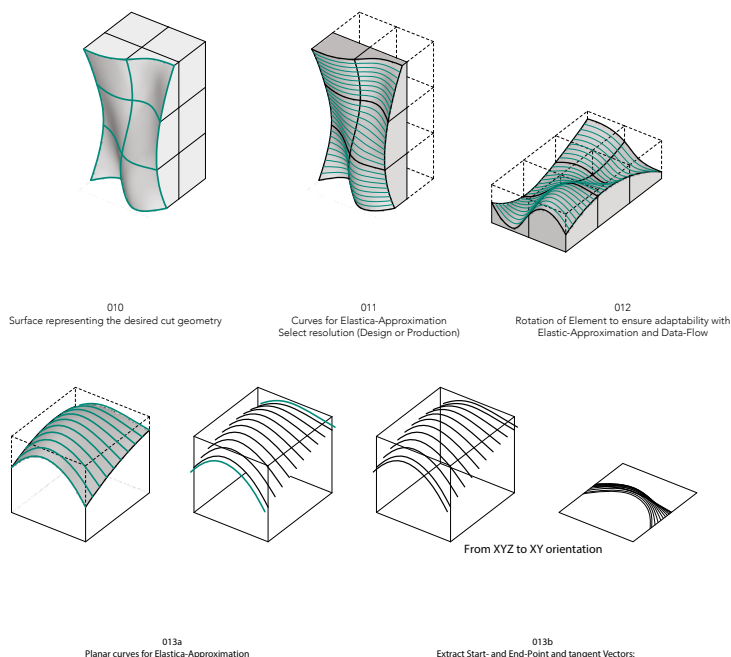
**Figure 21.** Description of production surfaces via swept elastica cross sections.



014a (Geometry)
Geometry representation with Elastica Curves

014b (Geometry)
Geometry representation from "Design input"

014c (Data)
Export Data phrased in a predefined setup for the
"Mathematical Elastica Extension" tool
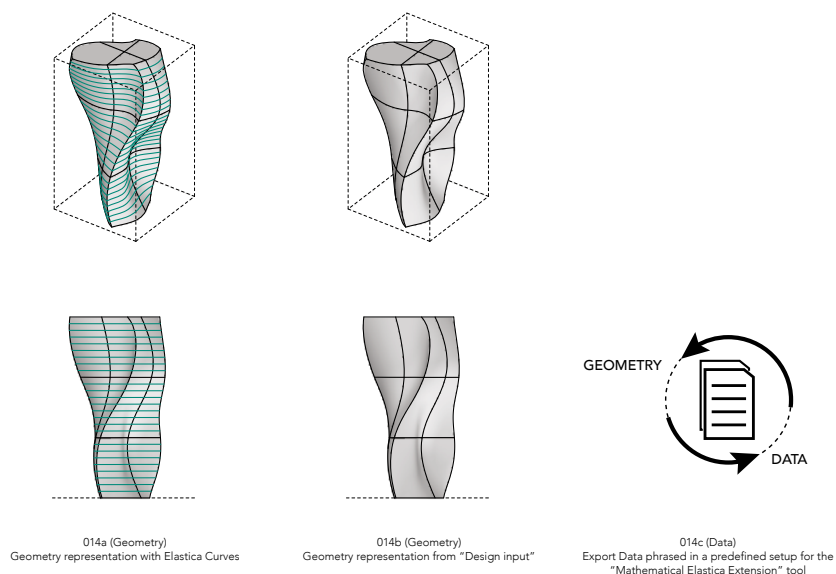
GEOMETRY

DATA

**Figure 22.** Global orientation of constitutive elastica cross-sections.

**324**

exports to the '*Mathematical Elastica Extension*', while output two is representing the desired geometry by Elastica Curves. By defining a data-structure a mutual adaptation of data import and export was defined from Input, Process and Output. The digitised workflow outputs data from the '*Design with Elastica*' tool to the '*Mathematical Elastica Extension*' and weave the tools together. To ensure a smooth transition from one block boundary to the next, the necessity for data conversion is important to perform a mathematical extension that preserve the elastica properties.

The setup allows for a real-time *design to fabrication workflow* and a comparison between the *Design-Geometry* and the *Elastica-Geometry* are processed. While the Design-Geometry is an arbitrary input, the '*Euler Elastica Approximation*' curves are lofted with the setting on *tight*, which uses square root of chord length parameterisation in the loft direction.

## 5.6 Design Workshop

The developed toolset was subsequently tested in a workshop setting with 16 participants in the format of the Superform: Robotic Hot-Blade Cutting workshop, held March 15–18 2016 in extension to the Robarch 2016 conference at Walsh Bay, Sydney. The workshop tasked participants with formal explorations of hot-blade design potentials, produced through a dual robot setup consisting of 2x ABB IRB 1600 manipulators in a MultiMove configuration. The explorations uncovered several benefits of working directly in a production-ready geometry: Firstly, the exploitation of double (or more) cuts, in which two intersecting surfaces creates a sharp crease is a feature difficult to approximate through rationalisation (Fig. 13, second row, middle). Secondly, the design of expressive ripple or wave-effects (Fig. 14) requires careful alignment with blade-cutting direction and curvature description to remain feasible. As such, they exemplify design potentials difficult to achieve through linear rationalisation.

# 6. Conclusion

A set of methods has been proposed for design generation of surfaces which incorporates the constraints of an elastic blade swept mechanically by two or more industrial robot manipulators. The methods are implemented as prototype design tools in C++, MatLAB, Python, and GhPython to enable interaction with non-specialist designers. The toolset was tested with 16 participants in the RobArch 2016 workshop: Superform – robotic hotblade cutting. The workshop design experiments revealed several design features that would be difficult to achieve in pure rationalisation workflows, as a result of the direct incorporation of constraints and live design feedback enabled by the framework.

**Figure 23.** Examples of the workshop participants design explorations. Design left: Jill Smith & Phil Dench. Design, right: Dharman Gersch.

# Acknowledgements

# References

Brander, D., J. Gravesen, and T. Nørbjerg. Approximation by planar elastic curves. arXiv:1509.00703[math.NA].

Bruckstein, A.M., R.J. Holt, and A.N. Netravali. 2001. "Discrete Elastica." *Applicable Analysis* 78, 3–4: 453–485.

Bruckstein, A.M., A.N. Netravali, and T.J. Richardson. 2001. "Epi-Convergence of Discrete Elastica." *Applicable Analysis* 79: 137 –171.

Euler, L. 1744. *Methodus inveniendi lineas curvas maximi minimive proprietate gaudentes; Additamentum I: de curvis elasticis.*

Farin, Gerald. 2002. "A History of Curves and Surfaces in CAGD." In *Handbook of Computer Aided Geometric Design*: 1–23.

Hesse, Petra, Ed. 2012. "TailorCrete, Flight Assembled Architecture." In A*rchitekturteilchen. Modulares Bauen im Digitalen Zeitalter,* 126–127, 164–165. Köln..

Jepsen, C., M. Kristensen, and P. Kirkegaard, P. 2011. "Dynamic Double Curvature Mould System." In *Computational Design Modeling: Proceedings of the Design Modeling Symposium, Berlin.* Ed. Christoph Gengnagel, Axel Kilian, Norbert Palz, and Fabian Scheurer. Springer, 291–300.

Lim, S., R.A. Buswell, T.T. Le, S.A. Austin, A.G.F. Gibb, and A. Thorpe. 2012. "Development in Construction-Scale Additive Manufacturing Processes." *Automation in Construction* 21, 1: 262–268.

Lloret Ena, Amir R. Shahab, Linus Mettler, Robert J. Flatt, Fabio Gramazio, Matthias Kohler and Silke Langenberg. 2014. "Complex Concrete Structures: Merging Existing Casting Techniques with Digital Fabrication." *Sciencedirect.com*

Pottman et al. 2007. *Architectural Geometry.* Bentley Institute Press.

Søndergaard, A., J. Feringa, T. Nørbjerg, K. Steenstrup, D. Brander, G. Gravesen, S. Markvorsen, A. Bærentzen, K. Petkov, J. Hattel, K. Clausen, K. Jensen, L. Knudsen, and J. Kortbek. 2016. "Robotic Hot-Blade Cutting." In *Robotic Fabrication in Architecture, Art and Design 2016, proceedings of RobArch 2016.*

Truesdell, C. 1983. "The Influence of Elasticity on Analysis: The Classic Heritage." *Bulletin of the American Mathematical Society* 9, 3: 293–310.

Veenendaal, D, M. West, and P. Block. 2011. "History and Overview of Fabric Formwork: Using Fabrics for Concrete Casting." S*tructural Concrete* 12, 3.

Yamaguchi, F. 1988. *Curves and Surfaces in Computer Aided Geometric Design.* Berlin Heidelberg: Springer-Verlag.

# Cuttable Ruled Surface Strips for Milling

Kasper H. Steenstrup, Toke B. Nørbjerg, Asbjørn Søndergaard, Andreas Bærentzen, and Jens Gravesen

K. H. Steenstrup, T. B. Nørbjerg, A. Bærentzen, J. Gravesen
Technical University of Denmark, Denmark
khor@dtu.dk ✉
tono@dtu.dk
janba@dtu.dk
jgra@dtu.dk

A. Søndergaard
Odico Formwork Robotics, Denmark
asbjorn.sondergaard@aarch.dk

# Abstract

This paper proposes a novel pre-processing method for industrial robotic CNC-milling. The method targets a hybrid machining process, in which the main bulk of material is removed through robotic hot or abrasive wire cutting, after which regular CNC-machining is employed for removal of the remaining material volume. Hereby, the roughing process is significantly sped up, reducing overall machining time. We compare our method to the convex hull and remove between 5% and 75% more material; on most models we obtain a 50% improvement. Our method ensures that no overcutting happens and that the result is cuttable by wire cutting.

Keywords:
piecewise-ruled surfaces, CAD, milling, free form architecture

# 1. Introduction

Recent years have seen a dramatic increase in the exploration of industrial robots for the purpose of architectural production (Kohler et al. 2014). While predominantly still a topic of research, some of these developments have recently matured into commercialisation, targeting the deployment of industrial robots for large-scale production (Søndergaard 2014). Within subtractive processes, the Denmark start-up Odico has been successfully bringing robotic hot-wire cutting to market.

CNC milling is a well-established process in industrial production of, particularly, foam-casting moulds, but also digitally produced stonework and bespoke timber manufacturing. While the process enables a very high degree of surface control and design freedom, it is also inherently limited by vast machining times for larger-scale applications that require the removal of large quantities of material, such as the machining of foam for ship hulls, wind turbine blades, or architectural structures. This adversity becomes significantly amplified when applied to hard materials, such as CNC milling of stone (Steinhagen et al. 2016). Wire cutting on the other hand, enables a dramatic reduction in production times, as volumetric artefacts can be produced in one or few swipes (McGee et al. 2013). However, here the precondition is that production geometries be described via ruled surfaces, which thus constrains the design freedom for the benefit of production efficiency. The wire-cutting methodology and its implications are extendable to abrasive wire sawing of, for instance, stoneworks, exemplified at the works of the Sagrada Familia cathedral (Burry 2016) as well as robotic abrasive wire sawing, as explored by Feringa and Søndergaard (2015).

The development of robotic hot-blade cutting (Søndergaard et al. 2016) provides a cost-effective and time-efficient manufacturing process for general curved foam geometries. However, this process is also constrained by the detail level achievable, and is inadequate for small surface details, while well suited for large-scale variations often deployed at industrial and architectural scale. In addition, so far, blade cutting is not applicable to non-foam materials.

The three processes milling, wire cutting, and blade cutting (see Figure 1) can be viewed as complementary, each covering a particular spectrum within subtractive machining. As such, an extension of the processes is to consider new ways for hybridisation.

One such possibility is the combination of milling and wire cutting, in which the latter is applied for removal of the initial volume which would otherwise be machined in CNC roughing processes. While CNC roughing is generally fast compared to CNC finishing, when assuming high target surface smoothness, the roughing process can represent substantial machining times when applied to voluminous subtractions. Additionally, certain architectural applications may enable the omission of surface finishing machining in favour of leaving roughed

**Figure 1.** Different cutting techniques: CNC-milling, hot wire cutting, and hot-blade cutting.
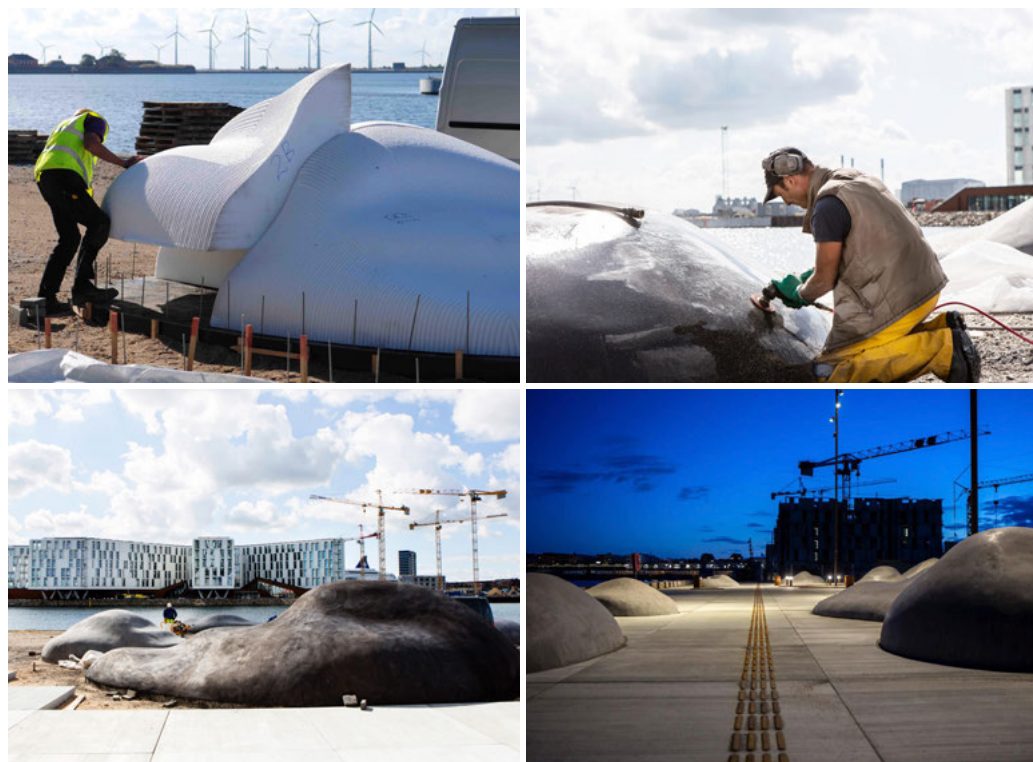


**Figure 2.** Creating an artificial concrete landscape in the urban harbour front of Copenhagen.
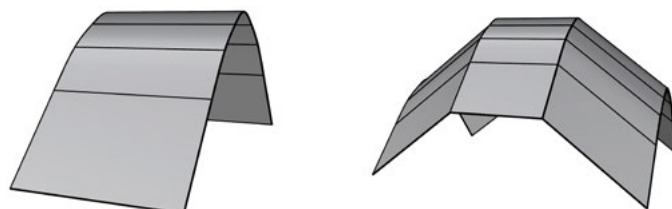


**Figure 3.** To the left a ruled surface defined by two curves. To the right a piecewise ruled surface defined by several curves.

surfaces for practical or aesthetic purposes. Two projects exemplifying this within the BladeRunner production portfolio, can be found in Feringa (2014). There, 212 m³ of expanded polystyrene foam were milled to achieve a three-dimensional guideline shape to be coated in-situ with 70–100 mm of polished spent, giving the final shape, see Figure 2. Only roughing processes were applied as for ensuring enhanced binding between the foam core and concrete shell, roughing representing approximately 92 direct machining hours.

Given the amount of machining hours spent on roughing, a hybrid approach would, for this case, have caused a reduction in processing time of between 69–72 %. In light of this finding, work was initiated to find a rationalisation algorithm that would cover any arbitrary three-dimensional shape with a set of non-convex ruled surfaces, such as to allow for a maximum of initial volume to be removed through wire cutting, while within the same robot cell shifting subsequently to aCNC tooling setup.

For this, we propose a method that combines fast wire cutting and precise CNC milling removing as much material as possible using a wire before the precise shape is milled. As we allow multiple cuts, the wire-cut surface is a piecewise ruled surface, and it can be considered as an approximation or *rationalisation* of the required surface. We can formulate the problem as follows: Given a surface, rationalise it with a piecewise ruled surface such that the rationalisation never intersects the original surface (no overcutting), and such that it can be manufactured by wire cutting. The latter implies that not only the rulings, but also the extension of the rulings never intersect the surface.

Usually a mould is composed by several blocks, and we do not consider the whole surface, but only a segment contained in a single block. As the final shape is milled, we do not need to consider any continuity conditions between the piecewise ruled rationalisations of the different segments.

A ruled surface is given by moving a line segment through space while it changes length and orientation. As a line segment is determined by its endpoints, the two curves described by the end points determine the surface uniquely, see Figure 3. A particular class of piecewise ruled surfaces is obtained by letting a polygon move through space while it changes shape, see Figure 3.

If the polygon at all times is on the outside of the original surface and furthermore is planar and convex, then we are certain that the extensions of the rulings never intersect the original surface, see Figure 4.

Piecewise ruled surfaces are well known in architecture: Flöry et al. (2012) describes a method to rationalise free form architecture, focussing on the smoothnessbetween rulings, and Flöry and Pottmann (2010) find areas where a good rationalisation can be done. Both papers use the asymptotic directions as guides for the rulings. In Wang and Elber (2014) large GPU-powered dynamic programming is used to minimise the distance between the original surface and the rationalisation.
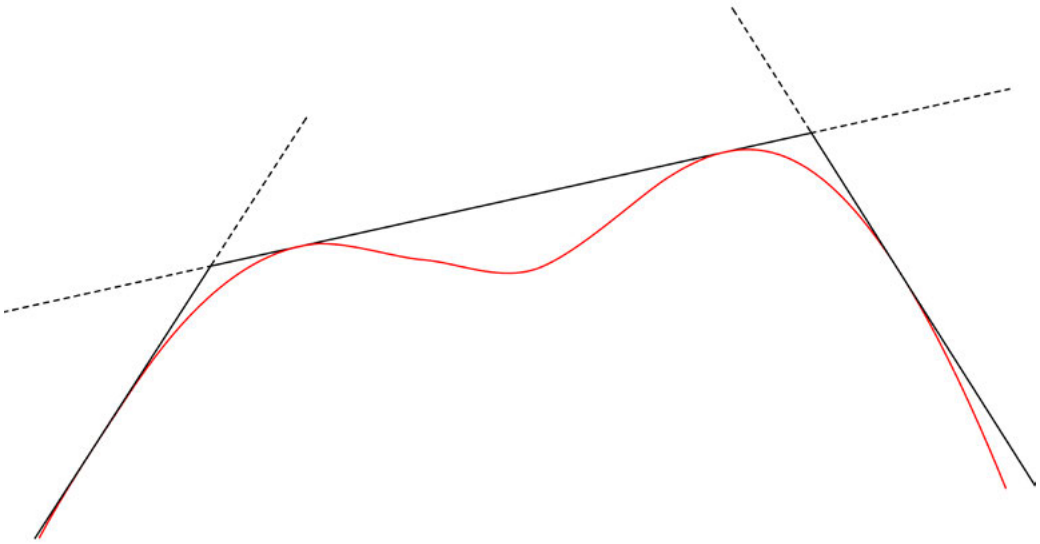
**Figure 4.** Planar intersection of the surface and the piecewise ruled rationalisation. If the rulings turn less than 180 ° then the convexity of the rulings guarantees that the extended rulings never intersect the surface.

The paper by Elber and Fish (1997) constructs a piecewise ruled approximation of a free-form surface using Bézier surfaces and a subdivision scheme to get the approximation within tolerated error, but global accessibility is not guaranteed. In Elber (1995), a free-form surface is approximated by piecewise developable surfaces, by using a simple developable primitive and a subdivision technique.

Milling with a cylindrical tool produces piecewise ruled surfaces, so they have also been studied in this context. To improve the tool path Chiou (2004) shows that the error in the rough milling can be lowered by separating the ruled surface into multiple strips. The paper Chu and Chen (2006) constructs a piecewise ruled/developable rationalisation where a subdivision scheme is used if a tolerance is not met. Tool interference is taken care of, but only to the extent of a fixed axis flank milling tool. In Cao and Dong (2015) the one-sided Hausdorff distance is used to minimise the overcutting.

The paper by Julius et al. (2005) uses an iterative algorithm to automatically obtainrationalisation consisting of developable patches. In Jiang et al. (2014) user input is used to create a Lobel mesh which has the utility to create developable patches.

Our method distinguishes itself by accepting a general free-form surface as input and guaranteeing the wire does not cut into the model (overcutting), and that the rationalisation is cuttable by a wire.

## 2. Method

Given a surface $\mathbf{f}$, we want to minimise the distance between it and a piecewise ruled spline surface $\mathbf{s}$ of the form:

(1)

$$\mathbf{s}(u,v) = \sum_{i=1}^{k} \sum_{j=1}^{h} \beta_i^p(u)\,\beta_j^1(v)\,\mathbf{c}_{i,j},$$

where $\mathbf{c} = \{\mathbf{c}_{i,j}\}$ is the set of control points and $\beta_i^p$ is a B-spline of degree $p$. Observe that $\mathbf{s}$ is a piecewise ruled surface since the basis function $\beta_i^1$ has degree 1. We now discretise the piecewise ruled surface s by choosing a uniform grid $(\mathbf{u}_i, \mathbf{v}_j)$, $i = 1, \ldots, N$, $j = 1, \ldots, M$, in the parameter plane and we discretise the original surface $\mathbf{f}$ by sampling points $\mathbf{f}_{i,j}$, $i = 1, \ldots, N$, $j = 1, \ldots, M$, on the surface. How the sampling is done is explained in Section 2.3 below. We furthermore make sure that the $v$-knots are among the parameter values $v_j$, i.e. we have indices $1 = j_1 < j_2 < \cdots < j_h = M$ such that the knot vector in the v direction is $v_{j1}, \ldots, v_{jh}$. We measure the distance between $\mathbf{f}$ and $\mathbf{s}$ by the discrete square distance

(2)

$$\sum_{i=1}^{N} \sum_{j=1}^{M} \|\mathbf{f}_{i,j} - \mathbf{s}(u_i, v_j)\|^2,$$

## 2.1 Constraints

We need several constraints in the optimisation, which we now describe one by one.

### One-sided approximation

To avoid overcutting, the rulings should all be on the outside of the model. So if $\mathbf{N}_{i,j}$ is the *outward* normal of $\mathbf{f}$ at the point $\mathbf{f}_{i,j}$ then we require that

(3)

$$\big(\mathbf{s}(u_i, v_i) - \mathbf{f}_{i,j}\big) \cdot \mathbf{N}_{i,j} \geq \varepsilon_1, \quad \text{for all } i, j.$$

If $\varepsilon_1 = 0$, overcutting is only prevented at the sample points $\mathbf{f}_{i,j}$, but with $\varepsilon_1 > 0$ and sufficiently dense sampling overcutting is prevented. Alternatively, if $\mathbf{f}$ is a spline surface the local (or strong) convex hull property (Piegl and Tiller 2012, P3.22, P4.25) can be used to guarantee that no overcutting happens.

## Planarity and convexity of rulings

The piecewise ruled surface $\mathbf{s}$ given by (1) can be considered as swept by a moving polygon, and we require that the polygon $\mathbf{s}(u_i, v_{j1}), \ldots, \mathbf{s}(u_i, v_{jh})$ is planar for all $i$. We now let $\mathbf{r}_{i,\ell} = \mathbf{s}(u_i, v_{j\ell+1}) - \mathbf{s}(u_i, v_{j\ell})$, i.e., it is one of the rulings. The difference in the other direction is denoted $\mathbf{w}_{i,\ell} = \mathbf{s}(u_{i+1}, v_{j\ell}) - \mathbf{s}(u_i, v_{j\ell})$. The cross product $\mathbf{n}_{i,\ell} = \mathbf{r}_{i,\ell} \times \mathbf{r}_{i,\ell+1}$ is a normal to the plane spanned by $\mathbf{r}_{i,\ell}$ and $\mathbf{r}_{i,\ell+1}$, see Figure 5. If all the normals $\mathbf{n}_{i,\ell}$, $\ell = 1, \ldots, h-1$ are parallel then the polygon is planar, and if they all point in the same direction then the polygon is convex or concave. We can formulate this condition as

(4)
$$\mathbf{n}_{i,\ell_1} \cdot \mathbf{n}_{i,\ell_2} = \left\| \mathbf{n}_{i,\ell_1} \right\| \left\| \mathbf{n}_{i,\ell_2} \right\|, \quad \ell_1, \ell_2 = 1, \ldots, h-1.$$

or to simplify it a bit

(5)
$$\mathbf{n}_{i,1} \cdot \mathbf{n}_{i,\ell} = \left\| \mathbf{n}_{i,1} \right\| \left\| \mathbf{n}_{i,\ell} \right\|, \quad \ell = 2, \ldots, h-1.$$

To rule out the possibility of a concave polygon, we require that the normal $\mathbf{n}_{i,\ell}$ points in roughly the same direction as $\mathbf{w}_{i,\ell}$. This can be formulated as

(6)
$$\mathbf{w}_{i,\ell} \cdot \mathbf{n}_{\ell,1} \geq \frac{1}{2} \left\| \mathbf{w}_{i,\ell} \right\| \left\| \mathbf{n}_{i,\ell} \right\|. \quad \ell = 1, \ldots, h-1.$$

or as (5) secures that $\mathbf{n}_{i,\ell}$ points in the same direction as $\mathbf{n}_{i,1}$ we can simplify it to

(7)
$$\mathbf{w}_{i,1} \cdot \mathbf{n}_{i,1} \geq \frac{1}{2} \left\| \mathbf{w}_{i,1} \right\| \left\| \mathbf{n}_{i,1} \right\|.$$
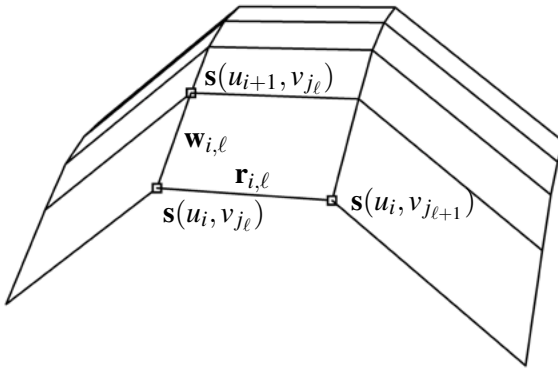
**Figure 5.** The discretised piecewise ruled surface from Figure 3. The points $\mathbf{s}(u_i, v_{j1}), \ldots, \mathbf{s}(u_i, v_{jh})$ form an instance of the moving polygon. The vector $\mathbf{r}_{i,\ell}$ is a leg in the polygon, i.e. a ruling. The vectors $\mathbf{w}_{i,1}, \ldots, \mathbf{w}_{i,h}$ goes from one polygon of rulings to the next.

### Boundary

Ultimately the rationalised surface $\mathbf{s}$ is supposed to be cut from a block, which we assume has the form of a box with axis parallel sides, given by $a_1 \leq x \leq a_2$, $b_1 \leq y \leq b_2$, and $d_1 \leq z \leq d_2$. So no part of the boundary is allowed to be strictly inside the block. We furthermore assume that we will be cutting roughly in the $x$ direction. So we require that

(8) (9)

$$
c^x_{1,j} \leq a_1, \qquad c^x_{k,j} \geq a_2, \qquad j = 1, \ldots, h,
$$
$$
c^y_{i,1} \leq b_1, \qquad c^y_{i,h} \geq b_2, \qquad i = 1, \ldots, k.
$$

where the superscript denotes the different components of the control points. In our implementation we start and end with the polygon on the block boundary, so in (8) the inequalities are replaced with equalities.

### Limit the directions of the rulings

The rulings are not allowed to turn more than 180°, and this can be secured if the y-coordinate is a strictly increasing function. This is the case if it holds for the control polygon, and we formulate this as

(10)

$$
c^y_{i+1,j} - c^y_{i,j} \geq \varepsilon_2,
$$

where $\varepsilon_2$ is some small positive number. Strictly speaking we only need the difference to be non-negative, but using an $\varepsilon_2 > 0$ also prevents any ruling from collapsing into a single point.

## 2.2 The Optimisation Problem

We are now able to formulate the optimisation problem

(11)

$$\underset{\mathbf{c}}{\text{minimize}} \sum_{i=1}^{N} \sum_{j=1}^{M} \|\mathbf{f}_{i,j} - \mathbf{s}(u_i, v_j)\|^2,$$

such that

$$c_{1,j}^x = a_1, \quad c_{k,j}^x = a_2, \quad j = 1,\ldots,h,$$

$$c_{i,1}^y \leq b_1, \quad c_{i,h}^y \geq b_2, \quad i = 1,\ldots,k,$$

$$(\mathbf{s}(u_i, v_j) - \mathbf{f}_{i,j}) \cdot \mathbf{N}_{i,j} \geq \varepsilon_1, \quad i = 1,\ldots,k, \quad j = 1,\ldots,h,$$

$$\mathbf{n}_{i,1} \cdot \mathbf{n}_{i,\ell} = \|\mathbf{n}_{i,1}\| \|\mathbf{n}_{i,\ell}\|, \quad \ell = 2,\ldots,h-1,$$

$$\mathbf{w}_{i,1} \cdot \mathbf{n}_{i,1} \geq \frac{1}{2} \|\mathbf{w}_{i,1}\| \|\mathbf{n}_{i,1}\|,$$

$$c_{i+1,j}^y - c_{i,j}^y \geq \varepsilon_2,$$

where

(12) (13) (14)

$$\mathbf{n}_{i,\ell} = \mathbf{r}_{i,\ell} \times \mathbf{r}_{i,\ell+1}, \qquad \ell = 1,\ldots,h-2,$$

$$\mathbf{r}_{i,\ell} = \mathbf{s}(u_i, v_{j_{\ell+1}}) - \mathbf{s}(u_i, v_{j_\ell}), \qquad \ell = 1,\ldots,h-1,$$

$$\mathbf{w}_{i,\ell} = \mathbf{s}(u_{i+1}, v_{j_\ell}) - \mathbf{s}(u_i, v_{j_\ell}), \qquad i = 1,\ldots,k-1.$$

We solve this optimisation problem using the interior point method as in Wächter and Biegler (2005).
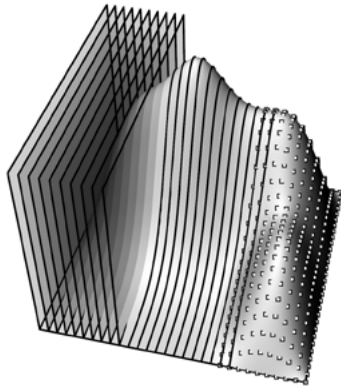
**Figure 6.** Illustration of the 3 steps that initialise the model into 900 points. Firstly: 10 of the 30 planes are shown, Secondly: 12 of the 30 intersection curves. Finally: 300 of the 900 discretisation points are shown.



Model 1    Model 2    Model 3

Model 4    Model 5
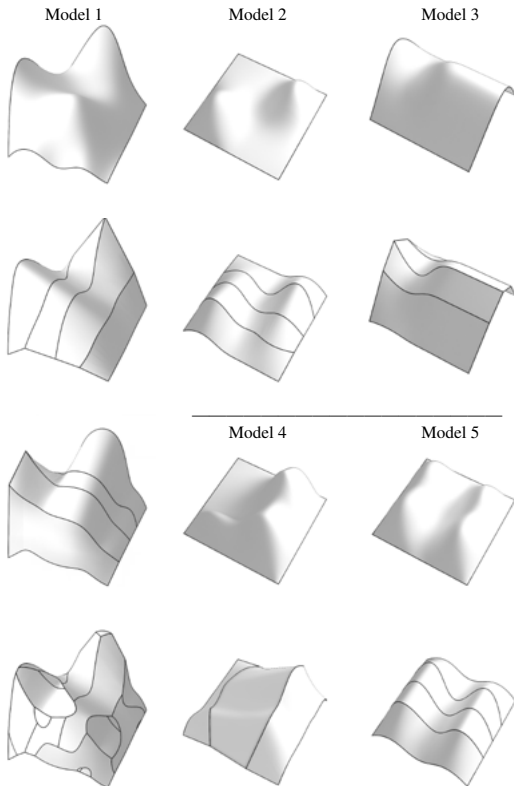
**Figure 7.** Five models rationalised by piece-wise ruled surfaces. Model one has been cut four times in one directions and four times in roughly the orthogonal direction. The four other models have been cut four times in one direction.

## 2.3 Initialisation

All that is left is to explain how we choose the sampling points $\mathbf{f}_{i,j}$ and initialise the optimisation.

First the coordinate system is chosen such that outward normal of the surface is roughly in the $z$-direction, i.e., upward. Then a cutting direction is chosen, and we create $N$ parallel planes orthogonal to the cutting direction and uniformly spaced. For each plane the intersection curve with the original surface $\mathbf{f}$ is found. Finally, each intersection curve is discretised into $M$ points. This is illustrated in Figure 6, where $N$ and $M$ both are 30.

# 3. Results

We have run our algorithm on the five models shown in Figure 7. Model 1 was cut in two different directions, four times in each directions, while Models 2–5 was cut four times in one direction. For comparison we have also calculated the convex hull, and the bounding box.

We have only considered cutting directions parallel to the sides of the blocks, but if we consider Model 2, diagonal cuts would be favourable. The depression in Model 4 poses a problem for wire cutting: No matter what direction a line at the depression has, it will cut into one of the 'mountains' at the edge. On the other hand, we see that even though we sweep the surface using a polygon with four legs the optimisation has put two of the legs on the same line. So we have in effect a polygon with only three legs and consequently only need three cuts to produce the rationalisation.

If we imagine the surface sitting inside the block and remove the outer part we are left with a solid object, see Figure 8. We have calculated the volume of that object in each case. The results are summarised in Table 1. We normalise all volumes with respect to the volume of the bounding box, i.e. we use Vol / Vol(BB). We show the volume of the model, but in the three other cases we show the volume that needs to be milled away, i.e., (Vol − Vol(Model))/ Vol(BB).

So for Model 1 we can see that the volume of the model is 49% of the bounding box volume, that our method has left 4% of the bounding box volume for milling, that the convex hull leaves 15% of the bounding box volume for milling, and that the bounding box (doing nothing) leaves 51% of the volume for milling. We also show how much more volume our method removes compared to the convex hull and the bounding box, respectively. That is we show (Vol − Vol(our))/ (Vol − Vol(Model)). For Model 1 this is 76% and 93%, respectively.
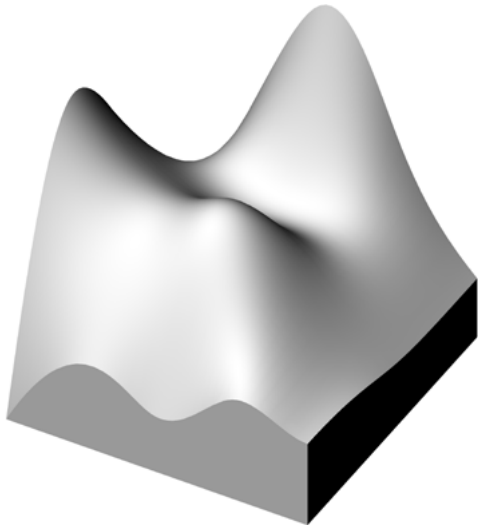
**Figure 8.** Model 1 with volume shown, the volume is created by intersection the bounding box with the surface.

| No. | Model | Ruled | Convex Hull | | Bounding Box | |
|-----|-------|-------|-------------|-----|--------------|-----|
| 1 | 0.4924 | 0.0374 | 0.1541 | 76% | 0.5076 | 93% |
| 2 | 0.2435 | 0.1520 | 0.3380 | 55% | 0.7565 | 80% |
| 3 | 0.5914 | 0.0201 | 0.0520 | 61% | 0.4086 | 95% |
| 4 | 0.3058 | 0.1379 | 0.1453 | 5% | 0.6942 | 80% |
| 5 | 0.4533 | 0.0798 | 0.2294 | 65% | 0.5467 | 85% |

Table 1. In the second column the volume of the model is shown. In columns 3,4, and 6 we show how much volume there is left for milling using our method, the convex hull, and the bounding box, respectively. All volumes are normalised with respect to the volume of the bounding box. In columns 5 and 7 we show how much more volume our method removes compared to the convex hull and the bounding box, respectively.

# 4. Conclusion and Future Work

We have described a novel method that finds a one-sided approximation of a free-form surface by a piecewise ruled surface. The method guarantees that no extension of the rulings cut through the original surface. This allows us to use the method and wire cutting as a pre-processing step for milling.

Compared to using the convex hull as a pre-processing step, we obtain an improvement from 5 to 75% and typically around 50%.

For simplicity we have limited ourselves to cuts parallel to the coordinate planes, but relaxing this conditions and allowing any cutting direction will improve the result.

We represent the piecewise ruled surface as a tensor product spline surface of degree one in one direction and the planarity condition of the rulings restrict the flexibility of the piecewise ruled surface. To overcome this, we can choose another representation where we explicitly move a planar polygon through space.

In this work we have assumed that the full architectural model has been segmented into block-sized portions, and we have only considered the piece inside a single block. An interesting possibility is to use our method to aid in the segmentation. If we allow for non-convex polygons in the optimisation, we will obtain a better fit and we could use the concave vertices to guide the segmentation.

Our system can be incorporated into a design workflow in one of several ways. The most obvious use is to simply run the method in order to reduce the amount of milling that is required to produce a given piece. However, the designer might also wish to create surfaces whose final design will change little when our method runs. In this case, we simply ensure that a design which is close to cuttable will, in fact, be so. Finally, our method seems to provides a distinct design expression with a plurality of intersection curves if cuts are made from several directions. We surmise that this could be used explicitly in some cases.

## Acknowledgements

## References

Burry, M. 2016. "Robots at the Sagrada Familia Basilica: A Brief History of Robotised Stone-Cutting." In *Robotic Fabrication in Architecture, Art and Design 2016.* Springer, 2–15.

Cao, L., and L. Dong. 2015. "Positioning Method of a Cylindrical Cutter for Ruled Surface Machining Based on Minimizing One-Sided Hausdorff Distance." *Chinese Journal of Aeronautics 28*, 5: 1564–1573.

Chiou, J. C. 2004. "Accurate Tool Position for Five-Axis Ruled Surface Machining by Swept Envelope Approach." *Computer-Aided Design 36*, 10: 967–974.

Chu, C.-H., and J.-T. Chen. 2006. "Tool Path Planning for Five-Axis Flank Milling with Developable Surface Approximation." *The International Journal of Advanced Manufacturing Technology 29*, 7-8: 707–713.

Elber, G., and R. Fish. 1997. "5-Axis Freeform Surface Milling Using Piecewise Ruled Surface Approximation." *Journal of Manufacturing Science and Engineering 119*, 3: 383–387.

Elber, G. 1995. "Model Fabrication Using Surface Layout Projection." *Computer-Aided Design 27*, 4: 283–291.

Feringa, J., and A. Søndergaard. 2015. "Fabricating architectural volume." *Fabricate*.

Feringa, J. 2014. "Entrepreneurship in Architectural Robotics: The Simultaneity of Craft, Economics and Design." *Architectural Design 84*, 3: 60–65.

Flöry, S., and H. Pottmann. 2010. "Ruled Surfaces for Rationalization and Design in Architecture. *LIFE in: formation. On Responsive Information and Variations in Architecture*, 103–109.

Flöry, S., Y. Nagai, F. Isvoranu, H. Pottmann, and J. Wallner. 2012. "Ruled Free Forms." In *Advances in Architectural Geometry*.

Jiang, C., C. Tang, M. Tomicic, J. Wallner, and H. Pottmann, H. 2014. "Interactive Modeling of Architectural Freeform Structures – Combining Geometry with Fabrication and Statics." In *Advances in Architectural Geometry*, ed. by P. Block, J. Knippers, and W. Wang. Springer.

Julius, D., V. Kraevoy, and A. Sheffer. 2005. "D-Charts: Quasi-Developable Mesh Segmentation." *Computer Graphics Forum*.

Kohler, F., M. Gramazio, and J. Willmann. 2014. "The robotic touch: How robots change architecture."

Mcgee, W., J. Feringa, and A. Søndergaard. 2013. *Rob – Arch 2012: Robotic Fabrication in Architecture, Art, and Design*. Vienna: Springer, ch. Processes for an Architecture of Volume, 62–71.

Piegl, L., and W. Tiller. 2012. *The NURBS book.* Springer Science & Business Media.

Søndergaard, A., J. Feringa, T. Nørbjerg, K. Steenstrup, D. Brander, J. Graversen, S. Markvorsen, A. Bærentzen, K. Petkov, J. Hattel, J., et al. 2016. "Robotic Hot-Blade Cutting." In *Robotic Fabrication in Architecture, Art and Design 2016*. Springer, 150–164.

Søndergaard, A. 2014. "Odico Formwork Robotics." *Architectural Design 84*, 3: 66–67.

Steinhagen, G., J. Braumann, J. Brüninghaus, M. Neuhaus, S. Brell-Cokcan, and B. Kuhlenkötter, B. 2016. „Path Planning for Robotic Artistic Stone Surface Production." In *Robotic Fabrication in Architecture, Art and Design 2016*. Springer, 122–135.

Wächter, A., and T. L. Biegler. 2005. "On the Implementation of an Interior-Point Filter Line-Search Algorithm for Large-Scale Nonlinear Programming." *Mathematical Programming 106*, 1: 25–57.

Wang, C. C., and G. Elber. 2014. "Multi-Dimensional Dynamic Programming in Ruled Surface Fitting." *Computer-Aided Design 51*: 39–49.

# The Armadillo Vault

## Computational Design and Digital Fabrication of a Freeform Stone Shell

Matthias Rippmann, Tom Van Mele, Mariana Popescu,
Edyta Augustynowicz, Tomás Méndez Echenagucia,
Cristián Calvo Barentin, Ursula Frick, and Philippe Block

M. Rippmann, T. Van Mele, M. Popescu, E. Augustynowicz, T. Echenagucia, C. Barentin, U. Frick, P. Block
Block Research Group, ETH Zurich, Switzerland

rippmann@arch.ethz.ch ✉
van.mele@arch.ethz.ch ✉
mariana.popescu@arch.ethz.ch
augustynowicz@arch.ethz.ch
mendez@arch.ethz.ch
calvo@arch.ethz.ch
frick@arch.ethz.ch
block@arch.ethz.ch ✉

# Abstract

This paper describes the development of an unreinforced, freeform vault consisting of 399 discrete limestone blocks with thicknesses ranging from 5 to 12 cm. The vault covers an area of 75 m$^2$ and spans more than 15 m in pure compression, without mortar between the blocks. We discuss how the design of the vault and its individual pieces was entirely driven by constraints related to the fabrication process and to the architectural and structural requirements and timeline of the project. Furthermore, we describe the form-finding process of the shell's funicular geometry, the discretisation of the thrust surface, the computational modelling and optimisation of the block geometry, and the machining process. Finally, we discuss some of the strategies that were developed for dealing with tolerances during fabrication and construction.

# 1. Introduction

Throughout history, master builders have discovered expressive forms through the constraints of economy, efficiency, and elegance, – not in spite of them. There is much to learn from their architectural and structural principles, their design and analysis methods, and their construction logics (Block et al. 2014). This paper revisits some of this lost knowledge in the context of computational geometry and digital fabrication applied to the design and construction of the presented project. It reports on the structural design, architectural geometry, and digital fabrication of an unreinforced, cut-stone vault constructed in the Corderie dell'Arsenale of the Architecture Biennale in Venice. The exhibition piece advocates for the logic of compression-only forms, not only because of their uniquely expressive aesthetics, but also because of their potential to achieve efficiency and stability through geometry.

The doubly curved vault consists of 399 individual limestone blocks or *voussoirs* assembled without mortar or other structural connections. The vault stands in compression and spans a total area of 75 m$^2$ with three linear supports along its boundary and one support in the middle. The structure has a more or less triangular shape in plan. The unsupported edges between the boundary supports create openings that provide access to the space underneath. Located in the centre of the exhibition space, the stone vault spans the central walkway between the two entrances and wraps around the existing columns. The columns penetrate the structure's surface through two large openings, one of which is partially supported (Fig. 1).

The voussoir geometry results from the discretisation pattern or *tessellation*, which determines the stone rows or *courses*. The exterior surface of the vault is called *extrados* and the interior *intrados*. The supports are made of 20 mm thick steel plates, and designed to distribute the weight of the vault as evenly as possible over the floor of the protected building. A system of steel ties connects the steel supports and absorbs the vault's horizontal thrust. The ties are necessary because no mechanical connections to the floor were allowed. Leaving them exposed shows and emphasises that the stone surface structure would not be stable without them.

Figure 2 depicts the design, analysis, and fabrication process of the cut-stone vault. The flowchart also serves as an overview of the structure of this paper. Section 2 summarises the structural and fabrication requirements for this project and defines the specific objectives of the presented applied research. Section 3 discusses the structural design of the vault, focussing on the initial form-finding process and the computational methods developed to generate the tessellation and voussoir geometry. Information about the structural analysis of the vault is not included in this paper. Section 4 describes the fabrication and assembly process. It focuses on the CAM process and the machining strategy before touching upon aspects related to the falsework and the actual assembly. Finally, Section 5 presents the completed structure and provides some concluding remarks.
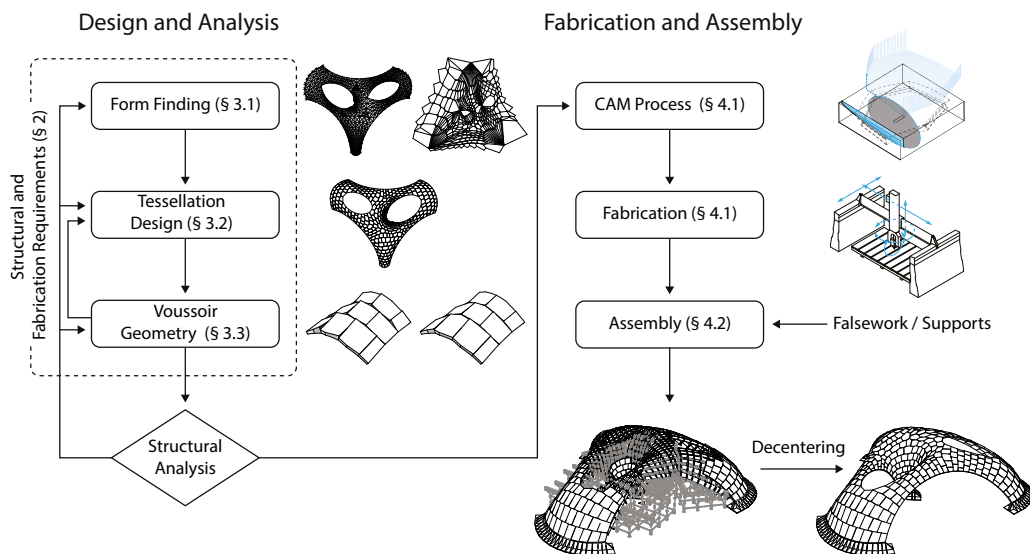
**Figure 2.** Flowchart summarising the structurally informed, fabrication driven, computational design process of the cut-stone vault. An online video documenting this process can be watched here: https://vimeo.com/167868985.

# 2. Structural and Fabrication Requirements

The design of the vault and its individual pieces was entirely driven by constraints related to the fabrication process and to the architectural and structural requirements and timeline of the project. In this section, we describe the structural and fabrication requirements in more detail.

## 2.1 Structural Requirements

First of all, the vault required an appropriate funicular overall shape that allows it to stand in compression without mortar or connections between the individual stone blocks. The form finding process of this funicular shape is briefly described in Section 3.1.

In addition, to comply with the prescribed weight limitations on the floor of the exhibition space in the protected building, the thickness of the stone shell had to be reduced to the absolute minimum. As a result, the thickness of the voussoirs at midspan of the large unsupported arches is only five centimetres, which is the minimum thickness required to avoid spalling of the stone and allow the integration of sufficiently large registration notches. High degrees of double curvature ensure that stable states of compressive stress can be developed
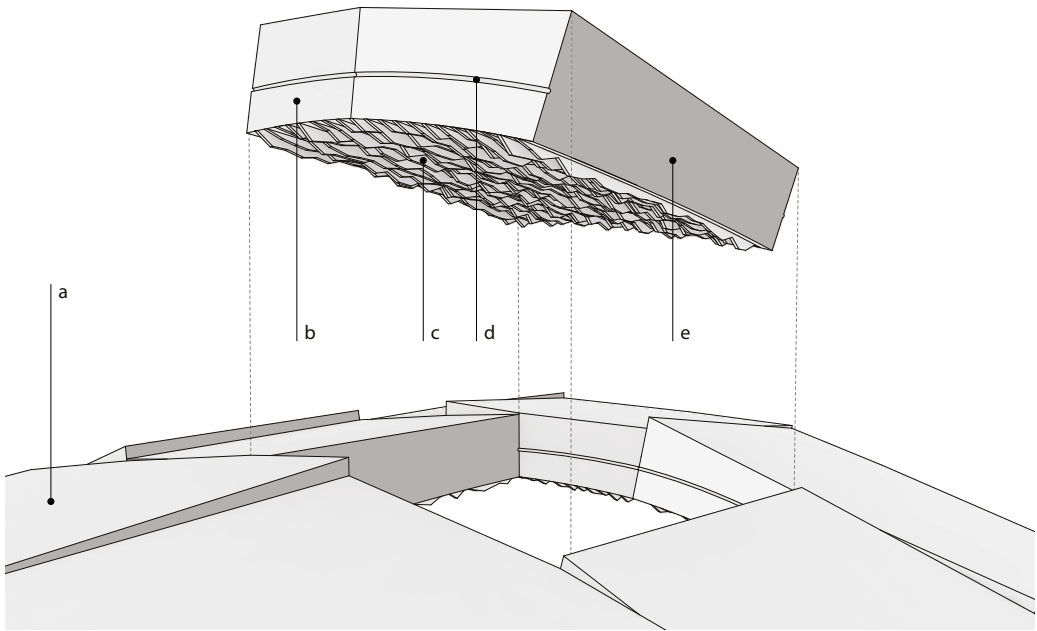
**Figure 3.** One voussoir lifted from the stone surface. Note that lifting a stone out of the structure would not be possible in reality because of the registration notches. (a) Flat extrados surface. (b) Doubly ruled, load-transferring surface. (c) Curved surface on intrados, generated with rough-cuts. (d) Registration notch. (e) Planarised, non-load-transferring side surface.

within the tight stone envelope under all loading conditions (self-weight, point loads, earthquake loads, etc.).

The total weight of the vault is approximately 23.7 tons, which is less than the load due to a crowd of people occupying the exclusion zones around the supports. To prevent too much of this weight from accumulating at the central support and also for aesthetic reasons, the overall shape of the vault is intentionally shallow. As previously discussed, the resulting outward thrust at the boundary supports is resisted by an internal system of ties. The vertical reaction forces are spread over a sufficiently large area by the footings such that the pressure underneath averages below the prescribed 600 kg/m².

Note that, due to the reduced thickness of the structure, the load-transferring surfaces between the voussoirs are small (Fig. 3). Since there is no mortar between the voussoirs, which could compensate for tolerances, these interfaces had to be flush and therefore precisely cut. This high degree of precision was (structurally) not required for the surfaces on the intrados and extrados.

Finally, the voussoirs were arranged in a staggered pattern and their load-transferring interfaces aligned to the force flow, to ensure sufficient interlocking, and to prevent sliding failure. Small male/female notches were added to these interfaces.
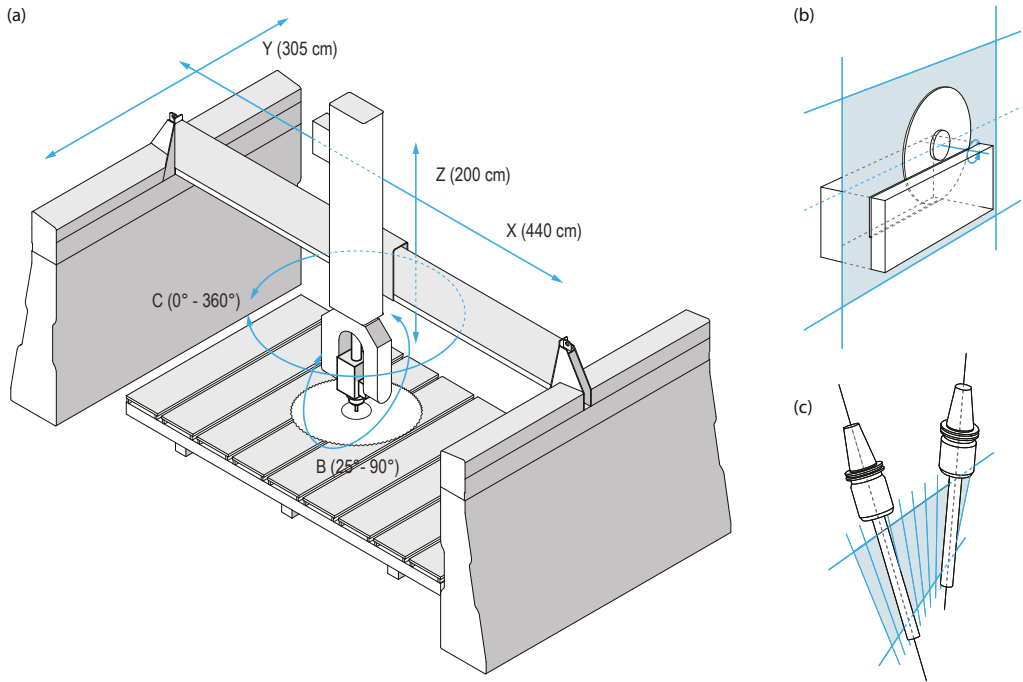
**Figure 4.** (a) 5-axis router OMAG Blade5 (Generation 3) with marked axes X, Y, Z, C and B. (b) Circular saw blades can only make planar cuts. (c) Profiling tools can create ruled surfaces.

They served primarily as registration marks during assembly (Fig. 3). Section 3.2 describes the design of the staggered voussoir pattern, and Section 3.3 the generation of the actual voussoir geometry.

## 2.2  Fabrication Requirements

The fabrication requirements resulted, on the one hand, from constraints of the CNC-machining process, and, on the other hand, from practical considerations regarding assembly. Due to the strict time constraints and high number of voussoirs, the main goal for the fabrication process was to limit the average cutting time. Additionally, the required precision of all bespoke stones demanded a highly accurate fabrication process.

All voussoirs for this vault were processed on a 5-axis router OMAG Blade5 (Generation 3) using a circular saw blade (Ø 81 cm) and customised profiling tools (Fig. 4). For the chosen limestone, the blade allows a relatively fast cutting procedure using, for example, a maximum feed rate of 445 cm/min for a 10 cm deep cut (Rippmann et al. 2013). However, such cuts are geometrically constrained to planar surfaces (Fig. 4b). In contrast, the profiling tools can be used to process

ruled surfaces efficiently, but operate at 5 to 10 times slower feed rates (Fig. 4c). Specifically, the use of circular blades demands a convex cutting geometry along the interfaces to avoid self-intersections with the blade trajectory and thus undesired cuts in the final voussoir.

In subtractive manufacturing processes, the three-dimensional treatment of a workpiece from all sides demands the flipping of the partly processed stone block and its precise re-referencing on the machine bed. To avoid this time-consuming procedure, and potential tolerance issues, all voussoirs were designed such that their extrados is planar. Hence, they could be cut from cuboid blanks that were mounted with one planar face against the machine table. After the exposed surfaces of the workpiece have been machined, this untreated planar face equals the extrados of the processed voussoir (Heyman 1997; Clifford & McGee 2013).

An additional measure to reduce the machining time of the voussoirs was to successively cut side-by-side grooves (with a larger step size than the blade's thickness) to approximate the doubly curved intrados surface. Usually, the resulting fragile fins are first knocked off manually to then continue with finer mill passes to obtain a smooth surface finish. We decided to stop after this first step and to use the "unfinished", rough, but nonetheless precise, aesthetic as a strength by carefully aligning these grooves with the force flow (see Section 3.2).

The maximum allowed weight of the voussoirs was limited to 45 kg on the top and 135 kg close to the supports. This constraint resulted from the fact that no heavy equipment, such as mobile cranes, could be used on the construction site, and thus ensured that all pieces could be handled safely by the masons assisted only by lightweight hoists mounted on the scaffolding.

# 3. Structural Design and Architectural Geometry

The design of an unreinforced, discrete, dry-set, cut-stone vault with complex geometry is a complicated process. Essentially, it can be summarised by the following steps. First, a thrust surface is designed through a form-finding process. This surface is taken as the middle surface of the cross-section of the vault. The intrados and extrados are created as offsets of this middle surface according to a local thickness, defined by the live loading cases. This stone envelope is then discretised into voussoirs following a tessellation pattern taking into account the fabrication and assembly requirements. Finally, the stability of the discretised geometry under different loading conditions can be verified with discrete element modelling. In this section, we describe the design of the thrust surface (Section 3.1), the tessellation design (Section 3.2), and the generation of the voussoir geometry (Section 3.3).

## 3.1 Form Finding

The funicular shape of the vault is the result of a form-finding process based on thrust network analysis (Block & Ochsendorf 2007). As a first step, preliminary design alternatives were sketched using RhinoVAULT (Rippmann et al. 2012). From this, a mesh was obtained and then refined, based on functional and aesthetic considerations. The updated mesh served as a target for a "best-fit" procedure that finds the closest possible network of compressive forces under the given loads (Van Mele et al. 2014).

During the form finding process, only the self-weight of the vault was considered. As discussed in Section 2.1, the allowable self-weight was dictated by the requirements of the site and the constraints imposed on the assembly process. A corresponding thickness distribution was computed based on experience, aesthetic considerations, and common sense. As depicted in Figure 5c, the thickness varies from 12 cm at the central support and the bottom leg, to 5 cm at the highest points and at midspan of the large unsupported arches.

The layout of force directions for the horizontal thrust in the network was derived from the geometric and structural features of the three-dimensional target geometry, and represented by the form diagram in Figure 5a. The best-fit algorithm was used to find the specific distribution of forces along those directions that maps the three-dimensional network as close as possible to the geometric target. During this process, the geometric target was updated to be able to find solutions that better distribute stresses along the supports and introduce more double curvature. The force diagram in Figure 5b is the final "best-fitting" distribution. Figure 5d is a visualisation of lumped stresses at the nodes. It shows that stresses are extremely low and do not even exceed 0.1 MPa. Note that this is two orders of magnitude below the compressive strength of the selected stone, which is a Cedar Hill limestone with a compressive strength of 22 MPa.

Finally, the resulting thrust network can then be converted to a mesh that, after subdivision and smoothing, represents the middle surface of the stone envelope of the vault.

## 3.2 Tessellation Design

The design of the tessellation geometry is subject to a comprehensive set of constraints derived from structural and fabrication requirements (Section 2), and from aesthetic considerations regarding tectonics and rhythm. Basically, the tessellation pattern must be staggered to ensure an interlocking voussoir arrangement and properly aligned to the force flow to prevent sliding failure, particularly along the unsupported boundaries.

The design of the tessellation pattern starts with the definition of course lines on the thrust surface. The thrust surface is represented by a quad mesh (Fig. 6a), whose faces are aligned with the layout of forces defined during the form-finding

process (see Section 3.1). This mesh gives a first indication regarding the orientation, singularities and spacing of the course line layout. The actual design of the courses was created manually from a set of geodesic curves on the thrust surface. Custom design and monitoring tools were used to help control the predefined minimum and maximum spacing of the courses such that, for example, the allowed weight of the average voussoir per row was not exceeded, while maintaining local alignment to the force flow (Fig. 6b).

A set of vertical lines was then generated per course aligned with the force flow. These lines define the side-by-side cuts resulting in the rough break-off edges on the intrados of the structure. A particular challenge was the alignment of cut lines from one course to the other such that the force flow becomes globally apparent (Fig. 6c). Constraints pertaining to the blade width and minimum and maximum allowable break-off widths had to be taken into account. The continuity of the cut lines was achieved by transferring the endpoints within one course to start points within the next. Given the varying geometry of the vault and the above-mentioned constraints, a strategy was developed for the gradual insertion or removal of additional cut lines.

Subsequently, an initial tessellation topology was defined by choosing more or less equally spaced vertical joint lines from the rough-cut pattern. The use of alternating boundary conditions for neighbouring courses guaranteed an initially staggered configuration. Locally, especially close to singularities, this tessellation topology was further modified manually. A more balanced staggering with larger overlaps between voussoirs was then created through an automated procedure that maximises the distance between joints of neighbouring courses. Ideally, the voussoirs of neighbouring courses are thus staggered by half of the length of one voussoir (Rippmann & Block, 2013; Rippmann 2016). In this iterative solving procedure, the vertical joint lines were automatically aligned with the local rough-cut pattern.

The final tessellation geometry was created by making all faces convex (Fig. 6d). This was achieved by scaling the vertical joint lines based on a user-defined scale factor and proportional to the course height. As a result, the degree of convexity increases towards the top, forming smoother transitions around the singularities.

## 3.3 Voussoir Geometry

The voussoir geometry was generated based on the tessellation of the thrust surface (Fig. 6d) and the chosen thickness distribution (Fig. 5c). The geometry of each of the surfaces of a voussoir (i.e. the intrados and extrados surfaces, the load-transferring side surfaces, and the non-load-transferring side surfaces) was determined by the limitations of the fabrication process and the limited amount of time in which the voussoirs had to be produced.

Each voussoir is convex and has a flat extrados surface. The non-load-transferring side surfaces (the surfaces transverse to the course lines) are also flat.
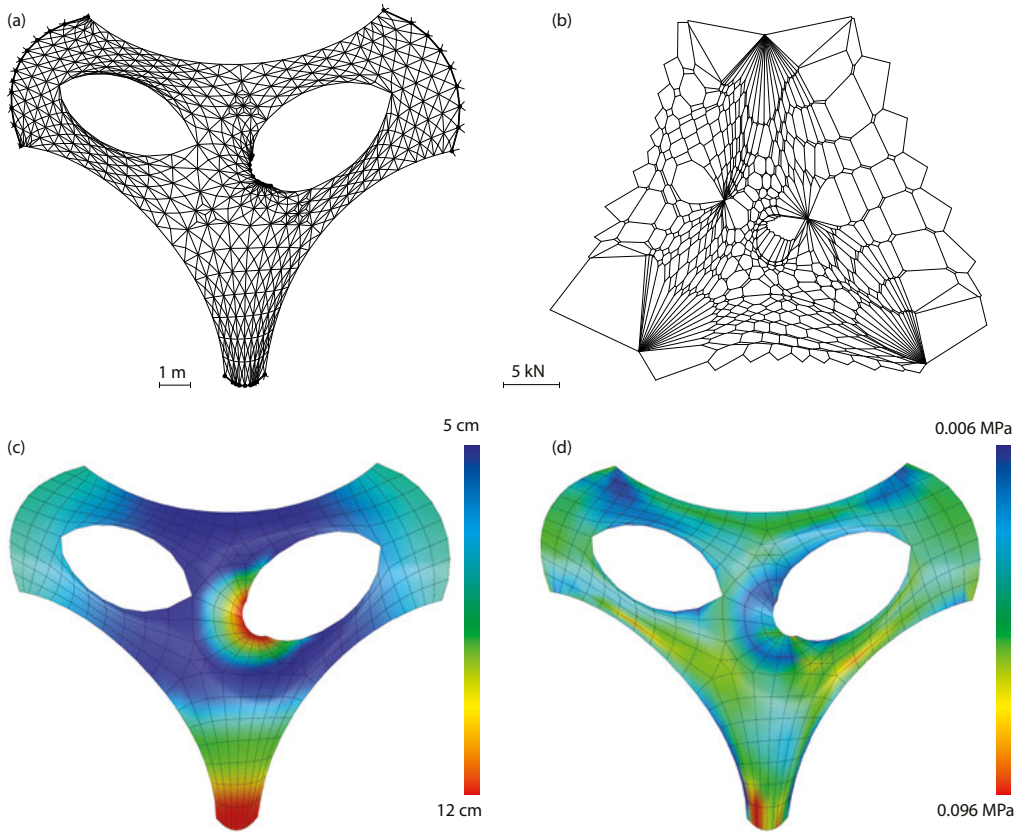
**Figure 5.** (a) The form diagram lays out the directions of horizontal forces in the three-dimensional thrust network. (b) The force diagram contains the force magnitude along each of the directions in the form diagram. (c) The distribution of thickness. (d) The stress in the surface resulting from the distribution of force and thickness.

The intrados surface of the voussoirs is curved like the intrados of the vault. It is created with parallel cuts by a circular blade leaving fins that are hammered off. The primary load-transferring surfaces (the surfaces aligned with the course lines) are ruled, because they are cut with a cylindrical profiling tool that creates the (male and female) notches.

Since the surface of the vault has areas with negative Gaussian curvature (i.e. in some areas it is anticlastic), it is not possible to create a connected flat-panel discretisation of the extrados with only convex faces (see Krieg et al. 2014; Li et al, 2015; Pottmann et al, 2015). Therefore, the extrados surface of each of the voussoirs was planarised individually creating a disconnected discretisation of the exterior of the vault.

The planarisation process is summarised in Figure 7. First, disconnected planar faces were based at the normal of the centroid of the original, smooth extrados
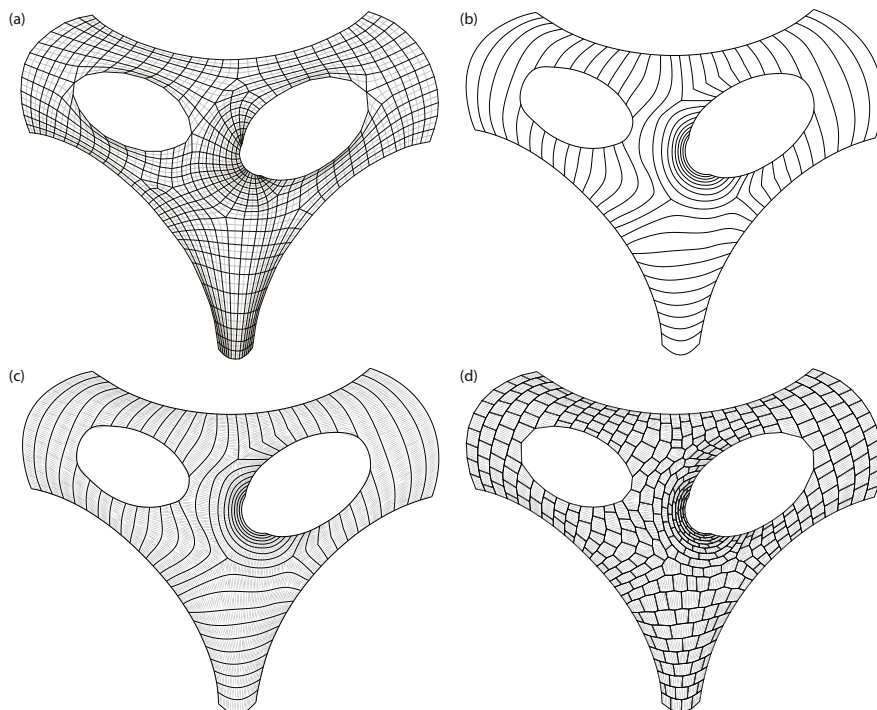
**Figure 6.** Overview of the tessellation design: (a) the mesh representing the thrust surface, (b) the course lines, (c) the rough-cut pattern on the intrados, and (d) the final tessellation of the thrust surface and aligned rough cuts.

surface (Fig. 7a). Note that this created large, erratic deviations from the original curved extrados at the corners of the voussoirs. These deviations were not aesthetically pleasing and significantly increased the weight of the vault. Therefore, in a second step, the planar faces were allowed to rotate around the normal at the centroid and move slightly up and down. The normals at the corners were allowed to rotate as well (Fig. 7b). During this procedure, the tessellation of the intrados was kept fixed. This means that the vectors connecting corresponding top and bottom corners of the voussoirs were no longer perfectly aligned with the normals of the thrust surface. However, this deviation was limited to 5 degrees from the original normal vector (Fig. 7b). Finally, in a post-processing step, the non-load-transferring faces were planarised, without changing the geometry of the load-transferring faces, and the notch lines were added.

After this optimisation process, the stepping from one stone to the next was between two and five cm in all locations. The lower bound was introduced to maintain a uniform and balanced appearance. The final configuration gave the vault a slightly rough, scale-like exterior that contrasts its smoothly curving interior surface.
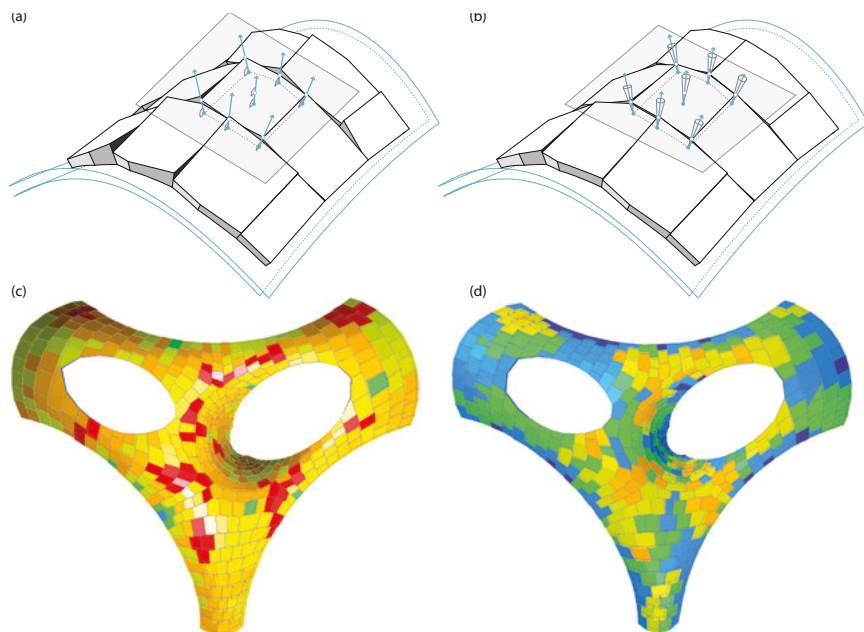
**Figure 7.** Overview of the design of the voussoir geometry: (a) disconnected, planar faces based at the centroids of the tessellation cells on the extrados create a rough, scale-like exterior with large deviations at the corners; (b) by rotating the faces and corner vectors a more balanced stepping from every voussoir to its neighbours is created; (c) deviation from allowed minimum and maximum corner stepping before normal adjustments (red voussoirs are outside of the imposed bounds); and (d) deviations afterwards.

# 4. Fabrication and Assembly

The fabrication and assembly of the cut-stone vault is a combination of traditional and digital methods, aimed at constructing the designed geometry with very high precision. The geometry of each voussoir is digitally processed and G-code is generated for CNC machining. The stones are cut using three different CNC machines to achieve a result that has very small tolerances and the desired finish, while keeping to a very tight schedule. The vault is assembled much in the same way as traditional masonry vaults were. Each voussoir is fully supported by a custom-made falsework. The stones are manually set, using shims, starting from all sides at the bottom and converging towards the "keystones" at the top.

## 4.1 CAM Process and Fabrication

The fabrication process of each voussoir starts with cutting a cuboid blank from a rough block of limestone (Fig. 8a). Its dimensions are defined by the bounding box of the voussoir. To save time and material during the cutting process of all

blanks, the 399 bounding boxes from the vault's voussoirs are categorised in 55 different sizes. The Pellegrini Single Wire Saw CNC machine is used to cut stone plates, which are then cut transversally and longitudinally according to the pre-defined ashlar sizes using a 3-axis blade-saw CNC machine.

The final shape of each voussoir was cut with the 5-axis CNC machine. To speed up the process, two cutting areas on opposite corners of the machining table were used, such that an already finished voussoir from one cutting area could be replaced while the next stone was being cut in the other area. Vacuum pods of different sizes and heights were used to hold the blanks in position and to keep the cutting tool from colliding with the table (Fig. 8b). Once the blank was in position, the side edges were cut with a circular saw (Ø81 cm). The result is a planar approximation of the final side edges. The next step is to shape the top face of the blank, which corresponds to the vault's intrados, by a series of side-by-side cuts (Fig. 8c). To save time during the cutting process of these grooves on top of the blank, the saw changes the direction of its trajectory each time it finishes a cut, tracing a zig-zagging path. Then, the fragile fins that result from the gap left between cuts are knocked off manually with a hammer.

To control the visual appearance of the pattern formed by the leftovers of the fins, the lead-in and lead-out of the circular blade was varied to create shallower, incomplete cuts at specific locations on the intrados (Fig. 9a). At these locations the fins would break off slightly higher (Fig. 9b), creating a balanced distribution of "highlights" on the rough, but overall smoothly curving surface.

The interfaces were finished using three different profiling tools (Fig. 8d). A simple cylindrical tool was used to finish the interfaces without registration notch. A tool with a 12 mm diameter semi-circular ridge was used to cut the female edges and one with a 12 mm diameter semi-circular groove to cut the males. To prevent potential tolerance problems, all side cuts were made following a right-to-left direction. With this cutting strategy, the tool always entered from the same side, and the rotation of the tool in relation with its trajectory was always the same as well. The resulting tolerances of the cutting process with the 5-axis CNC machine are between 0.4 and 0.8 mm.

The G-code of each voussoir was generated using dedicated CAM software after importing the cutting geometry of the voussoirs from Rhinoceros. This imported geometry contains the surfaces that define the shape of the voussoir and additional geometric elements used to define the cutting paths.

## 4.2 Falsework and Assembly

The voussoirs are assembled on top of a custom falsework consisting of standard scaffolding towers that support four marine-grade plywood waffle structures, one for each vault support (Fig. 10a). To minimise the amount of required material, the waffles are designed on separate orthogonal grids aligned to the main directions

**Figure 8.** Fabrication process: (a) The stones cut at the bounding boxes of the voussoirs. (b) Placement of the voussoir bounding box cut on the milling bed. (c) Rough cuts with a circular blade to create the intrados. (d) Processing of load-transferring side faces with custom-made tool to create the notch lines. (e) Adjacent stones test-assembled to verify alignment of rough-cut lines.
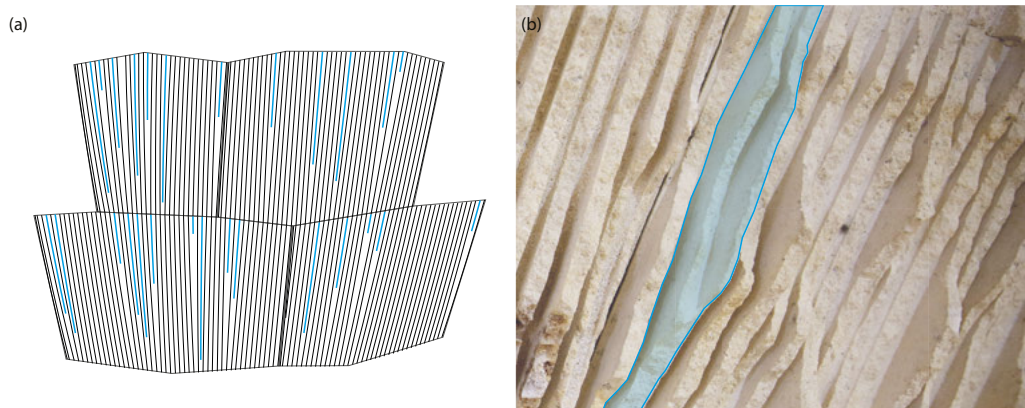


**Figure 9.** The break-off depth of rough-cut fins can be influenced by controlling the lead-in and lead-out of the circular blade to create a pattern of highlights on the intrados. (a) Distribution of highlights. (b) Example of different break-off depth.

of each support section. The elements in the longitudinal support directions are placed as perpendicular to the voussoirs as possible to increase stiffness. While non-orthogonal, geometrically complex waffles (Schwartzburg & Pauly 2013) could potentially be stiffer and lighter, the assembly time and complexity would be impractical and infeasible considering the tight schedule.

Each voussoir was placed on the waffle using shims, which allowed correcting the position and inclination of the voussoirs. The position of each stone was controlled with the registration notches and assessed by verifying the perfect alignment of the interfaces. In addition, total stations were used to measure the four corner points of the flat extrados of the voussoir, and compare them with the point cloud taken directly from the digital model (Fig. 10c).

Separate crews worked simultaneously on the different supports, starting from the bottom and working their way up to the "keystone" rows (Fig. 10b). This meant that imperfection and construction tolerances were accumulated at the top. The geometrical differences between the designed and the as-built vault were resolved by creating "keystones" that fit perfectly in the built geometry. The custom "keystones" were cut once all of the other voussoirs were placed and the correct shape for them had been measured on site (Fig. 10d). Note that an alternative solution is to assemble from the top down, thus taking the imperfections at the supports by grouting (Ochsendorf et al. 2016). However, considering the complexity of the support conditions caused by the loading limitations on the floor of the exhibition space, this type of corrections was not possible here.

# 5. Conclusions

This paper presents an overview of the structurally informed design and fabrication of the Armadillo Vault, a cut-stone vault presented at the 2016 Venice Architecture Biennale. The project was realised under extremely tight time and site constraints that drove the structural and geometrical design as well as the fabrication process.

The paper shows how a complex design and fabrication process is only possible with the aid of an integrated computational setup. The interaction and feedback from all of the steps in the process described above were an essential component to achieve such results, and to ensure a sound structure and very small construction tolerances.

The experience of the stone masons also informed the process, especially in the configuration of the keystone rows and the accumulation of imperfections in these last voussoirs. The high precision of the entire fabrication process described above minimises these errors, but does not completely eliminate them, or the need for a solution to tolerances. Therefore, manual adjustments during
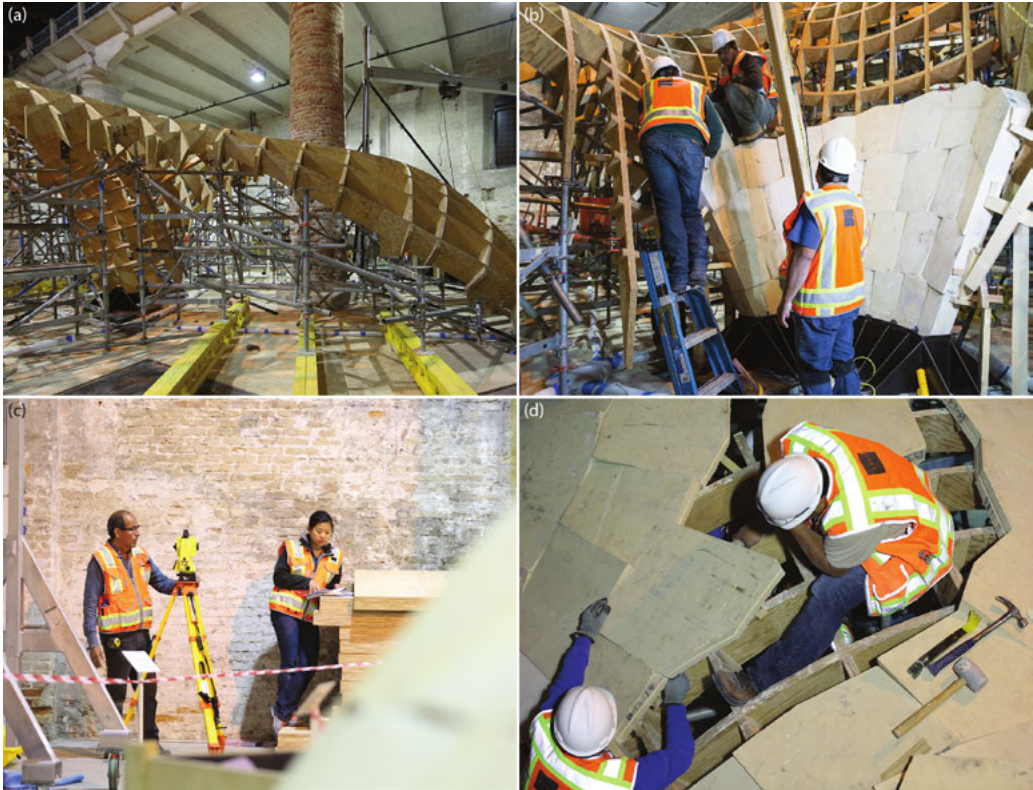
**Figure 10.** Assembly process: (a) Plywood waffle structure on top of standard scaffolding towers. (b) Voussoirs are placed starting from the supports. (c) The position of voussoirs was assessed using total stations, measuring the corner points of the flat extrados. (d) The keystones were cut after all other stones had been placed and the required geometry to compensate for the accumulation of tolerances could be determined.

assembly by the stone masons were needed due to the accumulation of tolerances. The execution of such manual adjustments can be facilitated by simplifying the voussoir geometry. For example, by optimising the geometry of the interfaces for planarity.

The resulting structure (Fig. 11) is a demonstration of how material and fabrication constraints are not equivalent to limited design possibilities, but can be the starting point for expressive and efficient structures.

# Acknowledgements

# References

Block, P., and J. Ochsendorf. 2007. "Thrust Network Analysis: A New Methodology for Three-Dimensional Equilibrium." J*ournal of the International Association for Shell and Spatial Structures* 48, 3: 1–8.

Block, P., M. Rippmann, and T. Van Mele. 2015. "Structural Stone Surfaces: New Compression Shells Inspired by the Past." AD Architectural Design. Ed. by A. Menges, *Material Synthesis: Fusing the Physical and the Computational*, 85, 5: 74–79. London: John Wiley & Sons.

Clifford, B., and W. McGee. 2013. "La Voûte de LeFevre." In *[En]Coding Architecture: The Book.* ed. by L.C. Werner, 122–127. Pittsburgh PA: Carnegie Mellon University School of Architecture.

Heyman, J. 1997. *The Stone Skeleton: Structural Engineering of Masonry Architecture*. Cambridge University Press. Cambridge, United Kingdom

Krieg, O.D., T. Schwinn, A. Menges, J. Li, J. Knippers, A. Schmitt, and V. Schwieger. 2014. „Biomimetic Lightweight Timber Plate Shells: Computational Integration of Robotic Fabrication, Architectural Geometry and Structural Design." In *Advances in Architectural Geometry 2014*, ed. by P. Block, J. Knippers, N.J. Mitra, and W. Wang, pp 109–125. Switzerland: Springer.

Li, Y., Y. Liu, and W. Wang. 2015. „Planar Hexagonal Meshing for Architecture." *IEEE Transactions on Visualization and Computer Graphics*, 21, 1: 95–106.

Ochsendorf, J., T. Helbig. C. Fivet, and J.M. Yoon. 2016. "Segmented Granite Vault in Cambridge." *Detail Structure* 1: 68–73

Pottmann, H. et al. 2015. "Architectural Geometry." *Computers and Graphics (Pergamon)*, 47: 145–164.

Rippmann, M., L. Lachauer, and P. Block. 2012. "Interactive Vault Design." *International Journal of Space Structures* 27, 4: 219–230.

Rippmann, M., and P. Block. 2013. "Rethinking Structural Masonry: Unreinforced, Cut-Stone Shells." *Proceedings of the ICE – Construction Materials* 166, 6: 378–389.

**Figure 11.** Finished cut-stone vault in the Corderie dell'Arsenale of the Architecture Biennale in Venice.

Rippmann, M., J. Curry, D. Escobedo, and P. Block. 2013. "Optimising Stone-Cutting Strategies for Freeform Masonry Vaults." In *Proceedings of the International Association for Shell and Spatial Structures (IASS) Symposium 2013*, ed. by J.B. Obrebski, and R. Tarczewski. Wroclaw, Poland.

Rippmann, M. 2016. F*unicular Shell Design: Geometric Approaches to Form Finding and Fabrication of Discrete Funicular Structures*. Ph. D. thesis, ETH Zurich, Department of Architecture.

Schwartzburg, Y., and M. Pauly. 2013. "Fabrication-Aware Design with Intersecting Planar Pieces." In *Proceedings of Eurographics 2013*, ed. by I. Navazo and P. Poulin. Girona, Spain.

Van Mele, T., D. Panozzo, O. Sorkine-Hornung, and P. Block. 2014. "Best-Fit Thrust Network Analysis – Rationalization of Freeform Meshes." In *Shell Structures for Architecture: Form Finding and Optimization*, ed. by S. Adriaenssens, P. Block, D. Veenendaal, and C. Williams. New York: Routledge.

# CASTonCAST Shell Structures

## Realisation of a 1:10 Prototype of a Post-Tensioned Shell Structure from Precast Stackable Components

Lluis Enrique and Joseph Schwartz

L. Enrique, J. Schwartz
Department of Architecture, ETH Zurich, Switzerland
enrique@arch.ethz.ch ✉
schwartz@arch.ethz.ch

# Abstract

This paper presents an important step towards the integration of structural concerns in the CASTonCAST system for the design and production of shell structures built from precast stackable components. This step consists of studying the application of prestressing for assembling the components and providing stiffness to the shell. This was tested in the realisation of a 1:10 prototype of a post-tensioned shell structure built from precast stackable components. This prototype is also the first one to be built in concrete using the CASTonCAST system.

Keywords:
shell structures, precast concrete, prestressing, architectural freeform surfaces, strut-and-tie models

# 1. Introduction

Between the 1920s and the 1970s, impressive reinforced concrete shell structures were built using the cast-in-place construction technique. After this period the construction of reinforced concrete shells declined due to the high costs associated to the intense labour required in the construction site and the high costs of formwork and scaffolding (Chilton 2000). During the last decades, the demand of freeform shapes in architecture has accentuated these problems, making the production of such curved structures in concrete more inefficient and unsustainable. For this reason, it is important to develop methods for the production of freeform shell structures which reduce the economic and environmental costs. Nowadays, new methods for producing efficient complex structures in concrete are being developed. It is worth mentioning the novel techniques for casting concrete building elements using flexible formwork (West 2001; Orr et al. 2011), flexible moulding systems (Schipper 2011; Pronk et al. 2009; Raun & Kirkegaard 2012), and additive manufacturing technologies (AM) such as D-shape (Dini 2006), Contour Crafting (Khoshnevis et al. 2004), Concrete Printing (Lim et al. 2009), and Smart Dynamic Casting (Lloret et al. 2015).

An alternative to these methods is the CASTonCAST system (Enrique et al. 2011; Enrique et al. 2016) (Fig. 1). This system deals with the design and production of architectural freeform shapes from precast stackable components. The system consists of two complementary parts:

(1) A novel manufacturing technique of complex building components which relies on producing a series of components in stacks by using the previous component as a mould for the next one.

(2) A new geometric method, which emerges from the constraints of the manufacturing technique, for the construction of freeform shapes by the connection of stackable solid tiles.

The system presents the following advantages: First, it eliminates the need for costly complex moulds. Second, the method allows one to transport the components to the construction site in stacks. This avoids the need to manufacture supporting structures for each component. Finally, the labour at the construction site consists in placing the components on a reusable scaffolding and assembling them. This increases the speed of erection and reduces the construction costs.

This research has the aim of applying the CASTonCAST system for the design of freeform shell structures. The first step in this direction consists of studying the way the components are assembled together and the shell gets stiffness. Attracted by the efficiency in construction of precast segmental bridges and
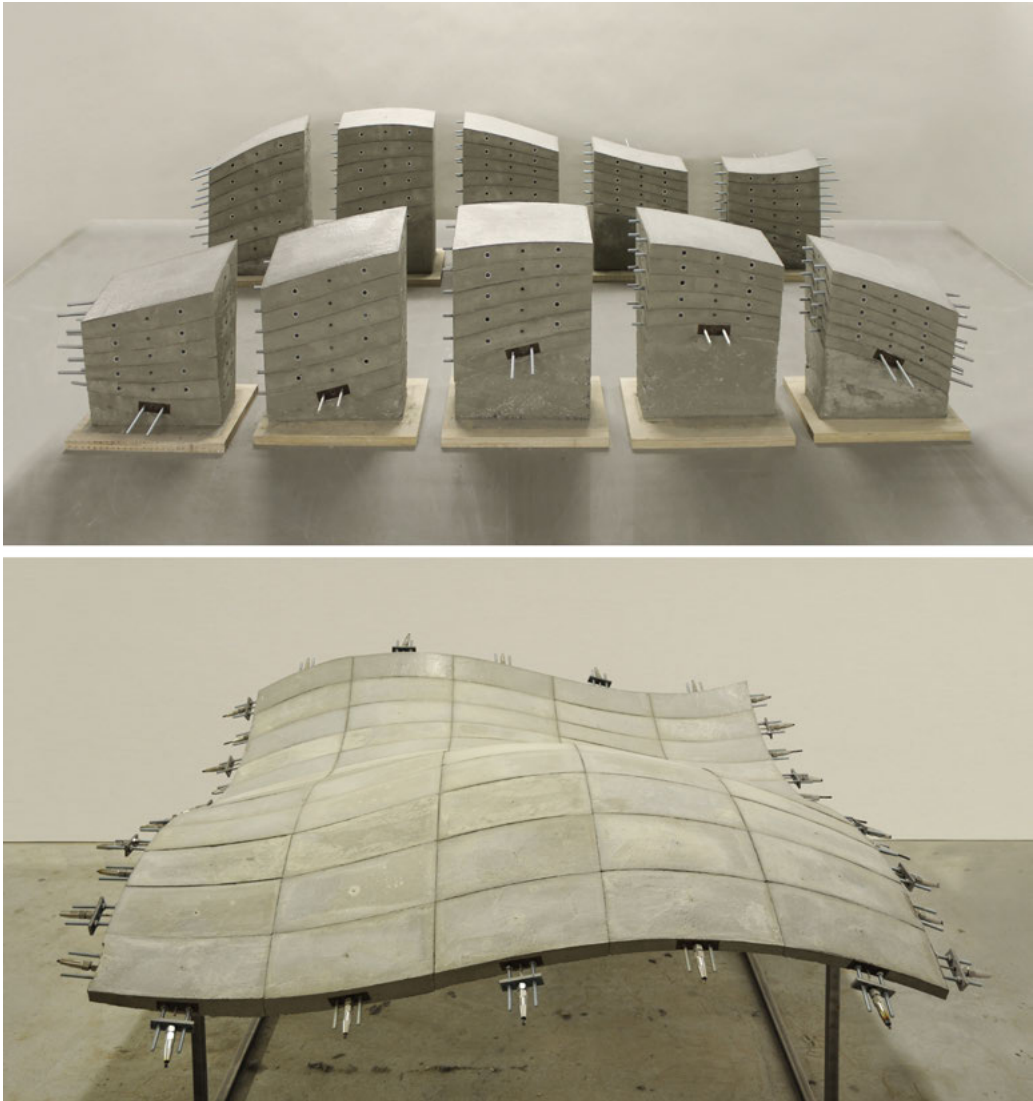
**Figure 1.** 1:10 Prototype of a post-tensioned shell structure built from precast stackable components: stacks of components (above) and post-tensioned shell (below).

inspired by built works such as the Jubilee Church designed by Richard Meier & Partners Architects, this research studies the application of prestressing in the CASTonCAST system for assembling the components and providing stiffness to the shell. In this paper this approach has been tested in the realisation of a 1:10 prototype of a post-tensioned shell structure built from precast stackable components (Fig. 1).

# 2. Prototype

The prototype is composed of 60 stackable concrete components of size 25 x 8-12 x 2.5-6 cm, arranged in a matrix of 5 by 12. These are assembled by a network of 17 post-tensioning steel cables of 4 mm diameter. The total size of the prototype is 140 x 140 x 2.5-6 cm, and its weight is approximately 135 kg. Since the components at real scale are meant to be around 2.5 m length by 1.2 m wide, we can say that the prototype is constructed approximately at a 1:10 scale. However, at real scale the thickness of a shell structure should be between 5 and 25 cm.

## 2.1 Geometry

The shell was designed using the CASTonCAST geometric method (Enrique et al. 2016). This method allows the construction of freeform shapes by the connection of stackable tiles which represent building components manufactured one on top of another. To achieve this, the same group of tiles must be able to be arranged in two clusters: stack and strip. The key of the method relies on simple requisite: for two tiles to be joined in two different clusters, both tiles must have two congruent surfaces between them (Fig. 2).

The shape of the shell was designed with the intention that its main surfaces have regions with both positive and negative Gaussian curvatures. During the design process it was important to control two main aspects in order to ensure that the components could be easily produced: First, the thickness of the shell had to be between 2.5 and 6 cm. Second, the curvature of the top surface of the components should not be too complex. To control these two aspects, a stack-to-strip modelling process was followed. This consists on modelling a stack of solid tiles and later arranging them in order to construct the resulting strip.

For modelling the stack, first the generating curves were created (Fig. 3). These curves represent a series of transversal sections of the shell, and therefore they define both the thickness and the curvature of the shell. This shows that there is an interesting relationship between the change of thickness and the global curvature of the shell. In this process, it was necessary to respect the range of admissible thicknesses previously defined. Since at real scale the range of admissible thicknesses is larger than at the prototype scale, the design space is also wider.

Then, the angle between the generating surfaces of the stack was defined (Fig. 3). This affects the curvature of the shell along the strips. In order to get more variation of the curvature along the strip, the shell was constructed from two stacks with a different angle between their generating surfaces. As Figure 3 shows, both stacks are linked. For this, the back face of the last tile of the first stack and the front face of the first tile of the second stack must be congruent. This
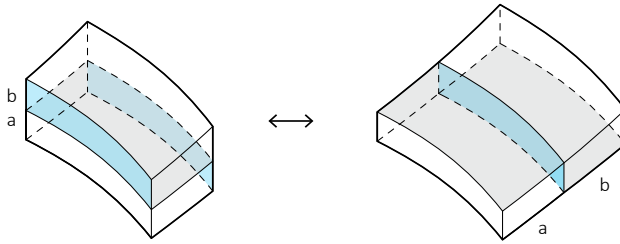
**Figure 2.** Stack and strip of two tiles



Generating
surfaces
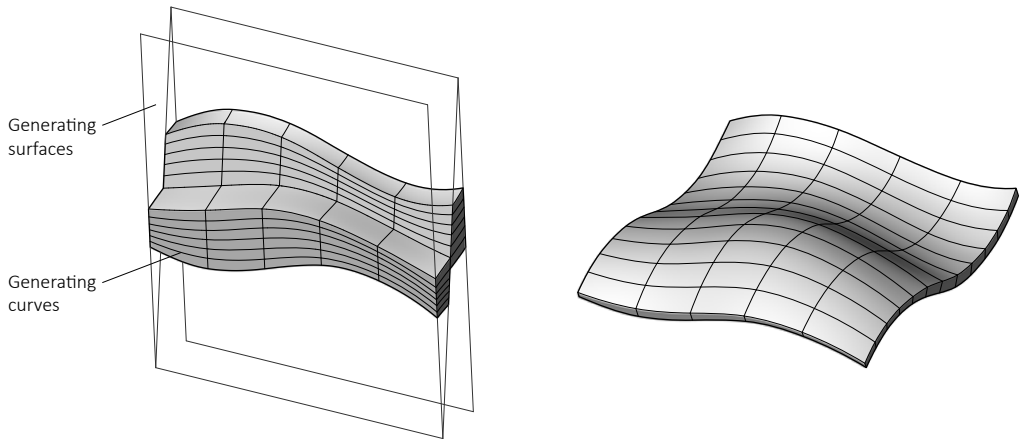
Generating
curves

**Figure 3.** Geometric modelling of the shell.

allowed joining the two shell patches corresponding to each of the stacks giving shape to the shell. Both the generating curves and the generating surfaces were manipulated until the desired shape was obtained.

Finally, once the shape of the shell was defined, the tiles of the stack were subdivided by a series of transversal planes into smaller tiles. This step allowed controlling the appropriate size of the components and the curvature of the top surface of the components.

## 2.2 Structure

A study of the structural behavior was developed in order to check the internal forces in the prestressed shell. In this study, two conditions had to be fulfilled: First, the effect of prestressing had to ensure that no internal tensile forces appear in the mass of concrete of the shell; this was important for ensuring that
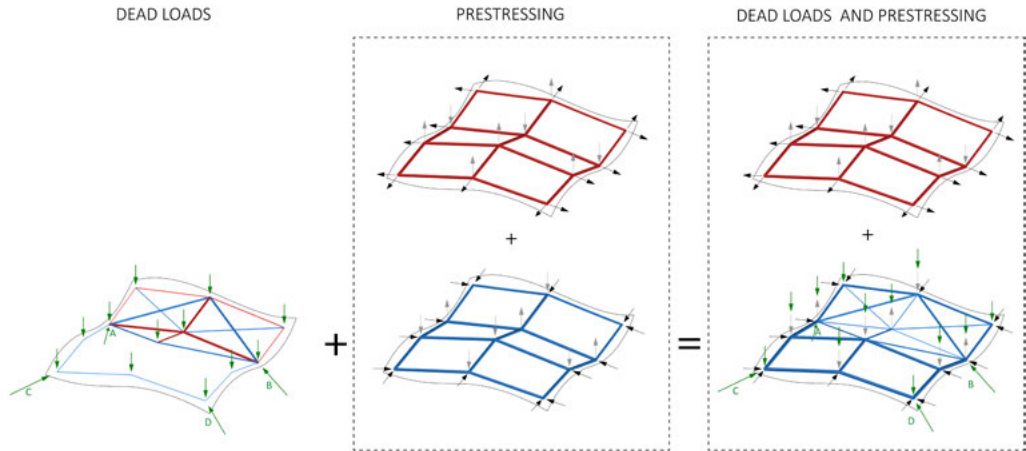
**Figure 4.** Study of the internal forces in the prototype using the Load Path Network Method. Compression in blue and tension in red.

the precast elements were appropriately compressed and also to prevent cracks from appearing. Second, the magnitude of the internal forces had to respect the yield conditions of the material. The available parameters to achieve this were: the shape of the shell, the thickness, the position of the supports and the amount of prestressing force.

The study was conducted using the Load Path Network Method (Enrique and Schwartz, 2016). LPNM is an equilibrium-based method for the generation of three-dimensional strut-and-tie models based on the lower-bound theorem of the theory of plasticity (Muttoni et al. 1997). This method allows one to construct and visualise possible paths of the internal forces in equilibrium in a given structure. Using this method, a scheme of a possible spatial configuration of the internal forces in equilibrium within the designed shape was modelled (Fig. 4). For this, first a possible load path of the self-weight was modelled. This path of internal forces shows that the shell takes advantage of its three-dimensional shape for distributing the internal forces by means of a network of compressive and tensile axial forces. In this step, the initial shape and the position of the supports had to be slightly modified in order to reduce the magnitude of the internal forces.

Then, a simplified network of prestressing cables was modelled. In order to fulfil the conditions defined before, the magnitude of the prestressing force in the cables needed to be larger than the largest tensile force of the first load path, and, at the same time, it had to respect the yield strength of the concrete mass and the steel cables. In this case, the required prestressing force in the cables was equivalent to 40% of the admissible tensile strength of a steel cable
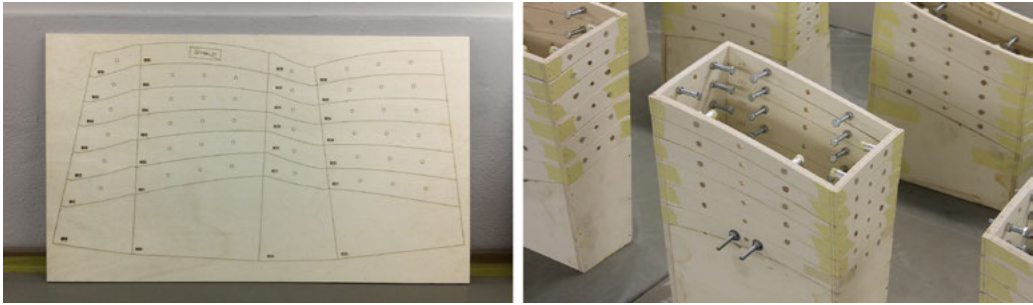
**Figure 5.** Production of the lateral moulds.

of 4 mm diameter. By superimposing the two systems of forces the mass of concrete of the shell remained only under compressive forces.

The equilibrium solution chosen might not be the one describing the real structural behavior of the shell; however, according to the lower-bound theorem of the theory of plasticity, the modelled solution of internal forces guarantees the structural safety (Muttoni et al. 1997).

## 2.3 Production

The CASTonCAST manufacturing technique (Enrique et al. 2016) consists of casting a series of components in stacks using the previous component as a bottom mould for the next component. The main steps for the production of this prototype were:

### 1. Production of the lateral moulds

For the production of a stack of components, moulds for the flat lateral faces of the components are required. Like the components, these lateral moulds are stackable. Thanks to this, they can be manufactured together by cutting their stackable parts from flat sheets of material (Fig. 5). This reduces the material waste and the production time. For the production of this prototype, a total of 10 flat sheets of timber of size 83 x 45 x 1 cm were required for producing lateral moulds of the 60 components.

The assembly devices were fixed in the lateral moulds. These are female-male stainless steel pin joints and two plastic tubes connecting the opposite faces of the mould for inserting the post-tensioning cables.
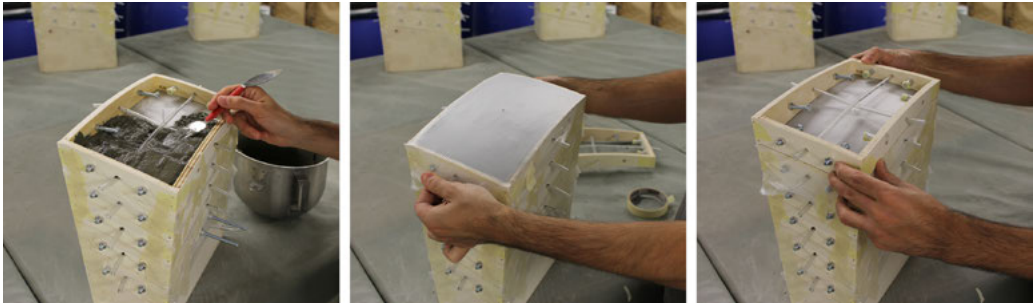
**Figure 6.** Production of the components: casting (left), placing the separation layer (centre) and placing the next lateral mould (right).

## 2. Production of the bases

The first component of the stacks did not have a bottom flat surface. Due to this, it was necessary first to manufacture bases. These were produced using lean concrete. For further prototypes, the bases will be produced from reusable materials in order to reduce the material waste.

## 3. Casting the components

For casting one component, first the mould was filled with concrete and later the top surface of the components was shaped manually using a bricklaying trowel (Fig. 6 left). To do this successfully, it was necessary to control during the design process that the curvature of the top surface of the components was not too complex. In addition, it was important to control the concrete rheology and workability.

The concrete mixture used contained a cement-sand ratio of 1:2 and a water-cement ratio of 0.6. Due to the small scale of the components, no gravel nor steel reinforcement was used. However, polypropylene fibres were added to the mixture in order to reduce the width of the cracks and improve the resistance to shrinkage during the curing.

Once the concrete had hardened, a thin plastic layer was applied on the top surface of the component in order to prevent that the material of the next component adheres to it. (Fig. 6 centre). This can also be achieved using a standard demoulding spray. Then, the next lateral mould was fixed in order to start the casting of the next component (Fig. 6 right). Each new component could be cast approximately 12 hours after casting the previous one. In order to reduce the production time, the stacks were cast by layers, starting by casting the first component for all the stacks, then, the second one for all the stacks, and so on.
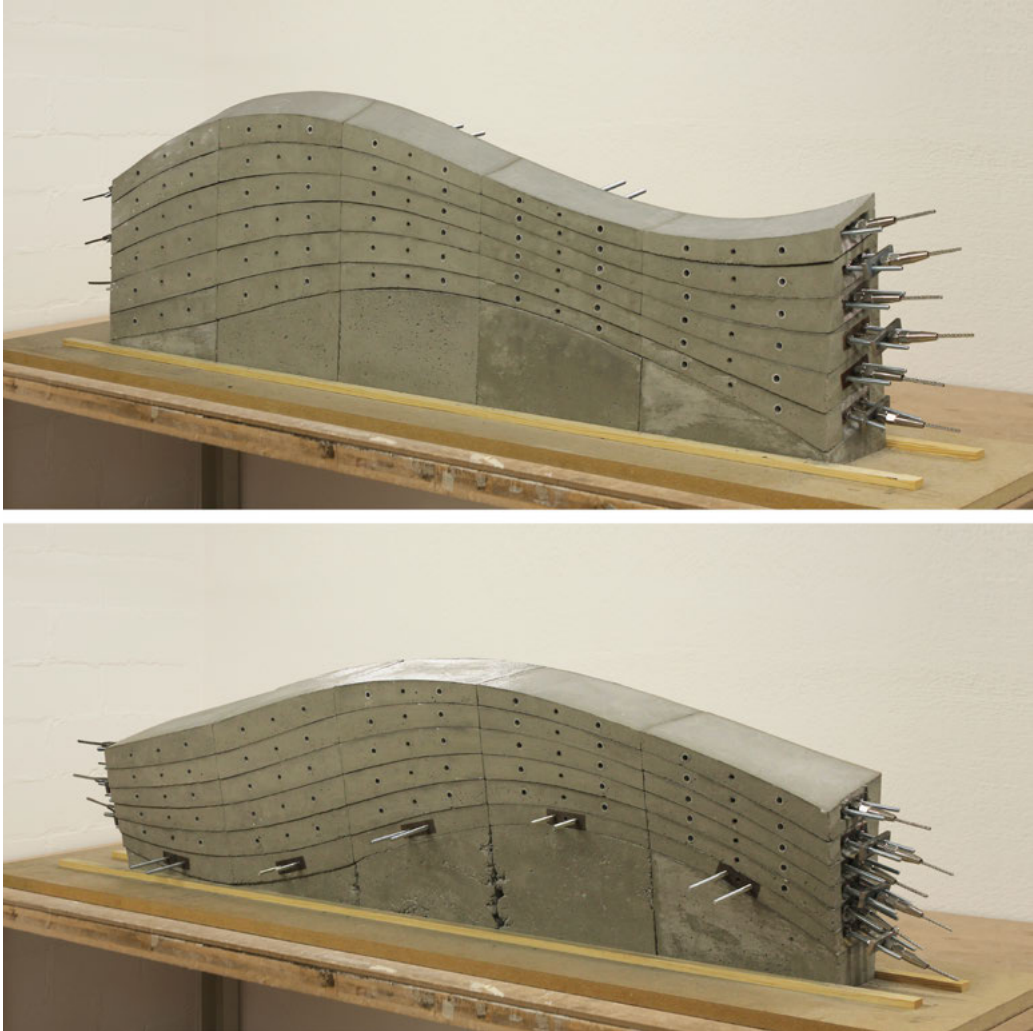
**Figure 7.** Longitudinal post-tensioning of the components.

Due to the manual production process, which at real scale must be carried out by skilled workers, the quality of the surface finish was that of handcrafted products. This finish could have been smoothed and improved by applying an optional surface polishing. Although the final quality of the surface finish may be rougher than when the components are cast using a mould, this method of manufacturing the components allows one to eliminate the need of producing complex non-reusable moulds and therefore reduces largely the material waste.

**Figure 8.** Assembly sequence.

## 2.4 Assembly

The assembly of the components was solved by means of two combined systems: female-male steel pin joints located in the lateral faces of the components and a bidirectional network of post-tensioning cables. The steel pin joints served to match the components precisely and make the shell stiff against shear forces. The bidirectional network of post-tensioning cables was in charge of joining the precast concrete components, providing stiffness to the shell structure and preventing cracks from appearing.

The post-tensioning process was done in two phases: longitudinal and transversal post-tensioning. The longitudinal post-tensioning consisted of assembling the components of adjacent stacks belonging to the same level. This process shaped two large stacks composed of six stackable post-tensioned curved beams each (Fig. 7). Since the components are stackable, the first curved beam could be post-tensioned directly on top of the bases and the subsequent curved beams could be post-tensioned on top of the previous ones. Thanks to this, there was no need of building custom support devices for the assembly process. This feature reduces the economic cost and the material waste involved in the manufacturing of such supporting structures.

After the longitudinal post-tensioning, the 12 curved beams were assembled together on top of a simple scaffolding (Fig. 8). This was composed of four MDF panels of 2 cm thickness which were produced using a CNC machine. Only two
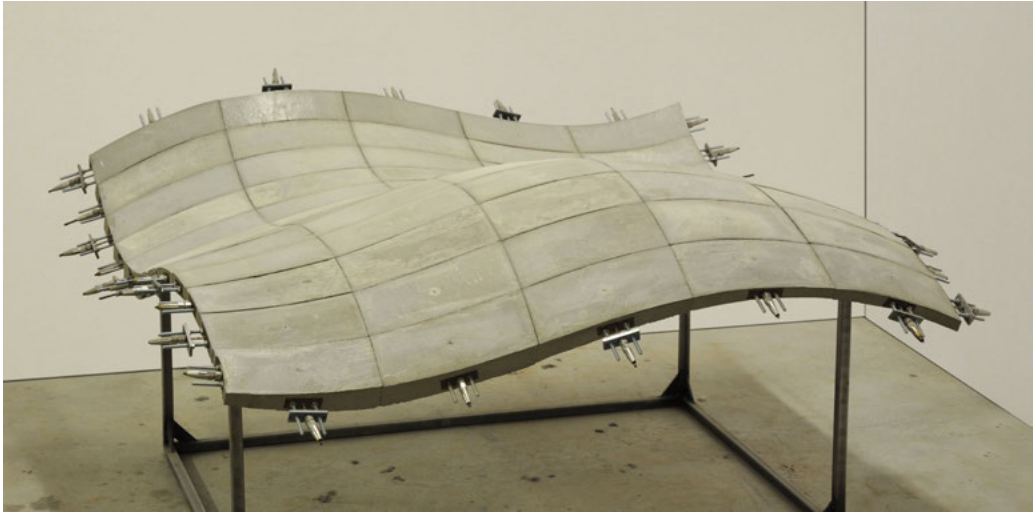
of these panels had a curved edge following the curvature of the shell in order to help placing the beams in their exact position. The beams were assembled by joining the back face of each beam with the front face of the next one. Due to inaccuracies during the fabrication process, it was required to slightly sand the steel pin joints with an electric circular saw. This showed that the production process requires a high level of precision. After connecting all the beams, these were assembled by means of five transversal post-tensioning cables. Finally, the shell was decentred and supported by a steel frame (Fig. 9).

At real scale, the longitudinal post-tensioning would take place at the manufacturing plant in order to reduce to time of erection at the construction site. Then, the stacks of post-tensioned curved beams would be transported to the construction site where the shell would be assembled. One of the two stacks of post-tensioned curved beams of the prototype, without the bases, built at a real scale would weight around 20-30 tons and would be 12.5 m long. This means that a four-axis trailer 14-16 m long with a valid loading capacity of 30-50 tons could transport the full shell to the construction site in two trips, carrying in each trip one full stack composed of 30 components. Once at the construction site, the curved beams would be placed on a scaffolding built from standard reusable elements. In this way, the construction of costly non-reusable scaffolding would be avoided.

# 3. Conclusions and Further Research

The results of this study show that bringing together the CASTonCAST system and prestressing has a great potential for the design and production of freeform precast prestressed shell structures. However, in order to apply the system at real scale, the next questions must be studied:

### 1. Geometry
The geometric method is currently being extended to the strip-to-stack approach in order to study how to efficiently tessellate a given freeform shape into stackable tiles.

### 2. Structure
At the moment, the structural analysis is used to check the structural behaviour of a modelled shape, but it does not actively participate in the design process. For this reason, the link between geometry and structure must be strengthened.

### 3. Fabrication
The production of the components at real scale is currently being investigated. This step involves solving important aspects such as controlling the rheology of the concrete mixture, shaping the top surface of the components, manufacturing the bases, adding steel reinforcement and testing the separation layer, among others.

### 4. Assembly
Further research needs to be done in order to study ways of assembling the shell on site only with the use of reusable standard scaffolding.

# Acknowledgements

# References

Chilton, John C., and Heinz Isler. 2000. *Heinz Isler: the engineer's contribution to contemporary architecture.* London: Telford.

Dini, Enrico. 2006. D-Shape. Accessed at http://www.d-shape.com.

Enrique, Lluis, and Joseph Schwartz. 2016. "Application of the Load Path Network Method for the Design of Prestressed Shell Structures." Paper accepted for presentation at the IASS2016 Annual International Symposium, Tokyo, Japan, September 26–30.

Enrique, Lluis, and Joseph Schwartz. 2016. "Load Path Network Method: An Equilibrium-Based Approach for the Design and Analysis of Structures." *Structural Engineering International.* (to be published).

Enrique, Lluis, Povilas Cepaitis, Diego Ordoñez, and Carlos Piles. 2011. CASTonCAST Fabrication System and Method. UK Patent Application GB1101013.9 filed January 20, 2011.

Enrique, Lluis, Povilas Cepaitis, Diego Ordoñez, and Carlos Piles. 2016. "CASTonCAST: Architectural Freeform Shapes from Precast Stackable Components." *VLC arquitectura. Research Journal 3,* no. 1: 85–102.

Khoshnevis, Behrokh. 2004. "Automated Construction by Contour Crafting-Related Robotics and Information Technologies." *Automation in Construction* 13, no. 1: 5–19.

Lim, Sungwoo, Thanh Le, John Webster, Richard Buswell, A. Austin, Alistair Gibb, and Tony Thorpe. 2009. "Fabricating Construction Components Using Layered Manufacturing Technology." In *Proc. Global Innovation in Construction Conference,* Loughborough University, Leicestershire, UK, pp. 13–16.

Lloret, Ena, Amir R. Shahab, Mettler Linus, Robert J. Flatt, Fabio Gramazio, Matthias Kohler, and Silke Langenberg. 2015. "Complex Concrete Structures: Merging Existing Casting Techniques with Digital Fabrication." *Computer-Aided Design* 60: 40–49.

Muttoni, Aurelio, Joseph Schwartz, and Bruno Thürlimann. 1997. *Design of Concrete Structures with Stress Fields.* Basel: Birkhäuser.

Orr, John J., A. P. Darby, T. J. Ibell, M. C. Evernden, and Mike Otlet. 2011. "Concrete Structures Using Fabric Formwork." *The Structural Engineer* 89, no. 8: 20–26.

Pronk, A., I. V. Rooy, and P. Schinkel. 2009. "Double-Curved Surfaces Using a Membrane Mould." In Proc. of the IASS 2009 Symposium. Valencia, September 28 – October 2.

Raun, Christian, and Poul Henning Kirkegaard. 2012. "Reconfigurable Double-Curved Mould." In *Proc. of the Second International Conference on Flexible Formwork. BRE CICM*, University of Bath, June 27–29.

Schipper, H. R., and Bas Janssen. 2011. "Manufacturing Double-Curved Elements in Precast Concrete Using a Flexible Mould: First Experimental Results." In *Proc. FIB Symposium: Concrete Engineering for Excellence and Efficiency*, Prague, 8–10 June. Czech Concrete Society and fib–International Federation for Structural Concrete.

West, Mark. 2001. "Fabric-Formed Concrete Structures." In *Proc. Of the First International Conference on Concrete and Development*, Tehran, Iran, April, pp. 133–142.

# Lightweight Conical Components for Rotational Parabolic Domes

## Geometric Definition, Structural Behaviour, Optimisation and Digital Fabrication

Roberto Narváez-Rodríguez and José Antonio Barrera-Vera

R. Narváez-Rodríguez, J. A. Barrera-Vera
University of Seville, Spain

roberto@us.es ✉
barrera@us.es ✉

# Abstract

Although initially intended for academic purposes, the research shown in this paper was drawn towards the development of hollow lightweight conical components to materialise rotational parabolic domes. The starting point is a projective interpretation of an Archimedean property of rotational paraboloid planar sections. This is used to discretise the parabolic surface with a set of tangent ellipses obtained via planar circle-packing algorithms. The ellipses are then materialised with components composed of three truncated conical surfaces, which may be composed of several laminar materials. The geometry and economy of the material, the good structural behaviour, the simple solution for fabrication and assembly, and the tests on a full-scale prototype prove this component to be an efficient self-supporting system for wide-span structures against the use of solid boundary rings, not only for rotational parabolic domes, but also for a possible translation to other types of surfaces.

# 1. Introduction

The use of computation, in contrast to computerization (Terzidis 2003), in architectural design has definitely opened a new paradigm in architecture. The focus of this new design strategy has moved from the object to the process itself. Algorithms acquire the role of the new means of representation as the language that translates human thinking into the power of combination of computer-based processes, with implications both in architectural practice and in the academic sphere.

Although postgraduate courses on computational architectural design have become commonplace, many architecture schools still run a mainly conventional syllabus for their bachelor-degree courses, which forces students to initiate their training in one paradigm and to end up having to change it for the postgraduate training or professional practice, with the acute inconvenience that this may impose. This is the reason why ever more university lecturers and schools are becoming involved in the preparation of architectural geometry (Pottmann et al. 2007) courses to implement the computational paradigm at the beginning of the undergraduate period, which is exactly when students mould their way of thinking, conceiving, and expressing their architectural work (Menges and Ahlquist 2011).

Ideally, these courses should cover competences in mathematics, geometry, computation, algorithmics and digital fabrication in order to provide students with a meaningful workflow to foster their motivation and consequently their learning. However, integrating an introduction on these disciplines in a single geometry course for beginner university students is not an easy task. In addition to the drawbacks of working at this stage, a new problem arises for the faculty if the course is designed to be guided by an original and attractive task that consistently includes the desired competences and without assuming impossible-to-achieve goals. This constitutes the design of a project or the ideation of a system appropriate for the aforementioned purposes.

This paper is intended to show the research carried out within the described context in order to provide a consistent architectural system that matches the needs of the new conception of architectural design for the initial stages of the undergraduate training period by integrating the newly required competences with traditional geometrical contents which provide competences further to those being rendered under the use of the new digital tools.

In this search among the variety of possibilities for an architectural system that holds appropriate contents for first-year students, three themes stand out as playing a major role in the research results shown in this paper. Although they appear to be classic geometry topics to be included in a geometry course under the paradigm of computational design, they remain under consideration due to two main factors: their benefits in understanding architectural history and conventional compositions, and their possible contributions towards the new paradigm. These themes include:

**Figure 1.** Photograph from the interior of the Archimedean Pavilion prototype, composed of inclined rotational parabolic domes materialised with lightweight conical components.

- Working with classic surfaces, which provides essential contents and competences that enable the student to address surfaces of a more complex nature at a later stage. In the case of this paper, rotational paraboloids.

- Understanding projective relationships, not only for representational purposes, but also as a source of composition and as a method to generate simpler algorithms for solving three-dimensional problems. In this case, a discretisation method based on a projective interpretation of an Archimedean property of rotational paraboloids is used.

- Using developable surfaces to materialise double-curved surfaces and complex compositions. This includes the use of digital fabrication for planar sheets of material, subsequently manipulated to form the three-dimensional shapes. In this case, elliptical and irregular conical surfaces to generate a lightweight component to populate the parabolic surface over the previous discretisation method.

The combination of these three topics, originally intended as part of a pedagogical plan, resulted in the constructive system developed in this paper: the use of hollow lightweight components made up of conical surfaces to materialise a specific discretisation of rotational paraboloids. The aim is to get economy of material, good structural behaviour, and ease of assembly to conform an efficient system for wide-span structures against the use of solid boundary rings for rotational parabolic domes.

# 2. An Archimedean Property of Rotational Paraboloids

Archimedes of Syracuse (287–212 B.C.) provides the background to this work. In his work "On Conoids and Spheroids", which can be consulted on Heath's translation into English (Archimedes 1897), among other topics, Archimedes proves the properties of various planar sections of rotational paraboloids. A projective interpretation of a theorem included in this work provides the starting point.

## 2.1 Archimedes' Proposition as a Projective Property

In "Proposition 12" of "On Conoids and Spheroids" Archimedes states that the planar section of a paraboloid of revolution, produced by a plane neither parallel nor perpendicular to the axis, is an ellipse. He then identifies the position of the major axis and proves that the minor axis is equal to the perpendicular distance between the two lines, parallel to the axis of the paraboloid, which pass through the extremes of the major axis.

Although it obvious that Archimedes does not refer to the definition of the ellipse as a projective property of the paraboloid, he uses lines parallel to the axis of the paraboloid (rays) and the orthogonal distance between them to define the minor axis. In terms of normal projection, it could be stated that the axes of the ellipse, on the surface of the paraboloid, are projected onto a plane perpendicular to the axis, with the same length; that is, the projection of the ellipse is a circle (Gentil Baldrich 1997).

In other words, by using the parallel projection defined by the direction of the axis of the paraboloid, any circle on a plane perpendicular to the axis of the paraboloid is projected onto the paraboloid's surface as an ellipse, which is a planar curve. This property, which is a particular case of a generalised theorem for rotational quadrics (Martin-Pastor, Narvaez-Rodriguez, & Hernandez-Macias 2016), means, among other things, that any circle-packing arrangement can be projected onto the paraboloid to obtain a discretisation of the surface based on planar elliptical faces tangent to each other at various points of the boundary.

## 2.2 Discretisation of Rotational Paraboloids

From the materialisation point of view, the previous theorem can be applied in several ways, not only for the whole circular base of the paraboloids, but also for any bounding area on the perpendicular plane. Additionally, there is also a variety of possible ways to materialise any initial discretisation: elliptical planar faces, polygonal planar faces, elliptical rings, elliptical arc-based frames, etc.

Whatever the arrangement chosen, it must be taken into account that ellipses increase their eccentricity the further away they are from the vertex of the
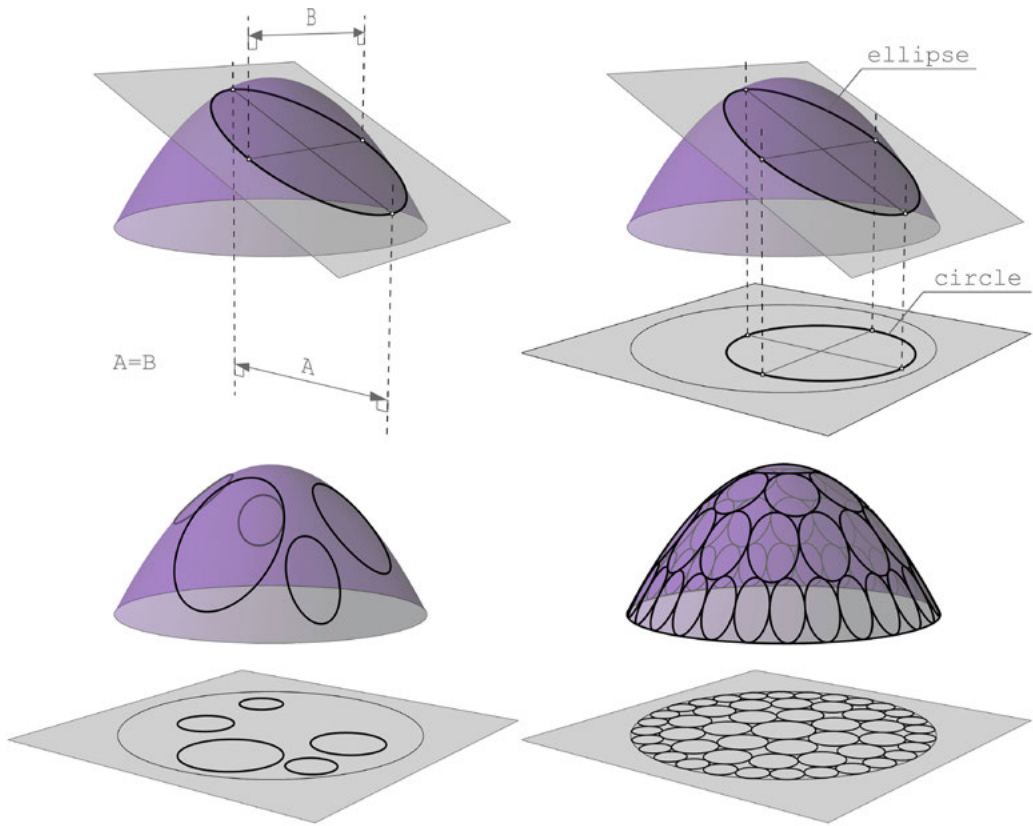
**Figure 2.** Top-left: Archimedes' definition of the minor axis of the ellipse (oblique planar section of the paraboloid) as the perpendicular distance between the lines parallel to the axis of the paraboloid passing through the extremes of the major axis. Top-right: Projective interpretation; the normal projection of the ellipse onto a plane perpendicular to the axis of the paraboloid is a circle. Bottom-left: with same normal projection, the projection of circles onto the paraboloid's surface as ellipses. Bottom-right: Discretisation of the paraboloid's surface with planar elliptical faces stemming from a circle-packing algorithm.
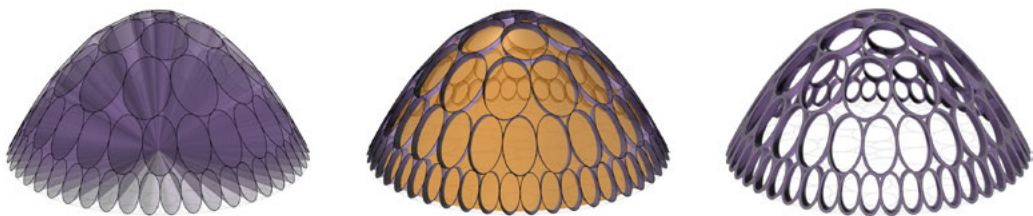


**Figure 3.** Left: Discretisation of the dome with elliptical rings and generation of the cones by extruding the ellipses to the centre of the base of the dome. Middle: Offset surface to trim the apex. Right: Thickening of the conical rings as an immediate solution to acquire rigidity.

paraboloid due to the increase in the slope of the surface, and hence the algorithm used for packing must implement control of this deformation by selecting the appropriate radii for the circles, in accordance with their position with respect to the centre of the paraboloid and the material and constructive constraints of the project.

This paper focusses on the design and analysis of a specific materialisation of rotational parabolic domes, which uses the resultant elliptical rings as the starting point. From the possibilities of materialising these ellipses, the one chosen is based on the construction of conical surfaces by extruding all the ellipses to a common apex. This is a principle that was already used by other authors in applications to spherical surfaces, such as the Packed Pavilion (Leidi et al. 2010) (Beorkrem 2013). However, further to the discretisation method and the fact of working with parabolic surfaces, there exists another circumstance which differentiates this research from the Packed Pavilion: the way in which the resultant elliptical cones are rigidified to provide global stability to the structure.

The immediate solution to providing rigidity to a conical surface, regardless of its material, is to thicken the surface up to the desired strength. Nevertheless, this solution can be prohibitively expensive due to the considerable amount of material needed, and it would impose a major increase in weight in real architectural applications beyond the construction of prototypes. Therefore, the objective is to conceive a more efficient system to rigidify the conical surfaces, whose use remains feasible in real architectural practice.

# 3. Lightweight Conical Components

The methodology used for conceiving a lightweight conical component can be related in different stages. The starting point is the design itself of a rigid geometrical shape from the elliptical cones. Once designed, the feasibility must be proved from two points of view; first the structural behaviour, and second the fabrication and assembly constraints. Finally, an optimisation process to minimise the amount of material is desirable. The main considerations of this process, together with the results obtained, are explained in the following points.

## 3.1 Geometry and Rigidity

Instead of adding material to the initial conical surface, sheets of material could be considered and a satisfactory three-dimensional shape could constitute an increase in the mass moment of inertia of the cross-section of the ring, and consequently provide a higher rigidity to the ring. In the search for a simple arrangement with the use of developable surfaces, the solution adopted consists of a set of three conical surfaces, which make up a triangular cross-section on the
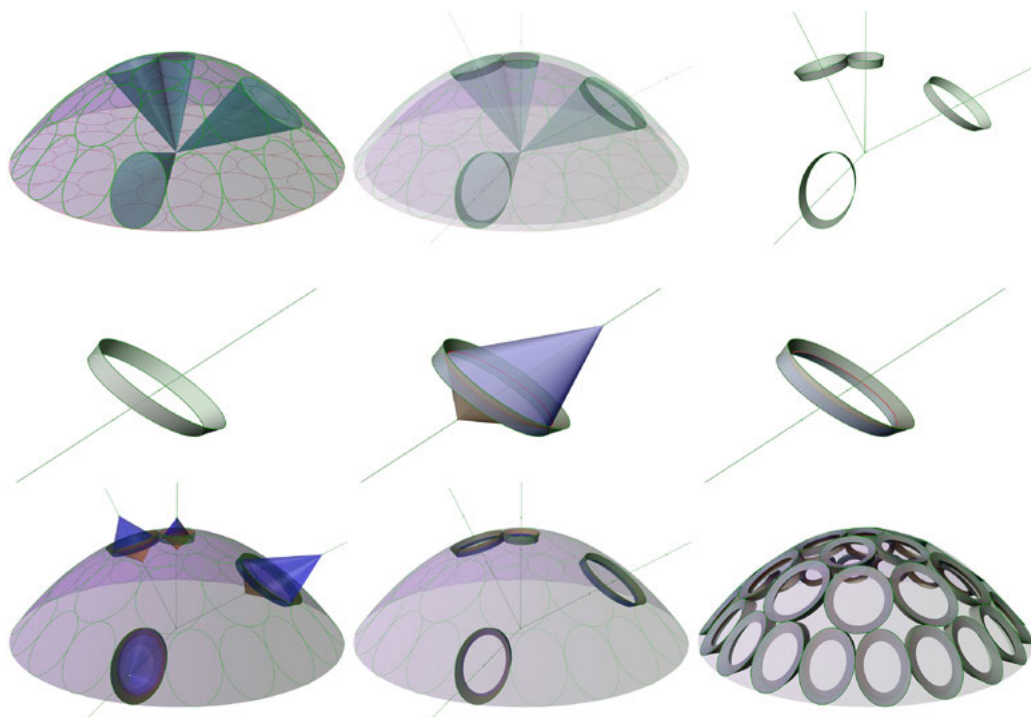
**Figure 4.** Top row: Initial discretisation, extrusion of four sample conical surfaces and the resulting truncated conical surfaces produced by the section with an offset surface. Middle row: Rigidification of the truncated conical surface by generating a component with two new cones with collinear vertices with the original cones. Bottom row: Reproduction of the previous rigidification for the four sample conical surfaces and the resulting dome by applying the process to all the elliptical rings.



**Figure 5. Left:** Photograph of the unrolled conical surfaces before assembly. Right: Result of the conical component after assembly and the emergence of the desired structural rigidity.

ring; the initial lateral surface of the elliptical conical ring, and two new cones, whose vertices are collinear with the original cones, and whose bases are coincident with the two existing bases of the initial truncated conical surface.

There are two major considerations to bear in mind when designing the component. The first is that of the triangular cross-section of the ring, which can be parameterised in the model according to various factors, such as the inner span desired (for lighting or other purposes) among others, but the most important factor is that relative to the rigidity of the component and the stability of the whole structure. As the mass moment of inertia of the cross-section strongly affects the rigidity of the component, the first factor to take into account must be the forces acting over the ring and provision of the cross-section matching the resistance needs. The second consideration is the aforementioned increasing eccentricity of the rings as they are further from the vertex of the paraboloid. In addition to the aesthetic repercussions, this also has implications on the structural behaviour. Both considerations are analysed in the following point (structural behaviour and optimisation).

The simple bending and assembly of low-rigidity sheets of polyethylene provides an idea of the effectiveness of the system due to the emergence of a surprising rigidity of the component just after the assembly of unrolled surfaces, whose initial rigidity is not enough to avoid the deformations due to their own weight. As many other emergent phenomena in nature (Weinstock 2010), the emergence of a good structural behaviour, out of simple low-rigidity elements, is by itself a first index of the efficiency of a system. In addition, active bending is also a sign of economy of material use (Lienhard et al. 2013). However, in the next point this will be technically tested.

## 3.2  Structural Behaviour and Optimisation

Once the component is designed, the first property to prove from the structural point of view is its rigidity, and the amount of material necessary to acquire it, compared to the solution of a solid boundary ring resulting from the thickening of the initial conical surface. A finite element analysis of the two components was therefore carried out over two equal sets of rings composed of steel sheets, with different eccentricities and subject to the same loads. The results are clear and enough reason to reject the solid boundary ring for its use in many architectural applications:

- The first test assigns the same amount of material and the same axial force, 2 kN, to the two systems. In the case of the lightweight conical component, a sheet thickness of 0.5 mm keeps the deformation under 1 mm, whereas a 1.5 mm-thick solid boundary ring (the same amount of material) reaches inadmissible values, thereby producing the collapse of the rings.
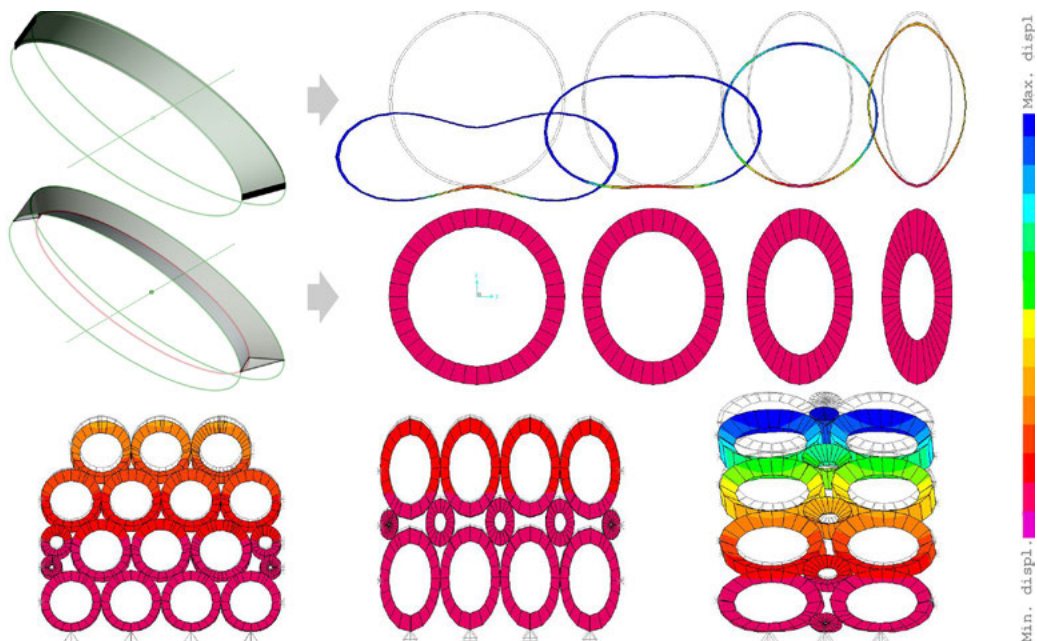
**Figure 6.** Top: Comparison of the solid boundary ring with the lightweight conical component (triangular cross-section). The rings analysed are made of steel and have a diameter of 1.2 m. Against the same loads, when the amount of material is the same, the deformation of the lightweight conical component is insignificant compared to the solid boundary ring. To perform the same deformation, the lightweight conical component needs a sheet of 0.5 mm thick whereas the solid boundary ring needs a plate of 30 mm thick (about 20 times more material). Bottom row: Comparison of the behaviour in groups of the lightweight conical component according to the eccentricity and the orientation of the ellipses.

- The second test strives towards finding the necessary amount of material such that both systems perform the same deformation against the same axial force of 2 kN. The lightweight conical component suffices with the thickness of 0.5 mm, whereas the solid boundary ring needs a thickness of 30 mm to match the same deformation. This contains up to 20 times more material than the lightweight conical component, thus having a weight twenty times heavier.

After testing the effectiveness and economy of the material of the lightweight conical component, the optimisation of the design is desirable in order to render the system even more efficient. There are numerous factors that carry influence, some of which are intrinsic to every component, due to their geometry, while others are produced by circumstances external to the component,

such as the value and the direction of the loads acting upon it, the position of the component within the whole structure, the number of tangency points with the adjacent components, etc. All these factors should be taken into account for every project in which the system is used, and it is always necessary to perform a customised optimisation to obtain the best results. Nevertheless, in order to facilitate the initial design and to take certain variables into account in the parameterisation, an additional analysis was carried out to facilitate the following conclusions being drawn about three important factors illustrated with the examples of deformation diagrams and the Pareto curves for the multi-objective optimisation (minimum material and minimum deformation):

- *Eccentricity of the components and loads*. Due to the constant existence of eccentricities of the initial ellipses, it is important to analyse the main influence of this factor in the structural behaviour. The diagrams show how the behaviour differs along the two different axes of the elliptical components. Two conclusions can be drawn in this sense: (1) The more eccentricity there is involved, the more widely different is the behaviour along each axis. (2) The loads parallel to the major axis are better supported than the loads perpendicular to this axis and are also better supported by components of a more eccentric nature than by those less eccentric with the same diameter.
  Taking into account that the most eccentric ellipses are located near the boundary of the base and linked to the ground, due to the nature of the discretisation method itself, and as long as the axis of the dome is vertical, then this factor turns out to be beneficial for the spreading of the forces. Since the axial forces concentrate as they approach the ground, this is where the most eccentric components lie.

- *Cross-section of the components.* The triangular section of the components is crucial for the success of the system and has a determining influence on the optimisation of the structure. On the one hand, there are three tests, each of which has a set inner radius of the component, a set area of the cross-section and a range of different proportions of the cross-section. The result in the optimum section, minimum amount of material and minimum deformation, varies depending on the inner span, although the values range around the equilateral section, for which the same amount of material supports a greater load than in the other cases. However, not only does the optimum depend on the proportion of the section, but also on the ratio between the area of the triangle and the inner span of the component measured in a perpendicular direction to the cross-section considered.
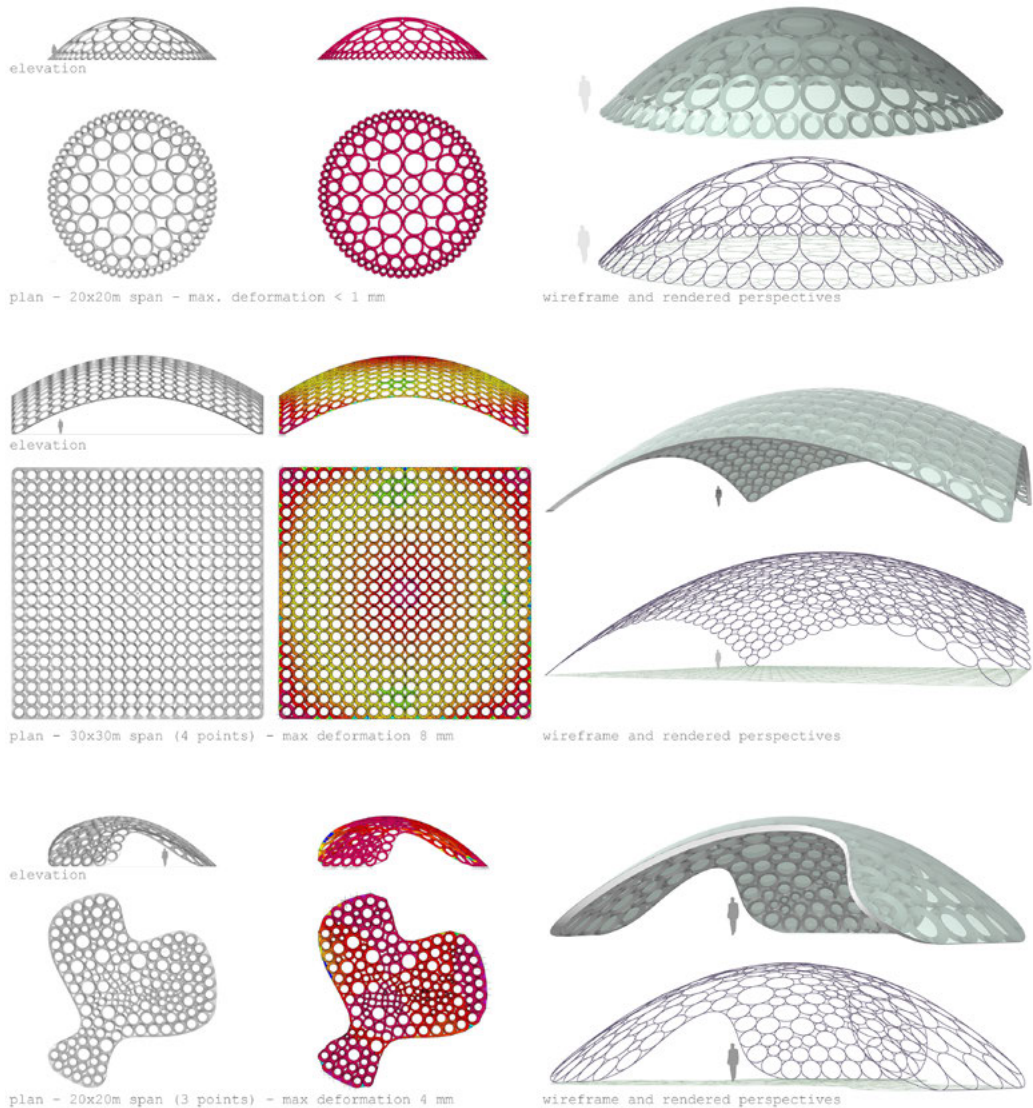
**Figure 7.** Feasibility of the system with three different wide-span design examples stemming from rotational paraboloids. The maximum deformations of the component system shown (finite element analysis) are for lightweight conical components executed with 0.5-mm-thick steel sheets and subject to the dead load of its own structure. Top row: Dome with a diameter of 20 m with a maximum deformation smaller than 1 mm. Middle row: Roof of 30 m x 30 m only resting on its four corners, with a maximum deformation of 8 mm. Bottom row: Pavilion with a diameter of 20 m resting on three boundary segments, with a maximum deformation of 4 mm.

The Pearson correlation coefficient between that ratio and the deformation of the component for a set external force is -0.98. Hence, for a set triangular section, there is better behaviour if the perpendicular inner span of the component is shorter. Since the triangular section of an eccentric component is variable along the boundary, the determination of the optimum turns out to be more complex than it may seem at first sight. Nevertheless, for a circular component with a constant equilateral cross-section, the optimum ratio between the height of the triangle and the inner span of the component is about 1/4.5.

- *Number of connections with adjacent components*. This factor seems to be obvious, but is still worth mentioning; the more connection points there are evenly spaced along the boundary, the more stable the component becomes. This is a factor that can be controlled via the initial circle-packing algorithm, in an effort to avoid non-triangular gaps between components.

## 3.3 Fabrication and Assembly Constraints

As far as digital fabrication and assembly of isolated components are concerned, this system, based on the use of laminar materials, is simple to execute and is normally fabricated from standard sheets or panels cut with a laser cutter or CNC milling machines. As in many other systems, the success of the constructive system relies on achieving consistency between the model for the structural analysis and the real execution of the components. In this sense, after the experience of constructing a full-scale prototype (the Archimedean Pavilion) there are three types of joints to execute with special care:

- *Surface seam.* When preparing the detailing algorithm for the digital fabrication, the unrolled development of the three conical surfaces involved must accomplish two important conditions. (1) The origin surface seam must be placed at a common location for the three surfaces to have a common origin for all the issues occurring on all three surfaces. (2) Additionally, the location of the seam must not coincide on high-curvature segments and should finally be executed obliquely to the generator of the surface. This ensures the continuity of the surface curvature after bending the sheet. The joint itself could be executed in many ways, but in this prototype an internal joint strip with rivets is the chosen solution.

- *Joints between the component's surfaces.* The most important property in the theoretical model that must be preserved in the execution is the continuity of this joint. In practice, this joint should be welded, in the case of weldable materials, or performed to work continuously. Maybe in the case
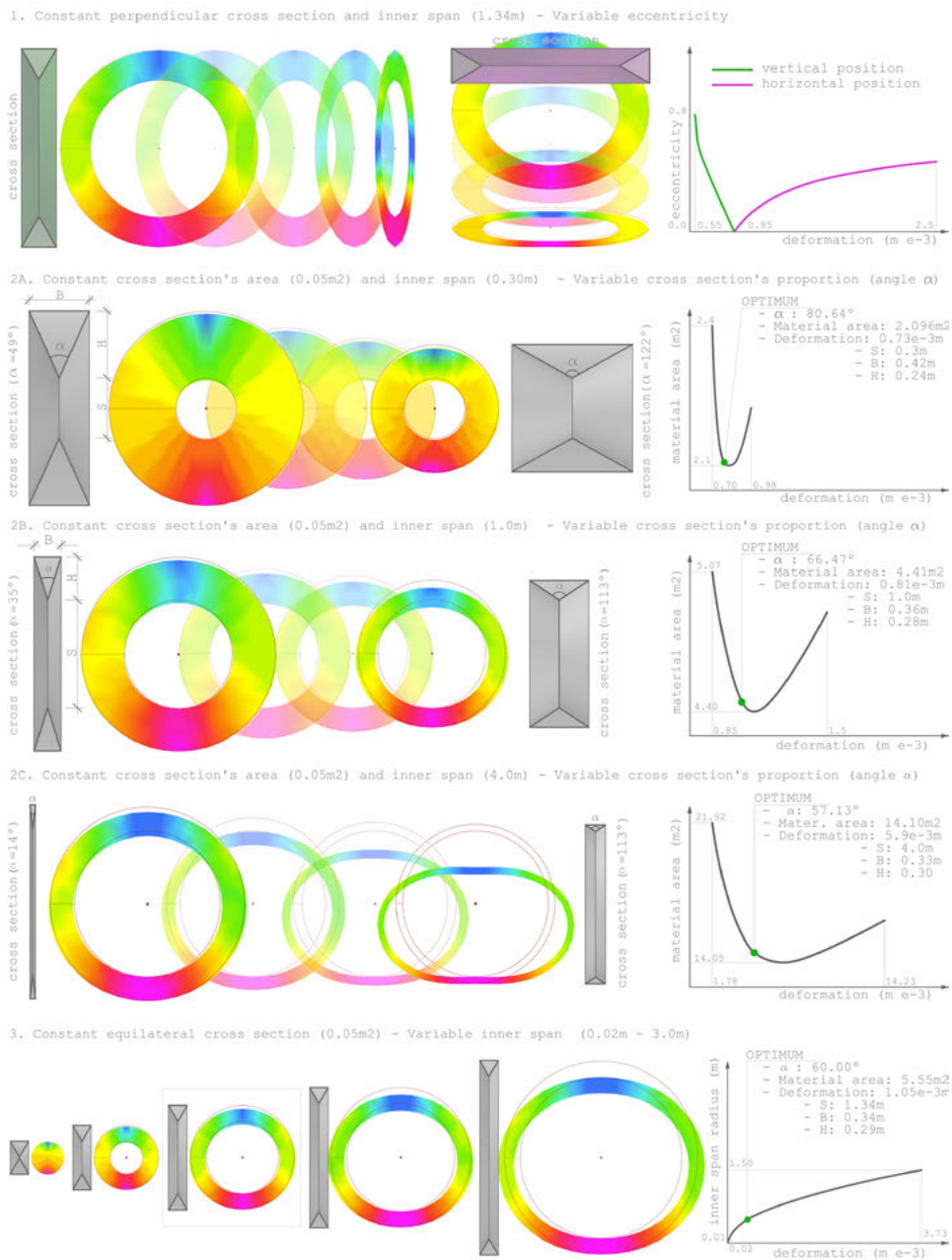
**Figure 8.** Finite element analysis to draw conclusions about the structural behaviour. Top row (1): Eccentricity tests and deformation graphs according to the position of the components. Three middle rows (2): Variable cross-section tests for three different inner spans and the graphs with the Pareto curves to determine their optimum. Bottom row (3): Tests on the constant equilateral cross-section with variable inner span. The optimum is a ring with equilateral cross-section and with an inner span of between 4 and 5 times the height of the triangle.

of wooden panels, a fingerjoint could provide a good solution, although it has yet to be tested by the team for these components.

- *Connections between various components*. Although the theoretical model is analysed with a continuous joint along the tangency line between adjacent cones, the practice has proved that this continuity is not as important as the previous continuity. It may be substituted by two bolts with nuts at the extremes of the tangency line, as long as there is a rigidifying element between the two points and the screws are tightened sufficiently to provoke a strong contact and friction between the two components.

It is also worth mentioning that glazing or panelling is feasible for the system. The plane containing the external ellipse of the components can be extended until it meets its neighbours, thus facilitating the creation of a 3D irregular mesh of planar faces which also has projective relationships with the initial circle packing; the projection of the mesh edges onto the circle packing plane results in a 2D Voronoi power diagram (Aurenhammer 1987).

## 3.4 Full-Scale Prototype

The teaching experience mentioned at the beginning of this paper was finally concluded with the installation of a full-scale prototype: the Archimedean Pavilion. Although the design remains part of the research carried out by the lecturers, students have participated in the process since the onset. They solved, with the help of their tutors, all the geometrical problems: parametric definition, through propagation-based systems (Aish & Woodbury 2005), to explore the design space composed of inclined rotational paraboloids; parametric definition to discretise the parabolic surfaces; parametric definition for the detailing and digital fabrication, assembly of rings, and the setting up of the installation.

Due to budget limitations, facilities available, and safety reasons, the material chosen for the prototype was high-density polyethylene (HDPE) in sheets of 1 mm thickness. The main advantages of this material include the laminar behaviour for the assembly process, similar to that of metal sheets or thin wooden panels in real applications, the cost, the lightness, the ease, and safety of use, since the manipulation and processing was wholly carried out by students and lecturers, and finally the possibility of testing all the assembly and setting up processes on a 1:1 scale upon a pavilion of about 10 x 6 m. On the other hand, this material presents certain properties that render it as non-appropriate for installations intended to last: non-linear deformation, variable behaviour according the temperature, and, mainly, creep or cold flow, which causes it to continue deforming when exposed to high levels of stress over long periods.

**Figure 9.** Two pictures and a photograph of the connections between components, including the drilling for the screw and the opening to operate on it.
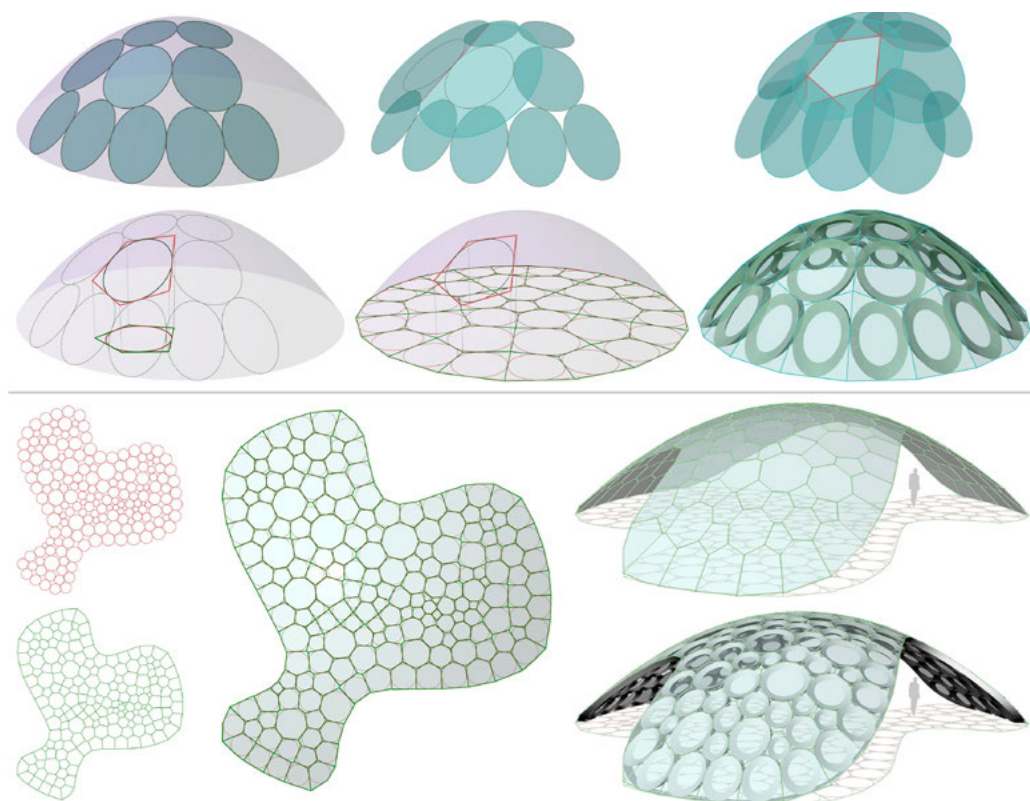


**Figure 10.** Generation of a mesh of planar faces containing the external ellipse of the components for glazing or panelling. Top: Geometrical operations to generate the mesh, projective relationship and the resulting glazing over the components. Bottom: Top view of another example of the same process including circle packing (red), 2D Voronoi power diagram (green), and 3D mesh over the circle packing (middle). Pictures of the result without and with the components.
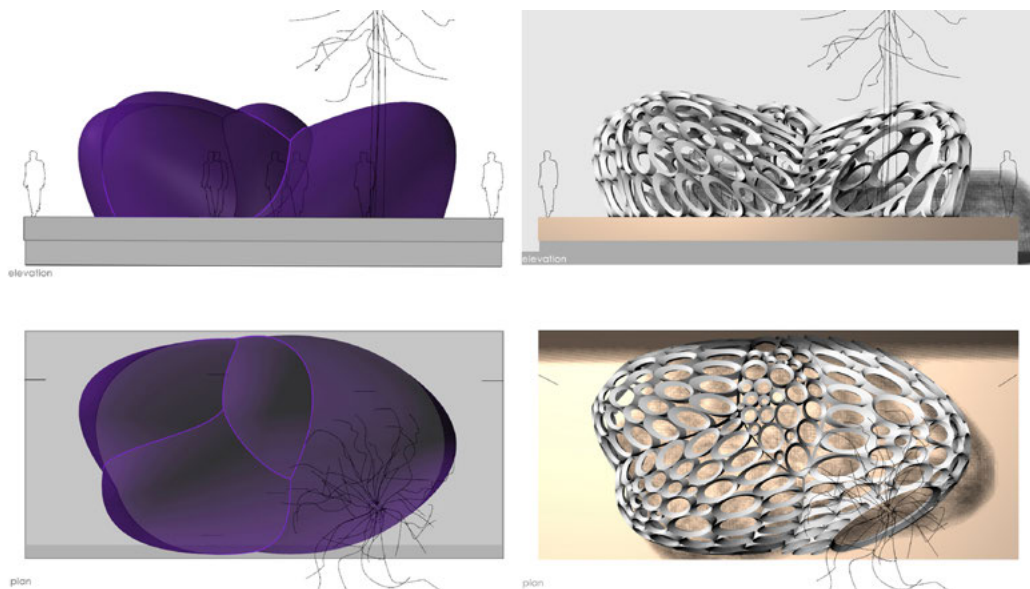
**Figure 11.** Left: Pictures of the composition with inclined rotational paraboloids which make up the space of the Archimedean Pavilion. Right: Picture of the resulting discretisation and materialisation with lightweight conical components.

# 4. Conclusion

The implementation of the paradigm of computational design in architecture at the beginning of the undergraduate training period, integrated into a geometry course, fosters the search for simple and ingenious geometrical solutions which may result in discovering applications for architectural practice in the real world.

The discretisation of rotational parabolic domes, based on the projective interpretation of the Archimedean property of oblique planar sections of the paraboloid, provides an appropriate framework to materialise this type of dome through the use of hollow lightweight conical components and facilitates the subsequent glazing or panelling.

In general, lightweight conical components provide an efficient system to materialise rotational parabolic domes. However, each component is rendered still more efficient under the following summarised conditions:

• When the axis of the rotational paraboloid is vertical.

• When the main loads are parallel to the major axis of the initial ellipses.

**394**

**Figure 12.** Photographs of the assembly and result of the Archimedean Pavilion.

- When the cross-section of the component is similar to an equilateral triangle and the inner span of the component, measured perpendicular to the cross-section, is approximately between four and five times the height of the triangular section.

- When there are several connections with adjacent components and these are evenly spaced along the boundary of the component.

In the fabrication and assembly process of the components, three types of joints must be carefully and accurately executed in order to match the theoretical conditions of the analysis, and consequently to ensure their expected behaviour; the seam of the surface, the joints between the surfaces of the component, and the connections between different components.

The materialisation system based on lightweight conical components provides economic use of material, good structural behaviour, and ease of assembly to form an efficient system for wide-span structures as opposed to the use of solid boundary rings, not only for parabolic domes, but also for a possible translation to other types of surface discretisation.

## Acknowledgements

# References

Aish, Robert, and Robert Woodbury. 2005. "Multi-Level Interaction in Parametric Design." *Smart Graphics*, 151–62. doi: 10.1007/11536482_13

Archimedes. 1897. *The Works of Archimedes*. Edited by T. L. Health. First edit. London: Cambridge University Press Warehouse. Accessed at https://archive.org/stream/worksofarchimede029517mbp#page/n9/mode/2up

Aurenhammer, Franz. 1987. "Power Diagrams: Properties, Algorithms and Applications." *SIAM Journal on Computing* 16, 1: 78–96. doi: 10.1137/0216006

Beorkrem, Christopher. 2013. *Material Strategies in Digital Fabrication*. Edited by Wendy Fuller. New York: Routledge (Taylor and Francis Group). Accessed at http://www.amazon.com/Material-Strategies-Fabrication-Christopher-Beorkrem/dp/041553366X

Gentil Baldrich, José María. 1997. *Sobre La Intersección de Cuádricas de Revolución de Ejes Paralelos*. Seville (Spain): Departamento de Expresión Gráfica Arquitectónica. Universidad de Sevilla.

Leidi, Michele, Dominik Zausinger, Min-Chieh Chen, and Tom Pawlofsky. 2010. "Packed Pavilion." Accessed at http://packed-pavilion.blogspot.com.es/

Lienhard, Julian, Holger Alpermann, Christoph Gengnagel, and Jan Knippers. 2013. "Active Bending, A Review on Structures Where Bending Is Used as a Self-Formation Process." *International Journal of Space Structures* 28, 3: 187–96. doi: 10.1260/0266-3511.28.3-4.187

Martin-Pastor, Andres, Roberto Narvaez-Rodriguez, and Daniel Hernandez-Macias. 2016. "A New Theorem about Quadrics Intersections. Speculations Around a Property of Rotational Paraboloids Stated by Archimedes." *Forthcoming publication*.

Menges, Achim, and Sean Ahlquist. 2011. *Computational Design Thinking*. Chichester: Wiley. Accessed at http://fama.us.es/record=b2487754~S5*spi

Pottmann, Helmut, Michael Hofer, Andreas Asperl, and Axel Kilian. 2007. *Architectural Geometry*. Exton, PA: Bentley Institute Press. Accessed at http://www.bentley.com/en-US/Training/Products/Resources/Books/Architectural Geometry.htm

Terzidis, Kostas. 2003. *Expressive Form: A Conceptual Approach to Computational Design*. New York: Spon Press – Taylor & Francis Group. doi: 10.4324/9780203586891

Weinstock, Michael. 2010. *The Architecture of Emergence: The Evolution of Form in Nature and Civilisation*. Edited by Helen Castle, Miriam Swift, and Calver Lezama. Chicester, UK: John Wiley & Sons Ltd.

# Author Biographies

Robert Aish is Visiting Professor of Design Computation at the Bartlett School of Architecture, where his research into the use of nonmanifold topology to represent architectural space is supported by the Leverhulme Trust. Previously, he was Director of Research at Bentley where he led the development of GenerativeComponents, and Director of Software Development at Autodesk, where he led the development of DesignScript. He is also a cofounder of the SmartGeometry group. He studied Industrial Design at the Royal College of Art and has a PhD in Human Computer Interaction from the University of Essex.

Aleksandra Anna Apolinarska is an architect and a PhD researcher at Gramazio Kohler Research, ETH Zurich, specialising in design and planning of geometrically complex architectural projects. After graduating from the Poznan University of Technology and the University of Stuttgart, she worked for various architecture offices across Europe, including design-toproduction and Foster+Partners, where she was involved in a number of challenging projects, such as Apple Campus 2, Kuwait Airport, and NBK Tower in Kuwait. In 2013 she joined ETH Zurich, and later Arch-Tec-Lab AG, to lead the development of the "Sequential Roof" project in the post-tender and execution phase.

Edyta Augustynowicz is an architect with versatile experience in design, focussed on the application of computational techniques in the built environment. She graduated from the Technical University in Poznan, Poland, majoring in Architecture and Urban Design. In 2010, she obtained a Master of Advanced Studies degree from ETH Zurich at the Chair of Computer Aided Architectural Design. For several years, she was a part of the Digital Technologies Department at Herzog & de Meuron, where she worked on various scale projects providing digital tools and developing advanced building geometries. She joined the Block Research Group (BRG) at ETH Zurich in 2015 to support works for the Venice Architecture Biennale 2016.

José Antonio Barrera-Vera holds a degree in Building Engineering, a master's degree and a PhD in Graphic Engineering. He has worked as a lecturer and a researcher in the University of Seville (Spain) since 1992. He lectures in both undergraduate and graduate courses and is the Head of the Department of Graphic Engineering. He has published several articles, given workshops, lectures and presented papers in several cities. His main research interest lies in the development of techniques for the documentation of complex geometries through the use of laser scanner and photogrammetry.

Olivier Baverel is Senior Researcher at Navier lab., Ecole des Ponts and Professor at the School of Architecture of Grenoble. He is Editor-in-Chief of the International Journal of Space Structures. His research focusses on grid shells, reciprocal systems, deployable structures, geometrical and structural rationalisation of free-form architecture.

Andreas Bærentzen is Associate Professor at the Department of Computer Science and Applied Mathematics, Technical University of Denmark, where he also received his MSc and PhD degrees. His research focus is on the representation and manipulation of digitally represented shapes, but he is broadly interested in computer graphics and geometry processing.

Ralph Bärtschi is a physicist and mathematician with long-time experience in software development and the direct control of computer-controlled machines for fabrication. He has profound knowledge in digital signal processing, geometric algorithms, and numerical methodologies. He is a founding partner of ROB Technologies AG.

Simon Bechert is a structural engineer and Research Associate at the Institute of Building Structures and Structural Design (ITKE) at the University of Stuttgart. His main research focusses on lightweight timber constructions and the structural design of integral timber joints.

Philippe Block is Associate Professor at the Institute of Technology in Architecture, ETH Zurich, where he directs the Block Research Group (BRG) together with Dr. Tom Van Mele, focussing on equilibrium analysis, computational form finding, optimisation, and fabrication of curved surface structures. He studied architecture and structural engineering at the Vrije Universiteit Brussel in Belgium and the Massachusetts Institute of Technology (MIT) in the USA, obtaining his PhD in 2009. With the BRG and as founding partner of Ochsendorf DeJong & Block (ODB Engineering), he applies his research to practice on the structural assessment of historical monuments and the design and engineering of compression structures.

Pengbo Bo is an Associate Professor at Harbin Institute of Technology at Weihai, China. His research interests are geometric modelling and geometry processing. He received his PhD. from the University of Hong Kong, where he worked on the problem of freeform surface modelling using Dupin cyclides and developable surfaces. He also received a B.S. and a M.S. degree in Computer Science from Shandong University, in 1997 and 2001, respectively.

Etienne Bouleau has degrees both in civil and geotechnics engineering. After graduation, Etienne Bouleau started his career at RFR office in Paris to work on lightweight and glazed structures, where he worked mainly on the Louis Vuitton's Foundation project. Etienne joined the INGENI SA team in 2010 and focusses on research and development to design vanguard structures such as the Jet d'Eau footbridge in Geneva.

David Brander is an Associate Professor of Mathematics at the Technical University of Denmark. He grew up in Australia and was educated in mathematics, physics, and computer science at Adelaide, Oxford, Univ. Penn. and the Australian National University. He has been at DTU since 2008, after completing postdoctoral positions at the TU Munich and Kobe University.

Cristián Calvo Barentin holds a degree in architecture from the Universidad Técnica Federico Santa María, Chile. He co-founded an electronics development firm, where he worked as an interaction designer. He also worked as a teaching and research assistant at the Universidad Técnica Federico Santa María, where he was responsible for the introduction of industrial robot arms in an architectural design studio, a first for South America. His research at the Block Research Group (BRG) at ETH Zurich focusses on physical modelling of masonry vault collapse and bending-active structural systems using force-sensitive robotic arms.

Kenn Clausen is an architect and parametric designer at GXN, the research and innovation unit of 3XN Architects in Denmark. He attended Aalborg University, specialising in architecture and digital design. He implements and utilises digital tools, workflow strategies, and advanced design technologies in a number of large-scale building projects from the new IOC headquarter in Lausanne to residential towers in Mumbai. He runs Bladerunner at GXN, a research project regarding the implementation of robot technologies in concrete formwork fabrication. His work experiences include Electrotexture LAB in Denmark and UNStudio in Amsterdam.

Xavier De Kestelier is Joint Head of Foster + Partners' Specialist Modelling Group. He has worked on Beijing Airport, Kai Tak Cruise Terminal, Kuwait Airport, and the Yachtplus super yachts. His team has been involved in ground-breaking research in the field of large-scale 3D printing as part of a consortium set up by the European Space Agency to explore 3D printing to construct lunar habitations. Xavier has been a Visiting Professor at Ghent University, Adjunct Professor at Syracuse University, a Teaching Fellow at The Bartlett School of Architecture and since 2010, one of the directors of Smartgeometry.

Mira Dedijer studied Civil Engineering at the University of Novi Sad, Serbia, and completed her Master degree in Structural Engineering in 2011 with main focus on concrete structures. Mira Dedijer gained her professional experience as a structural engineer in one of the leading designing companies in Bosnia and Herzegovina Projekt a.d. Banja Luka, being engaged in a variety of projects such as business and residential buildings, clinics, hydro power plants, and the design, construction and modernisation of roadways. In her research work she now focuses on the digital design of timber shell structures. Since 2015, she is a PhD researcher at the Timber Construction Laboratory IBOIS at EPFL Lausanne and the NCCR Digital Fabrication.

Cyril Douthe is a researcher at the IFSTTAR, Department of Material and Structural Engineering and Assistant Professor at the Ecole des Ponts ParisTech. His research activities cover aspects of structural morphology and design of lightweight structures, with an emphasis on problems of geometrically nonlinearity and instability.

Lluis Enrique Monzo received a Diploma in Architecture from the Polytechnic University of Catalonia (UPC) in 2008 and a Master of Architecture from the Architectural Association School of Architecture (AA) in London in 2011. His Master's thesis, entitled "Cast on Cast System: Architectural Freeform Shapes from Precast Stackable Components", was awarded prizes by the Holcim Foundation in Sustainable Construction in 2011 and 2012. In 2011, he received a grant to do doctoral studies from the La Caixa Foundation. Currently, he is finishing his PhD at the Chair of Structural Design lead by Professor Joseph Schwartz in the Swiss Federal Institute of Technology Zürich.

Ursula Frick holds a degree in architecture from the University of Innsbruck. She worked as architect and consultant in computational design and digital fabrication in the EU and the USA. She has held workshops and lectured at the AA, PennDesign, SCI-arc, and Tamkang University Taipei. In 2007, together with Thomas Grabner she founded the collective [uto]. They developed several software plugins that enhance workflow in parametric software. In 2014, she joined the Block Research Group (BRG) at ETH Zurich as PhD researcher in the NCCR Digital Fabrication. Her current research is concerned with structural design of discrete-element assemblies, taking into account constraints imposed by digital fabrication and automated assembly processes.

Reto Furrer is a structural engineer with special competences in lightweight structures, wind engineering, and parametric design. After receiving his engineering degree at Lucerne University of Applied Sciences and Arts (HSLU) he worked as a scientific assistant at the Competence Center Façade and Metal Engineering at HSLU (2008 – 2010). Since 2009 he is part of the firm Dr. Lüchinger+Meyer Bauingenieure AG in Zurich. As a senior engineer, an active member of the structural mechanic group as well as an experienced project leader, Reto Furrer has been responsible for many outstanding Swiss and international projects such as the wooden roof structure of the Arch_Tec_Lab building at ETH Zurich.

Fabio Gramazio is an architect with multi-disciplinary interests ranging from computational design and robotic fabrication to material innovation. In 2000, he founded the architecture practice Gramazio Kohler Architects in conjunction with his partner Matthias Kohler, where numerous award-wining designs have been realised. By opening the world's first

architectural robotic laboratory at the ETH Zurich, their research has been formative in the field of digital architecture, merging computational design and additive fabrication through the customised use of industrial robots. Fabio Gramazio's work has been widely published and internationally exhibited, and is comprehensively documented in the book "The Robotic Touch – How Robots Change Architecture".

Jens Gravesen is Associate Professor at Department of Computer Science and Applied Mathematics, Technical University of Denmark. He received his Cand. Scient. degree (MSc) in mathematics and physics from the University of Copenhagen in 1980 and his D.Phil. degree from Oxford University in 1988. His research area is geometry, in particular geometric modelling. He has published numerous papers in international journals, books and conference proceedings, has served as program officer for SIAM's activity group on geometric design, and is one of the organisers of the yearly European Study Group with Industry in Denmark.

Felix Günther earned his diploma degree in mathematics from Humboldt Universiẗat Berlin in 2011 and his Ph.D. from TU Berlin in 2014. As a fellow of the European Post-Doctoral Institute for Mathematical Sciences he is currently staying at the Max Planck Institute for Mathematics in Bonn. Before, he visited the Institut des Hautes É´tudes Scientifiques in Bures-sur-Yvette, the Isaac Newton Institute for Mathematical Sciences in Cambridge, and the Erwin Schrödinger International Institute for Mathematical Physics in Vienna. His research area is discrete differential geometry, in particular the theory of discrete Riemann surfaces.

Gabriele Guscetti is a civil engineer (EPFL) with a specialisation in structural engineering. He is also Founder Member and President of the Board at INGENI SA. Guscetti explores the use of different materials in the most original and innovative applications to achieve a conceptual and technical enhancement of the structure and thereby of the architectural project. He has carried out projects of different scales, from the smallest, most singular, to the largest, most impressive ones: Rolex buildings, Geneva, Langensand Bridge, Lucerne (Steel Award 2011), FIBA headquarters, Mies (Building Award 2015), Swiss Tech Convention Center, Lausanne, JTI headquarters, Geneva, and, the unique concept of a mobile footbridge to the Geneva Jet d'Eau.

Daniel Hambleton is the Director of MESH Consultants Inc., a Torontobased consulting firm that offers applied mathematics and development services to the digital design industry. He has worked extensively across a variety of markets, such as: architecture, product design, energy, software development, and engineering. Although his research is focussed on computational geometry and physics simulations, he has extensive experience with interdisciplinary projects and unique collaborations.

John Harding has studied and practiced as both an architect and engineer. He recently received his doctorate from The University of Bath in computational design, focussing on genetic programming for early-stage design exploration. His current research interests lie in structural form-finding, evolutionary computing, and machine-learning applications for design. He previously led the Ramboll Computational Design team in London before recently becoming Senior Lecturer in Architecture at the University of The West of England (UWE), UK.

Matthew Hayhurst studied Architecture at the University of Nottingham, graduating in 2007 with distinction. He was nominated for the RIBA President's Silver Medal. He joined Foster + Partners in 2007, working on a wide range of projects including The Sage Gateshead, Imperial College London, Corby Academy, and several international projects. He is currently the Lead Project Architect for the Edmond and Lily Safra Centre for Brain Sciences, which is currently under construction in Jerusalem and the mixed-use Royal Hamilius development in the heart of Luxembourg City. He is a visiting tutor and Lecturer at Nottingham and Birmingham City Universities.

Darron Haylock studied Architecture at De Montfort University, Leicester. He was made a Project Director at Foster+Partners in 2001 and a partner in 2004. He worked on the Thomas Deacon Academy project in Peterborough, which won the prestigious RIBA and Institution of Structural Engineer awards. More recently he worked as the Partner-in-Charge of Circle Hospitals, with sites at a variety of UK locations. He is also the Partner in Charge of Glebe Place, a high-end residential project in Chelsea, as well as being involved in several masterplan design competitions – in Beijing, Budapest, and Casablanca.

Caigui Jiang is a computer science Ph.D. student associated to the Visual Computing Center at King Abdullah University of Science and Technology (KAUST) in Saudi Arabia. He received his B.S. and M.S. degrees from Xi'an Jiaotong University in 2008 and 2011 respectively. His research interests include geometry processing, architectural geometry, and computer graphics.

Martin Kilian received degrees in Computer Science and Mathematics from Karlsruhe Institute of Technology in 2005 and a Ph.D. from TU Wien in 2008. From 2008 to 2014 he worked as a research assistant at TU Wien, where his research focussed on geometric folding algorithms and architectural geometry. With the support of a Erwin Schr̈odinger fellowship from the Austrian Science Fund, he spent 2015 as a research fellow at University College London, in the group of Niloy J. Mitra, returning to TU Wien afterwards.

Jan Knippers is partner of Knippers Helbig Advanced Engineering and Director of the Institute of Building Structures and Structural Design (ITKE) at the University of Stuttgart. He focusses in research and practice on innovative building structures and fibre-based materials.

Matthias Kohler is an architect with multi-disciplinary interests ranging from computational design and robotic fabrication to material innovation. In 2000, he founded the architecture practice Gramazio Kohler Architects in conjunction with his partner Fabio Gramazio, where numerous award-wining designs have been realised. By opening the world's first architectural robotic laboratory at ETH Zurich, their research has been formative in the field of digital architecture, merging computational design and additive fabrication through the customised use of industrial robots. Matthias Kohler's work has been widely published and internationally exhibited, and is comprehensively documented in the book "The Robotic Touch – How Robots Change Architecture". Since 2014, Matthias Kohler is also Director of the National Centre of Competence in Research (NCCR) Digital Fabrication.

Mina Konakovic studied Mathematics at the University of Belgrade, Serbia, where she received her Masters degree in 2014. Since 2015, she is a PhD researcher at the Computer Graphics and Geometry Laboratory at EPFL Lausanne and the NCCR Digital Fabrication.

Duks Koschitz is Assistant Professor of Design and Technology at Pratt Institute in Brooklyn and is the Director of the Design Lab at Pratt. He coordinates the first-year design sequence and integrates digital technologies in the curriculum. Duks wrote his dissertation on the curved-crease paperfolding work of David A. Huffman in the Design & Computation Group at the Massachusetts Institute of Technology. He has published articles on paperfolding, design theory and creative learning. He co-founded sparc, and worked as project architect at NMDA, Office da, Morphosis and Coop Himmelblau. Duks holds a Dipl.Ing. from the Technical University in Vienna.

Oliver David Krieg is a Research Associate and doctoral candidate at the Institute for Computational Design (ICD). With the completion of his Diploma degree in 2012 he also received the faculty's Diploma Price. With a profound interest in computational design processes and digital fabrication in architecture, he participated in several award-winning and internationally published research projects. In the context of computational design his research aims to investigate the architectural potentials of robotic fabrication in wood construction.

Riccardo La Magna is a structural engineer and PhD candidate at the Institute of Building Structures and Structural Design (ITKE) of the University of Stuttgart. In his research he focusses on simulation technology, innovative structural systems, and new materials for building applications.

Bruno Léger is a structural engineer and Technical Director at Quille Construction, a subsidiary company of Bouygues Construction. He has taken part in the design and planning of complex projects, like the Velodrome Stadium in Marseille.

Morten Norman Lund was educated as an engineer at Aalborg University, specializing in architecture. He has been at GXN as an architect for 5 years, working mainly on research projects that focus on materials, sustainability, and digital technologies as well as architecture projects. He is currently leading GXN's latest research into digital fabrication though the Digital Factory project. His current work at 3XN and GXN serves to bring digital tools into the later phases of the design process to allow more complex designs to be conceived and built.

Tomás Méndez Echenagucia is a postdoctoral fellow at the Block Research Group (BRG) at ETH Zurich. He holds a double degree in Architecture from Universidad Central de Venezuela and Politecnico di Torino, where he also obtained a PhD in Architecture and Building Design. He was awarded the Hangai Prize by the International Association of Shell and Spatial Structures in 2008. He has worked as an architect and a consultant on computational design in Europe and South America. His research is focussed on multidisciplinary search and optimisation tools for the early stages of architectural design, including acoustic, structural and environmental design.

Romain Mesnil is a structural engineer with master's degrees from MIT and l'Ecole des Ponts et Chaussées. He is currently a PhD candidate funded by Bouygues Construction at l'Ecole des Ponts et Chaussées in Paris. His research goal is to provide intuitive methods for geometrical and structural rationalisation of free-form architecture.

Zachary Mollica is a Canadian architect and maker whose work explores the integration of innovative digital methods alongside traditional craft knowledge. Zac completed his undergraduate studies at Dalhousie School of Architecture, Canada and has since worked for a number of architecture and design practices in Amsterdam, Lunenburg, Toronto, and Vancouver. Completing the Architectural Association's Design + Make programme in Hooke Park over the past 2 years, Zac led the development of the Tree Fork Truss within the Wood Chip Barn student project.

Josef Musil is an associate at Foster + Partners in London, as part of the research Specialist Modelling Group and focusses on applied research, application of new technologies, and algorithmic design to complex architectural and geometrical

challenges. He also specialises on the application of small robotics within the office. Josef studied as a Fulbright scholar at the University of Pennsylvania, where he received his MArch degree, and at the Czech Technical University. Josef is enthusiastic about bridging computer science or other sciences with architecture. Josef worked as a researcher or a tutor at UPenn, USC, UCL, and AA Visiting School.

Roberto Narváez-Rodríguez holds degrees in both Architecture and Building Engineering and a master's degree in Engineering. He has worked as a senior lecturer and a researcher at the University of Seville (Spain) since 1999. He lectures in both undergraduate and graduate courses and has been recognised with various awards on Excellence in Teaching and Architecture. He has published several articles, given workshops, lectures and presented papers in several cities. His main research interest lies in the integration of architectural geometry and digital technologies at the earliest stage of the undergraduate training period.

Paul Nicholas holds a PhD in Architecture from RMIT University, Melbourne, Australia. Having previously practiced with Arup Consulting Engineers from 2005 and AECOM/Edaw from 2009, Paul joined the Centre for Information Technology and Architecture (CITA), Copenhagen, Denmark, in 2011. Paul's particular interest is the development of innovative computational approaches that establish new bridges between design, structure, and materiality. His recent research explores sensor-enabled robotic fabrication, multi-scale modelling, and the idea that designed materials such as composites necessitate new relationships between material, representation, simulation and production.

Toke Bjerge Nørbjerg is a PhD student at the Department of Computer Science and Applied Mathematics, Technical University of Denmark. He received his Cand. Scient. degree (MSc) in mathematics from the University of Copenhagen in 2013. Toke's research concerns surface rationalisation in architecture, combining differential geometry, numerical optimisation and computational mathematics. His work forms the basis for a novel fabrication method for free-form surface designs.

Esben Clausen Nørgaard is a Research Assistant at the Centre for Information Technology and Architecture, Copenhagen, Denmark. He is a trained civil engineer with a specialty in architectural design from Aalborg University in 2014 and joined CITA following graduation. His primary research interest lies within prototyping, fabrication, and rationalisation. Since joining CITA, his primary focus has been on fabrication with industrial robots and how these can be used to create relationship between traditional craftsmanship and digital environments.

Mark Pauly is an associate professor at the School of Computer and Communication Sciences at EPFL. Prior to joining EPFL, he was assistant professor at the CS department of ETH Zurich since April 2005. From August 2003 to March 2005 he was a postdoctoral scholar at Stanford University, where he also held a position as visiting assistant professor during the summer of 2005. He received his Ph.D. degree (with distinction) in 2003 from ETH Zurich and his M.S. degree (with highest honors) in 1999 from TU Kaiserslautern. His research interests include computer graphics and animation, geometry processing, architectural geometry, shape modelling and analysis, and computational geometry. He received the ETH medal for outstanding dissertation and was awarded the Eurographics Young Researcher Award in 2006.

Mariana Popescu is a PhD researcher at the Block Research Group (BRG) and within the NCCR - Digital Fabrication at ETH Zurich. She holds a Bachelor and Master's degree in architecture from Delft University of Technology and has a strong interest in innovative ways of approaching the fabrication process and use of materials. Her current research focusses on knitted stay-in-place formwork for complex concrete structures. Previously, she was part of the start-up Hive Systems, developing a platform for complex interactive environments using distributed algorithms, and has been working as a parametric design specialist at Zwarts & Jansma Architects in Amsterdam.

Helmut Pottmann is Professor of Applied Geometry and Director of the Centre for Geometry and Computational Design at Vienna University of Technology. From 2009-2013, he was director of the Geometric Modelling and Scientific Visualisation Centre at King Abdullah University of Science and Technology. His research interests are in Applied Geometry and Visual Computing, in particular in Geometric Modelling, Geometry Processing and most recently in Geometric Computing for Architecture and Manufacturing. He has co-authored two books and more than 200 refereed articles.

Mette Ramsgaard Thomsen is a Professor and Head of Research Centre at the Centre for Information Technology and Architecture (CITA), Copenhagen, Denmark. Her research centres on the intersection between architecture and computer science. During the last 15 years her focus has been on the profound changes that digital technologies instigate in the way architecture is thought, designed and built. At CITA she piloted a special research focus on the new digital-material relations that digital technologies bring forth. By investigating advanced computer modelling, digital fabrication, and material specification, CITA has been central in the forming of an international research field examining the changes to material practice in architecture.

Gernot Riether is an Associate Professor at the College of Architecture and Design at the New Jersey Institute of Technology (NJIT), USA. In his Digital Design Build Studio he and his students develop and test new digital design and fabrication

methods. Previous projects from this studio include the AIA Pavilion in New Orleans, the Nuit Blanche Pavilion in Paris, the MAINX24 Pavilion in Chattanooga, and Urban Blanket in Atlanta. Riether's research has been exhibited internationally and is featured in prominent publications such as Architectural Record and DETAIL. Riether's studio has been funded by the AIA, the Austrian government, non-profit organisations, the industry, and universities.

Matthias Rippmann has been a member of the Block Research Group (BRG) at ETH Zurich since 2010, where he received his doctorate. In 2015, he joined the National Centre of Competence in Research (NCCR) Digital Fabrication at ETH as a postdoctoral fellow. He conducts research in the field of structurally informed design and digital fabrication and is lead developer of the form-finding software RhinoVAULT. He studied architecture at the University of Stuttgart and the University of Melbourne. He worked in Stuttgart at Behnisch Architekten, LAVA, the Institute for Lightweight Structures and Conceptual Design, and Werner Sobek Engineers. In 2010, he co-founded the architecture and consultancy firm Rippmann Oesterle Knauss GmbH (ROK).

Christopher Robeller is an architect and postdoctoral researcher at the Timber Construction Laboratory IBOIS at EPFL Lausanne. Christopher received his architecture diploma with distinction from London Metropolitan University in 2008 and worked at ICD Stuttgart from 2008-2010, where he developed integral timber plate joints for the award-winning ICD/ITKE Research Pavilion 2010. Since 2011 he is working at IBOIS and received a doctoral degree from EPFL in 2015 for his thesis entitled Integral Mechanical Attachment for Timber Folded Plate Structures. His research was published in journals and conferences such as Bauingenieur, ACADIA, RobArch and AAG, where he received the Best Paper Award 2014.

Elissa Ross is a Senior Associate at MESH Consultants Inc. She holds a PhD in mathematics from York University (Toronto) where her research focussed on the rigidity and flexibility of periodic (repetitive) structures. She has additional expertise in computational geometry, graph theory, and tilings/patterns, and a long history of collaborative and interdisciplinary projects. At MESH Consultants Inc., Elissa conducts research in architectural geometry, adds to the breadth of the geometry consulting services, and develops inhouse tools for 3D geometry applications.

Romana Rust studied architecture at TU Graz, Austria. With the diploma thesis "Integration of Digital and Physical Design Methods", which was awarded at both the GAD Awards 2012 and archdiplomaˇ13, she completed her architectural studies in 2012 with distinction. Together with Kathrin Dörfler, she founded the architecture collective dorfundrust. Since 2013, she is a PhD researcher at Gramazio Kohler Research at ETH Zurich focussing on adaptive fabrication techniques and their integration with computational design frameworks that place materiality as an a priori agent in the formulation of architectural building elements.

Simon Schleicher is an Assistant Professor in the Department of Architecture at the University of California, Berkeley. His transdisciplinary work draws from architecture, engineering, and biology. By cross-disciplinary pooling of knowledge he aims to transfer bending and folding mechanisms found in nature to lightweight and responsive systems in architecture.

Joseph Schwartz obtained his Diploma in civil engineering from ETH Zurich in 1981 and his doctoral degree in 1989. His dissertation was awarded the ETH silver medal. From 2001 to 2008 he was professor at the Lucerne University of Applied Sciences and Arts. Since 2008 he is Full Professor of Structural Design at the Department of Architecture at ETH Zurich. He is co-author of "Design of Concrete Structures with Stress Fields" (1996) and "Mauerwerk" (1998). From 1991 to 2001 he was associate partner of a consulting office in Zug. Since 2002 he is owner of a civil engineering office in Zug.

Tobias Schwinn is a Research Associate and doctoral candidate at the Institute for Computational Design (ICD). In his research he focusses on the integration of robotic fabrication and computational design processes. Prior to joining the ICD in January 2011, he worked as a Senior Designer for Skidmore, Owings and Merrill in New York and London applying computational design techniques to parametric form-finding, rationalisation, complex geometry, automation and environmental design.

Martin Self is Director of Hooke Park and Programme Co-Director of the March Design + Make programme based at Hooke Park, the Architectural Association's Woodland Campus. Holding degrees in aerospace engineering and architecture theory, he worked as a consultant engineer at Ove Arup & Partners between 1996 and 2007, where he was a founding member of its Advanced Geometry Group. Projects at AGU included collaborations with architects including Alvaro Siza, OMA, UNStudio, and Shigeru Ban, and artists Anish Kapoor and Chris Ofili. He has taught students in realising design-build projects at the Architectural Association since 2005.

Shen-Guan Shih is a Professor at Department of Architecture, National Taiwan University of Science and Technology, since 1994. He is interested in interdisciplinary research combining information science, architecture, and more. In recent years, he has participated in developing building-code checking systems for the Taipei city government. He also does research and teaching regarding generative modeling for building design.

Daniel Sonntag is a Research Associate at the Institute of Building Structures and Structural Design (ITKE) at the University of Stuttgart and has worked several years as a structural engineer for Knippers Helbig Advanced Engineering. His main research interests lie in the field of structural optimisation of segmented shells.

Asbjørn Søndergaard is an architectural researcher and technology entrepreneur working in the field of digital fabrication in its relation to architectural design. He is Chief Development Officer and co-founding partner of Odico Formwork Robotics, an advanced technology enterprise focussed on industrial scale development and application of architectural robotics. He is also a Ph.D. research fellow at Aarhus School of Architecture, and his ongoing doctoral research focusses on the coupling of structural optimisation with digital manufacturing. His work centres on the development of new manufacturing interfaces for the realisation of topology optimised architectural structures, explored through the fabrication of full-scale prototypes.

Dave Stasiuk is the Director of Applied Research at Proving Ground, a technology consultancy for architects, engineers, and manufacturers which focusses on the development of advanced computational tools that facilitate data-driven design and project collaboration. His academic research exists within the larger framework of CITA's "Complex Modelling" project, which investigates the digital infrastructures of design models and examines concerns of feedback and scale across the expanded digital design chain. His work concerns adaptive reparameterisation, focusing on the dynamic activation of data structures that allow for model networks to operate holistically as representational engines in the realisation of complex material assemblies.

Kasper Hornbak Steenstrup is a PhD student at the Department of Computer Science and Applied Mathematics, Technical University of Denmark. He received his Cand. Scient. degree (MSc) in computer science from the University of Copenhagen in 2013. His research focus is on geometry processing and numerical optimisation where he has public several paper adding architectural design.

Chengcheng Tang received his PhD in Applied Mathematics and Computational Sciences at King Abdullah University of Science and Technology (KAUST) in 2015, under the supervision of Professor Helmut Pottmann, after obtaining a corresponding master's degree in 2011. Before joining KAUST, he received his bachelor's degree in Materials Physics from Jilin University in 2009. Chengcheng is interested in applied geometry and computational design. He has published in venues like SIGGRAPH, ACM TOG, and AAG. He will join Stanford University as a postdoctoral scholar with Professor Leonidas Guibas in summer 2016.

Eilon Vaadia is the Director of the Edmond and Lily Safra Centre for Brain Science at the Hebrew University of Jerusalem. He was trained as a postdoctoral student at the Department of Biomedical Engineering of Johns Hopkins University. He was among the founders of Interdisciplinary Centre for Neural Computation and headed the ICNC Ph.D. program for 8 years. He was the Chairman of the Department of Physiology, a member of the Hebrew University Senate and a member of the HUJI Executive Committee. He was selected as the Jack H. Skirball Chair in Brain Research in 2005.

Tom Van Mele is Co-director of the Block Research Group (BRG) at ETH Zurich. He created and maintains the BRG computational framework, specifically focussing on the development of robust data structures and solvers for structural design and optimisation. He also manages BRG's web-based teaching and research platforms. His main research interests are geometry-based form-finding and analysis methods, three-dimensional collapse of masonry structures, and flexible formwork systems for concrete shell structures. In 2008, he received his PhD from the Department of Architectural Engineering at the Vrije Universiteit Brussel in Belgium.

Johannes Wallner is Professor of Geometry at Graz University of Technology since 2007. He received his Ph.D. in 1997 from TU Wien under the supervision of Helmut Pottmann. His research interests are in applied geometry, in particular discrete differential geometry and also nonlinear refinement processes. In the last decade he has been interested in the relationship between geometry as a mathematical discipline, on the one hand, and freeform architecture, on the other hand. He has co-authored and edited three books and about 100 articles.

Yves Weinand, architect and civil engineer, obtained his degree in architecture in 1986 at the Institut Saint-Luc, Liège, Belgium. After working as an independent architect in Helsinki, New York, and Brussels, he combined work with studies at the EPF Lausanne, graduating in 1994 with a degree in civil engineering. From then on, he took part in teaching and research in the field of engineering as an assistant to the Chair of Structural Studies at the Faculty of Architecture at the Polytechnical Institute of Rhein-Westfalen, Germany. Since 1996, Yves Weinand has been the proprietor of the Etudes Weinand Bureau, engineering and architectural consultants in Liège. In 2004, he was appointed Associate Professor and director of the Laboratory of Timber Constructions, IBOIS, at EPF Lausanne. He participated in numerous competitions, juries and exhibitions, both within and outside Belgium, and has designed and carried out projects which always combine architecture with civil engineering.

Samuel Wilkinson joined Foster + Partners in 2014 and is an environmental design analyst in the Specialist Modelling Group. He has been involved with initiating and coordinating various academic and industrial research initiatives, focussing on technology development of robotics and additive construction. He has also worked to develop large-scale robotic 3D concrete printing in the construction sector with an industrial research consortium, and on conceptual design research for an autonomous multi-robot additive construction system for a Mars habitat.

Andrew John Wit is the Assistant Professor of Digital Practice within Temple University's Tyler School of Art in Philadelphia, PA. Additionally he is a co-founder of WITO*, "Laboratory for Intelligent Environments", where he creates projects that fringe design, technology and robotics. Prior to his current appointment, Professor Wit taught courses and led workshops in architecture, urbanism, and robotics in both in the U.S. and in Japan. Andrew earned his Bachelor of Science in Architecture from the University of Texas at San Antonio, and his Masters in Architecture from M.I.T., where he also researched in the Media Lab's "Smart Cities Lab".

Mateusz Zwierzycki is a Research Assistant at the Centre for Information Technology and Architecture, Copenhagen, Denmark. He is an architect, designer, Grasshopper user, and co-author of the projektowanieparametryczne.pl (the first Polish website about parametric tools in architectural design), author of the Starling, Squid, Anemone and Mesh Tools plugins for Grasshopper and many more disassociated scripts scattered all over the Grasshopper community. He is also the founder of the Milkbox group, long-time workshop tutor, teacher, and parametric design populariser.

Advances in Architectural Geometry 2016

<span style="color:magenta">Editors</span>

Sigrid Adriaenssens – Princeton University, United States
Fabio Gramazio – ETH Zurich, Switzerland
Matthias Kohler – ETH Zurich, Switzerland
Achim Menges – University of Stuttgart, Germany
Mark Pauly – EPF Lausanne, Switzerland

<span style="color:magenta">Book design</span>

Frank Hyde-Antwi – www.twiddlethumbs.net

The Advances in Architectural Geometry (AAG) symposia serve as a unique forum where developments in the design, analysis and fabrication of building geometry are presented. With participation of both academics and professionals, each symposium aims to gather and present practical work and theoretical research that responds to contemporary design challenges and expands the opportunities for architectural form.

The fifth edition of the AAG symposia was hosted by the National Centre for Competence in Research Digital Fabrication at ETH Zurich, Switzerland, in September 2016.

This book contains the proceedings from the AAG2016 conference and offers detailed insight into current and novel geometrical developments in architecture. The 22 diverse, peer-reviewed papers present cutting-edge innovations in the fields of mathematics, computer graphics, software design, structural engineering, and the design and construction of architecture.

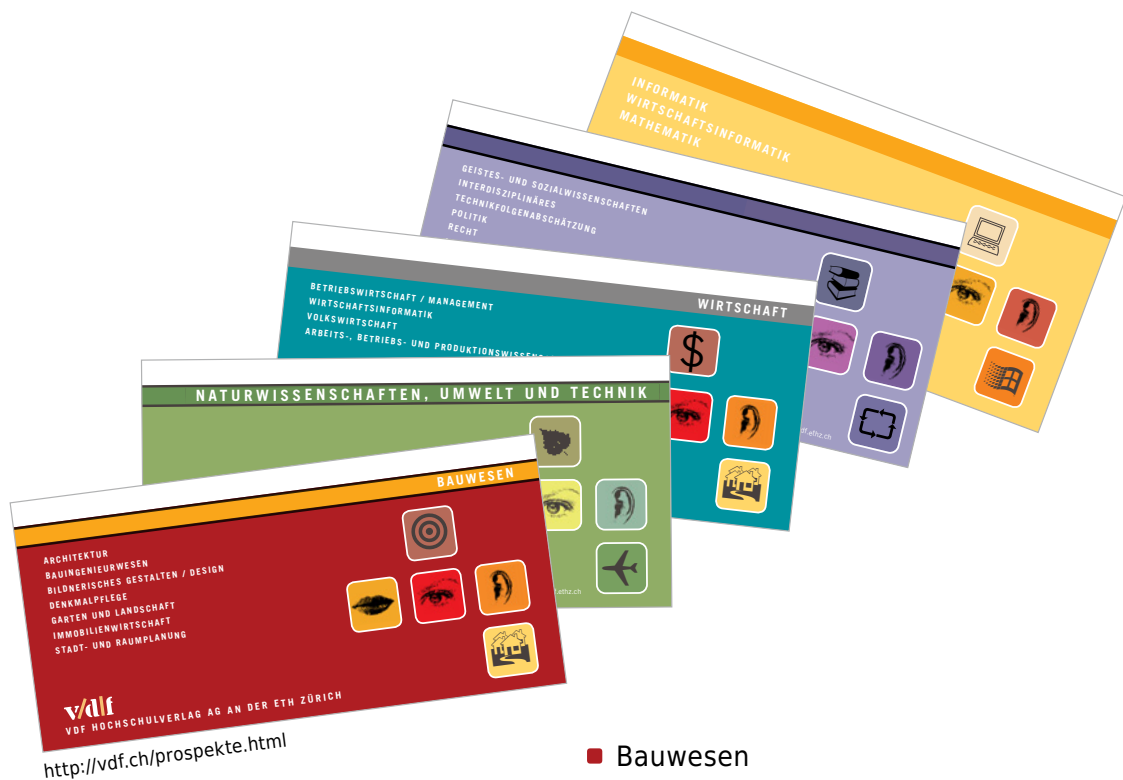# Weitere aktuelle vdf-Publikationen finden Sie in unseren **Fachbereichsprospekten:**

INFORMATIK
WIRTSCHAFTSINFORMATIK
MATHEMATIK

GEISTES- UND SOZIALWISSENSCHAFTEN
INTERDISZIPLINÄRES
TECHNIKFOLGENABSCHÄTZUNG
POLITIK
RECHT

BETRIEBSWIRTSCHAFT / MANAGEMENT
WIRTSCHAFTSINFORMATIK
VOLKSWIRTSCHAFT
ARBEITS-, BETRIEBS- UND PRODUKTIONSWISSENS...

WIRTSCHAFT

NATURWISSENSCHAFTEN, UMWELT UND TECHNIK

BAUWESEN

ARCHITEKTUR
BAUINGENIEURWESEN
BILDNERISCHES GESTALTEN / DESIGN
DENKMALPFLEGE
GARTEN UND LANDSCHAFT
IMMOBILIENWIRTSCHAFT
STADT- UND RAUMPLANUNG

v/d|f
VDF HOCHSCHULVERLAG AG AN DER ETH ZÜRICH

http://vdf.ch/prospekte.html

- Bauwesen
- Naturwissenschaften, Umwelt und Technik
- Wirtschaft
- Geistes- und Sozialwissenschaften, Interdisziplinäres, Militärwissenschaft, Politik, Recht
- Informatik, Wirtschaftsinformatik und Mathematik

v/d|f
**Hochschulverlag AG
an der ETH Zürich**

**Bücher als Websites und mehr...**

v/d|f-online.ch

NEWSLETTER ABONNIEREN